Petrogenesis of Archean granitoids: Insights from inverse and forward modelling

by

Jillian Kendrick

A thesis
presented to the University of Waterloo
in fulfillment of the
thesis requirement for the degree of
Doctor of Philosophy
in
Earth Sciences

Waterloo, Ontario, Canada, 2022

©Jillian Kendrick 2022

Examining Committee Membership

The following served on the Examining Committee for this thesis. The decision of the Examining Committee is by majority vote.

External Examiner	Dr. Thomas Chacko Professor
Supervisor	Dr. Chris Yakymchuk Associate Professor
Internal Members	Dr. Shoufa Lin Professor Dr. Brian Kendall Associate Professor
Internal-external Member	Dr. Vassili Karanassios Professor

Author's Declaration

This thesis consists of material all of which I authored or co-authored: see Statement of Contributions included in the thesis. This is a true copy of the thesis, including any required final revisions, as accepted by my examiners.

I understand that my thesis may be made electronically available to the public.

Statement of Contributions

Thesis Chapters 1 and 7 are authored solely by Jillian Kendrick with input from thesis supervisor Chris Yakymchuk. Chapters 2–6 are manuscripts prepared for submission to academic journals, with writing, data interpretation, and figure preparation done primarily by Jillian Kendrick as first author. All samples were collected by Jillian Kendrick, and sample analysis was also done by Jillian Kendrick when possible. Contributions from co-authors are summarized below for each chapter:

Chapter 2 was submitted to and accepted in *Geoscience Frontiers* in 2019 (Kendrick et al., 2020). The majority of this manuscript, including writing, figure preparation, modelling, and compilation of data from existing literature, was completed by Jillian Kendrick, with contributions from Chris Yakymchuk (supervisor). The manuscript includes revisions based on comments from *Geoscience Frontiers* reviewers Matthew Mayne and Richard White.

Citation: Kendrick, J., and Yakymchuk, C. 2020. Garnet fractionation, progressive melt loss and bulk composition variations in anatectic metabasites: Complications for interpreting the geodynamic significance of TTGs. Geoscience Frontiers 11, 745–763. doi:10.1016/j.gsf.2019.12.001.

Chapter 3 was submitted to and accepted in *Geology* in 2021 (Kendrick et al., 2022). This manuscript, including writing, figure preparation, data collection and interpretation, and modelling was primarily completed by Jillian Kendrick. Samples were collected by Jillian Kendrick, Carson Kinney, Sophie Gagnon, and Chris Yakymchuk (applicable for Chapters 3, 4, and 5). Jillian Kendrick conducted laser-ablation inductively coupled plasma mass spectrometry analysis with assistance from Ivan Edgeworth. Manuel Duguet (co-author, Ontario Geological Survey) was responsible for whole-rock lithogeochemical analysis and thin section preparation done at Ontario Geological Survey labs (applicable for Chapters 3, 4, and 5), and also contributed comments and suggestions on the manuscript. Chris Yakymchuk (supervisor) provided guidance and comments on the text, modelling results, and figures. The manuscript includes revisions based on comments from *Geology* reviewers J.-F. Moyen, Bruna Carvalho, and an anonymous reviewer.

Citation: Kendrick, J., Duguet, M., and Yakymchuk, C. 2022. Diversification of Archean tonalite-trondhjemite-granodiorite suites in a mushy middle crust. Geology 50, 76–80. https://doi.org/10.1130/G49287.1

Chapter 4 was submitted to *Earth and Planetary Science Letters* in 2021. Jillian Kendrick wrote the manuscript, created the figures, and interpreted the data. Sample crushing and zircon separation were done by Overburden Drilling Management and Jillian Kendrick prepared zircon crystals for analysis. Cathodoluminescence imaging of zircon was done by Nina Heinig. The U–Pb and Hf data from zircon were collected by co-authors Christopher Kirkland and Janne Liebmann, who also completed preliminary processing of these data. The other co-authors (Manuel Duguet, Shoufa Lin, Desmond Moser) provided comments on the manuscript, and supervisor Chris Yakymchuk additionally provided guidance on data interpretation. This manuscript is currently under review.

Chapter 5 will be submitted to *Journal of Petrology* in 2022. Jillian Kendrick completed all writing, created the figures, conducted the modelling, and interpreted the data. Sample crushing and garnet separation were done by Carson Kinney and Jillian Kendrick. Laser-ablation inductively coupled plasma mass spectrometry analysis of garnet was done by Jillian Kendrick with the assistance of Ivan Edgeworth. The Lu–Hf analysis (whole rock and garnet) was done by Jillian Kendrick at the Radiogenic Isotope and Geochronology Laboratory at Washington State University under the supervision of co-author Jeffrey Vervoort and with the assistance of Chao Zhang, Chris Fisher, Charles Knaack, and Da Wang. Zircon preparation and analysis were completed as described for Chapter 4. All co-authors, including Manuel Duguet, Desmond Moser, and Chris Yakymchuk provided feedback on the manuscript. Chris Yakymchuk provided advice and on guidance on interpretations.

Chapter 6 will be submitted for publication in 2022. Jillian Kendrick wrote the manuscript, created figures, and completed modelling and calculations. Co-author Jean Bédard provided a spreadsheet that he created for calculations related to parameterization of partition coefficients. Supervisor Chris Yakymchuk gave comments and feedback on the manuscript and guidance on interpretations.

Abstract

Archean granitoids are the earliest representation of continental crust on Earth. The Archean geological record is dominated by rocks of the tonalite–trondhjemite–granodiorite (TTG) suite, which are thought to have formed by partial melting of hydrated mafic crust. Two end-member settings of TTG formation have been proposed: partial melting of subducting oceanic slabs at mantle depth and partial melting of metabasite at a deep crustal level. Each scenario has different implications for Archean tectonic regimes. Although these scenarios are commonly distinguished based on the trace element compositions of TTGs (e.g., Sr/Y, La/Yb), factors that are unrelated to the setting of partial melting can also influence TTG compositions; further research is required to determine the effect of these additional factors. Furthermore, most exposed Archean crust is limited to formerly upper- to middle-crustal levels. Consequently, connections between TTGs at different crustal levels and the deep crustal processes that may affect or generate TTGs generally cannot be studied directly. In addition to TTGs, granitoids of the Archean sanukitoid suite have been considered as important indicators of ancient tectonic processes. The major and trace element characteristics of sanukitoids indicate a metasomatized mantle source and subduction is suggested as the driving force behind the change in mantle composition. However, the nature of the metasomatic agent introduced into the mantle and the processes that trigger mantle melting and sanukitoid generation remain unclear. In this thesis, the formation of Archean granitoids is explored both generally and in a crustal cross section of the Neoarchean Wawa-Abitibi terrane in the southern Superior Province known as the Kapuskasing Uplift.

Investigation of Archean granitoid generation in general is done in this thesis by combining phase equilibrium modelling with trace element partitioning between minerals and melt to calculate theoretical melt compositions under different conditions. Three potential influences on TTG compositions are explored using this approach: variations in source bulk composition, progressive melt loss at the source, and sequestration of garnet cores from the system. The modelling results indicate that although the trace element compositions of TTGs are sensitive to the pressure (i.e., depth) of melting—as is generally expected—other factors complicate this relationship. Compositions associated with high-pressure melting (elevated Sr/Y and La/Yb and low Nb and Ta) can be achieved at a range of pressure–temperature (*P*–*T*) conditions, particularly considering fractionation of trace elements into garnet and a range of possible source compositions. These results indicate that the trace element composition of TTGs may not be diagnostic of a particular geodynamic setting, as the end-member scenarios are generally distinguished by depth of melting.

Suites of TTGs and high-grade metabasites from the Kapuskasing Uplift are investigated using both modelling and geochemical data to better understand the evolution of these rocks and the potential connection between them. The TTGs exposed in a large grey gneiss domain at the mid-crustal level in this region exhibit a range of trace element compositions consistent with variable depths of source melting. However, these samples also show evidence of plagioclase accumulation and fractionation. The results of phase equilibrium and melt trace element modelling demonstrate that variable degrees of separation of early crystallizing plagioclase from coexisting melt can account for the range of TTG compositions. This may indicate that the grey gneiss domain was a long-lived crystal mush complex in which localized mush compactions resulted in the different compositional types of TTGs currently observed. Therefore, linking the trace element characteristics of TTGs to their source may be complicated by the behaviour of plagioclase after emplacement of the magma in the crust.

The Kapuskasing Uplift provides an opportunity to evaluate the isotopic record of TTGs from different crustal levels within a craton. In other cratons, isotopic data from Archean granitoids—typically from upper- to middle-crustal exposures—indicate that repeated reworking of the same crustal material was common. However, in the Kapuskasing Uplift, U–Pb and Hf isotopic data from zircon in TTGs indicates that three generations with different ages (one Neoarchean and two Mesoarchean) are present and each is derived from an isotopically distinct source. The oldest Mesoarchean TTG may represent a rifted fragment from other Mesoarchean subprovinces north of the Wawa subprovince as these rocks are isotopically compatible. The isotopic record is also heterogeneous across the crustal cross section. The youngest and most juvenile TTGs are volumetrically dominant at the upper- to middle-crustal level, and the least radiogenic TTGs (potentially derived from an ancient mafic source) are only found in the lower crust. This result highlights a potential bias in the Archean geological record; the typically inaccessible lower crust may contain volumetrically minor but isotopically distinct TTGs.

Deep-crustal metabasites exposed in the Kapuskasing Uplift show evidence of former partial melting and may represent potential TTG source rocks. This connection is tested by comparing the modelled compositions of anatectic melt, Lu–Hf isotopic data, and geochronological data of the metabasites to data from the natural TTGs at shallower crustal levels in the Kapuskasing Uplift. Based on modelling results, the composition of anatectic melt produced by the metabasites may have been comparable to TTGs. However, considering the different factors that may influence TTG compositions, trace elements alone are insufficient for linking these rocks to their source. The Lu–Hf isotopic data indicate that two isotopically distinct metabasites are present, which together are compatible with the

range of Hf isotopic compositions of zircon in TTGs at shallower crustal levels. The timing of metabasite partial melting, however, is coeval with only the youngest TTG magmatism; this metamorphic event likely resulted from late-stage processes during the stabilization of the southern Superior Province. Therefore, the lower crustal metabasites represent compatible source rocks for TTGs at shallower crustal levels in the Kapuskasing Uplift. Greater volumes of these metabasites were likely present previously and juxtaposition and partial melting of the two metabasic sources may have been a two-stage process.

Sanukitoid genesis is investigated using phase equilibrium modelling coupled with trace element partitioning modelling. Metasomatized mantle compositions are estimated assuming two possible metasomatic agents—TTG magma and partial melt from subducted sediments. Model melt reproduces some geochemical features of sanukitoids, but the large variations in natural sanukitoid compositions suggest that the process of sanukitoid generation was different for each craton. Model results indicate that a high degree of mantle melting with no (or minimal) garnet in the residue produces melt that is most similar to primitive sanukitoid compositions. These conditions require relatively low P and high T mantle melting that is consistent with asthenospheric upwelling, but not indicative of a specific tectonic setting.

The results of this thesis have two main implications for understanding Archean granitoids. First, coupled phase equilibrium and melt trace element modelling is a useful tool for exploring the effect of different processes on granitoid trace elements. However, the trace element characteristics of granitoids are the result of a confluence of many factors and do not indicate an unambiguous connection between granitoids and a particular source. Second, Lu–Hf isotopic data (coupled with geochronological data) from TTGs can provide more valuable insights into their sources than trace element data, particularly if Lu–Hf data from potential source rocks are also available.

Acknowledgements

I am very grateful to my supervisor, Dr. Chris Yakymchuk, for all of his guidance, support, and advice beginning even before I started my PhD program. Whether it was related to science, my career, or life in general, Chris always made time for a chat and I know that I will benefit from his advice for years to come. I would like to thank Dr. Manuel Duguet at the Ontario Geological Survey for his help in the field, thorough but quick editing of my (sometimes lengthy) manuscripts, and for overseeing the processing of my samples at the OGS and making sure I received the data. I would also like to thank my thesis committee members, Dr. Brian Kendall, Dr. Shoufa Lin, Dr. Vassili Karanassios, and Dr. Thomas Chacko. I also acknowledge NSERC, the Ontario Geological Survey, Alamos Gold Inc., and Vanier Canada Graduate Scholarships for financial support.

I am grateful to Dr. Jeffrey Vervoort and the group working in the Radiogenic Isotope and Geochronology Laboratory at Washington State University (Dr. Chao Zhang, Dr. Chris Fisher, Dr. Charles Knaack, and Dr. Da Wang) for their guidance and assistance while I processed and analyzed my samples. I would also like to thank Dr. Chris Kirkland and Dr. Janne Liebmann at Curtin University for analyzing my zircons and processing the data. Thank you to Dr. Nina Heinig at the Waterloo Advanced Technology Laboratory for operating the LEO for CL microscopy of zircon. I would also like to thank Dr. Dave Crabtree at OGS Geolabs and Dr. Wanda Aylward at Memorial University for assistance with electron probe microanalysis.

A big thanks goes to the friends who welcomed me to the department and Waterloo when I first arrived, including Katia Jellicoe, Stacey Parmenter, Ryan Truong, Sara Fellin, and Dr. Jen Parks (thanks Sara and Jen for looking after Petra during my many travels!). I must also thank Grant Hagedorn for the many office visits, great discussions, and all of his help with GeoCafe and ESGA events. Thank you to Dr. Oliver Schneider for advice and companionship during some stressful times.

Although the Yak Pak has changed a lot since I arrived, it has always been a wonderful and supportive group of people. I am very grateful to Carson Kinney for all of his help with fieldwork and processing my (our!) samples, and also for many fun discussions over the last few years. I would like to thank Sophie Gagnon for helping me with fieldwork and for being a wonderful office neighbour. I am very grateful to Ivan Edgeworth for doing his best to keep me sane during the isolation of the pandemic (and even after that… thanks for the soup) and for stepping up to take care of ESGA events and other

departmental affairs. I would also like to thank Sabastien Dyer for some great science-, bread-, and life-in-general-related discussions.

I thank my family for supporting me throughout this journey. I am very grateful to Dr. Katrina Hitchman and her family for their support from nearby, and to my family and friends in Nova Scotia for rooting for me from afar.

Table of Contents

Examining Committee Membership ii
Author's Declaration iii
Statement of Contributions iv
Abstract vi
Acknowledgements ix
List of Figures xvii
List of Tables xx
Chapter 1: Introduction 1
1.1 Outstanding questions about Archean Earth 1
1.2 The phase equilibrium modelling approach to investigating crustal evolution 2
1.3 Superior Province and regional geology 3
1.3.1 Overview of the Superior Province 3
1.3.2 The Wawa-Abitibi terrane 3
1.3.3 The Kapuskasing uplift 4
1.4 Thesis format and objectives 5
Chapter 2: Garnet fractionation, progressive melt loss and bulk composition variations in anatectic metabasites: Complications for interpreting the geodynamic significance of TTGs 11
Summary 11
2.1 Introduction 12
2.2 Methodology 14
2.2.1 Selection of source compositions 14
2.2.2 Phase equilibrium modelling 16
2.2.2.1 Open system behaviour 17
2.2.2.1.1 Melt loss 17
2.2.2.1.2 Garnet fractionation 17
2.3 Results 18
2.3.1 *P–T* pseudosections 18
2.3.2 *P–T* gradients 19
2.3.3 Major element compositions of modelled melts 21
2.3.4 Trace element compositions of modelled melts 23

2.4 Discussion 25
2.4.1 Limitations of the models 25
2.4.2 Comparison of modelled melts to natural TTGs 29
2.4.3 Implications for interpreting TTG trace element systematics 31
2.4.3.1 The role of bulk composition 31
2.4.3.2 The role of open system processes 32
2.4.4 Implications for linking TTG trace elements to depth of melting 33
2.5 Conclusions 36
2.6 References 37
Chapter 3: Diversification of Archean tonalite-trondhjemite-granodiorite suites in a mushy middle crust 60
Summary 60
3.1 Introduction 60
3.2 Methods 62
3.3 Results 62
3.4 Discussion 64
3.5 References 65
Chapter 4: Anatomy of a craton: isotopic heterogeneity across an Archean crustal cross section 74
Summary 74
4.1 Introduction 75
4.2 Regional Geology 76
4.3 Samples and Methodology 78
4.3.1 Samples 78
4.3.2 Whole-rock geochemical data 78
4.3.3 Zircon U–Pb and Lu–Hf analysis 79
4.4 Results 79
4.4.1 Whole-rock geochemical data 79
4.4.2 Zircon U–Pb geochronology 79
4.4.3 Hafnium isotopes 81
4.5 Discussion 83
4.5.1 Construction of the continental crust in the Kapuskasing Uplift 83
4.5.2 Insights into crustal evolution from a crustal cross section 84

4.6 Conclusions 86
4.7 References 87
Chapter 5: Testing the TTG–metabasite connection: an integrated geochemical, isotopic, and petrogenetic modelling approach 98
Summary 98
5.1 Introduction 98
5.2 Regional geology 100
5.3 Methods 101
5.3.1 Whole-rock geochemical analysis 101
5.3.2 *In situ* mineral chemical analysis 102
5.3.3 Phase equilibrium modelling and melt trace element modelling 102
5.3.4 Garnet Lu–Hf analysis 103
5.3.5 Zircon U–Pb and Hf analysis 104
5.4 Results 105
5.4.1 Field observations and petrography 105
5.4.1.1 17JK20 (metabasite) and 19JK15 (leucosome) 106
5.4.1.2 17JK12 (metabasite) 107
5.4.1.3 17JK09 (metabasite) 108
5.4.1.4 17JK08 (metatonalite) 109
5.4.1.5 19JK13 (leucosome) 110
5.4.1.6 19JK16 (leucosome) 110
5.4.2 Whole-rock composition 110
5.4.3 Phase equilibrium modelling 111
5.4.4 Melt composition modelling 112
5.4.5 Garnet Lu–Hf geochronology 114
5.4.6 Zircon U–Pb and Hf results 114
5.5 Discussion 115
5.5.1 Anatectic metabasites and TTGs – the trace element modelling perspective 115
5.5.2 Anatectic metabasites and TTGs – insights from Lu–Hf isotope systematics 118
5.5.3 Anatectic metabasites and TTGs – the geochronological connection 120
5.5.4 Interpretation of results in a regional tectonic framework 123
5.5.5 The TTG–metabasite connection 124

5.6 Conclusions 126
5.7 References 126
Chapter 6: Petrogenesis of Archean sanukitoids: insights from thermodynamic modelling 153
Summary 153
6.1 Introduction 154
6.2 Methodology 155
6.2.1 Data compilation and selection of compositions for modelling 155
6.2.2 Phase equilibrium modelling 157
6.2.3 Melt trace element modelling 157
6.3 Results 158
6.3.1 Characteristics of the sanukitoid dataset 158
6.3.2 Predicted phase equilibria of model metasomatized mantle 159
6.3.3 Composition of modelled melt from model metasomatized mantle 160
6.4 Discussion 162
6.4.1 Modelling limitations 162
6.4.1.1 Limitations of the metasomatized mantle compositions 162
6.4.1.2 The potential influence of accessory mineral behaviour in the source 164
6.4.1.3 Limitations of partition coefficients 164
6.4.2 Implications of models for interpreting sanukitoid compositions 165
6.4.3 Implications of the Eu anomaly in sanukitoids 167
6.4.4 Implications for the geodynamic setting of sanukitoid genesis 169
6.5 Summary and Conclusions 170
6.6 References 171
Chapter 7: Conclusions 190
7.1 Summary of research 190
7.2 Future work and recommendations 193
References 195
Appendices 202
Appendix S1 (Chapter 2 supplementary material) 202
Figure S1.1 Temperature–phase proportion diagrams 202
Figure S1.2 Model melt on granitoid classification diagrams 203
Table S1.1 Archean basalt data compilation 204

Table S1.2 Model melt trace elements 205
Appendix S2 (Chapter 3 supplementary material) **206**
Appendix S2.1 Detailed Methodology 206
Figure S2.1 Phase diagram of parental TTG 211
Figure S2.2 Measured rare earth elements of plagioclase 212
Table S2.1 Major and trace elements of TTGs (whole-rock) 213
Table S2.2 Plagioclase major element compositions 219
Table S2.3 Plagioclase trace element compositions 223
Table S2.4 Parental TTG compositions 225
Table S2.5 Partition coefficients 226
Appendix S3 (Chapter 4 supplementary material) **227**
Appendix S3.1 Methodology and zircon interpretations 227
Appendix S3.1.1 Methodology 227
Appendix S3.1.2 Zircon interpretations 229
Figure S3.1 Outcrop photos 237
Figure S3.2 CL images of zircon 238
Figure S3.3 Concordia and $^{207}Pb/^{206}Pb$ age versus $^{176}Hf/^{177}Hf(t)$ 239
Figure S3.4 Mean $^{207}Pb/^{206}Pb$ age versus mean $\varepsilon Hf(t)$ 240
Table S3.1 Major and trace elements of TTGs (whole-rock) 241
Table S3.2 U–Pb data (laser ablation split stream ICP-MS) 242
Table S3.3 Lu–Hf data (laser ablation split stream ICP-MS) 253
Appendix S4 (Chapter 5 supplementary material) **265**
Figure S4.1 Model melt major elements 265
Figure S4.2 Lu–Hf errorchron (17JK03) 266
Table S4.1 Metabasite and leucosome compositions 267
Table S4.1.1 QA/QC for whole-rock geochemical data 268
Table S4.2 Mineral composition data 272
Table S4.3 Trace element data from secondary reference materials 281
Table S4.3.1 Masses and dwell times 312
Table S4.4 Lu–Hf data (isotope dilution) 314
Table S4.5 U–Pb and Lu–Hf data (laser ablation split stream ICP-MS) 316
Table S4.6 Model melt major and trace elements 324

Table S4.7 Geochronological data compilation 325
Table S4.7.1 References 329
Appendix S5 (Chapter 6 supplementary material) **331**
Figure S5.1 Results of Archean upper crust modelling 331
Figure S5.2 Phase diagrams with different H_2O 332
Table S5.1 Sanukitoid data compilation 333
Appendix S6 ..... **340**
Table S6.1 Re–Os results 340
Table S6.2 Sm–Nd results 341

List of Figures

Figure 1.1 Schematic diagrams showing magma genesis in plate-tectonic and non-plate tectonic scenarios……7

Figure 1.2 Flow chart showing the process of coupling phase equilibrium modelling with melt trace element modelling. ……8

Figure 1.3 Simplified geological map of the Superior Province showing the location of the Wawa-Abitibi Terrane and the Kapuskasing uplift ……...……...9

Figure 1.4 Simplified geological map of the Kapuskasing uplift……...……10

Figure 2.1 Two-dimensional kernel density estimation of SiO_2 vs. MgO and Al_2O_3 vs. CaO from whole rock geochemical data in the Archean basalt compilation provided in Table S1.1…….47

Figure 2.2 *P–T* pseudosections for each of the modelled basalt compositions, the diagram for EAT has been modified from Palin et al. (2016b). ……..……..48

Figure 2.3 *P–T* diagrams with contours of weight fractions of garnet, plagioclase, and rutile for the three compositions in Fig. 2.2..……..…..……...49

Figure 2.4 Temperature–proportion diagrams illustrating the changes in phase weight proportions along the 500 °C/GPa, 750 °C/GPa, and 1000 °C/GPa thermal gradients in the closed system, melt loss, and garnet fractionation scenarios for the DAT (depleted Archean tholeiite) source composition (results for the other source compositions are provided in Fig. S1.1)……..……..50

Figure 2.5 Granitoid classification diagrams based on normative feldspar content after Barker (1979). Modelled melts from the closed system scenario are plotted for each source composition...…….51

Figure 2.6 Granitoid classification diagrams based on normative feldspar content after Barker (1979). Modelled melt compositions are plotted from the closed system, melt loss, and garnet fractionation scenarios for the DAT (depleted Archean tholeiite) bulk composition only……..…….52

Figure 2.7 *P–T* diagrams with contours of Sr/Y, La_N/Yb_N, and concentration of Nb (ppm) in the melt…53

Figure 2.8 Plots of Sr/Y vs. Y of modelled melts from each of the three compositions for each of the three scenarios……..54

Figure 2.9 Plots of La_N/Yb_N vs. Yb_N of modelled melts from each of the three compositions for each of the three scenarios……..……..55

Figure 2.10 Plots of Nb vs. Ta of modelled melts from each of the three compositions for each of the three scenarios……...……...56
Figure 2.11 Trace element compositions of modelled melts compared to (a and b) the high-pressure, medium-pressure, and low-pressure TTG groups and (b–d) natural TTG data……...57
Figure 3.1 A–C) Photographs of TTG outcrops in the Wawa Gneiss Domain, D–F) Photomicrographs of TTG samples……70
Figure 3.2 A) Chondrite-normalized trace element compositions of the Wawa Gneiss Domain TTGs collected in this study. B) Normative albite (Ab), anorthite (An), and orthoclase (Or) proportions of the TTG samples……..……..71
Figure 3.3 Phase equilibrium modeling of the crystallization sequence of the estimated parental TTG composition at 0.6 GPa. The full phase assemblage diagram is shown in Fig. S2.1……...72
Figure 3.4 A) Trace element trends of model TTG compositions, calculated by combining different proportions of crystals and melt, compared to interquartile ranges of natural TTG groups. B) Sr/Y vs. La/Yb of natural TTGs compared to model results.…..……..73
Figure 4.1 A) Simplified geological map of the Superior Province showing the location of relevant terranes B) Simplified geological map of the Kapuskasing Uplift……...……...93
Figure 4.2 U–Pb geochronological results from the nine TTG samples examined in this study.…...……94
Figure 4.3 $^{207}Pb/^{206}Pb$ age versus εHf(t) for zircon analyzed in this study and from Smith et al. (1987), Davis et al. (2005), and Mole et al. (2021)……..…..……...95
Figure 4.4 $^{207}Pb/^{206}Pb$ age versus εHf(t) for zircon from the Kapuskasing Uplift, including data from this study, Smith et al. (1987), and Mole et al. (2021)……...96
Figure 4.5 Schematic illustration of the distribution of felsic intrusive rocks from the three isotopic sources (Fig. 4.4) in the Kapuskasing uplift……97
Figure 5.1 Simplified geological maps of the study area. a) Location of the Superior Province in North America. b) Geological map of the Kapuskasing Uplift. c) Detailed geological map of the Kapuskasing Structural Zone……..…….137
Figure 5.2 Photographs of outcrops in the Kapuskasing Structural Zone..…….……..138
Figure 5.3 Photomicrographs of samples from the Kapuskasing Structural Zone. ……...……..139
Figure 5.4 Whole-rock geochemical compositions of samples from the Kapuskasing Structural Zone..140
Figure 5.5 Whole-rock geochemical compositions of leucosome samples from the Kapuskasing Structural Zone in comparison to natural TTG data from the Kapuskasing Uplift…..……...……..141

Figure 5.6 Pressure–temperature (*P–T*) phase diagrams for samples 17JK20 (a), 17JK12 (b), 17JK09 (c), 17JK08 (d) calculated by phase equilibrium modelling. ……..……142
Figure 5.7 Results of melt trace element modelling for metabasite samples 17JK20 and 17JK12…..…143
Figure 5.8 Trace element maps of Lu in garnet crystals from samples (a) 17JK20, (b) 17JK12, (c) 17JK09, and (d) 17JK08……144
Figure 5.9 Lu–Hf isochrons for samples (a) 17JK20, (b) 17JK12, (c) 17JK09, and (d) 17JK08…….....145
Figure 5.10 Tera-Wasserburg diagrams showing zircon U–Pb data for samples (a) 19JK15 and (b) 19JK16, with insets showing measured $^{176}Hf/^{177}Hf$ ratios…….146
Figure 5.11 (a) Results of melt trace element modelling compared to natural TTG samples from the Wawa Gneiss Domain and Michipicoten Greenstone Belt. (b) Comparison of metabasite whole-rock Lu–Hf data and Hf data from zircon in TTGs from the Wawa Gneiss Domain and Michipicoten Greenstone Belt. (c) Compilation of granitoid crystallization ages from previous work for samples from the Wawa Gneiss Domain and Michipicoten Greenstone Belt (Table S4.7) compared to results of garnet Lu–Hf and zircon U–Pb geochronology from this study..……...……147
Figure 5.12 Schematic diagram illustrating the formation of two generations of TTGs from two lower crustal metabasic sources……...148
Figure 6.1 Major element trends (wt. %) of sanukitoid compilation data (Table S5.1)……...……178
Figure 6.2 Trace element trends (µg/g, MgO in wt.%) of sanukitoid compilation data (Table S5.1)…..179
Figure 6.3 Phase diagrams of the calculated metasomatized mantle compositions, DMT (TTG-metasomatized depleted mantle) and DMS (metasediment-melt-metasomatized depleted mantle)…….180
Figure 6.4 Modal proportions (wt.%) of residual minerals predicted for model melt of DMT (TTG-metasomatized depleted mantle) and DMS (metasediment-melt-metasomatized depleted mantle)…….181
Figure 6.5 Major element trends (wt. %) of model melt of DMT (TTG-metasomatized depleted mantle) and DMS (metasediment-melt-metasomatized depleted mantle)……..182
Figure 6.6 Trace element trends (µg/g) of DMT model melt (TTG-metasomatized depleted mantle)…183
Figure 6.7 Trace element trends (µg/g) of DMS model melt (metasediment-melt-metasomatized depleted mantle)……..…….184
Figure 6.8 Major element trends (wt.%) of model melt compared to sanukitoid compilation data ……185
Figure 6.9 Trace element trends (µg/g, MgO in wt.%) of model melt compared to sanukitoid compilation data…….……186

List of Tables

Table 2.1 Archean basalt compositions selected for modelling (EAT = enriched Archean tholeiite, DAT = depleted Archean tholeiite, MAB = MgO-rich Archean basalt)……..58
Table 2.2 Bulk compositions used as input for THERMOCALC (EAT = enriched Archean tholeiite, DAT = depleted Archean tholeiite, MAB = MgO-rich Archean basalt)……..59
Table 5.1 Bulk compositions used for phase equilibrium modelling……149
Table 5.2 Lu and Hf data obtained from isotope dilution……...……..150
Table 5.3 U–Pb and Hf data from zircon……...……...151

Chapter 1

Introduction

1.1 Outstanding questions about Archean Earth

The origin and evolution of continental crust on early Earth is currently one of the most controversial issues in Earth Sciences (e.g., Bédard, 2018; Condie, 2018; Wyman, 2018; Brown et al., 2020a). Tectonic processes linked to global plate tectonics are thought to have generated continental crust during the Phanerozoic eon (e.g., Brown et al., 2020b; Merdith et al., 2021), however some researchers argue that the evolution of early Earth cannot be interpreted through the lens of uniformitarianism (Bédard, 2006; 2018). The oldest continental crust on Earth is preserved in Archean (4.0 Ga to 2.5 Ga) cratons, which are dominated by large volumes of granitoid crust and supracrustal greenstone belts; these rocks exhibit features that are distinct from younger crust (Moyen and Martin, 2012; Thurston, 2015). This distinction has spurred debate about the geodynamic setting in which early crust was generated—were processes similar to those of modern plate tectonics in operation during the Archean eon or did a unique tectonic regime exist at this time (Fig. 1.1)?

The most common lithological feature of Archean cratons are granitoids of the tonalite-trondhjemite-granodiorite (TTG) suite (Moyen and Martin, 2012). These rocks formed throughout the entire Archean eon and have been investigated extensively for geochemical evidence that links TTGs to a particular tectonic setting (e.g., Jahn et al., 1981; Drummond and Defant, 1990; Moyen, 2011; Nagel et al., 2012; Johnson et al., 2019). Based on experiments and modelling, TTGs may have formed by partial melting of a hydrated basaltic source (e.g., Rapp et al., 1991; Nair and Chacko, 2008; Qian and Hermann, 2013; Palin et al., 2016; Johnson et al., 2017), which could have been possible in two end-member tectonic scenarios: melting of a subducting slab (e.g., Drummond and Defant, 1990) or melting within thickened oceanic crust similar to a modern oceanic plateau (e.g., Bédard, 2006) (Fig. 1.1). In general, these scenarios are distinguished by depth of melting, and therefore TTG compositions are examined for geochemical indicators of "high-pressure" or "low-pressure" source melting (Moyen, 2011). These end-member settings of TTG generation have been linked to the broader tectonic regime of the Archean eon, as some workers consider subduction to be a hallmark of plate tectonics (e.g., van Hunen and Moyen, 2012). Alternatively, TTGs could have formed in a non-plate tectonic regime by mantle plume-driven crustal melting or by melting of "subcreted" (rather than subducted) basaltic crust (Bédard, 2006; 2018).

In addition, the extent to which factors other than source characteristics affect TTG compositions is currently a subject of debate, as fractional crystallization and crystal accumulation have been shown to obscure source-related geochemical signatures (e.g., Laurent et al., 2020; Kendrick et al., 2022 [Chapter 3]; Rollinson, 2021;). Determining the significance of TTG (and other Archean granitoid) geochemical compositions is essential to reconstructing the geodynamic processes that shaped continental evolution on early Earth.

1.2 The phase equilibrium modelling approach to investigating crustal evolution

Over the past decade, phase equilibrium modelling has emerged as a tool for testing hypotheses related to Archean crustal evolution. This has become possible with the formulation of activity–composition models relevant to partially molten systems (e.g., Holland et al., 2018), particularly models for tonalitic melt generated in metabasic systems (Green et al., 2016). With this technique, a potential granitoid source can be modelled to determine the pressure–temperature conditions of granitoid generation or investigate the effects of other variables on melt composition (e.g., Palin et al., 2016). In addition, the results of phase equilibrium modelling may be coupled with mineral–melt partition coefficients (Fig. 1.2) to calculate the trace element compositions of model melt, resulting in a powerful tool for investigating granitoid petrogenesis (e.g., Nagel et al., 2012; Hoffmann et al., 2014; Semprich et al., 2015; Johnson et al., 2017; Gardiner et al., 2018; Huang et al., 2020; Pourteau et al., 2020; Hernández-Montenegro et al., 2021). Recent work has focused on the generation of TTG magma from metabasic sources and has shown that melt with geochemical signatures typically associated with high-pressure melting can be formed at relatively low or moderate pressure (e.g., Johnson et al., 2017; Pourteau et al., 2020). Integration of isotope fractionation with phase equilibrium modelling represents another avenue for fruitful research on the formation of Archean granitoids (e.g., Gardiner et al., 2018; Antonelli et al., 2021). Overall, the development of increasingly more sophisticated thermodynamic models has provided a new tool for investigating Archean crustal evolution that builds upon existing work based on experimental petrology (e.g., Rapp et al., 1991; Qian and Hermann, 2013). However, as a necessary simplification of nature, these models require assumptions such as source to sink equilibrium; given the complexity inherent to Archean granitoid petrogenesis (Moyen, 2019), this assumption may not always be appropriate.

1.3 Superior Province and regional geology

1.3.1 Overview of the Superior Province

The Superior Province is the largest Archean craton exposed on Earth and is primarily located within the Canadian Shield in northern Quebec, Ontario, and Manitoba (Fig. 1.3; Percival et al., 2012). Rocks with ages spanning nearly the entire Archean eon have been identified in the Superior Province (Percival et al., 2012), and isotopic evidence supporting the former presence of Hadean crustal material has locally been identified (O'Neil et al., 2012; O'Neil and Carlson, 2017). In general, the Superior Province is composed of northeast-southwest-trending domains that are distinguished based on distinct lithological components (Percival et al., 2012). Most domains are dominated by granitoids (mainly TTGs) and greenstone belts, although domains composed mainly of sedimentary rocks are also present (Percival et al., 2012). The rocks exposed across the Superior Province mainly represent former upper to middle crustal levels, with less common high-grade metamorphic rocks representing deep crustal exposures (Percival et al., 2012).

The formation of the Superior Province has conventionally been viewed as the result of plate tectonic processes, with individual, far-travelled crustal components assembled by horizontal accretion (e.g., Cawood et al., 2006; Percival et al., 2012; Wyman, 2013). Assembly of the Superior Province is thought to have taken place during a series of collisional orogenic events from ca. 2720 Ma to ca. 2680 Ma (Percival et al, 2012). This plate tectonics-based interpretation is supported by the recognition of features associated with modern-day subduction zones such as granitoids with compositions similar to modern arc magmas (e.g., Polat and Kerrich, 2001), belts of sedimentary rocks resembling flysch deposits (Percival et al., 2012), and seismic reflections resembling suture zones (e.g., Calvert et al., 1995). An alternative view of the construction of the Superior Province advocates for growth of continental crust above a long-lived mantle plume and subsequent disaggregation and reassembly of this continent caused by changes in mantle flow (Bédard et al., 2013; Bédard and Harris, 2014).

1.3.2 The Wawa-Abitibi terrane

The Wawa-Abitibi terrane is located in the southern central Superior Province (Fig. 1.3) and represents the largest tract of juvenile crust in the Superior Province (Percival et al., 2012). Rocks of the Wawa-Abitibi terrane were primarily formed between ca. 2790 Ma and ca. 2680 Ma largely in an inferred oceanic environment (Percival et al., 2012). Volcanic rocks are abundant and show a large range of compositions, including komatiites, tholeiitic basalts, calc-alkaline basalts, andesites, dacites, and rhyolites (Polat, 2009; Wyman and Kerrich, 2010). Formation of these rocks has been attributed to a

complex history of interaction between oceanic plateaux, oceanic arcs, and mantle plume activity (Polat, 2009; Wyman and Kerrich, 2010). Alternatively, the basaltic crust of the Wawa-Abitibi terrane has been suggested to have formed primarily during rifting of older continental crust (e.g., Bédard and Harris, 2014; Mole et al., 2021). Granitoid rocks are also common in the Wawa-Abitibi terrane and are mainly of TTG affinity; these rocks are proposed to have formed by reworking of oceanic plateau crust and partial melting of a subducted slab (e.g., Benn and Moyen, 2008; Mole et al., 2021). Although the Wawa-Abitibi terrane is mainly composed of juvenile Neoarchean crust, evidence for localized Mesoarchean basement with an age of ca. 2900 Ma has been identified in the central Wawa-Abitibi terrane (Turek et al., 1992; Moser et al., 1996; Percival et al., 2012). The central Wawa-Abitibi terrane is also cross-cut by the transverse Kapuskasing Uplift structure, which interrupts local greenstone belts and granitoid units (Percival et al., 2012).

1.3.3 The Kapuskasing Uplift

The Kapuskasing Uplift is a fault-bound structure in the southern Superior Province interpreted as an intracratonic uplift exposed by southeastward-directed thrusting mainly during the Proterozoic (Percival and West, 1994). At the southern extent of the Kapuskasing Uplift (Fig. 1.4)—within the Wawa-Abitibi terrane—a near-complete crustal cross-section is exposed (Percival, 1990; Percival and West, 1994). The Kapuskasing Uplift comprises three main domains, each representing different crustal levels: the Michipicoten Greenstone Belt (upper crust), the Wawa Gneiss Domain (middle crust), and the Kapuskasing Structural Zone (lower crust).

The Michipicoten Greenstone Belt is composed of three main volcanic cycles dated at ca. 2900 Ma, ca. 2750, and ca. 2700 Ma (Turek et al., 1992; Sage, 1994). These rocks range from basaltic to rhyolitic in composition, with komatiites only present in the oldest (ca. 2900 Ma) cycle (Turek et al., 1992). Granitoid plutons of TTG composition that are synvolcanic with respect to each volcanic cycle have been identified in the Michipicoten Greenstone Belt, along with post-2700 Ma granitoid intrusions of mainly monzonite, granodiorite, and syenite (Turek et al., 1984; Turek et al., 1992; Sage et al., 1996). The greenstone belt was mainly metamorphosed at greenschist-facies conditions with amphibolite-facies rocks localized at the margins; amphibolite-facies metamorphism was likely caused by emplacement of granitoid plutons (Ayres, 1978; Sage, 1994). The intrusive contact at the eastern margin of the Michipicoten Greenstone Belt represents the transition to the Wawa Gneiss Domain.

The Wawa Gneiss Domain is mainly composed of granitoid plutons and gneisses with enclaves of supracrustal rocks up to a kilometer in size (Moser et al., 1996). Granitoid rocks in this area have been

described broadly as tonalitic, trondhjemitic, and granitic and have been metamorphosed at amphibolite-facies conditions (Moser et al., 1996) with estimated crystallization pressures of ~0.5–0.6 GPa (Percival, 1990). Crystallization ages of the granitoids are ca. 2920 Ma, ca. 2675 Ma, ca. 2660 Ma, and ca. 2645 Ma, with the latest two pulses of magmatism coinciding with late-stage extension in the Wawa Gneiss Domain (Moser et al., 1996). To the east, the Wawa Gneiss Domain shows a complex and gradational contact with the higher-grade metamorphic rocks of the Kapuskasing Structural Zone (Percival, 1983).

The Kapuskasing Structural Zone is an upper-amphibolite- to granulite-facies domain composed mainly of intermediate to mafic gneisses (Percival, 1983; Percival and West, 1994). Peak metamorphic conditions have been estimated to be 750–850°C and 10–11 kbar and metabasites show evidence of partial melting (Mäder et al., 1994; Hartel and Pattison, 1996). The geochronological record of the Kapuskasing Structural Zone is complex, with early work on U–Pb geochronology of zircon in mafic gneisses yielding ages of ca. 2660 Ma and ca. 2645 Ma primarily (Percival and Krogh, 1983; Krogh, 1993; Krogh and Moser, 1994) and more recent work identifying a near-continuous record of metamorphic zircon growth from ca. 2660 Ma to ca. 2580 Ma (Moser et al., 2008; Bowman et al., 2011). Earlier zircon growth has also been identified, with several crystals from mafic and tonalitic gneisses dated between ca. 3200 Ma and ca. 2700 Ma (Benn and Kamber, 2009). The abundance of zircon yielding ages of ca. 2660 Ma is interpreted to indicate that high-grade metamorphism was underway by this time (Percival and West, 1994; Krogh and Moser, 1994; Moser et al., 2008; Bowman et al., 2011), although metamorphic events prior to ca. 2700 Ma may have been possible (Benn and Kamber, 2009). The protracted record of zircon growth may be the result of sustained high temperatures (Moser et al., 2008), possibly driven by periodic lower crustal delamination events (Moser et al., 1996). Alternatively, protracted zircon growth may record slow cooling of the Kapuskasing Uplift, which is supported by Rb–Sr and Ar–Ar data (Hanes et al., 1994; Percival and Peterman, 1994; Percival and West, 1994). The Ivanhoe Lake Fault zone marks the eastern extent of the Kapuskasing Uplift, where high-grade metamorphic rocks of the Kapuskasing Structural Zone are juxtaposed with the Swayze region of the Abitibi Greenstone Belt (Percival and West, 1994).

1.4 Thesis format and objectives

This thesis is composed of seven chapters in total, with five of these (Chapters 2–6) prepared as standalone articles for publication in scientific journals, preceded by an introduction chapter (Chapter 1) and followed by a conclusions chapter (Chapter 7). Two chapters are studies based on phase equilibrium modelling of petrological processes in a general sense (Chapters 2 and 6) and the remaining three chapters

are directly related to samples and data collected from the Kapuskasing Uplift (Chapters 3, 4, and 5). Each chapter has an associated reference list and appendix with supplementary data and other material; an additional appendix is available for data collected as part of this thesis project but not used in any of the chapters (Appendix S6).

The overall objective of this thesis is to investigate the processes that influenced the evolution of Archean granitoids from source to sink. As the geochemical compositions of Archean granitoids—particularly TTG—are commonly viewed as indicators of early Earth tectonic processes, understanding all sources of geochemical variation is crucial. The research in this thesis employs both inverse and forward modelling techniques to test different hypotheses about granitoid evolution both in general and in the Kapuskasing Uplift. In the inverse modelling approach, data are collected from samples and used to reconstruct the petrogenesis of a rock or suite of rocks; this may include major and trace element concentrations, isotope compositions, and petrographic observations. Forward modelling requires an assumption about an earlier stage in the geological evolution of a rock. For granitoids, this assumption may be the composition of the source or of a parental magma, and a modelling technique such as phase equilibrium modelling can be used to predict features of a granitoid produced under a particular set of conditions. The inverse and forward modelling approaches have different advantages and disadvantages, which will be explored throughout this thesis. Overall, this work highlights the utility of forward modelling for predicting the result of a particular geological process (Chapter 2), but also the pitfalls of this technique when the complexity of a natural system cannot be adequately captured by the model (Chapters 6). Although inverse modelling alone provides important insights into the geological evolution of a particular region (Chapter 4), using inverse and forward modelling techniques in tandem is a powerful technique for unravelling complex geological histories (Chapters 3 and 5).

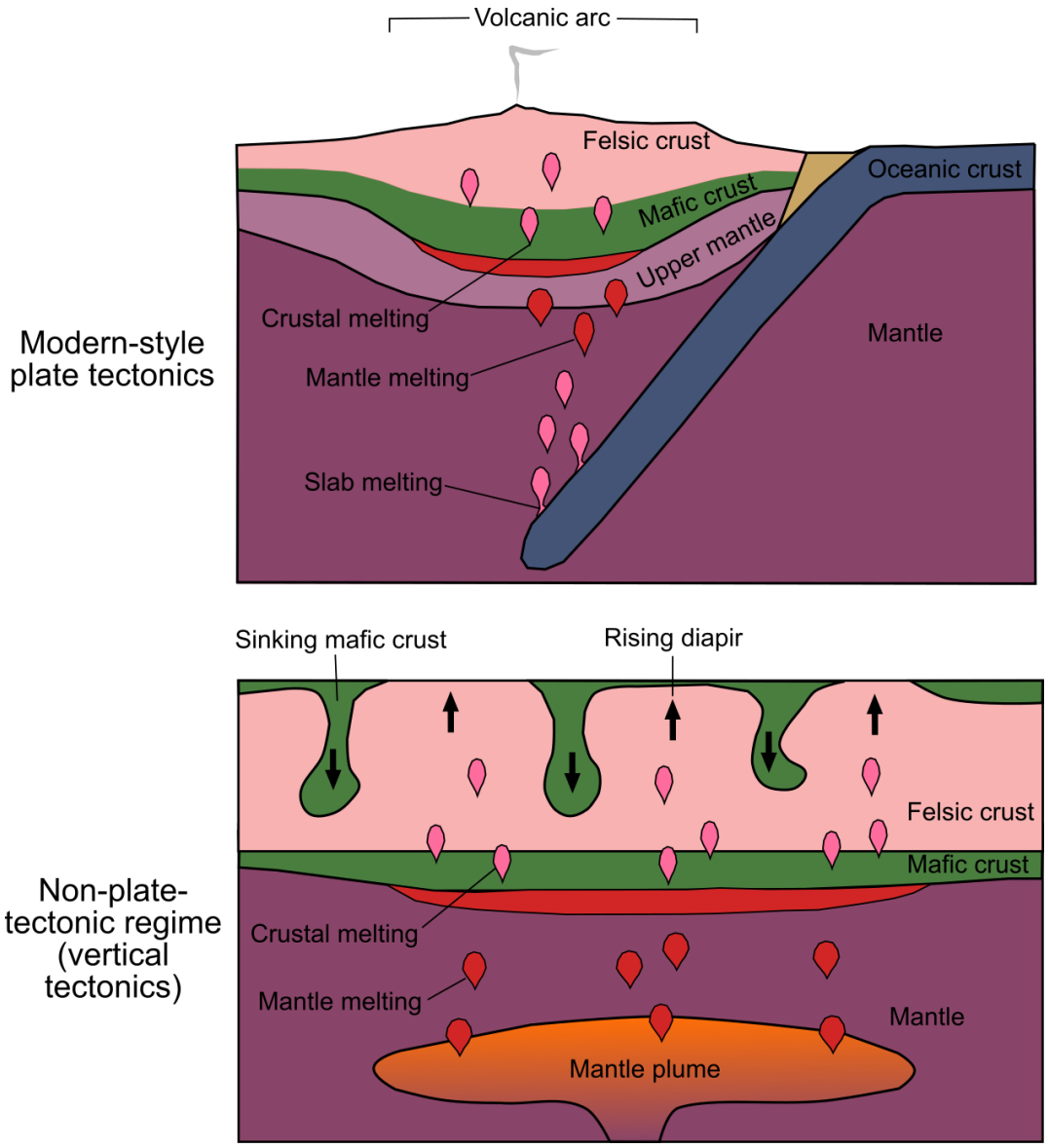


Fig. 1.1. Schematic diagrams showing Archean magma genesis in an arc (i.e., plate-tectonic style) setting (after Polat, 2012) and a non-plate tectonic setting (after Bédard, 2006).

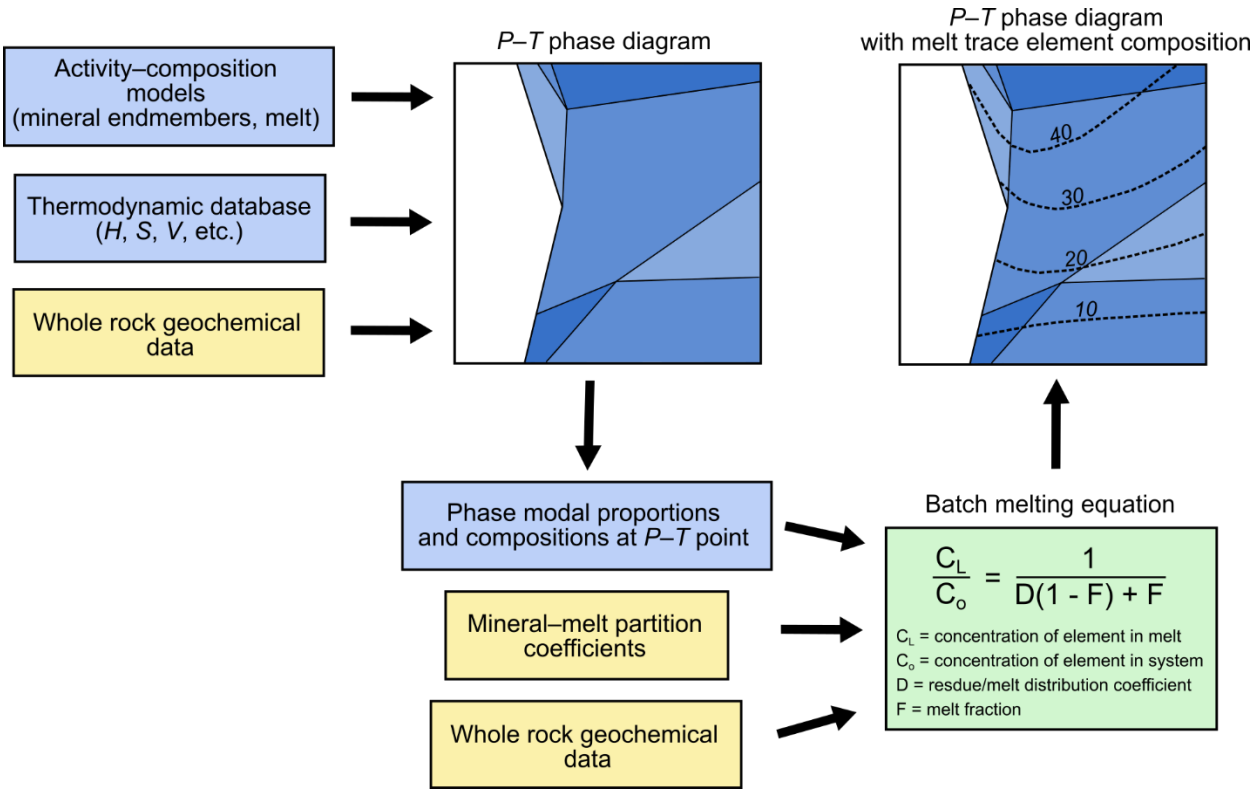


Fig. 1.2. Flow chart showing the process of coupling phase equilibrium modelling with melt trace element modelling. Batch melting equation from Shaw (1970).

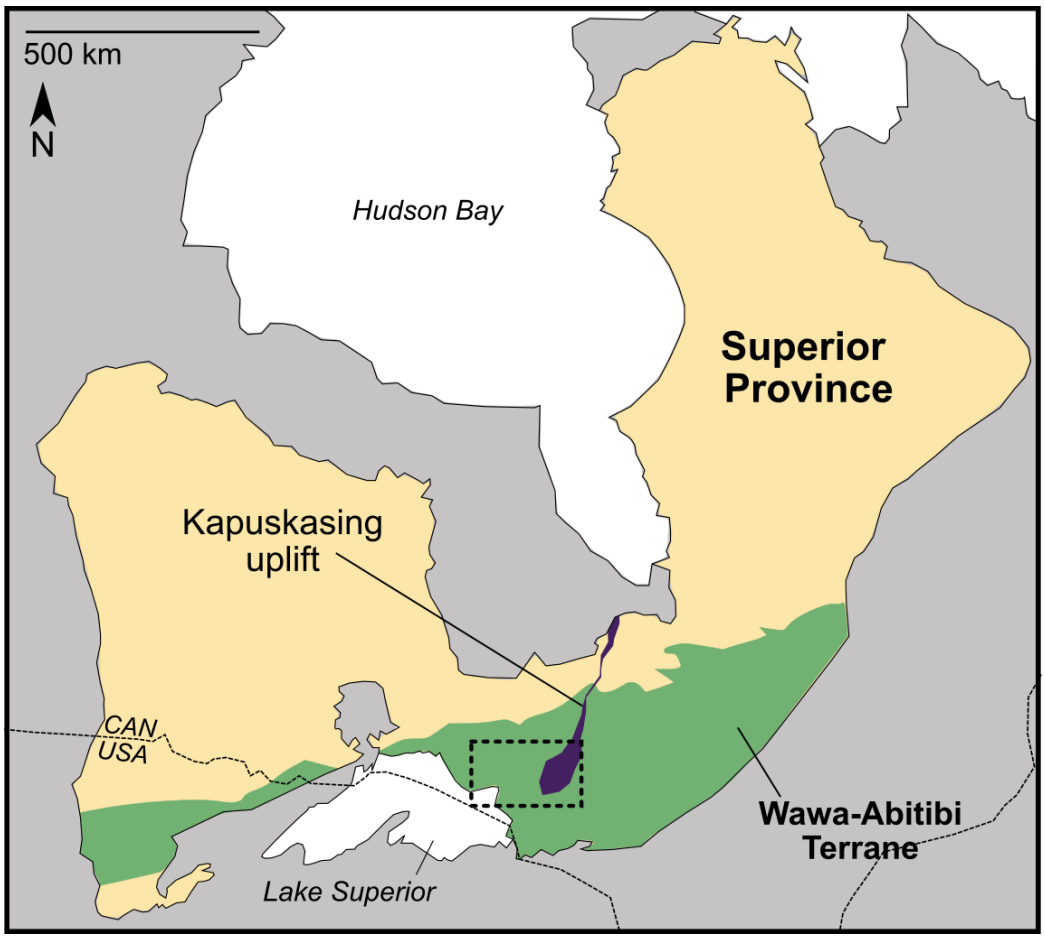


Fig. 1.3. Simplified geological map of the Superior Province showing the location of the Wawa-Abitibi Terrane and the Kapuskasing Uplift (modified from Percival et al., 2012). Dashed box represents the location of Fig. 1.4.

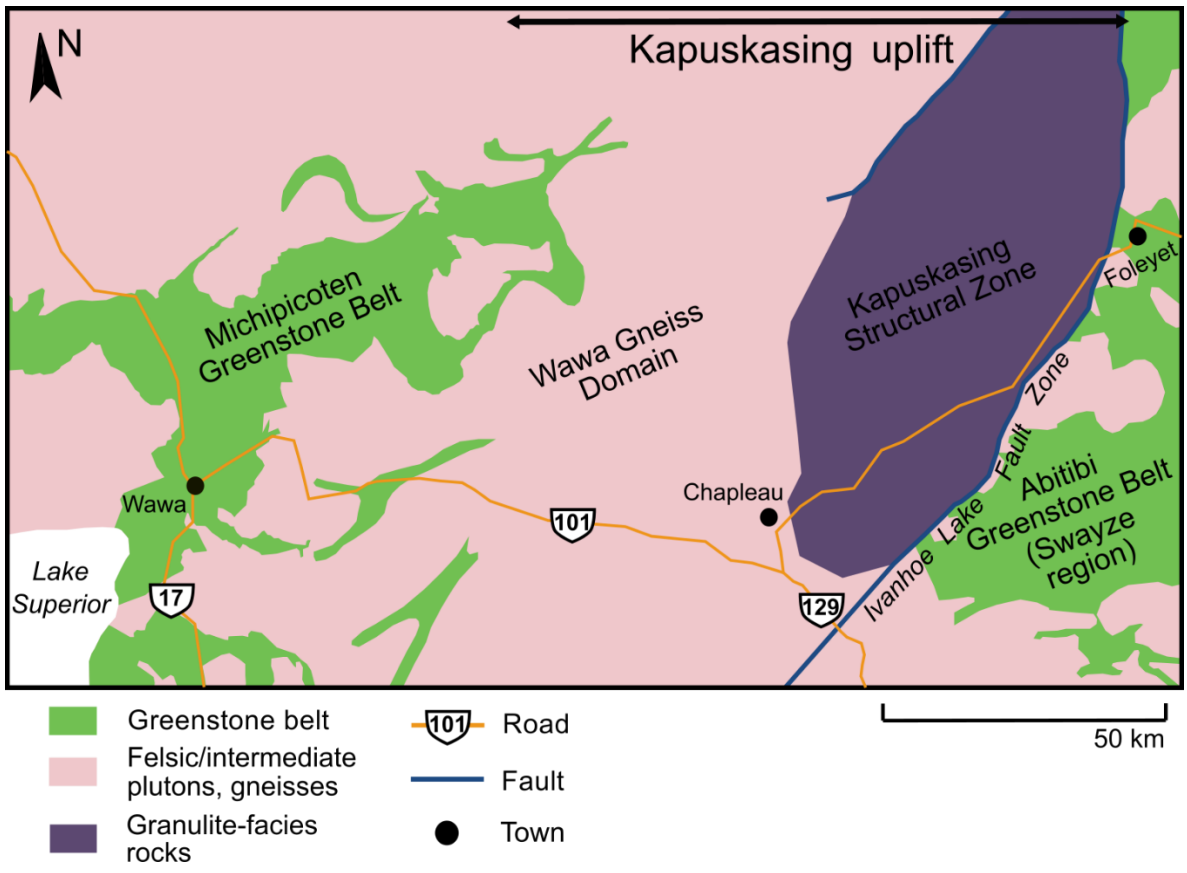


Fig. 1.4. Simplified geological map of the Kapuskasing Uplift (after Ontario Geological Survey, 2011).

Chapter 2

Garnet fractionation, progressive melt loss and bulk composition variations in anatectic metabasites: Complications for interpreting the geodynamic significance of TTGs

Summary

Tonalite-trondhjemite-granodiorite (TTG) suites constitute a large proportion of the Archean geological record; however, the geodynamic processes that generated them, and Archean continental crust in general, remain a subject of debate. The concentrations and ratios of Sr, Y, La, Yb, Nb, and Ta in TTGs are commonly used to determine the depth of melting of their metabasic sources. The trace element composition of melt produced by metabasic source rocks during anatexis is strongly affected by the presence and abundance of pressure-sensitive minerals, such as plagioclase (Sr-bearing), garnet (Y- and HREE-bearing), and rutile (Nb- and Ta-bearing). Elevated Sr/Y and La/Yb ratios and low concentrations of Nb and Ta in TTGs are generally considered to indicate melting at high pressures (≥2.0 GPa). The depth of melting is a key factor in determining the origin of TTGs as this provides critical information on the tectonic setting of their generation. We use phase equilibrium and trace element modelling to explore the effects of three potential influences on TTG trace element compositions: fractionation of trace elements into peritectic garnet cores, progressive melt loss from the source, and source bulk composition. We model three different compositions of Archean basalts along thermal gradients of 500 °C/GPa, 750 °C/GPa, and 1000 °C/GPa. The models produce major and trace element melt compositions that are generally consistent with measured compositions of TTGs. Although Sr/Y, La/Yb, Nb, and Ta exhibit pressure-dependent behaviour, other factors also affect these values. Garnet fractionation causes Sr/Y and La/Yb to reach much greater values and in this scenario, the values also increase with increasing temperature. Source bulk composition has an effect in all scenarios and most strongly influences La/Yb, Nb, and Ta. Overall, these results show that Sr/Y, La/Yb, Nb, and Ta can reach values generally considered to be indicative of high pressure melting at a range of *P*–*T* conditions including $P < 2.0$ GPa. Consequently, trace element compositions of TTGs alone may provide a misleading impression of the depth of melting of metabasites and the geodynamic environment of Archean crustal growth and reworking.

2.1 Introduction

Tonalite-trondhjemite-granodiorite suites, or TTGs, volumetrically dominate Archean cratons, but the geodynamic setting in which they formed remains contentious (Martin et al., 2005, Moyen, 2011, Bédard, 2018, Condie, 2018, Moyen and Laurent, 2018). It is generally accepted that TTGs are generated from the partial melting of hydrated metabasites (Rapp et al., 1991, Moyen and Martin, 2012, Nagel et al., 2012, Martin et al., 2014, Moyen and Laurent, 2018). Concentrations and ratios of specific trace elements in TTGs are commonly used to infer the depth of melting of their metabasic sources, and this is used to infer the tectonic processes that led to their genesis (Martin et al., 2005, Moyen and Stevens, 2006, Moyen and Martin, 2012). This has led to several interpretations for the genesis of TTGs that include partial melting of subducted oceanic crust (Drummond and Defant, 1990), melting of thickened crust in an arc-like setting (Nagel et al., 2012), and melting at the base of oceanic plateaux (Bédard, 2006). The depth of partial melting is a key distinguishing factor for these different settings and identifying evidence in TTGs for these processes has important implications for the origin and evolution of Archean cratons.

During partial melting of metabasites, a strong control on the trace element concentrations and ratios in equilibrated melt is the presence and abundance of garnet, plagioclase, and rutile (Drummond and Defant, 1990). These minerals have broadly pressure-sensitive stability fields in metabasites. In general, garnet is stable at high pressures and contains high concentrations of heavy rare earth elements (HREE) and Y, rutile is also stable at high pressures and is rich in Nb and Ta, and plagioclase is stable at relatively low pressures and is enriched in Sr. Regardless of the geodynamic processes involved, the presence (or absence) and abundance of these minerals in the source during melting is expected to impart a distinct trace element signature to the extracted melt that ultimately forms TTGs. Assuming all phases are in thermodynamic equilibrium, partial melting at high pressures is expected to proceed with garnet and rutile in the residue; these minerals preferentially partition the HREEs, Y, Nb, and Ta and this leaves the melt relatively depleted in these elements. By contrast, melting at low pressures in the plagioclase stability field will cause the melt to be depleted in Sr, but relatively enriched in HREEs, Y, Nb, and Ta due to the absence of garnet and rutile. Thus, the Sr/Y and La/Yb ratios of TTGs are commonly used as proxies of depth of melting (Moyen and Stevens, 2006, Moyen and Martin, 2012), as these ratios should increase with increasing pressure of melting as the metabasic source transitions from the plagioclase stability field to the garnet stability field. The depletion of Nb and Ta in TTGs is used as an additional indicator of high-pressure melting based on the stability of rutile. Based on Sr, Y, La, Yb, Nb, and Ta systematics in natural samples, Moyen

(2011) defined three groups of TTGs linked to depth of melting: the low-pressure group, produced at 1.0–1.2 GPa by a garnet-free, plagioclase-bearing source; the medium-pressure group, corresponding to approximately 1.5 GPa with garnet, some or no rutile, and no plagioclase in the source; and the high-pressure group, produced at ≥ 2.0 GPa in the presence of garnet and rutile without plagioclase. The different pressures of source melting can be linked to the conceptual geodynamic models of TTG generation, and this is crucial for understanding the formation, reworking, and stabilization of Archean cratons.

Recent advances in thermodynamic modelling of phase assemblages in anatectic metabasites (e.g. Palin et al., 2016b) coupled with trace element modelling (e.g. Johnson et al., 2017, Janoušek and Moyen, 2019) present an opportunity to forward model the major and trace element compositions of melt generated in metabasites at a range of *P–T* conditions and for various petrological scenarios. Although this technique has been used to model TTG trace element compositions assuming closed-system behaviour (Nagel et al., 2012, Johnson et al., 2017, Gardiner et al., 2018), previous studies have not investigated the various petrological factors that may influence Sr, Y, La, Yb, Nb, and Ta systematics in natural systems. In particular, open-system processes can modify the stability and modal proportions of minerals during high temperature metamorphism and anatexis (White et al., 2004; Yakymchuk and Brown, 2014, Yakymchuk and Brown, 2019; Mayne et al., 2016, Mayne et al., 2019; Stuck and Diener, 2018), and may affect trace element partitioning. Furthermore, fractionation of key trace elements into growing porphyroblasts such as garnet can limit their availability to the melt (e.g. Otamendi et al., 2002). In addition, mafic sources may have variable trace element compositions prior to melting, and differences in major element composition may cause garnet, plagioclase, and rutile to be produced at different *P–T* conditions and in different proportions, which has implications for linking trace elements of TTGs to depth of melting and their geodynamic settings.

Here we use forward modelling of three different mafic source compositions to demonstrate the effects of open-system melting (i.e. progressive melt loss), fractionation of trace elements into garnet, and source bulk composition on the trace element composition of TTGs. We assess the impact of these factors on the elements typically used to infer the depth of melting: Sr, Y, La, Yb, Nb, and Ta. Trace element concentrations were calculated for melt produced in each scenario for each bulk composition at a range of *P–T* conditions. The results of the modelling are evaluated in the context of natural TTG data (Moyen, 2011, Johnson et al., 2019) and the compositional groups defined by Moyen (2011). Overall, our results suggest that the Sr/Y, La/Yb, Nb, and Ta parameters of the melt

may not have a simple relationship with pressure, and these geochemical characteristics alone may give a misleading impression of the depth of melting and the nature of geodynamic processes that caused TTG generation in the Archean Eon.

2.2 Methodology

2.2.1 Selection of source compositions

Geochemical studies of TTGs and melting experiments have indicated that hydrated mafic crust is the most compatible source for TTGs (Jahn et al., 1981, Martin, 1986, Rapp et al., 1991, Rapp and Watson, 1995, Springer and Seck, 1997, Qian and Hermann, 2013) and large ion lithophile element (LILE) and light rare earth element (LREE) enrichment may be required (Martin et al., 2014); however, the chemical compositions of potential Archean basaltic sources are variable. Three recent phase equilibrium modelling studies used different approaches to select potential TTG sources. Nagel et al. (2012) chose to model melting of a modern mid-ocean ridge basalt (MORB) and an Eoarchean tholeiitic basalt from the Isua Supracrustal Belt in Greenland to determine the depth of melting required to reproduce the trace element compositions of Eoarchean TTGs. The Eoarchean tholeiite composition produced melts with the greatest similarity to Eoarchean TTGs, with the best fit corresponding to melts produced at 1.0 GPa and 1.4 GPa. Palin et al. (2016b) chose an average LILE- and LREE-enriched Archean tholeiite (EAT, Condie, 1981, Table 2.1) and an average LILE- and LREE-depleted Archean tholeiite (DAT, Condie, 1981, Table 2.1) and modelled the major element compositions of melts produced at varying *P*–*T* conditions in closed- and open-system scenarios. The modelling produced melt major element compositions consistent with those of natural TTGs at *P*–*T* conditions of 800–950 °C and ~1.0–1.8 GPa. Johnson et al. (2017) focused on modelling the major and trace element compositions of Palaeoarchean TTGs from the Pilbara Craton in Western Australia, for which a source basalt rich in incompatible trace elements has been proposed (Coucal basalts; Smithies et al., 2009). The compositions of the TTGs were reproduced by the model for melting at *P*–*T* conditions of 850–900 °C and <1.3 GPa. Therefore, various potential sources for TTGs have been modelled, and are in each case selected to suit the scope and purpose of the study.

For the purposes of this study, we chose to build upon the work of Palin et al. (2016b) and use two average Archean basalt compositions to evaluate the general effects of melt loss, garnet fractionation, and source bulk composition on the trace element composition of TTGs, but we acknowledge that understanding specific TTGs suites may require modelling of associated parental basalts (e.g. Johnson et al., 2017). To determine if EAT and DAT (Condie, 1981, Palin et al., 2016b)

represent average Archean basalts based on major element composition, we compared them to a compilation of whole rock geochemical data from 1435 Archean basalts (Fig. 2.1; Table S1.1) created using the sources cited in the basalt and komatiite geochemical database of Condie et al. (2016). Our criteria for selecting compositions to add to the compilation differ from those of Condie et al. (2016), who only included basalts with MgO concentrations of 7–17 wt.%. Given that the average Coucal basalt composition modelled by Johnson et al. (2017) contained only 3.80 wt.% MgO, we elected to include all basalts below 17 wt.% MgO (on an anhydrous basis). Additionally, the compositions were screened based on SiO_2 content (≤60 wt.% on an anhydrous basis) and any rocks stated to be of intrusive origin were not included. Plots of SiO_2 vs. MgO and Al_2O_3 vs. CaO (Fig. 2.1) produced from our database indicate that the major element compositions of EAT and DAT are typical of Archean basalts. Johnson et al. (2017) found that the low MgO content of the Coucal basalt composition allowed for stabilization of garnet at relatively low pressures. However, other workers have suggested that MgO-rich basalts were more common in the Archean and are underrepresented in the currently preserved Archean geological record (e.g. Palin and Dyck, 2018). Given the importance of garnet as a reservoir for Y and HREEs, the MgO content of the mafic source may be an important factor in melt trace element composition. To test this, we additionally selected a composition from a population of MgO-rich basalts (Fig. 2.1), which will be referred to here as the MgO-rich Archean basalt (MAB). The MAB composition, including major and relevant trace elements, is from a greenschist sample from the Tartoq Group supracrustal rocks in southwestern Greenland (sample 510878 of Szilas et al., 2013, Table 2.1).

The elements selected for melt trace element modelling were Sr, Y, La, Yb, Nb, and Ta as these are commonly linked to the depth of partial melting. For the three basalt compositions investigated, Sr, Y, La, and Yb concentrations were included in the source data (Condie, 1981, Szilas et al., 2013), and Nb and Ta were reported only for MAB (Szilas et al., 2013). We assigned to EAT the Nb and Ta of the average Coucal basalt (as reported by Johnson et al., 2017), as this suite of basalts shows trace element enrichment similar to EAT. This Nb concentration is relatively high, as it falls within the top 1% of Nb concentrations in a compilation of Archean basalt compositions from Australia (Smithies et al., 2018). However, suites of Nb-enriched basalts have been recognized in several Archean greenstone belts in the Superior province (Hollings and Kerrich, 2000, Wyman et al., 2000, Polat and Kerrich, 2001, Hollings, 2002), suggesting that basalts with high Nb concentrations are not a localized feature. Therefore, the concentration selected for EAT is considered here to be representative of a high-Nb endmember. For DAT, a moderate Nb concentration was chosen to differentiate it from EAT and the Nb-poor MAB. The Ta value for DAT was calculated based on the

established Nb/Ta value of the primitive mantle (17.5 ± 2; Green, 1995). The trace element compositions are specified in Table 2.1 for the three modelled compositions.

2.2.2 Phase equilibrium modelling

Phase equilibrium modelling was done in the Na_2O–CaO–K_2O–FeO–MgO–Al_2O_3–SiO_2–H_2O–TiO_2–Fe_2O_3 (NCKFMASHTO) chemical system using THERMOCALC version 3.45 (Powell and Holland, 1988) and the internally consistent thermodynamic dataset of Holland and Powell (2011; updated version ds62). The activity–composition (*a*–*x*) models used are as follows: tonalitic melt, amphibole, clinopyroxene (Green et al., 2016), orthopyroxene, garnet, biotite, muscovite, ilmenite (White et al., 2014), K-feldspar, plagioclase (Holland and Powell, 2003), and epidote (Holland and Powell, 2011). Rutile, quartz, titanite, and aqueous fluid (H_2O) were modelled as pure end members.

For each bulk composition (Table 2.2), phase assemblages were calculated from the solidus to 1050 °C and between 0.4 GPa and 2.2 GPa. Also, phase proportions and compositions were extracted from THERMOCALC across a grid at intervals of 25 °C and 0.1 GPa. For these calculations, the bulk H_2O contents of DAT, EAT, and MAB were reduced to minimally saturate melt in H_2O at the solidus at 1.2 GPa (Table 2.2). This was done because any free H_2O in suprasolidus rocks would be expected to partition into the melt (White and Powell, 2002, White et al., 2005). As FeO and Fe_2O_3 are not differentiated for MAB, an O value was assigned assuming a Fe^{2+}/Fe^{3+} ratio of 10. Additionally, phase proportion and composition data were collected along three *P*–*T* gradients for each bulk composition, 500 °C/GPa, 750 °C/GPa, and 1000 °C/GPa, which are considered to be plausible apparent geothermal gradients for Archean crust based on peak *P*–*T* estimates from Archean metamorphic rocks (Brown and Johnson, 2018). The 1000 °C/GPa thermal gradient was chosen for our modelling as a high d*T*/d*P* endmember based on the compilation of Brown and Johnson (2018), whereas 500 °C/GPa is the lowest d*T*/d*P* gradient recorded in Archean rocks in the compilation. These gradients are considered apparent thermal gradients and are simplified compared to natural *P*–*T* paths, which cannot typically be represented by a single gradient and may involve more complex prograde evolutions. For each of these *P*–*T* gradients, the H_2O contents of the bulk compositions were adjusted to just saturate melt in H_2O at the *P*–*T* conditions where the gradient intersects the solidus (Table 2.2). The data extracted from THERMOCALC were converted to weight fractions and then coupled with published partition coefficients (from Bédard, 2006) for various trace elements in metabasites to calculate the trace element composition of the melt (i.e. TTGs) and residue using a batch melting model (e.g. Presnall, 1969, Shaw, 1970, Hanson, 1978). These calculations represent a scenario where the composition of the system remains constant and there is equilibrium of major and

trace elements among all phases. This closed-system behaviour is considered here as a baseline scenario, and additional modelling was undertaken to simulate two open-system scenarios: loss of anatectic melt and fractionation of elements into garnet porphyroblasts.

2.2.2.1 Open-system behaviour

2.2.2.1.1 Melt loss

Loss of anatectic melt from suprasolidus rocks during prograde metamorphism is considered to be a common process, given that these rocks typically preserve peak metamorphic assemblages with minimal evidence of retrogression (White and Powell, 2002). This scenario was simulated here by removing 6 mol% melt (approximately equivalent to 6 vol% on a one-oxide basis) in pulses along each *P*–*T* gradient when a proportion of 7 mol% melt was reached (cf. Yakymchuk and Brown, 2014), which approximates the melt connectivity threshold of Rosenberg and Handy (2005). This leaves 1 mol% melt in the system, which is consistent with the presence of melt pseudomorphs in some anatectic metamorphic rocks (e.g. Holness and Sawyer, 2008). The bulk compositions of major and trace elements in the system were adjusted based on the extraction of melt with equilibrium concentrations at the 7 mol% threshold.

2.2.2.1.2 Garnet fractionation

The preservation of major and trace element zonation in garnet porphyroblasts is a well-documented feature (e.g. Spear and Kohn, 1996, Pyle and Spear, 1999) that provides strong evidence for sequestration of these elements during garnet growth. As garnet is an important reservoir for HREEs and Y in metabasites, garnet fractionation could have a significant impact on the availability of these elements to anatectic melt. In addition, the low diffusivity of the HREE and Y in garnet relative to divalent cations (e.g. Fe, Mg; Carlson, 2012) hinders diffusional equilibration of these elements due to thermally-activated volume diffusion. Garnet fractionation was modelled by removing garnet along the *P*–*T* gradients in increments of 4.5 mol% when 5 mol% was reached. This simulates continuous segregation of garnet cores from the equilibrium assemblage of the rock, leaving a thin reactive rim comprising a ~10 mol% fraction of the garnet, which is equivalent to a ~30 μm-thick rim for a garnet crystal with a diameter of ~2 mm and ~170 μm for a ~10 mm diameter crystal. In other forward models of garnet growth, this reactive rim is < 10 μm (Gaidies et al., 2008) or considered to be negligible (e.g. Evans, 2004), but we include a reactive rim here given the high temperatures and presence of melt in our models. The major and trace elements associated with the 4.5 mol% of garnet

sequestered from the system were removed from the modelled bulk compositions at each step, and the proportions of all residue phases were renormalized to a total of 1.

2.3 Results

2.3.1 *P–T* pseudosections

The *P–T* pseudosections produced for EAT (see also Palin et al., 2016b) and DAT have similar overall topologies, with modelled solidus temperatures ranging from approximately 625–725 °C; MAB shows distinct differences from the others, with a solidus at approximately 750 °C with a steep d*T*/d*P* (Fig. 2.2). Hornblende is predicted to be stable across a large portion of the three diagrams and is exhausted at 850–950 °C above 1.2–1.4 GPa. Similarly, quartz is stable at the solidus in all three diagrams, and is exhausted at temperatures as low as 800 °C at low *P*, but may persist up to 1000 °C at high *P*. Both clinopyroxene and orthopyroxene are predicted to be stable for all three bulk compositions, although their stability fields differ. Clinopyroxene is stable across the entire diagram for DAT, but for EAT and MAB, clinopyroxene is absent below 1.3 GPa and 750 °C and 1.9 GPa and 850 °C respectively. For EAT and DAT, orthopyroxene is restricted to pressures of ≤1.1 GPa at temperatures above 800–900 °C. For MAB, orthopyroxene is predicted to be stable at similar temperatures but persists up to at least 2.2 GPa.

The *P–T* stability fields of each of the trace element reservoirs of interest—garnet, rutile, and plagioclase—are comparable for EAT and DAT, and slightly different for MAB (Fig. 2.3). Garnet is predicted to be stable at pressures as low as 0.8 GPa for DAT, 0.9 GPa for EAT, and 1.1 GPa for MAB at approximately 900 °C (Fig. 2.3a–c); however, at temperatures close to the solidus, the lower pressure limit of garnet stability increases to 1.2 GPa for DAT and 1.4 GPa for EAT and MAB. At similar *P–T* conditions, the weight proportions of garnet predicted for DAT are approximately 5 wt.% higher than those of EAT and 15–30 wt.% higher than those of MAB. Plagioclase is stable up to 1.9 GPa for EAT and 1.8 GPa for DAT, and this maximum pressure corresponds to 850 °C–900 °C (Fig. 2.3d and e). With decreasing or increasing temperature from this point, the upper pressure limit of plagioclase stability decreases to ~1.0 GPa at the lowest. The model for DAT predicts greater proportions of plagioclase than those of EAT, particularly at lower pressures, where the DAT composition may have up to 10 wt.% more plagioclase than the EAT composition. For MAB, the maximum pressure of the plagioclase stability field is 1.2 GPa at temperatures above 950 °C and decreases to 0.5 GPa at the solidus at 750 °C (Fig. 2.3f). The amount of plagioclase predicted for MAB is typically 10–15 wt.% less than that of DAT at similar *P–T* conditions. The low-pressure limit

of the rutile stability field is at 0.9 GPa for DAT and 1.0 GPa for EAT from approximately 900 °C to 1050 °C, and at lower temperatures the field becomes restricted to pressures above 1.5 GPa–1.6 GPa (Fig. 2.3g and h). The model for MAB predicts the presence of rutile above 1.6 GPa to almost 1.8 GPa below 900 °C (Fig. 2.3i), and differs significantly from DAT and EAT above 900 °C, where rutile is expected to be stable to ≤0.4 GPa. At high *P–T*, the model predicts that EAT will have approximately 1.5 times more rutile than DAT and 3 times more than MAB.

2.3.2 *P–T* gradients

Assemblages and weight fractions of each phase were calculated along three *P–T* gradients for each bulk composition and for each of the three modelled scenarios: closed system, melt loss, and garnet fractionation. These gradients are intended to show simplified *P–T* paths up to peak metamorphic conditions recorded by Archean rocks (e.g. Brown and Johnson, 2018). The results from DAT are shown as an example (Fig. 2.4), as the same general trends are present for EAT and MAB (Fig. S1.1). For comparison, see also Palin et al. (2016b), where phase proportions for EAT and DAT were previously calculated for isobaric heating paths.

Along the 500 °C/GPa gradient in the closed-system scenario, the stable assemblage at the solidus is dominated by hornblende and quartz, with small amounts of clinopyroxene, garnet, and other minerals that are bulk composition-dependent (epidote, titanite, or muscovite). With increasing *P* and *T*, hornblende and quartz proportions decrease as garnet, clinopyroxene, and melt increase, and for DAT and EAT, plagioclase joins the modelled assemblage at ~800 °C. Rutile also becomes stable at this stage, at *P–T* conditions that vary with bulk composition. Near 900 °C and 1.8 GPa (925 °C and 1.85 GPa for MAB), hornblende is expected to be exhausted. At *P–T* conditions above hornblende out, changes in mineral proportions are relatively gradual, with quartz and plagioclase decreasing until plagioclase is exhausted, and garnet and clinopyroxene show little to no change in their modal proportions. Between 1000 °C and 1050 °C and 2.0 GPa and 2.1 GPa, quartz proportions reach zero, leaving an assemblage of garnet, clinopyroxene, rutile, and melt (and orthopyroxene for MAB). Proportions of melt continue to increase with clinopyroxene or garnet either increasing or decreasing slightly, depending on bulk composition; rutile proportions increase gradually for all compositions.

The mineral assemblages and trends in mineral proportions predicted along the 750 °C/GPa gradient in the closed-system scenario are broadly similar to those of the 500 °C/GPa gradient. The major differences, for all bulk compositions, is garnet and rutile production at relatively higher *P–T*, the exhaustion of quartz before hornblende, and the presence of biotite up to ~800 °C in EAT (Fig.

S1.1). Quartz persists until approximately 900 °C and 1.2 GPa for EAT and DAT and approximately 975 °C and 1.3 GPa for MAB, after which hornblende is exhausted around 975 °C and 1.3 GPa for EAT and DAT and 1050 °C and 1.4 GPa for MAB. For DAT and EAT, plagioclase is predicted to be present along most of the 750 °C/GPa gradient, and its proportions decrease steadily at high *P–T* where quartz is absent. Beyond hornblende exhaustion, plagioclase continues to be depleted as garnet, clinopyroxene, rutile, and melt proportions increase. The same general trends are predicted for the 1000 °C/GPa gradient in the closed-system scenario. Relative to the 750 °C/GPa gradient, quartz is exhausted at slightly lower *P–T* and hornblende persists to higher *P–T*, at least 1000 °C (at 1.0 GPa) for all bulk compositions. Garnet and rutile are stable at relatively higher *P–T* along this gradient, with no garnet predicted for MAB at *P–T* lower than 1050 °C and 1.05 GPa. For all bulk compositions, the 1000 °C/GPa gradient is predicted to produce the highest proportions of plagioclase and melt and the lowest proportions of garnet.

Mineral assemblages and proportions predicted for the open-system scenario with melt loss show minor differences relative to the closed system. Residue assemblages (i.e. without melt) for these two scenarios are shown and compared for all *P–T* gradients for DAT as an example (Fig. 2.4; see also Palin et al., 2016b). Compared to the closed-system model for the 500 °C/GPa gradient, the melt loss scenario generally predicts less garnet, clinopyroxene, and rutile, and more plagioclase, hornblende, and quartz. Instead of being exhausted at high temperatures, quartz and plagioclase (not stable for MAB) persist up to at least 1050 °C and 2.1 GPa with relatively minor proportions. Hornblende stability is extended by only 1–2 °C for DAT and EAT, and by 11 °C for MAB. Garnet, clinopyroxene, and rutile decrease to 80–90 wt.% of their closed-system weight proportions for DAT and EAT; changes in these minerals are much smaller for MAB. The 750 °C/GPa gradient shows similar changes relative to the closed-system scenario, with the major difference for all bulk compositions being the exhaustion of quartz at *P–T* conditions similar to the closed-system models and the extension of hornblende stability to at least 1050 °C and 1.4 GPa. Following this trend, greater proportions of hornblende are predicted to remain stable for the 1000 °C/GPa gradient for all bulk compositions. DAT and MAB are predicted to have a similar amount of plagioclase when compared to the closed-system scenario, whereas plagioclase proportions are increased for EAT. Unlike the closed-system models, no rutile is predicted to be stable along the 1000 °C/GPa gradient for all bulk compositions.

In general, relative to the closed-system scenario, the garnet fractionation model predicts that the proportions of all other minerals in the residue increase (as a consequence of renormalizing the

proportions of the phases to a total of 100 wt.% without garnet, as in Fig. 2.4). Overall, the residue assemblage (minus garnet) shows only minor differences from the closed-system scenario, such as the stability of hornblende and quartz extending to higher *P–T*. However, the exception to this is plagioclase, which is not stable along the 500 °C/GPa gradient for all bulk compositions, in contrast to its presence in closed-system models for DAT and EAT. With the removal of garnet, the residuum is predicted to be dominated by hornblende until 940–960 °C and 1.88–1.92 GPa, where clinopyroxene becomes most abundant. Along the 750 °C/GPa gradient, plagioclase is stable for DAT and EAT, and it reaches higher proportions in the residue than in the closed-system scenario; however, the melt loss model generally predicts the greatest proportions of plagioclase. Consequently, hornblende and clinopyroxene proportions are lower, though they remain the dominant minerals in the residue. Finally, the plagioclase content of the residue is predicted to be highest along the 1000 °C/GPa gradient compared to all other scenarios for DAT and EAT, reaching proportions similar to those of hornblende and clinopyroxene at approximately 900 °C and 0.9 GPa. Given that the 1000 °C/GPa gradient for MAB does not intersect the garnet stability field, the garnet fractionation scenario was not computed.

2.3.3 Major element compositions of modelled melts

The major element compositions of the modelled melts were evaluated using their CIPW normative ratios of anorthite, albite, and orthoclase (Fig. 2.5, Fig. 2.6) to classify them as tonalite, granodiorite, trondhjemite, or granite (O'Connor, 1965, Barker, 1979) and compare them to natural TTG compositions (from Moyen, 2011; the filtered and updated version of this database from Johnson et al., 2019, is used here). For comparison, see also Palin et al. (2016b), where melts from the EAT and DAT compositions were previously classified using this approach. Here, we produced these diagrams to compare melt compositions from the three bulk compositions in the closed-system scenario (Fig. 2.5) and to illustrate the general effects of melt loss and garnet fractionation on melt composition (Fig. 2.6; shown for DAT only, results from EAT and MAB are available in Fig. S1.2).

Each bulk composition is predicted to produce different melt compositions that are also controlled by the *P–T* gradients, or effectively the pressure, at which the source melted (Fig. 2.5). In general, for all bulk compositions, melt compositions tend to plot closer to or further within the trondhjemite field with increasing pressure; melts produced along the 500 °C/GPa gradient generally have the highest normative albite content. The 1000 °C/GPa melts plot closest to the anorthite apex and are mainly classified as tonalite or granodiorite. Nevertheless, melts from all gradients trend

toward higher normative anorthite proportions with increasing temperature, particularly between 950 °C and 1050 °C.

Of the three source compositions, melts modelled for DAT plot closest to the normative albite apex, with normative orthoclase content decreasing with increasing temperature for all *P–T* gradients. For DAT, the 500 °C/GPa gradient is predicted to produce mainly trondhjemitic melts, whereas melts from the 750 °C/GPa and 1000 °C/GPa gradients mostly plot as granodiorite and tonalite. EAT is predicted to produce different trends, with melts from all gradients showing increasing normative orthoclase proportions with increasing temperature, until an inflection between 750 °C and 850 °C coinciding with the exhaustion of muscovite or biotite, beyond which orthoclase decreases (see also Palin et al., 2016b, White et al., 2017). Thus, melts produced by EAT at temperatures lower than 850 °C for all *P–T* gradients are classified as granitic. Higher temperature melts from the 500 °C/GPa and 750 °C/GPa gradients are trondhjemitic, and those of the 1000 °C/GPa gradient are classified as granodiorite and tonalite. Relative to DAT and EAT, melts predicted to be produced by MAB generally plot closest to the anorthite apex. Melts generated between 750 °C and 850 °C plot in the high-anorthite portion of the granite field and orthoclase content is predicted to decrease with increasing temperature. From 850 °C to 950 °C, the melts are generally granodioritic, with the 500 °C/GPa melts showing the lowest normative anorthite content and plotting closest to the trondhjemite field. Between 950 °C and 1050 °C, melts produced along the 500 °C/GPa and 1000 °C/GPa gradients trend toward higher normative anorthite proportions; however, the 750 °C/GPa melts show increasing normative albite.

Open-system behaviour has a minor effect on melt major element composition compared to differences in source bulk composition (Fig. 2.6, Fig. S1.2). Relative to the closed-system scenario, the melt loss scenario is predicted to produce melts above 850 °C that have a higher normative albite content and lower normative orthoclase content, regardless of *P–T* gradient. For DAT and EAT, this effect is greatest for the 1000 °C/GPa gradient, whereas the 500 °C/GPa and 750 °C/GPa gradients are most affected for MAB. Garnet fractionation has an even smaller effect on the major element composition of the melt. Melts produced in this scenario show lower normative anorthite content and this is most apparent at higher temperatures (>850 °C), particularly for the 500 °C/GPa gradient. The melts generated by DAT are most affected, as EAT and MAB melt compositions show little to no change with garnet fractionation.

Of all modelled bulk compositions, the melts produced by DAT show the best agreement with the range of compositions of natural TTGs. For EAT and MAB, melts generated at temperatures

lower than 850 °C are generally predicted to have more normative orthoclase than the average TTG, and at higher temperatures along the 750 °C/GPa and 1000 °C/GPa gradients, MAB produces melts with higher normative anorthite contents than typical TTGs.

2.3.4 Trace element compositions of modelled melts

Modelled trends of melt trace elements show some differences among the three bulk compositions (Fig. 2.7) and can be linked to the modelled behaviour of garnet, plagioclase, and rutile (Fig. 2.3), as discussed above. For the closed-system scenario, melt Sr/Y ratios are predicted to reach up to 200 for DAT, 300 for EAT, and 200 for MAB (Fig. 2.7a–c); the values increase with pressure. Maximum values are near the solidus at ~750 °C for EAT, around 850 °C for DAT, and near 900 °C for MAB. The Sr/Y contours in *P–T* space are curved and mostly concave-up, broadly reflecting the shape of the contours of garnet modal proportions (Fig. 2.3); however, the curvature is inverted within the plagioclase stability field for DAT and EAT. Within the garnet stability field, MAB Sr/Y contours are predicted to closely match garnet contours, and in the plagioclase-present and garnet-free portion of the diagram, Sr/Y mirrors plagioclase contours. Modelled melt ratios of chondrite-normalized La/Yb (La_N/Yb_N) have a range up to 320 for EAT, 70 for DAT, and 80 for MAB (Fig. 2.7d–f), and these elevated values are predicted at the same *P–T* conditions as Sr/Y maxima. The shape of La_N/Yb_N contours is similar to that of garnet contours, and unlike Sr/Y, does not show a change in curvature in the plagioclase stability field. The highest modelled values of Nb in the melt for EAT and DAT, at 44 µg/g and 24 µg/g respectively, are predicted between 650 °C and 800 °C and 1.2 GPa and 1.5 GPa (Fig. 2.7g and h). The maximum Nb concentration of 3.4 µg/g for MAB is between 800 °C and 900 °C and 1.5 GPa and 1.8 GPa (Fig. 2.7i). Contours of the concentration of Nb in melt closely follow and are tightly spaced around the rutile-in boundary at lower temperatures (up to 850 °C for EAT and DAT and 950 °C for MAB) and have a similar overall shape to rutile modal proportion contours. The concentration of Nb is predicted to decrease with increasing temperature and pressure, with contours more strongly controlled by temperature.

The effect of bulk composition, *P–T* gradient, and closed- vs. open-system behaviour are shown for each of the modelled trace elements: Sr, Y, La, Yb, Nb, and Ta (Figs 2.8, 2.9, and 2.10). The tabulated results are presented in Table S1.2. Sr/Y is plotted against Y and in general, Sr/Y increases and Y decreases with increasing pressure, with the 500 °C/GPa gradient melts showing the highest Sr/Y (Fig. 2.8). For DAT and EAT, the melt loss scenario is predicted to produce melts with the lowest maximum Sr/Y (Fig. 2.8d and e); however, the differences between the melt loss and closed-system scenarios (Fig. 2.8a and b) are minor compared to the garnet fractionation scenario,

where maximum Sr/Y may be an order of magnitude higher (Fig. 2.8g and h). For MAB, the closed-system scenario melts are predicted to have lower Sr/Y (Fig. 2.8c) compared to the melt loss scenario (Fig. 2.8f) and Sr/Y is highest for the garnet fractionation scenario (Fig. 2.8i), though the effect is not as extreme compared to the other bulk compositions. In the closed- and open-system scenarios (Fig. 2.8a–f), MAB produces the highest Sr/Y melts of all bulk compositions, and the Sr/Y for DAT is slightly higher than EAT. Although melts with the maximum values are predicted to be produced along the 500 °C/GPa gradient, they do not correspond to the maximum pressure of 2.1 GPa explored in the model. In the closed system scenario, maximum Sr/Y is predicted at 1.87 GPa at 936 °C for DAT, 1.93 GPa at 965 °C for EAT, and 1.87 GPa at 934 °C for MAB (Fig. 2.8a–c; Table S1.2). In the melt loss scenario, the lower maximum Sr/Y for DAT and EAT is produced at only 1.58 GPa at 789 °C and 1.48 GPa at 742 °C respectively (Fig. 2.8d–f; Table S1.2). In the garnet fractionation scenario, maximum Sr/Y corresponds to melt produced at 1.98 GPa at 991 °C for DAT, 1.95 GPa at 974 °C for EAT, and 1.92 GPa at 960 °C for MAB (Fig. 2.8g–i; Table S1.2). For all bulk compositions and almost all scenarios, the melts from the 750 °C/GPa and 1000 °C/GPa gradients with the highest Sr/Y are predicted to be produced at or near the peak conditions of 1.4 GPa and 1050 °C and 1.05 GPa and 1050 °C respectively. A notable exception is the 1000 °C/GPa gradient in the closed-system and melt loss scenarios for MAB (Fig. 2.8c, f), which shows the opposite trend of Sr/Y decreasing steadily with increasing *P–T* conditions (Table S1.2); the 1000 °C/GPa gradient for MAB also has no stable garnet. Although Sr/Y mainly varies with pressure, some temperature dependence is also evident from the results at 1.4 GPa from each of the 500 °C/GPa and 750 °C/GPa gradients for DAT and EAT, which correspond to 700 °C and 1050 °C respectively. For the closed-system and melt loss scenarios, the value of Sr/Y at 1050 °C is predicted to be up to two times greater than that at 700 °C; however, in the garnet fractionation scenario, Sr/Y is one order of magnitude greater at 1050 °C than at 700 °C. At ~1.4 GPa along the 500 °C/GPa and 750 °C/GPa gradients for MAB, Sr/Y at 1050 °C is less than double the value at 700 °C for all modelled scenarios.

Chondrite normalized La/Yb vs. Yb of the modelled melts (Fig. 2.9) follow trends similar to Sr/Y vs. Y, with maximum values predicted to correspond to melts produced along the 500 °C/GPa gradient in all scenarios. The closed-system (Fig. 2.9a–c) and melt loss (Fig. 2.9d–f) scenarios yield similar results for all bulk compositions, whereas garnet fractionation (Fig. 2.9g–i) is predicted to produce La_N/Yb_N two to three orders of magnitude greater in comparison. In contrast to Sr/Y, melts derived from EAT have the highest La_N/Yb_N values in all scenarios (Fig. 2.9b, e, h); however, like Sr/Y, maximum La_N/Yb_N does not correspond to peak *P–T*. Melts produced by DAT and EAT along the 500 °C/GPa gradient reach maximum La_N/Yb_N at approximately 1.75 GPa and 877 °C for both the

closed and open systems (Fig. 2.9a, b, d, e; Table S1.2), which makes La_N/Yb_N decoupled from Sr/Y. However, for this *P–T* gradient, Sr/Y and La_N/Yb_N are coupled in the garnet fractionation scenario (Fig. 2.9g and h). In general, the 750 °C/GPa and 1000 °C/GPa gradient melts for DAT and EAT are predicted to reach maximum La_N/Yb_N at slightly lower *P–T* than maximum Sr/Y, typically by ≤ 0.1 GPa and ≤75 °C or 100 °C, depending on the gradient. For all *P–T* gradients and modelled scenarios, the La_N/Yb_N of melts produced by MAB are coupled to Sr/Y (Fig. 2.9c, f, i). Comparing La_N/Yb_N predicted at different temperatures but similar pressures from the 500 °C/GPa and 750 °C/GPa gradients yields similar results to Sr/Y. For DAT and EAT, La_N/Yb_N at 1.4 GPa and 1050 °C is up to three times greater than that at 1.4 GPa and 700 °C, and in the garnet fractionation scenario, the difference becomes two orders of magnitude. The temperature dependence is not as great for MAB, with La_N/Yb_N up to four times greater at high temperature compared to low temperature.

The Nb concentrations of the melts are plotted against Ta concentrations and, for each *P–T* gradient, the lowest Nb and Ta correspond to maximum *P–T* in all cases (Fig. 2.10). Differences between the closed-system, melt loss, and garnet fractionation scenarios are minor for all bulk compositions, and melts produced by EAT are predicted to have the highest and largest range of Nb and Ta concentrations (Fig. 2.10b, e, h); melts produced from MAB have the lowest and smallest range of concentrations (Fig. 2.10c, f, i). For DAT and EAT, Ta concentrations are overall higher with increasing thermal gradient and the opposite is predicted for MAB. The range of concentrations of Nb in the melt is similar for each gradient; however, in the melt loss scenario for all bulk compositions (Fig. 2.10d–f) and the garnet fractionation scenario for EAT (Figs. 10h), 1000 °C/GPa gradient melts are restricted to higher Nb. Almost all *P–T* gradients for each of the bulk compositions show an initial increase in Nb and Ta with increasing *P–T*, with maximum Nb typically produced at lower *P–T* than maximum Ta. With further *P–T* increase, both Nb and Ta decrease, and the concentrations predicted for different *P–T* gradients, particularly 500 °C/GPa and 750 °C/GPa, converge toward similar values.

2.4 Discussion

2.4.1 Limitations of the models

The modelled melt compositions presented here are subject to the limitations inherent to phase equilibrium modelling (e.g. Powell and Holland, 2008, Palin et al., 2016b, Forshaw et al., 2019, Lanari and Duesterhoeft, 2019), including the assumption of equilibrium (major and trace components) among all phases during melting. Although the clinopyroxene model we use is

considered appropriate across most of the investigated *P–T* conditions, it generally underestimates Na substitution at high pressure–low temperature conditions, which causes a shift in topology in this region of the phase diagram (Green et al., 2016). In addition, the *a–x* models used in our models do not consider Ti substitution in clinopyroxene or Ti incorporation in the melt (e.g. Ryerson and Watson, 1987, Forshaw et al., 2019). This results in an overestimation of the proportion of rutile in our models relative to nature, which in turn would cause concentrations of Nb and Ta in the melt to be lower in the models. For example, rutile is predicted to be stable to 0.4 GPa at high temperatures in the model for MAB (Fig. 2.3i), which may not be realistic. Given that the Fe^{2+}/Fe^{3+} ratio of MAB is unknown, this introduces further uncertainty to the *P–T* extent of the rutile stability field and modal proportions of rutile, which in turn adds uncertainty to the modelled concentrations of Nb and Ta in the melt. The Fe^{2+}/Fe^{3+} ratio may also have minor effects on the stability fields of the other minerals included in the modelling, as has been demonstrated for pelitic bulk compositions (Boger et al., 2012).

The partition coefficients used in the models (from Bédard, 2006) to calculate the concentrations of trace elements in the modelled melts are subject to uncertainty and are not constant values in nature. Although the values used are considered to be suitable for partial melting of metabasites (Bédard, 2006), partition coefficients generally vary with changes in temperature, pressure, melt composition, and mineral composition (Blundy and Wood, 2003). Nevertheless, we expect that the modelled trends in the trace element compositions of the melts are robust, as they are driven by strongly compatible behaviour between certain elements and minerals, and this behaviour should not change significantly with varying partition coefficients. For instance, an experimental study (Nicholls and Harris, 1980) of REE partitioning between andesitic melts and garnet at different temperatures reported a range in partition coefficients from ~10 to ~45 for Yb, which encompasses the value of 23.2 used in our models. Despite this range, all values are an order of magnitude greater than 1, indicating that Yb would be readily incorporated into garnet regardless of temperature. Consequently, uncertainty and variability in partition coefficients would affect the calculated concentrations of trace elements in the modelled melts, but the overall effect of melting in the garnet, plagioclase, or rutile stability field and the trends in the trace element concentrations in melt would be the same. Finally, measured concentrations of the HREE in hornblende in intermediate to metabasic migmatites are quite high relative to values predicted using existing partition coefficients (e.g. Reichardt and Weinberg, 2012, Yakymchuk et al., 2019), which suggests that hornblende may be a more important sink for the HREE in the residue in nature relative to the models.

Further limitations arise from assumptions made to simplify the natural process of partial melting of metamorphic rocks. In our models, we do not consider the effect of accessory minerals, which are commonly apatite and zircon in metabasites, on melt trace element compositions. Zircon is unlikely to have a significant effect because the concentration of Zr in Archean basalts is commonly relatively low (≤100 μg/g; Condie, 1985) resulting in little to no zircon in the source of TTGs. Relatively higher concentrations of P in Archean basalts (Condie, 1985) may stabilize apatite, which may be a significant reservoir for Y and REEs due to the high partition coefficients for these elements between apatite and melt (Bédard, 2006). However, apatite solubility is expected to be small for metaluminous melt compositions (e.g. Watson and Capobianco, 1981, Pichavant et al., 1992). Therefore, residual apatite is expected to slightly increase the Sr/Y composition of the melt relative to the scenarios modelled here, but it is not expected to significantly affect the La/Yb ratio considering the similar partition coefficients for the REE between melt and apatite (Bédard, 2006). In addition, some proportion of apatite and zircon may be trapped within peritectic phases such as garnet and not accessible to the melt (Watson et al., 1989, Sawyer, 1999), making the role of accessory minerals as trace element reservoirs difficult to model for a general scenario. Sequestration of rutile in unreactive or growing minerals could cause sequestration of Nb and Ta and consequently lower concentrations of these elements in the melt. Given that rutile preferentially incorporates Ta over Nb, this would cause the bulk and melt Nb/Ta to shift toward higher values.

In the garnet fractionation models, we assume complete sequestration of garnet cores, although realistically, limited thermally-activated diffusive exchange between garnet and other phases would be possible. Major elements such as Fe, Mg, and to a lesser extent, Ca, would be expected to diffuse readily, given their mobility in garnet at high temperatures (Carlson, 2006). In our models, the bulk compositions typically become progressively depleted in these elements as garnet is removed from the effective bulk composition (e.g., Lanari and Engi, 2017) with increasing temperature, particularly along the 500 °C/GPa gradient, which is predicted to produce the most garnet. This affects the *P–T* stability fields of other minerals that require these elements. For example, the 500 °C/GPa gradient for DAT and EAT intersects the plagioclase stability field in the closed-system and melt loss scenarios, but not in the garnet fractionation model. Therefore, in the garnet fractionation scenario, the plagioclase content of the residue may be underestimated and the Sr concentration of the melt may be overestimated. In addition, although trivalent cations (Y, HREE) in garnet diffuse about an order of magnitude slower than divalent cations (Carlson, 2012), these elements may not remain completely sequestered in the cores depending on the temperature, duration of heating, and size of the garnet. This would cause melt concentrations of the trace elements enriched in garnet—Y and Yb—to

be higher and Sr/Y and La_N/Yb_N ratios of melt to be lower. This may be particularly important in Archean cratons that remained at high temperatures for long durations (e.g. Kelly and Harley, 2005, Moser et al., 2008, Gardiner et al., 2019). Thus, our garnet fractionation model is likely an endmember representation of the natural process.

An important difference between the modelled melts and natural TTGs is that the models produce melt compositions in equilibrium with the residue in the source metamorphic rock, with no consideration of the processes that would modify the composition of the melt during extraction from the source, magma ascent, and emplacement. One potentially important process is the entrainment and subsequent dissolution of peritectic minerals in the melt during ascent. Evidence for peritectic garnet entrainment has been identified in natural felsic igneous rocks (Stevens et al., 2007, Taylor and Stevens, 2010), and the result of this would be a new melt composition that falls on a mixing line between the garnet and initial melt compositions (Moyen et al., 2009). This process could have a significant effect on the concentrations of trace elements in the melt, as dissolution of garnet would add Y and Yb, thereby lowering the Sr/Y and La_N/Yb_N ratios. Furthermore, any rutile inclusions within the entrained garnet could also break down, contributing Nb and Ta to the melt. Another potentially important process is mixing of the melts with other contemporaneous melts from different sources, such as the mantle or possibly heterogenous lower crust. The effect of magma mixing on trace element concentrations would vary depending on the source and degree of fractionation of the contaminating magma. Fractional crystallisation of minerals out of migrating melt that feeds TTG plutons has the potential to affect trace element content; however, the effect may be small. The relative timing of crystal fractionation of different minerals is crucial, and investigations of tonalite melting by thermodynamic modelling (Holland et al., 2018) and experiments (Stern et al., 1975, Schmidt and Thompson, 1996) have shown that plagioclase, hornblende, and possibly clinopyroxene are likely to be the most significant early (T > 900 °C) fractionating phases at pressures below 1.0 GPa. At higher pressures, melting experiments (Schmidt and Thompson, 1996) show that epidote and garnet may become more important, with garnet stable at a minimum pressure of approximately 1.4 GPa. Fractionation of plagioclase would cause a depletion of Sr, fractionation of epidote would remove Sr, Y and REEs (preferentially LREEs), and fractionation of garnet would reduce the concentrations of Y and HREE in the melt. However, fractionation modelling of tonalitic melts (Moyen et al., 2009) has indicated that changes to Sr and Y due to hornblende, epidote, and garnet fractionation would be minor, as the relatively low concentrations of FeO and MgO in the melt would inhibit significant production of these minerals. Furthermore, geochemical trends in suites of granitoid rocks commonly cannot be attributed to fractionation alone (Clemens et al., 2009), and

separation of relatively low-density silicate minerals from high-viscosity, silica-rich melts may be difficult (Glazner, 2014; Clemens, 2015).

2.4.2 Comparison of modelled melts to natural TTGs

In some scenarios modelled here, the trace element compositions of the melts match the range of the compositional groups of natural TTGs as defined by Moyen (2011) and the compilation of TTG geochemical data of Johnson et al. (2019), although there are some inconsistencies (Fig. 2.11). The Sr/Y and La_N/Yb_N ratios of melts from the closed-system models are shown in comparison to the high-pressure, medium-pressure, and low-pressure TTG groups as defined by Moyen (2011) (Fig. 2.11). The compositional differences that define the groups are considered to signify the different depths, or pressures, of melting, with low pressure representing 1.0–1.2 GPa, medium pressure representing approximately 1.5 GPa, and high pressure representing ≥2.0 GPa (Moyen, 2011). Notably, the pressures that Moyen (2011) assigned to these groups are based on the stabilities of plagioclase, garnet, and rutile observed during melting experiments of basalts (Moyen and Stevens, 2006); calculating the stability fields of these minerals by phase equilibrium modelling has produced different results (e.g. Palin et al., 2016a, Palin et al., 2016b, Johnson et al., 2017). The TTG groups are generally distinguished by Sr/Y and La_N/Yb_N, which are inferred to be higher for TTGs generated at higher pressures (Moyen, 2011). Overall, this trend is replicated in the models (Fig. 2.8, Fig. 2.9), with Sr/Y and La_N/Yb_N of the melts increasing with increasing *P*–*T* and reaching the highest values along the 500 °C/GPa gradient, which corresponds to the highest pressures. Most of the results from the 1000 °C/GPa gradient have lower Sr/Y and La_N/Yb_N than the low-pressure TTG group, with a few exceptions from EAT and MAB. Melts modelled along the 750 °C/GPa gradient plot within both the low-pressure and medium-pressure composition ranges, with those within the latter group generally corresponding to higher pressures. Finally, the 500 °C/GPa modelled melt compositions are most consistent with the medium-pressure group, with the highest Sr/Y and La_N/Yb_N melts for all bulk compositions reaching values in the overlap between medium-pressure and high-pressure TTGs. Notably, melts with the maximum Sr/Y and La_N/Yb_N are not produced at the maximum pressure considered in the model, which reflects the influence of temperature on garnet and plagioclase modal proportions (Fig. 2.3, Fig. 2.7). The compositions of melts produced in the melt loss model are similar to the compositions measured of the different TTG groups, though with slightly lower Sr/Y and slightly higher La_N/Yb_N (Fig. 2.8, Fig. 2.9d–f). However, in the garnet fractionation model, some melts produced at elevated *P*–*T* conditions have Sr/Y and La_N/Yb_N higher than all natural TTGs. The TTG groups of Moyen (2011) were not designed to encompass the compositions of all natural TTGs,

and therefore the maximum Sr/Y of approximately 300 and La_N/Yb_N of approximately 200 for the high-pressure group are exceeded by a small percentage of the TTGs in the Johnson et al. (2019) compilation. Although the maximum modelled Sr/Y of melts from DAT and EAT of ~2200 and ~1500 respectively, produced along the 500 °C/GPa gradient, are higher than the highest Sr/Y (1166) of the natural samples, the order of magnitude is consistent (Fig. 2.8g and h). However, the maximum La_N/Yb_N of the modelled melt is one (MAB) to two (DAT and EAT) orders of magnitude greater (Fig. 2.9g–i) than the highest La_N/Yb_N in the compilation of Johnson et al. (2019) of 527. Similarly, modelled melts from DAT and EAT in the garnet fractionation scenario along the high *P*–*T* portion of the 750 °C/GPa gradient have maximum Sr/Y consistent with the high-pressure group of TTGs (Fig. 2.8g and h), and maximum La_N/Yb_N an order of magnitude greater than natural TTGs (Fig. 2.9g and h). Thus, our garnet fractionation model may somewhat overestimate Sr/Y and greatly overestimate La_N/Yb_N relative to nature. The reason is apparent in the concentrations of these elements in modelled melts from the 500 °C/GPa gradient, which are generally in agreement with data from TTGs, except for the very low Y and Yb predicted in the garnet fractionation scenario (Fig. 2.11c and d). This suggests that diffusion of these elements out of the garnet cores and entrainment of peritectic garnet within natural melts may be common processes, resulting in increased concentrations of Y and Yb in natural melts relative to our models.

The Nb and Ta systematics of the modelled melts from the closed-system scenario are shown in comparison to the TTG groups and natural data (Fig. 2.11b). The groups are relatively well-defined by their Nb and Ta concentrations, which decrease with increasing pressure (Moyen, 2011). Although the Nb/Ta ratio of the modelled melts is consistent with observations from TTGs, their Nb and Ta concentrations do not show the same trend with increasing pressure as the TTG groups. All modelled melts from the three *P*–*T* gradients for MAB plot within the high-pressure group, despite being produced at a range of pressures from 0.75 GPa to 2.1 GPa. In contrast, all of the concentrations of Nb and Ta in modelled melts from EAT are higher than any of the TTG groups, whereas melts from DAT overlap with the medium and low-pressure groups. For each bulk composition, the different *P*–*T* gradients do not produce significantly different results. Given that each gradient corresponds to a different range of pressures, this indicates that pressure is not the main control on concentrations of Nb and Ta in the modelled melts. This is consistent with the stability of rutile in the models: although rutile becomes stable at high pressures, its modal proportions (Fig. 2.3) are controlled by the temperature-dependent breakdown of hornblende, the only other stable Ti-bearing phase in the rutile stability field. Therefore, changes in source bulk composition contribute to the greatest variety in Nb and Ta in the models. However, when compared to the natural TTG data, most modelled melts from

EAT and some from DAT have Nb and Ta concentrations that exceed the observed range. Given that rutile proportions are likely overestimated in the models (see section 2.4.1), which should result in an underestimation of Nb and Ta in the melt, this result may be indicative of the importance of rutile sequestration in natural systems. However, a more likely explanation is that the Nb and Ta concentrations assigned to EAT and DAT due to unavailable data (see section 2.2.1) are not representative of the average depleted or enriched Archean tholeiite; high-Nb basalts (such as the Coucal basalts, considered here to be analogous to EAT) may have been scarce. Although the concentrations of Nb and Ta in the modelled melts may not be realistic, the trends outlined above are independent of this and are therefore more meaningful.

2.4.3 Implications for interpreting TTG trace element systematics

2.4.3.1 The role of bulk composition

The mafic bulk compositions modelled here as TTG sources yield melts of different major and trace element compositions. In terms of major elements (Fig. 2.5), DAT produces melts with normative feldspar compositions most comparable with natural TTGs, whereas the modelled melts of EAT are comparable only at high temperatures. Melts produced by MAB have the poorest match with natural TTGs. The EAT and MAB compositions produce some melts with higher normative orthoclase content than typical TTGs, which may result from the higher K_2O/N_2O of these sources compared to DAT (Table 2.1). However, these melts are generally produced by a low degree of partial melting at low temperature. At proportions less than 7 mol% in a static system (Rosenberg and Handy, 2005), and potentially lower in a system undergoing syn-anatectic deformation (Brown, 2013), melt may not form a connected network along grain boundaries to allow extraction from the source. For each of the thermal gradients—500 °C/GPa, 750 °C/GPa, and 1000 °C/GPa—melt reaches 7 mol% at ~750 °C, ~820 °C, and ~830 °C for EAT and ~880 °C, ~900 °C, and ~880 °C for MAB. Therefore, some of the melts with high normative orthoclase would not be expected to be preserved in the geological record. Most of the melts produced by MAB at high temperatures along the 750 °C/GPa and 1000 °C/GPa gradients have a higher normative anorthite content than natural TTGs. Given that MAB has a similar wt.% CaO to DAT and EAT (Fig. 2.1), these melt compositions may reflect the relatively low Na_2O concentration of MAB (Table 2.1). Overall, the different mafic source compositions produce a range of melt compositions in terms of normative albite, anorthite, and orthoclase (Fig. 2.5), which may be controlled by the K_2O and Na_2O concentrations of the sources.

The trace element compositions of the melts are predicted by the models to be affected both by differences in the concentration of trace elements in the source and the residue mineral assemblage. The high concentration of La in EAT allows the melts to reach higher La_N/Yb_N and higher concentrations of La in melt than the other bulk compositions (Fig. 2.11d), suggesting that a LREE-enriched source is likely necessary to produce the most LREE-enriched natural TTGs (cf. Moyen and Martin, 2012); the same may also be true for Sr and Y (Fig. 2.11c). However, despite their relative depletion in La, Yb, Sr, and Y, DAT and MAB generate melts with concentrations of these elements comparable to TTGs (Fig. 2.11c and d). The Nb and Ta systematics of modelled melts are strongly controlled by the concentrations of Nb and Ta in the source, though this effect may be exaggerated by the large range of source Nb and Ta selected for this study. The reduced garnet stability field in the MAB composition relative to DAT and EAT in the *P–T* range of interest has a significant effect on Sr/Y and La_N/Yb_N of the melt in the garnet fractionation scenario. The maximum Sr/Y and La_N/Yb_N of melts produced by MAB, which are associated with the 500 °C/GPa gradient, are an order of magnitude less than those of DAT and EAT. Additionally, with garnet fractionation, melts produced along the 750 °C/GPa gradient by DAT and EAT reach Sr/Y and La_N/Yb_N consistent with the high-pressure TTG group of Moyen (2011), whereas those of MAB remain relatively low. Although these values are likely overestimated in our models, this trend indicates that the effect of garnet fractionation is weaker for MAB as a result of lower modal proportions of garnet.

2.4.3.2 The role of open-system processes

Of the open-system processes investigated here, melt loss and garnet fractionation, garnet fractionation potentially has the most significant consequences for the trace element composition of TTGs. The relatively small decrease in Sr/Y for DAT and EAT in the melt loss scenario can be attributed mainly to lower Sr concentrations due to the increased stability of plagioclase to higher *P–T* (Fig. 2.4). In contrast, the increased Sr/Y for melts produced by MAB and La_N/Yb_N of the modelled melts for all bulk compositions is the result of increased Sr and La melt concentrations likely caused by the smaller proportions of melt present in the system. The relatively minor effect of melt loss can be linked to the moderate partition coefficients between the melt and residue (or bulk distribution coefficient) for the elements of interest compared to the large partition coefficients for Y and Yb for garnet. Removal of garnet from the model has a greater potential to affect the bulk concentration of these trace elements, particularly for *P–T* gradients predicted to have high modal proportions of garnet. Although garnet fractionation, as modelled here, is an extreme scenario, the trends obtained for Sr/Y and La_N/Yb_N suggest that a more subdued version of this process in nature may be important.

The closed-system scenario fails to produce melts with Sr/Y considered to be characteristic of TTGs produced at 2.0 GPa or greater, despite 2.1 GPa being the maximum pressure investigated for the 500 °C/GPa gradient. Furthermore, Sr/Y is predicted in the models to decrease after reaching a peak value at approximately 1.9 GPa, which is linked to the concave-up shape of garnet modal proportion contours in *P*–*T* space (Fig. 2.3)—the elevated ratios observed in natural TTGs would not be achieved by melting at higher pressures along this gradient. Therefore, our results suggest that garnet fractionation in the source may be needed to yield melts with Sr/Y ratios significantly greater than 200. In contrast, the La_N/Yb_N ratios of modelled melts from the closed-system scenario cover the range of La_N/Yb_N represented by the three TTG groups of Moyen (2011). Owing to their high La concentrations, melts produced by EAT reproduce the high La_N/Yb_N expected of the medium- and high-pressure groups, whereas those of DAT and MAB do not. However, with garnet fractionation, it is conceivable that less LREE-enriched sources such as DAT and MAB could generate melts with elevated La_N/Yb_N (i.e., greater than 100). Another consequence of garnet fractionation is the potential for more temperature-dependent variation of Sr/Y and La_N/Yb_N ratios compared to the closed-system and melt loss scenarios. Given the moderate temperature dependence of garnet production predicted by the models (Fig. 2.3), garnet growth and Y and Yb fractionation away from the reactive bulk composition may occur by an isobaric temperature increase. The effect of this was described above in the results of the 500 °C/GPa and 750 °C/GPa gradients for DAT and EAT: at the same pressure, garnet fractionation caused Sr/Y and La_N/Yb_N to increase by one to two orders of magnitude from low to high temperature. This allowed Sr/Y and La_N/Yb_N at 1.4 GPa to exceed values expected for melts produced at $\geq$ 2.0 GPa.

2.4.4 Implications for linking TTG trace elements to depth of melting

Three geodynamic models have been proposed to explain the generation of TTGs in the Archean, and each implies melting of metabasites at different depths. The first scenario is reworking of thickened mafic crust, similar to modern oceanic plateaux, through processes unrelated to modern-style and horizontally-driven plate tectonics, which include mantle overturn, mantle plumes, and delamination of residual lower crust (Bédard, 2006, Bédard, 2018, Johnson et al., 2014, Sizova et al., 2015). The suggested thickness of Archean oceanic crust ranges from 25 km to 45 km based on the estimated degree of melting of the relatively hot Archean mantle (Herzberg et al., 2010, Herzberg and Rudnick, 2012), indicating a maximum depth of TTG generation of 45 km in this model. A second model invokes thickening of Archean mafic crust, which may be achieved in an arc environment (Nagel et al., 2012) or in a long-lived volcanic system driven by a mantle plume (Bédard et al., 2013). Melting

would therefore be possible at depths greater than 45 km—up to 60 km has been proposed (Bédard et al., 2013). The third scenario is melting of subducted mafic crust, a process that is inferred in modern subduction zones from the presence of adakites, which have geochemical characteristics indicative of melting of a garnet-bearing metabasite source (Drummond et al., 1996). Adakites have been proposed to be modern analogues of TTGs based on several geochemical similarities, leading to the interpretation that TTGs were produced by melting of subducted slabs (Drummond and Defant, 1990, Hastie et al., 2010). Given that mantle temperatures are inferred to have been higher in the Archean relative to modern Earth (Abbott et al., 1994, Herzberg et al., 2010), melting of subducting slabs may have been more common in the Archean (Moyen and Stevens, 2006). However, other workers oppose the slab melting model for TTG formation (e.g., Bédard, 2006) based on a lack of geochemical evidence for mantle interaction in many TTGs (Martin et al., 2005) and the potential for dehydration of the subducting slab before reaching solidus temperatures during hot subduction (Harry and Green, 1999). Our models cannot necessarily be used to test these hypotheses, given that we investigated only three Archean basalt compositions that may not fully encompass the source compositions expected for these different geodynamic environments. However, these scenarios are differentiated by the depth of melting, and our results have important implications for using particular geochemical characteristics of TTGs as proxies for pressure at the source.

In general, our modelled melt compositions from the lowest-pressure gradient, 1000 °C/GPa, are consistent with geochemical signatures attributed to low-pressure melting. These melts are produced in the models at pressures up to 1.0 GPa, which corresponds to a depth of ~34 km assuming overlying material is mafic with a density of 3000 kg/m^3. These melts are predicted to have low Sr/Y and La_N/Yb_N ratios in every scenario, consistent with or lower than the low-pressure group of TTGs of Moyen (2011), even for bulk compositions with a small proportion of stable garnet in this pressure range (DAT and EAT). Other basalt bulk compositions not represented here may stabilize garnet at lower pressures than our models; for instance, phase equilibrium modelling by Johnson et al. (2017) of a MgO-poor composition predicts garnet-present assemblages at pressures down to ~0.7 GPa, which is lower than the compositions modelled here (0.8–1.1 GPa; Fig. 2.3). Therefore, a range of Sr/Y and La_N/Yb_N ratios could be expected in melts produced along a 1000 °C/GPa thermal gradient, although modal proportions of garnet in the source would likely be too low to impart a high-pressure signature to the melt.

The modelled melt compositions from the 500 °C/GPa and 750 °C/GPa gradients suggest that distinguishing TTGs derived from melting at medium or high pressure may not be straightforward.

Although Sr/Y and La_N/Yb_N generally increase with increasing pressure along these thermal gradients, the influence of temperature on garnet modal proportions in the residue also plays a role. Along the linear *P*–*T* gradients modelled here, garnet modal proportions decrease with increasing *P*–*T* beyond 900 °C–950 °C (Fig. 2.3), suggesting that higher pressures of melting cannot be always equated with higher proportions of garnet. Fractionation of Y and Yb from the system by sequestration in garnet cores could produce melt with Sr/Y and La_N/Yb_N consistent with the high-pressure group of Moyen (2011) at moderate pressures and high temperatures. For instance, the modelled melts from DAT and EAT are predicted to have Sr/Y > 300 at ~1.4 GPa at > 1000 °C, corresponding to a depth of ~47 km assuming a crustal density of 3000 kg/m^3 (Fig. 2.8g and h; Table S1.2). By contrast, melts with Sr/Y > 300 are only possible for MAB in the garnet fractionation scenario at 1.9 GPa and 950 °C, or 65 km depth (Fig. 2.8i). Notably, MAB also produces melts that are the least consistent with natural TTGs in terms of normative feldspar composition, suggesting that this bulk composition may not be representative of typical TTG source rocks. Presumably, basalt compositions that may stabilize greater proportions of garnet, such as that modelled by Johnson et al. (2017), would be capable of producing melts with elevated Sr/Y and La_N/Yb_N at lower pressures than those modelled here considering garnet fractionation. The bulk composition of the melting metabasite evidently exerts a first order control on Sr/Y and La_N/Yb_N of the melt produced, and as this variable is typically unknown when investigating natural TTGs, this introduces uncertainty in assigning pressures or depths of melting to TTGs based on these geochemical characteristics. Similarly, we show that Nb and Ta concentrations of the melt are influenced by the concentrations of these elements in the source, with the potential to obscure the effect of Nb and Ta partitioning between melt and rutile at high pressure. Therefore, using these geochemical characteristics of TTGs to determine the depth of melting, and therefore their geodynamic setting, should be done with caution, and only in conjunction with other geological evidence.

The results of our modelling are consistent with the conclusions of Johnson et al. (2019) regarding the link between secular change in TTG compositions and the onset of plate tectonics on Earth. Based on their compilation of TTG geochemical data, Johnson et al. (2019) found that maximum Sr/Y and La_N/Yb_N values became greater with decreasing age, consistent with these rocks recording melting at greater depths due to the emergence of subduction with secular cooling of the mantle. Similarly, our modelling suggests that melting along a high d*T*/d*P* gradient, represented by 1000 °C/GPa, cannot reproduce this trend. Only the lower d*T*/d*P* gradients used in our modelling, 750 °C/GPa and 500 °C/GPa, can produce the higher maximum Sr/Y and La_N/Yb_N found in younger

TTGs, supporting the interpretation that these rocks could only be formed after cooling of the mantle allowed for melting of metabasites at greater depths, potentially by subduction.

2.5 Conclusions

Thermodynamic modelling of three Archean basalt compositions was coupled with trace element modelling to evaluate the effect of open-system processes during melting and source bulk composition on the Sr, Y, La, Yb, Nb, and Ta systematics of TTGs. The selected source compositions produce melts with a geochemical resemblance to natural TTGs in terms of normative feldspar composition, though many modelled melts of the MgO-enriched composition, MAB, are inconsistent with the natural record. Trace element modelling of melts from all sources produces trace element compositions consistent with TTGs that vary with source bulk composition and closed- vs. open-system behaviour. Concentrations of Sr, Y, La, Yb, Nb, and Ta in the melt reflect both the enrichment of these elements in the source and the stability fields and modal proportions of garnet, plagioclase, and rutile. The expected trends were observed: with increasing *P–T*, increasing proportions of garnet and rutile cause the concentrations of Y, Yb, Nb, and Ta to decrease in the melt, and decreasing proportions of plagioclase cause the concentration of Sr to increase in the melt. Consequently, Sr/Y and La_N/Yb_N generally increase with increasing *P–T* and show minor variations across the source compositions. The concentrations of Nb and Ta in the melt decrease with increasing rutile proportions but are also strongly controlled by the concentrations of Nb and Ta in the source. In the models, melt loss during anatexis has a relatively minor effect on melt trace element composition in comparison to garnet fractionation. In the latter scenario, Y and Yb are isolated from the melt, resulting in higher Sr/Y and La_N/Yb_N ratios relative to the other modelled scenarios. This allows the modelled melts to replicate the highest Sr/Y ratios of natural TTGs, which represent the high-pressure TTG group as defined by Moyen (2011). These high Sr/Y and La_N/Yb_N melts are produced at a range of *P* and *T*, rather than being restricted to $P \geq 2.0$ GPa (cf. Moyen, 2011).

The results of the modelling imply that geochemical parameters of TTGs commonly used as proxies for the pressure of melting may be sensitive to factors other than pressure, including the temperature of melting and the composition of the source, particularly with garnet fractionation. This, in turn, complicates the link between the composition of TTGs and their geodynamic setting, particularly when distinguishing ‘medium-pressure’ and ‘high-pressure’ melting. The trace element compositions of TTGs have traditionally been a key factor in determining the geodynamic processes that produced and reworked Archean continental crust. However, using this information in isolation

may be misleading, and a suite of geological evidence should be considered before reaching a conclusion.

2.6 References

Abbott, D., Drury, R., Smith, W.H.F., 1994. Flat to steep transition in subduction style. Geology 22, 937–940. https://doi.org/10.1130/0091-7613(1994)022<0937:FTSTIS>2.3.CO;2

Barker, F., 1979. Trondhjemite: definition, environment and hypotheses of origin. In: Barker, F. (Ed.), Trondhjemites, dacites, and related rocks. Amsterdam, Elsevier. Developments in Petrology 6, 1–12.

Bédard, J.H., 2006. A catalytic delamination-driven model for coupled genesis of Archaean crust and sub-continental lithospheric mantle. Geochimica et Cosmochimica Acta 70, 1188–1214. https://doi.org/10.1016/j.gca.2005.11.008

Bédard, J.H., 2018. Stagnant lids and mantle overturns: implications for Archaean tectonics, magmagenesis, crustal growth, mantle evolution, and the start of plate tectonics. Geoscience Frontiers 9, 19–49. https://doi.org/10.1016/j.gsf.2017.01.005

Bédard, J.H., Harris, L.B., Thurston, P.C., 2013. The hunting of the snArc. Precambrian Research 229, 20–48. https://doi.org/10.1007/s00145-016-9241-9

Blundy, J., Wood, B., 2003. Partitioning of trace elements between crystals and melts. Earth and Planetary Science Letters 210, 383–397. https://doi.org/10.1016/S0012-821X(03)00129-8

Boger, S.D., White, R.W., Schulte, B., 2012. The importance of iron speciation (Fe+2/Fe+3) in determining mineral assemblages: an example from the high-grade aluminous metapelites of southeastern Madagascar. Journal of Metamorphic Geology 30, 997–1018. https://doi.org/10.1111/jmg.12001

Brown, M., 2013. Granite: from genesis to emplacement. GSA Bulletin 125, 1079–1113. https://doi.org/10.1130/B30877.1

Brown, M., Johnson, T., 2018. Secular change in metamorphism and the onset of global plate tectonics. American Mineralogist 103, 181–196. https://doi.org/10.2138/am-2018-6166

Carlson, W.D., 2006. Rates of Fe, Mg, Mn, and Ca diffusion in garnet. American Mineralogist 91, 1–11. https://doi.org/10.2138/am.2006.2043

Carlson, W.D., 2012. Rates and mechanism of Y, REE, and Cr diffusion in garnet. American Mineralogist 97, 1598–1618. https://doi.org/10.2138/am.2012.4108

Clemens, J.D., 2015. Magmatic life at low Reynolds number: Comment. Geology 43, e357. https://doi.org/10.1130/G36512C.1

Clemens, J.D., Helps, P.A., Stevens, G., 2009. Chemical structure in granitic magmas - a signal from the source? Transactions of the Royal Society of Edinburgh-Earth Sciences 100, 159–172. https://doi.org/10.1017/S1755691009016053

Condie, K.C., 1981. Archean greenstone belts. Developments in Precambrian Geology. vol 3. Elsevier, New York.

Condie, K.C., 1985. Secular variation in the composition of basalts: an index to mantle evolution. Journal of Petrology 26, 545–563.

Condie, K.C., 2018. A planet in transition: the onset of plate tectonics on Earth between 3 and 2 Ga? Geoscience Frontiers 9, 51–60. https://doi.org/10.1016/j.gsf.2016.09.001

Condie, K.C., Aster, R.C., Van Hunen, J., 2016. A great thermal divergence in the mantle beginning 2.5 Ga: geochemical constraints from greenstone basalts and komatiites. Geoscience Frontiers 7, 543–553. https://doi.org/10.1016/j.gsf.2016.01.006

Drummond, M.S., Defant, M.J., 1990. A model for trondhjemite-tonalite-dacite genesis and crustal growth via slab melting: Archean to modern comparisons. Journal of Geophysical Research 95, 21,503–21,521.

Drummond, M.S., Defant, M.J., Kepezhinskas, P.K., 1996. Petrogenesis of slab-derived trondhjemite-tonalite-dacite/adakite magmas. Transactions of the Royal Society of Edinburgh-Earth Sciences 87, 205–215.

Evans, T.P., 2004. A method for calculating effective bulk composition modification due to crystal fractionation in garnet-bearing schist: implications for isopleth thermobarometry. Journal of Metamorphic Geology 22, 547–557. https://doi.org/10.1111/j.1525-1314.2004.00532.x

Forshaw, J.B., Waters, D.J., Pattison, D.R.M., Palin, R.M., Gopon, P., 2019. A comparison of observed and thermodynamically predicted phase equilibria and mineral compositions in mafic granulites. Journal of Metamorphic Geology 37, 153–179. https://doi.org/10.1111/jmg.12454

Gaidies, F., de Capitani, C., Abart, R., 2008. THERIA_G: a software program to numerically model prograde garnet growth. Contributions to Mineralogy and Petrology 155, 657–671. https://doi.org/10.1007/s00410-007-0263-z

Gardiner, N.J., Johnson, T.E., Kirkland, C.L., Smithies, R.H., 2018. Melting controls on the lutetium–hafnium evolution of Archaean crust. Precambrian Research 305, 479–488. https://doi.org/10.1016/j.precamres.2017.12.026

Gardiner, N.J., Kirkland, C.L., Hollis, J., Szilas, K., Steenfelt, A., Yakymchuk, C., Heide-Jørgensen, H., 2019. Building Mesoarchaean crust upon Eoarchaean roots: the Akia Terrane, West Greenland. Contributions to Mineralogy and Petrology 174, 20. https://doi.org/10.1007/s00410-019-1554-x

Glazner, A.F., 2014. Magmatic life at low Reynolds number. Geology 42, 935–938. https://doi.org/10.1130/G36078.1

Green, T.H., 1995. Significance of Nb/Ta as an indicator of geochemical processes in the crust-mantle system. Chemical Geology 120, 347–359. https://doi.org/10.1016/0009-2541(94)00145-X

Green, E.C.R., White, R.W., Diener, J.F.A., Powell, R., Holland, T.J.B., Palin, R.M., 2016. Activity–composition relations for the calculation of partial melting equilibria in metabasic rocks. Journal of Metamorphic Geology 34, 845–869. https://doi.org/10.1111/jmg.12211

Hanson, G.N., 1978. The application of trace elements to the petrogenesis of igneous rocks of granitic composition. Earth and Planetary Science Letters 38, 26–43. https://doi.org/10.1016/0012-821X(78)90124-3

Harry, D.L., Green, N.L., 1999. Slab dehydration and basalt petrogenesis in subduction systems involving very young oceanic lithosphere. Chemical Geology 160, 309–333. https://doi.org/10.1016/S0009-2541(99)00105-9

Hastie, A.R., Kerr, A.C., McDonald, I., Mitchell, S.F., Pearce, J.A., Wolstencroft, M., Millar, I.L., 2010. Do Cenozoic analogues support a plate tectonic origin for Earth's earliest continental crust? Geology 38, 495–498. https://doi.org/10.1130/G30778.1

Herzberg, C., Rudnick, R., 2012. Formation of cratonic lithosphere: an integrated thermal and petrological model. Lithos 149, 4–15. https://doi.org/10.1016/j.lithos.2012.01.010

Herzberg, C., Condie, K., Korenaga, J., 2010. Thermal history of the Earth and its petrological expression. Earth and Planetary Science Letters 292, 79–88. https://doi.org/10.1016/j.epsl.2010.01.022

Holland, T., Powell, R., 2003. Activity-compositions relations for phases in petrological calculations: an asymmetric multicomponent formulation. Contributions to Mineralogy and Petrology 145, 492–501. https://doi.org/10.1007/s00410-003-0464-z

Holland, T.J.B., Powell, R., 2011. An improved and extended internally consistent thermodynamic dataset for phases of petrological interest, involving a new equation of state for solids. Journal of Metamorphic Geology 29, 333–383. https://doi.org/10.1111/j.1525-1314.2010.00923.x

Holland, T.J.B., Green, E.C.R., Powell, R., 2018. Melting of peridotites through to granites: a simple thermodynamic model in the system KNCFMASHTOCr. Journal of Petrology 59, 881–900. https://doi.org/10.1093/petrology/egy048

Hollings, P., 2002. Archean Nb-enriched basalts in the northern Superior Province. Lithos 64, 1–14. https://doi.org/10.1016/S0024-4937(02)00154-8

Hollings, P., Kerrich, R., 2000. An Archean arc basalt-Nb-enriched basalt-adakite association: the 2.7 Ga Confederation assemblage of the Birch-Uchi greenstone belt, Superior Province. Contributions to Mineralogy and Petrology 139, 208–226. https://doi.org/10.1007/PL00007672

Holness, M.B., Sawyer, E.W., 2008. On the pseudomorphing of melt-filled pores during the crystallization of migmatites. Journal of Petrology 49, 1343–1363. https://doi.org/10.1093/petrology/egn028

Jahn, B.-M., Glikson, A.Y., Peucat, J.J., Hickman, A.H., 1981. REE geochemistry and isotopic data of Archean silicic volcanics and granitoids from the Pilbara Block, Western Australia: implications for the early crustal evolution. Geochimica et Cosmochimica Acta 45, 1633–1652. https://doi.org/10.1016/S0016-7037(81)80002-6

Janoušek, V., Moyen, J.-F., 2019. Whole-rock geochemical modelling of granite genesis – the current state of play. Geological Society, London, Special Publications 491, 267–291. https://doi.org/10.1144/sp491-2018-160

Johnson, T.E., Brown, M., Gardiner, N.J., Kirkland, C.L., Smithies, R.H., 2017. Earth's first stable continents did not form by subduction. Nature 543, 239–242. https://doi.org/10.1038/nature21383

Johnson, T.E., Brown, M., Kaus, B.J.P., VanTongeren, J.A., 2014. Delamination and recycling of Archaean crust caused by gravitational instabilities. Nature Geoscience 7, 47–52. https://doi.org/10.1038/ngeo2019.

Johnson, T.E., Kirkland, C.L., Gardiner, N.J., Brown, M., Smithies, R.H., Santosh, M., 2019. Secular change in TTG compositions: implications for the evolution of Archaean geodynamics. Earth and Planetary Science Letters 505, 65–75. https://doi.org/10.1016/j.epsl.2018.10.022

Kelly, N.M., Harley, S.L., 2005. An integrated microtextural and chemical approach to zircon geochronology: refining the Archaean history of the Napier Complex, east Antarctica. Contributions to Mineralogy and Petrology 149, 57–84. https://doi.org/10.1007/s00410-004-0635-6

Lanari, P., Duesterhoeft, E., 2019. Modeling metamorphic rocks using equilibrium thermodynamics and internally consistent databases: past achievements, problems and perspectives. Journal of Petrology 60, 19–56. https://doi.org/10.1093/petrology/egy105

Lanari, P., Engi, M., 2017. Local bulk composition effects on metamorphic mineral assemblages. Reviews in Mineralogy and Geochemistry 83, 55–102. https://doi.org/10.2138/rmg.2017.83.3

Martin, H., 1986. Effect of steeper Archean geothermal gradient on geochemistry of subduction-zone magmas. Geology 14, 753–756. https://doi.org/10.1130/0091-7613(1986)14<753

Martin, H., Smithies, R.H., Rapp, R., Moyen, J.-F., Champion, D., 2005. An overview of adakite, tonalite–trondhjemite–granodiorite (TTG), and sanukitoid: relationships and some implications for crustal evolution. Lithos 79, 1–24. https://doi.org/10.1016/j.lithos.2004.04.048

Martin, H., Moyen, J.-F., Guitreau, M., Blichert-Toft, J., Le Pennec, J.-L., 2014. Why Archaean TTG cannot be generated by MORB melting in subduction zones. Lithos 198–199, 1–13. https://doi.org/10.1016/j.lithos.2014.02.017

Mayne, M.J., Moyen, J.-F., Stevens, G., Kaislaniemi, L., 2016. Rcrust: a tool for calculating path-dependent open system processes and application to melt loss. Journal of Metamorphic Geology 34, 663–682. https://doi.org/10.1111/jmg.12199

Mayne, M.J., Stevens, G., Moyen, J.-F., 2019. A phase equilibrium investigation of selected source controls on the composition of melt batches generated by sequential melting of an average metapelite. Geological Society, London, Special Publications 491, 223–241.

Moser, D.E., Bowman, J.R., Wooden, J., Valley, J.W., Mazdab, F., Kita, N., 2008. Creation of a continent recorded in zircon zoning. Geology 36, 239–242. https://doi.org/10.1130/G24416A.1

Moyen, J.-F., 2011. The composite Archaean grey gneisses: petrological significance, and evidence for a non-unique tectonic setting for Archaean crustal growth. Lithos 123, 21–36. https://doi.org/10.1016/j.lithos.2010.09.015

Moyen, J.-F., Champion, D., Smithies, R.H., 2009. The geochemistry of Archaean plagioclase-rich granites as a marker of source enrichment and depth of melting. Transactions of the Royal Society of Edinburgh-Earth Sciences 100, 35–50. https://doi.org/10.1017/S1755691009016132

Moyen, J.-F., Laurent, O., 2018. Archaean tectonic systems: a view from igneous rocks. Lithos 302–303, 99–125. https://doi.org/10.1016/j.lithos.2017.11.038

Moyen, J.-F., Martin, H., 2012. Forty years of TTG research. Lithos 148, 312–336. https://doi.org/10.1016/j.lithos.2012.06.010

Moyen, J.-F., Stevens, G., 2006. Experimental constraints on TTG petrogenesis: implications for Archean geodynamics. In: Benn, K., Mareschal, J.-C., Condie, K.C. (Eds.), Archean Geodynamics and Environments. AGU, pp. 149–178.

Nagel, T.J., Hoffmann, J.E., Münker, C., 2012. Generation of Eoarchean tonalite-trondhjemite-granodiorite series from thickened mafic arc crust. Geology 40, 375–378. https://doi.org/10.1130/G32729.1

Nicholls, I.A., Harris, K.L., 1980. Experimental rare earth element partition coefficients for garnet, clinopyroxene and amphibole coexisting with andesitic and basaltic liquids. Geochimica et Cosmochimica Acta 44, 287–308. https://doi.org/10.1016/0016-7037(80)90138-6

O'Connor, J.T., 1965. A classification for quartz-rich igneous rocks based on feldspar ratios. U.S. Geological Survey Professionnal Paper, 525, pp. 79–84.

Otamendi, J.E., de la Rosa, J.D., Patino Douce, A.E., Castro, A., 2002. Rayleigh fractionation of heavy rare earths and yttrium during metamorphic garnet growth. Geology 30, 159–162. https://doi.org/10.1130/0091-7613(2002)030<0159:RFOHRE>2.0.CO;2

Palin, R.M., Dyck, B., 2018. Metamorphic consequences of secular changes in oceanic crust composition and implications for uniformitarianism in the geological record. Geoscience Frontiers 9, 1009–1019. https://doi.org/10.1016/j.gsf.2018.04.004

Palin, R.M., Weller, O.M., Waters, D.J., Dyck, B., 2016a. Quantifying geological uncertainty in metamorphic phase equilibria modelling; a Monte Carlo assessment and implications for tectonic interpretations. Geoscience Frontiers 7, 591–607. https://doi.org/10.1016/j.gsf.2015.08.005

Palin, R.M., White, R.W., Green, E.C.R., 2016b. Partial melting of metabasic rocks and the generation of tonalitic–trondhjemitic–granodioritic (TTG) crust in the Archaean: constraints from phase equilibrium modelling. Precambrian Research 287, 73–90. https://doi.org/10.1016/j.precamres.2016.11.001

Pichavant, M., Montel, J.-M., Richard, L.R., 1992. Apatite solubility in peraluminous liquids: experimental data and an extension of the Harrison-Watson model. Geochimica et Cosmochimica Acta 56, 3855–3861. https://doi.org/10.1016/0016-7037(92)90178-L

Polat, A., Kerrich, R., 2001. Magnesian andesites, Nb-enriched basalt-andesites, and adakites from late-Archean 2.7 Ga Wawa greenstone belts, Superior Province, Canada: implications for late Archean subduction zone petrogenetic processes. Contributions to Mineralogy and Petrology 141, 36–52. https://doi.org/10.1007/s004100000223

Powell, R., Holland, T.J.B., 1988. An internally consistent dataset with uncertainties and correlations: 3. Applications to geobarometry, worked examples and a computer program. Journal of Metamorphic Geology 6, 173–204. https://doi.org/10.1111/j.1525-1314.1988.tb00415.x

Powell, R., Holland, T.J.B., 2008. On thermobarometry. Journal of Metamorphic Geology 26, 155–179. https://doi.org/10.1111/j.1525-1314.2007.00756.x

Presnall, D.C., 1969. The geometrical analysis of partial fusion. American Journal of Science 267, 1178–1194.

Pyle, J.M., Spear, F.S., 1999. Yttrium zoning in garnet: coupling of major and accessory phases during metamorphic reactions. Geological Materials Research 1, 1–49.

Qian, Q., Hermann, J., 2013. Partial melting of lower crust at 10-15 kbar: constraints on adakite and TTG formation. Contributions to Mineralogy and Petrology 165, 1195–1224. https://doi.org/10.1007/s00410-013-0854-9

Rapp, R.P., Watson, E.B., 1995. Dehydration melting of metabasalt at 8–32 kbar: implications for continental growth and crust-mantle recycling. Journal of Petrology 36, 891–931.

Rapp, R.P., Watson, E.B., Miller, C.F., 1991. Partial melting of amphibolite/eclogite and the origin of Archean trondhjemites and tonalites. Precambrian Research 51, 1–25.

Reichardt, H., Weinberg, R.F., 2012. Hornblende chemistry in meta- and diatexites and its retention in the source of leucogranites: an example from the Karakoram Shear Zone, NW India. Journal of Petrology 53, 1287–1318. https://doi.org/10.1093/petrology/egs017

Rosenberg, C.L., Handy, M.R., 2005. Experimental deformation of partially melted granite revisited: implications for the continental crust. Journal of Metamorphic Geology 23, 19–28. https://doi.org/10.1111/j.1525-1314.2005.00555.x

Ryerson, F.J., Watson, E.B., 1987. Rutile saturation in magmas: implications for Ti-Nb-Ta depletion in island-arc basalts. Earth and Planetary Science Letters 86, 225–239.

Sawyer, E.W., 1999. Criteria for the recognition of partial melting. Physics and Chemistry of the Earth 24, 269–279. https://doi.org/10.1016/S1464-1895(99)00029-0

Schmidt, M.W., Thompson, A.B., 1996. Epidote in calc-alkaline magmas: an experimental study of stability, phase relationships, and the role of epidote in magmatic evolution. American Mineralogist 81, 462–474. https://doi.org/10.2138/am-1996-3-420

Shaw, D.M., 1970. Trace element fractionation during anatexis. Geochimica et Cosmochimica Acta 34, 237–243. https://doi.org/10.1016/0016-7037(70)90009-8

Sizova, E., Gerya, T., Stüwe, K., Brown, M., 2015. Generation of felsic crust in the Archean: a geodynamic modeling perspective. Precambrian Research 271, 198–224. https://doi.org/10.1016/j.precamres.2015.10.005

Smithies, R.H., Champion, D.C., Van Kranendonk, M.J., 2009. Formation of Paleoarchean continental crust through infracrustal melting of enriched basalt. Earth and Planetary Science Letters 281, 298–306. https://doi.org/10.1016/j.epsl.2009.03.003

Smithies, R.H., Ivanic, T.J., Lowrey, J.R., Morris, P.A., Barnes, S.J., Wyche, S., Lu, Y.J., 2018. Two distinct origins for Archean greenstone belts. Earth and Planetary Science Letters 487, 106–116. https://doi.org/10.1016/j.epsl.2018.01.034

Spear, F.S., Kohn, M.J., 1996. Trace element zoning in garnet as a monitor of crustal melting. Geology 24, 1099–1102. https://doi.org/10.1130/0091-7613(1996)024<1099:teziga>2.3.co;2

Springer, W., Seck, H.A., 1997. Partial fusion of basic granulites at 5 to 15 kbar: implications for the origin of TTG magmas. Contributions to Mineralogy and Petrology 127, 30–45.

Stern, C.R., Huang, W.-L., Wyllie, P.J., 1975. Basalt-andesite-rhyolite-H_2O: crystallization intervals with excess H_2O and H_2O-undersaturated liquidus surfaces to 35 kilobars, with implications for magma genesis. Earth and Planetary Science Letters 28, 189–196. https://doi.org/10.1016/0012-821X(75)90226-5

Stevens, G., Villaros, A., Moyen, J.-F., 2007. Selective peritectic garnet entertainment as the origin of geochemical diversity in S-type granites. Geology 35, 9–12. https://doi.org/10.1130/G22959A.1

Stuck, T.J., Diener, J.F.A., 2018. Mineral equilibria constraints on open-system melting in metamafic compositions. Journal of Metamorphic Geology 36, 255–281. https://doi.org/10.1111/jmg.12292

Szilas, K., Van Hinsberg, V.J., Kisters, A.F.M., Hoffmann, J.E., Windley, B.F., Kokfelt, T.F., Scherstén, A., Frei, R., Rosing, M.T., Münker, C., 2013. Remnants of arc-related Mesoarchaean oceanic crust in the Tartoq Group of SW Greenland. Gondwana Research 23, 436–451. https://doi.org/10.1016/j.gr.2011.11.006

Taylor, J., Stevens, G., 2010. Selective entrainment of peritectic garnet into S-type granitic magmas: evidence from Archaean mid-crustal anatectites. Lithos 120, 277–292. https://doi.org/10.1016/j.lithos.2010.08.015

Watson, E.B., Capobianco, C.J., 1981. Phosphorus and the rare earth elements in felsic magmas: an assessment of the role of apatite. Geochimica et Cosmochimica Acta 45, 2349–2358.

Watson, E.B., Vicenzi, E.P., Rapp, R.P., 1989. Inclusion/host relations involving accessory minerals in high-grade metamorphic and anatectic rocks. Contributions to Mineralogy and Petrology 101, 220–231. https://doi.org/10.1007/BF00375308

White, R.W., Palin, R.M., Green, E.C.R., 2017. High-grade metamorphism and partial melting in Archean composite grey gneiss complexes. Journal of Metamorphic Geology 35, 181–195. https://doi.org/10.1111/jmg.12227

White, R.W., Pomroy, N.E., Powell, R., 2005. An in situ metatexite-diatexite transition in upper amphibolite facies rocks from Broken Hill, Australia. Journal of Metamorphic Geology 23, 579–602. https://doi.org/10.1111/j.1525-1314.2005.00597.x

White, R.W., Powell, R., 2002. Melt loss and the preservation of granulite facies mineral assemblages. Journal of Metamorphic Geology 20, 621–632. https://doi.org/10.1046/j.1525-1314.2002.00206.x

White, R.W., Powell, R., Halpin, J.A., 2004. Spatially-focussed melt formation in aluminous metapelites from Broken Hill, Australia. Journal of Metamorphic Geology 22, 825–845. https://doi.org/10.1111/j.1525-1314.2004.00553.x

White, R.W., Powell, R., Holland, T.J.B., Johnson, T.E., Green, E.C.R., 2014. New mineral activity-composition relations for thermodynamic calculations in metapelitic systems. Journal of Metamorphic Geology 32, 261–286. https://doi.org/10.1111/jmg.12071

Wickham, H., 2011. ggplot2. Wiley Interdisciplinary Reviews: Computational Statistics 3, pp. 180–185. https://doi.org/10.1002/wics.147

Wyman, D.A., Ayer, J.A., Devaney, J.R., 2000. Niobium-enriched basalts from the Wabigoon subprovince, Canada: evidence for adakitic metasomatism above an Archean subduction zone. Earth and Planetary Science Letters 179, 21–30. https://doi.org/10.1016/S0012-821X(00)00106-0

Yakymchuk, C., Brown, M., 2014. Consequences of open-system melting in tectonics. Journal of the Geological Society 171, 21–40. https://doi.org/10.1144/jgs2013-039

Yakymchuk, C., Brown, M., 2019. Divergent behaviour of Th and U during anatexis: implications for the thermal evolution of orogenic crust. Journal of Metamorphic Geology, accepted manuscript. https://doi.org/10.1111/jmg.12469

Yakymchuk, C., Zhao, W., Wan, Y., Lin, S., Longstaffe, F.J., 2019. Fluid-present anatexis of Neoarchean tonalite and amphibolite in the Western Shandong Province. Lithos 326–327, 110–124. https://doi.org/10.1016/j.lithos.2018.12.014

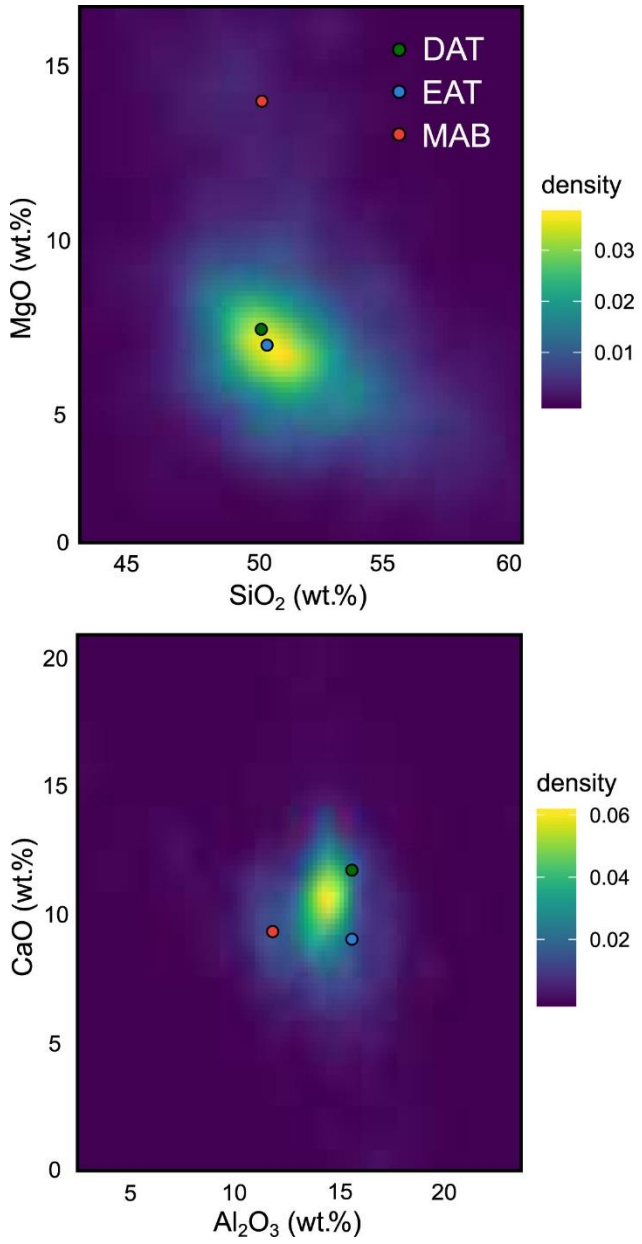


Fig. 2.1. Two-dimensional kernel density estimation of SiO_2 vs. MgO and Al_2O_3 vs. CaO from whole rock geochemical data in the Archean basalt compilation provided in Table S1.1. The plots were generated using the stat_density_2d function in the ggplot2 package (Wickham, 2011) available for the R programming language. DAT = depleted Archean tholeiite, EAT = enriched Archean tholeiite, MAB = MgO-rich Archean basalt.

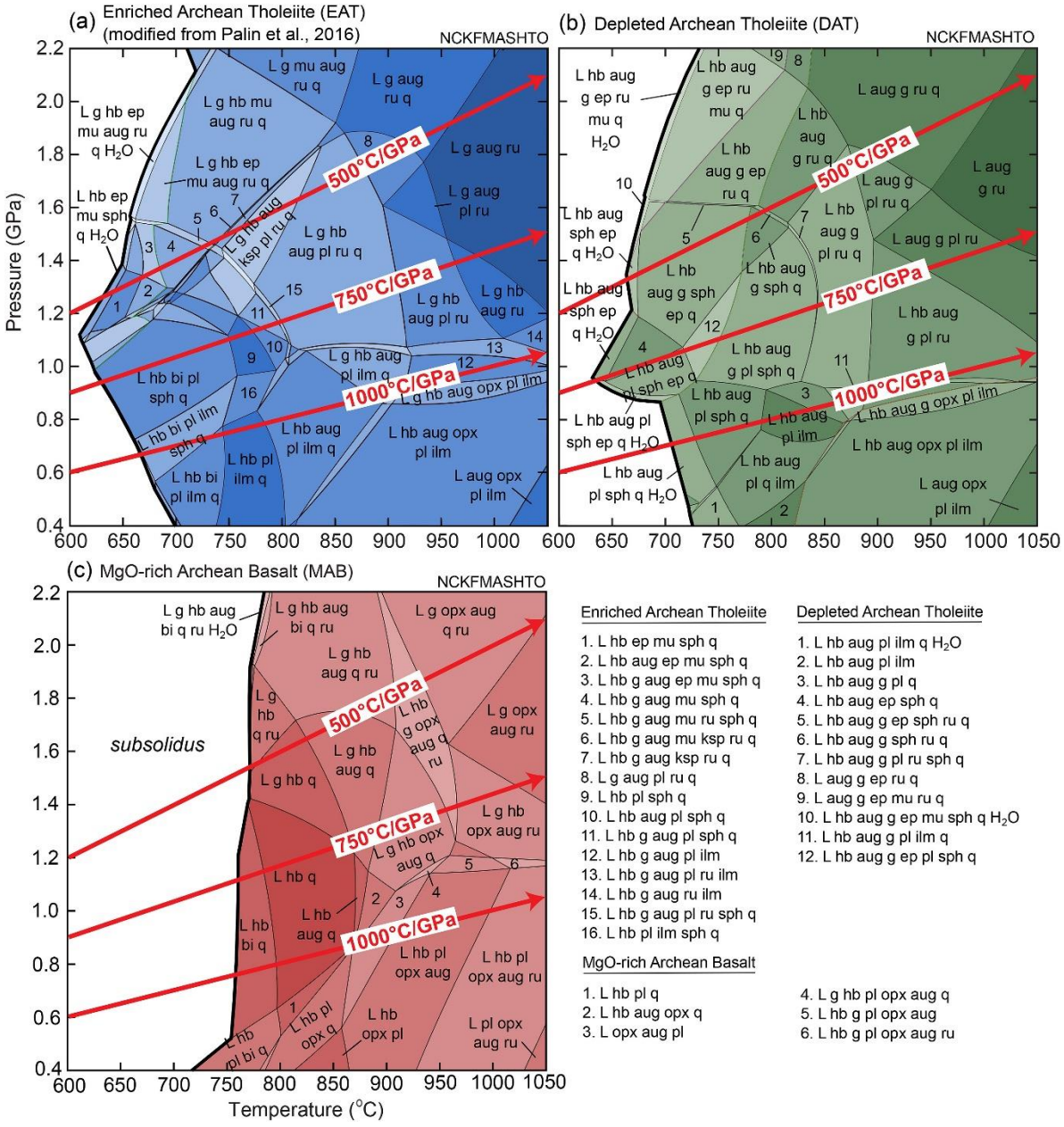


Fig. 2.2. *P–T* pseudosections for each of the modelled basalt compositions, the diagram for EAT has been modified from Palin et al. (2016b). The concentration of H_2O in each composition was selected to stabilize a minimal amount of free H_2O at the solidus at 1.2 GPa (Table 2.2). Phase abbreviations after Holland and Powell (2011).

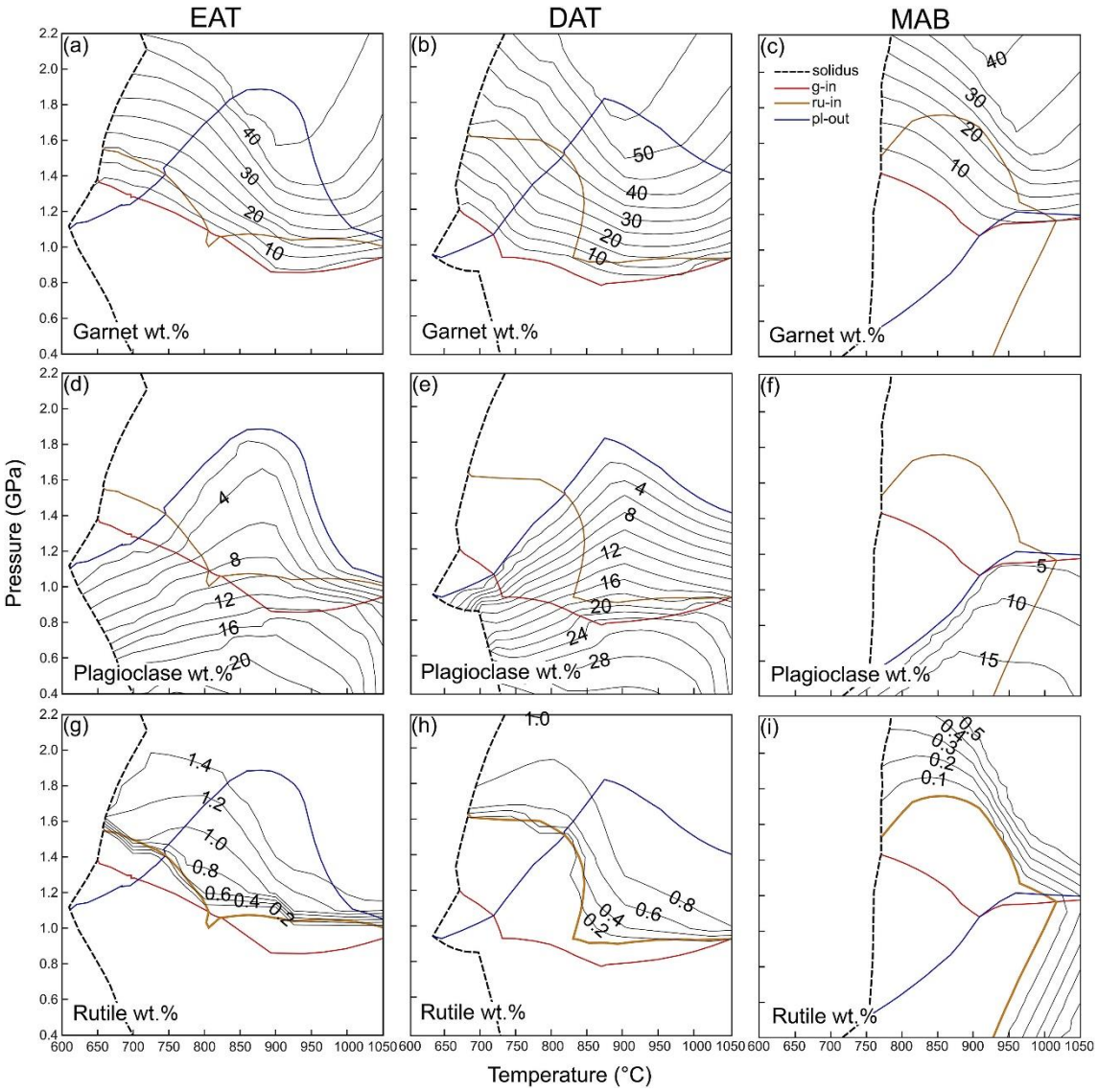


Fig. 2.3. *P–T* diagrams with contours of weight fractions of garnet, plagioclase, and rutile for the three compositions in Fig. 2.2. Note that some contours of rutile proportions appear slightly below the rutile-in boundary (g and h); this is an artifact of the lower resolution of the data used for contouring (increments of 25 °C and 0.1 GPa) compared with the higher resolution phase boundaries calculated using THERMOCALC (increments of 1–5 °C and 0.01–0.05 GPa). DAT = depleted Archean tholeiite, EAT = enriched Archean tholeiite, MAB = MgO-rich Archean basalt.

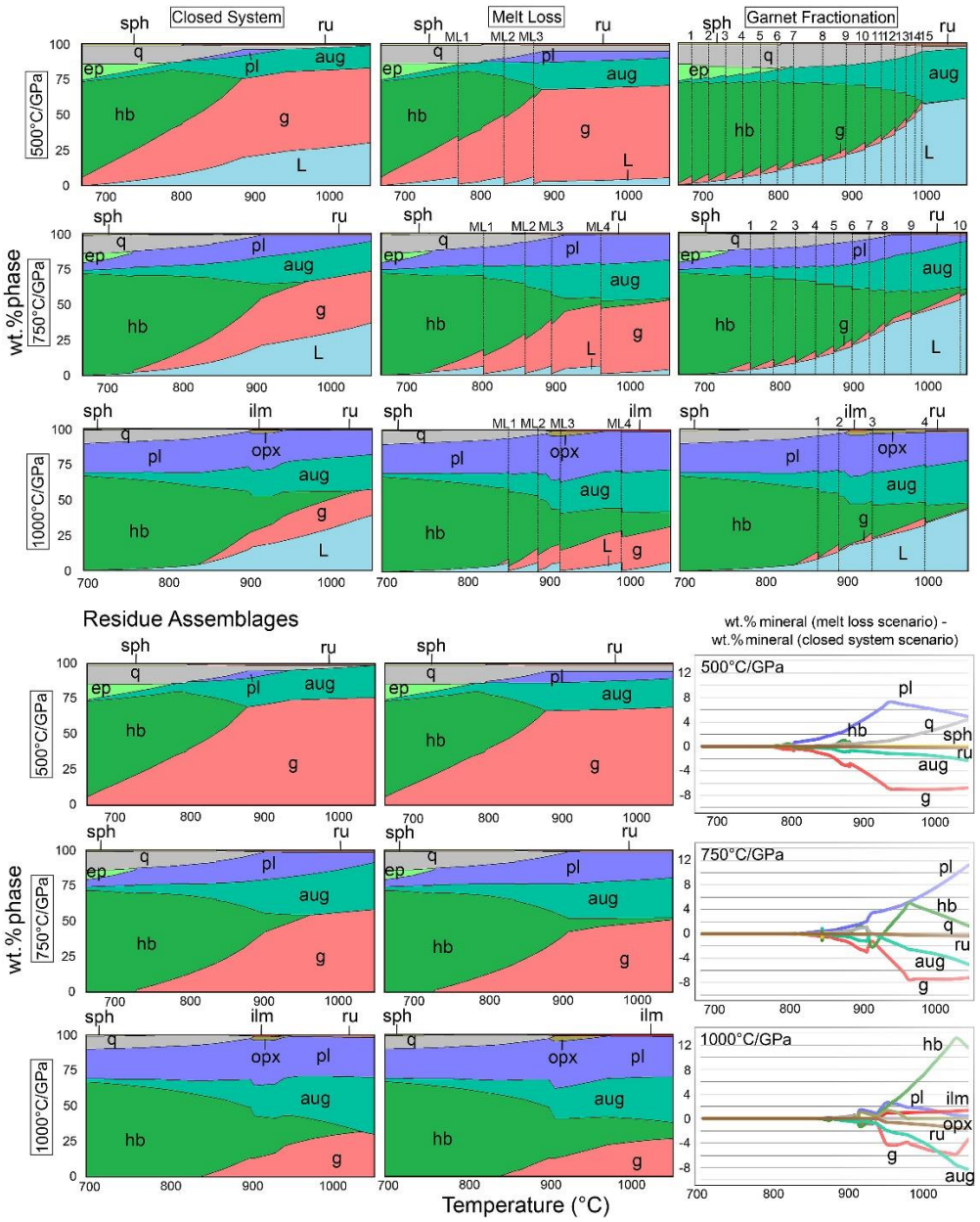


Fig. 2.4. Temperature–proportion diagrams illustrating the changes in phase weight proportions along the 500 °C/GPa, 750 °C/GPa, and 1000 °C/GPa thermal gradients in the closed system, melt loss, and garnet fractionation scenarios for the DAT (depleted Archean tholeiite) source composition (results for the other source compositions are provided in Fig. S1.1). Additional diagrams are shown excluding melt for the closed system and melt loss scenarios (lower half of figure) along with the relative changes in mineral proportions between the two scenarios (with melt excluded). Phase abbreviations after Holland and Powell (2011). Numbered labels on the melt loss and garnet fractionation diagrams (M1, M2, M3, 1, 2, 3, etc.) designate individual increments of melt or garnet extraction; the vertical dashed lines separate panels of different bulk composition resulting from each extraction.

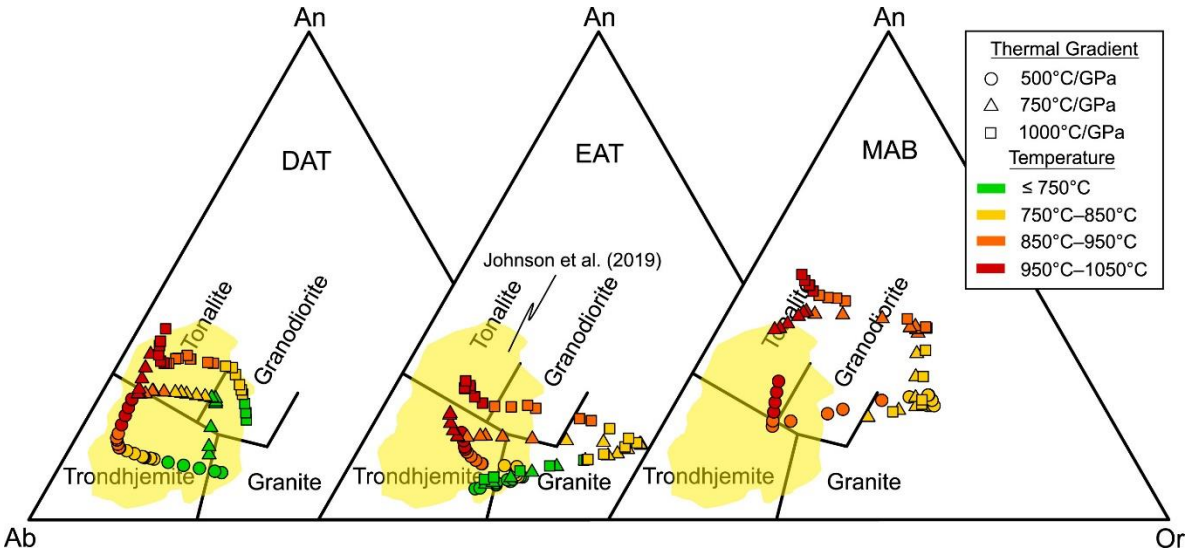


Fig. 2.5. Granitoid classification diagrams based on normative feldspar content after Barker (1979). Modelled melts from the closed system scenario are plotted for each source composition. Range of natural TTG compositions (after Johnson et al., 2019) is shown in yellow. DAT = depleted Archean tholeiite, EAT = enriched Archean tholeiite, MAB = MgO-rich Archean basalt, An = anorthite, Ab = albite, Or = orthoclase.

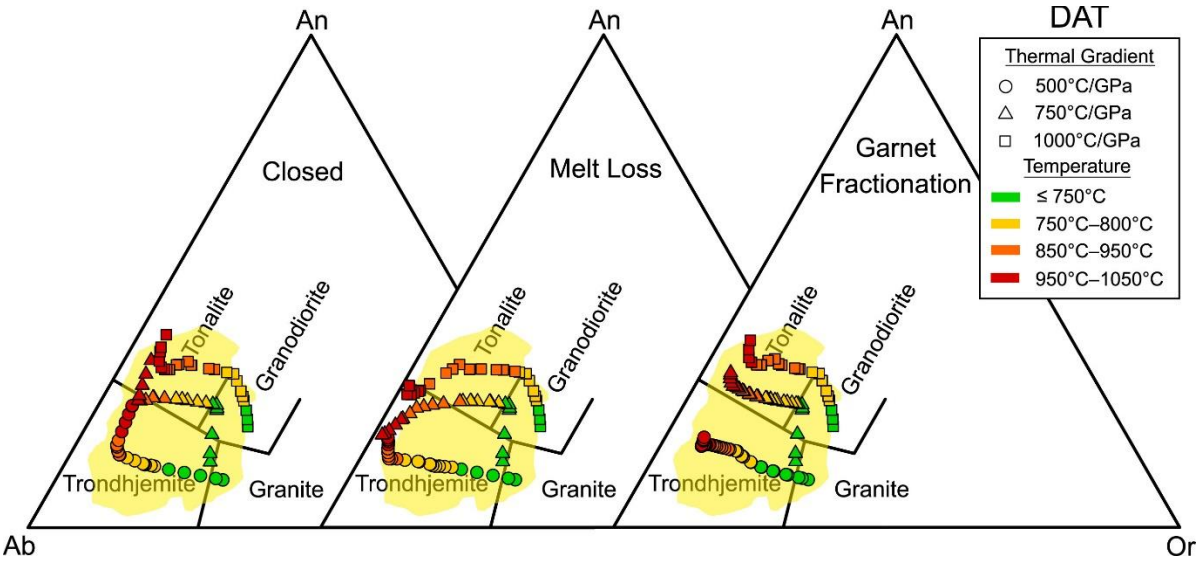


Fig. 2.6. Granitoid classification diagrams based on normative feldspar content after Barker (1979). Modelled melt compositions are plotted from the closed system, melt loss, and garnet fractionation scenarios for the DAT (depleted Archean tholeiite) bulk composition only. Range of natural TTG compositions (after Johnson et al., 2019) is shown in yellow. An = anorthite, Ab = albite, Or = orthoclase.

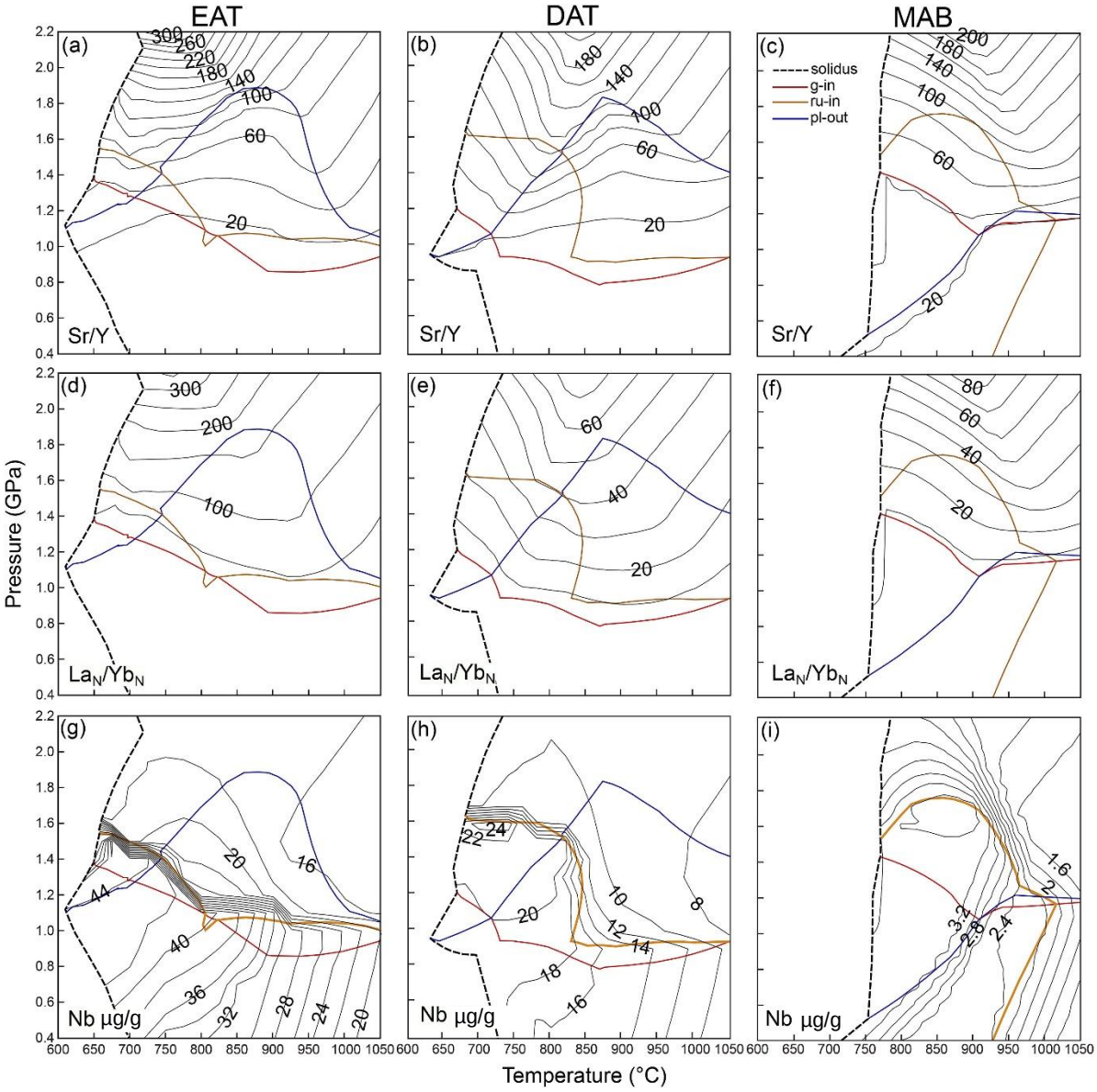


Fig. 2.7. *P–T* diagrams with contours of Sr/Y, La_N/Yb_N, and concentration of Nb (µg/g) in the melt. DAT = depleted Archean tholeiite, EAT = enriched Archean tholeiite, MAB = MgO-rich Archean basalt.

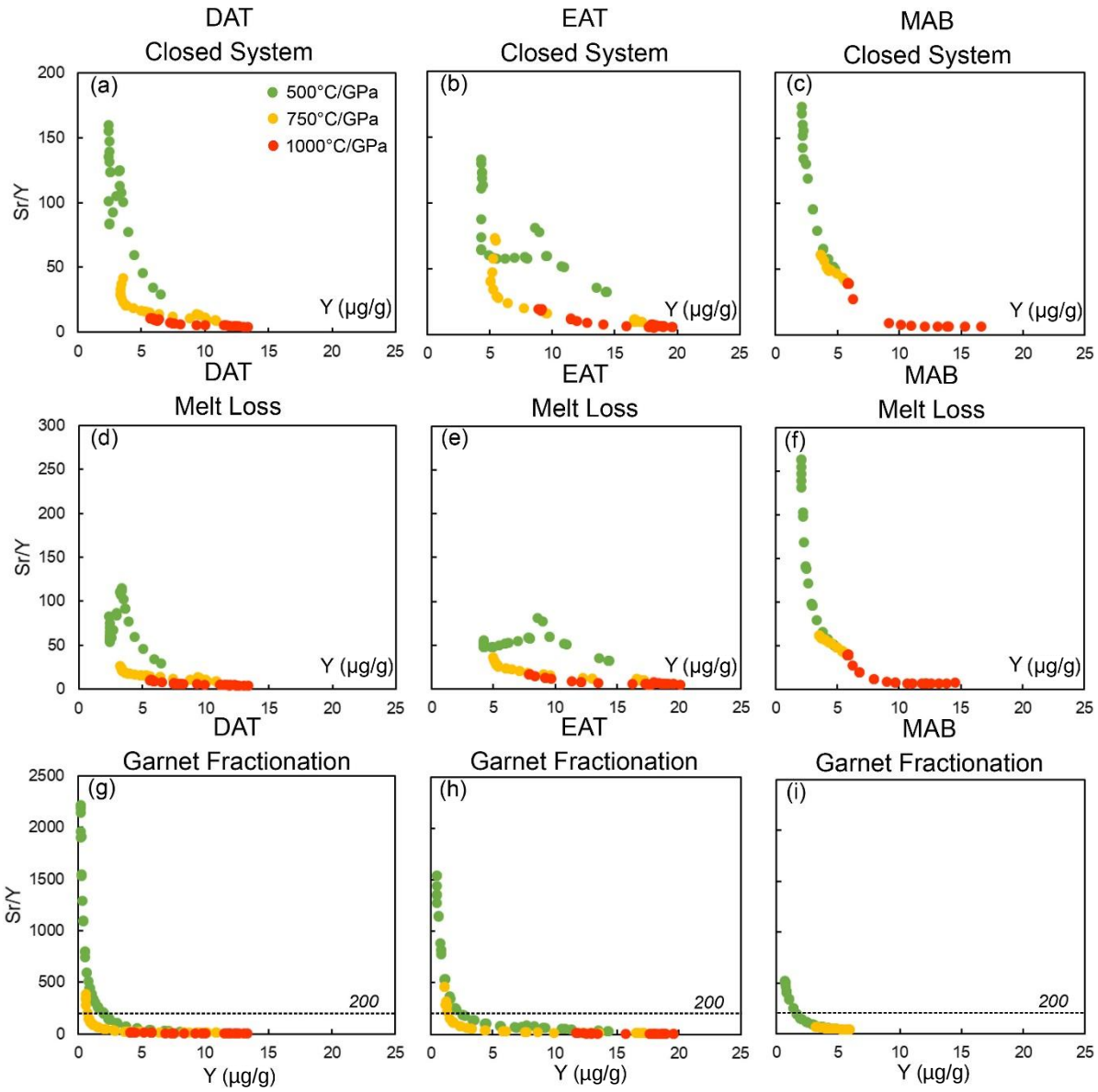


Fig. 2.8. Plots of Sr/Y vs. Y of modelled melts from each of the three compositions for each of the three scenarios. The garnet fractionation scenario was not modelled for the 1000 °C/GPa gradient for MAB due to lack of garnet. DAT = depleted Archean tholeiite, EAT = enriched Archean tholeiite, MAB = MgO-rich Archean basalt.

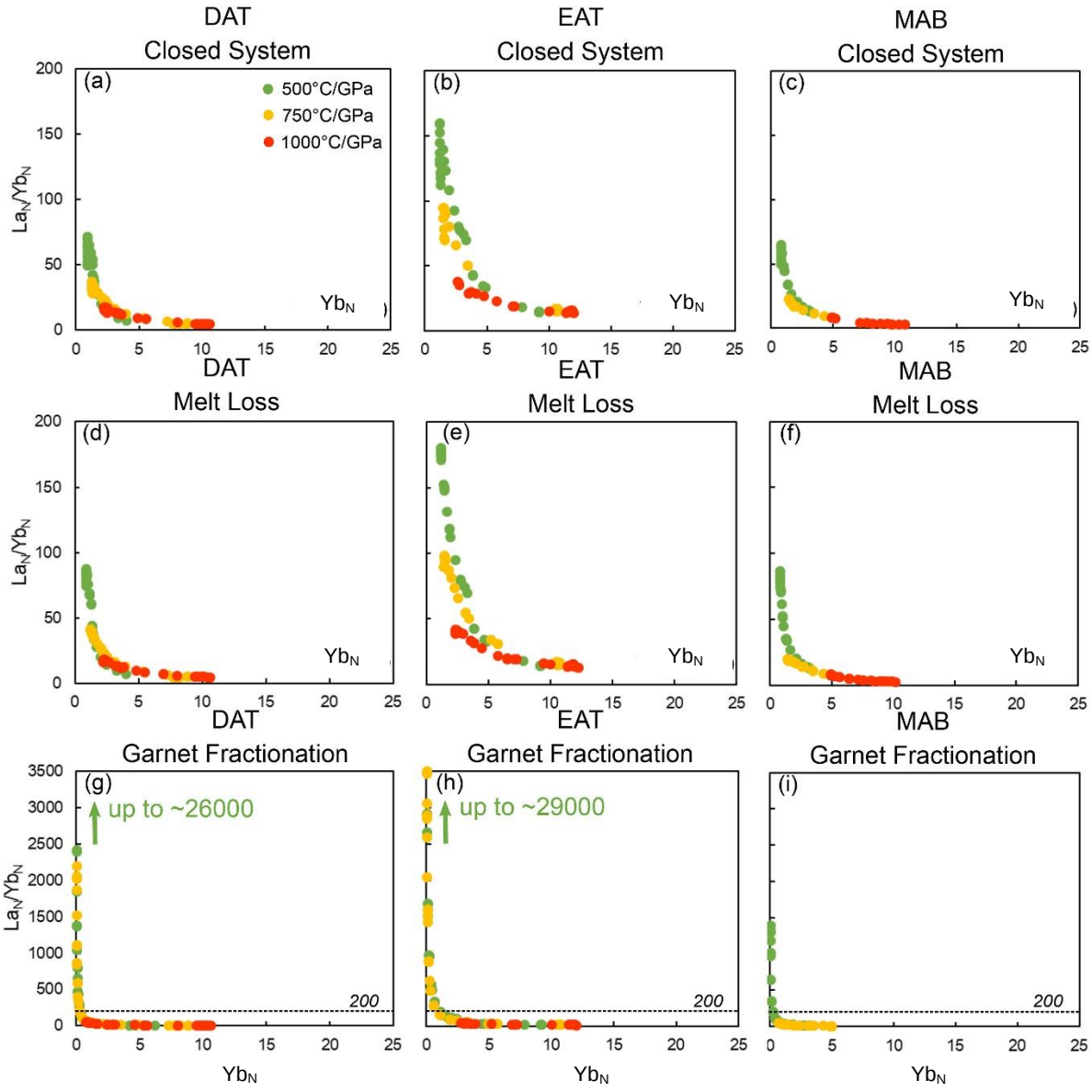


Fig. 2.9. Plots of La_N/Yb_N vs. Yb_N of modelled melts from each of the three compositions for each of the three scenarios. The garnet fractionation scenario was not modelled for the 1000 °C/GPa gradient for MAB due to lack of garnet. DAT = depleted Archean tholeiite, EAT = enriched Archean tholeiite, MAB = MgO-rich Archean basalt.

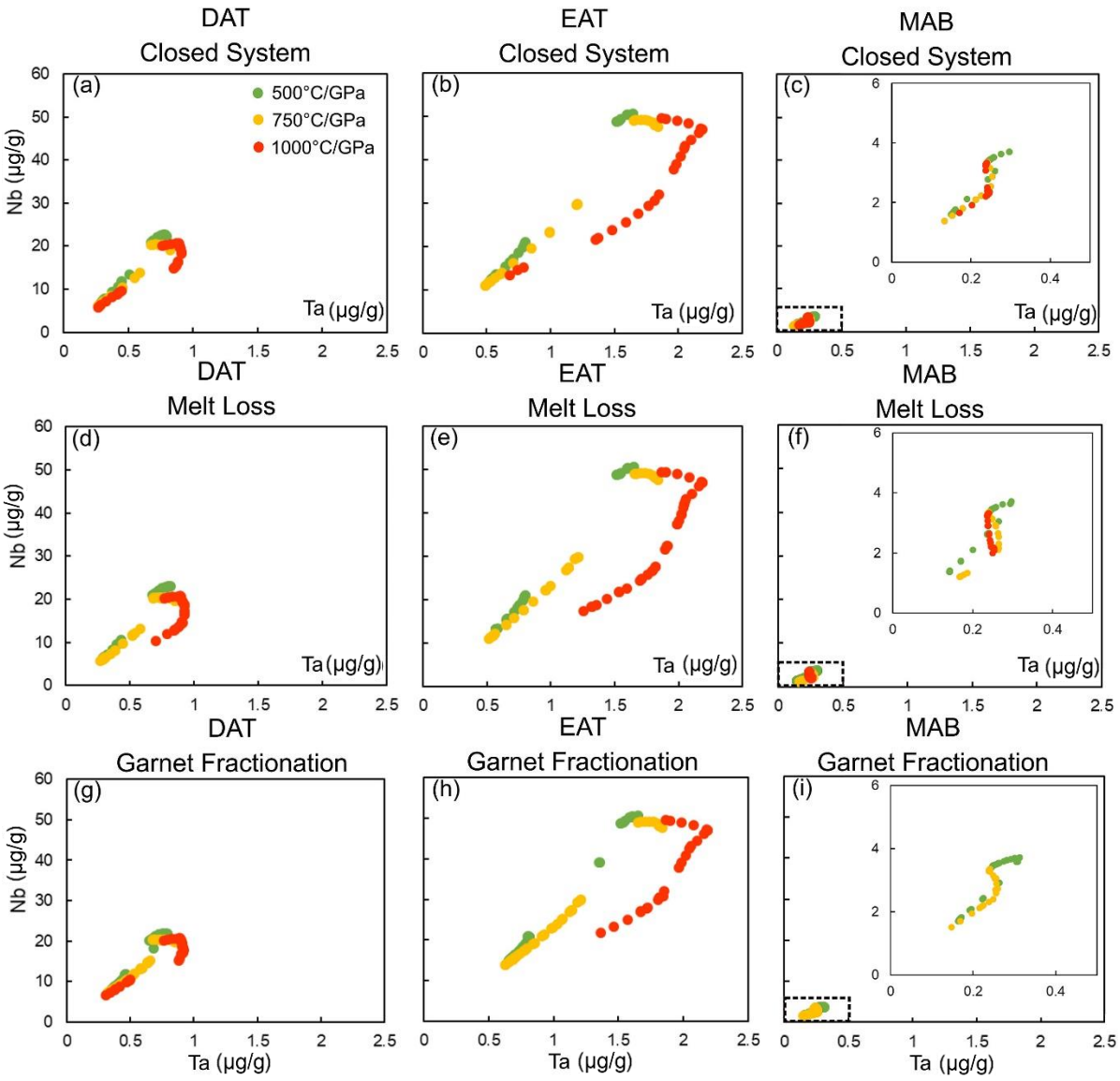


Fig. 2.10. Plots of Nb vs. Ta of modelled melts from each of the three compositions for each of the three scenarios. The garnet fractionation scenario was not modelled for the 1000 °C/GPa gradient for MAB due to lack of garnet. DAT = depleted Archean tholeiite, EAT = enriched Archean tholeiite, MAB = MgO-rich Archean basalt.

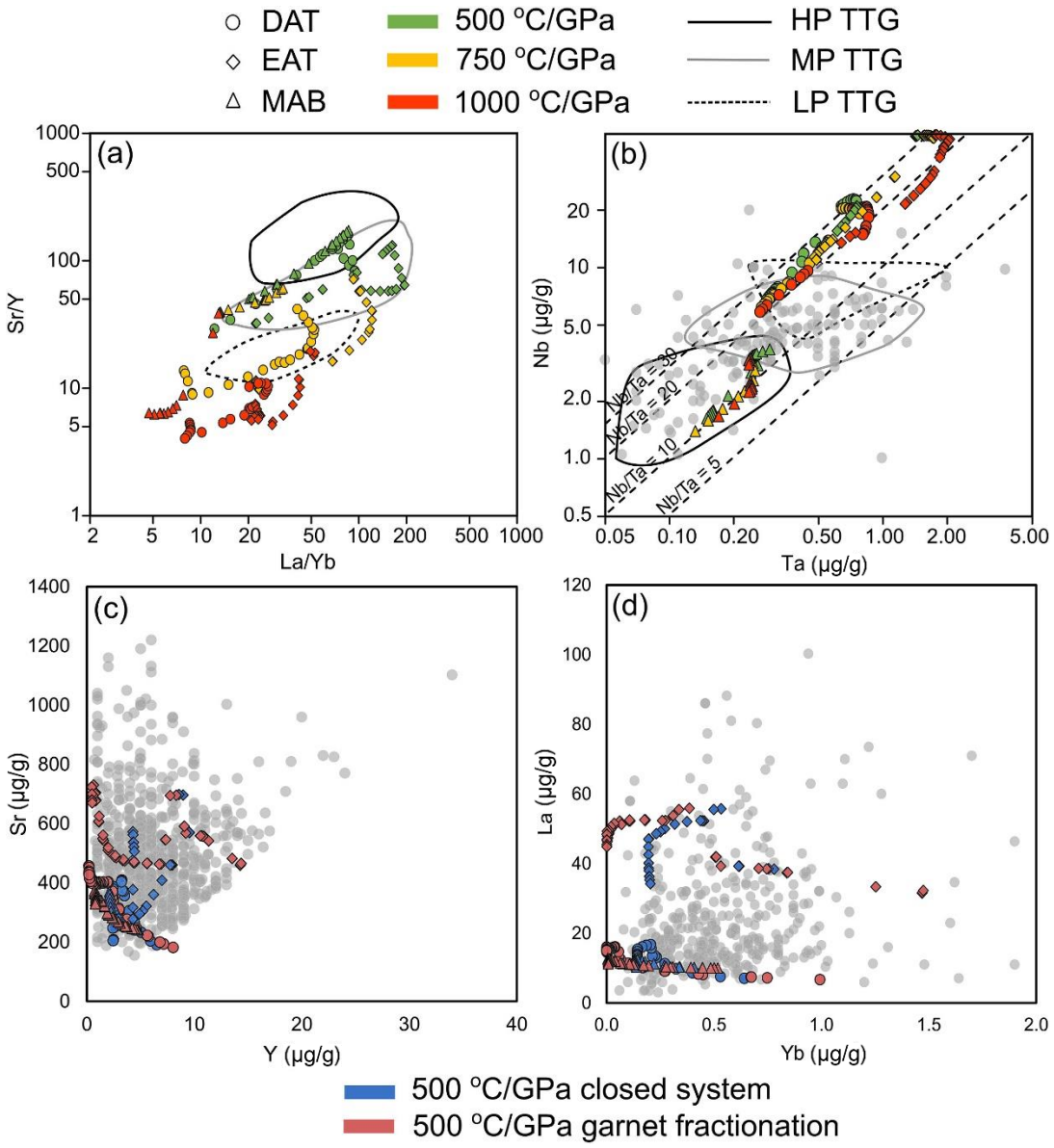


Fig. 2.11. Trace element compositions of modelled melts compared to (a and b) the high-pressure (HP), medium-pressure (MP), and low-pressure (LP) TTG groups (Moyen, 2011) and (b–d) natural TTG data (grey symbols, after Johnson et al., 2019). Diagrams in (a) and (b) include data from the closed-system scenario only. DAT = depleted Archean tholeiite, EAT = enriched Archean tholeiite, MAB = MgO-rich Archean basalt.

Table 2.1. Archean basalt compositions selected for modelling (EAT = enriched Archean tholeiite, DAT = depleted Archean tholeiite, MAB = MgO-rich Archean basalt).

	wt%										**µg/g**					
	SiO_2	TiO_2	Al_2O_3	FeO	Fe_2O_3	MnO	MgO	CaO	Na_2O	K_2O	Sr	Y	La	Yb	Nb	Ta
EAT	50.85	1.53	15.62	9.42	2.88	0.18	7.01	9.03	2.77	0.71	190	30	13	2.2	12.8	0.78
DAT	50.58	0.95	15.62	9.33	1.64	0.22	7.59	11.69	2.17	0.22	100	20	3.6	1.9	5	0.29
MAB	50.14	0.49	11.90	0.00	11.98[a]	0.19	14.27	9.29	1.36	0.33	78.9	12.6	2.7	1.24	0.8	0.1

[a] All Fe reported as Fe_2O_3

Table 2.2. Bulk compositions (mol%) used as input for THERMOCALC (EAT = enriched Archean tholeiite, DAT = depleted Archean tholeiite, MAB = MgO-rich Archean basalt).

	H_2O	SiO_2	Al_2O_3	CaO	MgO	FeO	K_2O	Na_2O	TiO_2	O	
DAT	6.10	49.36	9.89	12.22	11.04	8.82	0.14	2.05	0.70	0.60	sat 12 kbar
	5.29	49.30	9.88	12.21	11.03	8.81	0.14	2.05	0.70	0.60	sat 500°C/GPa
	5.23	49.33	9.89	12.21	11.03	8.82	0.14	2.05	0.70	0.60	sat 750°C/GPa
	4.53	49.70	9.96	12.30	11.12	8.88	0.14	2.06	0.70	0.60	sat 1000°C/GPa
EAT	6.83	49.69	8.99	9.21	10.21	9.81	0.44	2.63	1.13	1.06	sat 12 kbar
	5.87	50.20	9.08	9.31	10.31	9.92	0.45	2.66	1.14	1.07	sat 500°C/GPa
	5.11	50.61	9.16	9.38	10.39	10.00	0.45	2.68	1.15	1.08	sat 750°C/GPa
	4.82	50.76	9.19	9.41	10.43	10.03	0.45	2.69	1.15	1.08	sat 1000°C/GPa
MAB	5.80	49.72	6.96	9.87	21.10	4.47	0.22	1.30	0.37	0.23	sat 12 kbar
	5.56	49.84	6.97	9.89	21.15	4.48	0.22	1.30	0.37	0.23	sat 500°C/GPa
	5.82	49.72	6.96	9.87	21.10	4.47	0.22	1.30	0.37	0.23	sat 750°C/GPa
	5.83	49.72	6.96	9.87	21.10	4.47	0.22	1.30	0.37	0.23	sat 1000°C/GPa

Chapter 3

Diversification of Archean tonalite-trondhjemite-granodiorite suites in a mushy middle crust

Summary

Tonalite-trondhjemite-granodiorite (TTG) suites are the dominant component of Earth's first continents, but their origins are debated. The trace element concentrations of these rocks are conventionally linked to their source depth and inferred geodynamic setting, with the implicit assumption that TTG compositions are source controlled. Alternatively, their variable compositions may be caused by fractional crystallization in TTG plutons after emplacement and less clearly linked to source depth. Most TTGs in Archean mid-crustal exposures are the dominant component of igneous grey gneiss complexes; the processes that influence the evolution of TTG magmas in this setting are poorly understood. Here we present a petrological–geochemical model that explains the coexistence of TTGs in the middle crust with 'low-pressure' and 'high-pressure' geochemical trends, irrespective of tectonic setting or depth of the TTG source. We propose that mid-crustal TTGs were long-lived crystal mushes with compositions controlled by separation of early-crystallizing plagioclase and melt. Using phase equilibrium modeling, we demonstrate that a suite of TTGs from the southern Superior Province in Canada represents variably plagioclase-rich and melt-rich fractions from a common parent magma. The behavior of plagioclase may have a strong influence on the geochemical trends of TTGs, including the degree of rare earth element fractionation. Our results suggest that trace element compositions of TTGs may not primarily reflect the depth of the source and cannot be used alone to infer Archean geodynamic settings.

3.1 Introduction

Earth's earliest continents formed during the Archean Eon (4.0 Ga to 2.5 Ga) and their remnants today are predominantly composed of granitoid rocks of the tonalite-trondhjemite-granodiorite (TTG) suite (Martin, 1994). Determining the petrogenesis of these rocks is crucial to understanding the origin and evolution of continental crust. Rare earth element (REE) patterns of TTGs have been interpreted to record melting of mafic crust at different depths, leading to the high-, medium-, and low-pressure classification of TTGs (Moyen and Stevens, 2006; Moyen, 2011). Alternative

explanations of TTG trace element trends rely on fractional crystallization of tonalitic magma within the crust, with hornblende as a key fractionating mineral (Arth et al., 1978; Bédard, 2006; Smithies et al., 2019; Laurent et al., 2020). Recent work has suggested that differentiation can be driven by eruption of fractionated melt from crystal-rich, upper crustal TTG plutons (Laurent et al., 2020). However, the majority of TTGs were emplaced in the middle crust (i.e., at or below the brittle-ductile transition) where they rarely form recognizable plutons but rather comprise the main component of the ubiquitous 'Archean grey gneiss' (Martin, 1994). The processes that influenced the petrogenetic evolution of TTG magmas in this mid-crustal setting are still cryptic.

The presence of melt in felsic igneous middle crust has been previously recognized as an important factor in the evolution of Archean crust. Numerical models indicate that this scenario is required to achieve the low viscosity required for sagduction and diapirism (de Bremond d'Ars et al., 1999; Thébaud and Rey, 2013; Sizova et al., 2015), which were crucial in the evolution of some cratons (e.g., Collins et al., 1998; Lin, 2005). A melt-bearing Archean middle crust in these models is typically interpreted to result from anatexis of TTG-bearing grey gneiss (Collins et al., 1998; de Bremond d'Ars et al., 1999; Thébaud and Rey, 2013), but widespread partial melting of these rocks may be infeasible at ambient mid-crustal temperatures (White et al., 2017). Protracted U–Pb zircon geochronological records from TTGs in mid-crustal grey gneiss complexes (Kröner et al, 2014; Gardiner et al., 2017; Gardiner et al., 2019) support slow crystallization of TTG magmas within Archean crust. Accumulation of TTG magmas that remained above solidus temperatures for millions of years may have resulted in crystal mush complexes within the middle crust formed by fractional crystallization and mobilization of fractionated melt, analogous to zones of melt accumulation associated with some Archean metasedimentary migmatite terrains (Sawyer, 2020).

Here, we introduce a petrological–geochemical model that explains how diverse TTG trace element compositions can form from a parental magma in the middle crust by fractionation of plagioclase. We use thermodynamic modeling based on TTGs collected across the Wawa Gneiss Domain (WGD) in the southern Superior Province (Canada). The WGD is composed of a ~10 km-thick section dominated by TTGs (~0.5–0.65 GPa emplacement pressure) that structurally underlies a greenstone belt and overlies mafic to intermediate granulite-facies lower crust called the Kapuskasing Structural Zone (Percival and West, 1994; Percival et al., 2012). Most TTGs in the WGD were dated between 2695 and 2660 Ma (Ontario Geological Survey, 2019) and are strongly deformed with variable proportions of mafic enclaves at outcrop scale (Moser, 1994). Compositional and textural heterogeneities of these TTGs have been interpreted in part as the result of multiple magma injections

(Moser, 1994), however, our new observations support crystal–liquid separation (Fig. 3.1). Therefore, we suggest that the WGD is a candidate for a long-lived crystal mush complex composed of TTG magma at the mid-crustal scale. We model the effects of liquid–plagioclase fractionation and demonstrate that this process can generate geochemical signatures normally attributed to production of TTGs in different tectonic settings.

3.2 Methods

We collected whole-rock major and trace element data from each TTG sample of our WGD suite (Table S2.1). A subset of samples representing different geochemical groups was selected for *in situ* analyses of plagioclase major elements (Table S2.2) and trace elements (Table S2.3) by electron probe microanalysis and laser ablation–inductively coupled plasma–mass spectrometry, respectively. Phase equilibrium modeling of a putative parental TTG composition (Table S2.4) was done using the THERMOCALC software package. We calculated trace element compositions of modeled melt and minerals using mass balance and partition coefficients (Table S2.5) for plagioclase parameterized to anorthite content, melt composition, and temperature. A detailed account of the methodology is provided in Appendix S2.1.

A theoretical parental TTG composition was used for modeling, as the origin of TTGs in the WGD is unknown. To approximate a composition unaffected by plagioclase fractionation, we combined the medians of two groups in our TTG dataset—those representing fractionated melt and those with accumulated plagioclase (groups 1 and 2, respectively; see section 3.3)—to calculate a TTG composition with no Eu anomaly. This approach allows geochemical characteristics specific to TTGs in the WGD to be included, with medians providing overall trends without sensitivity to potential outliers; however, multiple TTG sources and parental melts may have been present.

3.3 Results

Outcrops along ~100 km of roads in the WGD are mainly TTGs with variable proportions of plagioclase + quartz + biotite and/or hornblende and minor amounts of K-feldspar, with less abundant leucocratic bodies composed mainly of plagioclase and quartz. The latter are patches commonly surrounding cm–dm-scale mafic enclaves (Fig. 3.1A–C) or cm-scale layers concordant with foliation. The main population of TTG samples (n = 27), each collected from different outcrops, has variable plagioclase modal proportions and microstructures, ranging from dispersed crystals to a framework of accumulated plagioclase (Fig. 3.1D, E). These samples are divided into two groups based on chondrite-normalized whole-rock REE trends: samples with a negative Eu anomaly are assigned to

group 1 and samples with a positive Eu anomaly comprise group 2 (Fig. 3.2A). The leucocratic samples (n = 9) are commonly dominated by plagioclase (Fig. 3.1F) and exhibit large positive Eu anomalies (Fig. 3.2A); these samples comprise group 3 based on the distinction in mineral assemblage from group 1 and 2 samples. When normalized to chondrite values, the trace element trends for all groups yield negative Nb–Ta anomalies and enrichment of LREE and Sr relative to HREE and Y; these geochemical trends are typical of TTGs (Moyen and Martin, 2012). The relative concentrations of HREE in TTGs have been linked to the depth of the source (Moyen, 2011; Johnson et al., 2017). Based on this classification, group 1 resembles low-pressure TTGs and group 2 is similar to high-pressure TTGs (Fig. 3.2A). Group 3 has the lowest concentrations of HREE, suggesting an even deeper source. However, the compositional trends of the three groups cannot be explained solely by the pressure-dependent mineral assemblage of a putative mafic source rock. Group 1 shows the highest concentrations of most trace elements and group 3 concentrations are consistently the lowest; group 2 values are intermediate. The exceptions are Ba and Sr—group 1 has negative anomalies and groups 2 and 3 have positive anomalies when normalized to chondrite values (Fig. 3.2A).

Based on trace element trends, group 1 is consistent with melt separated from early-crystallizing plagioclase. This results in enrichment of most trace elements except for those that preferentially partition into plagioclase (Eu, Sr, and Ba). Groups 2 and 3 show enrichment of trace elements found in plagioclase and relatively low concentrations of other trace elements, consistent with plagioclase accumulation. This is supported by cumulate microstructures that are preserved in several group 2 and group 3 samples, but absent from group 1 (Fig 3.1D–F). Furthermore, the normative albite-anorthite-orthoclase compositions of the samples (Fig. 3.2B), which are typical of TTGs (Moyen and Martin, 2012), show a general trend of decreasing orthoclase component from group 1 to 2 to 3, towards measured compositions of plagioclase in the TTGs.

The equilibrium crystallization sequence (Fig. 3.3; Fig. S2.1) of our estimated parental TTG composition was calculated at a pressure of 0.6 GPa to approximate the mid-crustal depth of the WGD. Plagioclase is predicted to crystallize at the liquidus followed by minor quartz and accessory ilmenite (Fig. 3.3). We modeled liquid–crystal separation at 40 mol% plagioclase crystallization, as the modeled feldspar composition closely matches the median measured composition (An_{25}, Fig. 3.3). The compositions of melt and the plagioclase-rich solid component were combined in different proportions, ranging from 100% melt to 100% crystals, to simulate different degrees of liquid–crystal separation. The spectrum of modeled trace element trends encompasses the natural trends of the three

TTG groups from the WGD (Fig. 3.4A, B). The trace element compositions of groups 1, 2, and 3 are approximated by models calculated using 20%, 70%, and 100% crystals, respectively (Fig. 3.4A). Group 1 samples exhibit low Sr/Y and La/Yb, whereas these ratios are relatively elevated for group 3; group 2 is intermediate (Fig. 3.4B). The model results replicate this trend, evolving from compositions similar to group 1 toward group 3 compositions with increasing crystal proportion (Fig. 3.4B). This result illustrates that plagioclase behavior may affect both Sr/Y and LREE/HREE ratios in TTGs. This is supported by plagioclase trace element data collected from several of our TTG samples, which indicate enrichment of La relative to the HREE by up to four orders of magnitude (Fig. S2.2). The results of the thermodynamic modeling demonstrate that varying degrees of liquid–crystal separation in partially solidified parental magmas can account for the diversity of TTG compositions observed in the WGD.

3.4 Discussion

Our modeling results support our hypothesis that the WGD was a mid-crustal scale crystal mush complex where fractionated melt may have locally been mobilized, leaving behind plagioclase-rich cumulate. Melt, along with entrained crystals, pooled within the middle crust, resulting in TTGs composed of variable proportions of accumulated plagioclase and fractionated melt. In contrast to previous investigations of the role of fractional crystallization in the petrogenesis of TTG magmas (e.g., Smithies et al., 2019; Laurent et al., 2020), we replicated REE trends in our TTG suite without fractionation of hornblende. This is consistent with the small amount of hornblende in our samples that record crystal accumulation (groups 2 and 3)—and the scarcity of hornblende in many TTGs suites (Moyen and Martin, 2012). However, we do not exclude hornblende fractionation as a factor in the evolution of the real parental TTG magma prior to emplacement in the middle crust. Although the LREE/HREE ratio of plagioclase in our TTG samples is unclear due to HREE values below our limit of detection, our results highlight the potential of plagioclase to control whole-rock LREE/HREE ratios in TTGs. Enrichment of LREE relative to HREE in plagioclase has been identified in different igneous rock types (Henderson, 1984) and high LREE/HREE in plagioclase was reported previously in Archean granitoids (Carvalho et al., 2016). The positive zirconium anomalies of group 2 and 3 TTGs (Fig. 3.4A) are not replicated accurately in the model, which may indicate accumulation of early crystallized zircon along with plagioclase. This is supported by previous modeling (Kirkland et al., 2021), which showed zircon crystallization in TTGs beginning at a similar melt/solid ratio as our model system (~40–60% crystallization of the system).

The mechanisms of melt separation from crystals in silicic crystal mushes are debated, but variations in external stress fields may facilitate the process (Rutter and Neumann, 1995). Strong evidence for melt extraction driven by differential stress has been provided in studies of mid-crustal migmatites (Brown and Rushmer, 1997; Carvalho et al., 2016). However, compaction of crystal mushes may be driven by gravity, as proposed for less viscous mafic magmas (e.g., Philpotts et al., 1996). In the WGD, the association of mafic enclaves with plagioclase-rich cumulate (group 3 rocks; Fig. 3.1A–C) may indicate that compaction and melt extraction were favored in areas where stress could be focused, given the competency contrast between the enclaves and enveloping crystal-rich mush. The timing of protracted regional deformation in the WGD (2695–2640 Ma) in part overlaps with crystallization ages of TTGs in the area (Moser, 1994; Moser et al., 1996), supporting the possibility of differential stress causing compactions within the crystal mush complex. Regardless of the mechanism of crystal–liquid separation, our results support the existence of a melt-bearing mid-crustal layer in igneous Archean crust without widespread partial melting of TTGs in the middle crust, enabling the vertical tectonic processes that were important in some cratons (e.g., Collins et al., 1998; Lin, 2005; Vanderhaeghe et al., 2019).

Although geochemical diversity in TTGs in general has been shown to arise from variations in source depth and/or composition (Martin et al., 2005; Moyen, 2011; Palin et al., 2016; Kendrick and Yakymchuk, 2020 [Chapter 2]), our plagioclase fractionation model accounts for the coexistence of TTGs with apparent ‘low-pressure’ and ‘high-pressure’ geochemical signatures in the WGD without requiring multiple mafic sources at different depths (c.f. Mole et al., 2021). Although we do not exclude the possibility that geochemical variation within a mid-crustal TTG suite can be caused by multiple sources, we suggest that geochemical data alone may not be easily linked to TTG sources. Similar trace element trends can be generated both at the source and after emplacement of magma, ultimately obscuring the geodynamic significance of TTG compositions.

3.5 References

Arth, J.G., Barker, F., Peterman, Z.E., and Friedman, I., 1978, Geochemistry of the gabbro–diorite–tonalite–trondhjemite suite of Southwest Finland and its implications for the origin of tonalitic and trondhjemitic magmas: Journal of Petrology, v. 19, p. 289–316, doi:10.1093/petrology/19.2.289.

Bédard, J.H., 2006, A catalytic delamination-driven model for coupled genesis of Archaean crust and sub-continental lithospheric mantle: Geochimica et Cosmochimica Acta, v. 70, p. 1188–1214, doi:10.1016/j.gca.2005.11.008.

Brown, M., and Rushmer, T., 1997, The role of deformation in the movement of granite melt: Views from the laboratory and the field, in Holness, M.B. ed., Deformation-enhanced fluid transport in the Earth's crust and mantle: The Mineralogical Society Series 8, London, Chapman and Hall, p. 111–144.

Carvalho, B.B., Sawyer, E.W., and Janasi, V.A., 2016, Crustal reworking in a shear zone: Transformation of metagranite to migmatite: Journal of Metamorphic Geology, v. 34, p. 237–264, doi:10.1111/jmg.12180.

Collins, W.J., Van Kranendonk, M.J., and Teyssier, C., 1998, Partial convective overturn of Archaean crust in the east Pilbara Craton, Western Australia: Driving mechanisms and tectonic implications: Journal of Structural Geology, v. 20, p. 1405–1424, doi:10.1016/S0191-8141(98)00073-X.

de Bremond D'Ars, J., Lécuyer, C., and Reynard, B., 1999, Hydrothermalism and diapirism in the Archean: Gravitational instability constraints: Tectonophysics, v. 304, p. 29–39, doi:10.1016/S0040-1951(98)00303-5.

Gardiner, N.J., Hickman, A.H., Kirkland, C.L., Lu, Y., Johnson, T., and Zhao, J.X., 2017, Processes of crust formation in the early Earth imaged through Hf isotopes from the East Pilbara Terrane: Precambrian Research, v. 297, p. 56–76, doi:10.1016/j.precamres.2017.05.004.

Gardiner, N.J., Kirkland, C.L., Hollis, J., Szilas, K., Steenfelt, A., Yakymchuk, C., and Heide-Jørgensen, H., 2019, Building Mesoarchaean crust upon Eoarchaean roots: The Akia Terrane, West Greenland: Contributions to Mineralogy and Petrology, v. 174, 20, doi:10.1007/s00410-019-1554-x.

Henderson, P., 1984, General geochemical properties and abundances of the rare earth elements, in Henderson, P., ed, Rare Earth Element Geochemistry: Amsterdam, The Netherlands, Elsevier, p. 1–32.

Johnson, T.E., Brown, M., Gardiner, N.J., Kirkland, C.L., and Smithies, R.H., 2017, Earth's first stable continents did not form by subduction: Nature, v. 543, p. 239–242, doi:10.1038/nature21383.

Kendrick, J., and Yakymchuk, C., 2020, Garnet fractionation, progressive melt loss and bulk composition variations in anatectic metabasites: Complications for interpreting the geodynamic significance of TTGs: Geoscience Frontiers, v. 11, p. 745–763, doi:10.1016/j.gsf.2019.12.001.

Kirkland, C.L., Yakymchuk, C., Olierook, H.K.H., Hartnady, M.I.H., Gardiner, N.J., Moyen, J.-F., Hugh Smithies, R., Szilas, K., and Johnson, T.E., 2021, Theoretical versus empirical secular change in zircon composition: Earth and Planetary Science Letters, v. 554, 116660, doi:10.1016/j.epsl.2020.116660.

Kröner, A., Hoffmann, J.E., Xie, H., Münker, C., Hegner, E., Wan, Y., Hofmann, A., Liu, D., and Yang, J., 2014, Generation of early Archaean grey gneisses through melting of older crust in the eastern Kaapvaal craton, southern Africa: Precambrian Research, v. 255, p. 823–846, doi:10.1016/j.precamres.2014.07.017.

Laurent, O., Björnsen, J., Wotzlaw, J.F., Bretscher, S., Pimenta Silva, M., Moyen, J.-F., Ulmer, P., and Bachmann, O., 2020, Earth's earliest granitoids are crystal-rich magma reservoirs tapped by silicic eruptions: Nature Geoscience, v. 13, p. 163–169, doi:10.1038/s41561-019-0520-6.

Lin, S., 2005, Synchronous vertical and horizontal tectonism in the Neoarchean: Kinematic evidence from a synclinal keel in the northwestern Superior craton, Canada: Precambrian Research, v. 139, p. 181–194, doi:10.1016/j.precamres.2005.07.001.

Martin, H., 1994, The Archean grey gneisses and the genesis of continental crust, in Condie, K.C., ed., Archean Crustal Evolution: Amsterdam, The Netherlands, Elsevier, p. 205–259.

Martin, H., Smithies, R.H., Rapp, R., Moyen, J.-F., and Champion, D., 2005, An overview of adakite, tonalite–trondhjemite–granodiorite (TTG), and sanukitoid: Relationships and some implications for crustal evolution: Lithos, v. 79, p. 1–24, doi:10.1016/j.lithos.2004.04.048.

Mole, D.R., Thurston, P.C., Marsh, J.H., Stern, R.A., Ayer, J.A., Martin, L.A.J., and Lu, Y.J., 2021, The formation of Neoarchean continental crust in the south-east Superior Craton by two distinct geodynamic processes: Precambrian Research, v. 356, 106104, doi:10.1016/j.precamres.2021.106104.

Moser, D.E., 1994, The geology and structure of the mid-crustal Wawa gneiss domain: A key to understanding tectonic variation with depth and time in the late Archean Abitibi–Wawa orogen: Canadian Journal of Earth Sciences, v. 31, p. 1064–1080, doi:10.1139/e94-096.

Moser, D.E., Heaman, L.M., Krogh, T.E., and Hanes, J.A., 1996, Intracrustal extension of an Archean orogen revealed using single-grain U-Pb zircon geochronology: Tectonics, v. 15, p. 1093–1109, doi:10.1029/96TC00130.

Moyen, J.-F., 2011, The composite Archaean grey gneisses: Petrological significance, and evidence for a non-unique tectonic setting for Archaean crustal growth: Lithos, v. 123, p. 21–36, doi:10.1016/j.lithos.2010.09.015.

Moyen, J.-F., and Martin, H., 2012, Forty years of TTG research: Lithos, v. 148, p. 312–336, doi:10.1016/j.lithos.2012.06.010.

Moyen, J.-F., and Stevens, G., 2006, Experimental constraints on TTG petrogenesis: Implications for Archean geodynamics, in Benn, K., Mareschal, J.-C., and Condie, K.C. eds., Archean geodynamics and environments. AGU Geophysical Monograph, Washington, DC, American Geophysical Union, p. 149–178.

Ontario Geological Survey, 2019, Geochronology Inventory of Ontario: http://www.mndm.gov.on.ca/en/mines-and-minerals/applications/ogsearth/geochronology-inventory-ontario-compilation (accessed May 2021).

Palin, R.M., White, R.W., and Green, E.C.R., 2016, Partial melting of metabasic rocks and the generation of tonalitic–trondhjemitic–granodioritic (TTG) crust in the Archaean: Constraints from phase equilibrium modelling: Precambrian Research, v. 287, p. 73–90, doi:10.1016/j.precamres.2016.11.001.

Percival, J.A., and West, G.F., 1994, The Kapuskasing uplift: A geological and geophysical synthesis: Canadian Journal of Earth Sciences, v. 31, p. 1256–1286, doi:10.1139/e94-110.

Percival, J.A., Skulski, T., Sanborn-Barrie, M., Stott, G.M., Leclair, A.D., Corkery, M.T., and Boily, M., 2012, Geology and tectonic evolution of the Superior Province, Canada, in Percival, J.A., Cook, F.A., and Clowes, R.M. eds., Tectonic Styles in Canada: The LITHOPROBE Perspective, Geological Association of Canada, Special Paper 49, p. 321–378.

Philpotts, A.R., Carroll, M., and Hill, J.M., 1996, Crystal-mush compaction and the origin of pegmatitic segregation sheets in a thick flood-basalt flow in the Mesozoic Hartford Basin, Connecticut: Journal of Petrology, v. 37, p. 811–836, doi:10.1093/petrology/37.4.811.

Rutter, E.H., and Neumann, D.H.K., 1995, Experimental deformation of partially molten Westerly granite under fluid-absent conditions, with implications for the extraction of granitic magmas:

Journal of Geophysical Research: Solid Earth, v. 100, p. 15697–15715, doi:10.1029/94JB03388.

Sawyer, E.W., 2020, Petrogenesis of secondary diatexites and the melt budget for crustal reworking: Journal of Petrology, v. 61, egaa039, doi:10.1093/petrology/egaa039.

Sizova, E., Gerya, T., Stüwe, K., and Brown, M., 2015, Generation of felsic crust in the Archean: A geodynamic modeling perspective: Precambrian Research, v. 271, p. 198–224, doi:10.1016/j.precamres.2015.10.005.

Smithies, R.H. et al., 2019, No evidence for high-pressure melting of Earth's crust in the Archean: Nature Communications, v. 10, 5559, doi:10.1038/s41467-019-13547-x.

Thébaud, N., and Rey, P.F., 2013, Archean gravity-driven tectonics on hot and flooded continents: Controls on long-lived mineralised hydrothermal systems away from continental margins: Precambrian Research, v. 229, p. 93–104, doi:10.1016/j.precamres.2012.03.001.

Vanderhaeghe, O., Guergouz, C., Fabre, C., Duchêne, S., and Baratoux, D., 2019, Secular cooling and crystallization of partially molten Archaean continental crust over 1 Ga: Comptes Rendus - Geoscience, v. 351, p. 562–573, doi:10.1016/j.crte.2019.07.002.

White, R.W., Palin, R.M., and Green, E.C.R., 2017, High-grade metamorphism and partial melting in Archean composite grey gneiss complexes: Journal of Metamorphic Geology, v. 35, p. 181–195, doi:10.1111/jmg.12227.

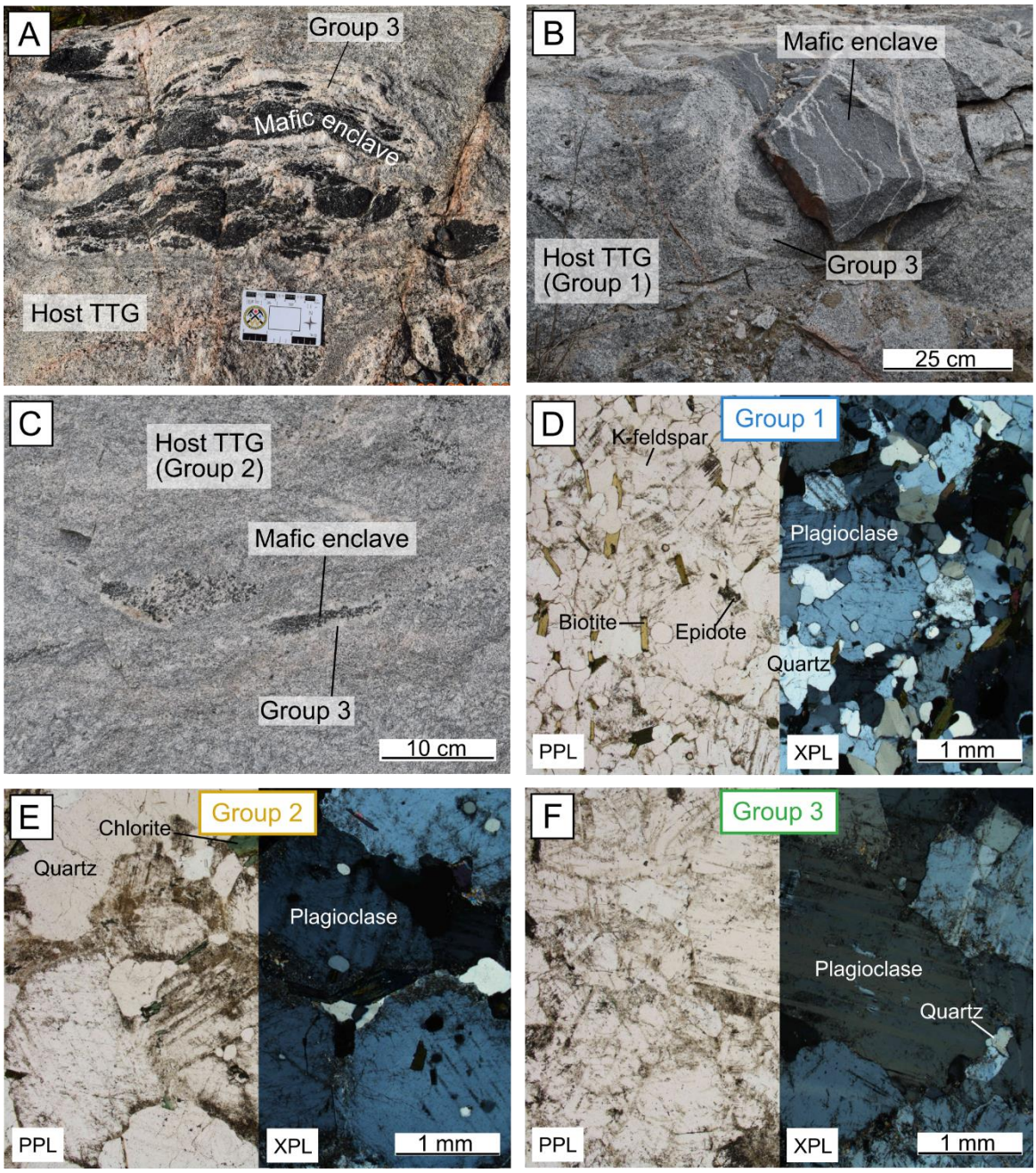


Figure 3.1. A–C) Photographs of TTG outcrops in the Wawa Gneiss Domain. Mafic enclaves are associated with leucocratic bodies (group 3). D) Photomicrograph of a group 1 sample: subhedral plagioclase with irregular grain boundaries is dispersed in a matrix of quartz, biotite, and anhedral K-feldspar. E) Photomicrograph of a group 2 sample: blocky plagioclase exhibits cumulate texture. F) Photomicrograph of a group 3 sample: plagioclase crystals are densely packed. PPL = plane-polarized light; XPL = cross-polarized light.

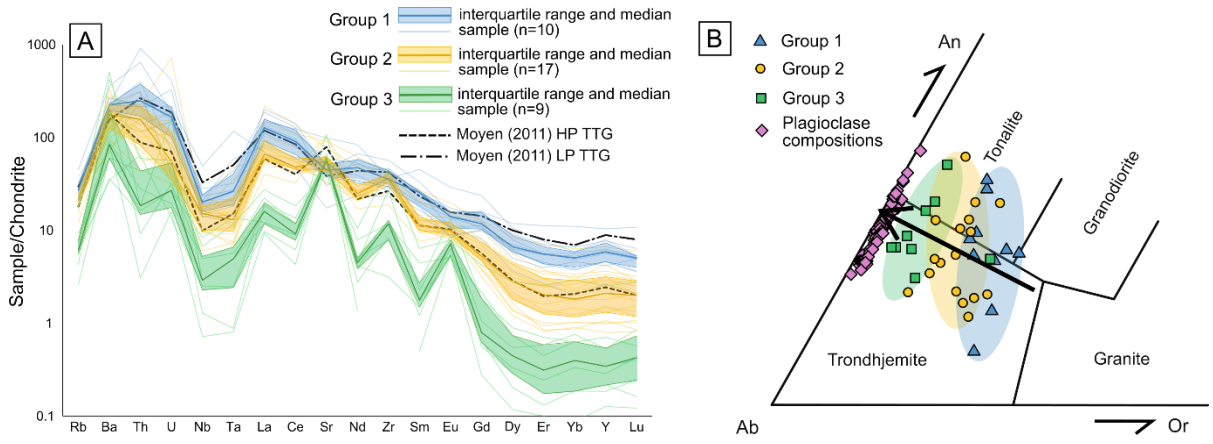


Figure 3.2. A) Chondrite-normalized trace element compositions of the Wawa Gneiss Domain TTGs collected in this study. Dashed lines are medians of the 'high-pressure' (HP) and 'low-pressure' (LP) TTG groups from Moyen (2011). B) Normative albite (Ab), anorthite (An), and orthoclase (Or) proportions of the TTG samples.

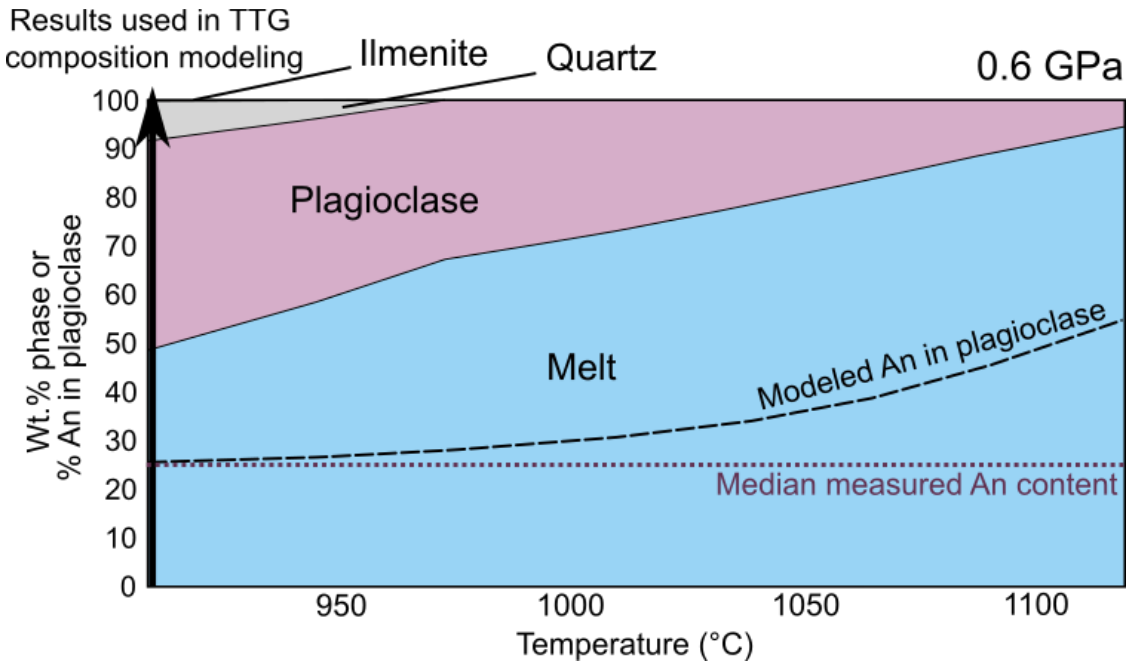


Figure 3.3. Phase equilibrium modeling of the crystallization sequence of the estimated parental TTG composition at 0.6 GPa. The full phase assemblage diagram is shown in Fig. S2.1.

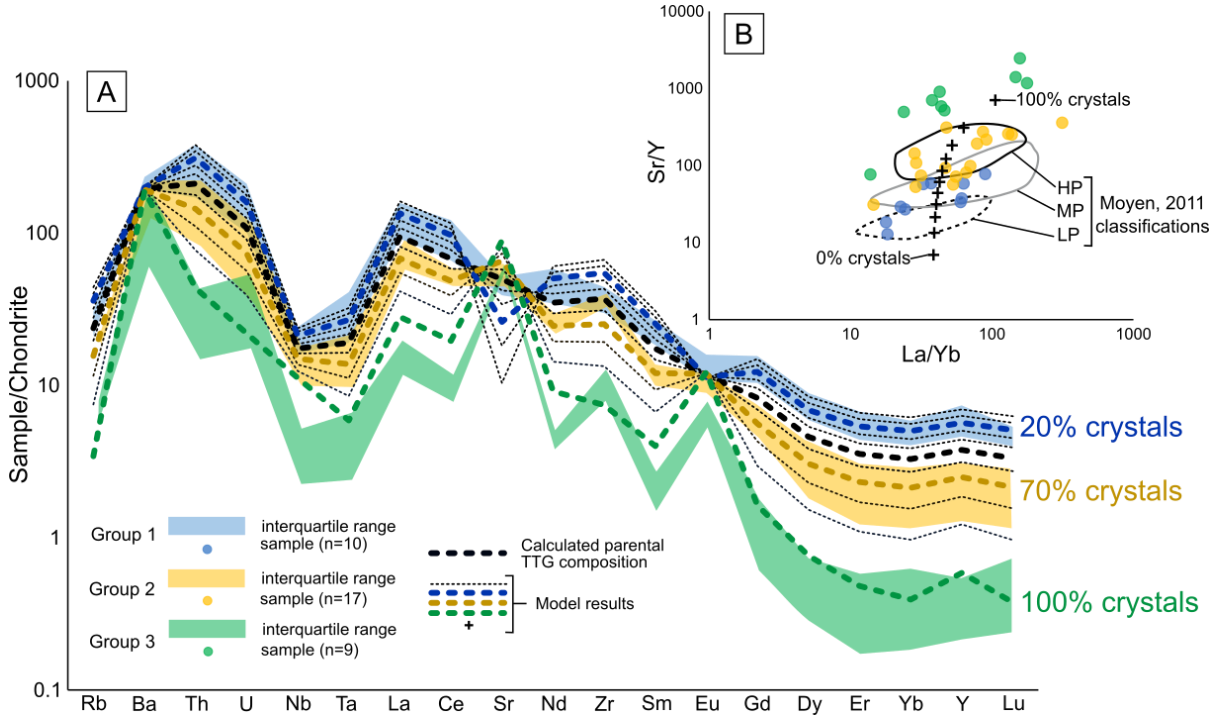


Figure 3.4. A) Trace element trends of model TTG compositions, calculated by combining different proportions of crystals and melt, compared to interquartile ranges of natural TTG groups. B) Sr/Y vs. La/Yb of natural TTGs compared to model results. Fields for high-pressure (HP), medium-pressure (MP), and low-pressure (LP) TTGs are after Moyen (2011).

Chapter 4

Anatomy of a craton: Isotopic heterogeneity across an Archean crustal cross section

Summary

The formation of granitoids, predominantly tonalite-trondhjemite-granodiorite (TTG) suites was a key process in the differentiation of Earth's earliest crust. However, the relative importance of intracrustal reworking versus input from external sources remains unclear. U–Pb and Hf isotopic data collected from zircon crystals in Archean granitoids commonly support reworking and partial melting of the same crustal material over time to produce subsequent generations of granitoids. Relatively few isotopic datasets indicate the presence of different generations of TTGs from unrelated sources in a single region. These end-member scenarios of granitoid generation have different implications for Archean crustal evolution. Here, we investigate TTGs from across a crustal cross section known as the Kapuskasing Uplift in the Neoarchean Wawa terrane of the southern Superior Province. We report U–Pb and Hf isotopic data from zircon in TTGs from the lower, middle, and upper crust to evaluate their sources. Results indicate three groups of TTGs: a ca. 2885 Ma upper-crustal TTG with chondritic εHf, ca. 2835–2820 Ma deep-crustal TTGs with subchondritic εHf, and ca. 2750–2685 Ma TTGs with suprachondritic εHf emplaced at middle- to upper-crustal level. Each group was derived from an isotopically distinct source. We propose that the Mesoarchean rocks exposed in the Kapuskasing Uplift represent a crustal fragment rifted from the margin of existing Mesoarchean terranes in the Superior Province. Subsequent Neoarchean juvenile magmatism dominates the upper and middle crust resulting in isotopic stratification of the Kapuskasing Uplift, as only the lower crust contains evidence of all three isotopic sources. Inferences about Archean crustal evolution in general rely on upper- to middle-crustal rocks (i.e., greenstone belts and grey gneiss), as these represent the majority of exposed Archean crust worldwide. The potential for the lower crust to be decoupled from overlying rocks implies that some parts of the Archean geological record may be preserved only at the deepest crustal levels—particularly rocks related to the most ancient sources.

4.1 Introduction

The processes that drove the evolution of Earth's early crust remain enigmatic. In general, crustal differentiation was driven by partial melting of hydrated basaltic crust to generate granitoids of the tonalite-trondhjemite-granodiorite (TTG) suite (Moyen and Martin, 2012). In a purely intracrustal model of crustal differentiation, TTGs are formed by partial melting of metabasite and subsequent generations of granitoids are formed by further crustal reworking; some isotopic datasets from Archean cratons support long-lived intracrustal reworking, where multiple generations of granitoids can be linked to the same isotopic source (e.g., Gardiner et al., 2017; O'Neil and Carlson, 2017). However, other isotopic datasets indicate that multiple unrelated sources were involved in the generation of felsic crust in a single region (e.g., Gardiner et al., 2020). Distinguishing between these scenarios has broad implications for Archean tectonics and crustal evolution, as evidence for multiple granitoid sources requires that Archean rocks of distinct origins were juxtaposed. This can be achieved, for instance, by accretion of exotic terranes through horizontal tectonic processes (e.g., Frieman et al., 2021) or emplacement of pulses of juvenile magmatism within existing ancient crust (e.g., Mulder et al., 2021).

A large proportion of exposed and accessible Archean crust is limited to rocks of the upper to middle crust (e.g., Percival et al., 2012), and consequently interpretations of continental evolution are commonly made without direct observations or data from rocks of the lower crust. However, the potential for the deep crust to be isotopically decoupled from overlying rocks has been demonstrated. For instance, inherited xenocrystic zircon in greenstone rocks can indicate the presence of an older basement (e.g., Van Kranendonk et al., 2013) and zircon transported as xenocrysts or within xenoliths from the deep Archean crust by post-Archean magmats may have distinct isotopic signatures from overlying rocks (e.g., Gardiner et al., 2020; Ma et al., 2020). Archean crustal xenoliths and xenocrysts can provide a valuable glimpse into the deep crust, though the lack of geological context and limited sample material may hinder their utility. Rarely, the lower levels of Archean crust are exposed in a crustal cross section, allowing for a comprehensive view of cratonic interiors.

Here, we investigate TTG samples collected across the Kapuskasing Uplift, a cross section of the Wawa terrane in the southern Superior Province (Fig. 4.1a) that extends from granulite-facies deep crust to the largely supracrustal shallow crust. This Archean crustal cross section provides a rare opportunity to evaluate the isotopic record preserved at different crustal levels, and we present the first U–Pb and Hf isotopic dataset of TTGs from across the Kapuskasing Uplift. We propose that

felsic crust in the Kapuskasing Uplift was generated by three main pulses of magmatism—two Mesoarchean and one Neoarchean—derived from three isotopically distinct sources. However, our results combined with previous data from the region demonstrate isotopic stratification within the crust; the upper and middle crust are biased toward the volumetrically dominant Neoarchean magmatism and only the deep crust preserves evidence of all three isotopic sources. We discuss the significance of these results within the context of the Superior Province and the Archean geological record in general.

4.2 Regional Geology

The Superior Province is the largest preserved Archean craton and has been used as a natural laboratory for testing hypotheses of different Archean tectonic processes (Lin, 2005; Percival et al., 2012; Bédard and Harris, 2014). The Wawa terrane, located in the southern Superior Province, contains the Kapuskasing Uplift, of which the southern portion is the focus of this study (Fig. 4.1a). Three domains in the Kapuskasing Uplift—exposed over ~150 km—broadly represent different crustal levels of the Wawa terrane. From shallowest to deepest, these include the Michipicoten Greenstone Belt (MGB), the Wawa Gneiss Domain (WGD), and the Kapuskasing Structural Zone (KSZ) (Fig. 4.1b).

The MGB represents some of the shallowest crust exposed in the Wawa terrane and is composed of three volcanic assemblages, with crystallization ages of ca. 2900 Ma, ca. 2750 Ma, and ca. 2700 Ma (Turek et al., 1992; Sage, 1994). Each cycle shows a progression from mafic volcanic rocks at the base to felsic volcanic rocks at the top (Turek et al., 1992). Within the MGB, TTG plutons have generally synchronous crystallization ages with the felsic portion of each volcanic cycle (Turek et al., 1984; Turek et al., 1992; Sage et al., 1996a). Monzonitic, granodioritic, and syenitic intrusions postdate the formation of the MGB and have no volcanic equivalents (Sage et al., 1996a). The oldest volcanic cycle, the Mesoarchean Hawk assemblage, contains the only ultramafic volcanic rocks in the MGB and is intruded by the ca. 2890–2880 Ma Hawk Lake granitic complex (Turek et al., 1984); these rocks are found only along the southeastern margin of the MGB (Fig. 4.1b; Sage, 1994). The Hawk assemblage has been hypothesized to be the remnant of the Hawk terrane, a basement of unknown extent upon which the Neoarchean rocks of the MGB were deposited (Turek et al., 1984; Percival et al., 2012).

The WGD represents the middle crustal level in the Wawa terrane and is dominated by granitoid plutons and gneisses containing supracrustal enclaves that are up to a kilometer in size (Moser et al., 1996). Most of the exposed granitoid rocks and gneisses in the WGD have compositions consistent with TTGs sensu stricto (Moser et al., 1996; Kendrick et al., 2022 [Chapter 3]). These TTGs exhibit a range of major and trace element compositions that are typically attributed to derivation from mafic sources at different depths (e.g., Moyen and Martin, 2012). However, the compositional diversity of these rocks was probably generated—or at least strongly influenced—by segregation of crystals and melt within a middle-crustal crystal mush (Kendrick et al., 2022 [Chapter 3]). Previous work has identified granitoid crystallization at ca. 2920 Ma, 2675 Ma, 2660 Ma, and 2645 Ma; the youngest ages represent local intrusions that accompanied late extension in the WGD (Moser et al., 1996). Granitoids of the WGD have a deformed intrusive contact with the MGB (Sage, 1994) and a less clearly defined, gradational contact with rocks in the KSZ to the east (Percival, 1983).

The KSZ represents the deepest crustal level exposed in the Wawa terrane and is composed of upper amphibolite- to granulite-facies rocks of predominantly intermediate to mafic composition (Percival, 1983). The origin and age of the protoliths are unclear, as high-grade metamorphism in the KSZ ($\geq$ 800°C, 1.0–1.1 GPa; Mäder et al., 1994; Hartel and Pattison, 1996) postdated most of the igneous activity in the Wawa and Abitibi terranes (Percival et al., 2012). Metamorphic zircon has yielded ages of ca. 2660 Ma and ca. 2645 Ma (Percival and Krogh, 1983; Krogh, 1993; Krogh and Moser, 1994), and some zircon populations were interpreted to record protracted metamorphic zircon growth from ca. 2660 Ma to ca. 2580 Ma (Moser et al., 2008). However, evidence of earlier metamorphism in KSZ rocks has been found, with metatonalite and metabasite yielding ca. 3200 Ma, 2850 Ma, and 2790 Ma ages from inferred metamorphic zircon (Benn and Kamber, 2009). Therefore, the thermal history of the KSZ may have been complex, with protoliths that may predate the largely Neoarchean history of the Wawa and Abitibi terranes. The lower crustal rocks of the Wawa terrane, exposed in the KSZ, are juxtaposed with greenstones of the Abitibi terrane to the east along the Ivanhoe Lake fault zone (Fig 4.1b); thrusting along this fault is inferred to have occurred in the Neoarchean and the Paleoproterozoic (Percival and West, 1994).

The origin of rocks exposed in the Kapuskasing Uplift has typically been interpreted within a modern-style plate tectonic framework. The Hawk terrane has been interpreted as a Mesoarchean microcontinent allochthonous to the proto-Superior Province (Percival et al., 2012). This

microcontinent became embedded within the Wawa-Abitibi terrane during the emplacement of magmatic and volcanic rocks from 2750 Ma to 2695 Ma in an inferred oceanic setting, and this composite body accreted to the Superior Province at ca. 2695 Ma (Percival et al., 2012). The origin of the lower crustal rocks of the KSZ has been explained by lateral tectonic underplating of allochthonous crustal material (Krogh, 1993) to the existing volcanic–plutonic complex (MGB and WGD). Moser et al. (1996) proposed multiple tectonic underplating events between ca. 2670 Ma and 2640 Ma, each followed by delamination and granulite-facies metamorphism.

4.3 Samples and Methodology

4.3.1 Samples

We report data from nine TTG samples collected across the Kapuskasing Uplift, mainly consisting of unfoliated to gneissic biotite tonalite or biotite–hornblende tonalite (Fig. S3.1). Six samples (18JK19, 19JK43, 19JK41, 19JK40, 18JK08, and 18JK53) are a subset from a larger group of TTG samples taken from the WGD that was previously examined by Kendrick et al. (2022) [Chapter 3]. The TTGs from the WGD selected for the present study include both plagioclase cumulate-rich samples and complementary residual melt-rich samples from Kendrick et al. (2022) [Chapter 3]. We also report results from a sample (19JK45B) collected at the edge of the Hawk Lake granitic complex, which we interpret as a TTG phase of this intrusive complex. The remaining two samples (17JK11 and 17JK26) were collected at the eastern margin of the KSZ; these outcrops contain garnet (<5% vol.%), granitic (sensu lato) leucosome (sample 17JK26 outcrop only) inferred to be the remnants of anatexis caused by high-temperature metamorphism, and a larger proportion of mafic enclaves in comparison to the other seven outcrops sampled (Fig. S3.1).

4.3.2 Whole-rock geochemical data

Of the nine TTG samples investigated in this study, whole-rock geochemical data for the six samples from the WGD have been previously reported in Kendrick et al. (2022 [Chapter 3]; samples 19JK43, 19JK41, and 19JK40 are listed as 18JK30, 18JK12, and 18JK24, respectively; see Table S2.1). We report whole-rock geochemical data from samples 19JK45B, 17JK11, and 17JK26, which were processed at the Ontario Geological Survey Geoscience Laboratories (Geolabs) (Sudbury, Canada). Major elements were analyzed by X-ray fluorescence and the trace elements were measured by inductively coupled plasma mass spectrometry. Reference materials, sample duplicates, and blanks

were used to ensure data quality. Detailed analytical methods are described in the Appendix S3.1.1 and whole-rock geochemical data from the three samples are provided in Table S3.1.

4.3.3 Zircon U–Pb and Lu–Hf analysis

Zircon mineral separates were obtained from each of the nine TTG samples for *in situ* U–Pb and Lu–Hf analysis. Cathodoluminescence (CL) images of the crystals were collected at the Waterloo Advanced Technology Laboratory at University of Waterloo to aid in the selection of locations for *in situ* analysis. U–Pb and Lu–Hf isotopic data were collected simultaneously by laser ablation split stream (LASS) analyses of zircon at the John de Laeter Centre for Mass Spectrometry at Curtin University following the methodology described by Gardiner et al. (2020). Matrix-matched reference materials were analyzed to ensure data quality. An extended description of the methodology is provided in the Appendix S3.1.1 and all data obtained from zircon separates and reference materials are available in Tables S3.2 and S3.3.

4.4 Results

4.4.1 Whole-rock geochemical data

The nine samples exhibit geochemical characteristics consistent with TTGs (e.g., Moyen and Martin, 2012), including SiO_2 > 64 wt.%, K_2O/Na_2O < 0.5, and enrichment of LREE relative to HREE (see Kendrick et al., 2022 [Chapter 3]; Table S3.1). The samples from the Hawk Lake granitic complex and the KSZ have overall higher concentrations of REE than many TTGs from the WGD, although there is variability within the WGD dataset (Kendrick et al., 2022 [Chapter 3]). The TTG samples from the KSZ also have higher maficity (FeOt + MgO + MnO + TiO_2, wt.%) than almost all of our other TTG samples from the Kapuskasing Uplift (see Kendrick et al., 2022 [Chapter 3]; Table S3.1). These major and trace element trends may indicate geochemical variability between suites of TTGs of different crustal levels within the Kapuskasing Uplift.

4.4.2 Zircon U–Pb geochronology

All U–Pb data from zircon analyses are included in Table S3.2, selected CL images from each zircon population are shown in Fig. S3.2, concordia and $^{207}Pb/^{206}Pb$ age versus $^{176}Hf/^{177}Hf$ trends are shown in Fig. S3.3, and detailed interpretations of the results from each sample are given in the Appendix S3.1.2; this information is also summarized here. For all samples, zircon varies from approximately 50 µm to 100 µm in width and 100 µm to 300 µm in length. Most zircon show oscillatory zoning in

CL images; many have distinct cores and rims. Only cores were targeted for analysis, as rims were typically < 50 μm thick. Analyses were considered to be discordant when the difference between the $^{238}U/^{206}Pb$ and $^{207}Pb/^{206}Pb$ ages was ≥ 5%. In three samples, an analysis yielded an age over 100 Myr older than others from the same sample, but with no distinguishable difference in $^{176}Hf/^{177}Hf$, resulting in $^{176}Hf/^{177}Hf(t)$ apparently more radiogenic than depleted mantle; these analyses could have been affected by common Pb and we consider these ages to be unreliable (c.f. Ge et al., 2018; Frieman et al., 2021; see Appendix S3.1.2). Analyses yielding young ages may have experienced ancient radiogenic Pb loss events, particularly if the concentration of U is high (>1000 μg/g). Any analyses that appeared to include both cores and rims, obvious cracks, or zones with a spongy texture (i.e., metamict zones) are also considered to be unreliable and are not discussed further.

Three groups of primary ages were identified: igneous zircon (Group I), xenocrystic components or discrete crystals (Group X), and metamorphic zircon (Group M). All samples yielded zircon populations with $^{207}Pb/^{206}Pb$ ages that overlapped with at least one other analysis within 2σ uncertainty (Fig. 4.2). The igneous crystallization age was calculated based on analyses from Group I, consistent with their dominant oscillatory zonation and location in core domains (Group I, Fig. 4.2). For each sample, Group I analyses were used to calculate a weighted mean $^{207}Pb/^{206}Pb$ age, interpreted as the igneous crystallization age of the sample. However, for four samples, a single statistically robust population was not found from Group I zircon analyses (see methods in Appendix S3.1.1), indicating either prolonged growth or secondary modification resulting in scatter along the concordia. Analyses that yielded ages older than Group I are inferred to have sampled xenocrystic components (Group X, Fig. 4.2). Metamorphic zircon growth (Group M, Fig. 4.2) is evident in samples that underwent high-grade metamorphism and such zircon ages are significantly younger than the dominant Group I population (samples 17JK11 and 17JK26). The significance of ages obtained from metamorphic zircon is not discussed further.

Three samples have Mesoarchean crystallization ages, including sample 19JK45B from the Hawk Lake granitic complex with an age of ca. 2885 Ma and two samples from the KSZ, 17JK11 yielding an age of ca. 2834 Ma, and 17JK26 with ages that vary from ca. 2835 to 2806 Ma (no statistically robust mean age). The analyses from sample 17JK26 show some correlation between $^{176}Hf/^{177}Hf$ and age (Fig. S3.3), which supports protracted zircon growth and not secondary modification. One analysis with a ca. 2885 Ma age from sample 17JK11 may represent a xenocrystic component.

The six remaining samples—all from the WGD—have Neoarchean crystallization ages. The oldest, sample 18JK19, yielded a population from ca. 2750 to 2715 Ma but lacks a single statistically robust mean age. The small range of $^{176}Hf/^{177}Hf$ values from this population (Table S3.2, Fig. S3.3) suggests that the range of ages reflects ancient Pb loss rather than protracted zircon growth in this sample. Samples 19JK43 and 18JK53 have indistinguishable weighted mean ages at ca. 2695 Ma and 18JK08 is the youngest sample at ca. 2685 Ma. Sample 19JK40 provided no single statistically robust mean age, with a population from ca. 2716–2679 Ma. A large number of analyses from sample 19JK40 yield $^{207}Pb/^{206}Pb$ ages younger than Group I that range from concordant to highly discordant (Fig. S3.3); the zircon population from this sample has likely experienced radiogenic Pb loss. Sample 19JK41 yields a similar population of ages to sample 19JK40, with a range of ca. 2706–2680 Ma and no statistically robust mean age. As these analyses show no correlation between $^{176}Hf/^{177}Hf$ values and $^{207}Pb/^{206}Pb$ age (Fig. S3.3), the range of ages likely reflects Pb loss. The populations of samples 19JK40 and 19JK41 broadly overlap with the ca. 2695–2685 Ma samples (Fig. 4.2); the crystallization ages of these samples are likely within this range. Assorted analyses with ages of ca. 2782–2720 Ma across the Neoarchean samples are consistent with xenocrystic zircon components.

4.4.3 Hafnium isotopes

The measured Lu–Hf isotopic data were coupled with the results of U–Pb geochronology to calculate an εHf(t) value for each analysis relative to the chondritic uniform reservoir (CHUR) (Fig. 4.3; dataset available in Table S3.3). Calculations included only zircon analyses within primary growth groups—the accepted igneous population (Group I), xenocrysts (Group X), or metamorphic growth (Group M). Populations were assigned their weighted mean age where possible; otherwise, the individual calculated $^{207}Pb/^{206}Pb$ age was used for spot analyses without a statistically robust weighted mean age. Alternatively, the significance of U–Pb and Hf isotopic data collected from zircon by LASS may be interpreted based on the mean $^{207}Pb/^{206}Pb$ age and the mean εHf(t) value of a zircon population (e.g., Salerno et al., 2021); both approaches yield similar results for our samples (Fig. S3.4).

Sample 19JK45B from the Hawk Lake granitic complex has a crystallization age of ca. 2885 Ma and εHf(t) overlaps CHUR at this time with values ranging from –1.0 to +1.5, similar to U–Pb–Hf data previously collected from this intrusive complex (Fig. 4.3; Smith et al., 1987). The two TTGs from the KSZ (17JK11 and 17JK26) yield the least radiogenic zircon εHf(t) values in our dataset. The main population between ca. 2835 Ma and ca. 2820 Ma has a range of εHf(t) values of approximately

–2.0 to –4.0 (Fig. 4.3). All samples from the WGD form a cluster of ages varying from ca. 2750 Ma to ca. 2685 Ma with relatively radiogenic εHf(t) values of +1.0 to +5.0. These juvenile, Neoarchean results are consistent with the majority of existing U–Pb and Hf data from the Wawa and Abitibi terranes of the southern Superior Province (Fig. 4.3).

All of our samples selected for zircon U–Pb and Hf isotopic analysis are TTGs, and therefore their source is likely to be basaltic (Moyen and Martin, 2012). Source evolution is approximated using $^{176}Lu/^{177}Hf = 0.023$ as a representative value chosen for mafic crust (from Vervoort and Kemp, 2016; see also Gardiner et al., 2018); however, we acknowledge the uncertainty associated with this ratio as we do not know the $^{176}Lu/^{177}Hf$ of the source rocks of these TTGs. Data from the Hawk Lake granitic complex are consistent with derivation from the same mafic source as samples from the Winnipeg River and Wabigoon terranes in the Superior Province (Hawk–Wabigoon–Winnipeg River array in Fig. 4.3); these terranes are located northwest of the Wawa terrane (Fig. 4.1a). A trend emanating from the oldest felsic rocks in the Hawk–Wabigoon–Winnipeg River array (ca. 3.0 Ga; Fig. 4.3), calculated using $^{176}Lu/^{177}Hf = 0.011$ (from Vervoort and Kemp, 2016; see also Gardiner et al., 2018), illustrates the expected range of εHf(t) values related to this array assuming melting of felsic crust. We interpret the two TTG samples from the KSZ as unrelated to the Hawk Lake granitic complex evolution trend. The high maficity of these two samples (Table S3.1) precludes a felsic source, suggesting that their low εHf(t) values required a mafic source with subchondritic $^{176}Hf/^{177}Hf$ by the Mesoarchean era.

Considering only data from the Kapuskasing Uplift (Fig. 4.4), our dataset comprises three different clusters of εHf(t) values at ca. 2835–2820 Ma, ca. 2885 Ma, and ca. 2750–2685 Ma, each consistent with derivation from increasingly radiogenic sources (sources 1, 2, and 3, respectively; Fig. 4.4). Assuming that the source lithology was broadly similar (i.e., mafic sources with $^{176}Lu/^{177}Hf = 0.023$) and derived from the same depleted mantle reservoir, calculated model ages differ for the three sources (Table S3.3): source 1 is the most ancient (ca. 3.8 Ga model age), source 2 is relatively younger (ca. 3.2 Ga model age), and source 3 is the youngest (ca. 2.9 Ga). Existing data from the MGB and WGD are relatively radiogenic and are consistent with source 3, except for two rhyolite samples (Fig. 4.4; Smith et al., 1987) with ages of ca. 2750 Ma and ca. 2710 Ma and near-chondritic $^{176}Hf/^{177}Hf$, consistent with source 2. Previously collected U–Pb and Hf data from pegmatite in the KSZ are compatible with both sources 2 and 3 (Fig. 4.4; Mole et al., 2021). The TTGs from the KSZ analyzed in our study are the only crustal material currently identified in the Kapuskasing Uplift that

was derived from source 1, the least radiogenic source (Fig. 4.4). Similar low εHf values are rare across the southern Superior Province (Fig. 4.3).

4.5 Discussion

4.5.1 Construction of the continental crust in the Kapuskasing Uplift

The Kapuskasing Uplift has been used as a natural laboratory for the composition of deep Archean crust (e.g., Rudnick and Fountain, 1995), but the origin and processes involved in the construction of the crust in this area are not well known. Our TTG dataset provides new insights into the formation of the crust exposed in the Kapuskasing Uplift within the broader context of the Superior Province, with implications for the construction of Archean crust in general.

Previous models explaining the origin of crustal components in the Kapuskasing Uplift region have relied on accretion of allochthonous crust to an existing cratonic nucleus (Moser et al., 1996; Percival et al., 2012). The Hawk terrane, which includes the volcanic Hawk assemblage and the Hawk Lake granitic complex at the base of the MGB, has been viewed as a Mesoarchean microcontinent embedded within the juvenile crust of the Wawa-Abitibi terrane, which accreted to the proto-Superior Province at ca. 2695 Ma (Percival et al., 2012). The lower crust of the Kapuskasing Uplift, exposed in the KSZ, has been interpreted as allochthonous crustal material that was tectonically incorporated into the base of the Wawa-Abitibi terrane during the Neoarchean (Krogh, 1993; Moser et al., 1996). Alternatively, the recognition of possible Mesoarchean protoliths in the KSZ has been interpreted as evidence for an attenuated continental margin underlying the Wawa and Abitibi terranes, possibly connected to older terranes to the north (Benn and Kamber, 2009).

Our U–Pb and Hf results from the Hawk Lake granitic complex link the Hawk terrane to older northern terranes and support the possibility of a Mesoarchean continental margin extending into the Wawa terrane. However, greenstone belts within the Wawa terrane north of the MGB do not contain evidence of an ancient continental basement and are geochemically compatible with an oceanic setting (Polat, 2009). We therefore suggest that the Hawk terrane was rifted from the Mesoarchean continental margin to the north during the Neoarchean, a model previously proposed for the Abitibi terrane (Bédard and Harris, 2014; Mole et al., 2021). The inherited ca. 2885 Ma component identified in sample 17JK11 from the KSZ may indicate that the deep crustal TTGs now exposed in the KSZ were emplaced at the base of the Hawk terrane at ca. 2830 Ma rather than being

tectonically accreted as allochthonous crust during the Neoarchean. The crystallization of these rocks coincides with a widespread ca. 2830 Ma magmatic episode within the Superior Province to the north and west of the Wawa terrane (Corfu and Stott, 1993; Davis et al., 1994; Tomlinson et al., 2003; Duguet et al., 2009; Bjorkman, 2017). Volcanic and plutonic rocks derived from source 3 were emplaced on top (MGB) and within (WGD) the composite Mesoarchean crust during continental rifting from ca. 2750–2690 Ma (Figs. 4.4 and 4.5; c.f. Mole et al., 2021). The abundance of source 3-related rocks obscures the relationship between and the extent of rocks from sources 1 and 2, as a large volume of Neoarchean TTG magma accumulated within the middle crust (Fig. 4.5). However, Hf isotopic data from pegmatites in the KSZ indicate that source 2-related rocks are not limited to the Hawk Lake granitic complex and may form part of the deep crust (Fig. 4.5).

The TTGs now exposed in the KSZ were derived from a relatively old mafic source with subchondritic εHf by the Mesoarchean; other granitoids produced by a similar source are older than the KSZ samples and scarce overall in the southern and western Superior Province (Fig. 4.3; Davis et al., 2005; Bjorkman et al., 2017). However, upper to middle crustal exposures are dominant in most terranes in the Superior Province (Percival et al., 2012). Our results may suggest granitoids generated from this ancient source are more widespread, but mainly restricted to the currently unexposed deep crust.

4.5.2 Insights into crustal evolution from a crustal cross section

Our isotopic dataset from across the Kapuskasing Uplift—a rare, nearly-complete exposure of Archean continental crust—implies episodic generation of felsic crust over at least ~200 Myr. In the simplest model of Archean felsic crust generation, purely intracrustal reworking would result in different generations of TTG magmatism that can be linked isotopically to a common source. We have identified three isotopically distinct groups of TTGs in the Kapuskasing Uplift, implying a complex history for the Wawa terrane requiring juxtaposition of three different mafic sources across the Mesoarchean and Neoarchean eras. However, data from the MGB or WGD in isolation would indicate a simpler evolution, dominated by a pulse of juvenile magmatism. Our results demonstrate that greenstone belts and mid-crustal grey gneiss domains can have limited potential for recording the isotopic complexity of Archean continental crust.

In exposures of Archean upper crust, greenstone belts associated with juvenile granitoids and felsic volcanic rocks may represent accretionary complexes marking the closure of an ocean, as suggested for example in the Kaapvaal Craton (Zeh et al., 2013), the Dharwar Craton (Praveen et al.,

2014), and the North China Craton (Tang et al., 2016). Distinguishing this tectonic setting from an intracontinental environment requires a lack of evidence for a cryptic—commonly unexposed—ancient basement; such evidence includes geochemical signatures and isotopic inheritance consistent with a crustal contaminant in greenstone belt rocks and their associated granitoids (Thurston, 2002; Bédard, 2006). However, these features can also be explained by introduction of crustal material into the mantle source by subduction (e.g., Tang et al., 2016). The isotopic data from the Kapuskasing Uplift demonstrate the limitations associated with determining the tectonic setting of upper crustal rocks without access to the deep crust. Although the volcanic rocks from the MGB exhibit geochemical characteristics associated with crustal contamination (Sage et al., 1996b), evidence for isotopic inheritance is apparently rare despite the underlying isotopically distinct crust. One possibility is that the volume of existing felsic rocks generated from sources 1 and 2 was relatively small and the crust was dominated by mafic rock. A large proportion of Mesoarchean mafic crust would be consistent with the lack of inherited zircon of that age (Turek et al., 1996) in the MGB. Therefore, the absence of isotopic inheritance in a greenstone belt could provide the false impression that isotopically complex basement rocks are also absent, which can in turn influence the interpreted tectonic setting.

Grey gneiss, mainly composed of TTG, is the dominant lithology exposed in Archean cratons (Moyen and Martin, 2012). Many inferences about Archean crustal evolution are therefore based on data from grey gneiss; examples include the East Pilbara Terrane (Gardiner et al., 2017), southwestern Greenland (Gardiner et al., 2019), and the Ancient Gneiss Complex in Swaziland (Zeh et al., 2011). The U–Pb and Hf isotopic data from these studies imply that many Archean granitoids in grey gneiss complexes are formed by reworking of existing TTGs from a single source. Our results suggest an isotopically homogeneous middle crust in the Wawa terrane, composed of juvenile TTGs generated from a single source (source 3; Figs 4.4 and 4.5). However, this voluminous pulse of magmatism from ca. 2750 Ma to ca. 2685 Ma began accumulating in the middle crust approximately 80 Myr after the deep crust had at least partially formed, as indicated by the ca. 2830 Ma TTGs now exposed in the KSZ (Fig. 4.5). The large volume of ca. 2750–2685 Ma TTGs requires an even larger volume of source 3, which suggests that this source material was likely located beneath the ca. 2830 Ma lower crustal TTGs. Evidence of reworking and partial melting is preserved in at least one ca. 2830 Ma TTG in the KSZ (17JK26). Nevertheless, of the TTGs investigated here and previously from the WGD (Mole et al., 2021; Fig. 4.4), none record evidence of inheritance from the underlying, isotopically distinct TTGs. Middle-crustal grey gneiss complexes may preserve an isotopic record that

is biased toward the most volumetrically significant magmatic episode in a particular region and decoupled from deeper, older crust. This highlights a strong potential for preservation bias in the Archean geological record, as rarely exposed deep crustal rocks can record distinct—though volumetrically limited—episodes of felsic magmatism. As we have shown for the Kapuskasing Uplift, these less expansive felsic intrusive bodies (i.e., the Hawk Lake granitic complex and the TTGs in the KSZ) can be crucial for reconstructing the crustal evolution of Archean cratons.

4.6 Conclusions

The new isotopic dataset from TTG samples collected across the crustal cross section exposed in the Kapuskasing Uplift provides important insights into Archean crustal evolution, both in the context of the Superior Province and felsic crust formation in general. The Mesoarchean to Neoarchean record of crustal evolution in the Kapuskasing Uplift indicates the presence of three pulses of TTG magmatism, each produced from isotopically distinct sources. In addition, the crust is stratified with different isotopic records preserved in the upper, middle, and lower crust. We have identified a Mesoarchean basement with two different generations of TTGs that was likely a crustal fragment rifted from the existing cratonic nucleus of the Superior Province. Juvenile Neoarchean volcanism and plutonism dominate the greenstone belt and grey gneiss domain, representing upper and middle crustal levels in the Kapuskasing Uplift, respectively. Isotopic inheritance is rare in these Neoarchean rocks, and alone they indicate a relatively simple crustal evolution dominated by a large pulse of juvenile magmatism. Only the deepest exposed crust preserves evidence of felsic magmatism generated from all three isotopically distinct sources. As most exposed Archean crust worldwide is upper- to middle-crustal greenstone belts and grey gneiss, interpretations about early Earth crustal evolution are biased toward the isotopic records of these rocks. This work demonstrates the potential for the lower crust to be isotopically decoupled from overlying rocks and preferentially contain material with a relatively ancient parentage. Portions of the Archean geological record may be preserved exclusively at the deepest and least accessible crustal levels; the involvement of multiple distinct sources in the construction of Archean felsic crust may be more common than implied by many zircon U–Pb and Hf isotope datasets.

4.7 References

Bédard, J.H., 2006. A catalytic delamination-driven model for coupled genesis of Archaean crust and sub-continental lithospheric mantle. Geochim. Cosmochim. Acta 70, 1188–1214. https://doi.org/10.1016/j.gca.2005.11.008

Bédard, J.H., Harris, L.B., 2014. Neoarchean disaggregation and reassembly of the Superior craton. Geology 42, 951–954. https://doi.org/10.1130/G35770.1

Benn, K., Kamber, B.S., 2009. In situ U/Pb granulite-hosted zircon dates, Kapuskasing Structural Zone, Ontario: a late Archean large igneous province (LIP) as a substrate for juvenile crust. J. Geol. 117, 519–541. https://doi.org/10.1086/600864

Bjorkman, K.E., 2017. 4D crust-mantle evolution of the Western Superior Craton: implications for Archaean granite-greenstone petrogenesis and geodynamics. PhD thesis, The University of Western Australia.

Corfu, F., Stott, G.M., 1993. U-Pb geochronology of the central Uchi Subprovince, Superior Province. Can. J. Earth Sci. 30, 1179–1196. https://doi.org/10.1139/e93-100

Davis, D.W., Amelin, Y., Nowell, G.M., Parrish, R.R., 2005. Hf isotopes in zircon from the western Superior province, Canada: implications for Archean crustal development and evolution of the depleted mantle reservoir. Precambrian Res. 140, 132–156. https://doi.org/10.1016/j.precamres.2005.07.005

Davis, W.J., Gariépy, C., Sawyer, E.W., 1994. Pre-2.8 Ga crust in the Opatica gneiss belt: a potential source of detrital zircons in the Abitibi and Pontiac subprovinces, Superior Province, Canada. Geology 22, 1111–1114. https://doi.org/10.1130/0091-7613(1994)022<1111:PGCITO>2.3.CO;2

Duguet, M., Lin, S., Davis, D.W., Corkery, M.T., McDonald, J., 2009. Long-lived transpression in the Archean Bird River greenstone belt, western Superior Province, Southeastern Manitoba. Precambrian Res. 174, 381–407. https://doi.org/10.1016/j.precamres.2009.09.001

Frieman, B.M., Kelly, N.M., Kuiper, Y.D., Monecke, T., Kylander-Clark, A., Guitreau, M., 2021. Insight into Archean crustal growth and mantle evolution from multi-isotope U-Pb and Lu-Hf analysis of detrital zircon grains from the Abitibi and Pontiac subprovinces, Canada. Precambrian Res. 357, 106136. https://doi.org/10.1016/j.precamres.2021.106136

Gardiner, N.J., Hickman, A.H., Kirkland, C.L., Lu, Y., Johnson, T., Zhao, J.X., 2017. Processes of crust formation in the early Earth imaged through Hf isotopes from the East Pilbara Terrane. Precambrian Res. 297, 56–76. https://doi.org/10.1016/j.precamres.2017.05.004

Gardiner, N.J., Johnson, T.E., Kirkland, C.L., Smithies, R.H., 2018. Melting controls on the lutetium–hafnium evolution of Archaean crust. Precambrian Res. 305, 479–488. https://doi.org/10.1016/j.precamres.2017.12.026

Gardiner, N.J., Kirkland, C.L., Hollis, J.A., Cawood, P.A., Nebel, O., Szilas, K., Yakymchuk, C., 2020. North Atlantic Craton architecture revealed by kimberlite-hosted crustal zircons. Earth Planet. Sci. Lett. 534, 116091. https://doi.org/10.1016/j.epsl.2020.116091

Gardiner, N.J., Kirkland, C.L., Hollis, J., Szilas, K., Steenfelt, A., Yakymchuk, C., Heide-Jørgensen, H., 2019. Building Mesoarchaean crust upon Eoarchaean roots: the Akia Terrane, West Greenland. Contrib. to Mineral. Petrol. 174, 1–19. https://doi.org/10.1007/s00410-019-1554-x

Ge, R., Wilde, S.A., Nemchin, A.A., Whitehouse, M.J., Bellucci, J.J., Erickson, T.M., Frew, A., Thern, E.R., 2018. A 4463 Ma apparent zircon age from the Jack Hills (Western Australia) resulting from ancient Pb mobilization. Geology 46, 303–306. https://doi.org/10.1130/G39894.1

Hartel, T.H.D., Pattison, D.R.M., 1996. Genesis of the Kapuskasing (Ontario) migmatitic mafic granulites by dehydration melting of amphibolite: the importance of quartz to reaction progress. J. Metamorph. Geol. 14, 591–611. https://doi.org/10.1046/j.1525-1314.1996.00404.x

Kendrick, J., Duguet, M., Yakymchuk, C., 2022. Diversification of Archean tonalite-trondhjemite-granodiorite suites in a mushy middle crust. Geology 50, 76–80. https://doi.org/10.1130/G49287.1

Krogh, T.E., 1993. High precision U-Pb ages for granulite metamorphism and deformation in the Archean Kapuskasing structural zone, Ontario: implications for structure and development of the lower crust. Earth Planet. Sci. Lett. 119, 1–18. https://doi.org/10.1016/0012-821X(93)90002-Q

Krogh, T.E., Moser, D.E., 1994. U–Pb zircon and monazite ages from the Kapuskasing uplift: age constraints on deformation within the Ivanhoe Lake fault zone. Can. J. Earth Sci. 31, 1096–1103. https://doi.org/10.1139/e94-098

Lin, S., 2005. Synchronous vertical and horizontal tectonism in the Neoarchean: kinematic evidence from a synclinal keel in the northwestern Superior craton, Canada. Precambrian Res. 139, 181–194. https://doi.org/10.1016/j.precamres.2005.07.001

Ma, Q., Xu, Y.-G., Huang, X.-L., Zheng, J.-P., Ping, X., Xia, X.-P., 2020. Eoarchean to Paleoproterozoic crustal evolution in the North China Craton: evidence from U-Pb and Hf-O isotopes of zircons from deep-crustal xenoliths. Geochim. Cosmochim. Acta 278, 94–109. https://doi.org/10.1016/j.gca.2019.09.009

Mäder, U.K., Percival, J.A., Berman, R.G., 1994. Thermobarometry of garnet–clinopyroxene–hornblende granulites from the Kapuskasing structural zone. Can. J. Earth Sci. 31, 1134–1145. https://doi.org/10.1139/e94-101

Mole, D.R., Thurston, P.C., Marsh, J.H., Stern, R.A., Ayer, J.A., Martin, L.A.J., Lu, Y.J., 2021. The formation of Neoarchean continental crust in the south-east Superior Craton by two distinct geodynamic processes. Precambrian Res. 356, 106104. https://doi.org/10.1016/j.precamres.2021.106104

Moser, D.E., Bowman, J.R., Wooden, J., Valley, J.W., Mazdab, F., Kita, N., 2008. Creation of a continent recorded in zircon zoning. Geology 36, 239–242. https://doi.org/10.1130/G24416A.1

Moser, D.E., Heaman, L.M., Krogh, T.E., Hanes, J.A., 1996. Intracrustal extension of an Archean orogen revealed using single-grain U-Pb zircon geochronology. Tectonics 15, 1093–1109. https://doi.org/10.1029/96TC00130

Moyen, J.-F., Martin, H., 2012. Forty years of TTG research. Lithos 148, 312–336. https://doi.org/10.1016/j.lithos.2012.06.010

Mulder, J.A., Nebel, O., Gardiner, N.J., Cawood, P.A., Wainwright, A.N., Ivanic, T.J., 2021. Crustal rejuvenation stabilised Earth's first cratons. Nat. Commun. 12, 1–7. https://doi.org/10.1038/s41467-021-23805-6

O'Neil, J., Carlson, R.W., 2017. Building Archean cratons from Hadean mafic crust. Science 355, 1199–1202. https://doi.org/10.1126/science.aah3823

Ontario Geological Survey, 2011. 1:250 000 scale bedrock geology of Ontario. Ontario Geol. Surv. Miscellaneous Release—Data 126–Revision 1

Percival, J.A., 1983. High-grade metamorphism in the Chapleau-Foleyet Area, Ontario. Am. Mineral. 68, 667–686.

Percival, J.A., Krogh, T.E., 1983. U–Pb zircon geochronology of the Kapuskasing structural zone and vicinity in the Chapleau–Foleyet area, Ontario. Can. J. Earth Sci. 20, 830–843. https://doi.org/10.1139/e83-073

Percival, J.A., West, G.F., 1994. The Kapuskasing uplift: a geological and geophysical synthesis. Can. J. Earth Sci. 31, 1256–1286. https://doi.org/10.1139/e94-110

Percival, J.A., Skulski, T., Sanborn-Barrie, M., Stott, G.M., Leclair, A.D., Corkery, M.T., Boily, M., 2012. Geology and Tectonic Evolution of the Superior Province, Canada, in: Percival, J.A., Cook, F.A., Clowes, R.M. (Eds.), Tectonic Styles in Canada: The LITHOPROBE Perspective. Geological Association of Canada, Special Paper 49, pp. 321–378.

Polat, A., 2009. The geochemistry of Neoarchean (ca. 2700 Ma) tholeiitic basalts, transitional to alkaline basalts, and gabbros, Wawa Subprovince, Canada: Implications for petrogenetic and geodynamic processes. Precambrian Res. 168, 83–105. https://doi.org/10.1016/j.precamres.2008.03.008

Praveen, M.N., Santosh, M., Yang, Q.Y., Zhang, Z.C., Huang, H., Singanenjam, S., Sajinkumar, K.S., 2014. Zircon U–Pb geochronology and Hf isotope of felsic volcanics from Attappadi, southern India: implications for Neoarchean convergent margin tectonics. Gondwana Res. 26, 907–924. https://doi.org/10.1016/j.gr.2013.08.004

Rudnick, R.L., Fountain, D.M., 1995. Nature and composition of the continental crust: a lower crustal perspective. Rev. Geophys. 33, 267–309. https://doi.org/10.1029/95RG01302

Sage, R.P., 1994. Geology of the Michipicoten Greenstone Belt. Ontario Geol. Surv. Open File Report 5888.

Sage, R.P., Lightfoot, P.C., Doherty, W., 1996a. Geochemical characteristics of granitoid rocks from within the Archean Michipicoten Greenstone Belt, Wawa Subprovince, Superior Province,

Canada: implications for source regions and tectonic evolution. Precambrian Res. 76, 155–190. https://doi.org/10.1016/0301-9268(95)00021-6

Sage, R.P., Lightfoot, P.C., Doherty, W., 1996b. Bimodal cyclical Archean basalts and rhyolites from the Michipicoten (Wawa) greenstone belt, Ontario: geochemical evidence for magma contributions from the asthenospheric mantle and ancient continental lithosphere near the southern margin of the Superior. Precambrian Res. 76, 119–153. https://doi.org/10.1016/0301-9268(95)00020-8

Salerno, R., Vervoort, J., Fisher, C., Kemp, A., Roberts, N., 2021. The coupled Hf-Nd isotope record of the early Earth in the Pilbara Craton. Earth Planet. Sci. Lett. 572, 117139. https://doi.org/10.1016/j.epsl.2021.117139

Smith, P.E., Tatsumoto, M., Farquhar, R.M., 1987. Zircon Lu-Hf systematics and the evolution of the Archean crust in the southern Superior Province, Canada. Contrib. to Mineral. Petrol. 97, 93–104. https://doi.org/10.1007/BF00375217

Tang, L., Santosh, M., Tsunogae, T., Teng, X.M., 2016. Late Neoarchean arc magmatism and crustal growth associated with microblock amalgamation in the North China Craton: evidence from the Fuping Complex. Lithos 248–251, 324–338. https://doi.org/10.1016/j.lithos.2016.01.022

Thurston, P.C., 2002. Autochthonous development of Superior Province greenstone belts? Precambrian Res. 115, 11–36. https://doi.org/10.1016/S0301-9268(02)00004-9

Tomlinson, K.Y., Davis, D.W., Stone, D., Hart, T.R., 2003. U–Pb age and Nd isotopic evidence for Archean terrane development and crustal recycling in the south-central Wabigoon subprovince, Canada. Contrib. to Mineral. Petrol. 144, 684–702. https://doi.org/10.1007/s00410-002-0423-0

Turek, A., Smith, P.E., Van Schmus, W.R., 1984. U-Pb zircon ages and the evolution of the Michipicoten plutonic-volcanic terrane of the Superior Province, Ontario. Can. J. Earth Sci. 21, 457–464. https://doi.org/10.1139/e84-049

Turek, A., Sage, R.P., Van Schmus, W.R., 1992. Advances in the U-Pb zircon geochronology of the Michipicoten greenstone belt, Superior Province, Ontario. Can. J. Earth Sci. 29, 1154–1165. https://doi.org/10.1139/e92-093

Turek, A., Heather, K.B., Sage, R.P., Van Schmus, W.R., 1996. U-Pb zircon ages for the Missanabie-Renabie area and their relation to the rest of the Michipicoten greenstone belt, Superior Province, Ontario, Canada. Precambrian Res. 76, 191–211. https://doi.org/10.1016/0301-9268(95)00063-1

Van Kranendonk, M.J., Ivanic, T.J., Wingate, M.T.D., Kirkland, C.L., Wyche, S., 2013. Long-lived, autochthonous development of the Archean Murchison Domain, and implications for Yilgarn Craton tectonics. Precambrian Res. 229, 49–92. https://doi.org/10.1016/j.precamres.2012.08.009

Vervoort, J.D., Kemp, A.I.S., 2016. Clarifying the zircon Hf isotope record of crust–mantle evolution. Chem. Geol. 425, 65–75. https://doi.org/10.1016/j.chemgeo.2016.01.023

Zeh, A., Gerdes, A., Millonig, L., 2011. Hafnium isotope record of the Ancient Gneiss Complex, Swaziland, southern Africa: evidence for Archaean crust–mantle formation and crust reworking between 3.66 and 2.73 Ga. J. Geol. Soc. London 168, 953–963. https://doi.org/10.1144/0016-76492010-117.Hafnium

Zeh, A., Jaguin, J., Poujol, M., Boulvais, P., Block, S., Paquette, J., 2013. Juvenile crust formation in the northeastern Kaapvaal Craton at 2.97 Ga—Implications for Archean terrane accretion, and the source of the Pietersburg gold. Precambrian Res. 233, 20–43. https://doi.org/10.1016/j.precamres.2013.04.013

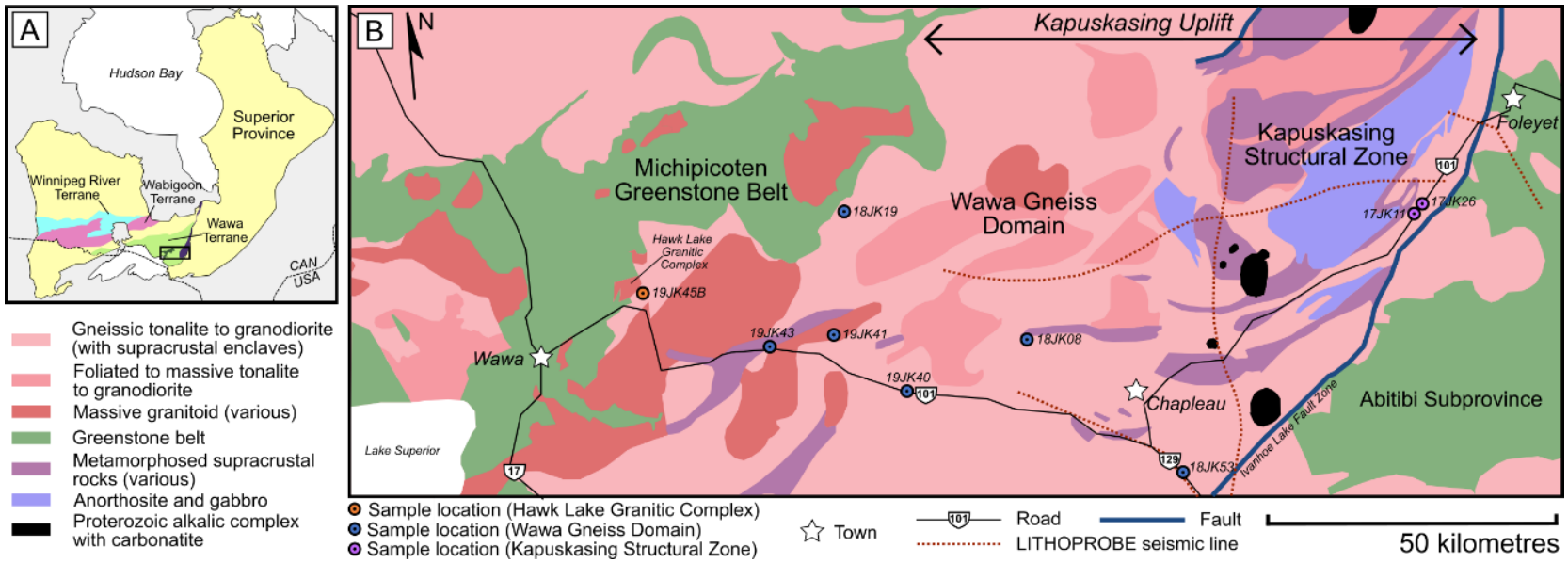


Figure 4.1. A) Simplified geological map of the Superior Province showing the location of relevant terranes (modified after Percival et al., 2012; extent of Wabigoon terrane from Mole et al., 2021). Box denotes location of the study area. B) Simplified geological map of the Kapuskasing Uplift (modified after Ontario Geological Survey, 2011).

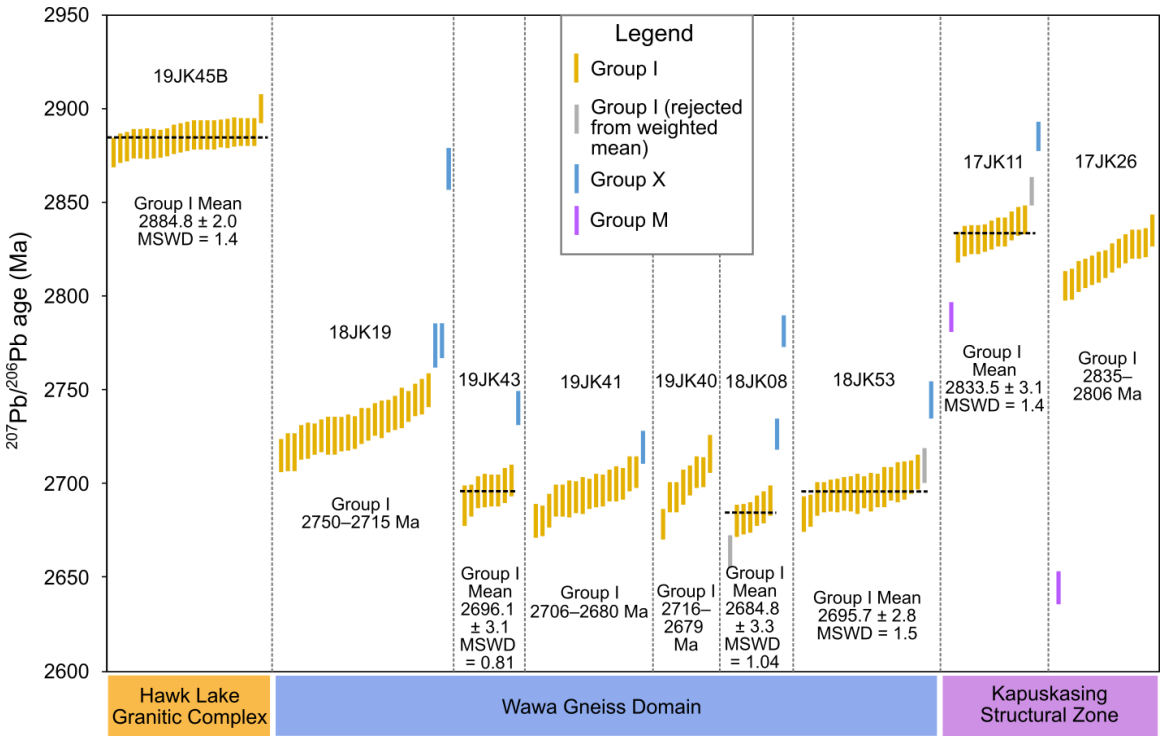


Figure 4.2. U–Pb geochronological results from the nine TTG samples examined in this study. All reported mean ages are weighted averages (see methods in Appendix S3.1.2 for more details).

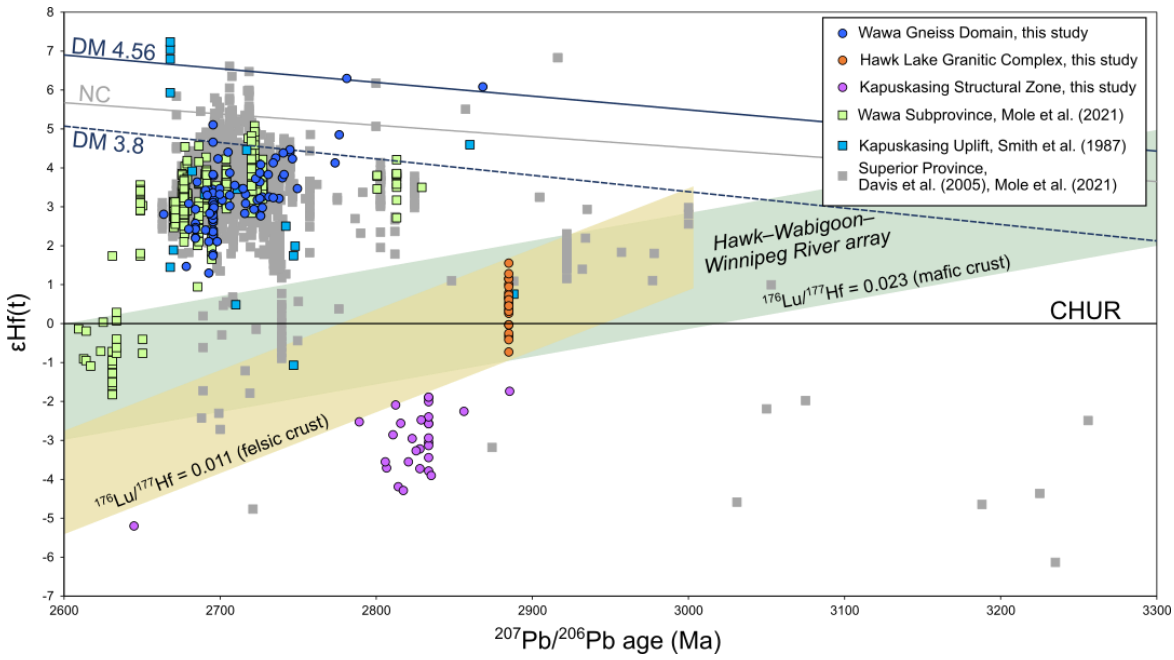


Figure 4.3. $^{207}Pb/^{206}Pb$ age versus εHf(t) for zircon analyzed in this study and from Smith et al. (1987), Davis et al. (2005), and Mole et al. (2021). DM = depleted mantle, NC = new crust, and CHUR = chondritic uniform reservoir (see methods in Appendix S3.1.2 for more details).

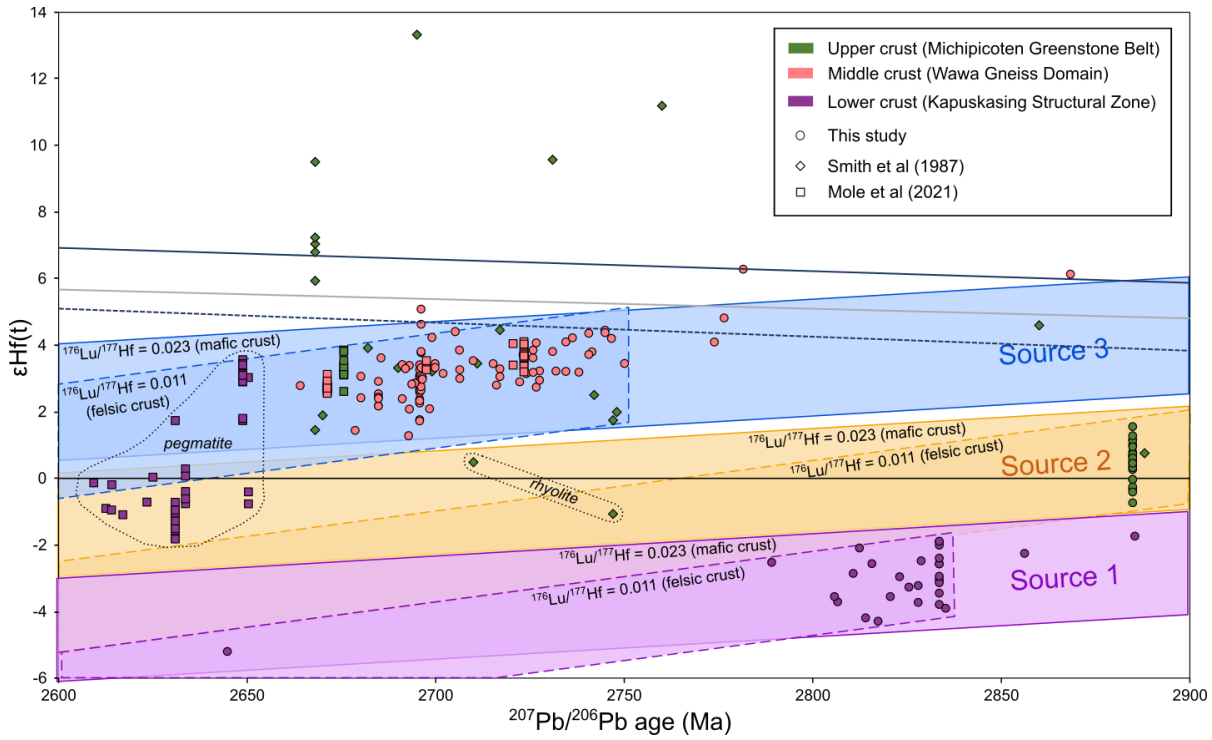


Figure 4.4. $^{207}Pb/^{206}Pb$ age versus εHf(t) for zircon from the Kapuskasing Uplift, including data from this study, Smith et al. (1987), and Mole et al. (2021).

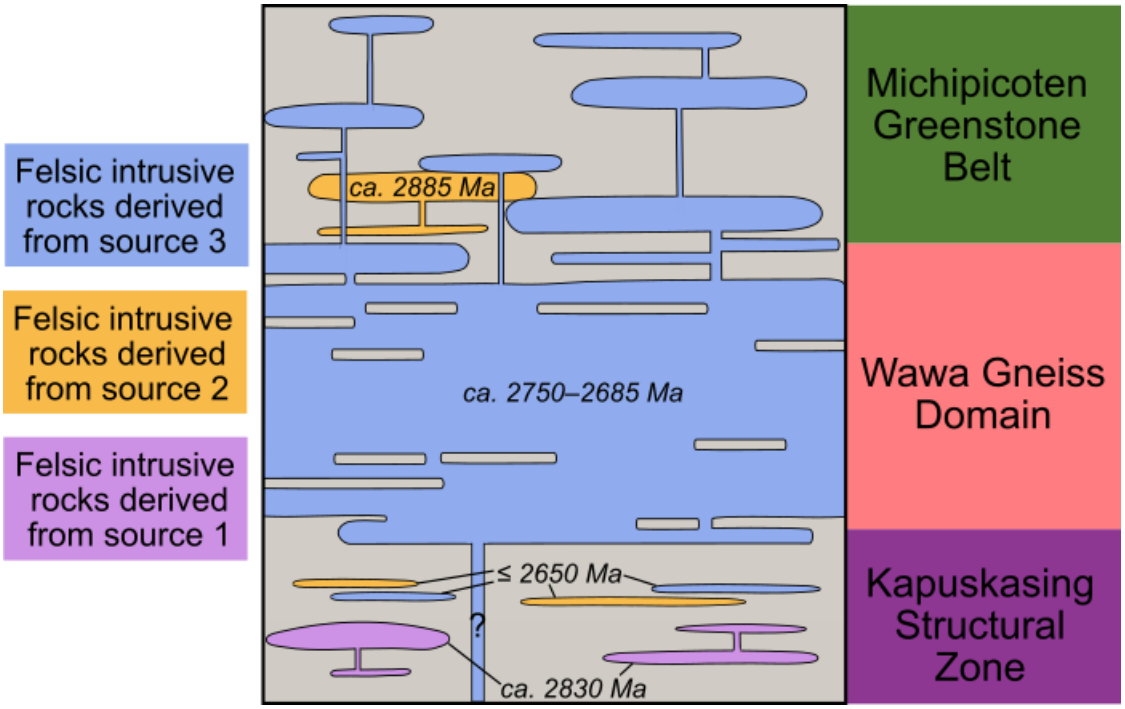


Figure 4.5. Schematic illustration of the distribution of felsic intrusive rocks from the three isotopic sources (Fig. 4.4) in the Kapuskasing uplift.

Chapter 5

Testing the TTG–metabasite connection: An integrated geochemical, isotopic, and petrogenetic modelling approach

Summary

Archean cratons are dominated by tonalite-trondhjemite-granodiorite (TTG) suites, the products of early crustal differentiation that formed early continental crust. These rocks may have been primarily generated by partial melting of hydrated basaltic crust in a variety of settings including subduction zones or the deep lithosphere. The processes that produced continental crust are mainly inferred from examination of TTGs alone, as potential source rocks are rarely exposed. In the southern Superior Province, Canada, the Kapuskasing Uplift exposes a rare crustal cross section with upper- to middle-crustal TTGs and lower-crustal metabasites, which have been shown to have produced trondhjemitic anatectic melt. Here, we hypothesize that the metabasites were the source of the Mesoarchean to Neoarchean TTGs in the Kapuskasing Uplift and test this connection by combining phase equilibrium and melt trace element modelling with whole-rock and zircon Hf isotope analysis and geochronology (garnet Lu–Hf and zircon U–Pb) of lower crustal samples. By comparison of the results with existing data from TTGs in the Kapuskasing Uplift, we determined that the metabasites are compatible sources for the TTGs. The Lu–Hf systematics of the metabasites and TTGs are the most robust evidence of a genetic connection. Modelling results indicate a possible connection and may support an increase in TTG source depth over time. Based on geochronological data, partial melting of the metabasites was coeval with crystallization of only the youngest TTGs. Overall, these results indicate a complex history of intracrustal differentiation in the Kapuskasing Uplift, with partial melting of two isotopically distinct lower-crustal metabasic sources at different times and depths.

5.1 Introduction

Tonalite-trondhjemite-granodiorite (TTG) suites are the dominant component of Archean cratons and represent the earliest granitoids generated on Earth. Based on partial melting experiments (e.g., Rapp et al., 1991; Nair and Chacko, 2008; Qian and Hermann, 2013) and thermodynamic models (e.g., Nagel et al., 2012; Palin et al., 2016; Johnson et al., 2017), anatexis of hydrated metabasite has been proposed as the dominant process by which TTGs were formed. Two endmember settings of

metabasite partial melting are generally considered: melting of a subducted oceanic slab due to a hotter Archean mantle compared to present (e.g., Drummond and Defant, 1990; Laurie et al., 2013) and melting at the base of thick basaltic crust (e.g., Bédard, 2006, Smithies et al., 2009). Understanding the nature of the TTG source is therefore crucial to broader interpretations about Archean tectonics and crustal differentiation. However, connecting a particular TTG suite to a potential metabasic source can seldom be directly achieved; subducting slabs were unlikely to have resurfaced and most preserved Archean crust records upper- to middle-crustal levels (e.g., Percival et al., 2012). Hence, rare exposures of deep Archean crust are valuable, as these may be the only direct window into potential TTG source regions and the partial melting process (e.g., Hoffmann et al., 2014; Yakymchuk et al., 2020).

In the Kapuskasing Uplift in the southern Superior Province, Canada, both deep-crustal anatectic metabasites and upper- to middle-crustal TTGs are exposed in a crustal cross section (Percival and West, 1994). Previous research in this area suggests that these metabasites represent appropriate source rocks for tonalitic to trondhjemitic melt (Hartel and Pattison, 1996), making the Kapuskasing Uplift a natural laboratory for testing the connection between lower crustal metabasite and TTGs. Here, we test the hypothesis that the anatectic metabasites were the source of upper- to middle-crustal TTGs in the Kapuskasing Uplift. We present phase equilibrium and melt trace element modelling and Lu–Hf and U–Pb isotopic data from a suite of anatectic metabasites, following previous work documenting the major and trace element composition and zircon U–Pb and Hf isotopic data from a suite of TTGs in the Kapuskasing Uplift (Kendrick et al., 2022 [Chapter 3]; Kendrick et al., submitted [Chapter 4]). Based on these new results, we aim to test the genetic connection between the metabasites and TTGs of the Kapuskasing Uplift by addressing three main questions:

1. Could the metabasites have produced melt with trace element compositions that are compatible with those of the TTGs in the Kapuskasing Uplift?
2. Are the Lu–Hf isotopic compositions of the metabasites compatible with those of TTGs in the Kapuskasing Uplift?
3. Was the timing of metabasite partial melting compatible with the timing of TTG magmatism in the Kapuskasing Uplift?

5.2 Regional geology

The Kapuskasing Uplift represents a near-complete cross section of the crust in the southern Superior Province and is the boundary between the Wawa and Abitibi subprovinces (Fig. 5.1). These two subprovinces have similar geological histories and may be contiguous across the fault zone marking the eastern extent of the Kapuskasing Uplift (Percival et al., 2012). In our study area, which is focused on the southern portion of the Kapuskasing Uplift, three domains broadly represent different crustal levels.

The Michipicoten Greenstone Belt (MGB; Fig. 5.1b) is composed of upper crustal rocks, including three volcanic cycles dated at ca. 2900 Ma, 2750 Ma, and 2700 Ma (Turek et al., 1992), which were metamorphosed at greenschist- to amphibolite-facies conditions (Sage, 1994). The volcanic rocks are mainly mafic to felsic, with ultramafic rocks only found in the ca. 2900 Ma cycle (Sage et al., 1996a). Intrusive magmatic rocks include synvolcanic granitoids—mainly TTG—and late- to post-tectonic (<2700 Ma) intrusions of mostly granodiorite, syenite, monzonite (Turek et al., 1992; Sage et al., 1996b). The MGB hosts several mineral deposits including the high-grade Island Gold deposit (Ciufo et al., 2020; Jellicoe et al., submitted).

The Wawa Gneiss Domain (WGD; Fig. 5.1b) has a deformed intrusive contact with the MGB and is dominated by plutons and grey gneisses of TTG composition (Moser et al., 1996; Kendrick et al. 2022 [Chapter 3]). These rocks represent a middle-crustal level and reached amphibolite-facies *P–T* conditions (Moser et al., 1996). A range of igneous crystallization ages has been identified, including ca. 2925 Ma, ca. 2707 Ma, ca. 2695 Ma, ca. 2685 Ma, ca. 2674 Ma, ca. 2660 Ma, and ca. 2645 Ma (Percival and Krogh, 1983; Moser et al., 1996; Kendrick et al., submitted [Chapter 4]). The range of trace element characteristics of these TTGs has been attributed largely to the behaviour of plagioclase post magma emplacement; plagioclase-rich cumulate is present in many outcrops (Kendrick et al., 2022 [Chapter 3]). The WGD has a polyphase deformation history ending with extension between ca. 2660 Ma and ca. 2645 Ma that was decoupled from the overlying MGB (Moser et al., 1996).

The Kapuskasing Structural Zone (KSZ; Figs 5.1b and c) has a gradational contact with the WGD characterized by an increase in metamorphic grade to upper-amphibolite and granulite facies (Percival, 1983). Meta-anorthositic, metatonalitic, and metabasic gneisses are the dominant lithologies and peak *P–T* conditions have been estimated at 750–850°C and 10–11 kbar, consistent with metamorphism at a deep crustal level (Mäder et al., 1994; Hartel and Pattison, 1996). Metamorphic zircon interpreted to have grown at high temperature have yielded ages from ca. 2690

Ma to ca. 2583 Ma; most ages are between ca. 2660 Ma and ca. 2645 Ma and continuous growth of metamorphic zircon rims has been documented from ca. 2660 Ma to ca. 2583 Ma (Krogh and Moser, 1994; Bowman et al., 2011). Several zircon ages from ca. 3191 Ma to ca. 2698 Ma (based on 13 *in situ* analyses; Benn and Kamber, 2009) were also interpreted as recording high-grade metamorphism. Both slow cooling and multiple thermal pulses have been proposed to explain the range of ages obtained from gneisses in the KSZ (Krogh and Moser, 1994; Percival and West, 1994; Benn and Kamber, 2009). Macroscopic evidence of anatexis is common in the metabasic gneisses and a previous investigation (Hartel and Pattison, 1996) determined that this was driven by an amphibole dehydration melting reaction of the general form

Hornblende + Plagioclase + Quartz = Garnet + Diopside + Titanite + Trondhjemitic melt.

The origin of TTGs in the Kapuskasing Uplift has been suggested to be fractionation of a mantle-derived (supra-subduction zone) magma contaminated by ancient felsic crust (Sage et al., 1996b) or partial melting of metabasic lower crust and subducted crust at different times (Benn and Kamber, 2009). Hartel and Pattison (1996) suggested that the metabasites exposed in the KSZ are representative of TTG source rocks in general, though no direct genetic connection has been made between the anatectic metabasites of the KSZ and overlying TTGs in the MGB and the WGD.

5.3 Methods

5.3.1 Whole-rock geochemical analysis

Whole-rock geochemical analysis (Table S4.1) was done at the Ontario Geological Survey (OGS) Geolabs. Samples were reduced to powder using an agate mill and fused with a borate flux for major element analysis by X-ray fluorescence (XRF) using Malvern-Panalytical Axios Advanced WD-XRF spectrometers. For trace elements, powdered samples were dissolved in a multi-acid solution in a closed vessel and analyzed by inductively coupled plasma mass spectrometry (ICP-MS) using a Thermo Scientific iCAP-Q ICP-MS. Concentrations of H_2O were measured by infrared absorption after heating samples to 105°C and 1000°C to release free water and crystalline water, respectively. Concentrations of ferrous iron were determined by titration using a permanganate solution standard. The quality of whole-rock geochemical data was monitored using sample duplicates, internal reference materials, and blanks (Table S4.1.1). Based on duplicate analyses, the precision of major element analyses was typically better than 2% (mainly 10–15% for H_2O and 10% for FeO) and trace element precision was generally better than 10%.

5.3.2 *In situ* mineral chemical analysis

The concentrations of major elements in garnet, plagioclase, clinopyroxene, amphibole, and biotite (Table S4.2) were measured by electron probe microanalysis (EPMA) with data collected by wavelength-dispersive spectrometers using a JEOL JXA-8230 SuperProbe at Memorial University of Newfoundland (samples 17JK20 and 17JK08) and a Cameca SX-100 electron microprobe at the OGS Geolabs (samples 17JK09 and 17JK12). At Memorial University of Newfoundland, operating conditions were 15 kV, 20 nA, and various beam diameters (focused for garnet, 3 µm for amphibole and clinopyroxene, and 5 µm for plagioclase and biotite) with 20–40 s count times on peak; matrix corrections were done using the ZAF method. At OGS Geolabs, 20 kV; 20 nA; a focused beam for garnet and clinopyroxene; rastered beams for amphibole, biotite (4 µm each), and plagioclase (8 µm); and 10–15 s on peak were used, with corrections done by the PAP method. A mix of natural and synthetic reference materials was used, including matrix-matched materials.

Chemical maps of garnet in polished thin sections were collected by laser ablation (LA) ICP-MS at the Metal Isotope Geochemistry Laboratory at University of Waterloo. A 193 nm Analyte G2 laser ablation system coupled to an Agilent 8800 quadrupole ICP-MS was used to raster across garnet crystals at scan speeds of 25–45 µm/s using circular spot sizes 20–25 µm in diameter, depending on the size of the map. Laser operating conditions were 10–15 Hz and fluence of 7 J/cm^2. The data were standardized using NIST 612 as the primary reference material and the quality of the data was monitored based on analyses of NIST 610 and BHVO-2G (results and mass integration times are available in Table S4.3 and Table S4.3.1, respectively); reference materials were analyzed after every 5–12 garnet scans. The data were reduced using the 'Trace Element' data reduction scheme and maps were generated using the Imaging function in Iolite v4.4.5 (Woodhead et al., 2007; Paton et al., 2011) with internal standardization based on Si content (using average concentrations of Si in garnet for each sample as determined by EPMA). Based on analyses of NIST 610, trace element precision and accuracy were typically better than 10% (rarely 10–20% for accuracy of REE). However, results from BHVO-2G commonly had a difference from accepted values and precision of up to 20–30%, particularly for REE. Therefore, we consider the trace element data in the maps to be semi-quantitative.

5.3.3 Phase equilibrium modelling and melt trace element modelling

Phase equilibrium modelling was done using THERMOCALC v.3.45 (Powell and Holland, 1988) with the internally consistent thermodynamic dataset ds62 (Holland and Powell, 2011) in the Na_2O–CaO–K_2O–FeO–MgO–Al_2O_3–SiO_2–H_2O–TiO_2–Fe_2O_3 chemical system with the metabasite set of

activity–composition (*a–x*) models (Green et al., 2016; files produced May 2016). The set includes models for tonalitic melt, clinopyroxene ('augite' model used here), amphibole (Green et al., 2016), orthopyroxene, garnet, biotite, muscovite, ilmenite (White et al., 2014), K-feldspar, plagioclase (Holland and Powell, 2003), and spinel (White et al., 2002). Rutile, quartz, titanite, and water were modelled as pure phases. The bulk compositions used for modelling were those measured by whole-rock geochemical analysis (Table 5.1, Table S4.1), including the crystalline H_2O values obtained from infrared absorption and the Fe^{2+}/Fe^{3+} ratio as determined from titration.

Melt trace element modelling was done by mass balance using the batch melting equation of Shaw (1970),

$$\frac{C_L}{C_o} = \frac{1}{D(1-F)+F}$$

where C_L is the concentration of a trace element in the melt, C_o is the concentration of a trace element in the system, D is the bulk distribution coefficient, and F is the weight fraction of melt. For the calculations done in this study, C_o is the whole-rock concentration of an element (Table S4.1). The value of D was calculated at each set of *P–T* conditions based on the modelled residue assemblage and partition coefficients relevant to anatexis of metabasites from Bédard (2006). The proportion of melt (converted to wt.%) from phase equilibrium modelling was used for F. The melt trace element modelling was done assuming a closed system, fixed partition coefficients for each mineral, and no involvement of accessory minerals.

5.3.4 Garnet Lu–Hf analysis

Garnet was separated from samples 17JK20, 17JK12, 17JK09, and 17JK08 at University of Waterloo by magnetic separation, heavy liquids, panning, and hand picking. Representative whole-rock samples were crushed manually and pulverized in an agate ball mill at University of Waterloo. Sample preparation for Lu–Hf analysis was done at the Radiogenic Isotope and Geochronology Laboratory (RIGL) at Washington State University (Pullman, USA). The protocols for sample dissolution and separation of Lu and Hf at this laboratory have been presented in detail in Johnson et al. (2018), and we summarize the process here. For each of the four samples selected for Lu–Hf analysis, two whole-rock powder fractions and four garnet separates were obtained, each weighing approximately 0.25 g. One whole-rock fraction and all garnet separates were dissolved in a concentrated HF and HNO_3 solution within sealed Savillex beakers on a 120°C hot plate at atmospheric pressure. This procedure is intended to limit dissolution of zircon, which may be

inherited from the protolith and not in isotopic equilibrium with metamorphic minerals. The remaining whole-rock fraction was digested in a HF and HNO_3 solution in a Teflon vessel within a Parr-type bomb heated in a furnace at 150°C to ensure complete dissolution of all minerals. The fractions were heated in a H_3BO_3 and HCl solution, and again in HCl in a Parr-type bomb in a 150°C furnace in preparation for ion exchange chromatography. After being spiked with ^{176}Lu–^{180}Hf tracer solutions, whole-rock and garnet fractions were passed through an initial stage of column chromatography to obtain Hf- and HREE-rich solutions. The solutions went through a second stage of column chromatography for further purification of Hf from other high field strength elements (Ti and Zr) and isolation of Lu from other HREE. The Hf solutions were further purified of any remaining HREE by a third stage "clean-up" column.

Isotopic analysis was done at RIGL using a Thermo-Finnigan Neptune Multi-Collector (MC) ICP-MS for Lu and the Thermo-Finnigan Neptune Plus MC-ICP-MS for Hf analysis. The procedures for analysis, data reduction (including interference and mass bias corrections), and isotope dilution calculations are described in Vervoort et al. (2004). The Hf isotope measurements were normalized relative to the JMC 475 Hf solution standard. External uncertainties were applied to the final ratios: 0.5% for $^{176}Lu/^{177}Hf$ and 0.005% (in quadrature) for $^{176}Hf/^{177}Hf$. Isochrons and Lu–Hf dates were calculated using Isoplot 4.15 (Ludwig, 2012). The results of Lu–Hf analysis are shown in Table 5.2 and Table S4.4 (including the results of a fourth metabasite sample, which yielded an errorchron shown in Figure S4.2 with a geologically meaningless age and is not discussed further).

5.3.5 Zircon U–Pb and Hf analysis

Zircon separates were obtained from two leucosome samples at Overburden Drilling Management Limited (Ottawa, Canada) by electric pulse disaggregation and density-based separation. Crystals were hand-picked and mounted in epoxy grain mounts, which were polished to expose the centres of grains. Zircon internal structures were imaged using cathodoluminescence (CL) microscopy at the Waterloo Advanced Technology Laboratory at University of Waterloo using a Zeiss Leo 1530 field emission scanning electron microscope with accelerating voltage of 20 kV and approximate current of 900 pA.

Isotopic analysis was performed at the John de Laeter Centre for Mass Spectrometry at Curtin University (Perth, Australia), where zircon U–Pb and Lu–Hf data (Table 5.3; Table S4.5) were collected simultaneously by laser ablation split-stream analysis, using a Resonetics RESOlution M–50A–LR system with a COMPex 102 193 nm excimer UV laser connected to an Agilent 8900 ICP-MS and a Nu Plasma II multi-collector ICP-MS. A 50 µm spot size was used for laser ablation, with

operating conditions of 10 Hz and 3 J/cm^2 fluence. Ablation time was 35 s after two cleaning pulses, with a total baseline acquisition of 65 s. The U–Pb data (Agilent) were processed using Iolite4 (Paton et al., 2011) with the OG-1 zircon standard as the primary reference material (Stern et al., 2009; 3465.4 ± 0.6 Ma). For Lu–Hf data (Nu Plasma II), processing was also completed in Iolite4 using a modified version of the data reduction scheme of Woodhead et al. (2004). Mud Tank zircon was the primary reference material for Hf analysis (Woodhead and Hergt, 2005; $^{176}Hf/^{177}Hf$ of 0.282507 ± 0.000006). Analyses of secondary reference materials (data available in Table S4.5) yielded $^{207}Pb/^{206}Pb$ ages and $^{176}Hf/^{177}Hf$ values within uncertainty of accepted values in most cases. Tera-Wasserburg diagrams were generated using Isoplot (Ludwig, 2012).

5.4 Results

5.4.1 Field observations and petrography

Outcrops in the southern KSZ were examined in areas of cleared vegetation along a northeast-trending road and associated small side roads (Fig. 5.1c). Although exposure was best along the road, outcrops in this area are sporadic (≤ 5% exposed). Metabasite (Figs 5.2a–c, e, f) and metatonalite (Fig. 5.2d) were the dominant observed lithologies with rare metapelite and meta-anorthosite. Flat-lying foliation was observed in many outcrops, generally defined by millimetre- to decimetre-scale compositional layers. Sampling was focused mainly on metabasite and metatonalite, with the aim of collecting a sample set representative of the variations observed in these lithologies.

Metabasite outcrops in the KSZ contain up to 30 vol.% stromatic to patchy leucosome that is composed primarily of plagioclase and quartz with variable amounts of garnet, clinopyroxene, and amphibole (Fig. 5.2a, b, e, f). Garnet and clinopyroxene have been interpreted as products of an amphibole breakdown reaction in the KSZ (Hartel and Pattison, 1996); we also infer that garnet and clinopyroxene porphyroblasts in the leucosome are peritectic, as the association of anhydrous minerals with leucosome is consistent with fluid-absent hydrate-breakdown melting (e.g., Brown, 2013). The metabasite mineral assemblages are typically dominated by amphibole and plagioclase, with or without garnet, clinopyroxene, biotite, and quartz. In all cases, samples used for whole-rock geochemical analysis were taken away from leucosome-rich areas, whereas both leucosome and melanocratic components were targeted for thin sections. Some outcrops are compositionally layered at the centimetre to decimetre scale, with leucosome-bearing amphibole + plagioclase (± garnet) layers and leucosome-poor garnet + clinopyroxene + plagioclase layers (Fig. 5.2c). Systematic variations in the characteristics of metabasite outcrops were observed across the study area, with

leucosome and garnet content broadly increasing from west to east. The prevalence of compositionally layered metabasite outcrops also increases from west to east. In exposures where both metabasite and metatonalite are present, metabasite bodies appear to be enclaves within metatonalitic gneiss, however poor exposure obscures the relationship between the two lithologies in most cases.

Metatonalite varies from homogeneous and moderately foliated to heterogeneous with strong foliation defined by millimetre- to centimetre-scale compositional banding (Fig. 5.2d). The proportion of amphibole is variable among metatonalite outcrops—and in some cases, within outcrop—resulting in relatively leucocratic and melanocratic varieties. The abundance of centimetre- to metre-scale metabasic enclaves also varies; these may comprise up to 25 vol.% of the outcrop. Stromatic leucosome is present in many metatonalite outcrops (up to 20 vol.%; Fig. 5.2d) and is dominantly composed of plagioclase + quartz ± K-feldspar but may also contain peritectic garnet or amphibole porphyroblasts. Garnet may also appear throughout melanocratic components of the metatonalite and is most common in the eastern portion of the study area and in more melanocratic outcrops (Fig. 5.2d).

From our sample set (53 collected in the KSZ), we have selected three metabasites and one metatonalite for further study. These samples represent a range of bulk compositions reflected in different proportions of rock-forming minerals—useful for phase equilibrium and melt composition modelling—and have sufficient garnet for Lu–Hf geochronology. At three metabasite outcrops, leucosome-rich samples were collected and trimmed to remove metabasite matrix to obtain leucosome bulk compositions and zircon separates for U–Pb and Hf analysis.

5.4.1.1 17JK20 (metabasite) and 19JK15 (leucosome)

Sample 17JK20 was collected from a heterogeneous outcrop of garnet + amphibole + clinopyroxene + plagioclase metabasite with abundant plagioclase + quartz leucosome (up to 30 vol.%; Fig. 5.2a). The leucosome forms a network-like structure across the outcrop, with some continuous stromatic leucosome (up to 3 cm wide) forming nearly orthogonal intersections with other centimetre-scale leucosome bodies. Millimetre-scale leucosome in the form of discontinuous layers or patches appears to be randomly oriented and are commonly in petrographic continuity (i.e., similar mineral assemblages, grains sizes, and modes) with larger leucosome bodies. Sample 19JK15 was taken from an area rich in centimetre-scale leucosome in this outcrop (Fig. 5.2a; sampled area not pictured) and was trimmed using a rock saw to remove metabasite.

At the thin section scale, sample 17JK20 is composed of garnet + amphibole + plagioclase + ilmenite + quartz ± clinopyroxene domains with a subgranoblastic texture and plagioclase + quartz leucosome domains. Garnet (up to 5 mm), amphibole, and plagioclase (both up to 1 mm) are subidioblastic and abundant (Fig. 5.3a, b). Subidioblastic clinopyroxene (up to 1 mm; Fig. 5.3b) is relatively uncommon. In the domains dominated by ferromagnesian minerals, rare quartz (up to 0.5 mm) is rounded or xenoblastic and commonly interstitial to the other minerals (Fig. 5.3b). The low dihedral angle and cuspate grain shapes of interstitial quartz are considered here (and in subsequent samples) to indicate the former presence of melt-filled pores (e.g., Holness and Sawyer, 2008). Opaque minerals in this sample include ilmenite, pyrrhotite, chalcopyrite, and pyrite. Biotite is rarely present at amphibole and garnet rims. Inclusions in garnet are typically quartz and ilmenite, with less common amphibole, biotite and Fe-sulphides. Leucosome domains are coarser grained overall with elongated plagioclase and quartz (commonly up to 5 mm). The peak metamorphic assemblage of this sample is inferred to be garnet + amphibole + clinopyroxene + plagioclase + quartz + ilmenite + melt.

In sample 17JK20, garnet has an average composition of $Alm_{58}Prp_{15}Grs_{24}Sps_{3}$ with weak, patchy zoning defined by variability in the concentrations of FeO and CaO ($Alm_{55–60}$ and $Grs_{23–27}$); the FeO content is highest at the rims. Plagioclase is homogeneous with an average composition of An_{38}. Clinopyroxene has a range of Mg# from 65 to 68 and is most Mg-rich at the edge of leucosome. Amphibole in sample 17JK20 is classified as pargasite and ferro-pargasite with no systematic zonation. The only biotite analyzed in this sample is an inclusion within garnet that yielded an Mg# of 52.

5.4.1.2 17JK12 (metabasite)

Sample 17JK12 was collected from a metabasite outcrop with an equigranular matrix dominated by millimetre-scale hornblende, plagioclase, and a small amount (≤ 5 vol.%) of garnet (Fig. 5.2b). The outcrop contains 5–10 vol.% discontinuous stromatic leucosome (millimetre- to centimetre-scale). Leucosome is mainly composed of quartz + plagioclase, but garnet porphyroblasts up to 1.5 cm (Fig. 5.2b) and less common clinopyroxene up to 0.5 cm are also present.

Two domains are present in sample 17JK12 and are both composed of garnet + amphibole + plagioclase + quartz + ilmenite. These two domains are distinguished based on the different modal proportions of minerals and the microstructures. Domains dominated by ferromagnesian minerals (Fig. 5.3c) contain abundant subidioblastic amphibole (up to 2 mm) with lesser amounts of subidioblastic garnet (up to 2 mm) and plagioclase (up to 1 mm). Quartz and ilmenite (up to 0.1 mm) are rare, xenoblastic, and interstitial to amphibole and plagioclase grains. Rare biotite is only present

at amphibole and garnet rims. Leucosome domains (Fig. 5.3d) are dominated by subidioblastic quartz and plagioclase (up to 6 mm), with subidioblastic to idioblastic amphibole (up to 5 mm) and skeletal, densely fractured, garnet porphyroblasts (up to 1.5 cm). Inclusions in the garnet porphyroblasts include apparently discontinuous but optically continuous patches of quartz and plagioclase (up to 4 mm), pyrrhotite, chalcopyrite, and ilmenite. We infer that the peak metamorphic assemblage was garnet + amphibole + clinopyroxene + plagioclase + quartz + ilmenite + melt, given the presence of clinopyroxene in outcrop near the sampled area (not observed in thin section).

Garnet in sample 17JK12 has an average composition of $Alm_{58}Prp_{17}Grs_{21}Sps_{4}$ and are zoned with the concentration of FeO increasing from core to rim (Alm_{56} to Alm_{61}) and MgO decreasing from core to rim (Prp_{19} to Prp_{14}). Plagioclase has an average composition of An_{37} with weakly decreasing CaO and increasing Na_2O from core to rim (An_{38} to An_{34}) in some crystals. Amphibole is mainly classified as pargasite with some magnesio-hornblende; one analysis of an amphibole rim is classified as ferro-pargasite. One biotite crystal associated with amphibole has an Mg# of 55.

5.4.1.3 17JK09 (metabasite)

Sample 17JK09 was collected from a compositionally layered metabasite outcrop, with centimetre- to decimetre-scale layers of two main types (Fig. 5.2c). The first type is melanocratic owing to the large proportion of amphibole and smaller amounts of plagioclase and garnet. Melanocratic layers contain variable amounts (~5–15 vol.%) of millimetre-scale to centimetre-scale stromatic or patchy leucosome. The second layer type is equigranular (millimetre-scale grain size) garnet + clinopyroxene + plagioclase metabasite that is leucosome-free and appears relatively leucocratic in outcrop. At this locality, only the second type of layer was sampled.

Sample 17JK09 is dominated by garnet + clinopyroxene + plagioclase + ilmenite (up to 2 mm) with a subgranoblastic texture (Fig. 5.3e). Quartz is uncommon, xenoblastic, and interstitial to the main minerals and is also the most abundant inclusion in garnet (Fig. 5.3f). Other inclusions found in garnet are clinopyroxene, green-brown amphibole, titanite, ilmenite, and apatite. Minor minerals in the matrix include green-blue amphibole and biotite—typically at the rims of garnet and clinopyroxene—rare green-brown amphibole, pyrrhotite, chalcopyrite, and pyrite. We suggest that the peak metamorphic assemblage was garnet + clinopyroxene + plagioclase + quartz + ilmenite + melt. This anhydrous assemblage and lack of visible leucosome suggest that most melt was drained from the system (e.g., White and Powell, 2002).

Garnet in sample 17JK09 is homogeneous with an average composition of $Alm_{58}Prp_{10}Grs_{29}Sps_{2}$. Plagioclase crystals are unzoned with a compositional range from An_{38} to An_{42}, although a plagioclase inclusion within garnet and plagioclase associated with amphibole have relatively lower concentrations of CaO (An_{34} and An_{23}, respectively). Clinopyroxene is generally homogeneous with an average Mg# of 58. Green-brown amphibole (as inclusions in garnet or rare matrix crystals) are classified as ferro-pargasite, whereas green-blue amphibole is ferro-hornblende. The two biotite crystals analyzed exhibit minor compositional differences, with Mg# of 48 and 44.

5.4.1.4 17JK08 (metatonalite)

Sample 17JK08 was collected from a gneissic metatonalite outcrop (Fig. 5.2d). Stromatic to lens-shaped leucosome layers constitute 15–20 vol.% of the outcrop, are mainly composed of plagioclase + quartz, and are up to 1.5 cm wide. These layers commonly contain garnet porphyroblasts up to 1 cm in size. Smaller garnet crystals are also present in the dominant metatonalitic layers of amphibole + biotite + plagioclase + quartz.

Sample 17JK08 contains amphibole + garnet + biotite + plagioclase + quartz domains and plagioclase + quartz + garnet + biotite domains, along with accessory apatite and allanite (Fig. 5.3g, h). Foliation in the sample is defined by alignment of the long axes of biotite and amphibole and the compositional banding. In the amphibole-rich domains, grains are subidioblastic and mainly up to 1 mm with some amphibole and garnet up to 4 mm. Quartz is generally subequant to equant, and rarely forms xenoblastic, interstitial grains (Fig. 5.3h). In leucosome domains, plagioclase and quartz are coarser (up to 5 mm) and elongate. Uncommon opaque minerals throughout the sample are ilmenite, chalcopyrite, pyrrhotite, and pyrite; these are also included in garnet along with quartz, apatite, and biotite. The peak metamorphic assemblage of this sample is inferred to be garnet + amphibole + biotite + plagioclase + quartz + ilmenite + melt.

Garnet in sample 17JK08 has an average composition of $Alm_{57}Prp_{21}Grs_{19}Sps_{4}$ with patchy zones that are relatively enriched in CaO (Grs_{22} maximum) and rims relatively enriched in FeO (Alm_{60} maximum). Plagioclase is homogeneous with an average composition of An_{36}. Amphibole in this sample is mainly classified as pargasite, with several analyses classified as magnesio-hornblende based on slight compositional fluctuations; a magnesio-hornblende inclusion in garnet shows minor enrichment in MgO and depletion of FeO relative to matrix amphibole. Matrix biotite is unzoned with an average Mg# of 54 and a biotite inclusion in garnet yielded an Mg# of 64.

5.4.1.5 19JK13 (leucosome)

Sample 19JK13 was collected from a leucosome-rich area (Fig. 5.2e) in a metabasite outcrop with compositional layering (as described for sample 17JK09). Melanocratic layers contain ~15 vol.% stromatic to patchy leucosome up to 10 cm wide, which is mainly composed of plagioclase + quartz with unevenly distributed garnet and clinopyroxene porphyroblasts up to 2 cm in size. The sampled leucosome contains garnet porphyroblasts.

5.4.1.6 19JK16 (leucosome)

Sample 19JK16 was obtained from a leucosome-rich area in a metabasite outcrop (Fig. 5.2f), which was also compositionally layered (as described for sample 17JK09). Leucosome is generally stromatic to patchy and up to 10 cm wide with heterogeneously distributed garnet and clinopyroxene porphyroblasts up to 1.5 cm and 3 cm in size, respectively. The leucosome constitutes up to 15 vol.% of the outcrop.

5.4.2 Whole-rock composition

Granulite-facies samples collected from the KSZ are broadly basic to tonalitic in composition. Distinguishing between intrusive and extrusive protoliths is difficult, as primary igneous textures are not preserved and contact relationships between different lithologies are unclear due to deformation and sporadic exposure. Geochemical classification diagrams based on volcanic rocks are used here qualitatively, as they may not be appropriate for all samples. In addition, loss of variable amounts of anatectic melt has likely influenced the bulk compositions of these rocks and they may be depleted in elements that are enriched in melt relative to their protoliths (e.g., SiO_2, Na_2O, K_2O, incompatible trace elements).

The metabasites from the KSZ examined here (17JK09, 17JK12, and 17JK20) are geochemically similar to basalt, and the metatonalite sample (17JK08) is similar to andesite based on SiO_2 versus $Na_2O + K_2O$ (wt.%) (Fig. 5.4a). The samples appear to be consistent with the tholeiitic series, based on total alkali content (Fig. 5.4a). Sample 17JK12 is relatively more magnesian (Mg# = 47) than 17JK20 and 17JK09 (Mg# = 35 and 34, respectively; see Table 5.1 for molar concentrations of MgO and FeO). Sample 17JK08, with ~60 wt% SiO_2, is intermediate in composition, sodic ($K_2O/Na_2O = 0.5$), and relatively magnesian compared to the metabasites (Mg# = 52). The trace element trends of the metabasite samples from the KSZ (Fig. 5.4b) are variable. The REE profiles are generally flat, with sample 17JK20 showing REE enrichment relative to samples 17JK09 and 17JK12. Sample 17JK20 also shows significantly lower concentrations of U and Th compared to the

other metabasite samples and Archean basalts on average (*Ar*-basalt of Martin et al., 2014; Fig. 5.4b). Trace element characteristics of sample 17JK08 are broadly similar to TTGs (e.g., Moyen and Martin, 2012), as the REE have an overall negative slope and a negative Nb–Ta anomaly is present.

The whole-rock chemical compositions of two leucosome samples (19JK13 and 19JK16) collected from metabasite outcrops in the KSZ are compared to TTGs from the WGD (Fig. 5.5). In terms of normative albite, anorthite, and orthoclase, the leucosome samples plot closer to the anorthite apex than the TTGs, but the low orthoclase content is similar to plagioclase cumulates associated with TTGs in the WGD (Fig. 5.5a). The chondrite-normalized trace element trends of the leucosome samples (Fig. 5.5b) are also comparable to the plagioclase cumulates, with strong positive Sr and Eu anomalies and low concentrations of other elements. Concentrations of HREE in the leucosome samples are relatively high compared to the cumulates. The presence of peritectic garnet may have contributed to higher HREE and normative anorthite content in the leucosomes in comparison to granitoid samples from the WGD.

5.4.3 Phase equilibrium modelling

Phase diagrams with modal isopleths of garnet were constructed for metabasite samples 17JK20, 17JK12, 17JK09, and metatonalite sample 17JK08 by phase equilibrium modelling (Fig. 5.6; modelled compositions in Table 5.1). The diagrams for 17JK20 and 17JK12 (Fig. 5.6a, b) are similar, with the *P*–*T* field of the inferred peak assemblage (amphibole + clinopyroxene + garnet + plagioclase + ilmenite + quartz + melt) constrained by the predicted stability fields of orthopyroxene at low *P*, rutile at high *P*, and biotite at low *T*; these minerals are either absent from the samples or not part of the inferred peak assemblage. With increasing temperature, hornblende is predicted to be exhausted first in 17JK20 whereas quartz is exhausted in 17JK12. The field containing the peak assemblage extends to lower *P* for sample 17JK20 (≥7 kb) than 17JK12 (>8 kb) as a result of the larger garnet stability field.

For sample 17JK09 (Fig. 5.6c), the inferred peak assemblage (clinopyroxene + garnet + plagioclase + ilmenite + quartz + melt) is predicted to be stable across a narrow range of *P*–*T* conditions. Amphibole, though observed in thin section, is not inferred to be part of the peak metamorphic assemblage in this sample. The predicted stability fields of rutile and orthopyroxene (not observed in the sample) constrain *P*, and the predicted stability of amphibole at lower temperatures constrains minimum *T*. At higher temperatures, quartz is predicted to be exhausted. Quartz is present in the sample and we interpret that it is part of the peak assemblage, although it is possible that some or most quartz formed upon cooling.

The inferred peak assemblage of metatonalite sample 17JK08 (amphibole + garnet + plagioclase + biotite + ilmenite + quartz) is not replicated by the model (Fig. 5.6d); clinopyroxene is predicted to be stable across most modelled *P*–*T* conditions, but was not found in the sample or in outcrop. Previous work using this set of THERMOCALC *a*–*x* models has reported an overestimation of clinopyroxene stability in amphibole-bearing rocks (Forshaw et al., 2019). The L + hb + aug + g + ksp + pl + ilm + q ± bi fields (Fig. 5.6d) may be the best fit for the peak assemblage, as orthopyroxene and rutile—both absent from the sample—are predicted at lower *P* and higher *P*, respectively, and amphibole is exhausted at high *T*. The modal proportion of biotite is underestimated in the model (~3 mol% maximum predicted in the peak field) compared to observations from 17JK08 (≥5 vol%). However, the predicted biotite stability field could potentially be expanded at the expense of clinopyroxene and K-feldspar, which both appear to be overestimated in the model (2–7 mol% of each predicted, depending on *P*–*T*), as neither is present in the sample.

The modelled *P*–*T* fields corresponding to the inferred peak metamorphic assemblages of each of the four samples overlap at approximately 850 ± 50°C and 10 ± 1 kbar (Fig. 5.6e). The modelled proportion of garnet at these conditions for each sample is broadly consistent with outcrop and thin section observations. Maximum temperature constraints are strongly dependent on whole-rock concentrations of H_2O, and measured values may not represent the concentration of H_2O in the system during granulite-facies metamorphism. Previous thermobarometric work on metabasite in the KSZ reporting < 800°C relied on Fe–Mg exchange (Mäder et al., 1994; Hartel and Pattison, 1996), which may have recorded post-peak temperatures. Our peak temperature estimate is consistent with subsequent work that compared data from rocks of the KSZ to experimental work (Pattison, 2003) and employed garnet–orthopyroxene Al-solubility thermobarometry including a correction for retrograde Fe–Mg exchange (Pattison et al., 2003). Therefore, our best estimate for peak conditions of the metabasites in the KSZ based on the pseudosections presented here and previous thermobarometric estimates are 850 ± 50°C and 10 ± 1 kbar.

5.4.4 Melt composition modelling

Of the four samples that are the focus of this study, 17JK20 and 17JK12 were considered to be most suitable for melt composition modelling, as they are amphibole-bearing metabasites with assemblages consistent with the melting reaction proposed to have produced trondhjemitic melt in the KSZ (Hartel and Pattison, 1996). We use the results of phase equilibrium modelling from each of these samples to calculate the trace element composition of partial melt expected at six sets of *P*–*T* conditions, ranging

from 7 kbar to 21 kbar and 850°C to 977.5°C (Fig. 5.7) to represent a range of thermal regimes (Brown and Johnson, 2018).

The major element compositions of model melt are mostly consistent with tonalite, trondhjemite, or granodiorite based on calculated normative feldspar content (Fig. S4.1), however melt fractions of ~10–17 wt.% (produced at 850°C to 875°C) are predicted to be granitic (i.e., enriched in K-feldspar content relative to TTGs). Variations in the concentrations of REE in modelled melt can be attributed to several factors. Garnet has the strongest influence on HREE in the models, with higher proportions of garnet correlated with lower concentrations of HREE in the model melt. Amphibole is the dominant repository for HREE in the residue when garnet is absent; this is apparent in the results at low pressure (950°C and 7 kbar), as hornblende is predicted to be present for sample 17JK12 but is absent for sample 17JK20. The concentration of LREE in the modelled melt is influenced by melt fraction, with lower melt fractions yielding higher concentrations. However, plagioclase and amphibole in the residue also affect LREE, as these minerals have higher partition coefficients for LREE in the Bédard (2006) set of values than the other minerals relevant to our models. These controls on REE behaviour result in strong LREE enrichment and strong HREE depletion in melt in equilibrium with a residue at high pressure, which is dominated by garnet and clinopyroxene; the La_N/Yb_N of the highest-pressure model melt (875°C and 21 kbar) is approximately 160 and 80 for samples 17JK20 and 17JK12, respectively. Negative Eu (and Sr) anomalies in the modelled melt can be correlated with the proportion of plagioclase in the residue and the Eu anomaly is slightly positive with small amounts or no plagioclase present. As whole-rock concentrations of REE indicate no Eu anomaly for 17JK12 and a negative anomaly for 17JK20 (Fig. 5.4b), the positive Eu anomaly in the modelled melt must originate from low partition coefficients for Eu relative to Sm and Gd for minerals in the modelled residue.

Trends in LILE (Rb, Ba, Th, and U) in modelled melt show a strong correlation with whole-rock trends (Fig. 5.4b), but overall concentrations of LILE also increase with decreasing melt fraction. Barium is preferentially sequestered in the residue relative to other LILE when plagioclase is present. Modelled melt in equilibrium with rutile have pronounced negative Nb–Ta anomalies. Modelled residues containing ilmenite are associated with comparatively weaker negative Nb–Ta anomalies in the melt, but the apparent magnitude of this anomaly is also dependent on the various factors that influence LILE and LREE in the modelled melt.

Overall, the melt trace element modelling of samples 17JK20 and 17JK12 predicts that increasing pressure is correlated with steepening of the expected melt REE profile, a shift from a

negative to positive Eu anomaly, and a stronger Nb–Ta anomaly. Melt fraction is expected to increase with temperature, which most strongly affects the predicted concentrations of LILE and LREE. At the inferred peak metamorphic conditions of 850°C and 10 kbar, the presence of garnet and plagioclase in the modelled residue imparts HREE depletion and negative Sr and Eu anomalies to the melt, and the Nb–Ta anomaly is expected to be weak due to the stability of ilmenite in these metabasites.

5.4.5 Garnet Lu–Hf geochronology

The distribution of the parent isotope within garnet provides insights into the significance of the Lu–Hf age, which may be biased toward core or rim growth depending on which portion of the crystal is enriched in Lu (Baxter and Scherer, 2013). We used semi-quantitative trace element maps to determine the distribution of Lu in representative garnet crystals from each of the four samples examined from the KSZ (Fig. 5.8). In sample 17JK20, garnet shows either no zoning or some enrichment of Lu in the core (Fig. 5.8a). The garnet population of sample 17JK12 is bimodal in terms of size, but the concentration of Lu is greatest in the rim for both small and large crystals (Fig. 5.8b). In garnet in sample 17JK09 (Fig. 5.8c), a weak enrichment in the rim or core have both been observed. Garnet zoning patterns are most complex in sample 17JK08 (Fig. 5.8d). Rims are enriched in Lu with a mantle of low concentration and an inner annulus of Lu-rich patches.

Six-point isochrons are used to evaluate the timing of Lu–Hf isotopic equilibration in each of the granulite-facies samples (Fig. 5.9). Each isochron is based on regression through the isotope dilution results for four aliquots of garnet and two whole-rock analyses (Table 5.2). Sample 17JK20 (Fig. 5.9a) yields an isochron with excess scatter (MSWD = 9.2), resulting in an apparent age with large uncertainty, 2669 ± 38 Ma (isochron age uncertainties are at 95% confidence). The isochron is well-constrained for sample 17JK12 (Fig. 5.9b, MSWD = 1.3) and yields the most precise age of the four samples, 2609.2 ± 6.4 Ma. For sample 17JK09, the isochron fit implies some scatter (MSWD = 3.3) and the calculated age is 2641 ± 26 Ma. Sample 17JK08 yields a well-constrained isochron (MSWD = 1.6) with a calculated age of 2684.5 ± 7.7 Ma.

5.4.6 Zircon U–Pb and Hf results

Zircon crystals from two leucosome samples (19JK15 and 19JK16) are elongate to equant with rounded edges (Fig. 5.10). Crystals range from 50 µm to 100 µm in sample 19JK15 and up to 200 µm in 19JK16. In sample 19JK15, zircon crystals comprise a core with oscillatory and sector zoning commonly surrounded by a weak-CL-response rim; a thin rim with strong CL response may also be present (Fig. 5.10a). Oscillatory zoning is also present in crystals from sample 19JK16 and scarce

rims all have relatively weak CL responses (Fig. 5.10b). Evidence of metamictization, which includes a very weak CL response and irregular microstructures and fractures, is most common in crystals from sample 19JK16.

In situ laser ablation analyses were focused on cores, as rims were typically smaller than the 50 μm laser beam diameter. A discordance filter was applied to the dataset to eliminate analyses where the difference between the $^{238}U/^{206}Pb$ and $^{207}Pb/^{206}Pb$ ages was ≥ 5%. In sample 19JK15, 15 analyses with $^{207}Pb/^{206}Pb$ ages ranging from ca. 2683 Ma to ca. 2609 Ma overlap with at least one other analysis within 2σ uncertainty. One analysis with an age of ca. 2720 Ma is older than the main population, and a ca. 2586 Ma analysis is younger than the main group. Sample 19JK16 yielded 18 analyses with ages that overlap within 2σ uncertainty from ca. 2656 Ma to ca. 2599 Ma, and two older analyses with ages of ca. 2785 Ma and ca. 2708 Ma. For both samples, the main leucosome populations do not yield single, statistically robust ages.

For sample 19JK15, the Hf isotopic data of the main population analyses correspond to a range in εHf(t) from +2.0 to +3.7 based on $^{207}Pb/^{206}Pb$ dates from individual analyses. The $^{176}Hf/^{177}Hf$ ratios for the main population from sample 19JK16 are more scattered, resulting in a range of εHf(t) from +1.5 to +4.5 for $^{207}Pb/^{206}Pb$ dates calculated from individual analysis.

5.5 Discussion

5.5.1 Anatectic metabasites and TTGs – the trace element modelling perspective

Pioneering work on connecting anatectic metabasites to TTGs was done in the Kapuskasing Uplift; Hartel and Pattison (1996) determined that the anatectic metabasites in the KSZ generated trondhjemitic melt based on observations and mass balance analysis. Our whole-rock geochemical data from leucosome in the KSZ (Fig. 5.5) support this conclusion. However, the leucosome compositions most strongly resemble plagioclase cumulate associated with TTGs in the WGD, which may suggest that the leucosomes do not represent primary melt compositions, but rather crystals that remained after melt expulsion (e.g., Sawyer, 1987; Carvalho et al., 2016; Brown et al., 2016; Koblinger and Pattison, 2017). Forward modelling of the melt produced by metabasite by phase equilibrium modelling coupled with trace element modelling has the potential to provide further insights into TTG generation, such as the *P–T* conditions of source melting (e.g., Johnson et al., 2017, 2021). However, recent work has emphasized the potential for open-system processes at the source to obscure the connection between TTG trace element composition and source *P–T* conditions, including progressive melt loss (Huang et al., 2020; Kendrick and Yakymchuk, 2020 [Chapter 2]),

fractionation of trace elements into peritectic minerals (Kendrick and Yakymchuk, 2020 [Chapter 2]; Antonelli et al., 2021), and fluid-fluxed melting (Pourteau et al., 2020).

Forward modelling of a TTG source and calculating the concentrations of trace elements in modelled melt requires assumptions that must be considered when comparing the modelled melt to natural TTGs, which have been discussed in detail previously (Huang et al., 2020; Kendrick and Yakymchuk, 2020 [Chapter 2]; Johnson et al., 2021). An important assumption is that partition coefficients are appropriate for the modelled system. For generation of tonalitic melt from a metabasic source, values from Bédard (2006) are commonly used (e.g., this study; Johnson et al., 2017; Kendrick and Yakymchuk, 2020 [Chapter 2]; Pourteau et al., 2020) and these are a useful approximation, given the parameterization done for plagioclase, clinopyroxene, and orthopyroxene partition coefficients. However, the REE partition coefficients for garnet in this set of values impart a negative Eu anomaly to modelled garnet. This may result in modelled melt with a positive Eu anomaly if the residue is garnet-rich and plagioclase-poor (e.g., Fig. 5.7). As negative Eu anomalies are rare in garnet in granulite- and eclogite-facies metabasites (e.g., Bea et al., 1997; Manton et al., 2017) and given the additional complication of potentially variable Eu valence states that was not considered in our modelling (e.g., Holder et al., 2020), we interpret the significance of our modelled Eu anomalies with caution.

Another assumption for modelling TTG genesis is appropriate source composition. The anatectic metabasites in the KSZ have likely lost melt (this study; Hartel and Pattison, 1996), resulting in depletion of elements that preferentially partitioned into early melt (i.e., H_2O, K_2O and incompatible trace elements). Our samples may have a lower concentration of H_2O than they did at subsolidus conditions, resulting in elevated solidus temperatures in the model. Progressive melt loss from metabasite during partial melting may also increase the *P*–*T* stability field of plagioclase (Palin et al., 2016; Stuck and Diener, 2018; Huang et al., 2020; Kendrick and Yakymchuk, 2020 [Chapter 2]), suggesting that our models may overestimate plagioclase proportions and *P*–*T* extent. Sample 17JK09 has likely been most affected by melt loss, given the relatively low whole-rock concentration of K_2O and anhydrous peak mineral assemblage. By contrast, samples 17JK20 and 17JK12 contain a large proportion of amphibole and therefore likely lost less melt than 17JK09 (cf. Hartel and Pattison, 1996). Characteristics of the phase diagrams for samples 17JK20 and 17JK12—such as the strongly pressure-dependent stability fields of garnet, rutile, and plagioclase—are consistent with suprasolidus metabasite phase equilibria previously determined from experiments and modelling (e.g., Moyen and

Stevens, 2006; Palin et al., 2016). Considering the various sources of uncertainty related to the modelled melt trace element compositions, trends are considered more robust than individual values.

For the purposes of comparing our modelling results to natural TTGs from the Kapuskasing Uplift, we divide TTGs from the MGB and WGD into three main groups based on age: 2885 Ma, 2750–2700 Ma, and 2695–2685 Ma. Although these groups are likely an oversimplification of the variety of TTGs present, they are based on a sample set of TTGs we have investigated previously (Kendrick et al., 2022 [Chapter 3]; Kendrick et al., submitted [Chapter 4]) for which major and trace element and zircon U–Pb and Hf isotope data are available.

Trace element trends of the 2885 Ma TTG in the MGB (negative Sr and Eu anomalies, $La_N/Yb_N \approx 11$; sample 19JK45B of Kendrick et al., submitted [Chapter 4]) are consistent with melting of metabasite in our model at low-pressure with a plagioclase-bearing and garnet-poor or garnet-absent residue (Fig. 5.11a). Trace element trends in this TTG and related rocks have previously been linked to feldspar fractionation (Sage et al., 1996b), though a complementary feldspar-rich cumulate of this age has not been documented. Therefore, depletions in Eu and Sr in the 2885 Ma TTG cannot be uniquely linked to a plagioclase-bearing source. However, the relatively elevated concentrations of HREE, Nb, and Ta in this TTG may be indicative of melting of a metabasic source at relatively low-pressure outside of the rutile stability field and in the presence of little to no garnet (i.e., ≤ 10 kbar).

For the 2750–2700 Ma TTG, the shallow slope of the REE ($La_N/Yb_N \approx 10$; sample 18JK19 of Kendrick et al., 2022 [Chapter 3] and Kendrick et al., submitted [Chapter 4]) appears to preclude a garnet-bearing residue, however this TTG also lacks an Eu anomaly, which is inconsistent with a plagioclase-bearing source. Models of our metabasite samples do not replicate this trend, as plagioclase is predicted to be present at all modelled *P*–*T* conditions where garnet is absent (Fig. 5.6a–c). However, previous modelling of suprasolidus phase equilibria for metabasites has shown that the stability field of plagioclase is expected to be reduced or absent when sufficient H_2O is added to the system for water-fluxed melting (Pourteau et al., 2020; Ferrero et al., 2021; Hernández-Montenegro et al., 2021). Therefore, low-pressure, water-fluxed melting could explain the trace element composition of the 2750–2700 Ma TTG. Yet, the apparent stability of plagioclase at peak metamorphic conditions in our samples and other anatectic metabasites in the KSZ (this study; Hartel and Pattison, 1996) does not support extensive water-fluxed melting (cf. Laurie et al., 2013; Pourteau et al., 2020; Ferrero et al., 2021), at least at the crustal level currently exposed.

In the WGD, several TTGs with ages of 2695–2685 Ma have been identified (Kendrick et al., submitted [Chapter 4]). The dated samples (n = 5, samples 19JK43, 19JK41, 19JK40, 18JK08, and

18JK53 of Kendrick et al., submitted [Chapter 4]; average composition using data from Kendrick et al., 2022 [Chapter 3] is shown in Fig. 5.11a) represent a mix of accumulated-plagioclase-rich and fractionated-melt-rich TTGs, and all five samples have greater La_N/Yb_N ($La_N/Yb_N \approx 15$ to 94, average of 51) and lower concentrations of Nb and Ta than the 2885 Ma TTG sample. These geochemical characteristics may support a deeper source for the ca. 2695–2685 Ma TTGs than the 2885 Ma TTG and possibly the 2750–2700 Ma TTG. The presence or absence of plagioclase in the source is difficult to determine based on the Eu anomalies of the TTGs, given the evidence for plagioclase fractionation and accumulation in the ca. 2695–2685 Ma samples (Kendrick et al., 2022 [Chapter 3]). We interpret the compositions of these TTGs as compatible with a source containing garnet and possibly also plagioclase. The strong negative Nb–Ta anomaly may indicate that the source contained rutile rather than ilmenite, which requires higher pressure (1–2 kbar) than is currently recorded at the current exposure level of the KSZ (~10 kbar; Fig. 5.6).

Between the two different metabasite samples chosen for melt trace element modelling (17JK20 and 17JK12), neither sample is a preferable source for the TTGs; trace element trends of the modelled melt are broadly similar for both metabasites. Given the limitations of the modelling and the possibility of fractional crystallization and crystal accumulation in natural TTGs (e.g. Laurent et al., 2020; Kendrick et al., 2022 [Chapter 3]; Rollinson, 2021), direct comparison between model results and TTG samples is problematic. However, in general, the modelled melt trace element compositions are compatible with the natural TTG compositions and our results may support an increase in source pressure between ca. 2885 Ma and 2685 Ma.

5.5.2 Anatectic metabasites and TTGs – insights from Lu–Hf isotope systematics

Measurements of Lu–Hf isotopes in zircon have been widely used to understand the origin of TTGs (e.g., Zeh et al., 2011; Næraa et al., 2012; Gardiner et al., 2017; Mole et al., 2021). Using this technique, inferences about the TTG source can only be made indirectly using an assumed source $^{176}Lu/^{177}Hf$ ratio. For a mafic source, recent common practice is to assume a $^{176}Lu/^{177}Hf$ ratio of ~0.02 (e.g., Zeh et al., 2011; Næraa et al., 2012; Gardiner et al., 2019) based on existing $^{176}Lu/^{177}Hf$ data from basalt and the assumption that juvenile crustal material is formed by melting of an average depleted mantle reservoir with higher $^{176}Lu/^{177}Hf$ (~0.038, Vervoort and Blichert-Toft, 1999). However, there are limitations to this approach—considerable variability in the $^{176}Lu/^{177}Hf$ ratios of Archean basalt has been observed (Vervoort and Kemp, 2016). The metabasites of the KSZ examined in this study provide a rare opportunity to evaluate Lu–Hf systematics in potential TTG source rocks directly.

Using whole-rock Lu–Hf isotopic data from three metabasites—samples 17JK20, 17JK12, and 17JK09 (whole-rock bomb values, Table 5.2)—we evaluate the Hf isotopic evolution of these rocks over time (Fig. 5.11b). During the relevant period for magmatism in the Kapuskasing Uplift (late Mesoarchean to Neoarchean), samples 17JK20 and 17JK09 were relatively radiogenic compared to the chondritic uniform reservoir (CHUR). The positive whole-rock εHf(t) of these metabasites is similar to the values obtained from zircon in leucosome (samples 19JK15 and 19JK16) and zircon in granitoids of the WGD and MGB (Mole et al., 2021; Kendrick et al., submitted [Chapter 4]), which are mainly between +2 and +4 at ca. 2750–2600 Ma (Fig. 5.11b). The evolution of sample 17JK12 (whole-rock) is close to CHUR and compatible with near-chondritic εHf(t) values from zircon in the ca. 2885 Ma TTG from the MGB.

The whole-rock $^{176}Lu/^{177}Hf$ ratios from samples 17JK20, 17JK12, and 17JK09 could be the primary ratios of their protoliths or may represent later modification, which may then affect the projected Hf isotopic evolution (Fig. 5.11b). A wide range of whole-rock $^{176}Lu/^{177}Hf$ ratios has been documented in basalts from different geological settings (e.g., Patchett and Tatsumoto, 1980), which has been linked to mantle melting processes (e.g., Blichert-Toft and Albarède, 1997; Chauvel and Blichert-Toft, 2001). Murphy et al. (2021) report whole-rock $^{176}Lu/^{177}Hf$ ratios of 0.017–0.034 from Archean basalt samples of the Pilbara Terrane, which are similar values to those from the metabasites in the KSZ (Table 5.2). Subsequent modification of primary Lu/Hf ratios is possible, for instance by mobilization of Hf in fluoride complexes that may form in the presence of a fluorine-bearing fluid phase (e.g., Allen et al., 1985; Smith et al., 1987). However, there is no clear evidence for percolation of such fluid through the KSZ or the Kapuskasing Uplift in general; fluid related to gold mineralization in the MGB, for instance, does not appear to have mobilized Hf (Ciufo et al., 2020).

The Lu/Hf ratios of metabasites can be modified by loss of anatectic melt in the presence of garnet; this would result in a residue relatively depleted in Hf (enriched in the melt) relative to Lu (enriched in garnet). Given the evidence for melt loss from KSZ metabasites (Hartel and Pattison, 1996; this study), this scenario should be considered. The potential for melt loss to modify whole-rock composition depends on the original fertility of the metabasites, which is a function of the relative modal proportions of quartz and hornblende (Hartel and Pattison, 1996). The mineral assemblage and modal proportions of sample 17JK12 are consistent with a quartz-poor endmember, where early exhaustion of quartz would have resulted in low melt production and preservation of a large proportion of amphibole (Fig. 5.3c). In contrast, sample 17JK09 likely contained sufficient quartz for amphibole dehydration melting to proceed until both amphibole and quartz were exhausted

or nearly so, resulting in an anhydrous mineral assemblage (Fig. 5.3e). Assuming production and loss of 10% melt for sample 17JK12 and 30% for sample 17JK09 (based on examination of similar rocks from the KSZ by Hartel and Pattison, 1996) and a melt $^{176}Lu/^{177}Hf$ ratio of 0.005 (based on whole-rock TTG values from Guitreau et al., 2012), estimates of melt-reintegrated $^{176}Lu/^{177}Hf$ are 0.029 for sample 17JK12 (measured value of 0.032) and 0.020 for 17JK09 (measured value of 0.027); these changes would not significantly affect our projected isotopic evolution of these metabasite samples (Fig. 5.11b). Therefore, we suggest that melt loss does not affect our overall interpretation: the Lu–Hf isotope data support the presence of a suprachondritic metabasic source consistent with Neoarchean TTGs in the Kapuskasing Uplift, and a near-chondritic metabasic source consistent with the Mesoarchean TTG from the MGB (Fig. 5.11b).

5.5.3 Anatectic metabasites and TTGs – the geochronological connection

Our garnet Lu–Hf and zircon U–Pb geochronology results provide insights into the timing of partial melting (heating) and partial melt crystallization (cooling) of the anatectic metabasites in the KSZ. This information is crucial for drawing a connection between the timing of metabasite anatexis and TTG magmatism of the Kapuskasing Uplift. Extraction of melt from anatectic deep crust toward shallower crustal levels has been suggested to take place during heating and melt production when a melt connectivity threshold is reached (e.g., Rosenberg and Handy, 2005; Yakymchuk and Brown, 2014). Melt extraction driven by deviatoric stress is also possible during heating or cooling (Carvalho et al., 2016; Sawyer, 2020). Therefore, the crystallization ages of TTGs produced by lower crustal anatexis should be generally coeval with partial melting or melt crystallization in the metabasic source.

The significance of geochronological data from garnet and zircon in metabasite depends on the growth history of these minerals. Garnet in metabasites grows as a result of prograde metamorphic reactions and may initiate at amphibolite-facies (i.e., subsolidus) conditions, although this is most likely at high pressure (>15 kbar, Green et al., 2016) or for Fe-rich bulk compositions (Pattison, 2003). At upper amphibolite- and granulite-facies (i.e., suprasolidus) conditions, garnet is typically present or expected at 8–10 kbar and above (Pattison, 2003; Moyen and Stevens, 2006; Green et al., 2016), however the pressure at which garnet may become stable depends on metabasite bulk composition, particularly Mg# (e.g., Johnson et al., 2017; Kendrick and Yakymchuk, 2020 [Chapter 2]; Huang et al., 2020). For metatonalitic bulk compositions, the garnet *P*–*T* stability field is similar to that of metabasites (e.g., Watkins et al., 2007; White et al., 2017), although relatively lower modal proportions of garnet are expected for metatonalites (White et al., 2017). In metabasite, zircon

is unlikely to grow as a result of metamorphic reactions during heating at subsolidus conditions (Kohn et al, 2015) and is generally expected to break down and potentially be dissolved completely during high-temperature partial melting reactions (Kohn et al, 2015; Yakymchuk et al., 2017). Therefore, for metabasite that reached suprasolidus conditions, most or all of the zircon is expected to have grown during cooling and crystallization of partial melt (Kohn et al, 2015; Yakymchuk et al., 2017).

Ideally, an age obtained from garnet Lu–Hf geochronology records the timing of the prograde metamorphic reactions that produced garnet. Based on field evidence (this study; Hartel and Pattison, 1996) and phase equilibrium modelling (Fig. 5.6), garnet was likely being produced during partial melting as a peritectic phase in metabasite and metatonalite in the KSZ, although growth could have initiated at subsolidus conditions. The garnet stability field extends to the lowest *P–T* conditions for samples 17JK20 and 17JK09 in our models (Fig. 5.6a, c), consistent with their low Mg# compared to samples 17JK12 and 17JK08. This implies that garnet growth could have begun earlier in 17JK20 and 17JK09, assuming all samples experienced a common *P–T* history. These two samples yield imprecise Lu–Hf ages that broadly overlap within uncertainty (Fig. 5.9a, c). However, there is a ~75 m.y. difference between the Lu–Hf ages of 17JK12 and 17JK08 (Fig. 5.9b, d); this is inconsistent with the relative timing of garnet growth based on phase equilibrium modelling alone.

The high peak metamorphic temperature of the KSZ (~850°C) and evidence for prolonged high-temperature conditions (~80 m.y. at 650–700°C, Moser et al., 2008) and slow cooling (<1°C/Ma, Percival and Peterman, 1994) could have promoted diffusion of Hf and Lu in garnet. Previous work on diffusion of Hf in garnet (Smit et al., 2013; Bloch et al., 2015) indicates that diffusion was possible in our samples given the thermal history of the KSZ. However, the diffusion rate of Lu within garnet has been shown to be faster than that of Hf (Smit et al., 2013; Bloch et al., 2015), implying that complete rehomogenization of Hf in a garnet crystal would be achieved after complete rehomogenization of Lu. A lack of or very weak Lu zoning was observed in samples 17JK20 and 17JK09, suggesting that at least partial diffusive Hf loss is permissible in these samples; this may explain the poorly constrained ages (Fig. 5.9a, c). Relatively complex Lu zoning is preserved in sample 17JK08 (Fig. 5.8d), which may indicate that the well-constrained age from this sample corresponds to the growth of garnet during heating and partial melting without resetting by diffusion. Although Lu zoning is preserved in some small crystals (~1–2 mm in diameter) in sample 17JK12, the densely fractured skeletal garnet porphyroblasts (Fig. 5.3d; up to ~1.5 cm in diameter) may have effectively behaved as clusters of very small garnet crystals (< 0.5 mm in diameter) that could have

been more readily rehomogenized. As these porphyroblasts were targeted for Lu–Hf analysis, the isochron age of 2609.2 ± 6.4 Ma from sample 17JK12 may record cooling rather than heating. The Lu–Hf isochron age from sample 17JK08 (2684.5 ± 7.7 Ma) is our best estimate of the timing of heating and partial melting of metatonalite—and therefore the proximal metabasite—in the KSZ.

The main leucosome populations of zircon from samples 19JK15 (ca. 2683–2609 Ma) and 19JK16 (ca. 2656–2599) exhibit oscillatory and sector zoning consistent with crystallization from melt (Rubatto, 2017), and we interpret that their ages broadly represent crystallization of partial melt during cooling of the anatectic metabasites. The oldest ages obtained from the leucosome population in 19JK15 are within uncertainty of our Lu–Hf age corresponding to heating; these zircon could have grown in localized Zr-oversaturated melt pockets and became trapped within peritectic garnet, preventing dissolution upon further melting. Three analyses (Fig. 5.10) that yielded ages > 2700 Ma may represent inherited components or crystals from the igneous protoliths of the metabasite or fluid-driven reprecipitation of igneous zircon at low temperature (e.g., Rubatto, 2017). The youngest analysis from sample 19JK15 may represent late zircon growth during cooling at high temperature, based on similar results from previous work on metamorphic zircon in the KSZ (Moser et al., 2008).

Based on existing geochronological data of the MGB and the WGD (Fig. 5.11c), granitoids mainly crystallized between ca. 2925 Ma and ca. 2645 Ma, with most tonalites and trondhjemites formed during two main pulses of magmatism at ca. 2925–2885 Ma and ca. 2747–2685 Ma. Several zircon analyses from previous work on metatonalite and metabasite of the KSZ have yielded ages of 2748 ± 15 Ma and 2698 ± 16, Ma coeval with documented pulses of TTG magmatism (Benn and Kamber, 2009). These data may indicate that rocks of the KSZ were metamorphosed at ca. 2750 Ma and ca. 2700 Ma, but zircon growth is difficult to link to heating and partial melting in metabasite (Kohn et al, 2015; Yakymchuk et al., 2017). Garnet can be directly linked to high-temperature conditions and anatexis based on phase equilibrium modelling (Fig. 5.6), and our results from garnet Lu–Hf geochronology suggest an onset of anatexis in the KSZ at ca. 2685 Ma, consistent with existing geochronological data from the KSZ (Krogh and Moser, 1994; Moser et al., 2008; Benn and Kamber, 2009). Considering the uncertainty of the ^{176}Lu decay constant (by propagating the uncertainty of the isochron slope with the decay constant uncertainty from Söderlund et al. (2004) in quadrature), our garnet Lu–Hf age from sample 17JK08 is 2684.5 ± 14.0 Ma, which partly overlaps with the ca. 2700–2695 Ma pulse of TTG magmatism documented in the Kapuskasing Uplift by zircon U–Pb geochronology (Fig. 5.11c).

The timing of partial melting and melt crystallization in the lower crust exposed in the KSZ is correlated with a shift toward relatively potassic granitoids (in comparison to TTGs) in the Kapuskasing Uplift starting at ca. 2685 Ma (Fig. 5.11c). The metabasites could have produced granodioritic to granitic (*s.s*) melt at low degrees of partial melting (~10–17% predicted at 850–875° C; Table S4.6; Fig. S4.1), though such melt fractions would result in a small volume of melt overall. In addition, late potassic granitoids in the MGB have been suggested to be sanukitoids, as their trace element compositions are consistent with a metasomatized mantle source (Sage et al., 1996b). Uncommon ≤ 2685 Ma tonalitic to trondhjemitic rocks (Fig. 5.11c) could have been generated by higher degrees of metabasite partial melting, as our geochronological data indicate that melt was present and crystallizing in the metabasites from ca. 2685 Ma to ca. 2600 Ma. However, the volume of such magma appears to have been limited, as tonalitic veins and a small sill in the WGD comprise the 2660–2645 Ma occurrences (Moser et al., 1996).

5.5.4 Interpretation of results in a regional tectonic framework

Metabasites exposed in the KSZ are compatible sources for ca. 2885 Ma and ca. 2750–2685 Ma TTGs in the Kapuskasing Uplift based on trace element modelling and Lu–Hf isotopic data. The results of geochemical modelling suggest that source depth may have increased from the Mesoarchean to the Neoarchean (Fig. 5.11a), and Lu–Hf data indicate that two isotopically distinct metabasic sources are present in the KSZ, together accounting for the Hf isotopic signatures of zircon in TTGs in the WGD and MGB (Fig. 5.11b). However, the high-grade metamorphic event that resulted in widespread crustal anatexis in the KSZ appears to have postdated most TTG magmatism (Fig. 5.11c). Here, we discuss the significance of these results in the tectonic framework of the southern Superior Province.

Mesoarchean TTGs are uncommon in the southern Superior Province (Percival et al., 2012). Our work suggests that the ca. 2885 Ma TTG in the MGB could have formed by isolated partial melting of existing basaltic crust at a relatively shallow level. Although no metamorphism in the KSZ coeval with the ca. 2885 Ma magmatism has been documented, we have determined that metabasite sample 17JK12 (Fig. 5.11b) from the KSZ represents a geochemically compatible source rock for the 2885 Ma TTGs.

Widespread juvenile magmatism—ranging in composition from komatiitic to rhyolitic—at ca. 2750–2685 Ma is well-documented throughout the southern Superior Province (Percival et al., 2012). The variety of juvenile igneous rocks may have been generated by plume-arc interaction (e.g., Wyman et al., 2002; Benn and Moyen, 2008) or a switch from rifting to subduction or subcretion with

or without simultaneous plume activity (e.g., Bédard and Harris, 2014; Mole et al., 2021). The source of TTGs of this age in the southern Superior Province has been suggested to be the base of recently formed basaltic crust or a subducting oceanic slab (e.g., Wyman et al., 2002; Benn and Moyen, 2008; Mole et al., 2021). We have identified metabasites in the KSZ with radiogenic εHf(t) (samples 17JK20 and 17JK09; Fig. 5.11b) compatible with juvenile ca. 2750–2685 Ma TTGs throughout the southern Superior Province (Mole et al., 2021), suggesting that a lower crustal source for the TTGs was possible. Although evidence for pre-2685 Ma metamorphism and metabasite partial melting is scarce at the currently exposed crustal level in the KSZ, the presence—or former presence—of additional, compositionally similar metabasite would have been necessary given the large volume of upper- to middle-crustal TTG plutons and gneiss in the Kapuskasing Uplift. The metabasic source rocks, either magmatically or tectonically incorporated at the base of the existing older crust (i.e., the 2885 Ma TTG and associated metabasic source rocks represented by sample 17JK12) may have delaminated (e.g., Bédard, 2006) after partial melting from ca. 2750 to ca. 2685 Ma.

High-temperature metamorphism in the KSZ at ca. 2685 Ma, perhaps in part driven by delamination of lower crust, is coeval or nearly coeval with late-stage events in the southern Superior Province, including sanukitoid magmatism (e.g., Sage et al., 1996b; Benn and Moyen, 2008) and mineralization of orogenic gold deposits (e.g., Davis and Lin, 2003; Ciufo et al., 2020; Jellicoe et al., submitted). Late middle-crustal extension and minor tonalitic and trondhjemitic magmatism between 2660 Ma and 2645 Ma (Moser et al., 1996) accompanied slow melt crystallization in the KSZ. These ≤ 2685 Ma events postdate most TTG magmatism in the southern Superior Province and appear to signify a shift away from the geodynamic setting in which continental crust was generated and toward the post-tectonic stabilization of the Superior Province (e.g. Percival et al., 2012).

5.5.5 The TTG–metabasite connection

Our work in the Kapuskasing Uplift highlights the challenges of testing the TTG–metabasite connection. Of the three lines of evidence that are the focus of this study and are supported by field and petrographic observations—melt composition modelling, Lu–Hf isotopic data, and geochronological data—the latter two appear crucial. As pulses of TTG magmatism are generally the result of crust-forming events, evidence of these events can be overprinted by later metamorphism associated with final continental assembly and stabilization. Therefore, the *P*–*T* conditions recorded in metabasite may result from processes unrelated to crust-forming TTG magmatism—we suggest that this situation is likely true for the KSZ. Although coupled phase equilibrium and melt composition modelling of basaltic or metabasic compositions has been used to demonstrate that such

rocks may be viable sources for TTGs (e.g., Nagel et al., 2012; Palin et al., 2016; Johnson et al., 2017; Kendrick and Yakymchuk, 2020 [Chapter 2]), linking a particular potential source rock to a specific suite of TTGs by this technique is challenging. Some aspects of TTG trace element compositions may be unrelated to the source (e.g., Laurent et al., 2020; Rollinson, 2021; Kendrick et al., 2022 [Chapter 3]) and the limitations of the models generally prohibit quantitative comparisons between model results and natural TTG compositions. Phase equilibrium and melt composition modelling results from KSZ metabasites compared to compositions of TTGs from the MGB and WGD suggest a possible increase in the depth of the source over time. However, melt composition modelling alone is not sufficient for distinguishing between different potential metabasic sources. Our work demonstrates that coupled Lu–Hf isotopic datasets from metabasites and TTGs are a more powerful tool for connecting TTGs to their sources. The isotopic data allowed us to identify two distinct lower-crustal metabasite sources, each compatible with a different generation of TTGs at shallower crustal levels.

The presence of two metabasite sources in the lower crust that apparently melted at different times and successively deeper crustal levels to generate upper- to middle-crustal TTGs adds complexity to the crustal-melting model of TTG genesis. In general, a lower-crustal TTG source is suggested to be basalt that was hydrated by interaction with water at the surface of the Earth and heated after burial under subsequent layers of basalt, resulting in conditions appropriate for TTG genesis (Bédard, 2006; Fig. 5.12a). For production of a second generation of TTGs from a separate, deeper source, new basaltic material could have been added to the previous generation of basalt by magmatic underplating or tectonic accretion (Fig. 5.12b). However, underplated magma would likely lack the hydration required for TTG genesis (Moyen and Martin, 2012) and tectonic accretion would result in a relatively cold interface that would inhibit partial melting (e.g., Sizova et al., 2010). A dehydrating subducting slab could introduce the required H_2O in the underplated magma scenario (e.g., Polat, 2012) and heat may be added by upwelling asthenosphere in the tectonic accretion scenario (Fig. 5.12c). Each case requires at least limited horizontal transport of crustal material to introduce H_2O at the deepest crustal levels. This generalized model of multigenerational TTG production, based on observations from the Kapuskasing Uplift, could be applicable more broadly where different generations of isotopically distinct TTGs are found together in the upper to middle crust.

5.6 Conclusions

Our work supports our hypothesis that lower crustal metabasites were the source of middle- to upper-crustal TTGs in the Kapuskasing Uplift. We have identified two isotopically distinct metabasites, which together are able to account for the Hf isotope variability of zircon in TTGs at relatively shallower crustal levels. Compositional modelling of anatectic melt from metabasite in the Kapuskasing Uplift generally supports a connection between the metabasites and the TTGs, but this technique was not useful for determining a connection between specific metabasites and TTGs. Modelling results suggest a possible increase in TTG source depth from the Mesoarchean to the Neoarchean. The timing of metamorphism in the Kapuskasing Uplift is coeval with the crystallization of relatively late TTGs. Two earlier pulses of TTG magmatism predate this high-grade metamorphism and crustal anatexis. The currently exposed lower-crustal metabasites in the Kapuskasing Uplift may represent a small portion of an originally larger volume of metabasite, which melted earlier and may have subsequently delaminated. Overall, the results indicate that continental crust in this region could have been generated from two metabasic sources that were juxtaposed in the deep crust; one melted in the Mesoarchean and the other in the Neoarchean. Archean intracrustal differentiation may have therefore been a complex process with H_2O introduced into the deep crust at more than one stage, likely requiring at least limited horizontal tectonism.

5.7 References

Allen, P., Condie, K. C. & Narayana, B. L. (1985). The geochemistry of prograde and retrograde charnockite-gneiss reactions in southern India. Geochimica et Cosmochimica Acta 49, 323–336.

Antonelli, M. A., Kendrick, J., Yakymchuk, C., Guitreau, M., Mittal, T. & Moynier, F. (2021). Calcium isotope evidence for early Archaean carbonates and subduction of oceanic crust. Nature Communications 12, 2534.

Barker, F. (1979). Trondhjemite: definition, environment and hypotheses of origin. In: Barker, F. (ed.) Trondhjemites, Dacites, and Related Rocks. Amsterdam: Elsevier, 1–12.

Baxter, E. F. & Scherer, E. E. (2013). Garnet geochronology: timekeeper of tectonometamorphic processes. Elements 9, 433–438.

Bea, F., Montero, P., Garuti, G. & Zacharini, F. (1997). Pressure-dependence of rare earth element distribution in amphibolite- and granulite- grade garnets. A LA-ICP-MS study. Geostandards Newsletter 21, 253–270.

Bédard, J. H. (2006). A catalytic delamination-driven model for coupled genesis of Archaean crust and sub-continental lithospheric mantle. Geochimica et Cosmochimica Acta 70, 1188–1214.

Bédard, J. H. & Harris, L. B. (2014). Neoarchean disaggregation and reassembly of the Superior craton. Geology 42, 951–954.

Benn, K. & Kamber, B. S. (2009). In situ U/Pb granulite-hosted zircon dates, Kapuskasing Structural Zone, Ontario: a late Archean large igneous province (LIP) as a substrate for juvenile crust. The Journal of Geology 117, 519–541.

Benn, K. & Moyen, J. F. (2008). The late Archean Abitibi-Opatica terrane, Superior Province: a modified oceanic plateau. Special Paper of the Geological Society of America 440, 173–197.

Blichert-Toft, J. & Albarède, F. (1997). The Lu-Hf isotope geochemistry of chondrites and the evolution of the mantle–crust system. Earth and Planetary Science Letters 148, 243–258.

Bloch, E., Ganguly, J., Hervig, R. & Cheng, W. (2015). ^{176}Lu–^{176}Hf geochronology of garnet I: experimental determination of the diffusion kinetics of Lu^{3+} and Hf^{4+} in garnet, closure temperatures and geochronological implications. Contributions to Mineralogy and Petrology 169, 12.

Bowman, J. R., Moser, D. E., Valley, J. W., Wooden, J. L., Kita, N. T. & Mazdab, F. K. (2011). Zircon U-Pb isotope, $\delta^{18}O$ and trace element response to 80 m.y. of high temperature metamorphism in the lower crust: sluggish diffusion and new records of Archean craton formation. American Journal of Science 311, 719–772.

Brown, C. R., Yakymchuk, C., Brown, M., Fanning, C. M., Korhonen, F. J., Piccoli, P. M. & Siddoway, C. S. (2016). From source to sink: Petrogenesis of cretaceous anatectic granites from the Fosdick migmatite-granite complex, West Antarctica. Journal of Petrology 57, 1241–1278.

Brown, M. (2013). Granite: From genesis to emplacement. Bulletin of the Geological Society of America 125, 1079–1113.

Brown, M. & Johnson, T. (2018). Secular change in metamorphism and the onset of global plate tectonics. American Mineralogist 103, 181–196.

Carvalho, B. B., Sawyer, E. W. & Janasi, V. A. (2016). Crustal reworking in a shear zone: transformation of metagranite to migmatite. Journal of Metamorphic Geology 34, 237–264.

Chauvel, C. & Blichert-Toft, J. (2001). A hafnium isotope and trace element perspective on melting of the depleted mantle. Earth and Planetary Science Letters 190, 137–151.

Ciufo, T. J., Jellicoe, K., Yakymchuk, C., Lin, S., Mercier-Langevin, P. & Wodicka, N. (2020). Geology, structural evolution, and hydrothermal alteration of the Island gold deposit, Michipicoten greenstone belt, Ontario. In: Mercier-Langevin, P., Lawley, C. J. M. & Castonguay, S. (eds) Targeted Geoscience Initiative 5: Contributions to the Understanding of Canadian Gold Systems. Geological Survey of Canada, Open File 8712, 143–156.

Davis, D. W. & Lin, S. (2003). Unraveling the geologic history of the Hemlo Archean gold deposit, superior province, Canada: a U-Pb geochronological study. Economic Geology 98, 51–67.

Drummond, M. S. & Defant, M. J. (1990). A model for trondhjemite-tonalite-dacite genesis and crustal growth via slab melting: Archean to modern comparisons. Journal of Geophysical Research 95, 21503–21521.

Ferrero, S., Wannhoff, I., Laurent, O., Yakymchuk, C., Darling, R., Wunder, B., Borghini, A. & O'Brien, P. J. (2021). Embryos of TTGs in Gore Mountain garnet megacrysts from water-fluxed melting of the lower crust. Earth and Planetary Science Letters 569, 117058.

Forshaw, J. B., Waters, D. J., Pattison, D. R. M., Palin, R. M. & Gopon, P. (2019). A comparison of observed and thermodynamically predicted phase equilibria and mineral compositions in mafic granulites. Journal of Metamorphic Geology 37, 153–179.

Gardiner, N. J., Hickman, A. H., Kirkland, C. L., Lu, Y., Johnson, T. & Zhao, J.-X. (2017). Processes of crust formation in the early Earth imaged through Hf isotopes from the East Pilbara Terrane. Precambrian Research 297, 56–76.

Gardiner, N. J., Kirkland, C. L., Hollis, J., Szilas, K., Steenfelt, A., Yakymchuk, C. & Heide-Jørgensen, H. (2019). Building Mesoarchaean crust upon Eoarchaean roots: the Akia Terrane, West Greenland. Contributions to Mineralogy and Petrology 174, 1–19.

Green, E. C. R., White, R. W., Diener, J. F. A., Powell, R., Holland, T. J. B. & Palin, R. M. (2016). Activity–composition relations for the calculation of partial melting equilibria in metabasic rocks. Journal of Metamorphic Geology 34, 845–869.

Guitreau, M., Blichert-Toft, J., Martin, H., Mojzsis, S. J. & Albarède, F. (2012). Hafnium isotope evidence from Archean granitic rocks for deep-mantle origin of continental crust. Earth and Planetary Science Letters 337–338, 211–223.

Hartel, T. H. D. & Pattison, D. R. M. (1996). Genesis of the Kapuskasing (Ontario) migmatitic mafic granulites by dehydration melting of amphibolite: the importance of quartz to reaction progress. Journal of Metamorphic Geology 14, 591–611.

Hernández-Montenegro, J. D., Palin, R. M., Zuluaga, C. A. & Hernández-Uribe, D. (2021). Archean continental crust formed by magma hybridization and voluminous partial melting. Scientific Reports 11, 5263.

Hoffmann, J. E., Nagel, T. J., Münker, C., Næraa, T. & Rosing, M. T. (2014). Constraining the process of Eoarchean TTG formation in the Itsaq Gneiss Complex, southern West Greenland. Earth and Planetary Science Letters 388, 374–386.

Hofmann, A. W. (1988). Chemical differentiation of the Earth: the relationship between mantle, continental crust, and oceanic crust. Earth and Planetary Science Letters 90, 297–314.

Holder, R. M., Yakymchuk, C. & Viete, D. R. (2020). Accessory mineral Eu anomalies in suprasolidus rocks: beyond feldspar. Geochemistry, Geophysics, Geosystems 21, e2020GC009052

Holland, T. & Powell, R. (2003). Activity–compositions relations for phases in petrological calculations: an asymmetric multicomponent formulation. Contributions to Mineralogy and Petrology 145, 492–501.

Holland, T. J. B. & Powell, R. (2011). An improved and extended internally consistent thermodynamic dataset for phases of petrological interest, involving a new equation of state for solids. Journal of Metamorphic Geology 29, 333–383.

Holness, M. B. & Sawyer, E. W. (2008). On the pseudomorphing of melt-filled pores during the crystallization of migmatites. Journal of Petrology 49, 1343–1363.

Huang, G., Palin, R., Wang, D. & Guo, J. (2020). Open-system fractional melting of Archean basalts: implications for tonalite–trondhjemite–granodiorite (TTG) magma genesis. Contributions to Mineralogy and Petrology 175, 1–25.

Janoušek, V., Farrow, C. M. & Erban, V. (2006). Interpretation of whole-rock geochemical data in igneous geochemistry: introducing Geochemical Data Toolkit (GCDkit). Journal of Petrology 47, 1255–1259.

Johnson, T. A., Vervoort, J. D., Ramsey, M. J., Aleinikoff, J. N. & Southworth, S. (2018). Constraints on the timing and duration of orogenic events by combined Lu–Hf and Sm–Nd

geochronology: an example from the Grenville orogeny. Earth and Planetary Science Letters 501, 152–164.

Johnson, T. E., Brown, M., Gardiner, N. J., Kirkland, C. L. & Smithies, R. H. (2017). Earth's first stable continents did not form by subduction. Nature 543, 239–242.

Johnson, T., Yakymchuk, C. & Brown, M. (2021). Crustal melting and suprasolidus phase equilibria: From first principles to the state-of-the-art. Earth-Science Reviews 221, 103778.

Kendrick, J. & Yakymchuk, C. (2020). Garnet fractionation, progressive melt loss and bulk composition variations in anatectic metabasites: Complications for interpreting the geodynamic significance of TTGs. Geoscience Frontiers 11, 745–763.

Kendrick, J., Duguet, M. & Yakymchuk, C. (2022). Diversification of Archean tonalite-trondhjemite-granodiorite suites in a mushy middle crust. Geology 50, 76–80.

Koblinger, B. M. & Pattison, D. R. M. (2017). Crystallization of heterogeneous pelitic migmatites: Insights from thermodynamic modelling. Journal of Petrology 58, 297–326.

Kohn, M. J., Corrie, S. L. & Markley, C. (2015). The fall and rise of metamorphic zircon. American Mineralogist 100, 897–908.

Krogh, T. E. & Moser, D. E. (1994). U–Pb zircon and monazite ages from the Kapuskasing uplift: age constraints on deformation within the Ivanhoe Lake fault zone. Canadian Journal of Earth Sciences 31, 1096–1103.

Laurent, O., Björnsen, J., Wotzlaw, J.-F., Bretscher, S., Pimenta Silva, M., Moyen, J.-F., Ulmer, P. & Bachmann, O. (2020). Earth's earliest granitoids are crystal-rich magma reservoirs tapped by silicic eruptions. Nature Geoscience 13, 163–169.

Laurie, A., Stevens, G. & Van Hunen, J. (2013). The end of continental growth by TTG magmatism. Terra Nova 25, 130–136.

Ludwig, K. R. (2012). User's manual for Isoplot 3.75: a geochronological toolkit for Microsoft Excel. Berkeley Geochronology Center Special Publication No. 5, 75 pp.

Mäder, U. K., Percival, J. A. & Berman, R. G. (1994). Thermobarometry of garnet–clinopyroxene–hornblende granulites from the Kapuskasing structural zone. Canadian Journal of Earth Sciences 31, 1134–1145.

Manton, R. J., Buckman, S., Nutman, A. P., Bennett, V. C. & Belousova, E. A. (2017). U-Pb-Hf-REE-Ti zircon and REE garnet geochemistry of the Cambrian Attunga eclogite, New England Orogen, Australia: implications for continental growth along eastern Gondwana. Tectonics 36, 1580–1613.

Martin, H., Moyen, J.-F., Guitreau, M., Blichert-Toft, J. & Le Pennec, J.-L. (2014). Why Archaean TTG cannot be generated by MORB melting in subduction zones. Lithos 198–199, 1–13.

McDonough, W. F. & Sun, S.-s. (1995). The composition of the Earth. Chemical Geology 120, 223–253.

Mole, D. R., Thurston, P. C., Marsh, J. H., Stern, R. A., Ayer, J. A., Martin, L. A. J. & Lu, Y. J. (2021). The formation of Neoarchean continental crust in the south-east Superior Craton by two distinct geodynamic processes. Precambrian Research 356, 106104.

Moser, D. E., Bowman, J. R., Wooden, J., Valley, J. W., Mazdab, F. & Kita, N. (2008). Creation of a continent recorded in zircon zoning. Geology 36, 239–242.

Moser, D. E., Heaman, L. M., Krogh, T. E. & Hanes, J. A. (1996). Intracrustal extension of an Archean orogen revealed using single-grain U-Pb zircon geochronology. Tectonics 15, 1093–1109.

Moyen, J.-F. & Martin, H. (2012). Forty years of TTG research. Lithos 148, 312–336.

Moyen, J.-F. & Stevens, G. (2006). Experimental constraints on TTG petrogenesis: implications for Archean geodynamics. In: Benn, K., Mareschal, J.-C. & Condie, K. C. (eds) Archean geodynamics and environments. AGU Geophysical Monograph. Washington, DC: American Geophysical Union, 149–178.

Murphy, D., Rizo, H., O'Neil, J., Hepple, R., Wiemer, D., Kemp, A. & Vervoort, J. (2021). Combined Sm-Nd, Lu-Hf, and 142Nd study of Paleoarchean basalts from the East Pilbara Terrane, Western Australia. Chemical Geology 578, 120301.

Næraa, T., Scherstén, A., Rosing, M. T., Kemp, A. I. S., Hoffmann, J. E., Kokfelt, T. F. & Whitehouse, M. J. (2012). Hafnium isotope evidence for a transition in the dynamics of continental growth 3.2 Gyr ago. Nature 485, 627–630.

Nagel, T. J., Hoffmann, J. E. & Münker, C. (2012). Generation of Eoarchean tonalite-trondhjemite-granodiorite series from thickened mafic arc crust. Geology 40, 375–378.

Nair, R. & Chacko, T. (2008). Role of oceanic plateaus in the initiation of subduction and origin of continental crust. Geology 36, 583–586.

Ontario Geological Survey (2011). 1:250 000 scale bedrock geology of Ontario. Ontario Geolocial Survey Miscellaneous Release Data 126, Revision 1.

Palin, R. M., White, R. W. & Green, E. C. R. (2016). Partial melting of metabasic rocks and the generation of tonalitic–trondhjemitic–granodioritic (TTG) crust in the Archaean: constraints from phase equilibrium modelling. Precambrian Research 287, 73–90.

Patchett, P. J. & Tatsumoto, M. (1980). Hafnium isotope variations in oceanic basalts. Geophysical Research Letters 7, 1077–1080.

Paton, C., Hellstrom, J., Paul, B., Woodhead, J. & Hergt, J. (2011). Iolite: freeware for the visualisation and processing of mass spectrometric data. Journal of Analytical Atomic Spectrometry 26, 2508.

Pattison, D. R. M. (2003). Petrogenetic significance of orthopyroxene-free garnet + clinopyroxene + plagioclase ± quartz-bearing metabasites with respect to the amphibolite and granulite facies. Journal of Metamorphic Geology 21, 21–34.

Pattison, D. R. M., Chacko, T., Farquhar, J. & McFarlane, C. R. M. (2003). Temperatures of granulite-facies metamorphism: constraints from experimental phase equilibria and thermobarometry corrected for retrograde exchange. Journal of Petrology 44, 867–900.

Percival, J. A. (1983). High-grade metamorphism in the Chapleau-Foleyet area, Ontario. American Mineralogist 68, 667–686.

Percival, J. A. & Krogh, T. E. (1983). U–Pb zircon geochronology of the Kapuskasing structural zone and vicinity in the Chapleau–Foleyet area, Ontario. Canadian Journal of Earth Sciences 20, 830–843.

Percival, J. A. & Peterman, Z. E. (1994). Rb–Sr biotite and whole-rock data from the Kapuskasing uplift and their bearing on the cooling and exhumation history. Canadian Journal of Earth Sciences 31, 1172–1181.

Percival, J. A., Skulski, T., Sanborn-Barrie, M., Stott, G. M., Leclair, A. D., Corkery, M. T. & Boily, M. (2012). Geology and tectonic evolution of the Superior Province, Canada. In: Percival, J. A., Cook, F. A. & Clowes, R. M. (eds) Tectonic Styles in Canada: The LITHOPROBE Perspective. Geological Association of Canada, Special Paper 49, 321–378.

Percival, J. A. & West, G. F. (1994). The Kapuskasing uplift: a geological and geophysical synthesis. Canadian Journal of Earth Sciences 31, 1256–1286.

Polat, A. (2012). Growth of Archean continental crust in oceanic island arcs. Geology 40, 383–384.

Pourteau, A., Doucet, L. S., Blereau, E. R., Volante, S., Johnson, T. E., Collins, W. J., Li, Z.-X. & Champion, D. C. (2020). TTG generation by fluid-fluxed crustal melting: direct evidence from the Proterozoic Georgetown Inlier, NE Australia. Earth and Planetary Science Letters 550, 116548.

Powell, R. & Holland, T. J. B. (1988). An internally consistent dataset with uncertainties and correlations: 3. Applications to geobarometry, worked examples and a computer program. Journal of Metamorphic Geology 6, 173–204.

Powell, R. & Holland, T. J. B. (2008). On thermobarometry. Journal of Metamorphic Geology 26, 155–179.

Qian, Q. & Hermann, J. (2013). Partial melting of lower crust at 10-15 kbar: constraints on adakite and TTG formation. Contributions to Mineralogy and Petrology 165, 1195–1224.

Rapp, R. P., Watson, E. B. & Miller, C. F. (1991). Partial melting of amphibolite/eclogite and the origin of Archean trondhjemites and tonalites. Precambrian Research 51, 1–25.

Rollinson, H. (2021). Do all Archaean TTG rock compositions represent former melts? Precambrian Research 367, 106448.

Rosenberg, C. L. & Handy, M. R. (2005). Experimental deformation of partially melted granite revisited: implications for the continental crust. Journal of Metamorphic Geology 23, 19–28.

Rubatto, D. (2017). Zircon: the metamorphic mineral. Reviews in Mineralogy and Geochemistry 83, 261–295.

Sage, R. P. (1994). Geology of the Michipicoten Greenstone Belt. Ontario Geological Survey Open File Report 5888.

Sage, R. P., Lightfoot, P. C. & Doherty, W. (1996a). Bimodal cyclical Archean basalts and rhyolites from the Michipicoten (Wawa) greenstone belt, Ontario: geochemical evidence for magma contributions from the asthenospheric mantle and ancient continental lithosphere near the southern margin of the Superior Province. Precambrian Research 76, 119–153.

Sage, R. P., Lightfoot, P. C. & Doherty, W. (1996b). Geochemical characteristics of granitoid rocks from within the Archean Michipicoten Greenstone Belt, Wawa Subprovince, Superior Province, Canada: implications for source regions and tectonic evolution. Precambrian Research 76, 155–190.

Sawyer, E. W. (1987). The role of partial melting and fractional crystallization in determining discordant migmatite leucosome compositions. Journal of Petrology 28, 445–473.

Sawyer, E. W. (2020). Petrogenesis of secondary diatexites and the melt budget for crustal reworking. Journal of Petrology 61, 1–23.

Scherer, E., Münker, C. & Mezger, K. (2001). Calibration of the lutetium-hafnium clock. Science 293, 683–687.

Shaw, D. M. (1970). Trace element fractionation during anatexis. Geochimica et Cosmochimica Acta 34, 237–243.

Sizova, E., Gerya, T., Brown, M. & Perchuk, L. L. (2010). Subduction styles in the Precambrian: insight from numerical experiments. Lithos 116, 209–229.

Smit, M. A., Scherer, E. E. & Mezger, K. (2013). Lu–Hf and Sm–Nd garnet geochronology: chronometric closure and implications for dating petrological processes. Earth and Planetary Science Letters 381, 222–233.

Smith, P. E., Tatsumoto, M. & Farquhar, R. M. (1987). Zircon Lu–Hf systematics and the evolution of the Archean crust in the southern Superior Province, Canada. Contributions to Mineralogy and Petrology 97, 93–104.

Smithies, R. H., Champion, D. C. & Van Kranendonk, M. J. (2009). Formation of Paleoarchean continental crust through infracrustal melting of enriched basalt. Earth and Planetary Science Letters 281, 298–306.

Söderlund, U., Patchett, P. J., Vervoort, J. D. & Isachsen, C. E. (2004). The ^{176}Lu decay constant determined by Lu–Hf and U–Pb isotope systematics of Precambrian mafic intrusions. Earth and Planetary Science Letters 219, 311–324.

Stern, R. A., Bodorkos, S., Kamo, S. L., Hickman, A. H. & Corfu, F. (2009). Measurement of SIMS instrumental mass fractionation of Pb isotopes during zircon dating. Geostandards and Geoanalytical Research 33, 145–168.

Stuck, T. J. & Diener, J. F. A. (2018). Mineral equilibria constraints on open-system melting in metamafic compositions. Journal of Metamorphic Geology 36, 255–281.

Turek, A., Sage, R. P. & Van Schmus, W. R. (1992). Advances in the U–Pb zircon geochronology of the Michipicoten greenstone belt, Superior Province, Ontario. Canadian Journal of Earth Sciences 29, 1154–1165.

Vervoort, J. D. & Blichert-Toft, J. (1999). Evolution of the depleted mantle: Hf isotope evidence from juvenile rocks through time. Geochimica et Cosmochimica Acta 63, 533–556.

Vervoort, J. D. & Kemp, A. I. S. (2016). Clarifying the zircon Hf isotope record of crust–mantle evolution. Chemical Geology 425, 65–75.

Vervoort, J. D., Patchett, P. J., Söderlund, U. & Baker, M. (2004). Isotopic composition of Yb and the determination of Lu concentrations and Lu/Hf ratios by isotope dilution using MC-ICPMS. Geochemistry, Geophysics, Geosystems 5, Q11002.

Watkins, J. M., Clemens, J. D. & Treloar, P. J. (2007). Archaean TTGs as sources of younger granitic magmas: melting of sodic metatonalites at 0.6–1.2 GPa. Contributions to Mineralogy and Petrology 154, 91–110.

White, R. W., Palin, R. M. & Green, E. C. R. (2017). High-grade metamorphism and partial melting in Archean composite grey gneiss complexes. Journal of Metamorphic Geology 35, 181–195.

White, R. W. & Powell, R. (2002). Melt loss and the preservation of granulite facies mineral assemblages. Journal of Metamorphic Geology 20, 621–632.

White, R. W., Powell, R. & Clarke, G. L. (2002). The interpretation of reaction textures in Fe-rich metapelitic granulites of the Musgrave Block, central Australia: constraints from mineral equilibria calculations in the system K_2O–FeO–MgO–Al_2O_3–SiO_2–H_2O–TiO_2–Fe_2O_3. Journal of Metamorphic Geology 20, 41–55.

White, R. W., Powell, R., Holland, T. J. B., Johnson, T. E. & Green, E. C. R. (2014). New mineral activity–composition relations for thermodynamic calculations in metapelitic systems. Journal of Metamorphic Geology 32, 261–286.

Woodhead, J. D. & Hergt, J. M. (2005). A preliminary appraisal of seven natural zircon reference materials for *in situ* Hf isotope determination. Geostandards and Geoanalytical Research 29, 183–195.

Woodhead, J. D., Hellstrom, J., Hergt, J. M., Greig, A. & Maas, R. (2007). Isotopic and elemental imaging of geological materials by laser ablation inductively coupled plasma-mass spectrometry. Geostandards and Geoanalytical Research 31, 331–343.

Woodhead, J., Hergt, J., Shelley, M., Eggins, S. & Kemp, R. (2004). Zircon Hf-isotope analysis with an excimer laser, depth profiling, ablation of complex geometries, and concomitant age estimation. Chemical Geology 209, 121–135.

Wyman, D. A., Kerrich, R. & Polat, A. (2002). Assembly of Archean cratonic mantle lithosphere and crust: plume–arc interaction in the Abitibi–Wawa subduction–accretion complex. Precambrian Research 115, 37–62.

Yakymchuk, C. & Brown, M. (2014). Consequences of open-system melting in tectonics. Journal of the Geological Society, London 171, 21–40.

Yakymchuk, C., Clark, C. & White, R. W. (2017). Phase relations, reaction sequences and petrochronology. Reviews in Mineralogy and Geochemistry 83, 13–53.

Yakymchuk, C., Kirkland, C. L., Hollis, J. A., Kendrick, J., Gardiner, N. J. & Szilas, K. (2020). Mesoarchean partial melting of mafic crust and tonalite production during high-T–low-P stagnant tectonism, Akia Terrane, West Greenland. Precambrian Research 339, 105615.

Zeh, A., Gerdes, A. & Millonig, L. (2011). Hafnium isotope record of the Ancient Gneiss Complex, Swaziland, southern Africa: evidence for Archaean crust–mantle formation and crust reworking between 3.66 and 2.73 Ga. Journal of the Geological Society, London 168, 953–963.

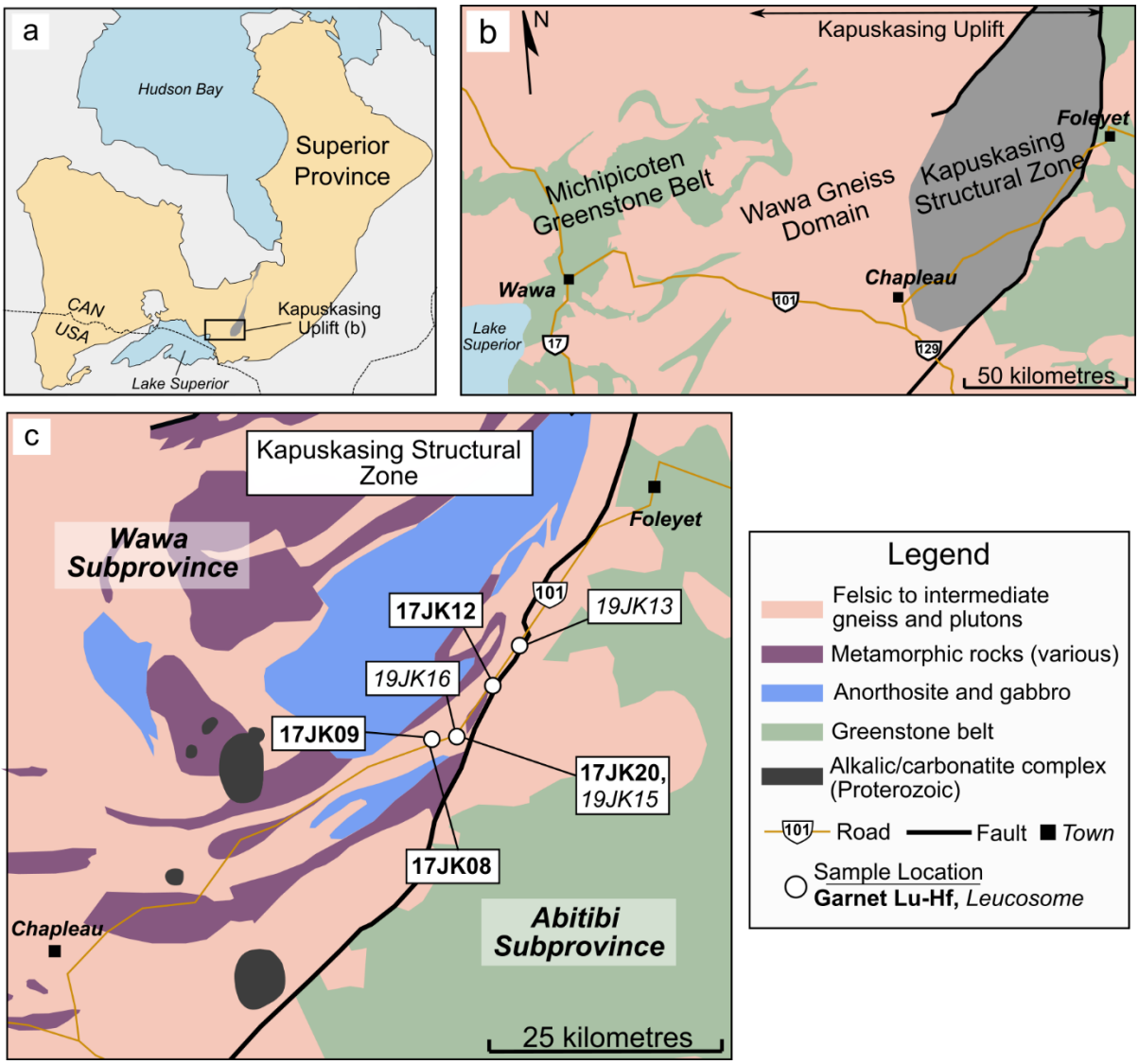


Figure 5.1. Simplified geological maps of the study area. a) Location of the Superior Province in North America (modified after Percival et al., 2012). b) Geological map of the Kapuskasing Uplift (modified after Ontario Geological Survey, 2011). c) Detailed geological map of the Kapuskasing Structural Zone (modified after Ontario Geological Survey, 2011) with locations of samples used in this study.

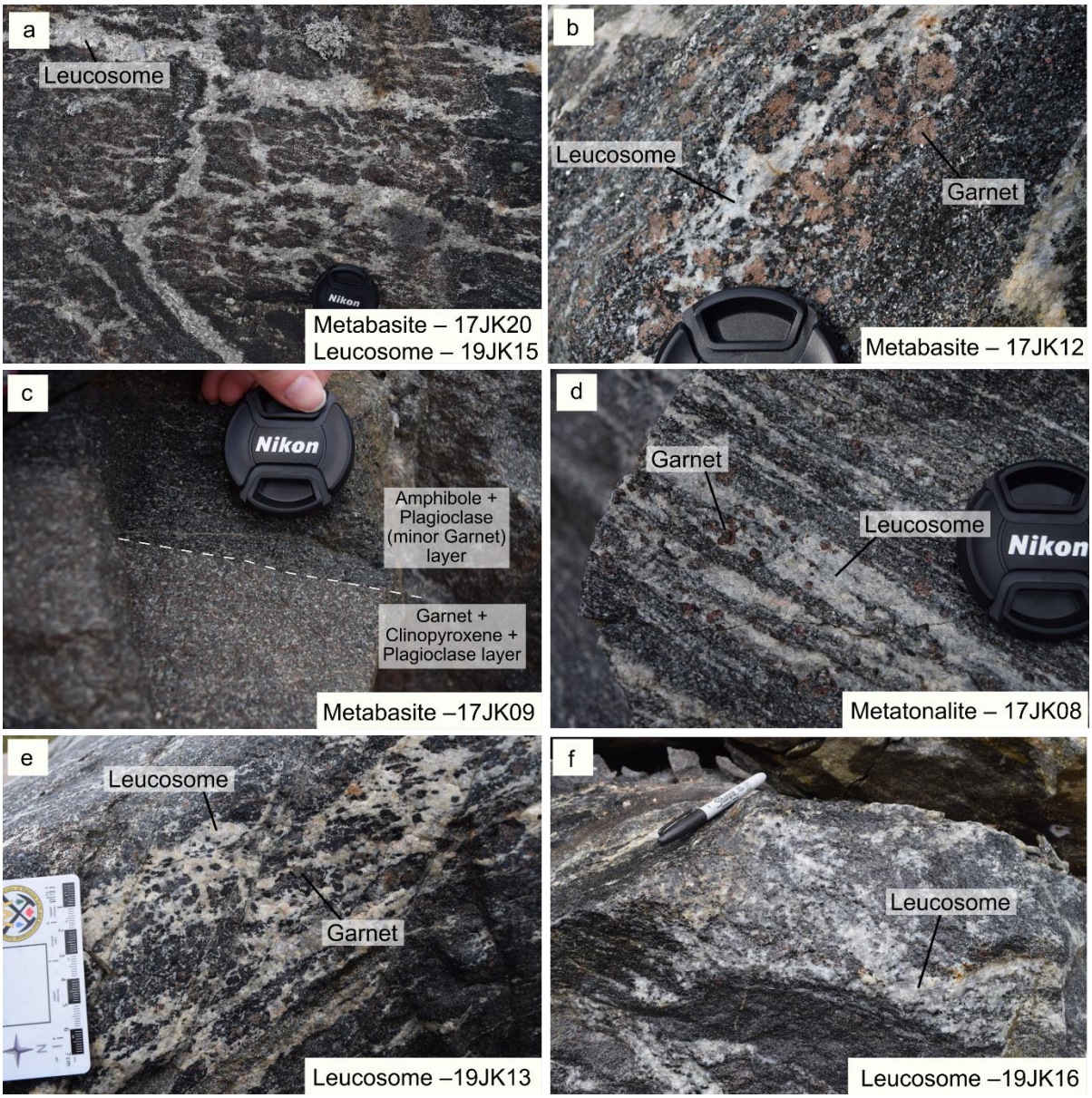


Figure 5.2. Photographs of outcrops in the Kapuskasing Structural Zone. a) Leucosome-rich metabasite outcrop where samples 17JK20 (metabasite) and 19JK15 (leucosome) were collected. b) Metabasite with leucosome and peritectic garnet, location of sample 17JK12 (metabasite). c) Compositionally layered metabasite, location of sample 17JK09 (metabasite). d) Metatonalite outcrop with leucosome and peritectic garnet, location of sample 17JK08 (metatonalite). e) Metabasite outcrop with leucosome and peritectic garnet, location of sample 19JK13 (leucosome). f) Leucosome-rich area of a metabasite outcrop, location of sample 19JK16 (leucosome).

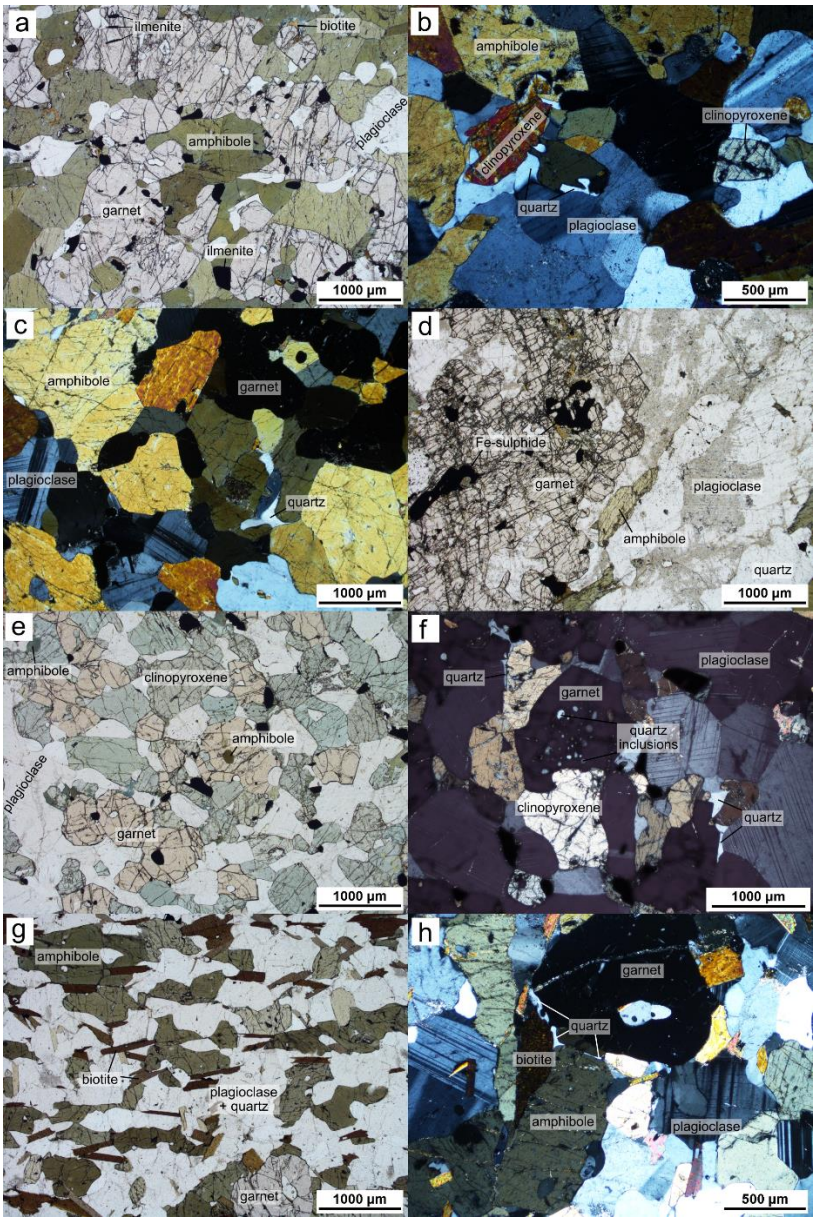


Figure 5.3. Photomicrographs of samples from the Kapuskasing Structural Zone. a) Amphibole- and garnet-rich domain in metabasite (PPL, 17JK20). b) Interstitial quartz associated with amphibole and clinopyroxene (XPL, 17JK20). c) Amphibole-, garnet-, and plagioclase-bearing domain with rare interstitial quartz in metabasite (XPL, 17JK12). d) Leucosome domain in metabasite with a skeletal garnet porphyroblast (PPL, 17JK12). e) Garnet-, clinopyroxene-, and plagioclase-rich metabasite with subgranoblastic texture (PPL, 17JK09). f) Xenoblastic quartz is interstitial to garnet, clinopyroxene, and plagioclase in metabasite (XPL, 17JK09). g) Foliated metatonalite with an assemblage of amphibole, biotite, plagioclase, and quartz with uncommon garnet (PPL, 17JK08). h) Interstitial quartz associated with garnet at the edge of leucosome in metatonalite (XPL, 17JK08). PPL = plane-polarized light, XPL = cross-polarized light.

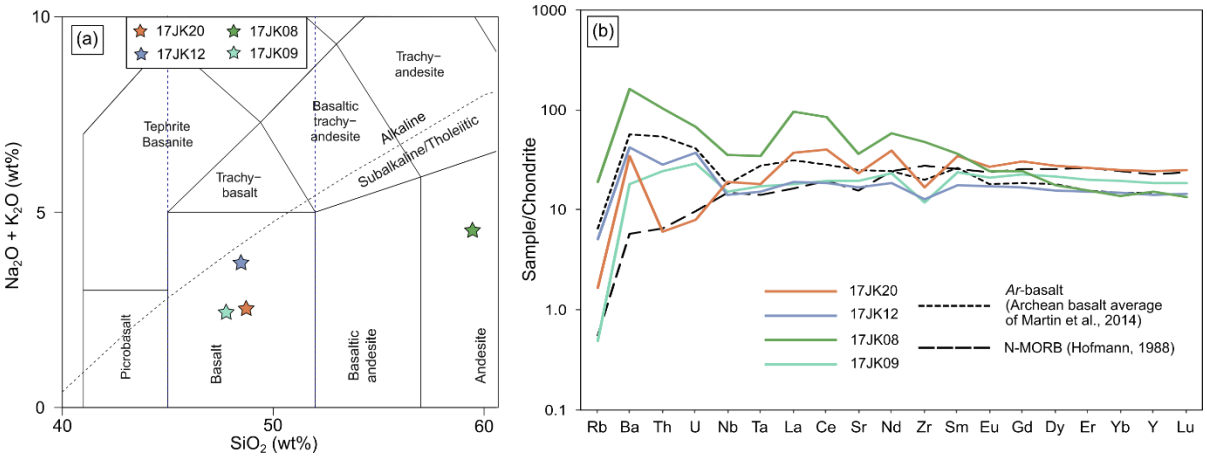


Figure 5.4. Whole-rock geochemical compositions of samples from the Kapuskasing Structural Zone. a) SiO_2 (wt.%) versus $Na_2O + K_2O$ (wt.%) of samples (plotted using GCDkit; Janoušek et al., 2006). b) Chondrite-normalized trace elements of samples (normalization values from McDonough & Sun, 1995) in comparison to N-MORB (Hofmann, 1988) and average Archean basalt (Martin et al., 2014).

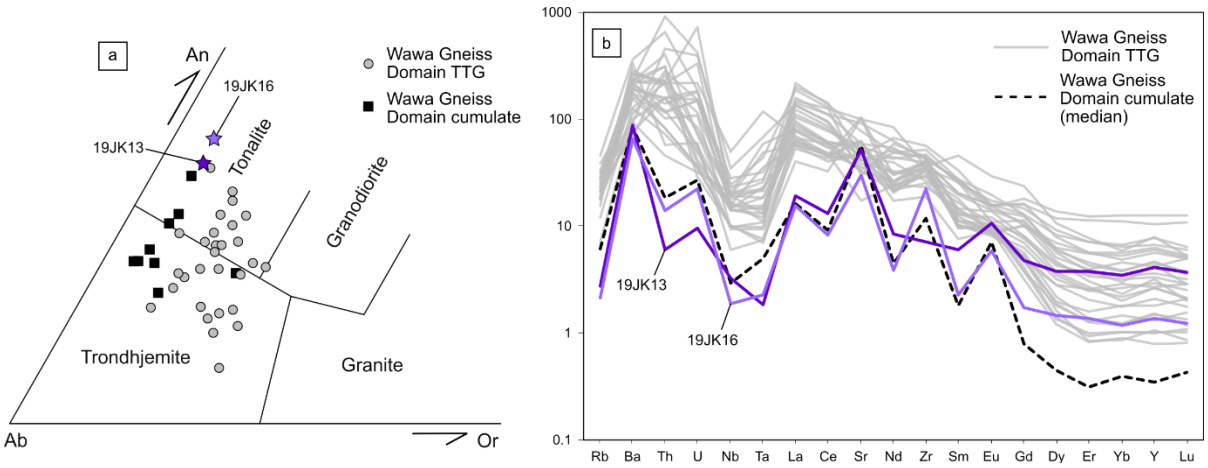


Figure 5.5. Whole-rock geochemical compositions of leucosome samples from the Kapuskasing Structural Zone in comparison to natural TTG data from the Kapuskasing Uplift (from Kendrick et al., 2022 [Chapter 3]). a) Normative feldspar compositions (An = anorthite, Ab = albite, Or = orthoclase) calculated using GCDkit with classifications from Barker (1979). b) Chondrite-normalized trace elements of samples (normalization values from McDonough and Sun, 1995).

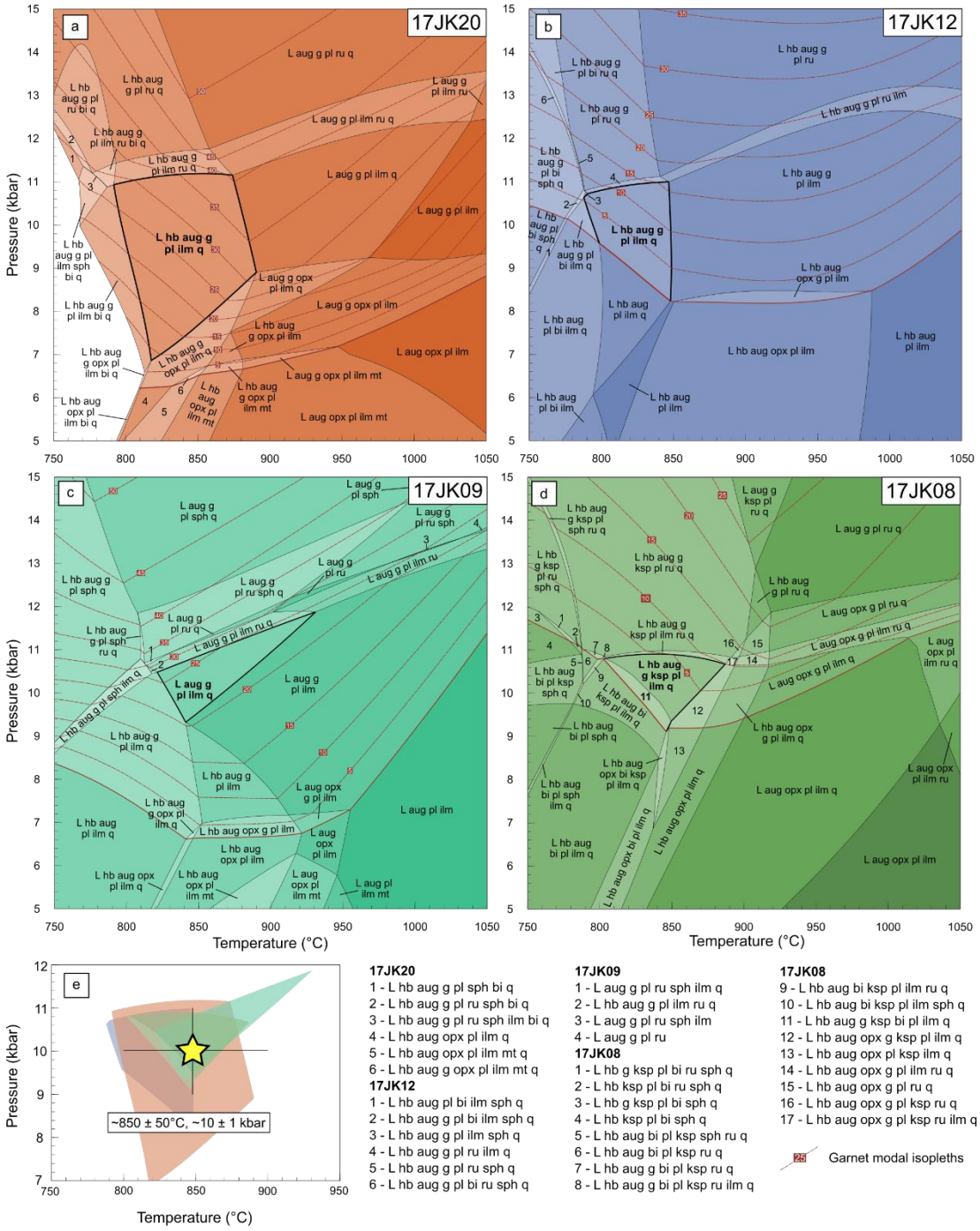


Figure 5.6. Pressure–temperature (*P*–*T*) phase diagrams for samples 17JK20 (a), 17JK12 (b), 17JK09 (c), 17JK08 (d) calculated by phase equilibrium modelling. Uncertainties for peak *P*–*T* conditions shown in (e) were estimated based on best practices (Powell & Holland, 2008). L = melt, hb = amphibole, g = garnet, aug = clinopyroxene, opx = orthopyroxene, pl = plagioclase, bi = biotite, ksp = K-feldspar, q = quartz, ilm = ilmenite, ru = rutile, sph = titanite.

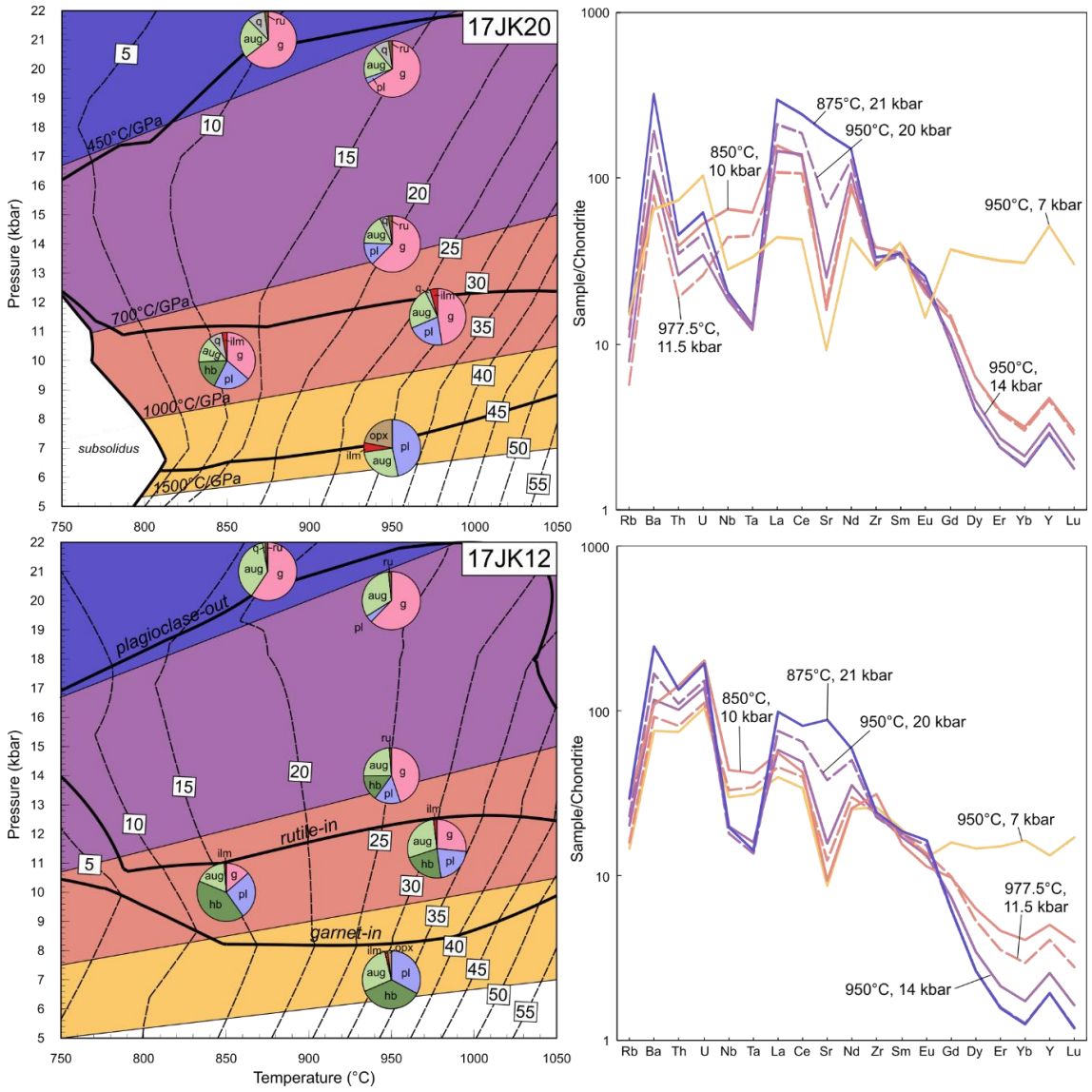


Figure 5.7. Results of melt trace element modelling for metabasite samples 17JK20 and 17JK12. hb = amphibole, g = garnet, aug = clinopyroxene, opx = orthopyroxene, pl = plagioclase, q = quartz, ilm = ilmenite, ru = rutile

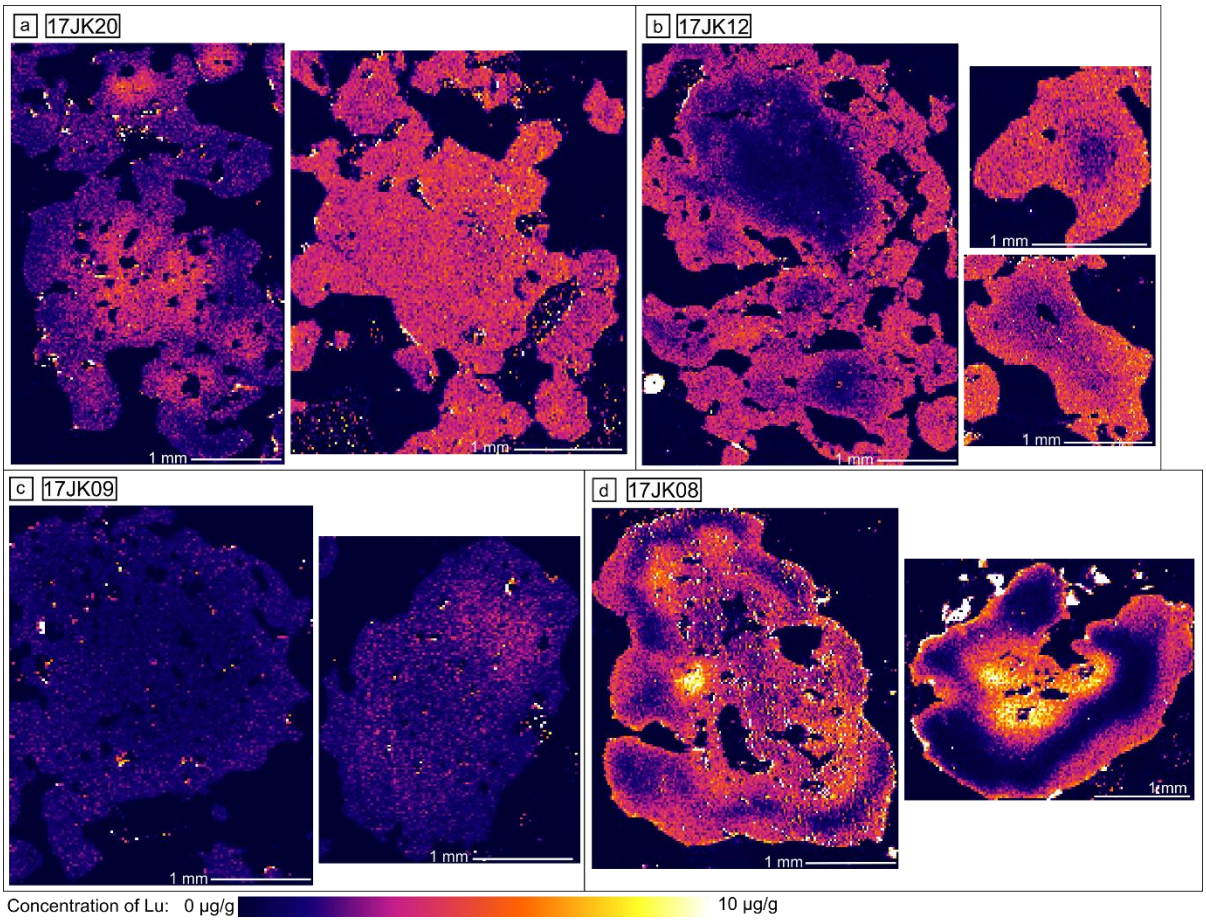


Figure 5.8. Trace element maps of Lu in garnet crystals from samples (a) 17JK20, (b) 17JK12, (c) 17JK09, and (d) 17JK08.

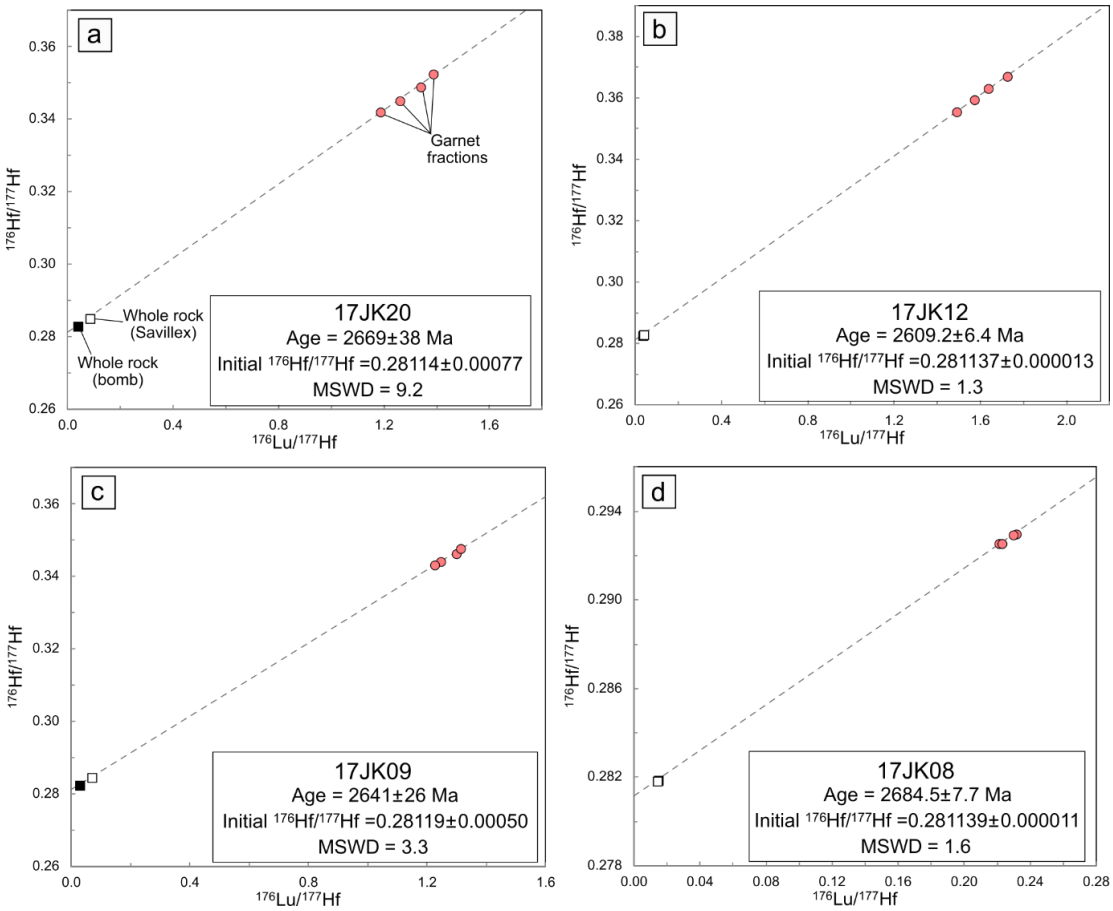


Figure 5.9. Lu–Hf isochrons for samples (a) 17JK20, (b) 17JK12, (c) 17JK09, and (d) 17JK08. Data point symbols are larger than uncertainties. Reported age uncertainties are 95% confidence errors (Ludwig, 2012).

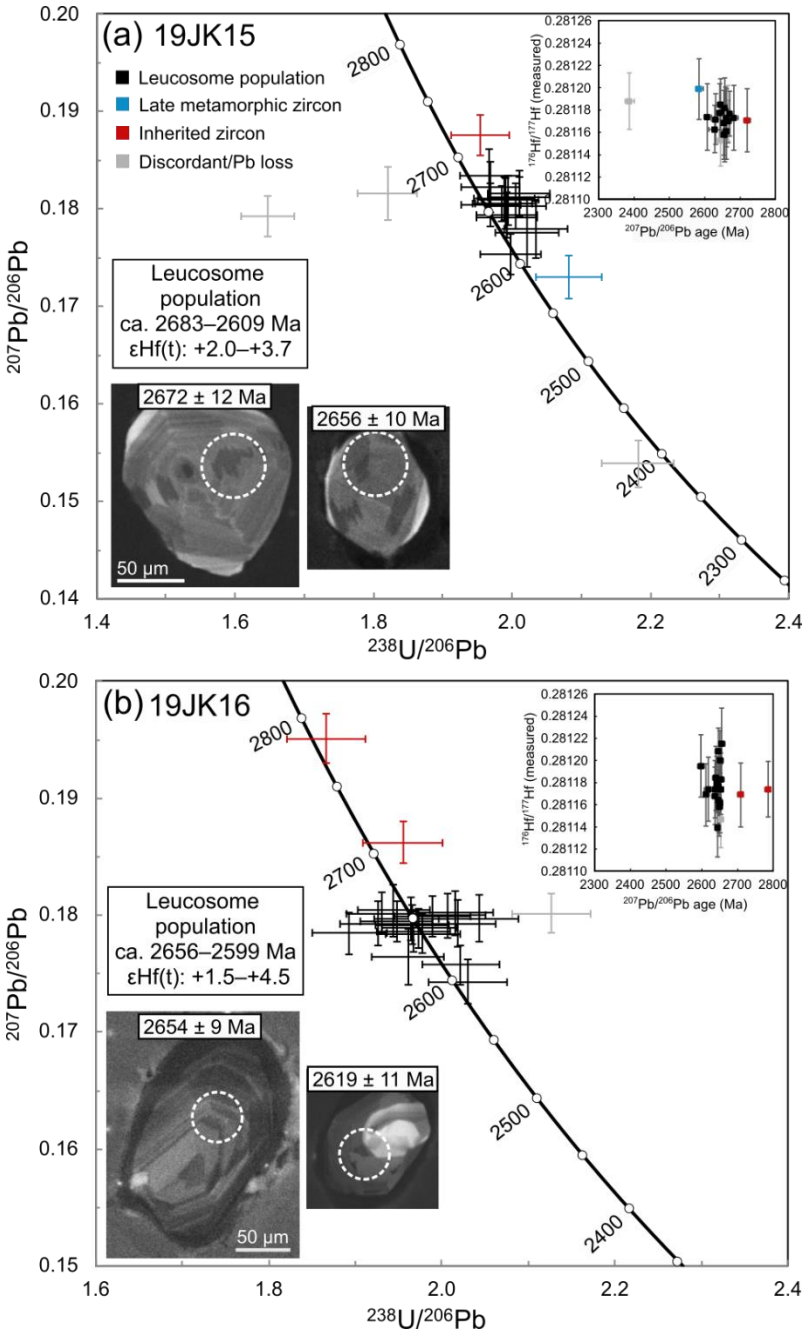


Figure 5.10. Tera-Wasserburg diagrams showing zircon U–Pb data for samples (a) 19JK15 and (b) 19JK16, with insets showing measured $^{176}Hf/^{177}Hf$ ratios.

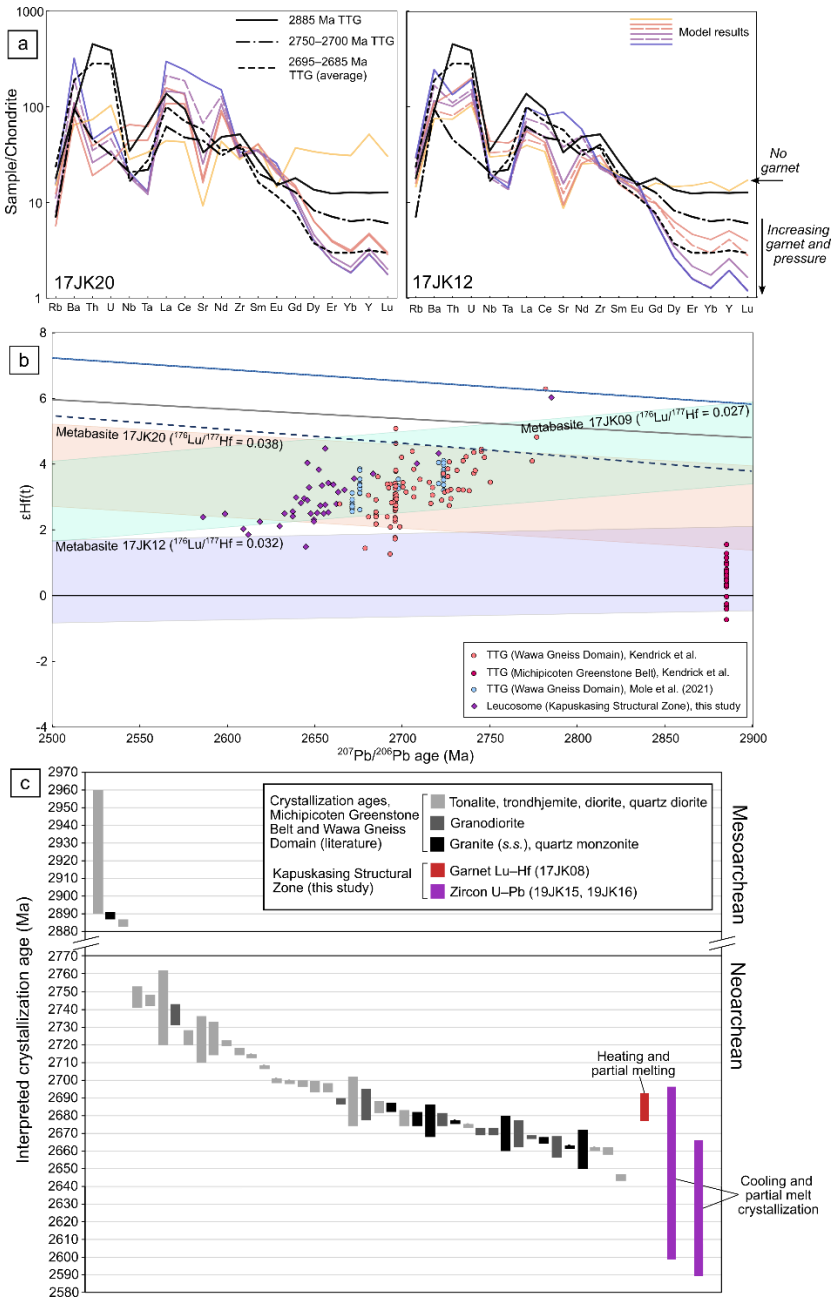


Figure 5.11. (a) Results of melt trace element modelling (Fig. 5.7) compared to natural TTG samples from the Wawa Gneiss Domain and Michipicoten Greenstone Belt (data from Kendrick et al., 2022 [Chapter 3]; Kendrick et al., submitted [Chapter 4]). (b) Comparison of metabasite whole-rock Lu–Hf data (samples 17JK20, 17JK12, and 17JK09) and Hf data from zircon in TTGs from the Wawa Gneiss Domain and Michipicoten Greenstone Belt (data from Kendrick et al., submitted [Chapter 4]; Mole et al., 2021). (c) Compilation of granitoid crystallization ages from previous work for samples from the Wawa Gneiss Domain and Michipicoten Greenstone Belt (Table S4.7) compared to results of garnet Lu–Hf and zircon U–Pb geochronology from this study. Solid bars represent the reported age uncertainties.

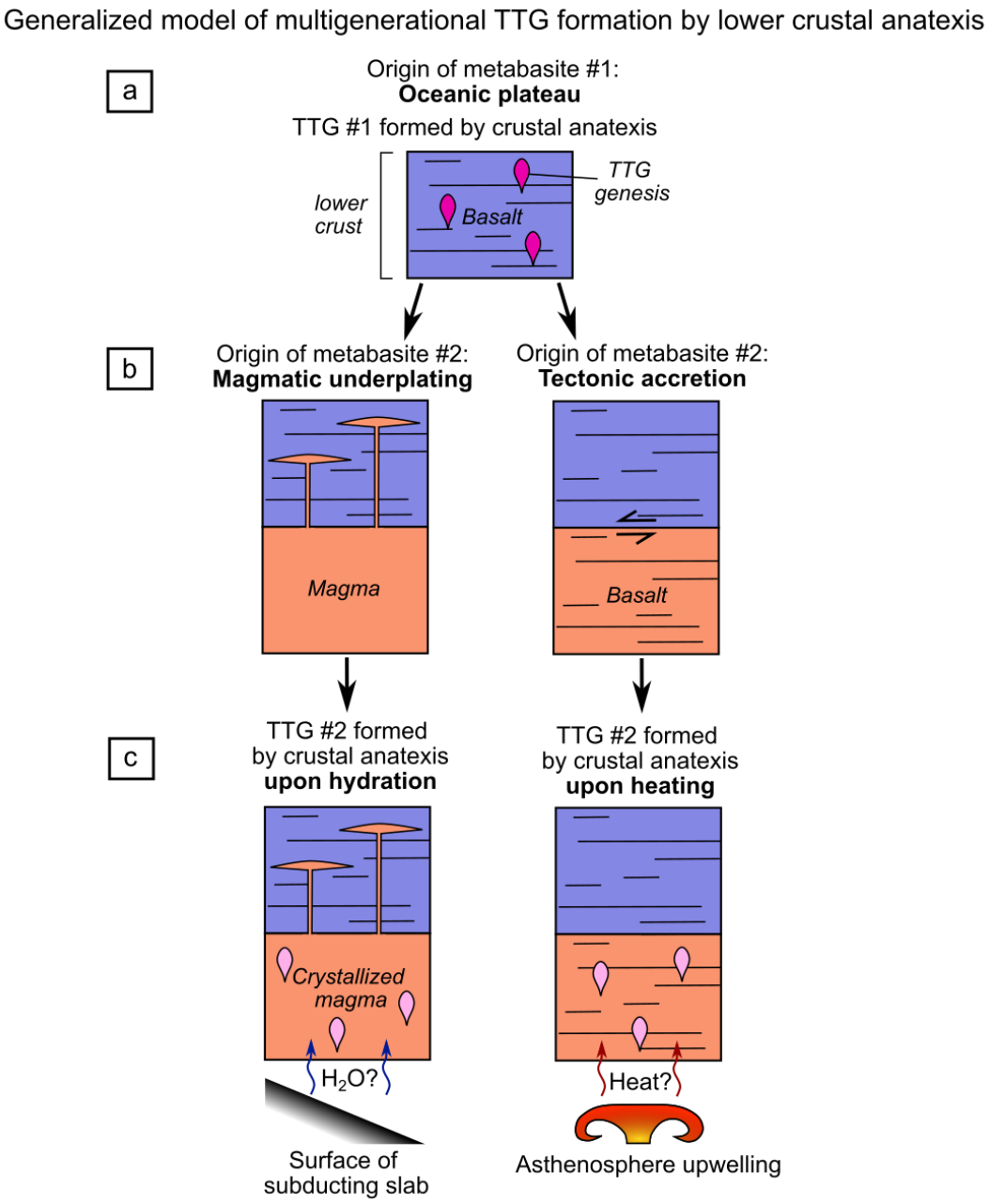


Figure 5.12. Schematic diagram illustrating the formation of two generations of TTGs from two lower crustal metabasic sources. a) The first TTG generation is produced by partial melting of basalt buried and metamorphosed at lower-crustal depth in an oceanic plateau setting. b) New mafic source material is added at the base of the existing lower-crustal metabasite either by magmatic underplating or tectonic accretion. c) Partial melting of new source material is initiated either by addition of H_2O from a subducting slab (magmatic underplating scenario) or addition of heat from upwelling asthenosphere (tectonic accretion scenario) to produce the second generation of TTG magma.

Table 5.1. Bulk compositions used for phase equilibrium modelling.

Sample	H_2O	SiO_2	Al_2O_3	CaO	MgO	FeO	K_2O	Na_2O	TiO_2	O/Fe_2O_3
mol%										*O*
17JK20	3.01	50.93	9.04	10.48	7.59	13.88	0.36	2.01	1.34	1.36
17JK12	4.79	49.14	9.41	10.97	9.64	10.78	0.48	2.90	0.89	0.99
17JK09	2.65	49.83	9.03	14.77	6.38	12.46	0.08	2.34	1.17	1.29
17JK08	3.53	61.18	9.11	7.08	7.18	6.63	0.99	3.02	0.73	0.56
wt.%										*Fe_2O_3*
17JK20	0.87	49.24	14.84	9.46	4.92	12.91	0.55	2.00	1.72	3.49
17JK12	1.42	48.49	15.76	10.10	6.38	10.39	0.74	2.95	1.17	2.59
17JK09	0.77	48.22	14.83	13.34	4.14	11.42	0.12	2.33	1.51	3.33
17JK08	1.03	59.49	15.04	6.43	4.68	6.41	1.51	3.03	0.95	1.44

Table 5.2. Lu and Hf data obtained from isotope dilution.

Sample	Lu (µg/g)	Hf (µg/g)	$^{176}Lu/^{177}Hf$	2s (abs)*	$^{176}Hf/^{177}Hf$	2s (abs)†
17JK20 – metabasite						
Whole rock – S§	0.660	1.138	0.0823	0.0004	0.285316	0.000015
Whole rock – B§	0.723	2.710	0.0379	0.0002	0.283107	0.000015
Garnet-1	2.229	0.254	1.2603	0.0063	0.345330	0.000018
Garnet-2	2.131	0.221	1.3882	0.0069	0.352558	0.000018
Garnet-3	2.223	0.238	1.3410	0.0067	0.349090	0.000018
Garnet-4	2.150	0.260	1.1874	0.0059	0.342068	0.000025
17JK12 – metabasite						
Whole rock – S	0.538	2.171	0.0351	0.0002	0.282897	0.000015
Whole rock – B	0.561	2.506	0.0318	0.0002	0.282716	0.000016
Garnet-1	3.507	0.293	1.7262	0.0086	0.367133	0.000020
Garnet-2	3.439	0.332	1.4909	0.0075	0.355567	0.000019
Garnet-3	3.382	0.297	1.6398	0.0082	0.363321	0.000019
Garnet-4	3.480	0.318	1.5750	0.0079	0.359586	0.000023
17JK09 – metabasite						
Whole rock – S	0.478	0.999	0.0680	0.0003	0.284621	0.000015
Whole rock – B	0.502	2.651	0.0268	0.0001	0.282549	0.000014
Garnet-1	1.407	0.154	1.3140	0.0066	0.347842	0.000018
Garnet-2	1.406	0.164	1.2274	0.0061	0.343455	0.000018
Garnet-3	1.415	0.156	1.2998	0.0065	0.346397	0.000018
Garnet-4	1.398	0.161	1.2466	0.0062	0.344209	0.000018
17JK08 – metatonalite						
Whole rock – S	0.408	4.291	0.0135	0.0001	0.281830	0.000015
Whole rock – B	0.430	4.283	0.0142	0.0001	0.281872	0.000015
Garnet-1	5.140	3.155	0.2316	0.0012	0.292993	0.000040
Garnet-2	5.109	3.286	0.2210	0.0011	0.292553	0.000015
Garnet-3	5.130	3.271	0.2229	0.0011	0.292565	0.000015
Garnet-4	5.072	3.138	0.2298	0.0011	0.292953	0.000015

* External uncertainty, 0.5%

† External uncertainty, 0.005% (in quadrature)

§ S – Savillex digestion (i.e., table-top); B – Bomb digestion

Table 5.3. U–Pb and Hf data from zircon.

Analysis No.	$^{207}Pb/^{206}Pb$ age (Ma)	2SE	$^{176}Hf/^{177}Hf$ measured	2SE	$^{176}Lu/^{177}Hf$	2SE	$^{176}Hf/^{177}Hf$ (t)*	εHf (t)	2SE	Classification†
19JK15 – Leucosome										
Zircon-1	2658	12	0.281158	0.000024	0.000035	0.0000039	0.281156	2.53	1.39	X
Zircon-2	2644	9	0.281178	0.000026	0.000020	0.0000003	0.281177	2.95	1.43	X
Zircon-3	2609	10	0.281174	0.000030	0.000010	0.0000002	0.281174	2.03	1.53	X
Zircon-4	2660	12	0.281179	0.000022	0.000017	0.0000003	0.281178	3.38	1.34	X
Zircon-5	2720	9	0.281171	0.000028	0.000102	0.0000026	0.281166	4.33	1.48	I
Zircon-6	2389	13	0.281188	0.000025	0.000009	0.0000003	0.281188	-2.55	1.40	D
Zircon-7	2662	10	0.281161	0.000025	0.000012	0.0000008	0.281160	2.79	1.41	X
Zircon-8	2656	10	0.281169	0.000029	0.000101	0.0000005	0.281164	2.76	1.50	X
Zircon-9	2667	11	0.28117	0.000019	0.000011	0.0000002	0.281169	3.22	1.29	X
Zircon-10	2646	10	0.281153	0.000023	0.000006	0.0000003	0.281153	2.13	1.37	D
Zircon-11	2667	12	0.281177	0.000025	0.000016	0.0000010	0.281176	3.46	1.41	D
Zircon-12	2658	8	0.281182	0.000027	0.000015	0.0000002	0.281181	3.43	1.46	X
Zircon-13	2663	10	0.281173	0.000026	0.000061	0.0000023	0.281170	3.15	1.43	X
Zircon-14	2655	11	0.281158	0.000022	0.000020	0.0000007	0.281157	2.50	1.34	X
Zircon-15	2672	12	0.281177	0.000020	0.000030	0.0000003	0.281175	3.56	1.31	X
Zircon-16	2630	17	0.281163	0.000021	0.000010	0.0000002	0.281163	2.11	1.32	X
Zircon-17	2633	14	0.281172	0.000023	0.000010	0.0000005	0.281171	2.50	1.36	X
Zircon-18	2647	11	0.281185	0.000023	0.000009	0.0000002	0.281185	3.29	1.37	X
Zircon-19	2683	13	0.281173	0.000029	0.000007	0.0000003	0.281173	3.71	1.50	X
Zircon-20	2586	11	0.281199	0.000027	0.000007	0.0000002	0.281199	2.39	1.45	L

Table 5.3 (continued)

19JK16 – Leucosome										
Zircon-1	2645	8	0.281139	0.000026	0.000076	0.0000008	0.281135	1.49	1.43	X
Zircon-2	2642	8	0.281179	0.000025	0.000091	0.0000012	0.281174	2.82	1.41	X
Zircon-3	2651	8	0.281162	0.000027	0.000042	0.0000021	0.281160	2.52	1.46	X
Zircon-4	2639	8	0.281184	0.000029	0.000060	0.0000008	0.281181	2.99	1.50	X
Zircon-5	2637	8	0.281174	0.000026	0.000079	0.0000005	0.281170	2.56	1.43	X
Zircon-6	2646	9	0.281208	0.000021	0.000032	0.0000012	0.281206	4.04	1.32	X
Zircon-7	2652	9	0.281200	0.000027	0.000073	0.0000018	0.281196	3.83	1.46	X
Zircon-8	2654	9	0.281183	0.000024	0.000028	0.0000009	0.281182	3.35	1.39	X
Zircon-9	2708	8	0.281169	0.000029	0.000077	0.0000033	0.281165	4.02	1.51	I
Zircon-10	2648	8	0.281164	0.000028	0.000046	0.0000008	0.281162	2.49	1.48	X
Zircon-11	2653	8	0.281147	0.000026	0.000079	0.0000055	0.281143	1.96	1.43	D
Zircon-12	2612	8	0.281169	0.000028	0.000042	0.0000007	0.281167	1.86	1.48	X
Zircon-13	2656	10	0.281215	0.000032	0.000059	0.0000053	0.281212	4.48	1.58	X
Zircon-14	2649	9	0.281158	0.000026	0.000052	0.0000008	0.281155	2.31	1.43	X
Zircon-15	2637	8	0.281168	0.000026	0.000040	0.0000008	0.281166	2.41	1.43	X
Zircon-16	2653	8	0.281174	0.000023	0.000179	0.0000018	0.281165	2.74	1.37	X
Zircon-17	2785	9	0.281174	0.000025	0.000048	0.0000019	0.281171	6.03	1.41	I
Zircon-18	2619	11	0.281174	0.000029	0.000008	0.0000002	0.281174	2.25	1.50	X
Zircon-19	2599	9	0.281195	0.000028	0.000034	0.0000006	0.281193	2.49	1.48	X
Zircon-20	2649	8	0.281159	0.000024	0.000103	0.0000021	0.281154	2.26	1.39	X
Zircon-21	2646	9	0.281177	0.000024	0.000052	0.0000009	0.281174	2.90	1.39	X

*The $^{207}Pb/^{206}Pb$ age in column 2 was used to calculate $^{176}Hf/^{177}Hf$ (t) for individual analyses. Decay constant for ^{176}Lu from Scherer et al. (2001).

†X = Leucosome population, I = Inherited zircon, D = Discordant/Pb loss, L = Late metamorphic zircon

Chapter 6

Petrogenesis of Archean sanukitoids: Insights from thermodynamic modelling

Summary

The sanukitoid suite is a series of Archean granitoid rocks that exhibit enrichment in both large ion lithophile elements (e.g., K_2O, Ba, Sr) and MgO, Ni, and Cr relative to the more common Archean tonalite-trondhjemite-granodiorite (TTG) suites. These characteristics have led to the interpretation that sanukitoids are formed by partial melting of a mantle source that was metasomatized by crustal material. Sanukitoids have been identified in many Archean cratons and are typically a relatively late feature in craton evolution, which may signal a change in tectonic processes late in the Archean eon. The chemical composition of sanukitoids has been used to understand characteristics of their source, such as the nature of the metasomatic agent introduced into the mantle, which in turn could be linked to tectonic regime more broadly. However, previous work has also linked trends in sanukitoid compositions to factors unrelated to source. In this work, we use phase equilibrium modelling coupled with melt trace element modelling to forward model potential sanukitoid sources and determine the effect of two variables on sanukitoid composition: source bulk composition and pressure–temperature conditions of source melting. We consider mantle sources metasomatized by two different metasomatic agents—TTG melt and partial melt of subducted metasedimentary rocks—and investigate predicted melt compositions between 1.5 GPa and 2.5 GPa at a range of melt fractions. These results are compared to a compilation of data from natural primitive (i.e., relatively mafic) sanukitoid samples from the Amazonian Craton, Baltic Shield, Kaapvaal Craton, North China Craton, and Superior Province. Overall, the model results replicated some geochemical trends of natural sanukitoid suites, with the TTG-melt-metasomatized mantle results in some cases showing a closer fit to natural data than those of the metasediment-melt metasomatized mantle. Trends in rare earth elements were best replicated by model melt produced by high degrees of partial melting with no residual garnet. This work also revealed that a negative Eu anomaly is a common feature of many natural sanukitoids, however this feature was not replicated in the models. In general, the results suggest that the geochemical diversity of natural sanukitoids could be attributed to variations in

pressure–temperature conditions of source melting, different source compositions, or a combination of these factors. Linking sanukitoid compositions to a particular mantle metasomatic agent or tectonic process is therefore difficult. The distinct geochemical features of different sanukitoid suites from different cratons likely reflects the influence of localized processes; the significance of sanukitoid compositions can best be assessed when these rocks are considered within their regional geological context and major and trace element compositions are coupled with isotopic data.

6.1 Introduction

The Archean sanukitoid suite, first defined based on observations from the Superior Province (Shirey and Hanson, 1984; Stern and Hanson, 1991), form a magmatic series from diorite to granite (Martin et al., 2009). Unlike the more abundant Archean tonalite-trondhjemite-granodiorite (TTG) granitoids that are characterized by elevated concentrations of Na_2O (Moyen, 2011), sanukitoids are more potassic with monzodiorites, granodiorites, and monzogranites as the most common rock types (Martin et al., 2009). The source of the sanukitoid suite is widely considered to be metasomatized mantle based on high concentrations of MgO, Ni, Cr, and large ion lithophile elements (LILE) in these rocks (Shirey and Hanson, 1984; Martin et al., 2009; Laurent et al., 2014a). Although TTGs are common throughout the Archean eon, sanukitoids are restricted temporally to the latest stages of Archean craton evolution globally and may represent a fundamental shift in tectonic regime at the end of the Archean eon (Laurent et al., 2014a). A subducting slab is commonly proposed as the source of mantle metasomatism resulting in the interpretation that sanukitoids mark the onset of modern-style arc magmatism (e.g., Stern and Hanson, 1991; Martin et al., 2009; de Oliveira et al., 2011; Laurent et al., 2014a; Singh et al., 2019). Alternatively, the appearance of sanukitoids late in the Archean geological record has been attributed to the emergence of continental crust above sea level at this time; according to this interpretation, the introduction of eroded K-rich sediments into the mantle at convergent margins is crucial to sanukitoid genesis (Bédard, 2018).

Some aspects of sanukitoid chemical compositions are commonly linked to characteristics of their source, including the degree of source melting and the nature of the metasomatic agent in the mantle, which may have been fluid released from the subducting slab, TTG melt derived from anatexis of the slab, or partial melt from anatexis of subducting sediments (Lobach-Zhuchenko, 2008; Martin et al., 2009; Laurent et al., 2011; Jiang et al., 2016). However, geochemical trends in sanukitoids have also been linked to fractional crystallization and magma mixing or contamination (Martin et al., 2009). In addition, a phase equilibrium modelling study of sanukitoid genesis showed

that variable ratios of metasomatic agent and mantle mixing could produce the geochemical variety observed in some sanukitoid suites (Semprich et al., 2015). Variability in sanukitoid compositions may be linked to multiple processes, and determining the extent to which each process can influence major and trace element compositions is important for determining the significance of sanukitoid compositions in the broader context of Archean tectonic processes.

Here, we explore the potential connection between major and trace element trends of sanukitoids and characteristics of their source. We employ phase equilibrium and melt trace element modelling to forward model partial melting of theoretical sanukitoid sources, considering two main source-related variables:

1. Source composition, which varies depending on the origin of the metasomatic agent that interacted with depleted mantle.
2. Pressure–temperature (*P*–*T*) conditions of melting, which control the melt fraction and residue mineral assemblage in the source and may be indicative of tectonic processes.

Our modelling results indicate that the major and trace element compositions of sanukitoids are the product of a complex combination of the two aforementioned variables and other factors, resulting in considerable geochemical variability among individual sanukitoid suites.

6.2 Methodology

6.2.1 Data compilation and selection of compositions for modelling

Our sanukitoid dataset was assembled from major and trace element geochemical data of 426 samples reported in the literature from five cratons: Amazonian Craton (de Oliveira et al., 2010), Baltic Shield (Lobach-Zhuchenko et al., 2005; Heilimo et al., 2010; Egorova, 2014), Kaapvaal Craton (Laurent et al., 2014b), North China Craton (Wang et al., 2009; Jiang et al., 2016), and Superior Province (Stern and Hanson, 1991; Stevenson et al, 1999). Many sanukitoid suites include a range of compositions from mafic rocks to granitoids, with the most SiO_2-rich samples typically interpreted as magma that evolved through fractional crystallization or contamination by felsic crustal material during emplacement (Martin et al., 2009). We restricted our dataset to the most primitive sanukitoids (i.e., least modified by aforementioned processes) by selecting only those with $SiO_2 < 62$ wt.% on an anhydrous basis (cf. Martin et al., 2009), resulting in 108 total samples (Table S5.1).

The models are designed to simulate melting of depleted mantle modified by two potential metasomatic agents: melt of TTG composition derived from a subducting slab or melt derived from partial melting of subducting sediment (Table 6.1). The depleted mantle composition used is from Workman and Hart (2005), which is an estimate of depleted MORB mantle (DMM). The composition of the TTG metasomatic agent was calculated using the Moyen (2011) TTG database, which is divided into high-, medium-, and low-pressure groups. Given that a subducting slab would be the expected source of metasomatic fluid in the mantle, only the high-pressure TTG group was used. If a 500°C/GPa thermal gradient is assumed for the slab (based on thermal gradients from Archean metamorphic rocks; Brown and Johnson, 2018), then melting at mantle depth would proceed at high temperature (≥ 1000°C); metabasite melting experiments and models at such conditions yield melt with SiO_2 < 70 wt.% (Rapp et al., 1991; Rapp & Watson, 1995; Palin et al., 2016). Therefore, an average of the Moyen (2011) high-pressure TTGs with SiO_2 < 70 wt.% was used as the TTG metasomatic component in this study (HP TTG, Table 6.1). This approach removes evolved granitoids from the average TTG composition, resulting in a better approximation of the primary TTG melt composition that would have been generated by a melting slab. Melt produced by subducted Archean sediments was approximated by phase equilibrium modelling of the average Archean upper crust composition of Taylor and McLennan (1985) (Fig. S5.1). Although there are limitations associated with this composition, this is a first-order approximation of the crustal material that generated the detritus that would have been incorporated into Archean subduction zones. Assuming relatively hot conditions for subduction (500°C/GPa), dehydration of the sediments prior to melting would be expected (e.g., Harry and Green, 1999); minimal H_2O (1000 µg/g) was used in the modelled Archean upper crust composition (i.e., the subducted sediments) to reflect this. The redox state of Archean sediments is difficult to constrain, but was assumed to be relatively reduced because atmospheric oxygen was low during the Archean Eon (e.g., Canfield et al., 2000). For the model, 5% of the FeO in the Archean upper crust estimate was converted to Fe_2O_3. Metasediment melt compositions were calculated at 1.5 GPa, 2.0 GPa, and 2.5 GPa (AUC1.5, AUC2.0, and AUC2.5 in Table 6.1) to represent different depths of melting along a 500°C/GPa thermal gradient (at 1.5 GPa, 750°C is below the solidus and the melt composition at 760°C was selected instead; Fig. S5.1).

The depleted mantle composition was mixed with the TTG and sediment partial melt metasomatic agents in different proportions to simulate metasomatized mantle (Table 6.1). Hereafter, the modelled TTG-metasomatized depleted mantle is referred to as DMT and the sediment-melt metasomatized depleted mantle is denoted as DMS. Three different DMS compositions (DMS1.5,

DMS2.0, DMS2.5, Table 6.1) were computed using the metasediment melt compositions calculated at different pressures. After iterative calculations, models indicated 40% metasomatic agent and 60% depleted mantle as an appropriate composition to produce partial melt with SiO_2 in the same range as the dataset of primitive sanukitoids. The concentrations of H_2O in DMT and DMS were fixed based on estimates of mantle H_2O in modern subduction zones, which generally range from 250–2500 µg/g (Peslier, 2010). Diagrams were constructed using 200 µg/g, 1000 µg/g, and 2000 µg/g H_2O for each composition; only the results of the 1000 µg/g scenario will be discussed in detail, as trends are similar for all scenarios (results from 200 µg/g and 2000 µg/g H_2O diagrams are provided in Fig. S5.2). Reported estimates of oxygen fugacity for the Archean upper mantle are variable but generally reducing relative to the fayalite-magnetite-quartz (FMQ) buffer (Ballhaus, 1993; Aulbach & Stagno, 2016). Given that the redox state of the metasomatic agents cannot be reliably estimated, DMT and DMS were assigned a low Fe_2O_3/FeO ratio (5% of FeO as Fe_2O_3) to represent generally reducing conditions. Although the redox state of DMT and DMS could affect partition coefficients for certain trace elements (e.g., Eu), this effect is not quantified here and will be discussed qualitatively.

6.2.2 Phase equilibrium modelling

Phase equilibrium modelling was done in the chemical system K_2O–Na_2O–CaO–FeO–MgO–Al_2O_3–SiO_2–H_2O–TiO_2–Fe_2O_3–Cr_2O_3 using THERMOCALC version 3.50 and the internally consistent thermodynamic dataset of Holland and Powell (2011; version 6.33 produced June 23, 2017). The set of activity–composition models used were those described by Holland et al. (2018), which includes models for melt, olivine, orthopyroxene, clinopyroxene, garnet, and spinel developed by Holland et al. (2018), feldspar models from Holland and Powell (2003), the amphibole model of Green et al. (2016), and a modified version of the biotite model from White et al. (2014). Quartz was modelled as a pure phase.

6.2.3 Melt trace element modelling

The trace element compositions of modelled melt were calculated at different *P*–*T* conditions by a mass-balance approach using a batch melting equation (e.g., Shaw, 1970),

$$\frac{C_L}{C_o} = \frac{1}{D(1-F)+F}$$

where C_L is the concentration of an element in the melt, C_o is the concentration of an element in the system, F is the melt fraction (in wt.%), and D is the bulk distribution coefficient between the melt

and residue. The value of D was computed using the residue assemblage calculated by THERMOCALC (converted to wt%) and parameterized Kd values from the equations of Bédard (2005; 2006; 2007; 2014) for olivine, plagioclase, orthopyroxene, and clinopyroxene; parameterizations for amphibole and biotite are also from Bédard (unpublished data). Sources for Kds where parameterization was not possible are Barth et al. (2002) for garnet, Bea et al. (1994) for K-feldspar, and Foley et al. (2000) for rutile. All Kds for quartz and elements not included in aforementioned sources were set to 0.000001.

6.3 Results

6.3.1 Characteristics of the sanukitoid dataset

Compositional trends in sanukitoid suites may be the result of fractional crystallization, magma contamination or mixing, source characteristics, or a combination of these factors. Although field observations and chemical analyses of minerals are required to understand all sources of compositional variability of a particular sanukitoid suite, we characterize broad trends of our dataset of sanukitoid whole-rock compositions. As high-SiO_2 samples were filtered from this dataset, we expect that sanukitoids generated by large degrees of fractional crystallization have been removed. Major and trace elements are compared to the concentration of MgO in the sanukitoid samples as MgO is a proxy for igneous differentiation (e.g., Stern and Hanson, 1991), or alternatively characteristics of the source (composition and degree of melting; Martin et al., 2009) The concentrations of major elements exhibit similar trends across the selected sanukitoid suites (Fig. 6.1). Increasing MgO is generally correlated with decreasing SiO_2 (Fig. 6.1a), Al_2O_3 (Fig. 6.1b), and Na_2O (Fig. 6.1c) and increasing FeO(t) (Fig. 6.1d) and CaO (Fig. 6.1e). Both K_2O (Fig. 6.1f) and TiO_2 (Fig. 6.1g) do not show a clear relationship with MgO overall. However, the Kaapvaal and Superior data show a negative correlation between MgO and K_2O (Fig. 6.1f).

The trace elements we examine here include those that are characteristically enriched in sanukitoids, such as Sr and Ba—here proxies for the LILE—and Cr (Martin et al., 2009). We also evaluate trends in Zr (a proxy for the HFSE) and the behaviour of REE, as these elements could provide important indications of sanukitoid source characteristics (e.g., Lobach-Zhuchenko et al., 2008; Laurent et al., 2011; Semprich et al. 2015; Jiang et al., 2016). In our sanukitoid dataset, the combined concentrations of Sr and Ba (generally $\geq$ 1000 µg/g; Fig. 6.2a) and the concentration of Zr (Fig. 6.2b) show no clear correlation with MgO, however Cr (Fig. 6.2c) shows a positive correlation with MgO. The majority of samples have Eu/Eu* $\leq$ 1 (Fig. 6.2d), indicating a negative Eu anomaly in

their chondrite-normalized REE profiles (Fig. 6.2f; values for chondrite normalization from McDonough and Sun, 1995). Most sanukitoid samples have $La_N/Yb_N < 40$ (Fig. 6.2e) and samples with elevated La_N/Yb_N also have low concentrations of Yb relative to the rest of the dataset (Fig. 6.2e and f).

6.3.2 Predicted phase equilibria of model metasomatized mantle

Phase diagrams of DMT and DMS were constructed to evaluate the residue assemblage and composition and proportion of partial melt at different *P–T* conditions. For DMT, calculations were done between 1.5–2.5 GPa and 700–1600°C (Fig. 6.3a). The modelled solidus is between 750°C and 870°C, and solidus temperature decreases as pressure increases. Biotite and hornblende are stable only near the solidus (<900°C and <1000°C respectively) for the full pressure range and the stability of plagioclase ($An_{22–35}$) is restricted to <1.9 GPa and <1170°C. Quartz and garnet have strongly temperature-dependent stability fields, which extend to 1160°C and 1370°C, respectively; with decreasing pressure they are restricted to lower temperature, particularly within the plagioclase stability field. Clinopyroxene is predicted to be exhausted with increasing temperature—1300°C at 1.5 GPa and 1480°C at 2.5 GPa. For the entire investigated range of pressure and temperature, orthopyroxene is predicted to be stable, with the exception of a small field at high pressure.

For DMS, three separate phase diagrams (Fig. 6.3b) were constructed from 700°C to 1600°C and 1.4–1.6 GPa, 1.9–2.1 GPa, and 2.4–2.6 GPa to reflect the different bulk compositions calculated at 1.5 GPa, 2.0 GPa, and 2.5 GPa, respectively (Table 6.1). The solidus is predicted to be between 890°C and 1000°C and Mg-rich biotite and K-feldspar are stable only near the solidus (<1010°C); these minerals are not present in the highest-pressure diagram, where quartz is stable close to the solidus instead. Olivine is stable across most of the 1.4–1.6 GPa diagram at temperature >1000°C and mainly at relatively low pressure. In contrast, olivine is predicted within a small field between 1060°C and 1170°C at 1.9–2.1 GPa and is absent at 2.4–2.6 GPa. Garnet is exhausted at ~1050°C at 1.4–1.6 GPa, ~1210°C at 1.9–2.1 GPa, and ~1360°C at 2.4–2.6 GPa. In the two lower-pressure diagrams, orthopyroxene is stable across almost the entire modelled range of *P–T* conditions, except above 1580°C at 1.4–1.6 GPa. At 2.4–2.6 GPa, orthopyroxene is absent between ~1030°C and ~1310°C. Clinopyroxene is predicted to be stable across the entirety of the three DMS diagrams.

6.3.3 Composition of modelled melt from model metasomatized mantle

Major and trace element compositions were calculated for partial melt of DMT (Table 6.2) and DMS (Table 6.3) at melt fractions of 5 mol%, 10 mol%, 20 mol%, and 30 mol% at 1.5 GPa, 2.0 GPa, and 2.5 GPa using the predicted residue assemblages (Fig. 6.4) for mineral–melt trace element partitioning. Clinopyroxene dominates the residue in most scenarios and orthopyroxene is typically also present, with greater proportions at lower pressure. Garnet is a component of the residue for both DMT and DMS, but the proportion decreases with increasing melt fraction until garnet is absent (or nearly so) at 30 mol% melt. Subordinate residue minerals—amphibole, plagioclase, and quartz for DMT and K-feldspar and biotite for DMS—decrease in abundance with increasing melt fraction and pressure.

Model melt of DMT show similar major element trends across the modelled pressure range (Figs 6.5a–c). The concentration of SiO_2 ranges from ~58 wt.% to ~69 wt.% (see Table 6.2) and generally increases with decreasing melt fraction; results at 1.5 GPa show a smaller range of SiO_2 (Fig. 6.5a), likely reflecting the presence of plagioclase in the residue (Fig. 6.4a). The range of Al_2O_3 is ~15 wt.% to ~21 wt.% and is slightly elevated in results at 1.5 GPa (Fig. 6.5a), which may be caused by the lack of garnet in the residue compared to results at higher pressures (Fig. 6.4a–c). Ranges of FeO(t) (~0.6–4.5 wt.%), MgO (~2.0–6.7 wt.%), and CaO (~1.1–5.8 wt.%) are similar at different pressures, and each decreases in concentration with decreasing melt fraction. The concentration of Na_2O has a range from ~3.7 wt.% to ~7.4 wt.% and decreases slightly with increasing pressure and decreasing melt fraction. For K_2O, there is a strong decrease from ~7.0 wt.% at 5 mol.% melt to ~2.0 wt.% at 30 mol.% melt. The concentration of TiO_2 is low for all results, with a range of ~0.2–0.6 wt.%.

Results for DMS (Figs 6.5d–f) show some similarities to DMT, but differences in melt compositions across the modelled pressures are more pronounced owing to the different metasomatic agent compositions used. The concentration of SiO_2 mainly ranges from ~53 wt.% to ~55 wt.%, except at 2.5 GPa (Fig. 6.5f) with ~57 wt.% and ~63 wt.% at melt fractions of 10 mol.% and 5 mol.%, respectively (see Table 6.3). For Al_2O_3, concentrations range from ~18 wt.% to ~23 wt.% and decrease with increasing pressure and melt fraction. The concentrations of FeO(t), MgO, and CaO are relatively restricted at 1.5 GPa (~0.7–3.3 wt.%; Fig. 6.5d) and become broader with increasing pressure (~0.7–4.6 wt.% at 2.0 GPa, Fig. 6.5e; ~0.8–8.0 wt.% at 2.5 GPa, Fig. 6.5f), and these values increase with higher melt fractions. The range for Na_2O is ~2.2 wt.% to ~5.1 wt.%, and

concentrations increase with higher melt fraction. Concentrations of K_2O are strongly pressure-dependent, with generally higher values at 1.5 and 2.0 GPa (~10–15 wt.%; Figs 6.5d and e) compared to results at 2.5 GPa (~3.8–12 wt.%, Fig. 6.5f). The concentrations of TiO_2 in model melt are low overall (≤ 0.9 wt.%).

The concentrations of trace elements in the model melt show variation with both pressure and melt fraction. For DMT (Fig. 6.6), Sr and Ba show similar results at 2.0 GPa (~600–2750 µg/g, Fig. 6.6b; see Table 6.2) and 2.5 GPa (~600–3400 µg/g, Fig. 6.6c), with increasing concentrations with decreasing melt fractions. However, at 1.5 GPa, Ba shows a restricted range (~600–750 µg/g, Fig. 6.6a) and Sr is relatively low (~125–700 µg/g, Fig. 6.6a) with the lowest values associated with low melt fractions. Concentrations of Zr are similar across the pressure range, with a minimum of ~160–200 µg/g and maximum of ~475–620 µg/g and values increasing with decreasing melt fraction. The concentration of Cr is lowest overall at 1.5 GPa (~40–170 µg/g; Fig. 6.6a) compared to higher values at 2.0 GPa (~20–240 µg/g; Fig. 6.6b) and 2.5 GPa (~35–340 µg/g; Fig. 6.6c), and increasing Cr is correlated with higher melt fractions. The REE for results from DMT (Fig. 6.6d–f) show a negative slope when normalized to chrondrite values and LREE generally increase with decreasing melt fraction. Model melt at 2.0 GPa and 2.5 GPa have relatively low HREE for melt fractions of 5 mol.%, 10 mol.%, and 20 mol.% (Fig. 6.6e and f), whereas results at 30 mol. % melt are similar across the range of modelled pressures.

For DMS, Ba and Sr show similar results at 1.5 GPa (~280–570 µg/g for Ba, ~60–120 µg/g for Sr; Fig. 6.7a) and 2.0 GPa (~460–820 µg/g for Ba, ~160–320 µg/g for Sr; Fig. 6.7b), with decreasing melt fraction correlated with decreasing Ba and increasing Sr (see Table 6.3). The concentrations of Ba and Sr are higher at 2.5 GPa (~550–2340 µg/g Ba and ~380–1260 µg/g Sr; Fig. 6.7c), and both increase with decreasing melt fraction. Trends in Zr are similar across the range of pressures, with concentrations increasing with decreasing melt fraction and a range broadly from ~190 µg/g to ~600 µg/g. The range of concentrations of Cr is more restricted at 1.5 GPa (~40–140 µg/g; Fig. 6.7a) and 2.0 GPa (~60–290 µg/g; Fig. 6.7b) compared to results at 2.5 GPa (~30–540 µg/g; Fig. 6.7b), and Cr increases with higher melt fractions. Chondrite-normalized REE trends have a negative slope (Figs 6.7d–f) and decreasing melt fraction is associated with increasing LREE and decreasing HREE.

6.4 Discussion

6.4.1 Modelling limitations

6.4.1.1 Limitations of the metasomatized mantle compositions

The metasomatic agents used to calculate the DMT and DMS sanukitoid sources in this study are each associated with different limitations. By calculating our TTG melt metasomatic agent based on a compilation of natural data, we implicitly assume that TTG compositions represent primary melt that underwent no significant modification after separating from the source. However, recent work has shown that fractional crystallization of amphibole and plagioclase may strongly influence the composition of TTGs (Laurent et al., 2020; Rollinson, 2021; Kendrick et al., 2022 [Chapter 3]). The trace element characteristics of "high-pressure" TTGs—used in this study to calculate DMT—have been attributed to hornblende fractionation and/or plagioclase accumulation after emplacement of TTG magma in the crust (Smithies et al., 2019; Laurent et al., 2020; Rollinson, 2021; Kendrick et al., 2022 [Chapter 3]). Many high-pressure TTGs in the compilation used in this study (Moyen, 2011) have Eu/Eu* > 1 resulting in our TTG metasomatic agent also exhibiting a positive Eu anomaly, which is consistent with plagioclase accumulation and potentially also hornblende fractionation. Therefore, the TTG metasomatic agent used here may have some characteristics that would not exist in a primary TTG melt derived from a subducting slab at mantle depth, but is otherwise a reasonable approximation of TTG melt generated at high pressure.

The sediment melt metasomatic agents were determined using the Taylor and McLennan (1985) estimate of Archean upper crust composition, which is based on compositions of Archean sedimentary rocks. The REE trends of Archean sedimentary rocks are variable, reflecting derivation from different lithologies that dominate Archean upper crust—basalt (relatively flat chondrite-normalized REE) and TTG (relatively steep chondrite-normalized REE) (Taylor and McLennan, 1995). This suggests that subducting sediments may have had variable compositions leading to variable compositions of metasomatized mantle; our DMS represents a first-order approximation. Our approach of modelling Archean sediment melting and selecting melt compositions at 1.5 Ga, 2.0 Ga, and 2.5 Ga along a 500 °C/GPa gradient also introduces uncertainty. At 1.5 Ga, the result is very near the solidus and the melt fraction is 3 mol% (Fig. S5.1), resulting in very high concentrations of many trace elements in the model melt (Table 6.1). This scenario may not be realistic, as the concentration of H_2O expected in sediments melting in a subduction zone—and therefore the position of the solidus

in *P*–*T* space in the model—is uncertain. Given that we calculated the DMS composition using 40% metasomatic agent and 60% depleted mantle, a metasomatic agent produced by 3 mol% melting of subducting sediments would produce a very small volume of metasomatized mantle, which may not be a realistic source for sanukitoid magma. Overall, our modelling results provide a general approximation of a mantle source metasomatized by melt from subducted Archean sediments.

The most uncertain variables for both types of metasomatized mantle compositions modelled here are the concentration of H_2O and the ratio of Fe_2O_3/FeO. The most significant effect of H_2O in the models is the modelled position of the solidus in *P*–*T* space and also the near-solidus mineral assemblages. Increased H_2O would result in a lower solidus temperature and therefore increased *P*–*T* stability fields of hydrous minerals—amphibole and biotite—in coexistence with partial melt. Some studies investigating the petrogenesis of sanukitoid suites have inferred the presence of biotite and amphibole in the metasomatized mantle source based on trace element trends (e.g., LILE, Ni, Cr) and geochemical modelling (e.g., Lobach-Zhuchenko et al., 2008; Heilimo et al., 2010; Laurent et al., 2011). In our model for DMT, no biotite is stable at 5 mol.% melt and above, and amphibole is only stable with 5 mol.% melt at 1.5 GPa. For DMS, biotite stability extends up to 20 mol.% melt at 1.5 GPa and 10 mol.% at 2.0 GPa and no stable amphibole is predicted at suprasolidus conditions, although amphibole is present in the DMS model with elevated H_2O (Fig. S5.2). As the selected concentrations of H_2O for modelling are poorly constrained, the *P*–*T* conditions of the solidus and hydrous mineral stability in the models should be treated with caution.

The amount of Fe_2O_3 in DMT and DMS was estimated to be low to generate relatively reducing conditions in our models. Some investigations of mantle xenoliths have identified a connection between metasomatism and mantle oxidation (e.g., Yaxley et al., 2012; Hanger et al., 2015), although it is unclear if these xenoliths extracted from Phanerozoic mantle are analogues for the Archean mantle. Most of the phases in our models have both Fe^{2+} and Fe^{3+} incorporated into their activity–composition models (melt, garnet, orthopyroxene, clinopyroxene, biotite, amphibole), and therefore the Fe_2O_3/FeO ratio of the bulk composition could affect the *P*–*T* stability fields of these phases. The effect of Fe_2O_3/FeO on oxygen fugacity also has implications for trace element partitioning. Overall, we expect that the compositions of our modelled melt are not strongly influenced by source redox conditions, except in the case of trace elements with redox-sensitive behaviour (discussed further below).

6.4.1.2 The potential influence of accessory mineral behaviour in the source

Although our models of metasomatized mantle melting do not include accessory minerals, zircon, apatite, and other accessory minerals have been described in metasomatized mantle rocks (e.g., Haggerty, 1995; Konzett et al., 2000; O'Reilly and Griffin, 2000; Grieco et al., 2001). Zircon in metasomatized mantle would sequester Zr and HREE, resulting in partial melt with lower concentrations of these elements compared to our model melt. Based on analyses of mantle apatite (O'Reilly and Griffin, 2000), Sr and REE (preferentially LREE) may be sequestered in the mantle source if apatite is present. However, many mineral assemblages described in metasomatized mantle rocks have been linked to Phanerozoic metasomatic events (e.g., Konzett et al., 2000; O'Reilly and Griffin, 2000; Grieco et al., 2001) and may not be representative of Archean metasomatized mantle.

6.4.1.3 Limitations of partition coefficients

In this study, partition coefficients are calculated for each model melt with variables including temperature, pressure, melt composition, and mineral compositions based on the parameterizations by Bédard (2005; 2006; 2007; 2014; unpublished data). These parameterizations were developed by regression analysis of mainly experimental and some natural data; in some cases, these data were sparse and/or scattered (e.g., Ba for clinopyroxene and orthopyroxene). Uncertainties in the calculated partition coefficients are also derived from these original data, as different laboratories conducting partitioning experiments may have different sources of systematic error and disequilibrium is common in natural systems (Bédard, 2014). Although some partition coefficient parameterizations for elements relevant to this study incorporated fO_2 (only Eu for plagioclase and clinopyroxene), we did not include fO_2 in the partition coefficient calculations because we do not have a robust constraint on this value for metasomatized Archean mantle. Oxygen fugacity can affect trace element partitioning both by influencing the valence state of elements that may have different charges across the range of terrestrially relevant fO_2 conditions (many transition metals, Eu; e.g, Mallmann and O'Neill, 2009; Dygert et al., 2020) or by affecting the size of crystallographic sites of some minerals (e.g., Dalpé and Baker, 2000). In general, our approach of partition coefficient parameterization likely yields the most realistic values for our models, as experimental data relevant to our modelled scenarios are not available.

Partition coefficients used for garnet are likely subject to greater uncertainty than the parameterized values used for other minerals, as the garnet values were selected from a single experimental study (Barth et al., 2002). These partitioning experiments were run at relatively high *P*–

T conditions (1.8 GPa and 1000–1040°C), but simulated melting of crustal eclogite rather than mantle rocks. Therefore, these partition coefficients for garnet may not be accurate for our modelled system, but the overall trends (e.g., REE trends) are likely realistic. The chosen partition coefficients for K-feldspar are from a natural study of migmatite samples (Bea et al., 1994), which is a poor match for our modelled system in terms of melt composition and *P*–*T* conditions. However, many K-feldspar partitioning studies report data for few elements or less appropriate igneous systems. In the melting models, K-feldspar is only predicted to be stable in residue for DMS in relatively low proportions (~5 mol.% or less), which suggests that the effect of these partition coefficients on model melt composition is minor overall.

6.4.2 Implications of models for interpreting sanukitoid compositions

The variability of both major and trace elements in the natural primitive sanukitoid dataset is indicative of the variety of sanukitoid source characteristics (Figs 6.1 and 6.2). Some elements that generally exhibit incompatible behaviour—such as K_2O, Ba, Sr, and Zr—are not clearly correlated with MgO in the sanukitoids, suggesting that igneous differentiation or variable degrees of source melting are not the primary control for these elements. As the sanukitoid samples are all relatively primitive (< 62 wt.%), enrichment in incompatible elements likely indicates an enriched source. The Kaapvaal samples in particular show trends that differ from other sanukitoids (elevated TiO_2 and Zr), which have been attributed to enrichment of a mantle source by a siliceous melt derived from subducted sediments (Laurent et al., 2011). For other sanukitoid suites in our dataset, such as those from the Baltic Shield (Lobach-Zhuchenko, 2008; Heilimo et al., 2010) and the North China Craton (Jiang et al., 2016), a fluid rich in H_2O and possibly also CO_2 is the preferred metasomatic agent based on low concentrations of HFSE and high concentrations of LILE. The distinct geologic histories of each craton probably contributed different geochemical characteristics to each suite, and therefore a single petrogenetic model for sanukitoids is not realistic.

Although we do not expect our models to represent the variety of sanukitoid compositions in the natural dataset, the trends of calculated model melt compositions are informative. Increasing melt fraction is generally associated with increasing MgO in the models (Fig. 6.8). Major element trends with respect to MgO in natural sanukitoids are broadly replicated in the models, though the concentrations of FeO(t) (Fig. 6.8d) are very low in model results, CaO (Fig. 6.8e), and TiO_2 (Fig. 6.8g) are somewhat underestimated in model melt, and K_2O (Fig. 6.8f) is very high in some model results. This suggests that changing source characteristics—in this case, degree of melting and

therefore source temperature—can generate major element trends observed in natural samples. Model melt from DMS show some characteristics that differ from many sanukitoids, such as relatively low SiO_2 and FeO (Fig. 6.8a, d) and Na_2O (Fig. 6.8c) and high Al_2O_3 (Fig. 6.8b) and K_2O (Fig. 6.8f). No model results have elevated TiO_2 (Fig. 6.8g) similar to the Kaapvaal samples, suggesting that some processes or characteristics of the source of these rocks are not replicated in the models.

Trace element trends of model melt show some similarities to the natural sanukitoids (Fig. 6.9). The concentrations of Sr and Ba combined show a range in the models that is similar to the sanukitoid dataset. Model results at low melt fractions (5 and 10 mol.%) show relatively low concentrations (Sr + Ba ≤ 1000 μg/g) or high values (Sr + Ba > 6000 μg/g); the low values reflect the presence of amphibole (DMT) or biotite and K-feldspar (DMS) in the residue, which were predicted to be most abundant at relatively low pressure (Fig. 6.4). The concentration of Zr in the model is predicted to decrease with increasing MgO. Results at a melt fraction of 5 mol.% show concentrations of Zr that are similar to the Kaapvaal sanuktoid suite, whereas 30 mol.% melt has lower Zr content that is consistent with the other suites. The concentration of Cr in the model melt increases with increasing MgO and the trend is very similar to the natural sanukitoid dataset. These results indicate that a large range of concentrations of LILE (here Sr and Ba) and HFSE (represented by Zr) could be expected based on different degrees of source melting or melting at different pressure, despite the concentrations of these elements having been previously attributed to a fluid or silicate melt metasomatic agent (Lobach-Zhuchenko, 2008; Jiang et al., 2016). This suggests that enrichment or depletion of these elements may not always be a reliable indicator of the nature of the mantle metasomatic agent involved in sanukitoid genesis.

The REE trends of our model melt exhibit important differences from the natural sanukitoid dataset. For all model results, Eu/Eu* is predicted to be greater than 1 (Fig. 6.9d), corresponding to a positive Eu anomaly in a chondrite-normalized REE plot. This contrasts with the sanukitoid dataset: nearly all samples have Eu/Eu* ≤ 1. The majority of model melt compositions have values of Yb_N that are lower than the natural sanukitoid dataset (all > 3) and the La_N/Yb_N of model results are higher than most natural samples (almost all < 50; Fig. 6.9e). The trends in Yb_N versus La_N/Yb_N in the model melt are correlated with the proportion of garnet in the residue; this mineral sequesters HREE, resulting in melt with low Yb_N and high La_N/Yb_N. Model melt of DMS reach higher La_N/Yb_N compared to DMT (Fig. 6.9e), reflecting the large proportion of garnet in the residue of the modelled metasediment melt metasomatic agents. In general, high melt fractions (20 and 30 mol.%) yield Yb_N

and La_N/Yb_N that are most similar to the sanukitoid dataset. Chondrite-normalized REE are overall lower in the model results compared to the natural sanukitoids, except for LREE in some cases (Fig. 6.9f, g). Model melt with no or very little garnet in the residue (results at 30 mol.% melt or low pressure; Fig. 6.4) show REE trends most similar to the sanukitoid dataset. This result contrasts with previous interpretations of the petrogenesis of the Kaapvaal suite (Laurent et al., 2011) and one of the North China Craton suites (Wang et al., 2009) in our sanukitoid dataset, for which garnet was proposed to be a residue mineral. Martin et al. (2009) noted that the geochemical diversity of sanukitoid suites in general could indicate variable amounts of residual garnet, but also suggested that the REE fractionation observed in sanukitoids could have been inherited from the metasomatic agent. Our model results support the latter interpretation; both DMT and DMS exhibit fractionated REE (Table 6.1) inherited from the TTG and metasediment melt metasomatic agents, respectively, contributing to moderate depletion of HREE in model melt without residual garnet (Fig. 6.9e–g).

In summary, our model results generally support primitive sanukitoid magma production by relatively large melt fractions (20 mol.% or 30 mol.%) and with source residue assemblages composed of mainly clinopyroxene and orthopyroxene with little to no garnet. Several natural sanukitoid samples exhibit elevated La_N/Yb_N (>40) that may indicate the presence of garnet in the source locally (Fig. 6.2e). Our results show that depleted mantle metasomatized by silicic melt can replicate several broad trends in primitive sanukitoids including many major elements (Fig. 6.8) and Sr, Ba, and Cr (Fig. 6.9a and c). Some model melt of DMS show trends that are inconsistent with sanuktioids, however given the limitations of the models, we do not suggest that metasediment melt is an unsuitable metasomatic agent for sanukitoid sources. The large compositional variation of the model melt from both sources implies that distinguishing a silicic melt metasomatic agent from a fluid metasomatic agent for a sanukitoid suite based on concentrations of major and trace elements may not be possible.

6.4.3 Implications of the Eu anomaly in sanukitoids

Our analysis of the natural sanukitoid dataset identified a negative Eu anomaly ($Eu/Eu^* < 1$) in many samples. Previous investigations of sanukitoid petrogenesis have reported negligible Eu anomalies in these rocks overall (Martin et al., 2009) or negative Eu anomalies associated with magma differentiation due to feldspar fractionation (Stevenson et al., 1999). We have limited our sanukitoid dataset to relatively primitive samples (i.e., low degrees of differentiation) and the Eu/Eu* of these samples do not show a correlation with the concentration of MgO (a proxy for igneous differentiation;

Fig. 6.9d). The compositional trends of these rocks therefore do not support development of the Eu anomaly by differentiation.

Our model melt results exhibit Eu/Eu* > 1, which appears to be linked to the selected partition coefficients for garnet from Barth et al (2002), as the partition coefficient for Eu is low compared to those of Sm and Gd. The experimental assembly used by Barth et al (2002) generated highly reducing conditions near the iron-wüstite (IW) buffer, likely resulting in elevated Eu^{2+}/Eu^{3+}. As garnet is expected to preferentially incorporate Eu^{3+} over Eu^{2+} (e.g., Holder et al., 2020), reducing conditions would result in low concentrations of Eu in garnet relative to other REE (i.e., negative Eu anomaly) and elevated Eu in coexisting melt (i.e., positive Eu anomaly). As many of our modelled residue assemblages contain garnet, positive Eu anomalies in our model results were therefore caused by garnet partition coefficients relevant for strongly reducing conditions. This suggests that the model results may have implications for redox conditions of the metasomatized sources that generated sanukitoids, although we consider garnet to be a subordinate residue mineral compared to clinopyroxene and orthopyroxene. Experimental data (Fabbrizio et al., 2021) suggest that reducing conditions—and therefore high Eu^{2+}/Eu^{3+}—are correlated with lower Eu partition coefficients for clinopyroxene and potentially also for orthopyroxene relative to other REE, similar to garnet. However, partitioning of Eu^{2+} and Eu^{3+} into pyroxene may also be influenced by melt and pyroxene composition (Shearer et al., 2006), suggesting that the pyroxene Eu/Eu* may not be directly correlated to fO_2. To generate the negative Eu anomalies observed in the sanukitoids, clinopyroxene and/or orthopyroxene must incorporate Eu^{2+} preferentially over the dominantly trivalent REE, and the conditions under which this scenario would be expected are unclear. In general, the negative Eu anomalies in the natural sanukitoid samples may indicate that they were not generated under strongly reducing conditions, as positive Eu anomalies would be more likely under such conditions.

The evolution of the mantle redox state throughout the Archean is a subject of debate, with some data supporting little change in mantle oxygen fugacity from the early Archean to present (e.g., Nicklas et al., 2018). However, evidence for secular oxidation of the mantle has also been identified (e.g., Nicklas et al., 2019), and the implications of crustal recycling for the redox state of Archean mantle remain unclear (e.g., Aulbach et al., 2019; Nicklas et al., 2019). Quantitative estimates of the redox conditions of sanukitoid sources—based on the behaviour of Eu and other redox-sensitive elements—could provide important insights into the role of mantle metasomatism in the chemical evolution of the Archean mantle.

6.4.4 Implications for the geodynamic setting of sanukitoid genesis

Our modelling results provide new insights into the *P–T* conditions of sanukitoid genesis, which in turn have implications for the tectonic processes that triggered melting of the metasomatized mantle. Due to the limitations of the models (particularly with respect to the concentration of H_2O in the metasomatized mantle), the predicted *P–T* conditions of melting should be considered qualitatively. The model results that most closely resemble natural sanukitoids are predicted at relatively high melt fractions of 20 and 30 mol.%, which require relatively high temperatures (1100–1300°C in the model, depending on pressure; Fig. 6.3). Above the maximum pressure in our models (2.5 GPa) even higher melt fractions and temperatures would be required for melting in the garnet-free pyroxenite stability field (Fig. 6.3). However, increasing melt fraction would be associated with a decrease in the concentrations of many trace elements that are characteristically elevated in sanukitoids, particularly LILE. We suggest that sanukitoid genesis at pressure greater than 2.5 GPa may have been unlikely, but probably cannot be ruled out completely.

Geodynamic models of sanukitoid genesis commonly invoke break off of a subducting slab as the cause of asthenospheric upwelling that ultimately triggered partial melting of the metasomatized mantle (e.g., Lobach-Zhuchenko et al., 2008; Heilimo et al., 2010; de Oliveira et al., 2011; Laurent et al., 2014a; Singh et al., 2019), although mantle plume activity could have also driven partial melting (e.g., de Oliveira et al., 2011). Alternatively, subcretion and subsequent delamination of Archean oceanic crust at the edge of a continent could have driven mantle metasomatism, asthenospheric upwelling, and melting of the mantle without the operation of modern-style subduction (Bédard, 2018). The *P–T* conditions of sanukitoid genesis indicated in our models are broadly consistent with all of these scenarios, and therefore the presence of sanukitoids alone is likely not diagnostic of a particular tectonic process. In addition, the large range of compositions replicated in our models indicate that connecting sanukitoid genesis uniquely to a particular metasomatic agent is challenging. Both TTG melt and melt from subducted sediments may be suitable metasomatic agents, in contrast to the interpretation of Bédard (2018) that interaction of sediments with the mantle source was required for sanukitoid genesis.

The appearance of sanukitoids generally during the latest stages of Archean craton evolution could be attributed to two possible scenarios: upper mantle metasomatism (potentially by a particular metasomatic agent) began in the late Archean (e.g., Bédard, 2018; Moreira et al., 2020) or mantle metasomatism was ongoing during the Archean and the processes that triggered mantle partial

melting were characteristic of the final stages of craton evolution (e.g., de Oliveira et al., 2011; Laurent et al., 2014a; Singh et al., 2019). Each scenario has different implications for the evolution of Archean mantle and tectonic regime in general, as mantle metasomatism by crustal material has been linked to subduction or subcretion (i.e., horizontal tectonic processes; e.g., Laurent et al., 2014a; Bédard, 2018; Singh et al., 2019 Moreira et al., 2020). The variety of sanukitoid compositions generated by our models suggests that major and trace element trends in these rocks cannot be uniquely connected to a particular tectonic scenario. In addition, our models do not include the possibility of post-emplacement chemical modification (by igneous differentiation or crustal contamination), which further complicates the connection between geochemical trends in sanukitoid suites and source processes. Therefore, the major and trace element compositions of sanukitoids alone likely provide limited insights into the geodynamic setting of their source and Archean tectonic regimes overall. However, the variability of sanukitoid compositions from different cratons suggests that detailed investigations of sanukitoid suites within their regional geological context could provide important insights into local tectonic evolution, particularly if sanukitoid major and trace elements can be coupled with isotope compositions and geochronology (e.g., Laurent et al., 2011; de Oliveira et al., 2011; Heilimo et al., 2013; Jiang et al., 2016).

6.5 Summary and Conclusions

The main conclusions of this work can be summarized as follows:

- Model results show that some geochemical trends of sanukitoids can be replicated by different degrees of mantle melting at different pressure.
- Many sanukitoids have chemical compositions compatible with relatively high degrees of melting (20–30 mol.%) of a garnet-free pyroxenite source.
- The common negative Eu anomaly in sanukitoids is not replicated in the models and the origin of this characteristic is unclear, but may have implications for the redox state of the Archean mantle.
- The nature of the metasomatic agent that modified the mantle source of a sanukitoid suite is difficult to determine based on the chemical composition of sanukitoids alone.
- Considerable geochemical variability in natural sanukitoid trends suggests that sanukitoid petrogenesis is complex and different for each craton, and the significance of these rocks is best evaluated within their regional geological context.

6.6 References

Aulbach, S. & Stagno, V. (2016). Evidence for a reducing Archean ambient mantle and its effects on the carbon cycle. Geology 44, 751–754.

Aulbach, S., Woodland, A. B., Stern, R. A., Vasilyev, P., Heaman, L. M. & Viljoen, K. S. (2019). Evidence for a dominantly reducing Archaean ambient mantle from two redox proxies, and low oxygen fugacity of deeply subducted oceanic crust. Scientific Reports 9, 20190.

Ballhaus, C. (1993). Redox states of lithospheric and asthenospheric upper mantle. Contributions to Mineralogy and Petrology 114, 331–348.

Barth, M. G., Foley, S. F. & Horn, I. (2002). Partial melting in Archean subduction zones: Constraints from experimentally determined trace element partition coefficients between eclogitic minerals and tonalitic melts under upper mantle conditions. Precambrian Research 113, 323–340.

Bea, F., Pereira, M. D. & Stroh, A. (1994). Mineral/leucosome trace-element partitioning in a peraluminous migmatite (a laser ablation-ICP-MS study). Chemical Geology 117, 291–312.

Bédard, J. H. (2005). Partitioning coefficients between olivine and silicate melts. Lithos 83, 394–419.

Bédard, J. H. (2006). Trace element partitioning in plagioclase feldspar. Geochimica et Cosmochimica Acta 70, 3717–3742.

Bédard, J. H. (2007). Trace element partitioning coefficients between silicate melts and orthopyroxene: Parameterizations of D variations. Chemical Geology 244, 263–303.

Bédard, J. H. (2014). Parameterizations of calcic clinopyroxene—Melt trace element partition coefficients. Geochemistry, Geophysics, Geosystems 15, 303–336.

Bédard, J. H. (2018). Stagnant lids and mantle overturns: Implications for Archaean tectonics, magmagenesis, crustal growth, mantle evolution, and the start of plate tectonics. Geoscience Frontiers 9, 19–49.

Brown, M. & Johnson, T. (2018). Secular change in metamorphism and the onset of global plate tectonics. American Mineralogist 103, 181–196.

Canfield, D. E., Habicht, K. S. & Thamdrup, B. (2000). The Archean sulfur cycle and the early history of atmospheric oxygen. Science 288, 658–661.

Dalpé, C. & Baker, D. R. (2000). Experimental investigation of large-ion-lithophile-element- and rare-earth-element-partitioning between calcic amphibole and basaltic melt: the effects of pressure and oxygen fugacity. Contributions to Mineralogy and Petrology 140, 233–250.

de Oliveira, M. A., Dall'Agnol, R. & de Arimatéia Costa de Almeida, J. (2011). Petrology of the Mesoarchean Rio Maria suite and the discrimination of sanukitoid series. Lithos 127, 192–209.

de Oliveira, M. A., Dall'Agnol, R. & Scaillet, B. (2010). Petrological constraints on crystallization conditions of Mesoarchean sanukitoid rocks, southeastern Amazonian craton, Brazil. Journal of Petrology 51, 2121–2148.

Dygert, N., Draper, D. S., Rapp, J. F., Lapen, T. J., Fagan, A. L. & Neal, C. R. (2020). Experimental determinations of trace element partitioning between plagioclase, pigeonite, olivine, and lunar basaltic melts and an fO_2 dependent model for plagioclase-melt Eu partitioning. Geochimica et Cosmochimica Acta 279, 258–280.

Egorova, Y. S. (2014). Sanukitoids of Fenno-Karelian Province, the Baltic shield: geology, composition, magmatic sources. Ph.D. thesis. St. Petersburg Press, p. 209 (in Russian).

Fabbrizio, A., Schmidt, M. W. & Petrelli, M. (2021). Effect of fO_2 on Eu partitioning between clinopyroxene, orthopyroxene and basaltic melt: Development of a Eu^{3+}/Eu^{2+} oxybarometer. Chemical Geology 559, 119967.

Foley, S. F., Barth, M. G. & Jenner, G. A. (2000). Rutile/melt partition coefficients for trace elements and an assessment of the influence of rutile on the trace element characteristics of subduction zone magmas. Geochimica et Cosmochimica Acta 64, 933–938.

Green, E. C. R., White, R. W., Diener, J. F. A., Powell, R., Holland, T. J. B. & Palin, R. M. (2016). Activity-composition relations for the calculation of partial melting equilibria in metabasic rocks. Journal of Metamorphic Geology 34, 845–869.

Grieco, G., Ferrario, A., Von Quadt, A., Koeppel, V. & Mathez, E. A. (2001). The zircon-bearing chromitites of the phlogopite peridotite of Finero (Ivrea zone, Southern Alps): Evidence and geochronology of a metasomatized mantle slab. Journal of Petrology 42, 89–101.

Haggerty, S. E. (1995). Upper mantle mineralogy. Journal of Geodynamics 20, 331–364.

Hanger, B. J., Yaxley, G. M., Berry, A. J. & Kamenetsky, V. S. (2015). Relationships between oxygen fugacity and metasomatism in the Kaapvaal subcratonic mantle, represented by garnet peridotite xenoliths in the Wesselton kimberlite, South Africa. Lithos 212–215, 443–452.

Harry, D. L. & Green, N. L. (1999). Slab dehydration and basalt petrogenesis in subduction systems involving very young oceanic lithosphere. Chemical Geology 160, 309–333.

Heilimo, E., Halla, J., Andersen, T. & Huhma, H. (2013). Neoarchean crustal recycling and mantle metasomatism: Hf–Nd–Pb–O isotope evidence from sanukitoids of the Fennoscandian shield. Precambrian Research 228, 250–266.

Heilimo, E., Halla, J. & Hölttä, P. (2010). Discrimination and origin of the sanukitoid series: Geochemical constraints from the Neoarchean western Karelian Province (Finland). Lithos 115, 27–39.

Holder, R. M., Yakymchuk, C. & Viete, D. R. (2020). Accessory mineral Eu anomalies in suprasolidus rocks: beyond feldspar. Geochemistry, Geophysics, Geosystems 21, e2020GC009052.

Holland, T. J. B., Green, E. C. R. & Powell, R. (2018). Melting of peridotites through to granites: a simple thermodynamic model in the system KNCFMASHTOCr. Journal of Petrology 59, 881–900.

Holland, T. & Powell, R. (2003). Activity-compositions relations for phases in petrological calculations: An asymetric multicomponent formulation. Contributions to Mineralogy and Petrology 145, 492–501.

Holland, T. J. B. & Powell, R. (2011). An improved and extended internally consistent thermodynamic dataset for phases of petrological interest, involving a new equation of state for solids. Journal of Metamorphic Geology 29, 333–383.

Jiang, N., Guo, J., Fan, W., Hu, J., Zong, K. & Zhang, S. (2016). Archean TTGs and sanukitoids from the Jiaobei terrain, North China craton: insights into crustal growth and mantle metasomatism. Precambrian Research 281, 656–672.

Kendrick, J., Duguet, M. & Yakymchuk, C. (2022). Diversification of Archean tonalite-trondhjemite-granodiorite suites in a mushy middle crust. Geology 50, 76–80.

Konzett, J., Armstrong, R. A. & Günther, D. (2000). Modal metasomatism in the Kaapvaal craton lithosphere: Constraints on timing and genesis from U–Pb zircon dating of metasomatized peridotites and MARID-type xenoliths. Contributions to Mineralogy and Petrology 139, 704–719.

Laurent, O., Björnsen, J., Wotzlaw, J. F., Bretscher, S., Pimenta Silva, M., Moyen, J. F., Ulmer, P. & Bachmann, O. (2020). Earth's earliest granitoids are crystal-rich magma reservoirs tapped by silicic eruptions. Nature Geoscience 13, 163–169.

Laurent, O., Martin, H., Doucelance, R., Moyen, J. F. & Paquette, J. L. (2011). Geochemistry and petrogenesis of high-K "sanukitoids" from the Bulai pluton, Central Limpopo Belt, South Africa: Implications for geodynamic changes at the Archaean-Proterozoic boundary. Lithos 123, 73–91.

Laurent, O., Martin, H., Moyen, J. F. & Doucelance, R. (2014a). The diversity and evolution of late-Archean granitoids: Evidence for the onset of "modern-style" plate tectonics between 3.0 and 2.5 Ga. Lithos 205, 208–235.

Laurent, O., Rapopo, M., Stevens, G., Moyen, J. F., Martin, H., Doucelance, R. & Bosq, C. (2014b). Contrasting petrogenesis of Mg–K and Fe–K granitoids and implications for post-collisional magmatism: Case study from the Late-Archean Matok pluton (Pietersburg block, South Africa). Lithos 196–197, 131–149.

Lobach-Zhuchenko, S. B. et al. (2005). The Archaean sanukitoid series of the Baltic Shield: Geological setting, geochemical characteristics and implications for their origin. Lithos 79, 107–128.

Lobach-Zhuchenko, S. B., Rollinson, H., Chekulaev, V. P., Savatenkov, V. M., Kovalenko, A. V., Martin, H., Guseva, N. S. & Arestova, N. A. (2008). Petrology of a Late Archaean, highly potassic, sanukitoid pluton from the baltic shield: Insights into late archaean mantle metasomatism. Journal of Petrology 49, 393–420.

Mallmann, G. & O'Neill, H. S. C. (2009). The crystal/melt partitioning of V during mantle melting as a function of oxygen fugacity compared with some other elements (Al, P, Ca, Sc, Ti, Cr, Fe, Ga, Y, Zr and Nb). Journal of Petrology 50, 1765–1794.

Martin, H., Moyen, J.-F. & Rapp, R. (2009). The sanukitoid series: magmatism at the Archaean–Proterozoic transition. Earth and Environmental Science Transactions of the Royal Society of Edinburgh 100, 15–33.

McDonough, W. F. & Sun, S. s. (1995). The composition of the Earth. Chemical Geology 120, 223–253.

Moreira, H., Storey, C., Fowler, M., Seixas, L. & Dunlop, J. (2020). Petrogenetic processes at the tipping point of plate tectonics: Hf-O isotope ternary modelling of Earth's last TTG to sanukitoid transition. Earth and Planetary Science Letters 551, 116558.

Moyen, J.-F. (2011). The composite Archaean grey gneisses: Petrological significance, and evidence for a non-unique tectonic setting for Archaean crustal growth. Lithos 123, 21–36.

Nicklas, R. W., Puchtel, I. S. & Ash, R. D. (2018). Redox state of the Archean mantle: Evidence from V partitioning in 3.5–2.4 Ga komatiites. Geochimica et Cosmochimica Acta 222, 447–466.

Nicklas, R. W., Puchtel, I. S., Ash, R. D., Piccoli, P. M., Hanski, E., Nisbet, E. G., Waterton, P., Pearson, D. G. & Anbar, A. D. (2019). Secular mantle oxidation across the Archean-Proterozoic boundary: Evidence from V partitioning in komatiites and picrites. Geochimica et Cosmochimica Acta 250, 49–75.

O'Reilly, S. Y. & Griffin, W. L. (2000). Apatite in the mantle: Implications for metasomatic processes and high heat production in Phanerozoic mantle. Lithos 53, 217–232.

Palin, R. M., White, R. W. & Green, E. C. R. (2016). Partial melting of metabasic rocks and the generation of tonalitic–trondhjemitic–granodioritic (TTG) crust in the Archaean: Constraints from phase equilibrium modelling. Precambrian Research 287, 73–90.

Peslier, A. H. (2010). A review of water contents of nominally anhydrous natural minerals in the mantles of Earth, Mars and the Moon. Journal of Volcanology and Geothermal Research 197, 239–258.

Rapp, R. & Watson, E. B. (1995). Dehydration melting of metabasalt at 8—32 kbar: Implications for continental growth and crust-mantle recycling. Journal of Petrology 36, 891–931.

Rapp, R., Watson, E. B. & Miller, C. F. (1991). Partial melting of amphibolite/eclogite and the origin of Archean trondhjemites and tonalites. Precambrian Research 51, 1–25.

Rollinson, H. (2021). Do all Archaean TTG rock compositions represent former melts? Precambrian Research 367, 106448.

Semprich, J., Moreno, J. A. & Oliveira, E. P. (2015). Phase equilibria and trace element modeling of Archean sanukitoid melts. Precambrian Research 269, 122–138.

Shaw, D. M. (1970). Trace element fractionation during anatexis. Geochimica et Cosmochimica Acta 34, 237–243.

Shearer, C. K., Papike, J. J. & Karner, J. M. (2006). Pyroxene europium valence oxybarometer: Effects of pyroxene composition, melt composition, and crystallization kinetics. American Mineralogist 91, 1565–1573.

Shirey, S. B. & Hanson, G. N. (1984). Mantle-derived Archaean monozodiorites and trachyandesites. Nature 310, 222–224.

Singh, P. K., Verma, S. K., Singh, V. K., Moreno, J. A., Oliveira, E. P. & Mehta, P. (2019). Geochemistry and petrogenesis of sanukitoids and high-K anatectic granites from the Bundelkhand Craton, India: Implications for late-Archean crustal evolution. Journal of Asian Earth Sciences 174, 263–282.

Smithies, R. H. et al. (2019). No evidence for high-pressure melting of Earth's crust in the Archean. Nature Communications 10, 1–12.

Stern, R. A. & Hanson, G. N. (1991). Archean high-Mg granodiorite: A derivative of light rare earth element-enriched monzodiorite of mantle origin. Journal of Petrology 32, 201–238.

Stevenson, R., Henry, P. & Gariépy, C. (1999). Assimilation-fractional crystallization origin of Archean sanukitoid suites: Western Superior Province, Canada. Precambrian Research 96, 83–99.

Taylor, S. R. & McLennan, S. M. (1985). The continental crust: its composition and evolution. Oxford: Blackwell Scientific.

Taylor, S. R. & McLennan, S. M. (1995). The geochemical the continental evolution crust. Reviews in Mineralogy and Geochemistry 33, 241–265.

Wang, Y., Zhang, Y., Zhao, G., Fan, W., Xia, X., Zhang, F. & Zhang, A. (2009). Zircon U–Pb geochronological and geochemical constraints on the petrogenesis of the Taishan sanukitoids

(Shandong): Implications for Neoarchean subduction in the Eastern Block, North China Craton. Precambrian Research 174, 273–286.

White, R. W., Powell, R., Holland, T. J. B., Johnson, T. E. & Green, E. C. R. (2014). New mineral activity-composition relations for thermodynamic calculations in metapelitic systems. Journal of Metamorphic Geology 32, 261–286.

Workman, R. K. & Hart, S. R. (2005). Major and trace element composition of the depleted MORB mantle (DMM). Earth and Planetary Science Letters 231, 53–72.

Yaxley, G. M., Berry, A. J., Kamenetsky, V. S., Woodland, A. B. & Golovin, A. V. (2012). An oxygen fugacity profile through the Siberian Craton – Fe K-edge XANES determinations of $Fe^{3+}/\sum Fe$ in garnets in peridotite xenoliths from the Udachnaya East kimberlite. Lithos 140–141, 142–151.

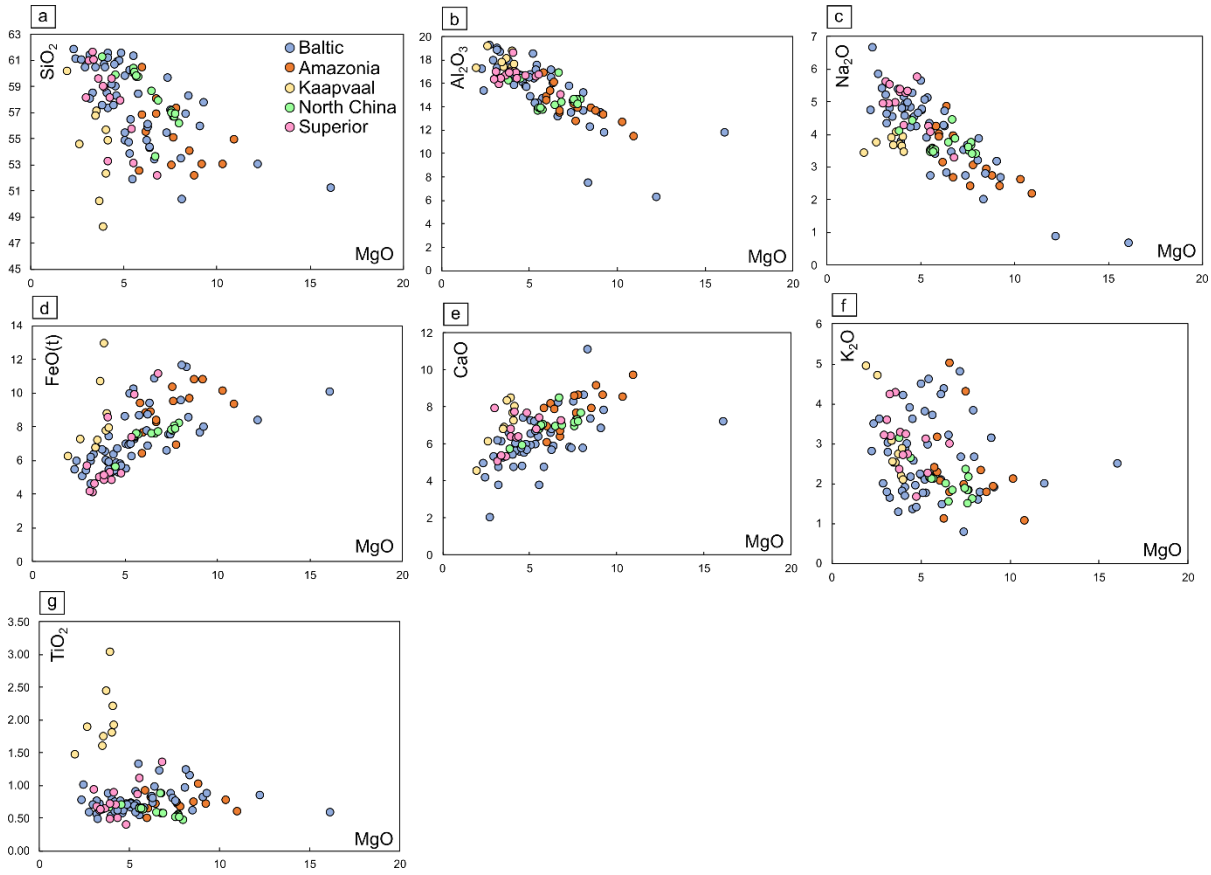


Figure 6.1. Major element trends (wt. %) of sanukitoid compilation data (Table S5.1).

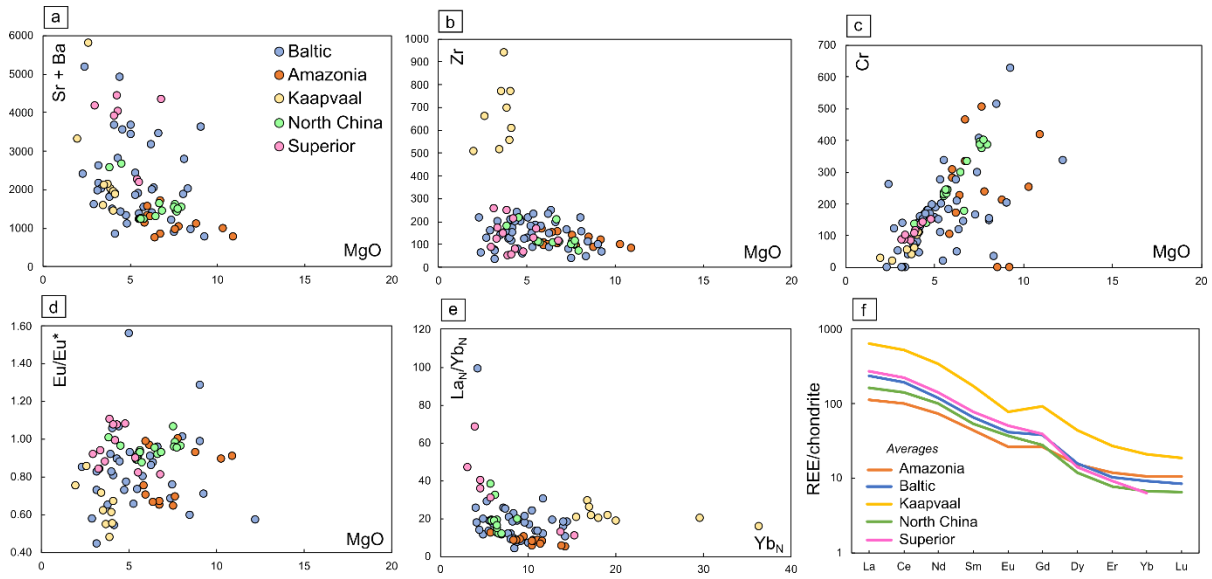


Figure 6.2. Trace element trends (µg/g, MgO in wt.%) of sanukitoid compilation data (Table S5.1).

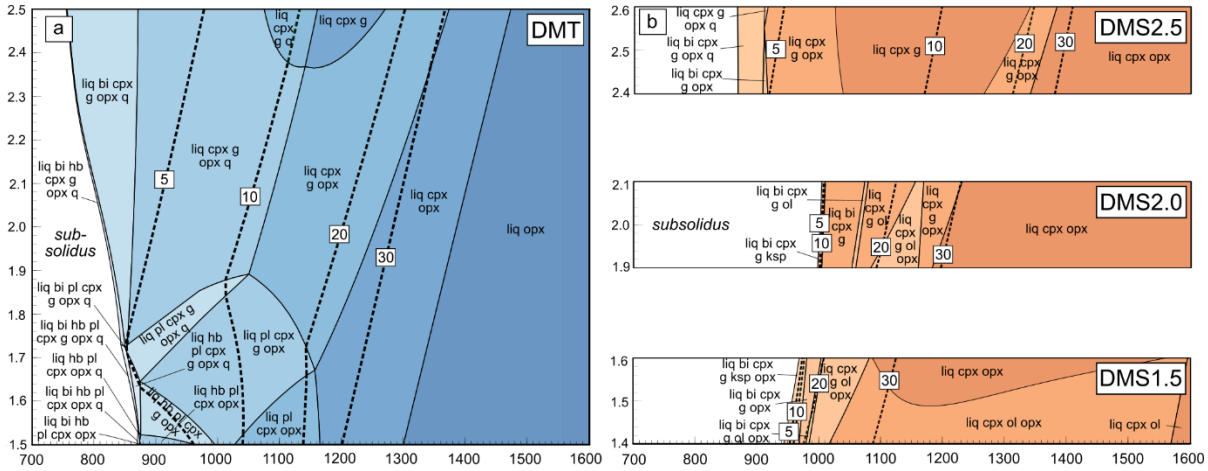


Figure 6.3. Phase diagrams of the calculated metasomatized mantle compositions, DMT (TTG-metasomatized depleted mantle) and DMS (metasediment-melt-metasomatized depleted mantle) (see Table 6.1). Abbreviations: liq = melt, bi = biotite, ksp = K-feldspar, pl = plagioclase, hb = amphibole, cpx = clinopyroxene, opx = orthopyroxene, g = garnet, ol = olivine, q = quartz

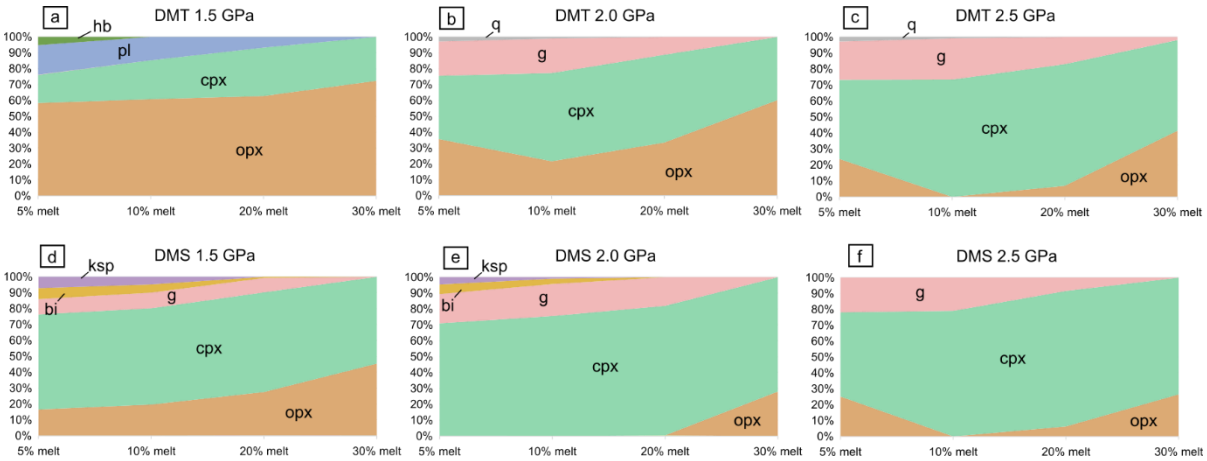


Figure 6.4. Modal proportions (wt.%) of residual minerals predicted for model melt of DMT (TTG-metasomatized depleted mantle; a–c) and DMS (metasediment-melt-metasomatized depleted mantle; d–f).

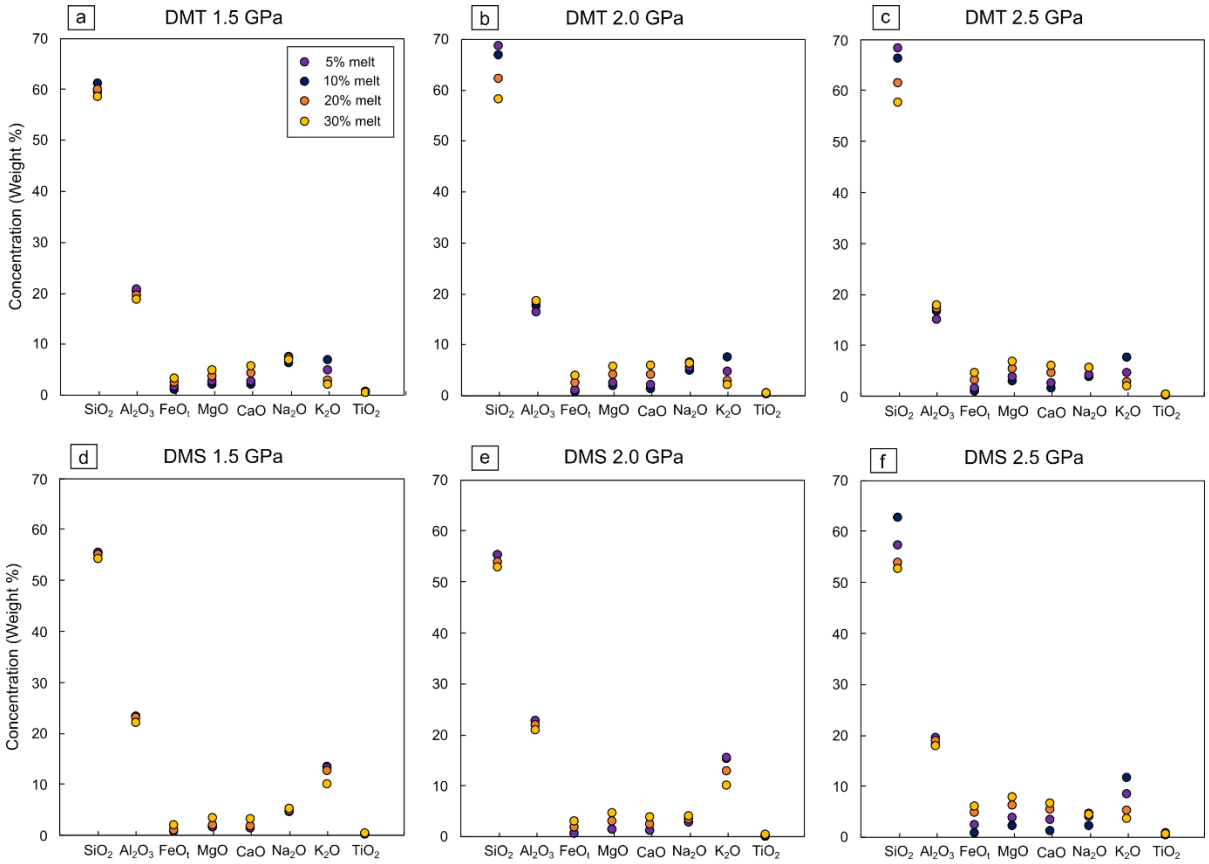


Figure 6.5. Major element trends (wt. %) of model melt of DMT (TTG-metasomatized depleted mantle; a–c) and DMS (metasediment-melt-metasomatized depleted mantle; d–f).

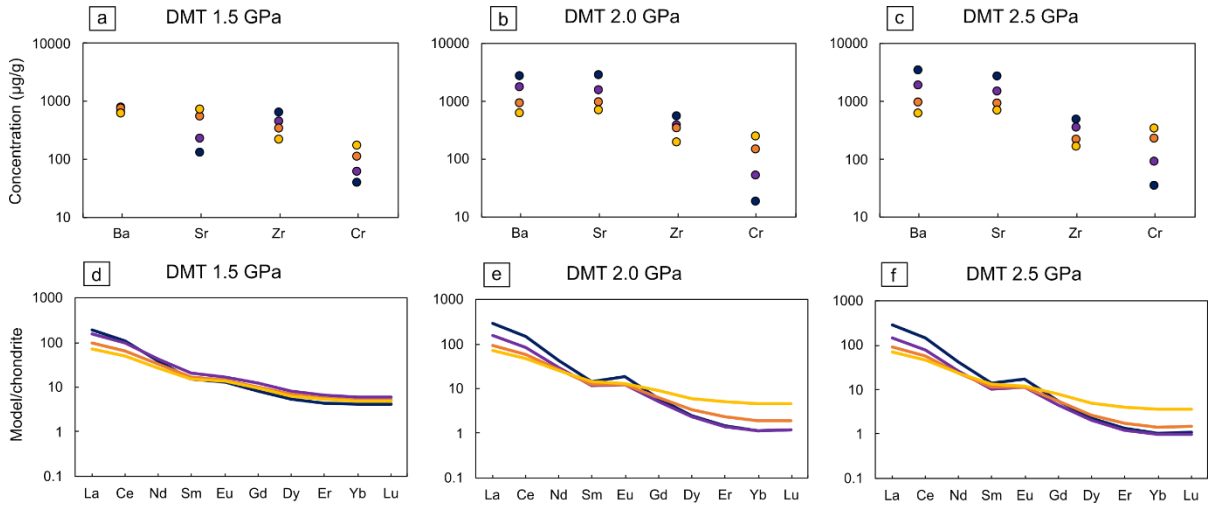


Figure 6.6. Trace element trends (µg/g) of model melt of DMT (TTG-metasomatized depleted mantle).

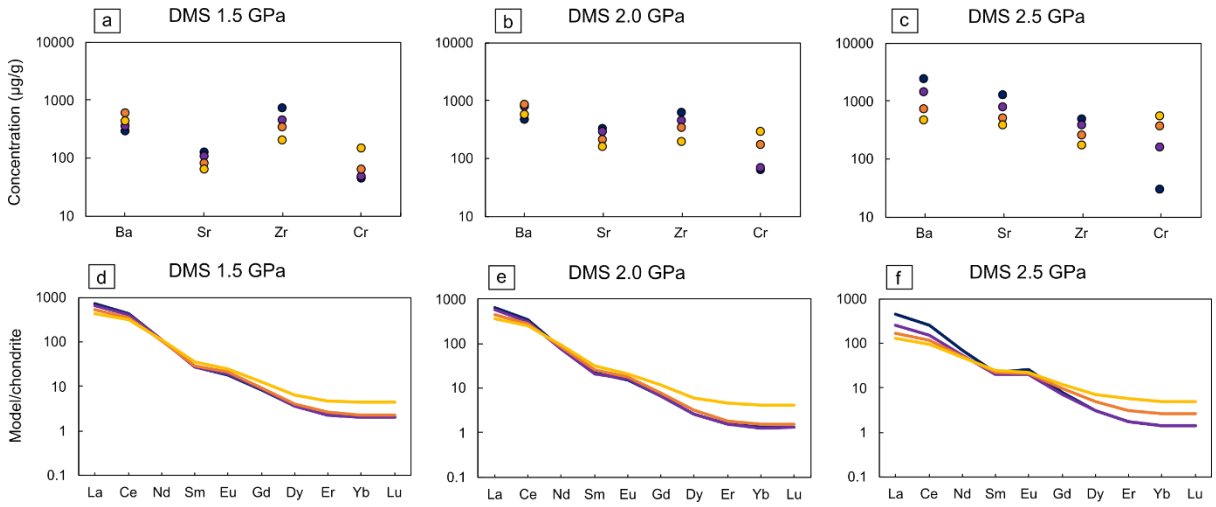


Figure 6.7. Trace element trends (µg/g) of model melt of DMS (metasediment-melt-metasomatized depleted mantle).

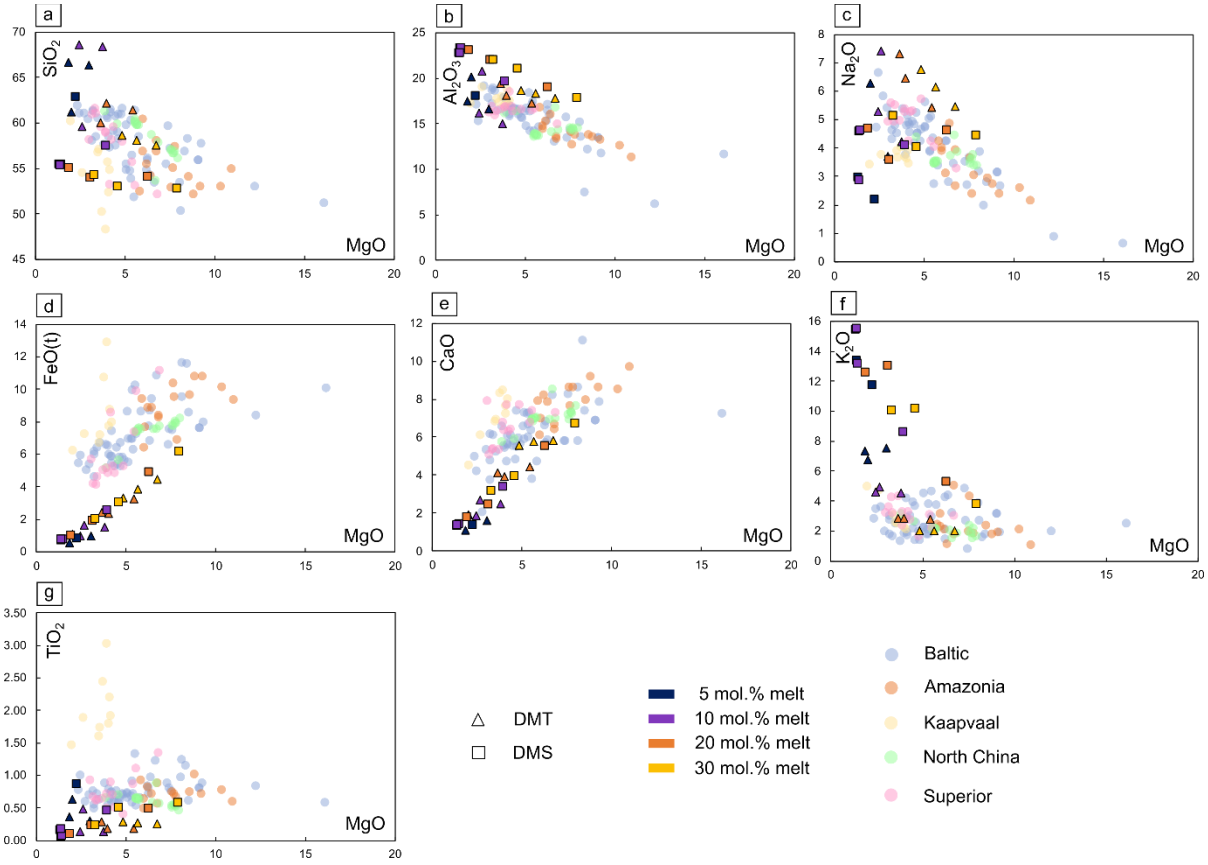


Figure 6.8. Major element trends (wt.%) of model melt (DMT = TTG-metasomatized depleted mantle, DMS = metasediment-melt-metasomatized depleted mantle) compared to sanukitoid compilation data (Table S5.1).

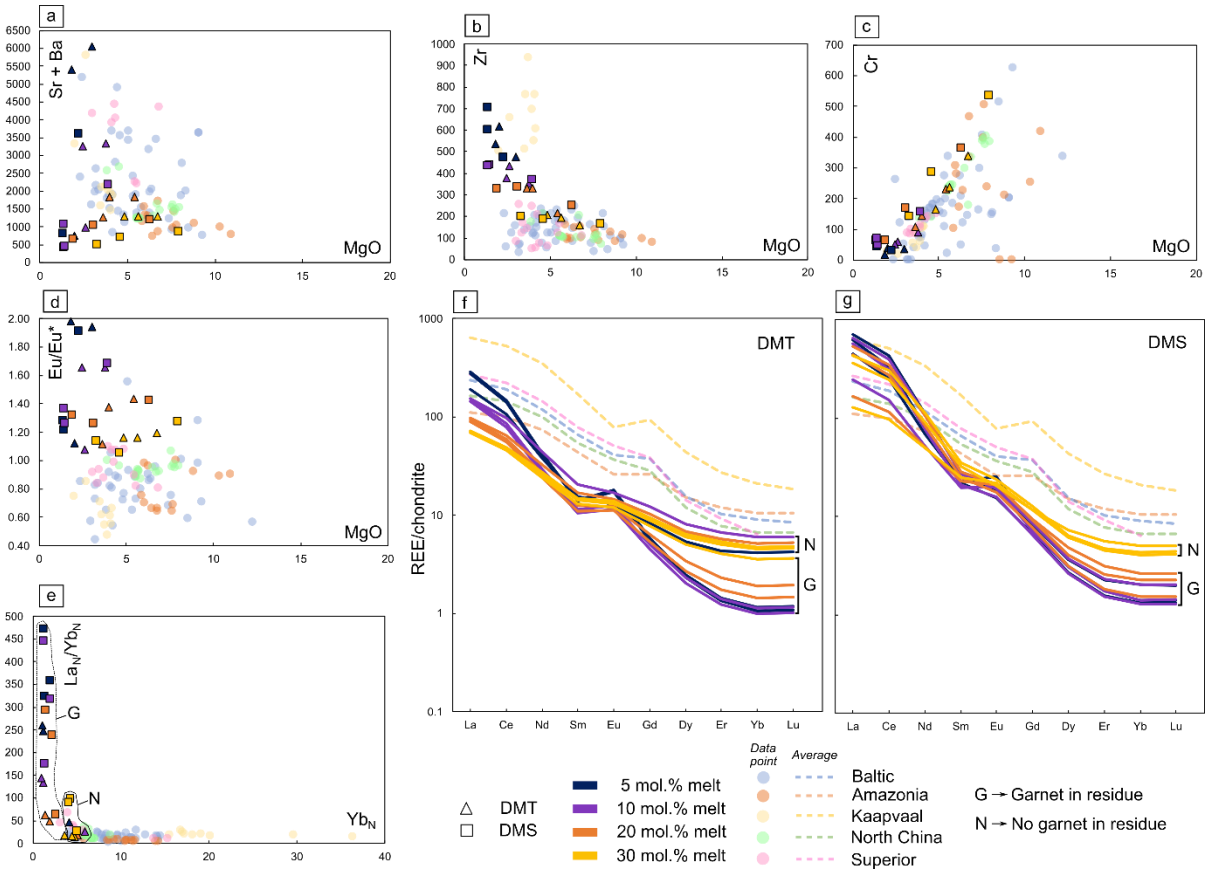


Figure 6.9. Trace element trends (µg/g, MgO in wt.%) of model melt (DMT = TTG-metasomatized depleted mantle, DMS = metasediment-melt-metasomatized depleted mantle) compared to sanukitoid compilation data (Table S5.1).

Table 6.1. Depleted mantle composition, metasomatic agent compositions, and metasomatized mantle compositions (mol% for major elements, μg/g for trace elements).

		Metasomatic agents				*Metasomatized mantle*			
	DMM	HP TTG	AUC1.5	AUC2.0	AUC2.5	DMT	DMS1.5	DMS2.0	DMS2.5
SiO_2	38.51	72.90	72.81	71.63	69.97	52.27	52.23	51.76	51.09
TiO_2	0.08	0.33	1.18	1.68	0.89	0.18	0.52	0.72	0.41
Al_2O_3	2.02	10.70	11.76	11.39	9.34	5.49	5.92	5.77	4.95
FeOt	5.89	2.67	0.73	1.31	3.87	4.60	3.83	4.06	5.08
MgO	49.73	2.28	1.76	1.74	3.83	30.75	30.54	30.54	31.37
CaO	2.93	4.82	1.67	2.63	5.69	3.68	2.42	2.81	4.03
Na_2O	0.11	5.40	5.00	4.41	4.58	2.22	2.06	1.83	1.90
K_2O	0.00	0.91	5.09	5.21	1.82	0.37	2.04	2.09	0.73
Cr_2O_3	0.194	0.002	0.000	0.000	0.001	0.117	0.116	0.117	0.117
Sr	7.664	598.77	47.72	142.44	341.80	244.10	23.69	61.57	141.32
Ba	0.563	513.05	373.08	471.03	385.54	205.56	149.57	188.75	154.55
Zr	5.082	123.62	457.63	355.52	154.60	52.50	186.10	145.26	64.89
La	0.192	14.69	100.57	87.34	28.63	5.99	40.34	35.05	11.57
Ce	0.55	26.67	202.56	170.10	59.22	11.00	81.36	68.37	24.02
Nd	0.581	11.67	68.87	58.48	26.16	5.02	27.89	23.74	10.81
Sm	0.239	2.14	8.14	7.72	4.65	1.00	3.40	3.23	2.00
Eu	0.096	0.74	2.01	1.80	1.56	0.35	0.86	0.78	0.68
Gd	0.358	1.75	3.97	3.87	3.03	0.91	1.80	1.76	1.43
Dy	0.505	1.26	2.16	2.14	2.07	0.81	1.17	1.16	1.13
Er	0.348	0.61	0.86	0.86	0.92	0.45	0.55	0.55	0.58
Yb	0.365	0.50	0.73	0.72	0.77	0.42	0.51	0.51	0.53
Lu	0.058	0.08	0.11	0.11	0.12	0.07	0.08	0.08	0.08
La_N/Yb_N	0.36	19.99	93.71	82.81	25.10	9.72	53.67	47.10	14.85
Eu/Eu*	1.00	1.16	1.07	1.00	1.26	1.12	1.06	0.99	1.23

DMM = depleted MORB mantle (Workman and Hart, 2005)

HP = high-pressure

AUC = Archean upper crust (Taylor and McLennan, 1985)

DMT = TTG-metasomatized depleted mantle

DMS = metasediment-melt-metasomatized depleted mantle

Table 6.2. Compositions of model melt of DMT (TTG-metasomatized depleted mantle)

Melt fraction (mol%)	5	10	20	30	5	10	20	30	5	10	20	30
Pressure (GPa)	1.5	1.5	1.5	1.5	2.0	2.0	2.0	2.0	2.5	2.5	2.5	2.5
Temperature (°C)	962	1041	1139	1201	898	1040	1203	1284	978	1133	1303	1368
Major elements (wt%)												
SiO_2	61.20	59.60	59.97	58.59	66.62	68.51	62.14	58.06	66.27	68.33	61.34	57.52
Al_2O_3	20.23	20.78	19.47	18.73	17.52	16.21	18.19	18.35	16.65	15.06	17.24	17.81
FeOt	1.07	1.58	2.38	3.28	0.55	0.95	2.36	3.82	0.94	1.48	3.20	4.45
MgO	2.01	2.61	3.63	4.82	1.83	2.44	3.98	5.63	3.01	3.78	5.42	6.72
CaO	1.90	2.67	4.12	5.56	1.08	1.86	3.90	5.75	1.60	2.48	4.44	5.83
Na_2O	6.25	7.39	7.28	6.74	4.70	5.29	6.44	6.14	3.69	4.20	5.43	5.45
K_2O	6.71	4.89	2.85	2.00	7.35	4.62	2.81	1.98	7.54	4.55	2.76	1.96
TiO_2	0.63	0.47	0.28	0.28	0.35	0.12	0.17	0.26	0.30	0.13	0.17	0.25
Trace elements (μg/g)												
Sr	126	218	529	698	2743	1524	930	689	2647	1449	899	678
Ba	623	765	732	597	2669	1730	900	604	3393	1894	936	614
Cr	38.50	59.38	109	166	17.85	51.16	144	238	34.80	89.03	229	338
Zr	622	435	332	210	538	379	331	194	476	355	217	163
La	45.61	36.39	23.13	17.04	68.03	36.27	22.15	16.73	65.95	33.91	21.21	16.33
Ce	65.23	59.16	39.47	30.11	89.88	52.16	36.09	29.24	86.73	48.04	33.95	28.18
Nd	3.50	4.04	3.01	2.51	3.89	2.71	2.45	2.38	3.76	2.46	2.22	2.23
Sm	7.03	9.42	7.68	6.86	6.56	5.20	5.68	6.44	6.38	4.75	5.07	5.93
Eu	1.87	2.52	2.17	2.04	2.68	1.86	1.82	1.92	2.53	1.68	1.65	1.77
Gd	0.46	0.69	0.58	0.53	0.33	0.28	0.36	0.49	0.31	0.25	0.30	0.44
Dy	1.06	1.60	1.36	1.27	0.49	0.46	0.68	1.19	0.45	0.40	0.54	1.01
Er	0.16	0.24	0.21	0.19	0.05	0.05	0.08	0.18	0.05	0.04	0.06	0.15
Yb	1.03	1.46	1.26	1.17	0.28	0.28	0.47	1.11	0.26	0.24	0.35	0.87
Lu	0.23	0.33	0.28	0.26	0.06	0.06	0.11	0.25	0.06	0.06	0.08	0.20
La_N/Yb_N	46.13	25.84	19.05	15.10	248	134	49.12	15.68	261	145	62.47	19.38
Eu/Eu*	1.12	1.08	1.12	1.16	1.98	1.66	1.38	1.16	1.95	1.66	1.44	1.19

Table 6.3. Compositions of model melt of DMS (metasediment-melt-metasomatized depleted mantle)

Melt fraction (mol%)	5	10	20	30	5	10	20	30	5	10	20	30
Pressure (GPa)	1.5	1.5	1.5	1.5	2	2	2	2	2.5	2.5	2.5	2.5
Temperature (°C)	963	968	992	1106	1004	1006	1109	1212	930	1183	1329	1394
Major elements (wt%)												
SiO_2	55.40	55.40	54.97	54.19	55.38	55.32	53.89	52.87	62.79	57.42	54.00	52.68
Al_2O_3	23.32	23.27	23.06	22.04	22.79	22.74	21.95	21.02	18.07	19.63	18.98	17.86
FeOt	0.67	0.71	0.98	1.96	0.71	0.74	1.84	2.98	0.79	2.53	4.87	6.10
MgO	1.41	1.47	1.91	3.30	1.37	1.41	3.11	4.61	2.28	3.95	6.30	7.95
CaO	1.29	1.39	1.77	3.16	1.28	1.33	2.42	3.89	1.34	3.36	5.53	6.68
Na_2O	4.57	4.60	4.66	5.11	2.93	2.82	3.56	4.00	2.16	4.08	4.60	4.41
K_2O	13.30	13.10	12.57	10.02	15.41	15.48	13.01	10.14	11.72	8.57	5.25	3.75
TiO_2	0.04	0.05	0.08	0.22	0.14	0.16	0.22	0.49	0.85	0.45	0.47	0.57
Trace elements (μg/g)												
Sr	122	104	80.27	61.77	323	282	202	158	1257	765	500	381
Ba	278	341	570	423	464	769	821	546	2342	1402	694	463
Cr	42.64	47.20	63.23	142	62.53	67.93	167	286	29.46	156	363	535
Zr	706	441	328	201	602	435	336	187	475	371	252	166
La	171	154	128	102	147	135	106	86.48	107	58.84	39.71	30.78
Ce	264	245	215	188	206	192	171	153	154	93.83	71.90	59.66
Nd	10.39	10.13	9.82	10.51	7.60	7.20	7.75	8.55	6.48	4.86	4.74	4.59
Sm	12.51	12.56	13.03	16.14	10.01	9.65	11.43	14.73	10.40	9.05	10.42	11.36
Eu	2.74	2.88	3.16	3.56	2.29	2.37	2.59	3.02	3.75	2.96	3.10	3.23
Gd	0.48	0.49	0.52	0.71	0.37	0.36	0.44	0.66	0.44	0.40	0.53	0.67
Dy	0.72	0.74	0.81	1.28	0.53	0.52	0.62	1.21	0.62	0.61	0.96	1.44
Er	0.08	0.08	0.09	0.17	0.06	0.06	0.07	0.16	0.06	0.06	0.11	0.20
Yb	0.50	0.50	0.56	1.07	0.32	0.32	0.38	1.01	0.34	0.35	0.65	1.24
Lu	0.11	0.11	0.12	0.24	0.07	0.07	0.08	0.23	0.08	0.08	0.14	0.28
La_N/Yb_N	358	318	238	98.47	471	445	293	89.21	324	175	63.86	25.83
Eu/Eu*	1.21	1.26	1.32	1.14	1.28	1.37	1.26	1.05	1.91	1.69	1.43	1.27

Chapter 7

Conclusions

7.1 Summary of research

The research presented in this thesis provides new insights into the petrogenesis of Archean granitoids. The fundamental issue addressed in this work is the extent to which these rocks record geochemical information that can be linked to their sources, which has important implications for reconstructing the geodynamic history of Archean Earth (e.g., Martin et al., 2014; Palin et al., 2016; Johnson et al., 2017; Johnson et al., 2019; Kendrick and Yakymchuk, 2020 [Chapter 2]; Laurent et al., 2020; Rollinson, 2021; Kendrick et al., 2022 [Chapter 3]). Using novel forward modelling techniques and inverse modelling approaches based on data collected from TTGs of the Kapuskasing Uplift in the Superior Province, the research in this thesis highlights the complexity of the Archean granitoid record and the variety of factors that may influence granitoid composition. However, this complexity can be unraveled to understand the source-to-sink processes that influence granitoid compositions, which are crucial to broadening our understanding of the evolution of continental crust on Earth.

Forward modelling the compositions of melt produced by theoretical basaltic TTG source rocks (Chapter 2) showed that TTG trace elements could have been affected by several source characteristics or processes. Archean tholeiitic basalts were predicted to produce TTG-like melt, but a high-Mg Archean basalt—a composition not previously investigated in models of TTG genesis—was determined to be a less suitable TTG source. Although residue mineral assemblages were predicted to be broadly pressure-dependent—resulting in pressure-dependent variability of Sr/Y, La/Yb, Nb, and Ta in melt that becomes TTG magma—other factors were also important. The bulk composition of the model source was also reflected in model TTG compositions, as the source enriched in La, Nb, and Ta generally yielded melt with greater concentrations of these elements. The concentrations of major elements in the source affected the *P*–*T* stability of minerals in the residue, which in turn affected predicted melt compositions. Modal proportions of minerals in the residue assemblages were also predicted to be affected by temperature; for instance, the highest proportion of garnet was typically not at the highest pressure along a modelled *P*–*T* gradient. In models simulating sequestration of garnet cores from the system, Sr/Y and La/Yb in the model melt were predicted to be elevated relative to models without garnet fractionation at the same *P*–*T* conditions. The implication

of these results is that the concentrations of elements typically considered as indicators of TTG source depth (Sr/Y, La/Yb, Nb, and Ta) are not uniquely controlled by the pressure of source partial melting, adding complexity to the link between TTG compositions and the tectonic settings in which they formed. This work was at the forefront of evaluating TTG petrogenesis using coupled phase equilibrium and melt trace element modelling of potential source rocks, particularly with respect to open system processes, and several modelling studies that complement or build upon on this work have followed (e.g., Huang et al., 2020; Hernández-Montenegro et al., 2021; Antonelli et al., 2021).

A suite of mid-crustal TTGs from the Kapuskasing Uplift exhibits a range of trace element compositions consistent with TTGs derived from both "low-pressure" and "high-pressure" sources (Chapter 3). Petrographic observations and major element geochemistry indicated that these TTGs contain variable proportions of accumulated plagioclase and phase equilibrium modelling of a theoretical parental TTG predicted early crystallization of plagioclase. Combining variable proportions of modelled plagioclase and fractionated melt resulted in a spectrum of trace element compositions similar to the range of compositions in the natural TTG suite. Increasing proportions of accumulated plagioclase are associated with increasing Sr/Y and La/Yb, suggesting that these ratios may not be reliable indicators of source depth. These results suggest that the mid-crustal grey gneiss domain in the Kapuskasing Uplift may represent a former crystal mush complex where a large volume of TTG magma cooled slowly and underwent compactions resulting in localized accumulation of plagioclase and fractionated melt. This work also highlighted the potential for plagioclase to drive fractionation of LREE from HREE in TTG magma, which has typically not been considered in models of TTG petrogenesis. The importance of fractional crystallization as a driver of compositional diversity in TTGs has recently become a high-profile subject of debate (e.g., Laurent et al., 2020; Rollinson, 2021) and has important implications for linking TTGs to Archean tectonics. This work represents the first use of coupled phase equilibrium and trace element modelling to assess fractional crystallization in TTGs, and shows that the behaviour of plagioclase can obscure the connection between TTGs compositions and their sources.

In the Kapuskasing Uplift—a rare cross section of Archean crust—TTGs are present at upper, middle, and lower crustal levels and U–Pb and Hf isotopes of zircon were collected from TTGs at each level (Chapter 4). These data revealed an isotopically stratified crustal architecture with three isotopically distinct sources involved in TTG generation. A population of juvenile Neoarchean TTGs (ca. 2750–2685 Ma) dominate the middle crust and are also found in the upper crust, whereas two

types of Mesoarchean TTGs are present: a 2885 Ma TTG with chondritic εHf in the upper crust and 2835–2820 Ma TTGs with subchondritic εHf that are restricted to the lower crust. The Hf isotope data suggest that the three TTG sources have different ages; TTGs produced by the most ancient source are only present in the deep crust. These results indicate that a fragment of Mesoarchean crust may have rifted from the cratonic nucleus of the Superior Province and was later intruded by juvenile magma during the formation of the Neoarchean Wawa-Abitibi terrane. Overall, this work demonstrates the utility of Hf isotopes for distinguishing TTGs with different sources and unravelling the complex magmatic evolution of Archean crust and represents the most detailed isotopic study of an Archean crustal cross section to date.

Deep crustal anatectic metabasites are considered as a possible source of TTGs, however limited access to exposed Archean lower crust prevents connections between lower and upper crustal rocks from being made in many Archean cratons. The crustal cross section exposed in the Kapuskasing Uplift provides a rare opportunity to evaluate the potential connection between deep-crustal high-grade anatectic metabasites and TTGs within the same region (Chapter 5). This work combined phase equilibrium modelling, zircon U–Pb and garnet Lu–Hf geochronology, and whole-rock Lu–Hf isotope compositions of deep-crustal metabasites to determine the compatibility of these rocks with middle-to-upper-crustal TTGs. Melt compositions of Kapuskasing Uplift metabasites predicted by forward modelling are broadly consistent with TTGs at shallower crustal levels. The results indicate that source depth may have increased in the Neoarchean, however it was not possible to distinguish different metabasic sources based on the modelling. Geochronological data from the metabasite indicate that partial melting of the deep crust post-dated most TTG magmatism (mostly ca. 2925 Ma to ca. 2685 Ma). However, whole-rock Lu–Hf isotope data indicate that two isotopically distinct metabasites are present in the Kapuskasing Uplift—one with suprachondritic εHf consistent with Neoarchean TTGs and another with near-chondritic εHf consistent with the upper crustal Mesoarchean TTG. These results indicate that appropriate source rocks for the TTGs in the Kapuskasing Uplift may have been present in the deep crust. Although the metamorphic event recorded in the currently exposed metabasites is temporally decoupled from TTG crystallization, earlier melting of similar metabasic material that is not exposed could have generated the TTGs. This two-stage history of lower crustal melting requires juxtaposition of the two hydrated basaltic sources in the deep crust, likely involving horizontal tectonic processes. These results support models of horizontal growth of the Superior Province, but indicate that melting of a subducting slab may not have been necessary to generate TTGs.

Phase equilibrium and melt trace element modelling of calculated metasomatized mantle sources was done to evaluate the potential signature of source composition and *P–T* conditions recorded in sanukitoids (Chapter 6). In this work, data from sanukitoid suites from Archean cratons worldwide were collated to evaluate common geochemical trends in these rocks. Two potential mantle sources for sanukitoids were investigated—one metasomatized by TTG melt and another by melt from subducted sediments—and each yielded similar melt compositions. A large range of melt compositions was predicted with changing melt fraction and *P–T* conditions, suggesting that it is difficult to link a sanukitoid suite to a particular type of metasomatized source based on trace element composition alone. In addition, a common negative Eu anomaly was identified in the dataset of natural sanukitoids compiled in this study and was not replicated in the models. For both modelled sources, model melt showed the closest agreement with natural sanukitoid compositions when the temperature of melting was relatively high (20–30 mol.%) and the residue assemblage was composed of clinopyroxene and orthopyroxene with no or only very little garnet. This result is broadly consistent with the interpretation that asthenospheric upwelling was the trigger for melting of the metasomatized mantle and sanukitoid genesis. However, the diverse compositional trends identified in the natural sanukitoid suites indicate that processes that influenced sanukitoid compositions may be distinct to different cratons.

7.2 Future work and recommendations

The results of this thesis provide avenues for future research, both related to the crustal evolution of the Superior Province and the petrogenesis of TTGs more generally. In this work, a distinct suite of TTGs with crystallization ages of ca. 2835–2820 Ma and subchondritic εHf was identified in the deep-crustal rocks (Kapuskasing Structural Zone) exposed in the Kapuskasing Uplift based on results from two samples. Although the Mesoarchean crust in this region is interpreted in this thesis as a rifted fragment from northern subdomains in the Superior Province, the data from these samples could not be clearly linked to existing U–Pb and Hf data from Mesoarchean subdomains in the Superior Province. The source of the Kapuskasing Structural Zone TTGs may have been older than the Wawa-Abitibi terrane and potentially some of the northern subdomains of the Superior Province, as calculated depleted mantle model ages for the ca. 2835–2820 Ma TTGs are Eoarchean. More isotopic data from the Kapuskasing Structural Zone are required to characterize possible ancient crustal components that were present in the deep crust. Additional TTGs from the Kapuskasing Structural Zone should be examined to determine the extent of the ca. 2835–2820 Ma suite and if

other Mesoarchean or older TTG suites are present. Also, the ancient metabasic source of the ca. 2835–2820 Ma TTG suite could be identified by whole-rock isotope analyses (Lu–Hf or Sm–Nd) of more metabasite samples in the Kapuskasing Structural Zone. The presence of a distinct Eoarchean crustal component in the deep crust exposed Kapuskasing Structural Zone could indicate that Mesoarchean subdomains of the Superior Province are underlain by ancient crust, implying long-lived bottom-to-top construction of the Mesoarchean crust in the Superior Province.

The research presented in this thesis has shown that TTG trace element compositions can only be linked to the depth of source melting when alternative explanations are ruled out. For any TTG suite, field and petrographic observations must be done to determine if crystal fractionation may have influenced TTG compositions. These effects complicate the use of forward modelling to link a particular source rock to a TTG suite. However, phase equilibrium modelling coupled with melt trace element modelling represents a powerful tool for evaluating the possible effects of various source processes on TTG (and other granitoid) compositions. Future work employing this technique could focus on the effect of source redox conditions on TTG composition and integrating stable isotope partitioning in addition to trace element partitioning. As the basaltic source rocks of TTGs are interpreted to be hydrated possibly by interaction with seawater (e.g., Drummond and Defant, 1990; Bédard, 2018), the oxidation state of the oceans could have been recorded in these basalts. Variable redox conditions can be simulated in models of potential TTG source rocks, and the effect of these changes on TTG composition can be evaluated. Therefore, it may be possible to determine if ocean oxidation was underway in the Archean (e.g, Anbar et al., 2007; Kendall et al., 2015)—either globally or in the vicinity of a particular Archean craton—by examining the TTG record. The compositions of stable isotopes in TTGs are increasingly being used as tracers of source processes (e.g., André et al., 2019; Doucet et al., 2020; Antonelli et al., 2021; Smithies et al., 2021; André et al., 2022). In particular, $\delta^{18}O$ data from zircon in TTGs from different cratons are becoming abundant (e.g., Mole et al., 2021; Smithies et al., 2021). Integrating $\delta^{18}O$ with phase equilibrium modelling of potential TTG sources could provide a framework for interpreting the zircon $\delta^{18}O$ record of TTGs, which in turn can be used to determine a surficial versus mantle source of H_2O in the TTG source with implications for early Earth tectonic processes and cycling of H_2O (Valley et al., 2005; Smithies et al., 2021).

As the TTG record spans the entire Archean eon, it holds great potential for evaluating the secular evolution of early Earth. Future work should continue to explore this but must also acknowledge the influence of local processes on TTG composition.

References

Anbar, A. D. et al. (2007). A whiff of oxygen before the great oxidation event? Science 317, 1903–1906.

André, L., Abraham, K., Hofmann, A., Monin, L., Kleinhanns, I. C. & Foley, S. (2019). Early continental crust generated by reworking of basalts variably silicified by seawater. Nature Geoscience 12, 769–773.

André, L., Monin, L. & Hofmann, A. (2022). The origin of early continental crust: New clues from coupling Ge/Si ratios with silicon isotopes. Earth and Planetary Science Letters 582, 117415.

Antonelli, M. A., Kendrick, J., Yakymchuk, C., Guitreau, M., Mittal, T. & Moynier, F. (2021). Calcium isotope evidence for early Archaean carbonates and subduction of oceanic crust. Nature Communications 12, 2534.

Ayres, L. D. (1978). Metamorphism in the Superior Province of northwestern Ontario and its relationship to crustal development. In: Fraser, J. A. & Heywood, W. W. (eds) Metamorphism in the Canadian Shield, Geological Survey of Canada, Paper, 1–367.

Bédard, J. H. (2006). A catalytic delamination-driven model for coupled genesis of Archaean crust and sub-continental lithospheric mantle. Geochimica et Cosmochimica Acta 70, 1188–1214.

Bédard, J. H. (2018). Stagnant lids and mantle overturns: Implications for Archaean tectonics, magmagenesis, crustal growth, mantle evolution, and the start of plate tectonics. Geoscience Frontiers 9, 19–49.

Bédard, J. H. & Harris, L. B. (2014). Neoarchean disaggregation and reassembly of the Superior craton. Geology 42, 951–954.

Bédard, J. H., Harris, L. B. & Thurston, P. C. (2013). The hunting of the snArc. Precambrian Research 229, 20–48.

Benn, K. & Kamber, B. S. (2009). In Situ U/Pb Granulite-Hosted Zircon Dates, Kapuskasing Structural Zone, Ontario: A Late Archean Large Igneous Province (LIP) as a Substrate for Juvenile Crust. The Journal of Geology 117, 519–541.

Benn, K. & Moyen, J. F. (2008). The late Archean Abitibi-Opatica terrane, Superior Province: A modified oceanic plateau. Special Paper of the Geological Society of America 440, 173–197.

Bowman, J. R., Moser, D. E., Valley, J. W., Wooden, J. L., Kita, N. T. & Mazdab, F. K. (2011). Zircon U-Pb isotope, $\delta^{18}O$ and trace element response to 80 m.y. of high temperature

metamorphism in the lower crust: Sluggish diffusion and new records of Archean craton formation. American Journal of Science 311, 719–772.

Brown, M., Johnson, T. & Gardiner, N. J. (2020a). Plate tectonics and the Archean Earth. Annual Review of Earth and Planetary Sciences 48, 291–320.

Brown, M., Kirkland, C. L. & Johnson, T. E. (2020b). Evolution of geodynamics since the Archean: Significant change at the dawn of the Phanerozoic. Geology 48, 488–492.

Calvert, A. J., Sawyer, E. W., Davis, W. J. & Ludden, J. N. (1995). Archaean subduction inferred from seismic images of a mantle suture in the Superior Province. Nature 375, 670–674.

Cawood, P. A., Kröner, A. & Pisarevsky, S. (2006). Precambrian plate tectonics: Criteria and evidence. GSA Today 16, 4–11.

Condie, K. C. (2018). A planet in transition: The onset of plate tectonics on Earth between 3 and 2 Ga? Geoscience Frontiers 9, 51–60.

Doucet, L. S., Laurent, O., Ionov, D. A., Mattielli, N., Debaille, V. & Debouge, W. (2020). Archean lithospheric differentiation: Insights from Fe and Zn isotopes. Geology 48, 1028–1032.

Drummond, M. S. & Defant, M. J. (1990). A model for trondhjemite-tonalite-dacite genesis and crustal growth via slab melting: Archean to modern comparisons. Journal of Geophysical Research, 95, 21,503-21,521.

Gardiner, N. J., Johnson, T. E., Kirkland, C. L. & Smithies, R. H. (2018). Melting controls on the lutetium–hafnium evolution of Archaean crust. Precambrian Research 305, 479–488.

Green, E. C. R., White, R. W., Diener, J. F. A., Powell, R., Holland, T. J. B. & Palin, R. M. (2016). Activity-composition relations for the calculation of partial melting equilibria in metabasic rocks. Journal of Metamorphic Geology 34, 845–869.

Hanes, J. A., Archibald, D. A., Queen, M. & Farrar, E. (1994). Constraints from $^{40}Ar/^{39}Ar$ geochronology on the tectonothermal history of the Kapuskasing uplift in the Canadian Superior Province. Canadian Journal of Earth Sciences 31, 1146–1171.

Hartel, T. H. D. & Pattison, D. R. M. (1996). Genesis of the Kapuskasing (Ontario) migmatitic mafic granulites by dehydration melting of amphibolite: The importance of quartz to reaction progress. Journal of Metamorphic Geology 14, 591–611.

Hernández-Montenegro, J. D., Palin, R. M., Zuluaga, C. A. & Hernández-Uribe, D. (2021). Archean continental crust formed by magma hybridization and voluminous partial melting. Scientific Reports 11, 1–9.

Hoffmann, J. E., Nagel, T. J., Münker, C., Næraa, T. & Rosing, M. T. (2014). Constraining the process of Eoarchean TTG formation in the Itsaq Gneiss Complex, southern West Greenland. Earth and Planetary Science Letters 388, 374–386.

Holland, T. J. B., Green, E. C. R. & Powell, R. (2018). Melting of peridotites through to granites: A simple thermodynamic model in the system KNCFMASHTOCr. Journal of Petrology 59, 881–900.

Huang, G., Palin, R., Wang, D. & Guo, J. (2020). Open-system fractional melting of Archean basalts: Implications for tonalite–trondhjemite–granodiorite (TTG) magma genesis. Contributions to Mineralogy and Petrology 175, 1–25.

Jahn, B. M., Glikson, A. Y., Peucat, J. J. & Hickman, A. H. (1981). REE geochemistry and isotopic data of Archean silicic volcanics and granitoids from the Pilbara Block, Western Australia: Implications for the early crustal evolution. Geochimica et Cosmochimica Acta 45, 1633–1652.

Johnson, T. E., Brown, M., Gardiner, N. J., Kirkland, C. L. & Smithies, R. H. (2017). Earth's first stable continents did not form by subduction. Nature 543, 239–242.

Johnson, T. E., Kirkland, C. L., Gardiner, N. J., Brown, M., Smithies, R. H. & Santosh, M. (2019). Secular change in TTG compositions: Implications for the evolution of Archaean geodynamics. Earth and Planetary Science Letters 505, 65–75.

Kendall, B., Creaser, R. A., Reinhard, C. T., Lyons, T. W. & Anbar, A. D. (2015). Transient episodes of mild environmental oxygenation and oxidative continental weathering during the late Archean. Science Advances 1, e1500777.

Kendrick, J., Duguet, M. & Yakymchuk, C. (2022). Diversification of Archean tonalite-trondhjemite-granodiorite suites in a mushy middle crust. Geology 50, 76–80.

Kendrick, J. & Yakymchuk, C. (2020). Garnet fractionation, progressive melt loss and bulk composition variations in anatectic metabasites: Complications for interpreting the geodynamic significance of TTGs. Geoscience Frontiers 11, 745–763.

Krogh, T. E. (1993). High precision U-Pb ages for granulite metamorphism and deformation in the Archean Kapuskasing structural zone, Ontario: Implications for structure and development of the lower crust. Earth and Planetary Science Letters 119, 1–18.

Krogh, T. E. & Moser, D. E. (1994). U–Pb zircon and monazite ages from the Kapuskasing uplift: Age constraints on deformation within the Ivanhoe Lake fault zone. Canadian Journal of Earth Sciences 31, 1096–1103.

Laurent, O., Björnsen, J., Wotzlaw, J. F., Bretscher, S., Pimenta Silva, M., Moyen, J. F., Ulmer, P. & Bachmann, O. (2020). Earth's earliest granitoids are crystal-rich magma reservoirs tapped by silicic eruptions. Nature Geoscience 13, 163–169.

Mäder, U. K., Percival, J. A. & Berman, R. G. (1994). Thermobarometry of garnet–clinopyroxene–hornblende granulites from the Kapuskasing structural zone. Canadian Journal of Earth Sciences 31, 1134–1145.

Martin, H., Moyen, J.-F., Guitreau, M., Blichert-Toft, J. & Le Pennec, J.-L. (2014). Why Archaean TTG cannot be generated by MORB melting in subduction zones. Lithos 198–199, 1–13.

Merdith, A. S. et al. (2021). Extending full-plate tectonic models into deep time: Linking the Neoproterozoic and the Phanerozoic. Earth-Science Reviews 214, 103477.

Mole, D. R., Thurston, P. C., Marsh, J. H., Stern, R. A., Ayer, J. A., Martin, L. A. J. & Lu, Y. J. (2021). The formation of Neoarchean continental crust in the south-east Superior Craton by two distinct geodynamic processes. Precambrian Research 356, 106104.

Moser, D. E., Bowman, J. R., Wooden, J., Valley, J. W., Mazdab, F. & Kita, N. (2008). Creation of a continent recorded in zircon zoning. Geology 36, 239–242.

Moser, D. E., Heaman, L. M., Krogh, T. E. & Hanes, J. A. (1996). Intracrustal extension of an Archean orogen revealed using single-grain U-Pb zircon geochronology. Tectonics 15, 1093–1109.

Moyen, J.-F. (2011). The composite Archaean grey gneisses: Petrological significance, and evidence for a non-unique tectonic setting for Archaean crustal growth. Lithos 123, 21–36.

Moyen, J.-F. (2019). Archean granitoids: Classification, petrology, geochemistry and origin. Geological Society, London, Special Publications 489, 15–49.

Moyen, J.-F. & Martin, H. (2012). Forty years of TTG research. Lithos 148, 312–336.

Nagel, T. J., Hoffmann, J. E. & Münker, C. (2012). Generation of Eoarchean tonalite-trondhjemite-granodiorite series from thickened mafic arc crust. Geology 40, 375–378.

Nair, R. & Chacko, T. (2008). Role of oceanic plateaus in the initiation of subduction and origin of continental crust. Geology 36, 583–586.

O'Neil, J. & Carlson, R. W. (2017). Building Archean cratons from Hadean mafic crust. Science 355, 1199–1202.

O'Neil, J., Carlson, R. W., Paquette, J. L. & Francis, D. (2012). Formation age and metamorphic history of the Nuvvuagittuq Greenstone Belt. Precambrian Research 220–221, 23–44.

Ontario Geological Survey (2011). 1:250 000 scale bedrock geology of Ontario. Ontario Geolocial Survey Miscellaneous Release Data 126, Revision 1.

Palin, R. M., White, R. W. & Green, E. C. R. (2016). Partial melting of metabasic rocks and the generation of tonalitic–trondhjemitic–granodioritic (TTG) crust in the Archaean: Constraints from phase equilibrium modelling. Precambrian Research 287, 73–90.

Percival, J. A. (1983). High-grade metamorphism in the Chapleau-Foleyet Area, Ontario. American Mineralogist 68, 667–686.

Percival, J. A. (1990). A Field Guide to the Kapuskasing Uplift, a Cross Section through the Archean Superior Province. In: Salisbury, M. H. & Fountain, D. M. (eds) Exposed Cross-Sections of the Continental Crust. NATO ASI Series (Series C: Mathematical and Physical Sciences), vol 317. Dordrecht: Springer, 227–283.

Percival, J. A. & Krogh, T. E. (1983). U–Pb zircon geochronology of the Kapuskasing structural zone and vicinity in the Chapleau–Foleyet area, Ontario. Canadian Journal of Earth Sciences 20, 830–843.

Percival, J. A. & Peterman, Z. E. (1994). Rb–Sr biotite and whole-rock data from the Kapuskasing uplift and their bearing on the cooling and exhumation history. Canadian Journal of Earth Sciences 31, 1172–1181.

Percival, J. A., Skulski, T., Sanborn-Barrie, M., Stott, G. M., Leclair, A. D., Corkery, M. T. & Boily, M. (2012). Geology and Tectonic Evolution of the Superior Province, Canada. In: Percival, J. A., Cook, F. A. & Clowes, R. M. (eds) Tectonic Styles in Canada: The LITHOPROBE Perspective. Geological Association of Canada, Special Paper 49, 321–378.

Percival, J. A. & West, G. F. (1994). The Kapuskasing uplift: A geological and geophysical synthesis. Canadian Journal of Earth Sciences 31, 1256–1286.

Polat, A. (2009). The geochemistry of Neoarchean (ca. 2700 Ma) tholeiitic basalts, transitional to alkaline basalts, and gabbros, Wawa Subprovince, Canada: Implications for petrogenetic and geodynamic processes. Precambrian Research 168, 83–105.

Polat, A. (2012). Growth of Archean continental crust in oceanic island arcs. Geology 40, 383–384.

Polat, A. & Kerrich, R. (2001). Magnesian andesites, Nb-enriched basalt-andesites, and adakites from late-Archean 2.7 Ga Wawa greenstone belts, Superior Province, Canada: Implications for late Archean subduction zone petrogenetic processes. Contributions to Mineralogy and Petrology 141, 36–52.

Pourteau, A., Doucet, L. S., Blereau, E. R., Volante, S., Johnson, T. E., Collins, W. J., Li, Z. X. & Champion, D. C. (2020). TTG generation by fluid-fluxed crustal melting: Direct evidence from the Proterozoic Georgetown Inlier, NE Australia. Earth and Planetary Science Letters 550, 116548.

Qian, Q. & Hermann, J. (2013). Partial melting of lower crust at 10-15 kbar: Constraints on adakite and TTG formation. Contributions to Mineralogy and Petrology 165, 1195–1224.

Rapp, R., Watson, E. B. & Miller, C. F. (1991). Partial melting of amphibolite/eclogite and the origin of Archean trondhjemites and tonalites. Precambrian Research 51, 1–25.

Rollinson, H. (2021). Do all Archaean TTG rock compositions represent former melts? Precambrian Research 367, 106448.

Sage, R. P. (1994). Geology of the Michipicoten Greenstone Belt. Ontario Geological Survey Open File Report 5888.

Sage, R. P., Lightfoot, P. C. & Doherty, W. (1996). Geochemical characteristics of granitoid rocks from within the Archean Michipicoten Greenstone Belt, Wawa Subprovince, Superior Province, Canada: Implications for source regions and tectonic evolution. Precambrian Research 76, 155–190.

Semprich, J., Moreno, J. A. & Oliveira, E. P. (2015). Phase equilibria and trace element modeling of Archean sanukitoid melts. Precambrian Research, 122–138.

Shaw, D. M. (1970). Trace element fractionation during anatexis. Geochimica et Cosmochimica Acta 34, 237–243.

Smithies, R. H. et al. (2021). Oxygen isotopes trace the origins of Earth's earliest continental crust. Nature 592, 70–75.

Thurston, P. C. (2015). Igneous rock associations 19. Greenstone Belts and granite−greenstone terranes: Constraints on the nature of the Archean world. Geoscience Canada 42, 437–484.

Turek, A., Sage, R. P. & Van Schmus, W. R. (1992). Advances in the U-Pb zircon geochronology of the Michipicoten greenstone belt, Superior Province, Ontario. Canadian Journal of Earth Sciences 29, 1154–1165.

Turek, A., Smith, P. E. & Van Schmus, W. R. (1984). U-Pb zircon ages and the evolution of the Michipicoten plutonic-volcanic terrane of the Superior Province, Ontario. Canadian Journal of Earth Sciences 21, 457–464.

Valley, J. W. et al. (2005). 4.4 billion years of crustal maturation: Oxygen isotope ratios of magmatic zircon. Contributions to Mineralogy and Petrology 150, 561–580.

van Hunen, J. & Moyen, J.-F. (2012). Archean subduction: Fact or fiction? Annual Review of Earth and Planetary Sciences 40, 195–219.

Wyman, D. A. (2013). A critical assessment of Neoarchean “plume only” geodynamics: Evidence from the superior province. Precambrian Research 229, 3–19.

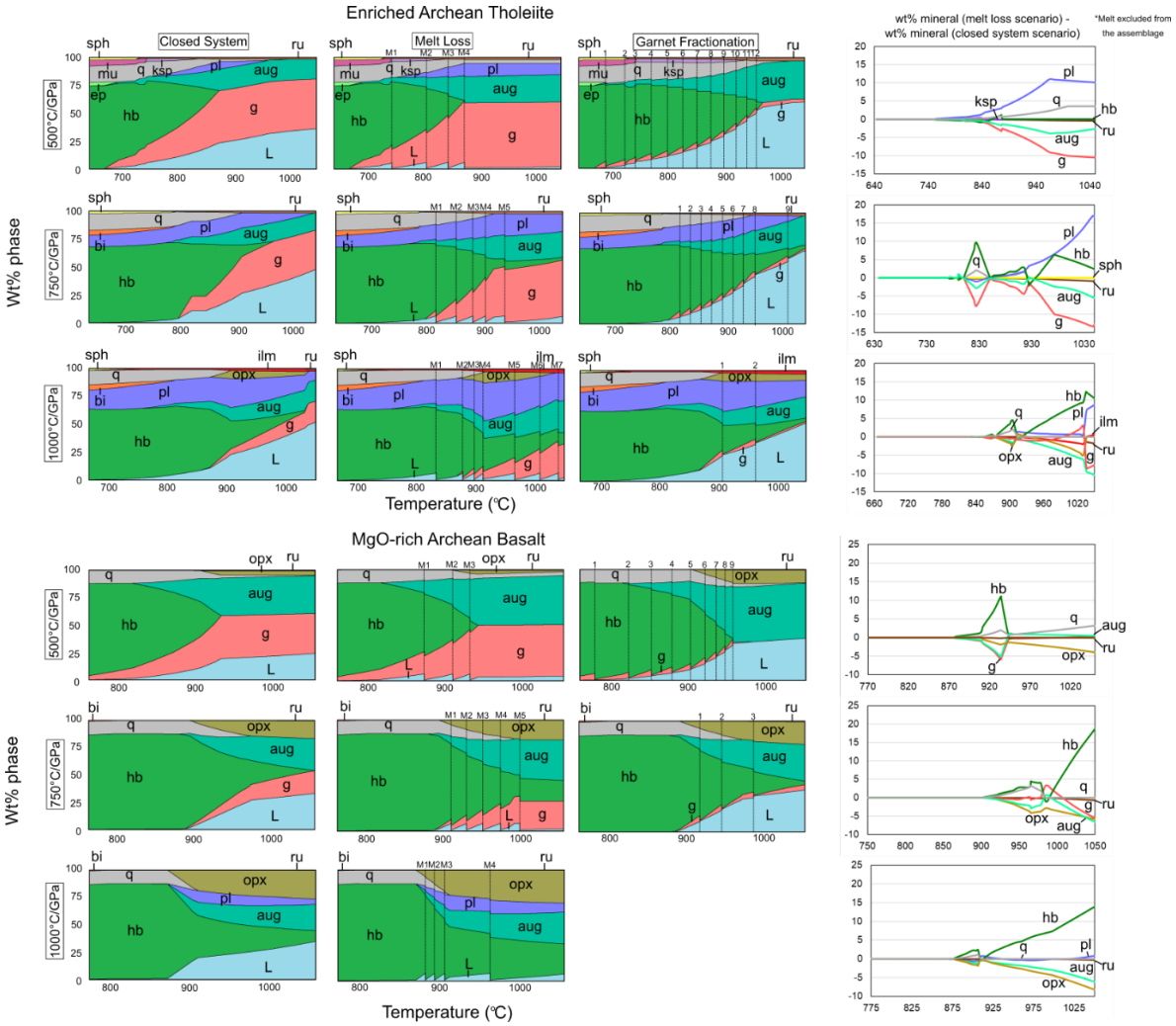
Wyman, D. (2018). Do cratons preserve evidence of stagnant lid tectonics? Geoscience Frontiers 9, 3–17.

Wyman, D. & Kerrich, R. (2010). Mantle plume - volcanic arc interaction: Consequences for magmatism, metallogeny, and cratonization in the Abitibi and Wawa subprovinces, Canada. Canadian Journal of Earth Sciences 47, 565–589.

Appendices

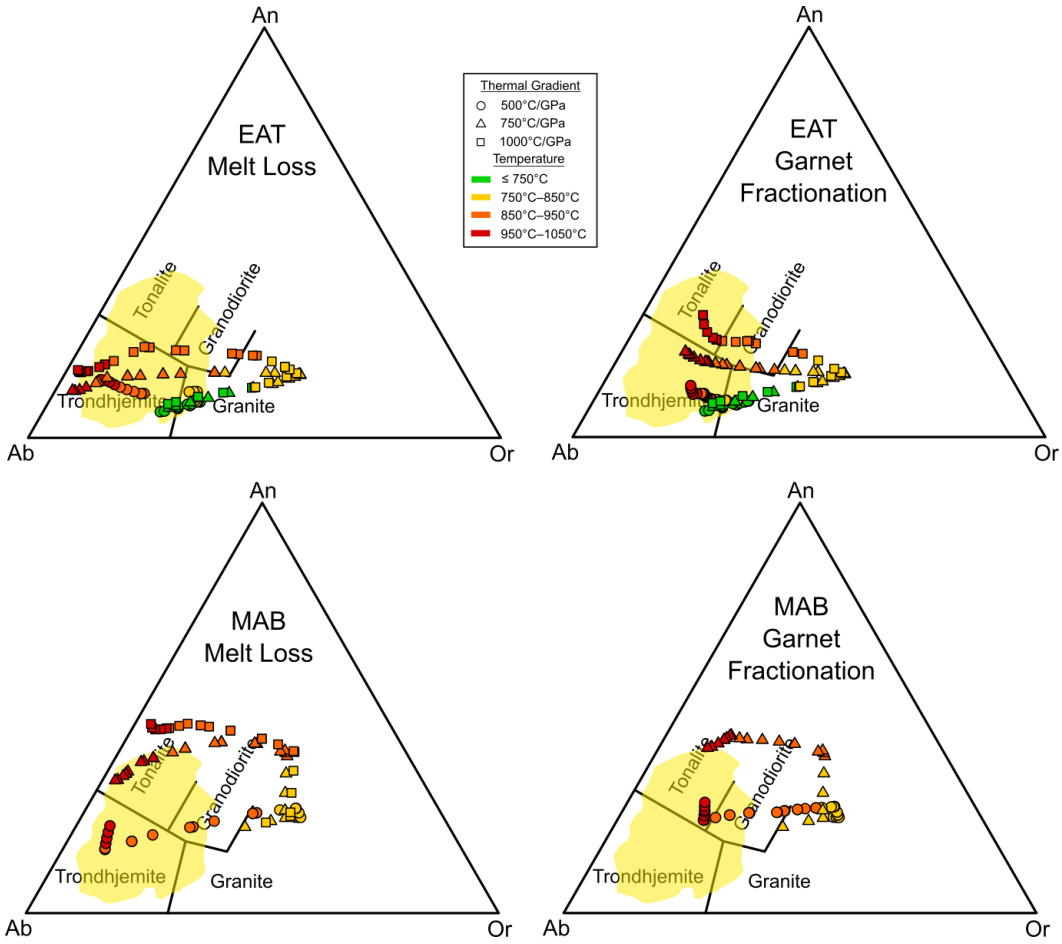
Appendix S1

Figure S1.1



Temperature–proportion diagrams illustrating the changes in phase weight proportions along the 500 °C/GPa, 750 °C/GPa, and 1000 °C/GPa thermal gradients in the closed system, melt loss, and garnet fractionation scenarios for the EAT and MAB bulk compositions.

Figure S1.2



Granitoid classification diagrams based on normative feldspar content after Barker (1979) showing classification of melts produced by the EAT and MAB compositions in the melt loss and garnet fractionation scenarios. Range of natural TTG compositions (after Johnson et al., 2019) is shown in yellow. EAT = enriched Archean tholeiite, MAB = MgO-rich basalt, An = anorthite, Ab = albite, Or = orthoclase.

Barker, F., 1979. Trondhjemite: definition, environment and hypotheses of origin. In: Barker, F. (Ed.), Trondhjemites, dacites, and related rocks. Amsterdam, Elsevier. Developments in Petrology 6, 1–12.

Johnson, T.E., Kirkland, C.L., Gardiner, N.J., Brown, M., Smithies, R.H., Santosh, M., 2019. Secular change in TTG compositions: implications for the evolution of Archaean geodynamics. Earth and Planetary Science Letters 505, 65–75. https://doi.org/10.1016/j.epsl.2018.10.022

Table S1.1

Compilation of whole rock geochemical data from Archean basalts based on the database of Condie et al. (2016).

Below is an excerpt from this table, full table is available in Appendix A Supplementary data as Supplementary Table 1 in:

Kendrick, J., and Yakymchuk, C. 2020. Garnet fractionation, progressive melt loss and bulk composition variations in anatectic metabasites: Complications for interpreting the geodynamic significance of TTGs. Geoscience Frontiers, 11: 745–763. doi:10.1016/j.gsf.2019.12.001.

		Wt%, from source														
Reference	Location	SiO_2	TiO_2	Al_2O_3	FeO_T/FeO	Fe_2O_{3T}/Fe_2O_3	MnO	MgO	CaO	Na_2O	K_2O	P_2O_5	H_2O	LOI	Total	Sum
Svetov et al 2004	Krasnaya Rechka Structure, Sumian, Karelia	49.98	1.26	15.94	6.1	7.82	0.16	5.5	2.8	5.46	0.5		0.26	4.41	100.19	100.19
Svetov et al 2004	Krasnaya Rechka Structure, Sumian, Karelia	50.72	1.24	16.2	7.06	3.05	0.17	6.7	3.08	4.26	0.94		0.18	6	99.6	99.6
Svetov et al 2004	Krasnaya Rechka Structure, Sumian, Karelia	53.26	1.02	14.29	7.29	6.3	0.13	6.63	1.54	3.18	1.41		0.26	4.48	99.79	99.79
Svetov et al 2004	Krasnaya Rechka Structure, Sumian, Karelia	49.52	0.88	12.27	10.34	2.81	0.21	9.08	7.43	1	3.29		0.03	2.7	99.56	99.56
Svetov et al 2004	Krasnaya Rechka Structure, Sumian, Karelia	56.06	0.94	12.76	8.69	1.94	0.18	5.7	5.54	4.11	1.31		0.13	2.16	99.52	99.52
Svetov et al 2004	Krasnaya Rechka Structure, Sumian, Karelia	54.16	0.9	12.83	4.89	5.17	0.19	7.06	7.15	3.46	2.08		0.1	1.56	99.55	99.55
Svetov et al 2004	Krasnaya Rechka Structure, Sumian, Karelia	53.6	0.83	12.31	8.74	1.19	0.2	8.47	7.29	3.88	0.6		0.1	2.38	99.59	99.59
Svetov et al 2004	Krasnaya Rechka Structure, Sumian, Karelia	56.04	0.92	12.83	8.05	1.06	0.17	6.6	6.1	4.82	1.02		0.13	1.87	99.61	99.61
Svetov et al 2004	Krasnaya Rechka Structure, Sumian, Karelia	55.3	0.93	14.14	8.12	1.38	0.16	5.29	6.24	3.57	2.6		0.08	1.85	99.66	99.66
Svetov et al 2004	Krasnaya Rechka Structure, Sumian, Karelia	55.22	1	15.45	7.26	1.94	0.15	4.18	6.1	5.4	0.6		0.13	2.44	99.87	99.87
Svetov et al 2004	Krasnaya Rechka Structure, Sumian, Karelia	51.58	1.12	14.14	10.66	1.96	0.2	5.7	6.24	3.43	1.4		0.13	2.97	99.53	99.53
Svetov et al 2004	Krasnaya Rechka Structure, Sumian, Karelia	54.5	1.03	13.62	9.94	1.26	0.17	5.44	5.33	4.88	1		0.12	2.35	99.64	99.64
Svetov et al 2004	Krasnaya Rechka Structure, Sumian, Karelia	51.58	1.06	15.45	9.7	1.42	0.22	5.56	5.26	4.36	2.1		0.15	3.15	100.01	100.01
Svetov et al 2004	Krasnaya Rechka Structure, Sumian, Karelia	49.4	1.14	16.74	11.25	1.39	0.23	5.29	4.7	4.33	1.72		0.16	3.63	99.98	99.98
Svetov et al 2004	Krasnaya Rechka Structure, Sumian, Karelia	54.78	1.07	14.25	9.33	1.82	0.19	4.83	4.56	4.18	1.72		0.21	2.65	99.59	99.59
Svetov et al 2004	Krasnaya Rechka Structure, Sumian, Karelia	56.92	0.84	13.87	7.41	2.97	0.17	4.6	5.18	3.5	1.9		0.18	2.35	99.89	99.89
Svetov et al 2004	Krasnaya Rechka Structure, Sumian, Karelia	50.26	1.05	15.03	10.77	1.73	0.23	6.07	4.76	4.03	1.26		0.26	4.36	99.81	99.81
Svetov et al 2004	Krasnaya Rechka Structure, Sumian, Karelia	46.06	1.1	16.05	12.21	1.93	0.26	6.95	4.76	4.08	1.02		0.3	5.41	100.13	100.13

Table S1.2

Calculated trace element compositions (Sr, Y, La, Yb, Nb, and Ta, in μg/g) of modelled melts produced in the closed system, melt loss, and garnet fractionation scenarios by each bulk composition along each thermal gradient.

This content is available in Appendix A Supplementary data as Supplementary Table 2 in:

Kendrick, J., and Yakymchuk, C. 2020. Garnet fractionation, progressive melt loss and bulk composition variations in anatectic metabasites: Complications for interpreting the geodynamic significance of TTGs. Geoscience Frontiers, 11: 745–763. doi:10.1016/j.gsf.2019.12.001.

Below is an excerpt from this table:

DAT 500 closed

P (kbar)	T (°C)	melt Sr	melt Y	Sr/Y	melt La	melt Yb	La/Yb	melt Nb	melt Ta	Nb/Ta	norm La	norm Yb	La_N/Yb_N
13.24	662.60	190	6.52	29.2	7.08	0.64	7.51	20.94	0.68	30.92	29.52	4.00	7.37
13.50	675.00	204	5.93	34.3	7.58	0.53	9.72	21.37	0.69	30.81	31.57	3.31	9.54
14.00	700.00	232	5.07	45.8	8.64	0.40	14.68	22.08	0.72	30.48	36.00	2.50	14.40
14.50	725.00	265	4.44	59.7	9.85	0.32	20.70	22.55	0.75	30.03	41.06	2.02	20.31
15.00	750.00	305	3.95	77.3	11.29	0.27	28.29	22.75	0.77	29.45	47.06	1.70	27.76
15.50	775.00	356	3.53	101	13.07	0.23	38.27	22.62	0.79	28.73	54.46	1.45	37.56
15.62	781.34	371	3.43	108	13.60	0.22	41.33	22.52	0.79	28.52	56.65	1.40	40.56
15.90	795.25	373	3.31	113	13.53	0.21	43.21	22.27	0.80	27.99	56.39	1.33	42.40
15.96	797.58	408	3.27	125	15.78	0.21	51.52	13.54	0.51	26.49	65.74	1.30	50.56
15.96	798.68	405	3.26	125	16.76	0.21	55.19	11.83	0.45	26.18	69.85	1.29	54.16
16.00	800.00	402	3.24	124.	16.76	0.21	55.54	11.78	0.45	26.15	69.85	1.28	54.50
16.50	825.00	314	2.99	105	16.52	0.18	60.77	10.71	0.42	25.47	68.84	1.15	59.64
17.00	850.00	253	2.74	92.3	16.11	0.16	66.35	9.38	0.38	24.83	67.14	1.03	65.11
17.50	875.00	208	2.48	83.8	15.49	0.15	72.32	7.87	0.32	24.28	64.53	0.91	70.98
17.54	877.37	204	2.45	83.1	15.41	0.14	72.86	7.72	0.32	24.23	64.20	0.90	71.50
18.00	900.00	246	2.44	101	14.76	0.14	70.16	7.58	0.31	24.18	61.52	0.89	68.85
18.50	925.00	327	2.42	135	14.02	0.14	67.01	7.41	0.31	24.11	58.43	0.89	65.76
18.72	935.68	387	2.42	160	13.70	0.14	65.66	7.33	0.30	24.08	57.09	0.89	64.43
19.00	950.00	377	2.43	155	13.38	0.14	63.77	7.27	0.30	24.02	55.73	0.89	62.59
19.50	975.00	361	2.45	147	12.82	0.14	60.54	7.15	0.30	23.90	53.42	0.90	59.41
20.00	1000.00	345	2.48	140	12.27	0.15	57.27	7.02	0.30	23.77	51.11	0.91	56.21
20.50	1025.00	330	2.51	131	11.71	0.15	53.95	6.89	0.29	23.64	48.80	0.92	52.94
20.95	1047.83	315	2.54	124	11.19	0.15	50.80	6.76	0.29	23.51	46.64	0.94	49.86
21.00	1050.00	314	2.54	123	11.17	0.15	50.66	6.75	0.29	23.51	46.55	0.94	49.71

Appendix S2

Appendix S2.1 Detailed Methodology

Whole-rock geochemical analyses

Thirty-six new analyses of felsic intrusive rocks are presented in this study. After weathered surfaces and cross-cutting veins were removed from the rock samples using a rock saw, the majority (34 of 36 total) were sent to the Ontario Geological Survey Geoscience Laboratories (Geolabs) for whole-rock lithogeochemical analysis. The rocks were pulverized using an agate mill. Major elements (Si, Ti, Al, Cr, Fe, Mn, Mg, Ca, Na, K, P; Table S2.1) and a set of trace elements (not reported here) were analysed by X-ray fluorescence (XRF). For XRF, samples are heated to 105 °C under nitrogen atmosphere and 1000°C under oxygen atmosphere and then fused with a borate flux. Samples were subsequently analysed using Malvern-Panalytical Axios Advanced WD-XRF spectrometers. Trace elements (including Ba, Be, Bi, Cd, Ce, Co, Cr, Cs, Cu, Dy, Er, Eu, Ga, Gd, Hf, Ho, In, La, Li, Lu, Mo, Nb, Nd, Ni, Pb, Pr, Rb, Sb, Sc, Sm, Sn, Sr, Ta, Tb, Th, Ti, Tl, Tm, U, V, W, Y, Yb, Zn, Zr; Table S2.1) were analysed by inductively coupled plasma mass spectrometry (ICP-MS). For ICP-MS, samples were first digested using a multi-acid solution in a closed vessel, before analysis using a Thermo Scientific iCAP-Q ICP-MS. The concentration of ferrous iron was measured using potentiometric titration with a permanganate solution standard. Water content was determined by heating samples to 105 °C to release free water and then 1000 °C for crystalline water; the concentration of water was subsequently measured by infrared absorption. Data quality was monitored by insertion of sample duplicates, internal reference materials and blanks.

One batch of samples (2 of 36 total) was sent to Activation Laboratories in Ontario for lithogeochemical analysis. Samples were crushed by a steel mill, fused using lithium metaborate/tetraborate, and digested in a weak nitric acid solution. Major elements (Si, Al, Fe, Mn, Mg, Ca, Na, K, Ti, P; Table S2.1) were analysed by ICP-optical emission spectrometry using a Varian Vista 735 ICP. Trace elements (Sc, Be, V, Cr, Ca, Ni, Cu, Zn, Ga, Ge, As, Rb, Sr, Y, Zr, Nb, Mo, Ag, In, Sn, Sb, Cs, Ba, La, Ce, Pr, Nd, Sm, Eu, Gd, Tb, Dy, Ho, Er, Tm, Yb, Lu, Hf, Ta, W, Tl, Pb, Bi, Th, U; Table S2.1) were measured by ICP-MS using a Perkin Elmer Sciex ELAN 6100 ICPMS. The concentration of ferrous iron was obtained by titration.

Mineral chemical analysis

Feldspar compositions (Table S2.2) were obtained by electron probe microanalysis (EPMA) at the Ontario Geological Survey Geolabs using a Cameca SX-100 Electron Probe Micro Analyser.

Minerals were analysed using an accelerating voltage of 20 kV and beam current of 20 nA with an 8-micron rastered beam, and on-peak counting times were 10 s to 15 s. The data were acquired by wavelength-dispersive spectroscopy.

Concentrations of trace elements in plagioclase (Table S2.3) were measured by laser ablation ICP-MS at the Metal Isotope Geochemistry Laboratory at University of Waterloo. A 193 nm Analyte G2 laser ablation system coupled to an Agilent 8800 quadrupole ICP-MS were used for in situ analysis of plagioclase in standard size polished thin sections. A suite of elements (^{29}Si, ^{31}P, ^{39}K, ^{43}Ca, ^{47}Ti, ^{85}Rb, ^{88}Sr, ^{89}Y, ^{90}Zr, ^{93}Nb, ^{137}Ba, ^{139}La, ^{140}Ce, ^{141}Pr, ^{146}Nd, ^{147}Sm, ^{153}Eu, ^{157}Gd, ^{159}Tb, ^{163}Dy, ^{165}Ho, ^{166}Er, ^{169}Tm, ^{172}Yb, ^{175}Lu, ^{181}Ta, ^{208}Pb, ^{232}Th, ^{238}U) was measured during line scans with laser beam parameters of 110 µm spot diameter, 8 Hz, 4.50 J/cm^2, and of 3 µm/s scan speed. Groups of three plagioclase line scans (~30 minutes) were bracketed by analysis of reference materials, including NIST-610 (primary standard), NIST-612, and BHVO-2G (secondary standards) at the same conditions with a reduced beam diameter of 65 µm. The data were processed using Iolite v4.4.5 (Paton et al., 2011) with internal standardization using ^{29}Si based on the average SiO_2 content of plagioclase in each sample from EPMA analyses. Segments of the line analyses were chosen for processing based on homogeneity and apparent lack of mineral inclusions, however minor spatial variations in LREE concentrations were commonly present and could not be completely avoided. The limit of detection was calculated using the method of Howell et al. (2010). Measured concentrations of REE in NIST-612 and BHVO-2G were within 6% and 8% of accepted values respectively, except for overestimation of Lu in BHVO-2G by ~20%. Measured values from secondary reference materials are available in Table S2.3.

Calculation of the parental TTG composition for modeling

The modeled TTG composition (Table S2.4) was calculated by combining the median values for group 1 and 2 TTGs in proportions of 40% and 60% respectively to produce a theoretical parental melt composition with a neutral (1.00) Eu anomaly relative to chondrite-normalized REE values. Group 3 was not incorporated in the calculation because it constitutes a very minor volumetric component of the overall TTG population in the Wawa Gneiss Domain. Though multiple TTG parental melts may have existed in the region, we have elected to calculate a single, representative parental melt to simplify modeling and to allow the effect of fractionation and accumulation to be shown clearly. The approach of combining TTG group compositions was taken for three main reasons, 1) petrographic evidence supports the hypothesis that the groups represent cumulates and complementary melt-rich domains; 2) an insignificant Eu anomaly has classically been included in

the geochemical definition of TTG (Moyen and Martin, 2012); and 3) the geochemical characteristics specific to the TTGs of the Wawa Gneiss Domain are incorporated into the parental melt. Other approaches for estimating an unmodified TTG composition, such as selecting a published melt composition obtained from basalt partial melting experiments (Rapp et al., 1991), require an assumed source composition that may not be appropriate for the Kapuskasing Uplift. For modeling, the concentration of H_2O and Fe_2O_3/FeO ratio of the parental melt composition were calculated from the measured values of the TTG samples, combining both the crystalline moisture and free moisture measurements for H_2O. We recognize the limitations of this approach, as these compositional parameters may be affected by post-crystallization processes; measures were taken in sample preparation to minimize inclusion of rock that underwent chemical changes after complete crystallization (see Whole-rock geochemical analyses).

Phase equilibrium modeling

Phase equilibrium modeling was done in the Na_2O–CaO–K_2O–FeO–MgO–Al_2O_3–SiO_2–H_2O–TiO_2–Fe_2O_3–Cr_2O_3 chemical system using the THERMOCALC software package, including THERMOCALC version 3.50 (Dec 2019), thermodynamic dataset version 6.33 (June 2017) of Holland and Powell (2011) and the igneous set of activity–composition models from Holland et al. (2018) (updated Dec 2019). Individual models are as follows: silicate melt (Holland et al., 2018); plagioclase (Holland and Powell, 2003); amphibole (Green et al., 2016); biotite (White et al., 2014); clinopyroxene (Holland et al., 2018); epidote (Holland and Powell, 2011); ilmenite (White et al., 2000). Quartz and water were modeled as pure phases.

A phase diagram (Fig. S2.1) was constructed from 0.4 GPa to 0.8 GPa and 400 °C to 1300 °C, with modeled phase assemblage boundaries calculated from the solidus (620 °C to 690 °C) to the liquidus (1150 °C to 1160 °C). The modal proportions of phases were calculated at 0.6 GPa from ~908 °C at 40 mol% plagioclase crystallization to ~1119 °C at 5 mol% plagioclase crystallization, with data collected from the model at 10 mol%, 15 mol%, 20 mol%, 25 mol%, 30 mol%, and 35 mol% plagioclase and at the calculated quartz-in and ilmenite-in boundaries. Further modeling below ~908 °C was not done, as amphibole is predicted to become stable beyond 40 mol% plagioclase crystallization (Fig. S2.1) and the interpreted cumulates (group 3) are predominantly composed of plagioclase and quartz, only rarely with minor amphibole. The anorthite content of model plagioclase, as calculated by THERMOCALC, was also collected at each step.

Melt trace element modeling

Melt trace element modeling was done by a mass balance approach using the batch melting equation (Shaw, 1970):

$$\frac{C_L}{C_o} = \frac{1}{D(1-F)+F}$$

where C_L is the concentration of an element in the melt, C_o is the concentration of the element in the system, D is the bulk distribution coefficient, and F is the melt fraction. The value for C_o for each element is the concentration calculated for the parental TTG composition (Table S2.4). For D, partition coefficients were calculated for plagioclase (Table S2.5) based on parameterizations developed by Bédard (2006). Partition coefficients for ilmenite are from Ewart and Griffin (1994) based on data from natural high-silica rhyolites. In our modeling, quartz was assumed to have no effect on the trace elements of interest.

Calculations using TTG compositions (natural samples and modeled melt)

The normative anorthite, albite, and orthoclase contents (Fig. 3.2) of the natural TTG samples were calculated using the GeoChemical Data toolkit (GCDkit) software Janoušek et al. (2006), the compositional fields of the granitoids are after Barker (1979). Trace element compositions of natural and modeled TTGs are normalized to the chondrite values of McDonough and Sun (1995) for spider diagrams and the calculation of the europium anomaly, which was done using the equation:

$$\frac{Eu}{Eu^*} = \frac{Eu_N}{\sqrt{Sm_N \times Gd_N}}$$

Barker, F., 1979, Trondhjemite: Definition, environment and hypotheses of origin, *in* Developments in Petrology, Elsevier, v. 6, p. 1–12, doi:10.1016/B978-0-444-41765-7.50006-X.

Bédard, J.H., 2006, Trace element partitioning in plagioclase feldspar: Geochimica et Cosmochimica Acta, v. 70, p. 3717–3742, doi:10.1016/j.gca.2006.05.003.

Ewart, A., and Griffin, W.L., 1994, Application of proton-microprobe data to trace-element partitioning in volcanic rocks: Chemical Geology, v. 117, p. 251–284, doi:10.1016/0009-2541(94)90131-7.

Green, E.C.R., White, R.W., Diener, J.F.A., Powell, R., Holland, T.J.B., and Palin, R.M., 2016, Activity–composition relations for the calculation of partial melting equilibria in metabasic rocks: Journal of Metamorphic Geology, v. 34, p. 845–869, doi:10.1111/jmg.12211.

Holland, T., and Powell, R., 2003, Activity–composition relations for phases in petrological calculations: An asymmetric multicomponent formulation: Contributions to Mineralogy and Petrology, v. 145, p. 492–501, doi:10.1007/s00410-003-0464-z.

Holland, T.J.B., and Powell, R., 2011, An improved and extended internally consistent thermodynamic dataset for phases of petrological interest, involving a new equation of state for solids: Journal of Metamorphic Geology, v. 29, p. 333–383, doi:10.1111/j.1525-1314.2010.00923.x.

Holland, T.J.B., Green, E.C.R., and Powell, R., 2018, Melting of peridotites through to granites: A simple thermodynamic model in the system KNCFMASHTOCr: Journal of Petrology, v. 59, p. 881–900, doi:10.1093/petrology/egy048.

Howell, D., Griffin, W.L., Pearson, N.J., Powell, W., Wieland, P., and O'Reilly, S.Y., 2013, Trace element partitioning in mixed-habit diamonds: Chemical Geology, v. 355, p. 134–143, doi:10.1016/j.chemgeo.2013.07.013.

Janoušek, V., Farrow, C.M., and Erban, V., 2006, Interpretation of whole-rock geochemical data in igneous geochemistry: Introducing Geochemical Data Toolkit (GCDkit): Journal of Petrology, v. 47, p. 1255–1259, doi:10.1093/petrology/egl013.

McDonough, W.F., and Sun, S.-s., 1995, The composition of the Earth: Chemical Geology, v. 120, p. 223–253, doi:10.1016/0009-2541(94)00140-4.

Moyen, J.-F., and Martin, H., 2012, Forty years of TTG research: Lithos, v. 148, p. 312–336, doi:10.1016/j.lithos.2012.06.010.

Paton, C., Hellstrom, J., Paul, B., Woodhead, J., and Hergt, J., 2011, Iolite: Freeware for the visualisation and processing of mass spectrometric data: Journal of Analytical Atomic Spectrometry, v. 26, 2508, doi:10.1039/c1ja10172b.

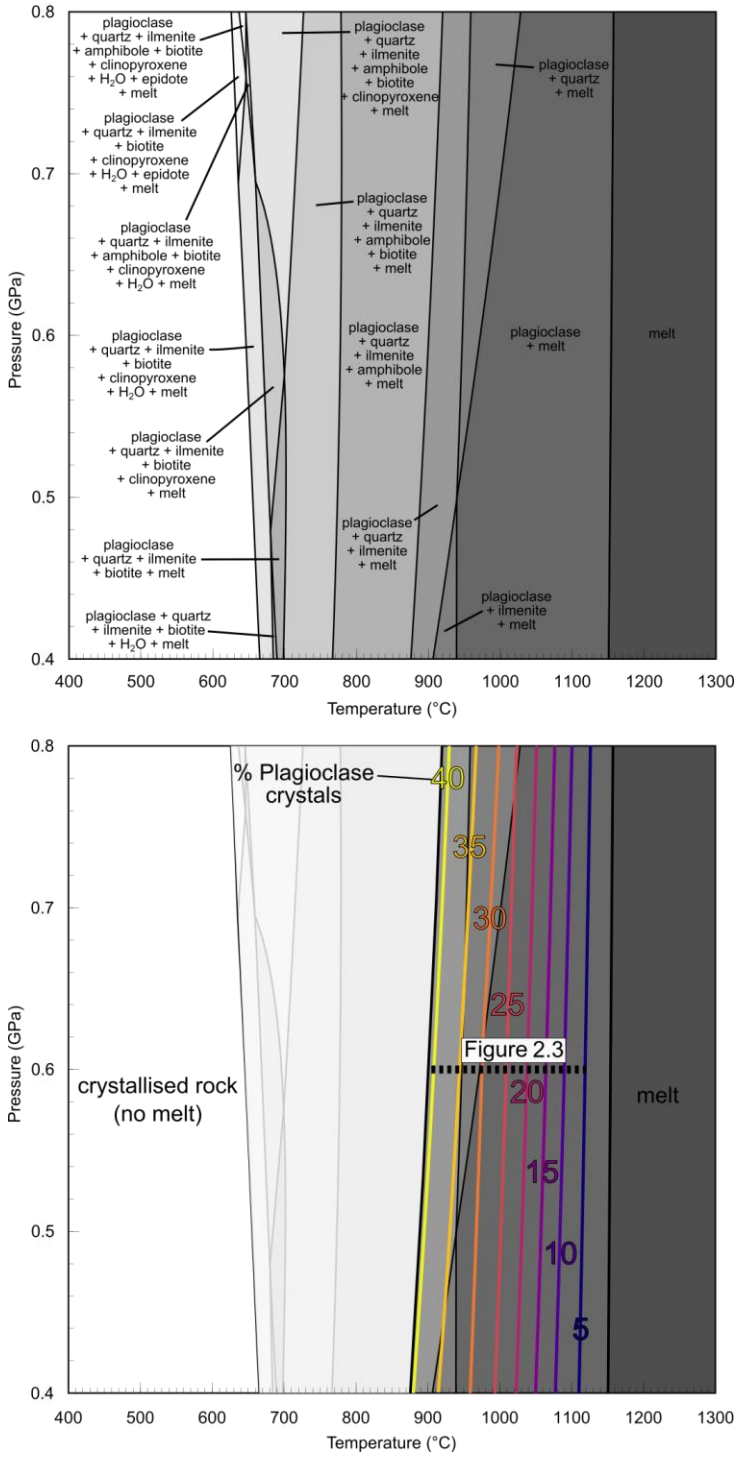
Rapp, R., Watson, E.B., and Miller, C.F., 1991, Partial melting of amphibolite/eclogite and the origin of Archean trondhjemites and tonalites: Precambrian Research, v. 51, p. 1–25, doi:10.1016/0301-9268(91)90092-O

Shaw, D.M., 1970, Trace element fractionation during anatexis: Geochimica et Cosmochimica Acta, v. 34, p. 237–243, doi:10.1016/0016-7037(70)90009-8.

White, R.W., Powell, R., Holland, T.J.B., and Worley, B.A., 2000, The effect of TiO_2 and Fe_2O_3 on metapelitic assemblages at greenschist and amphibolite facies conditions: Mineral equilibria calculations in the system K_2O–FeO–MgO–Al_2O_3–SiO_2–H_2O–TiO_2–Fe_2O_3: Journal of Metamorphic Geology, v. 18, p. 497–511, doi:10.1046/j.1525-1314.2000.00269.x.

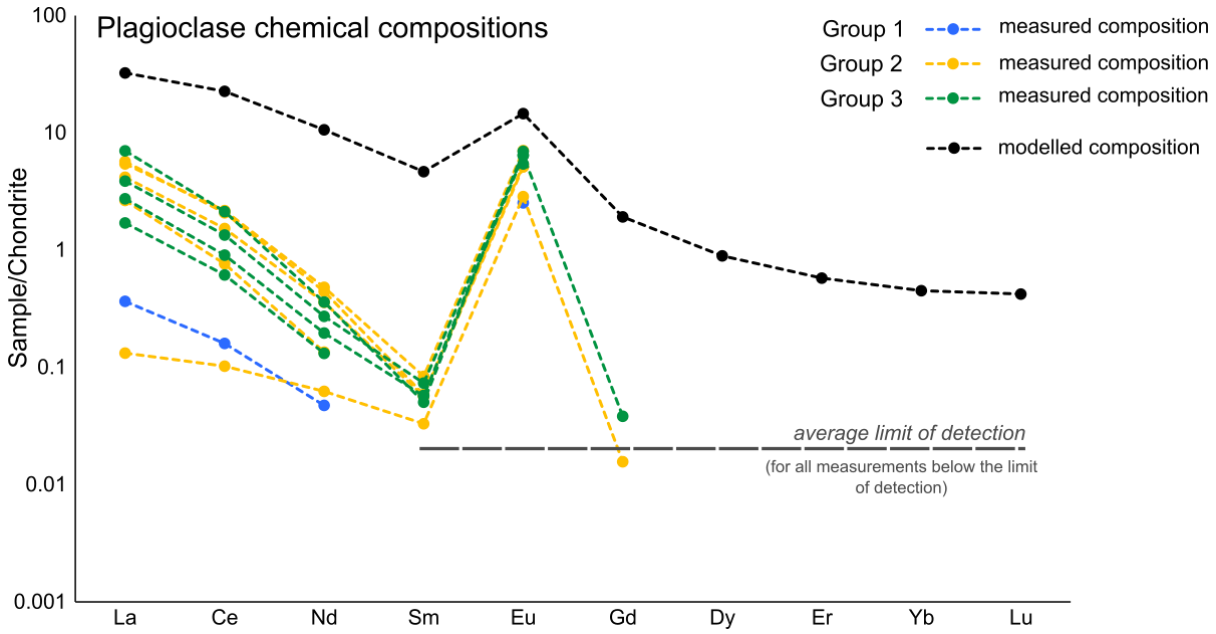
White, R.W., Powell, R., Holland, T.J.B., Johnson, T.E., and Green, E.C.R., 2014, New mineral activity–composition relations for thermodynamic calculations in metapelitic systems: Journal of Metamorphic Geology, v. 32, p. 261–286, doi:10.1111/jmg.12071.

Figure S2.1



Phase diagram of the estimated parental TTG composition.

Figure S2.2



Chondrite-normalized REE trends measured in plagioclase in TTGs. Limit of detection is shown where elemental abundance was too low to measure.

Table S2.1

Whole-rock compositions of Wawa Gneiss Domain TTGs

Sample	Datum	Latitude	Longitude	SiO_2	TiO_2	Al_2O_3	Fe_2O_3	Cr_2O_3	MnO
Group 1				Major elements in wt.%					
18JK04A	WGS84	47.848735	-83.735641	66.95	0.46	15.69	4.11	0.012	0.068
18JK09A	WGS84	47.869557	-83.570475	68.69	0.28	16.65	2.83	0.009	0.04
*18JK11-A	WGS84	47.949322	-84.114086	66.25	0.584	15.69	5.26	n/a	0.064
*18JK12-A	WGS84	47.969014	-84.106142	71.57	0.331	14.75	3.16	n/a	0.051
18JK13A	WGS84	48.010572	-84.116655	72.78	0.27	14.67	2.45	0.008	0.037
18JK23A	WGS84	47.864015	-83.861213	70.34	0.28	15.58	2.65	0.007	0.046
18JK27A	WGS84	48.038422	-84.543392	75.52	0.1	13.86	1.41	0.009	0.04
18JK30A	WGS84	47.959365	-84.259835	74.84	0.17	14.25	1.26	0.009	0.016
19JK02	WGS84	47.887095	-83.454814	68.43	0.25	17.31	1.89	0.006	0.027
19JK03	WGS84	47.956662	-83.434177	64.34	0.48	16.25	3.97	0.009	0.062
Group 2									
18JK03A	WGS84	47.848368	-83.742534	71.01	0.26	15.83	2.2	0.007	0.026
18JK07A	WGS84	47.792634	-83.533751	66.74	0.44	16.23	3.92	0.008	0.05
18JK08A	WGS84	47.935618	-83.651791	71.77	0.23	15.67	1.75	0.01	0.024
18JK19A	WGS84	48.16282	-84.057254	64.24	0.63	16.51	5	0.007	0.066
18JK24A	WGS84	47.869943	-83.944452	71.95	0.3	15.71	2	0.007	0.027
18JK25A	WGS84	47.894398	-84.04136	71.76	0.27	15.9	1.79	0.008	0.021
18JK29A	WGS84	47.944221	-84.148235	72.48	0.22	15.62	1.8	0.008	0.021
18JK32A	WGS84	47.93891	-84.498985	73.14	0.21	15.09	1.79	0.01	0.028
18JK35A	WGS84	47.981543	-83.92826	70.99	0.26	15.87	2.42	0.007	0.043
18JK36A	WGS84	47.967404	-83.829407	71.55	0.28	15.95	2.55	0.007	0.032
18JK38A	WGS84	47.906016	-83.78956	75.74	0.1	14.62	1.06	0.005	0.016
18JK52	WGS84	47.68329	-83.29956	68.18	0.46	16.39	3.98	0.004	0.041
18JK53	WGS84	47.70449	-83.31361	65.03	0.47	17.61	3.77	0.005	0.033
19JK01	WGS84	47.768898	-83.37602	67.5	0.41	16.89	2.79	0.005	0.027
19JK18	WGS84	47.845696	-83.33422	70.61	0.36	14.9	3.21	0.005	0.038
19JK21	WGS84	48.062667	-83.40209	65.19	0.56	16.5	4.04	0.012	0.047
19JK32A	WGS84	48.199117	-84.079013	71.81	0.2	15.47	1.51	0.005	0.021
Group 3									
18JK24C	WGS84	47.869943	-83.944452	74.76	0.02	16.25	0.23	0.006	0.005
18JK28B	WGS84	47.857237	-83.801506	75.5	0.04	14.95	0.48	0.006	0.009
18JK31B	WGS84	47.963479	-84.332022	77.66	0.01	14.18	0.29	0.006	0.005
19JK34	WGS84	47.75732	-83.41483	63.27	0.14	21.22	1.25	0.004	0.014
19JK35B	WGS84	47.774025	-83.465713	71.88	0.13	16.22	0.96	0.004	0.011
19JK36A	WGS84	47.77607	-83.506466	72.93	0.18	14.41	1.99	0.005	0.036
19JK46	WGS84	47.816284	-83.571851	72.55	0.06	16.77	0.54	0.008	0.008
19JK47	WGS84	47.820824	-83.669976	67.98	0.15	19.41	1.05	0.003	0.013
19JK48B	WGS84	47.848664	-83.729803	73.355	0.055	16.34	0.41	0.003	0.007

Table S2.1 (continued)

Sample	MgO	CaO	Na_2O	K_2O	P_2O_5	Total	Total LOI 1000	Crystalline Moisture
Group 1								
18JK04A	1.6	4.369	4.34	1.25	0.144	98.99	1.2	1.4
18JK09A	1.14	3.769	5.18	1.6	0.105	100.29	0.7	1.06
*18JK11-A	1.5	4.8	4.25	1.17	0.16	99.73	0.69	n/a
*18JK12-A	0.73	3.1	4.85	1.59	0.1	100.23	0.37	n/a
18JK13A	0.73	2.786	4.19	2.07	0.087	100.08	0.66	0.87
18JK23A	0.96	3.171	4.75	2.09	0.079	99.95	0.69	0.93
18JK27A	0.21	1.71	4.76	2.16	0.019	99.80	0.77	0.82
18JK30A	0.51	1.094	5.38	2.34	0.053	99.92	0.65	0.93
19JK02	0.74	3.239	5.49	2.24	0.075	99.70	0.7	0.88
19JK03	2.3	4.649	5.19	1.53	0.256	99.04	1.23	1.01
Group 2								
18JK03A	0.69	3.003	5.17	1.4	0.076	99.67	0.62	0.71
18JK07A	1.46	4.421	4.71	1.26	0.091	99.33	0.75	0.83
18JK08A	0.58	2.889	5.33	1.13	0.076	99.46	0.75	0.84
18JK19A	1.79	5.309	4.42	0.74	0.164	98.88	1.18	1.33
18JK24A	0.69	2.83	5.3	1.24	0.084	100.14	0.78	1.1
18JK25A	0.65	2.706	5.63	1.21	0.079	100.02	0.7	0.96
18JK29A	0.49	2.305	5.4	1.71	0.064	100.12	0.56	0.89
18JK32A	0.45	2.164	5.24	2	0.056	100.18	0.35	0.75
18JK35A	1.24	1.729	5.11	1.96	0.068	99.70	1.3	1.49
18JK36A	0.83	2.292	5.78	1.03	0.091	100.39	0.89	1.36
18JK38A	0.27	2.06	4.82	2.04	0.014	100.75	0.32	0.76
18JK52	1.24	3.813	4.9	1.32	0.156	100.48	0.56	0.88
18JK53	1.33	4.721	5.73	0.94	0.133	99.77	0.86	1.11
19JK01	1.11	3.731	5.25	1.53	0.116	99.36	0.8	0.73
19JK18	0.96	3.275	4.64	1.17	0.083	99.25	0.71	0.88
19JK21	2.21	4.511	4.56	1.64	0.238	99.51	0.68	0.8
19JK32A	0.61	2.367	5.73	2.01	0.067	99.80	0.44	0.82
Group 3								
18JK24C	0.08	3.139	5.96	0.46	0.008	100.92	0.41	0.71
18JK28B	0.15	2.712	4.7	1.83	0.003	100.38	0.49	0.71
18JK31B	0.07	2.247	5.23	0.93	0.002	100.63	0.25	0.67
19JK34	0.49	5.136	6.64	0.89	0.044	99.10	0.93	0.81
19JK35B	0.37	3.303	6	0.53	0.006	99.41	0.8	0.8
19JK36A	1.08	4.868	4.09	0.48	0.006	100.08	0.4	0.63
19JK46	0.19	3.501	5.95	0.61	0.008	100.20	0.42	0.64
19JK47	0.42	4.504	6.26	0.75	0.038	100.58	0.32	0.66
19JK48B	0.17	3.155	5.84	0.77	0.014	100.12	0.32	0.66

Table S2.1 (continued)

Sample	Free Moisture	Ba	Be	Bi	Cd	Ce	Co	Cr	Cs	Cu	Dy
Group 1		Trace elements in µg/g									
18JK04A	0.68	268.6	1.14	<0.47	0.055	58.97	11.26	74	0.756	32.7	2.916
18JK09A	0.67	542.6	1.25	<0.47	0.039	67.54	7.13	57	1.409	6.5	1.512
*18JK11-A	n/a	387	< 1	< 0.1		49.1	11	110	1.7	< 10	2.26
*18JK12-A	n/a	499	1	< 0.1		37.1	5	80	4.1	< 10	1.55
18JK13A	0.67	863.7	1.17	<0.47	0.029	87.49	5.03	47	4.694	11.3	1.942
18JK23A	0.68	539.2	1.15	<0.47	0.048	37.4	6.81	44	3.258	16.1	1.433
18JK27A	0.65	638	1.6	<0.47	0.033	29.24	1.42	59	0.99	1.7	1.727
18JK30A	0.67	557.2	1.37	<0.47	0.016	78.63	2.47	67	1.955	1.8	1.238
19JK02	0.57	559.9	1.21	<0.47	0.016	52.16	5.65	27	1.106	17.3	0.901
19JK03	0.59	462.9	1.39	<0.47	0.054	76.09	13.59	63	1.146	3.3	2.598
Group 2											
18JK03A	0.65	452.6	0.87	<0.47	0.03	35.99	4.43	44	1.565	10	0.442
18JK07A	0.67	421	0.79	<0.47	0.028	27.85	10.62	45	1.162	20.2	1.064
18JK08A	0.64	372.8	1.12	<0.47	0.026	32.86	3.75	65	0.865	2.1	0.402
18JK19A	0.68	226.9	0.7	<0.47	0.043	29.5	12.65	40	0.529	40	2.043
18JK24A	0.67	544.9	1.05	<0.47	0.025	37.79	4.77	39	1.743	4.8	0.333
18JK25A	0.67	240.6	1.24	<0.47	0.019	28	4.88	63	2.11	6.5	0.696
18JK29A	0.66	479.8	1.09	<0.47	0.023	27.24	3.15	46	1.418	3	0.463
18JK32A	0.65	540	1.43	<0.47	0.032	24.84	3.23	85	4.111	4.4	0.777
18JK35A	0.68	305.8	1.4	<0.47	0.021	35.79	6.18	52	1.515	6.1	0.689
18JK36A	0.7	180.8	1.79	<0.47	0.017	28.38	5.4	36	1.723	8.2	0.486
18JK38A	0.65	651.8	0.75	<0.47	0.02	26.09	1.5	25	0.989	<1.4	0.297
18JK52	0.67	425.3	0.71	<0.47	0.038	47.81	8.83	22	1.067	27.7	1.14
18JK53	0.71	304.9	0.7	<0.47	0.047	28.18	9.32	29	0.674	27.9	1.108
19JK01	0.56	512.35	0.985	<0.47	0.016	84.115	8.47	28.5	1.219	15.85	0.3435
19JK18	0.58	167.9	1.24	<0.47	0.022	33.96	6.96	25	1.689	7.5	0.854
19JK21	0.6	683.2	0.98	<0.47	0.024	67.83	14.5	79	0.741	8.8	1.383
19JK32A	0.59	798.1	1.21	<0.47	0.014	19.89	3.96	24	0.485	<1.4	0.531
Group 3											
18JK24C	0.67	203	0.68	<0.47	<0.013	2.64	0.69	37	0.427	2.7	0.029
18JK28B	0.66	1228	0.93	<0.47	<0.013	4.79	1.19	37	0.88	5.9	0.11
18JK31B	0.65	1031.1	0.95	<0.47	<0.013	8.35	0.55	46	0.209	1.4	0.182
19JK34	0.56	487.6	1.29	<0.47	0.025	5.61	4.03	23	0.255	11.7	0.22
19JK35B	0.58	216.1	1.1	<0.47	<0.013	7.26	4	24	0.479	21.8	0.071
19JK36A	0.55	146.2	0.98	<0.47	0.028	11.25	7.89	26	0.177	14.3	0.684
19JK46	0.55	83.7	1.37	<0.47	<0.013	7.23	1.74	18	0.307	12.8	0.05
19JK47	0.56	144.1	1.21	<0.47	<0.013	5.47	3.61	13	0.617	8.3	0.134
19JK48B	0.54	86.8	1.34	<0.47	0.013	3.8	0.865	14.5	0.4855	<1.4	0.0815

Table S2.1 (continued)

Sample	Er	Eu	Ga	Gd	Hf	Ho	In	La	Li	Lu	Mo
Group 1											
18JK04A	1.8	0.8951	19.51	3.164	4.23	0.5948	0.032	31.6	12.8	0.265	2.8
18JK09A	0.691	0.8047	21.19	2.454	3.4	0.2722	0.029	37.8	16.5	0.088	2.34
*18JK11-A	1.13	0.978	22	2.87	4.2	0.42	< 0.1	26		0.157	< 2
*18JK12-A	0.88	0.779	22	2.15	3	0.3	< 0.1	19.2		0.126	< 2
18JK13A	0.9	0.8775	17.26	3.2	5.45	0.3507	0.0266	47.6	50.9	0.121	1.98
18JK23A	0.727	0.4778	19.48	2.027	2.92	0.2692	0.0257	20.2	32.7	0.09	1.88
18JK27A	0.897	0.5041	20.03	1.964	2.97	0.3264	0.0167	16.6	6.5	0.13	3
18JK30A	0.635	0.6101	16.79	2.233	4.57	0.2227	0.0096	44.3	14.1	0.122	3.05
19JK02	0.428	0.5948	21.8	1.611	2.57	0.1567	0.0132	28.9	15.7	0.051	1.14
19JK03	1.227	1.6453	20.99	4.719	3.33	0.4546	0.0307	35.3	17.3	0.131	0.85
Group 2											
18JK03A	0.206	0.5542	19.48	0.753	3.94	0.0747	0.0086	21.5	28.4	0.038	1.99
18JK07A	0.576	0.6797	19.33	1.494	3.04	0.2259	0.02	15.7	23.8	0.079	1.69
18JK08A	0.135	0.5276	19.93	0.97	3.63	0.0649	0.0108	18.2	12.1	0.021	3.1
18JK19A	1.126	0.9002	20.25	2.55	3.86	0.4033	0.0291	14.8	8.7	0.149	1.31
18JK24A	0.161	0.5612	19.64	0.75	3.41	0.0598	0.0095	22.5	8.3	0.025	2.02
18JK25A	0.415	0.4695	20.03	0.965	3.29	0.1507	0.0046	13.5	26.8	0.071	2.83
18JK29A	0.202	0.5684	22	1.016	3.35	0.0829	0.009	14.8	23	0.033	2.3
18JK32A	0.397	0.4854	22.34	1.253	3.61	0.154	0.0146	13.4	24.6	0.062	4.07
18JK35A	0.326	0.4538	20.4	1.048	3.21	0.1225	0.0177	15.7	34.1	0.043	2.14
18JK36A	0.256	0.5017	22.48	0.932	4.09	0.0862	0.0069	13.7	24	0.051	1.73
18JK38A	0.131	0.5054	18.04	0.637	2.22	0.0449	0.0067	12.5	17.4	0.02	1.14
18JK52	0.489	0.8827	21.18	2.019	3.78	0.188	0.0233	24.5	33.4	0.049	0.94
18JK53	0.545	0.7756	21.46	1.599	3.55	0.1996	0.0231	14.4	23.6	0.071	1.09
19JK01	0.149	0.6278	19.66	0.8185	3.665	0.0553	0.0068	51.65	21.55	0.0265	1.005
19JK18	0.408	0.5751	19.51	1.398	3.92	0.1512	0.017	18.7	19.9	0.052	0.89
19JK21	0.6	1.1087	19.13	2.535	3.54	0.2435	0.0189	33.7	15.5	0.07	0.66
19JK32A	0.219	0.4795	22.3	1.124	2.76	0.0833	0.0151	9.5	15.9	0.029	0.74
Group 3											
18JK24C	0.016	0.3057	11.59	0.055	<0.14	0.0061	0.0018	2.2	2	0.003	1.82
18JK28B	0.05	0.4017	16.92	0.158	2.42	0.0187	<0.0018	2.8	7.1	0.01	1.71
18JK31B	0.072	0.2863	16.67	0.43	1.9	0.0288	<0.0018	4.7	3.1	0.018	2.11
19JK34	0.113	0.746	22.62	0.366	1.13	0.0401	0.0075	3.8	6.8	0.014	0.66
19JK35B	0.028	0.3614	18.38	0.112	0.37	0.0096	0.0029	5.3	8.8	0.004	1.13
19JK36A	0.405	0.4419	13.99	0.847	3.81	0.1426	0.0127	6.5	8.7	0.068	0.93
19JK46	0.021	0.2918	18.11	0.128	0.84	0.0083	0.0022	4.4	1.9	0.006	0.89
19JK47	0.094	0.4923	19.65	0.209	2.45	0.0296	0.0032	2.9	11.8	0.021	0.57
19JK48B	0.039	0.4168	18.51	0.124	0.865	0.01415	0.0028	2.3	6.1	0.0105	0.635

Table S2.1 (continued)

Sample	Nb	Nd	Ni	Pb	Pr	Rb	Sb	Sc	Sm	Sn	Sr	Ta
Group 1												
18JK04A	6.758	23.67	14.6	9.5	6.556	48.85	<0.04	9	3.956	2.05	299.5	0.436
18JK09A	3.368	24.44	8.6	11.24	7.229	47.47	<0.04	8.1	3.773	1	424.9	0.177
*18JK11-A	5.6	19.7	< 20	7	5.37	41	< 0.2	9	3.77	1	326	0.37
*18JK12-A	4.9	14.9	< 20	12	4.09	71	0.3	4	2.92	1	276	0.8
18JK13A	4.788	30.57	5.1	14.33	9.021	104.06	0.04	3.3	4.914	1.14	332.4	0.35
18JK23A	3.575	14.61	7.9	12.74	4.131	63.14	<0.04	6.6	2.642	1.01	386.4	0.248
18JK27A	11.857	10.95	1	12.36	3.084	65.45	<0.04	2.5	2.14	2.22	126.1	1.586
18JK30A	5.798	27.04	3.5	13.33	8.403	75.13	<0.04	1.7	3.813	1.05	218.4	0.593
19JK02	3.365	18.03	4.9	11.42	5.507	61.39	<0.04	3.1	2.441	0.47	319.1	0.202
19JK03	4.649	38.37	32.1	10.3	9.886	40.23	<0.04	9	6.691	1	716.7	0.287
Group 2												
18JK03A	3.471	11.38	6	8.94	3.585	51.18	<0.04	1.8	1.409	0.38	445.8	0.164
18JK07A	3.651	10.95	13.7	5.24	3.076	42.54	<0.04	6.6	1.898	0.64	300.7	0.213
18JK08A	2.383	11.88	2.1	10.12	3.54	42.14	<0.04	1.5	1.69	0.97	430.7	0.102
18JK19A	4.946	14.07	14.9	2.83	3.543	16.31	<0.04	10.2	2.978	0.72	320	0.299
18JK24A	4.295	12.13	5.2	9.14	3.835	58.17	<0.04	<1.1	1.412	0.71	402.4	0.3
18JK25A	4.565	9.38	5.4	10.96	2.782	52.41	<0.04	<1.1	1.499	0.49	452.8	0.653
18JK29A	2.358	10.58	2.1	9.44	3.029	43.35	<0.04	1.2	1.669	0.51	444.8	0.148
18JK32A	3.815	9.73	2.3	9.74	2.747	63.86	<0.04	2.7	1.652	0.87	337.8	0.485
18JK35A	4.583	9.65	10	6.65	3.073	88.53	<0.04	3.5	1.496	1.19	235.7	0.25
18JK36A	3.509	10.15	3.5	9.68	2.992	48.08	<0.04	<1.1	1.512	1.25	263.4	0.314
18JK38A	2.245	7.82	1.2	12.29	2.367	48.02	<0.04	1.2	1.123	0.27	342	0.126
18JK52	3.833	19.94	6	3.98	5.518	43.66	<0.04	4.7	3.016	0.62	402.3	0.195
18JK53	2.418	13.67	7.2	4.02	3.493	27.86	0.08	5.2	2.146	0.55	754	0.095
19JK01	2.4075	22.375	11.7	9.315	7.7445	49.515	<0.04	1.2	2.028	0.595	554.15	0.134
19JK18	4.582	12.14	6.5	7.96	3.566	53.87	<0.04	5.4	1.936	0.68	235.6	0.177
19JK21	4.021	28.28	42.7	7.57	7.7	53.43	<0.04	5.5	4.027	0.73	664.6	0.15
19JK32A	1.443	10.04	7.4	10.72	2.514	35.65	<0.04	2.4	1.833	0.53	737.8	0.101
Group 3												
18JK24C	0.172	0.63	1.4	8.81	0.222	12.84	<0.04	<1.1	0.074	<0.16	491.8	0.011
18JK28B	0.697	1.76	2.8	14.08	0.523	41.71	<0.04	<1.1	0.255	<0.16	315.5	0.067
18JK31B	0.308	3.62	0.8	9.31	0.948	9.81	<0.04	<1.1	0.662	<0.16	440.8	0.012
19JK34	1.193	2.23	10.3	11.9	0.581	17.03	<0.04	1.8	0.402	0.43	778.8	0.077
19JK35B	1.262	1.91	5.6	7.58	0.628	18.06	<0.04	<1.1	0.22	0.2	397.9	0.09
19JK36A	1.615	4.84	15.6	5.86	1.28	6.05	<0.04	5.2	0.946	0.35	302	0.159
19JK46	0.603	2.34	2.1	11.62	0.78	13.12	<0.04	<1.1	0.264	0.19	405.9	0.034
19JK47	2.012	2.05	6.1	9.16	0.559	21.03	<0.04	<1.1	0.336	0.19	415.2	0.186
19JK48B	0.5485	1.26	1.85	8.505	0.3695	14.155	<0.04	<1.1	0.179	0.16	406.6	0.033

Table S2.1 (continued)

Sample	Tb	Th	Ti	Tl	Tm	U	V	W	Y	Yb	Zn	Zr
Group 1												
18JK04A	0.475	8.171	2631	0.266	0.2727	1.116	61.6	0.09	16.32	1.777	62.6	162
18JK09A	0.2992	11.569	1611	0.265	0.0951	0.536	40.1	0.12	7.29	0.601	55	133
*18JK11-A	0.42	3.31		0.25	0.164	1.09	75	< 0.5	12.1	1.07	100	178
*18JK12-A	0.3	4.02		0.39	0.136	1.34	34	< 0.5	9.5	0.85	70	124
18JK13A	0.4081	18.741	1652	0.691	0.1184	1.376	25.3	0.05	8.89	0.78	58.1	217
18JK23A	0.2727	6.193	1578	0.335	0.0985	2.429	37.9	0.13	7.17	0.618	56.2	110
18JK27A	0.3	6.266	606	0.303	0.1332	1.602	6	0.11	9.85	0.912	45.4	88
18JK30A	0.258	26.501	999	0.365	0.1018	3.096	11.3	0.05	6.53	0.741	19.4	170
19JK02	0.1804	9.044	1400	0.319	0.054	0.31	20.8	<0.05	4.12	0.325	37.5	100
19JK03	0.5396	4.489	2755	0.237	0.1527	0.627	62.3	0.07	12.52	0.951	67.3	138
Group 2												
18JK03A	0.085	4.579	1546	0.325	0.0318	0.413	21.6	0.09	2.06	0.236	45.4	155
18JK07A	0.2047	2.372	2485	0.249	0.08	0.269	57.9	<0.05	5.71	0.545	56	111
18JK08A	0.1031	2.405	1343	0.255	0.0196	0.269	18.3	0.08	1.68	0.14	48.3	139
18JK19A	0.377	1.316	3467	0.089	0.1549	0.234	78.1	0.1	10.37	1.021	59.4	154
18JK24A	0.0746	6.506	1731	0.355	0.0205	5.345	23.6	0.09	1.6	0.163	43.2	135
18JK25A	0.128	4.547	1610	0.288	0.0679	1.357	23.5	0.15	4.2	0.464	35.1	127
18JK29A	0.1035	2.951	1327	0.242	0.0256	0.809	18.5	0.05	2.32	0.189	49.9	130
18JK32A	0.1549	3.431	1266	0.324	0.0607	1.107	17.8	<0.05	4.59	0.426	49.2	126
18JK35A	0.1385	6.325	1522	0.389	0.0461	0.857	25.8	0.09	3.3	0.283	50.4	117
18JK36A	0.1027	4.601	1609	0.256	0.0395	1.121	26.4	0.11	2.83	0.293	41.7	151
18JK38A	0.0634	6.504	612	0.275	0.0192	0.382	7.1	<0.05	1.25	0.145	27.5	72
18JK52	0.2455	3.52	2665	0.229	0.0551	0.37	49.1	<0.05	4.98	0.373	75.2	151
18JK53	0.2077	2.121	2706	0.152	0.0756	0.255	54.2	0.6	5.27	0.508	72	147
19JK01	0.06885	8.9805	2432	0.303	0.0217	0.2135	44	<0.05	1.55	0.165	47.95	166
19JK18	0.1681	7.552	2141	0.326	0.0503	0.543	36.5	0.05	4.17	0.353	57.7	158
19JK21	0.2817	6.046	3485	0.314	0.0817	0.285	65.5	<0.05	6.76	0.48	63.3	159
19JK32A	0.1159	1.656	1249	0.187	0.0306	0.439	21.7	<0.05	2.38	0.2	50.1	96
Group 3												
18JK24C	0.0052	0.089	131	0.081	0.0023	0.118	2.3	<0.05	0.2	0.014	5.9	<6
18JK28B	0.0184	0.535	275	0.238	0.007	1.17	4.1	<0.05	0.54	0.064	11	49
18JK31B	0.0452	1.737	114	0.052	0.0114	0.417	3.2	<0.05	0.85	0.102	6.1	45
19JK34	0.049	0.266	833	0.088	0.0151	0.237	16	<0.05	1.11	0.101	20.8	49
19JK35B	0.0143	0.814	776	0.091	0.0035	0.143	12.6	<0.05	0.34	0.03	15.9	12
19JK36A	0.1124	1.264	1035	0.029	0.0625	0.396	39.9	<0.05	3.96	0.471	23.1	175
19JK46	0.011	1.873	353	0.066	0.004	0.101	5.1	0.05	0.29	0.03	11.7	30
19JK47	0.0265	0.471	847	0.102	0.0158	0.199	11.1	<0.05	0.84	0.122	18.7	105
19JK48B	0.01425	0.4315	288	0.069	0.00595	0.1305	2.85	<0.05	0.45	0.054	10.85	32

*= analyzed at Activation Laboratories, all others analyzed at Ontario Geological Survey Geoscience Laboratories

Table S2.2

Plagioclase major element analysis. n.d. = not detected

	Weight %												
Sample	SiO_2	TiO_2	Al_2O_3	Cr_2O_3	MgO	CaO	MnO	FeO_T	SrO	BaO	Na_2O	K_2O	Total
18JK04_core	61.14	n.d.	24.22	n.d.	n.d.	6.22	n.d.	0.06	n.d.	n.d.	8.16	0.27	100.08
18JK04_rim	61.64	n.d.	23.71	n.d.	n.d.	5.67	n.d.	0.18	0.13	n.d.	8.59	0.13	100.04
18JK04_core	61.06	n.d.	24.27	n.d.	n.d.	6.16	n.d.	0.04	n.d.	n.d.	8.23	0.13	99.87
18JK04_core	61.22	n.d.	24.10	n.d.	0.01	6.08	n.d.	0.10	n.d.	n.d.	8.27	0.25	100.03
18JK04_rim	61.44	n.d.	24.09	n.d.	n.d.	6.00	n.d.	0.07	0.13	n.d.	8.36	0.14	100.23
18JK04_rim	61.33	n.d.	24.06	n.d.	n.d.	5.90	n.d.	0.08	n.d.	n.d.	8.49	0.19	100.04
18JK04_core	61.12	n.d.	24.22	n.d.	n.d.	6.19	n.d.	0.06	0.13	n.d.	8.20	0.23	100.14
18JK04_rim	61.47	n.d.	24.37	n.d.	n.d.	6.05	n.d.	n.d.	0.09	n.d.	8.25	0.11	100.34
18JK04	61.19	n.d.	24.02	n.d.	n.d.	6.18	n.d.	0.05	n.d.	n.d.	8.15	0.28	99.87
18JK04	61.00	n.d.	24.22	n.d.	n.d.	6.03	n.d.	0.03	0.12	n.d.	8.36	0.12	99.87
18JK04	61.12	n.d.	24.29	n.d.	n.d.	6.04	n.d.	n.d.	n.d.	n.d.	8.37	0.13	99.95
18JK11_core	61.56	n.d.	24.14	n.d.	n.d.	5.97	n.d.	0.04	n.d.	n.d.	8.38	0.23	100.31
18JK11_rim	61.52	n.d.	24.05	n.d.	n.d.	5.90	n.d.	0.05	n.d.	n.d.	8.45	0.12	100.08
18JK11_core	61.28	n.d.	24.01	n.d.	n.d.	5.95	n.d.	0.06	n.d.	n.d.	8.27	0.27	99.83
18JK11_rim	61.58	n.d.	24.00	n.d.	n.d.	5.96	n.d.	0.04	n.d.	n.d.	8.38	0.14	100.09
18JK11_core	61.86	n.d.	24.07	n.d.	n.d.	5.81	n.d.	n.d.	n.d.	n.d.	8.51	0.07	100.32
18JK11_rim	61.23	n.d.	23.85	n.d.	n.d.	5.87	n.d.	0.06	0.17	n.d.	8.39	0.09	99.65
18JK11_core	61.79	n.d.	24.12	n.d.	n.d.	5.88	n.d.	0.05	n.d.	n.d.	8.49	0.13	100.44
18JK11_rim	61.46	n.d.	24.14	n.d.	n.d.	5.87	n.d.	n.d.	n.d.	n.d.	8.52	0.09	100.09
18JK11	61.49	n.d.	24.06	n.d.	n.d.	5.88	n.d.	0.08	n.d.	n.d.	8.49	0.10	100.10
18JK11	61.61	n.d.	23.99	n.d.	n.d.	5.86	n.d.	0.06	0.1	n.d.	8.36	0.21	100.18
18JK07	61.92	n.d.	24.18	n.d.	n.d.	5.76	n.d.	0.06	n.d.	n.d.	8.57	0.16	100.65
18JK07_rim	61.88	n.d.	24.04	n.d.	n.d.	5.67	n.d.	0.07	n.d.	n.d.	8.41	0.18	100.24
18JK07_rim	62.07	n.d.	24.10	n.d.	n.d.	5.78	n.d.	0.10	n.d.	n.d.	8.48	0.19	100.71
18JK07	61.89	n.d.	23.97	n.d.	n.d.	5.67	n.d.	0.08	n.d.	0.07	8.59	0.19	100.45
18JK07_core	61.67	n.d.	24.10	n.d.	n.d.	5.85	0.028	0.05	0.13	n.d.	8.45	0.20	100.48
18JK07	61.85	n.d.	24.05	n.d.	n.d.	5.69	n.d.	0.09	n.d.	n.d.	8.46	0.20	100.35
18JK07_core	61.73	n.d.	24.03	n.d.	n.d.	5.69	n.d.	0.07	n.d.	n.d.	8.69	0.21	100.42
18JK07_rim	61.75	n.d.	23.99	n.d.	n.d.	5.68	n.d.	0.06	n.d.	n.d.	8.60	0.22	100.29
18JK07_core	61.73	n.d.	23.98	n.d.	n.d.	5.69	n.d.	0.07	n.d.	n.d.	8.59	0.23	100.28
18JK12_rim	63.34	n.d.	22.87	n.d.	n.d.	4.57	n.d.	0.04	n.d.	n.d.	9.27	0.09	100.16
18JK12_core	64.05	n.d.	22.64	n.d.	n.d.	4.01	n.d.	n.d.	0.13	n.d.	9.65	0.09	100.57
18JK12_core	63.46	n.d.	23.02	n.d.	n.d.	4.38	n.d.	0.09	0.1	n.d.	9.43	0.10	100.58
18JK12_rim	63.70	n.d.	23.09	n.d.	n.d.	4.42	n.d.	0.05	n.d.	n.d.	9.48	0.10	100.84
18JK12_rim	63.76	n.d.	22.89	n.d.	n.d.	4.36	n.d.	0.09	n.d.	n.d.	9.33	0.15	100.59
18JK12	63.83	n.d.	23.09	n.d.	n.d.	4.29	n.d.	0.07	n.d.	n.d.	9.44	0.16	100.88
18JK12	63.67	n.d.	22.94	n.d.	n.d.	4.37	n.d.	0.11	n.d.	n.d.	9.37	0.18	100.64
18JK12	63.41	n.d.	22.82	n.d.	n.d.	4.33	n.d.	0.09	0.13	n.d.	9.16	0.26	100.20
18JK12_core	63.64	n.d.	22.80	n.d.	n.d.	4.27	n.d.	0.06	n.d.	n.d.	9.26	0.33	100.35
18JK19_core	60.18	n.d.	24.84	n.d.	n.d.	6.72	n.d.	0.04	n.d.	n.d.	8.00	0.08	99.86
18JK19_rim	60.71	n.d.	24.48	n.d.	n.d.	6.24	n.d.	n.d.	n.d.	n.d.	8.30	0.07	99.80
18JK19	60.29	n.d.	25.01	n.d.	n.d.	6.97	n.d.	0.04	n.d.	n.d.	7.80	0.07	100.18
18JK19	60.01	n.d.	25.07	n.d.	n.d.	6.82	n.d.	n.d.	n.d.	n.d.	8.03	0.07	100.00
18JK19	60.80	n.d.	24.53	n.d.	n.d.	6.13	n.d.	0.04	0.1	n.d.	8.40	0.07	100.08
18JK19	60.53	n.d.	24.55	n.d.	n.d.	6.44	n.d.	0.06	n.d.	n.d.	8.23	0.06	99.87
18JK19	58.92	n.d.	25.56	n.d.	n.d.	7.70	n.d.	0.04	n.d.	n.d.	7.49	0.05	99.76
18JK19	61.12	n.d.	24.49	n.d.	n.d.	6.28	n.d.	n.d.	n.d.	n.d.	8.25	0.05	100.20

Table S2.2 (continued) Weight %

Sample	SiO_2	TiO_2	Al_2O_3	Cr_2O_3	MgO	CaO	MnO	FeO_T	SrO	BaO	Na_2O	K_2O	Total
18JK19_core	60.48	n.d.	24.78	n.d.	n.d.	6.46	n.d.	n.d.	0.11	n.d.	8.13	0.06	100.02
18JK19_rim	60.71	n.d.	24.70	n.d.	n.d.	6.31	n.d.	n.d.	n.d.	n.d.	8.23	0.07	100.02
18JK19	60.70	n.d.	24.83	n.d.	n.d.	6.47	n.d.	0.03	n.d.	n.d.	8.12	0.06	100.20
18JK19	60.59	n.d.	24.47	n.d.	n.d.	6.36	n.d.	0.05	n.d.	n.d.	8.15	0.05	99.67
18JK53_rim	62.15	n.d.	23.61	n.d.	n.d.	5.31	n.d.	0.09	n.d.	n.d.	8.80	0.22	100.17
18JK53_core	62.25	n.d.	23.47	n.d.	n.d.	5.30	n.d.	0.09	0.25	n.d.	8.68	0.22	100.27
18JK53	62.11	n.d.	23.65	n.d.	n.d.	5.24	n.d.	0.08	0.16	n.d.	8.82	0.20	100.25
18JK53	61.91	n.d.	23.94	0.02	n.d.	5.56	n.d.	n.d.	0.13	0.06	8.49	0.18	100.29
18JK53	61.94	n.d.	23.84	n.d.	n.d.	5.35	n.d.	0.07	0.14	n.d.	8.77	0.20	100.31
18JK53	61.90	n.d.	23.82	n.d.	n.d.	5.34	n.d.	n.d.	0.13	n.d.	8.67	0.18	100.03
18JK53_core	61.91	n.d.	23.58	0.03	n.d.	5.22	n.d.	0.06	0.15	n.d.	8.80	0.28	100.01
18JK53_rim	61.67	n.d.	23.49	n.d.	n.d.	5.22	n.d.	0.07	n.d.	n.d.	8.83	0.19	99.46
18JK53	61.41	n.d.	23.88	n.d.	n.d.	5.64	n.d.	0.10	0.12	0.08	8.58	0.17	99.97
18JK53	61.60	n.d.	23.72	n.d.	n.d.	5.36	n.d.	0.05	0.16	n.d.	8.75	0.13	99.77
18JK53	61.73	n.d.	23.76	n.d.	n.d.	5.51	n.d.	0.09	n.d.	n.d.	8.65	0.20	99.94
18JK53	62.05	n.d.	23.67	n.d.	n.d.	5.32	n.d.	0.07	0.09	n.d.	8.72	0.17	100.08
18JK24A_core	63.59	n.d.	22.87	n.d.	n.d.	4.35	n.d.	0.07	n.d.	n.d.	9.38	0.16	100.41
18JK24A_rim	63.43	0.04	22.88	n.d.	n.d.	4.33	n.d.	n.d.	0.12	n.d.	9.27	0.18	100.25
18JK24A_rim	63.36	n.d.	23.28	n.d.	n.d.	4.70	n.d.	0.05	n.d.	n.d.	9.07	0.19	100.64
18JK24A_rim	63.47	n.d.	22.97	n.d.	n.d.	4.33	n.d.	0.10	n.d.	n.d.	9.37	0.21	100.45
18JK24A_rim	63.28	n.d.	22.70	n.d.	n.d.	4.36	n.d.	0.06	n.d.	n.d.	9.38	0.21	99.99
18JK24A_rim	63.22	n.d.	22.90	n.d.	n.d.	4.34	n.d.	0.07	n.d.	n.d.	9.27	0.21	100.00
18JK24A_rim	63.44	n.d.	22.91	n.d.	n.d.	4.42	n.d.	0.07	n.d.	n.d.	9.15	0.22	100.21
18JK24A_core	63.22	n.d.	23.21	n.d.	n.d.	4.63	n.d.	0.05	0.14	n.d.	9.14	0.23	100.62
18JK24A_core	63.32	n.d.	23.01	n.d.	n.d.	4.33	n.d.	0.08	n.d.	n.d.	9.17	0.24	100.14
18JK24A_core	63.59	n.d.	22.72	n.d.	n.d.	4.10	n.d.	0.08	0.14	n.d.	9.39	0.25	100.27
18JK24A_core	63.49	n.d.	23.03	n.d.	n.d.	4.47	n.d.	0.09	0.11	0.07	9.09	0.25	100.59
18JK24A_core	63.66	n.d.	22.93	n.d.	n.d.	4.33	n.d.	0.07	n.d.	n.d.	9.25	0.26	100.49
18JK13	62.51	n.d.	23.64	n.d.	n.d.	5.30	0.03	0.05	n.d.	n.d.	8.83	0.06	100.42
18JK13_rim	62.34	n.d.	23.58	n.d.	n.d.	5.26	n.d.	n.d.	0.15	n.d.	9.01	0.09	100.43
18JK13	62.04	n.d.	23.37	n.d.	n.d.	5.25	n.d.	n.d.	0.09	n.d.	8.86	0.09	99.70
18JK13_rim	62.18	n.d.	23.63	n.d.	n.d.	5.41	n.d.	n.d.	0.11	n.d.	8.86	0.10	100.28
18JK13	61.72	n.d.	23.86	n.d.	n.d.	5.48	n.d.	0.04	n.d.	n.d.	8.78	0.11	99.99
18JK13_rim	62.03	n.d.	23.68	n.d.	n.d.	5.28	n.d.	0.05	0.11	n.d.	8.84	0.12	100.10
18JK13_core	61.90	n.d.	23.84	n.d.	n.d.	5.40	n.d.	0.05	n.d.	n.d.	8.85	0.14	100.17
18JK13_core	61.87	n.d.	24.13	n.d.	n.d.	5.69	n.d.	n.d.	0.14	n.d.	8.68	0.15	100.66
18JK13	62.15	n.d.	23.52	n.d.	n.d.	5.17	n.d.	0.04	n.d.	n.d.	9.01	0.20	100.08
18JK13_core	61.78	n.d.	23.51	n.d.	n.d.	5.30	n.d.	0.05	n.d.	n.d.	8.83	0.24	99.72
19JK46_rim	62.08	n.d.	23.36	n.d.	n.d.	5.12	n.d.	n.d.	n.d.	n.d.	9.00	0.17	99.73
19JK46_rim	61.91	n.d.	23.38	n.d.	n.d.	5.21	n.d.	0.06	n.d.	n.d.	8.97	0.18	99.70
19JK46_core	62.36	n.d.	23.41	n.d.	n.d.	5.01	n.d.	0.04	n.d.	n.d.	9.04	0.18	100.04
19JK46_rim	62.37	n.d.	23.49	n.d.	n.d.	5.11	n.d.	0.05	n.d.	n.d.	9.00	0.19	100.21
19JK46_core	62.28	n.d.	23.31	n.d.	n.d.	4.83	n.d.	0.06	n.d.	n.d.	9.22	0.21	99.91
19JK46_core	62.47	n.d.	23.30	n.d.	n.d.	4.96	n.d.	0.06	n.d.	n.d.	9.12	0.21	100.12
19JK46_rim	62.49	n.d.	23.53	n.d.	n.d.	5.02	n.d.	0.07	0.12	n.d.	9.06	0.22	100.50
19JK46_rim	62.12	n.d.	23.44	n.d.	n.d.	5.24	n.d.	0.06	n.d.	n.d.	8.91	0.23	99.99
19JK46_core	62.35	n.d.	23.49	n.d.	n.d.	5.13	n.d.	0.09	n.d.	n.d.	8.94	0.25	100.26
19JK46_rim	62.60	n.d.	23.49	n.d.	n.d.	5.01	n.d.	0.09	n.d.	n.d.	9.06	0.25	100.49
19JK46_core	62.53	n.d.	23.18	n.d.	n.d.	4.82	n.d.	0.04	n.d.	n.d.	9.23	0.26	100.06
19JK46_core	61.89	n.d.	23.66	n.d.	n.d.	5.30	n.d.	0.12	n.d.	n.d.	8.89	0.29	100.14

Table S2.2 (continued) atoms per formula unit (apfu)

Sample	Si	Ti	Al	Cr	Mg	Ca	Mn	Fe	Sr	Ba	Na	K	An	Ab	Or
18JK04_core	2.72	n.d.	1.27	n.d.	n.d.	0.30	n.d.	0.00	n.d.	n.d.	0.70	0.02	29	69	2
18JK04_rim	2.74	n.d.	1.24	n.d.	n.d.	0.27	n.d.	0.01	0.00	n.d.	0.74	0.01	27	73	1
18JK04_core	2.72	n.d.	1.27	n.d.	n.d.	0.29	n.d.	0.00	n.d.	n.d.	0.71	0.01	29	70	1
18JK04_core	2.72	n.d.	1.26	n.d.	0.00	0.29	n.d.	0.00	n.d.	n.d.	0.71	0.01	28	70	1
18JK04_rim	2.73	n.d.	1.26	n.d.	n.d.	0.29	n.d.	0.00	0.00	n.d.	0.72	0.01	28	71	1
18JK04_rim	2.73	n.d.	1.26	n.d.	n.d.	0.28	n.d.	0.00	n.d.	n.d.	0.73	0.01	27	71	1
18JK04_core	2.72	n.d.	1.27	n.d.	n.d.	0.30	n.d.	0.00	0.00	n.d.	0.71	0.01	29	70	1
18JK04_rim	2.72	n.d.	1.27	n.d.	n.d.	0.29	n.d.	n.d.	0.00	n.d.	0.71	0.01	29	71	1
18JK04	2.73	n.d.	1.26	n.d.	n.d.	0.29	n.d.	0.00	n.d.	n.d.	0.70	0.02	29	69	2
18JK04	2.72	n.d.	1.27	n.d.	n.d.	0.29	n.d.	0.00	0.00	n.d.	0.72	0.01	28	71	1
18JK04	2.72	n.d.	1.27	n.d.	n.d.	0.29	n.d.	n.d.	n.d.	n.d.	0.72	0.01	28	71	1
18JK11_core	2.73	n.d.	1.26	n.d.	n.d.	0.28	n.d.	0.00	n.d.	n.d.	0.72	0.01	28	71	1
18JK11_rim	2.73	n.d.	1.26	n.d.	n.d.	0.28	n.d.	0.00	n.d.	n.d.	0.73	0.01	28	72	1
18JK11_core	2.73	n.d.	1.26	n.d.	n.d.	0.28	n.d.	0.00	n.d.	n.d.	0.71	0.02	28	70	1
18JK11_rim	2.73	n.d.	1.26	n.d.	n.d.	0.28	n.d.	0.00	n.d.	n.d.	0.72	0.01	28	71	1
18JK11_core	2.74	n.d.	1.26	n.d.	n.d.	0.28	n.d.	n.d.	n.d.	n.d.	0.73	0.00	27	72	0
18JK11_rim	2.73	n.d.	1.25	n.d.	n.d.	0.28	n.d.	0.00	0.00	n.d.	0.73	0.00	28	72	0
18JK11_core	2.73	n.d.	1.26	n.d.	n.d.	0.28	n.d.	0.00	n.d.	n.d.	0.73	0.01	27	72	1
18JK11_rim	2.73	n.d.	1.26	n.d.	n.d.	0.28	n.d.	n.d.	n.d.	n.d.	0.73	0.01	27	72	1
18JK11	2.73	n.d.	1.26	n.d.	n.d.	0.28	n.d.	0.00	n.d.	n.d.	0.73	0.01	28	72	1
18JK11	2.73	n.d.	1.25	n.d.	n.d.	0.28	n.d.	0.00	0.00	n.d.	0.72	0.01	28	71	1
18JK07	2.73	n.d.	1.26	n.d.	n.d.	0.27	n.d.	0.00	n.d.	n.d.	0.73	0.01	27	72	1
18JK07_rim	2.74	n.d.	1.25	n.d.	n.d.	0.27	n.d.	0.00	n.d.	n.d.	0.72	0.01	27	72	1
18JK07_rim	2.74	n.d.	1.25	n.d.	n.d.	0.27	n.d.	0.00	n.d.	n.d.	0.73	0.01	27	72	1
18JK07	2.74	n.d.	1.25	n.d.	n.d.	0.27	n.d.	0.00	n.d.	0.00	0.74	0.01	26	72	1
18JK07_core	2.73	n.d.	1.26	n.d.	n.d.	0.28	0.00	0.00	0.00	n.d.	0.73	0.01	27	72	1
18JK07	2.74	n.d.	1.25	n.d.	n.d.	0.27	n.d.	0.00	n.d.	n.d.	0.73	0.01	27	72	1
18JK07_core	2.73	n.d.	1.25	n.d.	n.d.	0.27	n.d.	0.00	n.d.	n.d.	0.75	0.01	26	73	1
18JK07_rim	2.74	n.d.	1.25	n.d.	n.d.	0.27	n.d.	0.00	n.d.	n.d.	0.74	0.01	26	72	1
18JK07_core	2.74	n.d.	1.25	n.d.	n.d.	0.27	n.d.	0.00	n.d.	n.d.	0.74	0.01	26	72	1
18JK12_rim	2.80	n.d.	1.19	n.d.	n.d.	0.22	n.d.	0.00	n.d.	n.d.	0.79	0.01	21	78	1
18JK12_core	2.82	n.d.	1.17	n.d.	n.d.	0.19	n.d.	n.d.	0.00	n.d.	0.82	0.01	19	81	1
18JK12_core	2.79	n.d.	1.19	n.d.	n.d.	0.21	n.d.	0.00	0.00	n.d.	0.81	0.01	20	79	1
18JK12_rim	2.80	n.d.	1.19	n.d.	n.d.	0.21	n.d.	0.00	n.d.	n.d.	0.81	0.01	20	79	1
18JK12_rim	2.80	n.d.	1.19	n.d.	n.d.	0.21	n.d.	0.00	n.d.	n.d.	0.80	0.01	20	79	1
18JK12	2.80	n.d.	1.19	n.d.	n.d.	0.20	n.d.	0.00	n.d.	n.d.	0.80	0.01	20	79	1
18JK12	2.80	n.d.	1.19	n.d.	n.d.	0.21	n.d.	0.00	n.d.	n.d.	0.80	0.01	20	79	1
18JK12	2.80	n.d.	1.19	n.d.	n.d.	0.21	n.d.	0.00	0.00	n.d.	0.78	0.01	20	78	1
18JK12_core	2.81	n.d.	1.18	n.d.	n.d.	0.20	n.d.	0.00	n.d.	n.d.	0.79	0.02	20	78	2
18JK19_core	2.68	n.d.	1.31	n.d.	n.d.	0.32	n.d.	0.00	n.d.	n.d.	0.69	0.00	32	68	0
18JK19_rim	2.71	n.d.	1.29	n.d.	n.d.	0.30	n.d.	n.d.	n.d.	n.d.	0.72	0.00	29	70	0
18JK19	2.68	n.d.	1.31	n.d.	n.d.	0.33	n.d.	0.00	n.d.	n.d.	0.67	0.00	33	67	0
18JK19	2.67	n.d.	1.32	n.d.	n.d.	0.33	n.d.	n.d.	n.d.	n.d.	0.69	0.00	32	68	0
18JK19	2.71	n.d.	1.29	n.d.	n.d.	0.29	n.d.	0.00	0.00	n.d.	0.72	0.00	29	71	0
18JK19	2.70	n.d.	1.29	n.d.	n.d.	0.31	n.d.	0.00	n.d.	n.d.	0.71	0.00	30	70	0
18JK19	2.64	n.d.	1.35	n.d.	n.d.	0.37	n.d.	0.00	n.d.	n.d.	0.65	0.00	36	64	0
18JK19	2.71	n.d.	1.28	n.d.	n.d.	0.30	n.d.	n.d.	n.d.	n.d.	0.71	0.00	29	70	0
18JK19_core	2.69	n.d.	1.30	n.d.	n.d.	0.31	n.d.	n.d.	0.00	n.d.	0.70	0.00	30	69	0
18JK19_rim	2.70	n.d.	1.29	n.d.	n.d.	0.30	n.d.	n.d.	n.d.	n.d.	0.71	0.00	30	70	0
18JK19	2.70	n.d.	1.30	n.d.	n.d.	0.31	n.d.	0.00	n.d.	n.d.	0.70	0.00	30	69	0
18JK19	2.70	n.d.	1.29	n.d.	n.d.	0.30	n.d.	0.00	n.d.	n.d.	0.71	0.00	30	70	0
18JK53_rim	2.76	n.d.	1.23	n.d.	n.d.	0.25	n.d.	0.00	n.d.	n.d.	0.76	0.01	25	74	1

Table S2.2 (continued) apfu

Sample	Si	Ti	Al	Cr	Mg	Ca	Mn	Fe	Sr	Ba	Na	K	An	Ab	Or
18JK53_core	2.76	n.d.	1.23	n.d.	n.d.	0.25	n.d.	0.00	0.01	n.d.	0.75	0.01	25	74	1
18JK53	2.75	n.d.	1.24	n.d.	n.d.	0.25	n.d.	0.00	0.00	n.d.	0.76	0.01	24	74	1
18JK53	2.74	n.d.	1.25	0.00	n.d.	0.26	n.d.	n.d.	0.00	0.00	0.73	0.01	26	73	1
18JK53	2.74	n.d.	1.25	n.d.	n.d.	0.25	n.d.	0.00	0.00	n.d.	0.75	0.01	25	74	1
18JK53	2.75	n.d.	1.25	n.d.	n.d.	0.25	n.d.	n.d.	0.00	n.d.	0.75	0.01	25	74	1
18JK53_core	2.75	n.d.	1.24	0.00	n.d.	0.25	n.d.	0.00	0.00	n.d.	0.76	0.02	24	74	2
18JK53_rim	2.75	n.d.	1.24	n.d.	n.d.	0.25	n.d.	0.00	n.d.	n.d.	0.76	0.01	24	75	1
18JK53	2.73	n.d.	1.25	n.d.	n.d.	0.27	n.d.	0.00	0.00	0.00	0.74	0.01	26	73	1
18JK53	2.74	n.d.	1.25	n.d.	n.d.	0.26	n.d.	0.00	0.00	n.d.	0.76	0.01	25	74	1
18JK53	2.74	n.d.	1.24	n.d.	n.d.	0.26	n.d.	0.00	n.d.	n.d.	0.75	0.01	26	73	1
18JK53	2.75	n.d.	1.24	n.d.	n.d.	0.25	n.d.	0.00	0.00	n.d.	0.75	0.01	25	74	1
18JK24A_core	2.80	n.d.	1.19	n.d.	n.d.	0.21	n.d.	0.00	n.d.	n.d.	0.80	0.01	20	79	1
18JK24A_rim	2.80	0.00	1.19	n.d.	n.d.	0.20	n.d.	n.d.	0.00	n.d.	0.79	0.01	20	79	1
18JK24A_rim	2.79	n.d.	1.21	n.d.	n.d.	0.22	n.d.	0.00	n.d.	n.d.	0.77	0.01	22	77	1
18JK24A_rim	2.80	n.d.	1.19	n.d.	n.d.	0.20	n.d.	0.00	n.d.	n.d.	0.80	0.01	20	79	1
18JK24A_rim	2.80	n.d.	1.18	n.d.	n.d.	0.21	n.d.	0.00	n.d.	n.d.	0.81	0.01	20	79	1
18JK24A_rim	2.80	n.d.	1.19	n.d.	n.d.	0.21	n.d.	0.00	n.d.	n.d.	0.80	0.01	20	79	1
18JK24A_rim	2.80	n.d.	1.19	n.d.	n.d.	0.21	n.d.	0.00	n.d.	n.d.	0.78	0.01	21	78	1
18JK24A_core	2.79	n.d.	1.21	n.d.	n.d.	0.22	n.d.	0.00	0.00	n.d.	0.78	0.01	22	77	1
18JK24A_core	2.80	n.d.	1.20	n.d.	n.d.	0.20	n.d.	0.00	n.d.	n.d.	0.79	0.01	20	78	1
18JK24A_core	2.81	n.d.	1.18	n.d.	n.d.	0.19	n.d.	0.00	0.00	n.d.	0.80	0.01	19	79	1
18JK24A_core	2.80	n.d.	1.20	n.d.	n.d.	0.21	n.d.	0.00	0.00	0.00	0.78	0.01	21	78	1
18JK24A_core	2.80	n.d.	1.19	n.d.	n.d.	0.20	n.d.	0.00	n.d.	n.d.	0.79	0.01	20	78	1
18JK13	2.76	n.d.	1.23	n.d.	n.d.	0.25	0.00	0.00	n.d.	n.d.	0.76	0.00	25	75	0
18JK13_rim	2.76	n.d.	1.23	n.d.	n.d.	0.25	n.d.	n.d.	0.00	n.d.	0.77	0.00	24	75	0
18JK13	2.76	n.d.	1.23	n.d.	n.d.	0.25	n.d.	n.d.	0.00	n.d.	0.76	0.01	25	75	1
18JK13_rim	2.75	n.d.	1.23	n.d.	n.d.	0.26	n.d.	n.d.	0.00	n.d.	0.76	0.01	25	74	1
18JK13	2.74	n.d.	1.25	n.d.	n.d.	0.26	n.d.	0.00	n.d.	n.d.	0.76	0.01	25	74	1
18JK13_rim	2.75	n.d.	1.24	n.d.	n.d.	0.25	n.d.	0.00	0.00	n.d.	0.76	0.01	25	75	1
18JK13_core	2.74	n.d.	1.25	n.d.	n.d.	0.26	n.d.	0.00	n.d.	n.d.	0.76	0.01	25	74	1
18JK13_core	2.73	n.d.	1.26	n.d.	n.d.	0.27	n.d.	n.d.	0.00	n.d.	0.74	0.01	26	73	1
18JK13	2.76	n.d.	1.23	n.d.	n.d.	0.25	n.d.	0.00	n.d.	n.d.	0.77	0.01	24	75	1
18JK13_core	2.75	n.d.	1.23	n.d.	n.d.	0.25	n.d.	0.00	n.d.	n.d.	0.76	0.01	25	74	1
19JK46_rim	2.76	n.d.	1.23	n.d.	n.d.	0.24	n.d.	n.d.	n.d.	n.d.	0.78	0.01	24	75	1
19JK46_rim	2.76	n.d.	1.23	n.d.	n.d.	0.25	n.d.	0.00	n.d.	n.d.	0.77	0.01	24	75	1
19JK46_core	2.77	n.d.	1.22	n.d.	n.d.	0.24	n.d.	0.00	n.d.	n.d.	0.78	0.01	23	76	1
19JK46_rim	2.76	n.d.	1.23	n.d.	n.d.	0.24	n.d.	0.00	n.d.	n.d.	0.77	0.01	24	75	1
19JK46_core	2.77	n.d.	1.22	n.d.	n.d.	0.23	n.d.	0.00	n.d.	n.d.	0.79	0.01	22	77	1
19JK46_core	2.77	n.d.	1.22	n.d.	n.d.	0.24	n.d.	0.00	n.d.	n.d.	0.78	0.01	23	76	1
19JK46_rim	2.76	n.d.	1.23	n.d.	n.d.	0.24	n.d.	0.00	0.00	n.d.	0.78	0.01	23	76	1
19JK46_rim	2.76	n.d.	1.23	n.d.	n.d.	0.25	n.d.	0.00	n.d.	n.d.	0.77	0.01	24	75	1
19JK46_core	2.76	n.d.	1.23	n.d.	n.d.	0.24	n.d.	0.00	n.d.	n.d.	0.77	0.01	24	75	1
19JK46_rim	2.77	n.d.	1.22	n.d.	n.d.	0.24	n.d.	0.00	n.d.	n.d.	0.78	0.01	23	76	1
19JK46_core	2.77	n.d.	1.21	n.d.	n.d.	0.23	n.d.	0.00	n.d.	n.d.	0.79	0.01	22	76	1
19JK46_core	2.75	n.d.	1.24	n.d.	n.d.	0.25	n.d.	0.00	n.d.	n.d.	0.76	0.02	24	74	2

Table S2.3

Plagioclase and secondary reference material trace element data (µg/g).

	P	K	Ca	Ti	Rb	Sr	Y	Zr	Nb	Ba	La	Ce	Pr
18JK12A_line_1	<LOD	1863	2.67E+04	7.51	0.717	383	0.003	0.018	<LOD	63.4	0.087	0.098	0.008
18JK24A_line_1	13.65	1686	2.95E+04	17.88	0.354	583	0.002	0.015	<LOD	154	1.347	1.274	0.081
18JK24A_line_2	20.28	1502	2.87E+04	13.37	1.036	589	<LOD	0.019	0.001	137	0.627	0.468	0.025
18JK24A_line_3	11.31	1856	2.84E+04	16.98	2.097	594	0.006	0.086	0.002	183	1.287	1.332	0.090
18JK53_line_2	37.19	1494	4.60E+04	11.86	0.111	1177	0.005	<LOD	0.001	129	0.990	0.938	0.061
18JK53_line_3	6.75	1636	3.17E+04	7.21	0.146	945	0.006	0.019	<LOD	119	0.031	0.063	0.007
19JK46_line_1	30.39	1969	3.01E+04	13.18	0.284	508	0.004	0.020	<LOD	36.1	0.650	0.557	0.033
19JK46_line_2	25.85	2064	3.14E+04	14.53	0.294	523	0.007	0.020	<LOD	58.9	0.919	0.824	0.048
19JK46_line_3	20.60	1424	3.34E+04	10.30	0.084	529	0.003	0.007	<LOD	33.4	0.404	0.375	0.024
19JK46_line_4	18.87	1678	3.40E+04	15.70	0.127	545	0.005	0.008	<LOD	48.1	1.665	1.306	0.072
BHVO2G													
	1094	3841	7.52E+04	1.39E+04	9.01	359	22.06	157	16.85	120	14.54	36.40	5.20
	1100	3758	7.41E+04	1.42E+04	9.11	362	23.17	159	16.48	120	14.76	35.82	5.04
	1136	3648	7.51E+04	1.42E+04	8.56	351	23.05	154	16.61	119	14.31	34.51	5.05
	1119	3608	7.70E+04	1.45E+04	9.40	369	23.49	161	16.39	124	14.76	36.08	5.22
	1132	3972	7.71E+04	1.48E+04	8.94	371	22.70	156	16.50	124	14.76	36.85	5.28
NIST612													
	45.20	75.61	8.44E+04	39.63	32.54	78.68	38.50	39.14	39.68	38.46	37.31	39.67	39.40
	43.57	74.87	8.21E+04	40.83	33.32	79.16	40.46	41.31	39.51	38.15	38.11	39.41	39.58
	34.97	72.55	8.17E+04	40.14	32.17	77.68	39.53	39.05	39.23	37.21	36.25	38.96	39.52
	36.02	83.06	8.24E+04	40.40	33.00	81.06	39.01	38.79	38.59	39.23	37.04	39.61	38.94
	39.94	86.01	8.29E+04	39.47	31.87	82.52	39.12	38.16	38.61	39.80	36.71	39.93	38.83

Table S2.3 (continued)

	Nd	Sm	Eu	Gd	Tb	Dy	Ho	Er	Tm	Yb	Lu	Ta	Pb	Th	U
18JK12A_line_1	0.022	<LOD	0.143	<LOD	<LOD	<LOD	<LOD	<LOD	<LOD	<LOD	<LOD	<LOD	11.65	<LOD	<LOD
18JK24A_line_1	0.203	0.009	0.302	<LOD	<LOD	<LOD	<LOD	<LOD	<LOD	<LOD	<LOD	<LOD	11.10	<LOD	0.008
18JK24A_line_2	0.062	<LOD	0.290	<LOD	<LOD	<LOD	<LOD	<LOD	<LOD	<LOD	<LOD	<LOD	10.80	<LOD	0.010
18JK24A_line_3	0.220	0.012	0.398	<LOD	<LOD	<LOD	<LOD	<LOD	<LOD	<LOD	<LOD	<LOD	11.20	0.003	0.106
18JK53_line_2	0.164	0.008	0.289	<LOD	<LOD	<LOD	<LOD	<LOD	<LOD	<LOD	<LOD	<LOD	6.62	<LOD	<LOD
18JK53_line_3	0.028	0.005	0.161	0.003	<LOD	<LOD	<LOD	<LOD	<LOD	<LOD	<LOD	<LOD	5.46	<LOD	<LOD
19JK46_line_1	0.090	0.008	0.361	<LOD	<LOD	<LOD	<LOD	<LOD	<LOD	<LOD	<LOD	<LOD	14.72	<LOD	0.001
19JK46_line_2	0.125	0.011	0.362	0.008	<LOD	<LOD	<LOD	<LOD	<LOD	<LOD	<LOD	<LOD	16.01	<LOD	<LOD
19JK46_line_3	0.060	<LOD	0.306	<LOD	<LOD	<LOD	<LOD	<LOD	<LOD	<LOD	<LOD	<LOD	15.50	<LOD	<LOD
19JK46_line_4	0.165	0.007	0.391	<LOD	<LOD	<LOD	<LOD	<LOD	<LOD	<LOD	<LOD	<LOD	15.70	<LOD	0.001
BHVO2G															
	22.26	5.55	2.53	5.63	0.985	4.65	1.06	2.40	0.383	2.00	0.417	1.16	2.09	1.31	0.719
	22.43	5.80	2.05	5.99	0.964	5.04	1.04	2.52	0.344	1.92	0.300	1.13	1.79	1.22	0.456
	22.95	5.75	2.08	5.79	0.924	4.85	0.963	2.44	0.362	1.89	0.327	1.12	1.79	1.25	0.512
	23.25	5.81	2.11	6.05	0.984	5.12	1.03	2.33	0.362	2.06	0.363	1.25	2.41	1.24	0.597
	23.70	6.19	2.13	5.80	0.908	4.85	1.01	2.41	0.357	1.90	0.317	1.13	2.44	1.22	0.617
NIST612															
	34.61	37.16	36.64	36.98	38.83	35.08	39.06	37.92	38.19	38.03	37.72	37.75	38.92	38.86	38.74
	36.04	38.44	37.02	39.48	39.73	37.13	41.18	39.87	39.98	39.85	39.73	40.47	37.52	40.57	38.40
	35.64	37.35	37.01	37.47	38.57	36.04	39.54	37.94	38.52	37.94	37.63	39.31	36.84	38.69	38.06
	35.62	38.45	38.11	38.63	38.61	36.23	40.23	38.86	39.19	38.28	39.21	39.00	37.29	38.78	38.94
	35.35	37.80	36.95	37.97	38.51	35.73	39.72	38.31	38.11	38.12	38.18	38.51	36.81	39.59	38.37

Table S2.4

Calculated parental TTG composition.

Wt%	SiO_2	TiO_2	Al_2O_3	Fe_2O_3	Cr_2O_3	MgO	CaO	Na_2O	K_2O	H_2O	
Parental TTG	70.74	0.28	15.75	2.58	0.008	0.88	3.026	5.05	1.43	1.58	
Mol%	SiO_2	TiO_2	Al_2O_3	FeO	Cr_2O_3	MgO	CaO	Na_2O	K_2O	H_2O	O
Parental TTG	72.33	0.22	9.49	1.99	0.003	1.34	3.31	5.00	0.93	5.37	0.22

µg/g	Rb	Ba	Th	U	Nb	Ta	La	Ce	Sr	Nd	Zr
Parental TTG	53.4	470.9	5.997	0.784	4.151	0.254	22.1	40.81	369	15.63	139
	Sm	Eu	Gd	Dy	Er	Yb	Y	Lu			
Parental TTG	2.523	0.659	1.61	1.104	0.554	0.516	5.78	0.08			

Table S2.5

Partition coefficients calculated for model plagioclase and values from literature used for ilmenite.

	Rb	Ba	Th	U	Nb	Ta	La	Ce	Sr
Plagioclase	0.093	1.123	0.135	0.134	0.177	0.113	0.201	0.195	10.293
Ilmenite			0.427	0.063	65.600	18.000	1.310	1.190	0.415

	Nd	Zr	Sm	Eu	Gd	Dy	Er	Yb	Y	Lu
Plagioclase	0.175	0.097	0.151	1.313	0.128	0.106	0.087	0.073	0.099	0.067
Ilmenite	0.960	6.190	0.684	0.400	0.380	0.370		0.550	0.315	0.740

Appendix S3

Appendix S3.1 Methodology and zircon interpretations

Appendix S3.1.1 Methodology

Whole rock geochemical data

Three TTG samples were processed at the Ontario Geological Survey Geoscience Laboratories (Geolabs) in Sudbury, Ontario, where the rocks were pulverised using an agate mill. For major elements, crushed samples were heated and then fused with a borate flux to be analyzed by X-ray fluorescence (XRF) using Malvern-Panalytical Axios Advanced Wavelength Dispersive-XRF spectrometers. For trace elements, powdered samples were digested by a multi-acid solution in a closed vessel and subsequently analysed by inductively coupled plasma mass spectrometry (ICP-MS) using a Thermo Scientific iCAP-Q ICP-MS. Data quality was monitored by insertion of internal reference materials, sample duplicates, and blanks. Based on duplicate data, precision of major element concentrations is better than 1% for most elements (rarely up to 2.0–3.0% for TiO_2, Na_2O, K_2O, and MgO, up to 22% for MnO in one case) and precision for trace elements is better than 10% for most elements (rarely up to 14% for HREE).

Zircon U–Pb and Lu–Hf analysis

Zircon mineral separates were obtained from nine TTGs for *in situ* U–Pb and Lu–Hf analysis. Overburden Drilling Management Limited (Ottawa, Canada) conducted the mineral separation beginning with electric pulse disaggregation for sample breakdown. The disaggregated sample was concentrated on a shaking table and further refined to a zircon-rich concentrate by panning. Zircon crystals were hand-picked using a binocular microscope and mounted in epoxy resin inside 1-inch round plastic mounts, which were subsequently polished using diamond lapping film to expose the cores of the zircon crystals. The mounts were coated with a film of gold and the internal structures of the crystals were imaged using cathodoluminescence (CL) microscopy at the Waterloo Advanced Technology Laboratory at University of Waterloo (Waterloo, Canada) using a Zeiss Leo 1530 field emission scanning electron microscope (FESEM) operating at 20 kV with a current of approximately 900 pA.

Laser ablation split stream (LASS) analyses of zircon crystals were conducted at the John de Laeter Centre for Mass Spectrometry at Curtin University in Perth, Australia using a Resonetics RESOlution M–50A–LR system with a COMPex 102 193 nm excimer UV laser. Detailed analytical procedures for this laboratory are reported in Gardiner et al. (2020). The laser operating conditions were 50 μm spot size, 10 Hz, and 3 J/cm^2 fluence, with 35 s of ablation time after two cleaning pulses; baseline acquisition was 65 s in total. The U–Pb and Th isotopic data were collected using an Agilent 8900 ICP-MS and processed using Iolite (Paton et al., 2011). The primary reference material for the U–Pb geochronological results was the OG-1 zircon standard (Stern et al., 2009; 3465.4 ± 0.6 Ma) and concentrations of U and Th were calculated using the 91500 zircon standard (Wiedenbeck et al., 1995). The Lu–Hf isotopic data were collected from the same sampled material used for U–Pb analysis using a Nu Plasma II multi-collector ICP-MS. Faraday cups were used for all isotopes collected using the Nu Plasma II (^{180}Hf, ^{179}Hf, ^{178}Hf, ^{177}Hf, ^{176}Hf, ^{175}Lu, ^{174}Hf, ^{173}Yb, ^{172}Yb and ^{171}Yb). The time-resolved data were processed using Iolite (data reduction scheme after Woodhead et al., 2004). Mud Tank zircon (Woodhead and Hergt, 2005; ^{176}Hf/ ^{177}Hf of 0.282507 ± 0.000006) was used as the primary reference material for the Hf isotopic data.

For U–Pb (Table S3.2), the ^{207}Pb/^{206}Pb weighted mean ages from secondary reference zircons FC1 (1099.74 ± 2.17 Ma; MSWD = 1.98; n = 9/9) and GJ1 (605.22 ± 2.42 Ma; MSWD = 1.13; n = 15/18) were indistinguishable from the accepted values of 1099 ± 0.6 Ma (Paces and Miller, 1993) and 608.8 ± 1.8 Ma (Horstwood et al., 2016), respectively. Two reference zircons, 91500 (1068.2 ± 3.25 Ma; MSWD = 2.37; n = 15/18), Maniitsoq (3003.13 ± 1.96 Ma; MSWD = 1.27; n = 5/8) yielded ages that were distinguishable from accepted values, 1062.4 ± 0.4 Ma (Wiedenbeck et al., 1995) and 3008.7 ± 0.72 Ma (Marsh et al., 2019), respectively.

For Hf isotopic analysis (Table S3.3), weighted mean ^{176}Hf/ ^{177}Hf values of most secondary reference zircons were within uncertainty of accepted values, including MUNZirc (0.282132 ± 0.000013, MSWD = 1.3, n = 8/9; 0.282135 ± 0.000007 from Fisher et al., 2011), FC1 (FC1 0.282164 ± 0.000015, MSWD = 2.5, n = 10/10; 0.282184 ± 0.000016 from Woodhead and Hergt, 2005), Maniitsoq zircon (0.280843 ± 0.000014, MSWD = 1.9, n = 9/9;

0.280862 ± 0.000021 from Marsh et al., 2019) and GJ1 (0.281996 ± 0.000008, MSWD = 0.79, n = 15/15; 0.282000 ± 0.000005 from Morel et al., 2008). Two reference zircons yielded weighted mean values that were distinguishable from accepted values, Plešovice (0.282451 ± 0.000012, MSWD = 1.8, n = 10/10; 0.282482 ± 0.000013 from Sláma et al., 2008) and 91500 (0.282282 ± 0.000010, MSWD = 1.3, n = 18/18; 0.282308 ± 0.000006 from Blichert-Toft, 2008). For all standard and unknown analyses, the $^{180}Hf/^{177}Hf$ ratio was collected to monitor the accuracy of the mass bias correction and the average corrected $^{180}Hf/^{177}Hf$ is within the range of values reported by Thirlwall and Anczkiewicz (2004).

Calculations for concordia plots and weighted mean values (95% confidence and using 2σ uncertainty in all cases, including $^{207}Pb/^{206}Pb$ ages and $^{176}Hf/^{177}Hf$ values of reference materials) were done using Isoplot version 4.15 (Ludwig, 2003). We determined an acceptable MSWD for the population of $^{207}Pb/^{206}Pb$ ages of Group I for each sample based on the 2σ range of the MSWD, calculated using $1 + 2\sqrt{2/(n-1)}$ (Wendt and Carl, 1991; Spencer et al., 2017), where n is the number of analyses in Group I. If the MSWD is greater than this value, there is a less than 5% probability that the ages represent a single population; in this scenario, we report the range of Group I ages only (samples 18JK19, 19JK41, 19JK40, and 17JK26). For Figure S3.4, weighted mean $^{207}Pb/^{206}Pb$ ages of Group I were used for all samples for illustrative purposes. The εHf values were calculated using the Lu–Hf decay constant of Scherer et al. (2001) and the Lu–Hf isotopic values of chondrites from Blichert-Toft and Albarède (1997). Depleted mantle curves in Figs 4.3, 4.4, and S3.4 and depleted mantle model ages were calculated using Lu–Hf values from Vervoort and Blichert-Toft (1999). In Figs 4.3, 4.4, and S3.4, "DM 4.56" refers to a depleted mantle reservoir established at 4.56 Ga and "DM 3.8" was calculated assuming a depleted mantle formed at 3.8 Ga (after Fisher and Vervoort, 2018). The new crust evolution line in Figs 4.3, 4.4, and S3.4 was calculated based on values from Dhuime et al. (2011).

Appendix S3.1.2 Zircon interpretations

All ages reported in this section are $^{207}Pb/^{206}Pb$ ages. In general, the interpretation of xenocrystic components (Group X analyses) is based on an older $^{207}Pb/^{206}Pb$ age than the

main zircon population from the same sample (Group I analyses) and textures that may support the presence of a xenocrystic core. Three older analyses with $^{177}Hf/^{176}Hf$ ratios that are indistinguishable from Group I are considered to be unreliable (Group H, see Fig. S3.3). Although these could represent xenocrystic components, we choose to distinguish them from Group X and treat them with caution, as their $^{177}Hf/^{176}Hf(t)$ is greater than depleted mantle at the $^{207}Pb/^{206}Pb$ age of the analysis (with no overlap within 2SE, see Fig. S3.3).

Sample 19JK45B

Zircon crystals are subhedral and brown in colour with a rounded overall shape. The population exhibits a somewhat weak CL response, particularly in the cores, with subtle oscillatory zoning or ambiguous gradational CL textures. Many of the zircon grains are pitted. The cores are surrounded by a rim with higher CL response, which typically shows smooth zoning to lower CL response at the edges of the crystals. Twenty-seven zircon crystals were analyzed, and most ablation pits were located in cores. Two analyses are discordant (>5%). Two more crystals yield ages that are younger than the main population, one of which (2855 ± 8 Ma) has a high concentration of U (> 1000 µg/g) and a pitted appearance, supporting possible ancient Pb loss. The second crystal (2841 ± 11 Ma) appears texturally similar to the rest of the population, however the ablation pit may have partially sampled the rim, suggesting that the age is mixed between an igneous core and a metamorphic rim. The 23 remaining crystals form a continuous population from 2900 ± 8 Ma to 2877 ± 8 Ma with a weighted age of 2884.8 ± 2 Ma (MSWD = 1.4, 95% confidence, no rejections), which is interpreted to represent the igneous crystallisation age of this sample.

Sample 18JK19

Zircon crystals are subhedral to euhedral and light brown with a variety of crystal shapes. The crystals exhibit well-developed oscillatory zoning and a similar overall range of CL intensity, though several cores have a low CL response. Thirty zircon crystals were analysed within cores where possible. Four of the analyses are discordant (>5%). Three analyses (2868 ± 11 Ma, 2774 ± 12 Ma, and 2776 ± 9 Ma) may have sampled xenocrysts or xenocrystic components, however the reliability of these ages is unclear, as the ablation pit may have overlapped both a xenocrystic core and a later rim in one crystal. The remaining 23 analyses

yield a continuous population from to 2750 ± 9 Ma to 2715 ± 9 Ma. A meaningful population age cannot be derived from this group.

Sample 19JK43

Zircon crystals are subhedral and light brown, and exhibit a variety of textures in CL. Many exhibit oscillatory zoning with cores of variable CL response. Cores with a low CL response commonly have an unzoned, spongy, or chaotic internal structure. Twenty-one zircon crystals were analysed and most ablation pits avoided low CL response cores. Ten analyses are discordant (>5%). Two analyses yielded ages that are older than the rest of the population but with $^{177}Hf/^{176}Hf$ ratios indistinguishable from the others; the 3092 ± 24 Ma age is considered to be unreliable but the 2741 ± 9 Ma analysis may have sampled a xenocryst. One analysis (2712 ± 8 Ma) was eliminated from the population because the ablation pit partly includes a low-CL-response, pitted core. The remaining 8 analyses exhibit oscillatory zoning and form a continuous population from 2702 ± 8 Ma to 2689 ± 11 Ma with a weighted age of 2696.1 ± 3.1 Ma (MSWD = 0.81, 95% confidence), considered to be the igneous crystallisation age of this sample.

Sample 19JK41

Zircon crystals are subhedral to euhedral and light brown with variable CL response. All crystals exhibit oscillatory zoning, in several this is very well-developed with a strong overall CL response. Some have a low CL response core and most of these have a spongy or patchy texture. An uneven, very thin rim with a high CL response is present in most crystals. Twenty-five zircon crystals were analysed and ablation pits are within cores with oscillatory zoning. Four analyses are discordant (>5%). One analysis yielded an age that is older than the rest (2933 ± 19 Ma) with $^{177}Hf/^{176}Hf$ similar to the main population, indicating possible common Pb. Another analysis sampled a core with textures indicative of resorption; this is interpreted as a xenocrystic core (2720 ± 9 Ma). For the three remaining analyses, the ablation pits appeared to only partly include a resorbed core and may represent mixed ages. The 16 remaining analyses form a continuous population from 2706 ± 8 Ma to 2680 ± 9 Ma; a meaningful population age cannot be derived from this group.

Sample 19JK40

Zircon crystals are subhedral with a thin, elongated morphology and rounded ends. They are light brown to brown in colour. Most of the cores exhibit poorly-developed oscillatory zoning with an overall weak CL response. An annulus of uneven thickness and high CL response surrounds the core, and in some cases constitutes the rim of the crystals. Others have a low CL response rim that is unzoned or shows faint oscillatory zoning and this is rarely followed by another high CL response ring. Twenty-nine zircon crystals were analyzed. Ten of the analyses yielded discordant ages (<5%) and the majority of these have cores with a low CL response, some with a mottled texture. All but three of the crystals that gave discordant ages are approximately 50 µm wide, necessitating inclusion of the core and rim zones in the ablation pit, which may explain the excessive discordance. Three analyses that gave concordant ages younger than the main population (2616 ± 9 Ma, 2620 ± 8 Ma, 2647 ± 8 Ma) also included both cores and rims. These may be mixed ages that imply the existence of young overgrowths, but given the overall high concentration of U in zircon crystals (average of approximately 620 µg/g from all analyses) and high degree of discordance (seven analyses ≥10% discordant) in this sample, these young ages are unlikely to be meaningful. The oldest analysis with an age of 2878 ± 10 Ma has a $^{177}Hf/^{176}Hf$ ratio that is indistinguishable from the younger crystals, indicating possible common Pb. Of the remaining 15 analyses, the ablation pits of eight are almost entirely within a relatively high CL response core with oscillatory zoning and yield an overlapping range of ages from 2716 ± 10 Ma to 2679 ± 8 Ma. A meaningful population age cannot be derived from this group.

Sample 18JK08

Zircon crystals are subhedral with rounded ends, and many are fragments of elongated grains. The crystals are brown overall, indicative of elevated U. Most exhibit well-defined oscillatory zoning in the core, surrounded by a thin annulus with high CL response, followed by a low CL response rim commonly with subtle oscillatory zoning. Several crystals have cores with a gradient of CL response, but no obvious zoning, and a few others have a spongy texture. Analyses of 21 zircon grains were obtained from this sample, and due to the small size of the crystals, almost all of the ablation pits included the core, annulus and rim zones. Six analyses are discordant (>5%). One analysis is over 100 Myr younger than the rest (2475

± 9 Ma), but the very high U content (> 3000 µg/g) supports Pb loss rather than a meaningful age. Two analyses (2727 ± 8 Ma and 2782 ± 8 Ma) appear to have sampled resorbed cores, which may represent xenocrystic components. Twelve analyses yield a continuous population from 2712 ± 9 to 2661 ± 8 Ma, however three of these have high concentrations of U (>1000 µg/g), which is strongly correlated with disturbance to the U–Pb system in this sample. Of those with lower concentrations of U, one does not show clear oscillatory zoning and in another, the ablation pit sampled a high CL response crack, indicating that these ages may not be reliable. Based on seven analyses where ablation pits are almost entirely contained within cores that exhibit oscillatory zoning, a weighted age of 2684.8 ± 3.3 Ma (MSWD = 1.04, 95% confidence, one rejection) is obtained and is interpreted to represent the igneous crystallisation age of this sample.

Sample 18JK53

Zircon crystals are subhedral to euhedral and pale in colour with a variety of crystal shapes. Many have well-developed oscillatory zoning commonly with sector zoning. Several crystals have an annulus exhibiting a very low CL response with weak zoning. A few others have a low CL response core with weak oscillatory or chaotic zoning, surrounded by a rim with oscillatory zoning. Twenty-three crystals were analyzed in areas with oscillatory zoning, with several ablation pits including the low CL response annulus. Two analyses are discordant (>5%). One analysis (2745 ± 10 Ma) yields an age that is older than the main population and may represent a xenocryst. One crystal exhibits several 10 µm-wide crosscutting features and was eliminated from the group, as these may be evidence of late disturbance. Nineteen analyses form a continuous population from 2710 ± 9 Ma to 2684 ± 9 Ma and yield a weighted age of 2695.7 ± 2.8 Ma (MSWD = 1.5, 95% confidence, 1 rejection), which is considered as the igneous crystallisation age of this sample.

Sample 17JK11

Zircon crystals are subhedral and brown with a range of crystal shapes. Most exhibit oscillatory zoning with a relatively low CL response; in several crystals the zoning is very faint or poorly-developed. Many of the grains are surrounded by an unzoned, higher CL response rim of irregular thickness. Twenty-two zircon crystals were analyzed. One analysis

yields a discordant (>5%) age. Three analyses yielded ages younger than the main population; of these, one ablation pit appears to overlap a core and rim and another may have sampled a metamict core. The third (2789 ± 8 Ma) is within a broad rim and may represent a metamorphic age. One analysis with oscillatory zoning is older (2885 ± 8 Ma) and has no overlap with other ages, representing a possible xenocrystic component. The ages of 17 other analyses are within 2σ error of at least one other age. Of these, five ablation pits appear to include both a core and a rim and may represent mixed ages. The 12 remaining analyses are within zircon cores with oscillatory zoning and give a continuous range of ages from 2856 ± 8 Ma to 2826 ± 8 Ma with a weighted average of 2833 ± 3.4 Ma (MSWD = 1.5, 95% confidence, 1 rejected age), interpreted as the igneous crystallisation age of this sample.

Sample 17JK26

Zircon crystals are subhedral with rounded ends and are brown in colour. Many exhibit low CL response cores with oscillatory zoning of variable quality; several are extensively pitted. Most of the cores are surrounded by a higher CL response rim that is weakly zoned or unzoned. Eighteen crystals were analyzed, mostly within the cores. One analysis yields a discordant (>5%) age. Two analyses partially sampled a broad, high CL response rim and the core; the ages (2777 ± 9 Ma and 2802 ± 8 Ma) may represent a mixture of a metamorphic rim and an igneous core. An analysis within a crystal with patchy zoning yielded a young age that may be metamorphic (2645 ± 9 Ma). The remaining 14 analyses yield a population from 2835 ± 9 Ma to 2806 ± 8 Ma; a meaningful weighted mean age cannot be calculated from this population. The igneous crystallisation age likely falls within this range.

References

Blichert-Toft, J., 2008. The Hf isotopic composition of zircon reference material 91500. Chem. Geol. 253, 252–257. https://doi.org/10.1016/j.chemgeo.2008.05.014

Blichert-Toft, J., Albarède, F., 1997. The Lu-Hf isotope geochemistry of chondrites and the evolution of the mantle-crust system. Earth Planet. Sci. Lett. 148, 243–258.

Dhuime, B., Hawkesworth, C., Cawood, P., 2011. When continents formed. Science 331, 154–155.

Fisher, C.M., Hanchar, J.M., Samson, S.D., Dhuime, B., Blichert-Toft, J., Vervoort, J.D., Lam, R., 2011. Synthetic zircon doped with hafnium and rare earth elements: A reference material for in situ hafnium isotope analysis. Chem. Geol. 286, 32–47. https://doi.org/10.1016/j.chemgeo.2011.04.013

Fisher, C.M., Vervoort, J.D., 2018. Using the magmatic record to constrain the growth of continental crust—The Eoarchean zircon Hf record of Greenland. Earth Planet. Sci. Lett. 488, 79–91. https://doi.org/10.1016/j.epsl.2018.01.031

Gardiner, N.J., Kirkland, C.L., Hollis, J.A., Cawood, P.A., Nebel, O., Szilas, K., Yakymchuk, C., 2020. North Atlantic Craton architecture revealed by kimberlite-hosted crustal zircons. Earth Planet. Sci. Lett. 534, 116091. https://doi.org/10.1016/j.epsl.2020.116091

Horstwood, M.S.A., Košler, J., Gehrels, G., Jackson, S.E., McLean, N.M., Paton, C., Pearson, N.J., Sircombe, K., Sylvester, P., Vermeesch, P., Bowring, J.F., Condon, D.J., Schoene, B., 2016. Community-derived standards for LA-ICP-MS U-(Th-)Pb geochronology – uncertainty propagation, age interpretation and data reporting. Geostand. Geoanalytical Res. 40, 311–332. https://doi.org/10.1111/j.1751-908X.2016.00379.x

Ludwig, K. R., 2003. User's manual for Isoplot 3.75–4.15: A geochronological toolkit for Microsoft Excel. Berkeley Geochronology Center Special Publication No. 5, 75 pp.

Marsh, J.H., Jørgensen, T, R.C., Petrus, J.A., Hamilton, M.A., Mole, D.R., 2019. U-Pb, trace element, and hafnium isotope composition of the Maniitsoq zircon: A potential new Archean reference material, in: Goldschmidt Abstracts.

Morel, M.L.A., Nebel, O., Nebel-Jacobsen, Y.J., Miller, J.S., Vroon, P.Z., 2008. Hafnium isotope characterization of the GJ-1 zircon reference material by solution and laser-ablation MC-ICPMS. Chem. Geol. 255, 231–235. https://doi.org/10.1016/j.chemgeo.2008.06.040

Paces, J.B., Miller, J.D., 1993. Precise U-Pb ages of Duluth Complex and related mafic intrusions, northeastern Minnesota: Geochronological insights to physical, petrogenetic, paleomagnetic, and tectonomagmatic processes associated with the 1.1 Ga Midcontinent Rift System. J. Geophys. Res. 98, 13997–14013.

Paton, C., Hellstrom, J., Paul, B., Woodhead, J., Hergt, J., 2011. Iolite: Freeware for the visualisation and processing of mass spectrometric data. J. Anal. At. Spectrom. 26, 2508. https://doi.org/10.1039/c1ja10172b

Scherer, E., Münker, C., Mezger, K., 2001. Calibration of the lutetium-hafnium clock. Science 293, 683–687.

Sláma, J., Košler, J., Condon, D.J., Crowley, J.L., Gerdes, A., Hanchar, J.M., Horstwood, M.S.A., Morris, G.A., Nasdala, L., Norberg, N., Schaltegger, U., Schoene, B., Tubrett, M.N., Whitehouse, M.J., 2008. Plešovice zircon — A new natural reference material for U–Pb and Hf isotopic microanalysis. Chem. Geol. 249, 1–35. https://doi.org/10.1016/j.chemgeo.2007.11.005

Spencer, C.J., Yakymchuk, C., Ghaznavi, M., 2017. Visualising data distributions with kernel density estimation and reduced chi-squared statistic. Geosci. Front. 8, 1247–1252. https://doi.org/10.1016/j.gsf.2017.05.002

Stern, R.A., Bodorkos, S., Kamo, S.L., Hickman, A.H., Corfu, F., 2009. Measurement of SIMS Instrumental Mass Fractionation of Pb Isotopes During Zircon Dating. Geostand. Geoanalytical Res. 33, 145–168. https://doi.org/10.1111/j.1751-908X.2009.00023.x

Thirlwall, M.F., Anczkiewicz, R., 2004. Multidynamic isotope ratio analysis using MC–ICP–MS and the causes of secular drift in Hf, Nd and Pb isotope ratios. Int. J. Mass Spectrom. 235, 59–81. https://doi.org/10.1016/j.ijms.2004.04.002

Vervoort, J.D., Blichert-Toft, J., 1999. Evolution of the depleted mantle: Hf isotope evidence from juvenile rocks through time. Geochim. Cosmochim. Acta 63, 533–556.

Wendt, I., Carl, C., 1991. The statistical distribution of the mean squared weighted deviation. Chem. Geol. (Isotope Geosci. Sect.) 86, 275–285.

Wiedenbeck, M., Allé, P., Corfu, F., Griffin, W.L., Meier, M., Oberli, F., Von Quadt, A., Roddick, J.C., Spiegel, W., 1995. Three natural zircon standards for U-Th-Pb, Lu-Hf, trace element and REE analyses. Geostand. Newsletter 19, 1–23. https://doi.org/10.1111/j.1751-908X.1995.tb00147.x

Woodhead, J.D., Hergt, J.M., 2005. A preliminary appraisal of seven natural zircon reference materials for in situ Hf isotope determination. Geostand. Geoanalytical Res. 29, 183–195. https://doi.org/10.1111/j.1751-908X.2005.tb00891.x

Woodhead, J., Hergt, J., Shelley, M., Eggins, S., Kemp, R., 2004. Zircon Hf-isotope analysis with an excimer laser, depth profiling, ablation of complex geometries, and concomitant age estimation. Chem. Geol. 209, 121–135. https://doi.org/10.1016/j.chemgeo.2004.04.026

Figure S3.1

Outcrop photos.

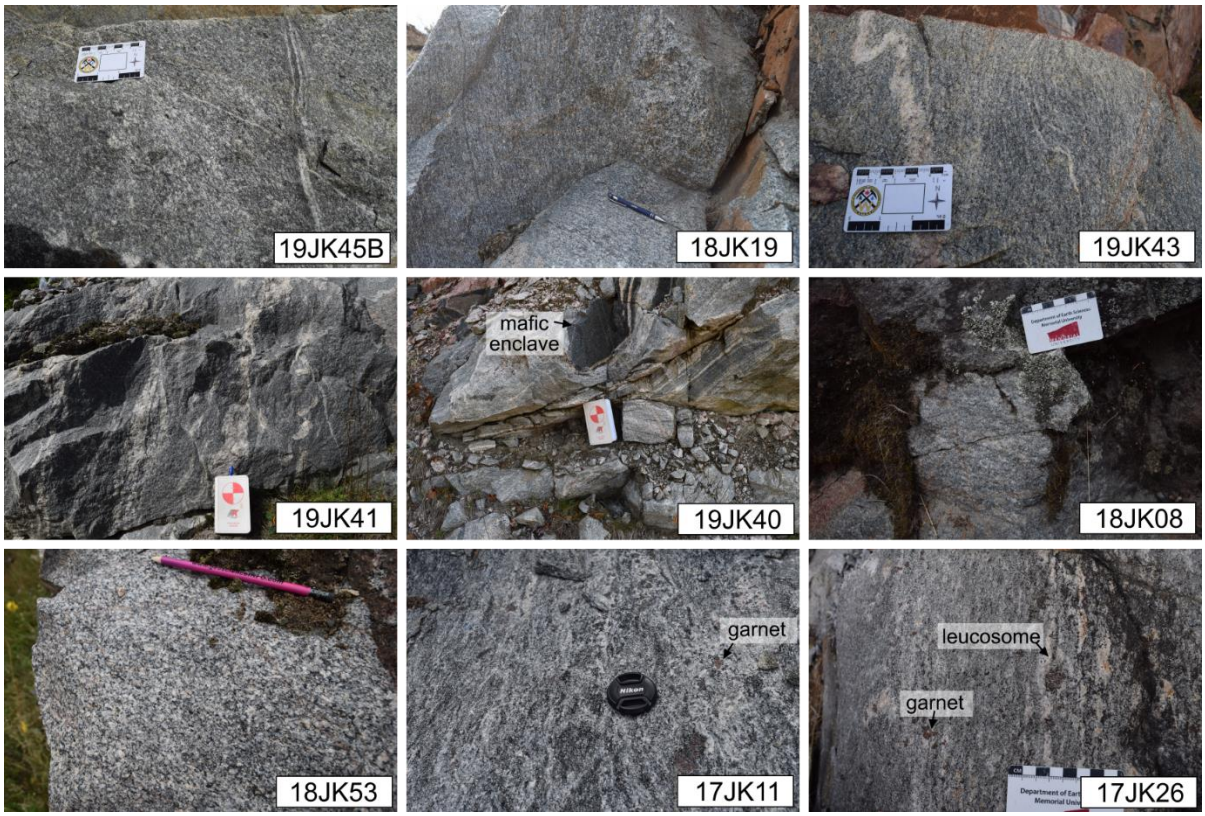


Figure S3.2

Representative CL images of zircon.

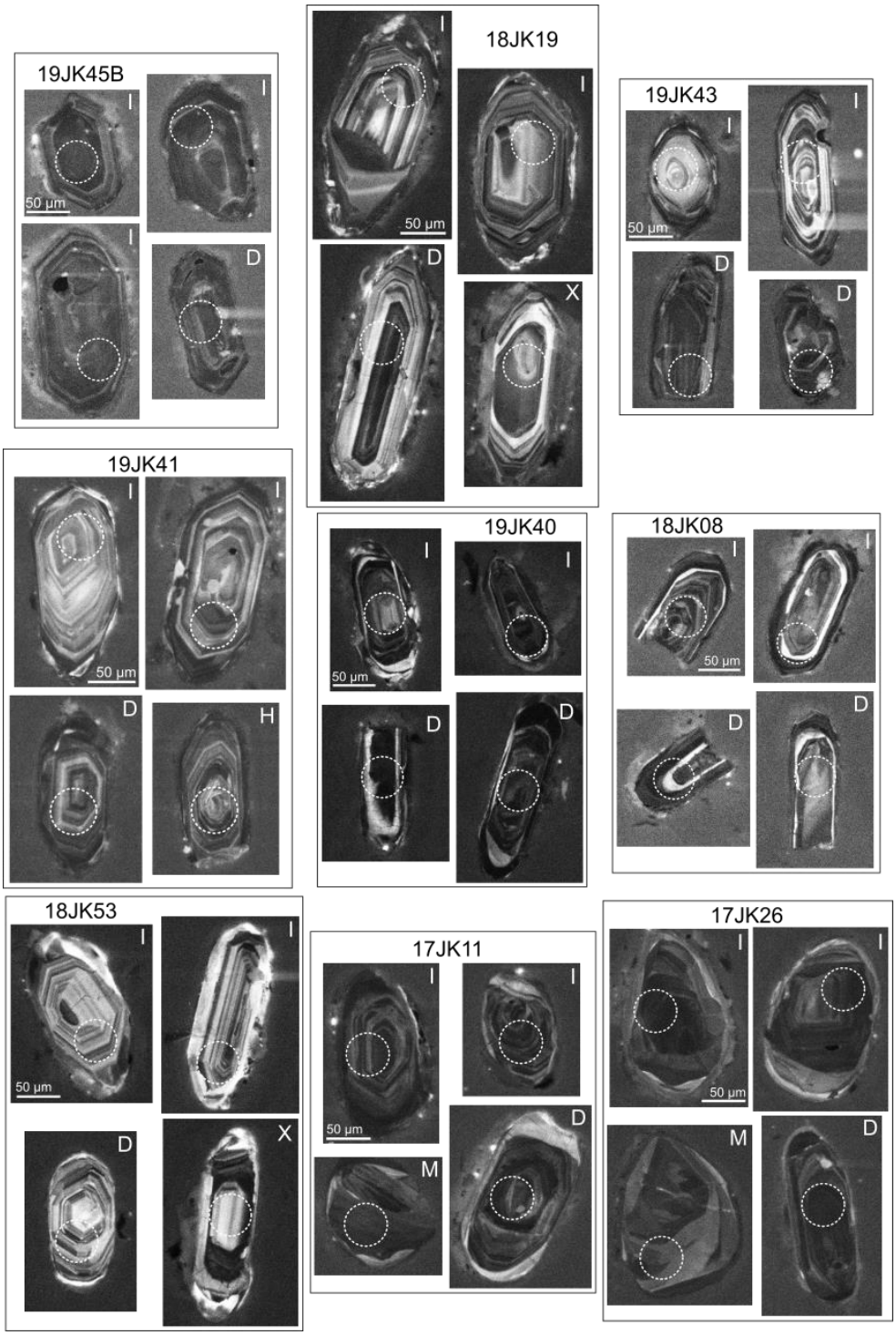


Figure S3.3

Concordia diagrams and $^{207}Pb/^{206}Pb$ age versus $^{176}Hf/^{177}Hf(t)$ from zircon analyses.

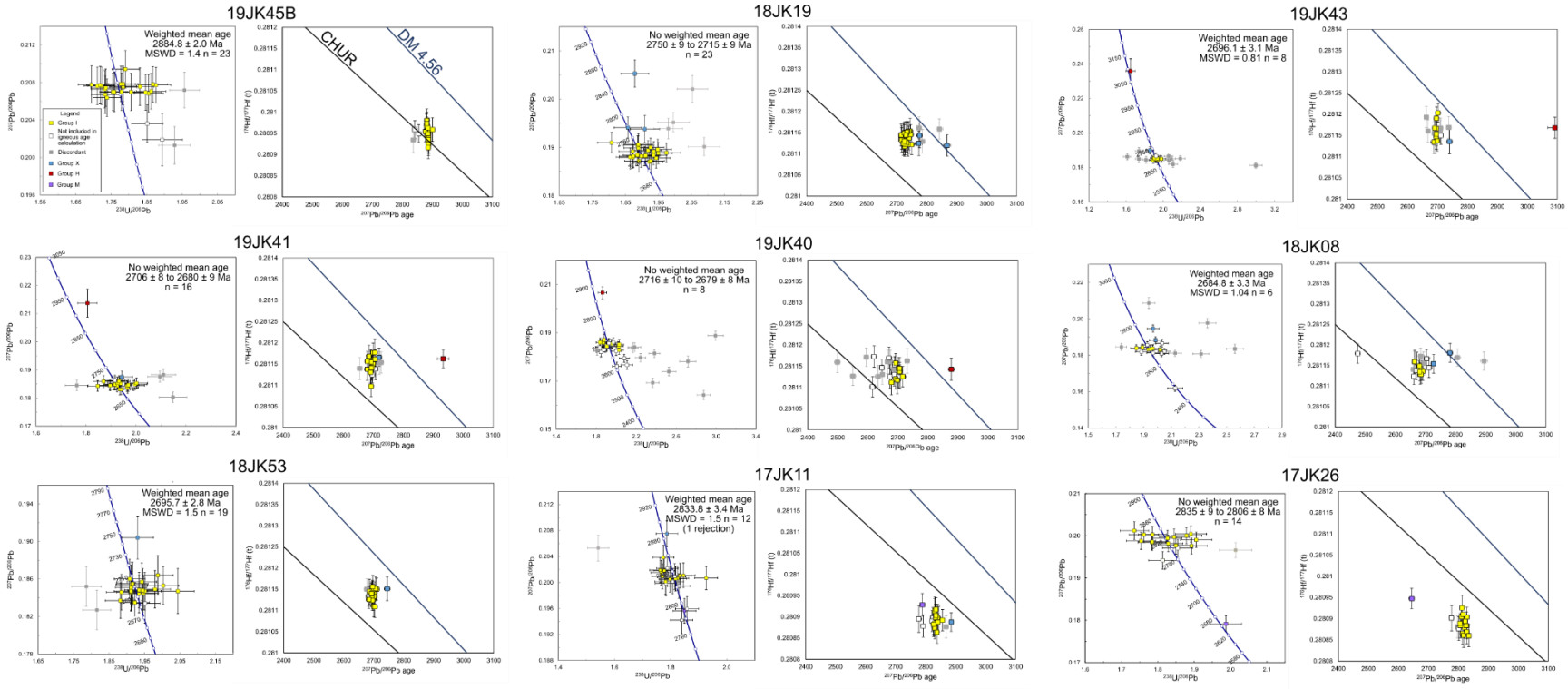


Figure S3.4

Mean $^{207}Pb/^{206}Pb$ age versus mean εHf(t) of each zircon population from the TTG samples.

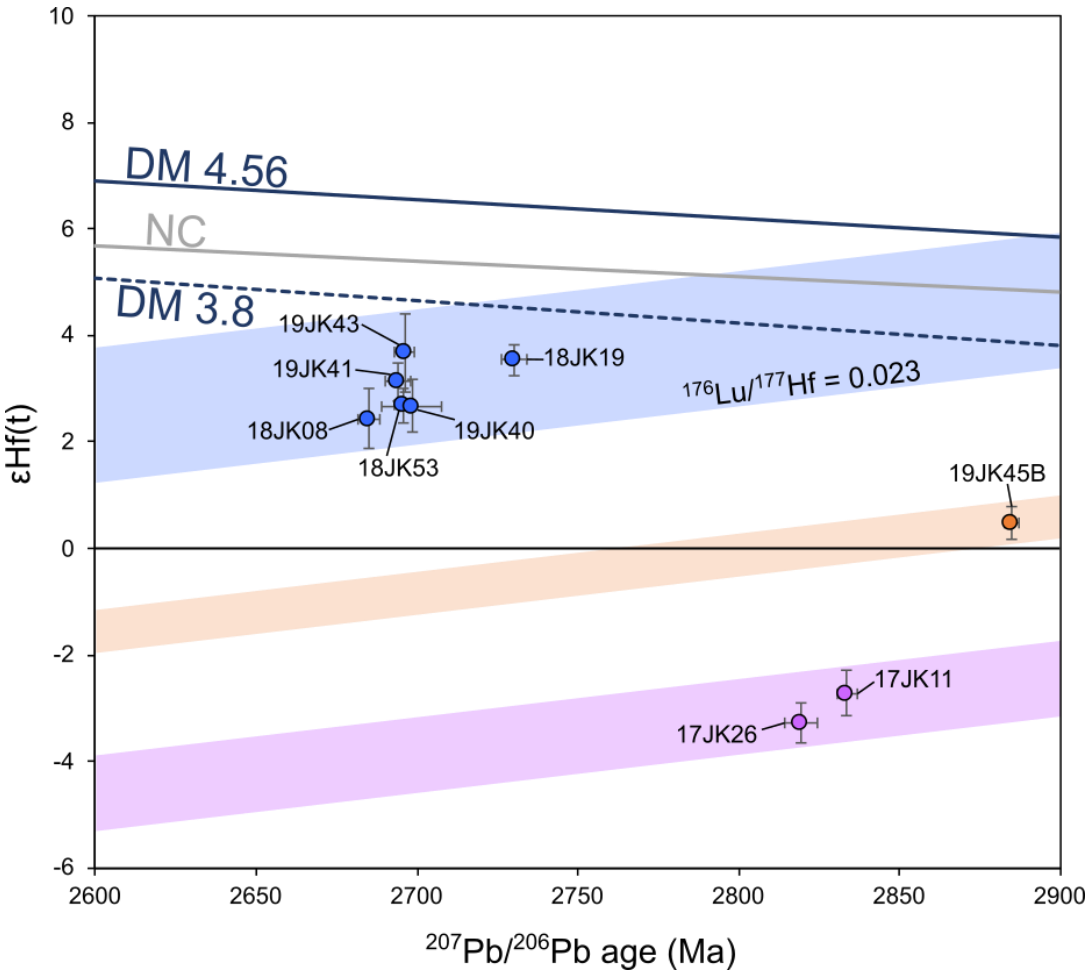


Table S3.1

Whole-rock geochemical data (major elements in wt.%, trace elements in µg/g) of TTGs from the Kapuskasing Structural Zone (samples 17JK11 and 17JK26) and the Hawk Lake granitic complex (sample 18JK34A). Geochemical data for the other samples are available in Table S2.1.

Sample	Latitude	Longitude	SiO_2	TiO_2	Al_2O_3	FeO_T	MgO	MnO	CaO	Na_2O	K_2O	P_2O_5
18JK34A*	48.05903	-84.54878	71.72	0.39	14.42	3.48	1.38	0.06	3.24	3.95	1.27	0.10
17JK11	48.06515	-82.71096	64.97	0.70	15.62	5.27	2.74	0.08	5.43	3.53	1.49	0.18
17JK26	48.08456	-82.68714	68.22	0.67	15.38	4.54	1.40	0.06	4.43	3.75	1.40	0.16

Sample	Ba	Rb	Sr	Y	Th	U	Nb	Ta	La	Ce	Pr	Nd	Sm
18JK34A*	222	41.46	244	19.8	13.067	2.876	8.277	0.918	32.5	57.78	6.277	22	4.059
17JK11	750	32.16	327	12.1	5.665	0.52	4.738	0.217	34.7	59.98	6.186	22.07	3.679
17JK26	1017	41.18	293	14.9	19.991	0.622	5.07	0.138	88.9	152.5	14.71	48.19	6.116

Sample	Eu	Gd	Tb	Dy	Ho	Er	Yb	Lu
18JK34A*	0.849	3.55	0.535	3.328	0.6743	1.98	2.043	0.31
17JK11	1.079	2.896	0.382	2.276	0.4452	1.313	1.201	0.18
17JK26	1.345	3.928	0.522	2.928	0.5674	1.587	1.373	0.22

*18JK34A was sampled from the same outcrop as 19JK45B

Table S3.2

LA-ICP-MS U–Pb data from zircon, including samples and standards. Concentrations of Th and U are in µg/g. Calculated dates ($^{238}U/^{206}Pb$ – column 10, $^{207}Pb/^{206}Pb$ – column 12, concordia age – column 14) are in Ma. Zircon classifications: I = igneous, D = >5% discordant, X = xenocrystic, H = old $^{207}Pb/^{206}Pb$ age with same $^{176}Hf/^{177}Hf$ as igneous population, M = metamorphic. Abbreviations: macq = Maniitsoq, Disc = discordance.

sample	spot id	$^{238}U/^{206}Pb$	2SE	$^{207}Pb/^{206}Pb$	2 SE	Th	U	Th/U	$^{238}U/^{206}Pb$	2SE	$^{207}Pb/^{206}Pb$	2 SE	Concordia	2 SE	Disc	Comment	Class
18JK08	18JK08 - 1	2.1277	0.0543	0.1619	0.0017	746	3460	0.22	2484	26	2475	9	2476	8	-0.3	>1000 µg/g U	
18JK08	18JK08 - 2	2.3613	0.0613	0.1977	0.0026	211	1519	0.14	2276	25	2807	11	2738	9	18.9	>5% discordant	D
18JK08	18JK08 - 3	2.1272	0.0453	0.1811	0.0017	248.6	1400	0.18	2484	22	2662	8	2644	7	6.7	>5% discordant	D
18JK08	18JK08 - 4	1.9685	0.0426	0.1947	0.0020	490	616	0.80	2648	24	2782	8	2767	8	4.8	Xenocrystic	X
18JK08	18JK08 - 5	1.9272	0.0446	0.1857	0.0018	294	853	0.34	2695	26	2704	8	2703	8	0.3	Core/rim overlap	
18JK08	18JK08 - 6	1.9861	0.0434	0.1883	0.0019	254	982	0.26	2629	24	2727	8	2716	8	3.6	Xenocrystic	X
18JK08	18JK08 - 7	2.0333	0.0455	0.1866	0.0021	1007	1770	0.57	2579	24	2712	9	2695	8	4.9	>1000 µg/g U	
18JK08	18JK08 - 8	1.8474	0.0410	0.1839	0.0019	82.3	291.9	0.28	2789	25	2688	9	2699	8	-3.8	Oscillatory zoning	I
18JK08	18JK08 - 9	2.0296	0.0494	0.1810	0.0017	408	1497	0.27	2582	26	2661	8	2655	7	3.0	>1000 µg/g U	
18JK08	18JK08 - 10	2.5595	0.0622	0.1835	0.0025	341.7	1593	0.21	2126	22	2684	11	2586	10	20.8	>5% discordant	D
18JK08	18JK08 - 11	1.8907	0.0429	0.1843	0.0018	615	914	0.67	2737	25	2691	8	2696	8	-1.7	Oscillatory zoning	I
18JK08	18JK08 - 12	1.9689	0.0465	0.1813	0.0019	164.6	289	0.57	2648	26	2664	9	2662	8	0.6	Oscillatory zoning	I
18JK08	18JK08 - 13	2.3154	0.0590	0.1808	0.0018	364	892	0.41	2314	25	2659	8	2630	7	13.0	>5% discordant	D
18JK08	18JK08 - 14	2.0500	0.0462	0.1821	0.0017	156.5	1330	0.12	2561	24	2671	8	2661	7	4.1	>1000 µg/g U	
18JK08	18JK08 - 15	2.0202	0.0449	0.1831	0.0019	256	455	0.56	2592	24	2680	9	2671	8	3.3	Oscillatory zoning	I
18JK08	18JK08 - 16	1.9482	0.0417	0.1833	0.0018	158.5	501.2	0.32	2671	23	2682	8	2681	8	0.4	Oscillatory zoning	I
18JK08	18JK08 - 17	1.8829	0.0425	0.1819	0.0018	229.9	464.6	0.49	2746	25	2670	8	2677	8	-2.9	Overlaps cracks	
18JK08	18JK08 - 18	1.9658	0.0425	0.1837	0.0018	462.1	881	0.52	2651	24	2686	8	2682	8	1.3	Oscillatory zoning	I
18JK08	18JK08 - 19	1.9376	0.0451	0.2087	0.0030	449	540	0.83	2683	26	2895	12	2860	10	7.3	>5% discordant	D
18JK08	18JK08 - 20	1.9342	0.0412	0.1832	0.0018	223.9	524.1	0.43	2687	23	2681	8	2682	8	-0.2	Oscillatory zoning	I
18JK08	18JK08 - 21	1.7385	0.0393	0.1846	0.0019	70.1	211	0.33	2929	27	2694	9	2718	8	-8.7	>5% discordant	D

Table S3.2 (continued)

sample	spot id	$^{238}U/^{206}Pb$	2SE	$^{207}Pb/^{206}Pb$	2 SE	Th	U	Th/U	$^{238}U/^{206}Pb$	2SE	$^{207}Pb/^{206}Pb$	2 SE	Concordia	2 SE	Disc	Comment	Class
18JK53	18JK53 - 1	1.9508	0.0457	0.1847	0.0020	131.4	204.4	0.64	2668	26	2695	9	2692	8	1.0	Oscillatory zoning	I
18JK53	18JK53 - 2	1.9120	0.0475	0.1847	0.0021	58.1	149.9	0.39	2712	28	2695	9	2697	9	-0.6	Oscillatory zoning	I
18JK53	18JK53 - 3	1.9309	0.0447	0.1904	0.0023	63.4	114.6	0.55	2690	26	2745	10	2738	9	2.0	Xenocrystic	X
18JK53	18JK53 - 4	1.8159	0.0396	0.1827	0.0021	65	120.6	0.54	2828	25	2677	10	2697	9	-5.6	>5% discordant	D
18JK53	18JK53 - 5	1.9124	0.0439	0.1851	0.0024	60.2	107.1	0.56	2712	25	2698	11	2700	10	-0.5	Oscillatory zoning	I
18JK53	18JK53 - 6	1.8850	0.0426	0.1846	0.0019	116.2	236.2	0.49	2744	25	2694	9	2699	8	-1.8	Oscillatory zoning	I
18JK53	18JK53 - 7	1.9346	0.0449	0.1844	0.0020	223	257	0.87	2686	26	2692	9	2691	8	0.2	Oscillatory zoning	I
18JK53	18JK53 - 8	1.9139	0.0440	0.1854	0.0024	37.31	76.6	0.49	2710	25	2701	11	2702	10	-0.3	Oscillatory zoning	I
18JK53	18JK53 - 9	1.9164	0.0441	0.1855	0.0023	54	104.8	0.52	2707	25	2702	10	2703	10	-0.2	Oscillatory zoning	I
18JK53	18JK53 - 10	1.9128	0.0402	0.1846	0.0020	90.3	182.5	0.49	2711	23	2694	9	2696	8	-0.6	Oscillatory zoning	I
18JK53	18JK53 - 11	1.9350	0.0412	0.1848	0.0019	239.1	271.2	0.88	2686	23	2696	8	2695	8	0.4	Oscillatory zoning	I
18JK53	18JK53 - 12	2.0442	0.0460	0.1847	0.0024	48	72.1	0.67	2567	24	2695	11	2674	10	4.7	Oscillatory zoning	I
18JK53	18JK53 - 13	1.8822	0.0425	0.1837	0.0019	147.2	202	0.73	2747	25	2686	9	2692	8	-2.3	Oscillatory zoning	I
18JK53	18JK53 - 14	1.9877	0.0435	0.1864	0.0021	65.83	113.8	0.58	2627	24	2710	9	2699	9	3.1	Oscillatory zoning	I
18JK53	18JK53 - 15	1.7860	0.0415	0.1852	0.0021	40.67	101.4	0.40	2866	27	2699	9	2718	9	-6.2	>5% discordant	D
18JK53	18JK53 - 16	1.9084	0.0437	0.1860	0.0021	59.3	86.5	0.69	2716	25	2706	9	2708	9	-0.4	Oscillatory zoning	I
18JK53	18JK53 - 17	1.9231	0.0407	0.1835	0.0021	42.25	92	0.46	2699	23	2684	9	2686	9	-0.6	Oscillatory zoning	I
18JK53	18JK53 - 18	1.9451	0.0416	0.1848	0.0023	27.6	71.9	0.38	2674	23	2696	10	2692	9	0.8	Oscillatory zoning	I
18JK53	18JK53 - 19	2.0028	0.0441	0.1853	0.0020	129.9	159.1	0.82	2611	24	2700	9	2689	8	3.3	Oscillatory zoning	I
18JK53	18JK53 - 20	1.9520	0.0419	0.1834	0.0021	46.64	104.9	0.44	2666	23	2683	9	2681	9	0.6	Overlaps cracks	
18JK53	18JK53 - 21	1.9425	0.0415	0.1857	0.0020	74.5	110.5	0.67	2677	23	2704	9	2700	8	1.0	Oscillatory zoning	I
18JK53	18JK53 - 22	1.9478	0.0417	0.1845	0.0018	157.8	209.4	0.75	2671	23	2693	8	2691	8	0.8	Oscillatory zoning	I
18JK53	18JK53 - 23	1.9798	0.0431	0.1849	0.0020	96.1	157.4	0.61	2636	24	2697	9	2689	8	2.3	Oscillatory zoning	I

Table S3.2 (continued)

sample	spot id	$^{238}U/^{206}Pb$	2SE	$^{207}Pb/^{206}Pb$	2 SE	Th	U	Th/U	$^{238}U/^{206}Pb$	2SE	$^{207}Pb/^{206}Pb$	2 SE	Concordia	2 SE	Disc	Comment	Class
19JK40	19JK40 - 1	2.0268	0.0452	0.1845	0.0018	130.8	393	0.33	2585	24	2693	8	2682	7	4.0	Oscillatory zoning	I
19JK40	19JK40 - 2	2.0820	0.0520	0.1794	0.0017	232	698	0.33	2529	26	2647	8	2637	7	4.5	Metamict	
19JK40	19JK40 - 3	2.3838	0.0557	0.1814	0.0017	901	728	1.24	2258	22	2665	8	2629	7	15.3	>5% discordant	D
19JK40	19JK40 - 4	2.0012	0.0481	0.1824	0.0018	86.1	288.6	0.30	2613	26	2674	8	2669	8	2.3	Core/rim overlap	
19JK40	19JK40 - 5	2.7181	0.0813	0.1781	0.0023	279.4	1182	0.24	2020	26	2635	11	2568	9	23.3	>5% discordant	D
19JK40	19JK40 - 6	1.9596	0.0422	0.1852	0.0019	179.2	314	0.57	2658	24	2699	8	2695	8	1.5	Core/rim overlap	
19JK40	19JK40 - 7	2.3663	0.0616	0.1693	0.0019	498	1815	0.27	2272	25	2550	9	2520	8	10.9	>5% discordant	D
19JK40	19JK40 - 8	1.9073	0.0437	0.1845	0.0018	148.7	409	0.36	2717	25	2693	8	2695	8	-0.9	Oscillatory zoning	I
19JK40	19JK40 - 9	1.8106	0.0393	0.1825	0.0018	73.26	219.4	0.33	2835	25	2675	8	2691	8	-6.0	>5% discordant	D
19JK40	19JK40 - 10	2.1683	0.0517	0.1838	0.0020	59.4	172.9	0.34	2445	24	2687	9	2660	8	9.0	>5% discordant	D
19JK40	19JK40 - 11	2.5284	0.0703	0.1739	0.0018	130.7	1036	0.13	2148	25	2595	9	2558	7	17.2	>5% discordant	D
19JK40	19JK40 - 12	1.8776	0.0423	0.1871	0.0023	43.43	124.2	0.35	2752	25	2716	10	2721	9	-1.3	Oscillatory zoning	I
19JK40	19JK40 - 13	2.9949	0.0789	0.1888	0.0019	134	600	0.22	1857	21	2731	8	2661	6	32.0	>5% discordant	D
19JK40	19JK40 - 14	2.0080	0.0444	0.1761	0.0018	597.3	1930	0.31	2605	24	2616	9	2615	8	0.4	>1000 µg/g U	
19JK40	19JK40 - 15	1.9724	0.0428	0.1861	0.0019	51	233.5	0.22	2644	24	2707	8	2700	8	2.3	Core/rim overlap	
19JK40	19JK40 - 16	2.2442	0.0504	0.1796	0.0017	57.5	759	0.08	2376	22	2648	8	2622	7	10.3	>5% discordant	D
19JK40	19JK40 - 17	1.8369	0.0405	0.1839	0.0018	182	462	0.39	2802	25	2688	8	2699	8	-4.2	Core/rim overlap	
19JK40	19JK40 - 18	1.9279	0.0446	0.1857	0.0019	79.7	410	0.19	2694	26	2704	8	2703	8	0.4	No oscillatory zoning	
19JK40	19JK40 - 19	2.1097	0.0579	0.1766	0.0018	86.5	429	0.20	2501	28	2620	8	2611	8	4.6	Core/rim overlap	
19JK40	19JK40 - 20	1.9512	0.0457	0.1855	0.0018	183.8	494	0.37	2667	26	2702	8	2699	8	1.3	Oscillatory zoning	I
19JK40	19JK40 - 21	2.8769	0.0654	0.1642	0.0019	482	1640	0.29	1923	19	2499	10	2401	8	23.0	>5% discordant	D
19JK40	19JK40 - 22	1.8477	0.0444	0.1820	0.0020	189.9	275.1	0.69	2789	27	2670	9	2683	9	-4.4	Core/rim overlap	
19JK40	19JK40 - 23	2.0292	0.0453	0.1829	0.0018	297	502.7	0.59	2583	24	2679	8	2669	8	3.6	Oscillatory zoning	I
19JK40	19JK40 - 24	1.8734	0.0421	0.1860	0.0019	239.4	521.3	0.46	2757	25	2706	8	2712	8	-1.9	Oscillatory zoning	I
19JK40	19JK40 - 25	1.8406	0.0407	0.1860	0.0018	428.2	505	0.85	2797	25	2706	8	2715	8	-3.4	Oscillatory zoning	I
19JK40	19JK40 - 26	1.8632	0.0417	0.2066	0.0025	249.6	425.4	0.59	2770	25	2878	10	2864	9	3.8	Same $^{176}Hf/^{177}Hf$	H
19JK40	19JK40 - 27	2.0313	0.0454	0.1851	0.0021	82.6	217.8	0.38	2581	24	2698	9	2683	9	4.4	Oscillatory zoning	I
19JK40	19JK40 - 28	2.1853	0.0621	0.1840	0.0018	490	925	0.53	2429	29	2689	8	2672	7	9.7	>5% discordant	D
19JK40	19JK40 - 29	1.9033	0.0435	0.1841	0.0020	189	259.3	0.73	2722	25	2689	9	2693	9	-1.2	Core/rim overlap	

Table S3.2 (continued)

sample	spot id	$^{238}U/^{206}Pb$	2SE	$^{207}Pb/^{206}Pb$	2 SE	Th	U	Th/U	$^{238}U/^{206}Pb$	2SE	$^{207}Pb/^{206}Pb$	2 SE	Concordia	2 SE	Disc	Comment	Class
19JK41	19JK41 - 1	2.0956	0.0483	0.1876	0.0019	449	570	0.79	2515	24	2720	8	2700	8	7.6	>5% discordant	D
19JK41	19JK41 - 2	1.9128	0.0402	0.1847	0.0018	403	510	0.79	2711	23	2695	8	2697	8	-0.6	Oscillatory zoning	I
19JK41	19JK41 - 3	1.9172	0.0404	0.1849	0.0020	143.1	206.6	0.69	2706	23	2697	9	2698	8	-0.3	Oscillatory zoning	I
19JK41	19JK41 - 4	1.9350	0.0412	0.1831	0.0020	196.5	241.6	0.81	2686	23	2680	9	2681	8	-0.2	Oscillatory zoning	I
19JK41	19JK41 - 5	1.8471	0.0409	0.1843	0.0019	171.4	297.1	0.58	2789	25	2691	9	2702	8	-3.6	Oscillatory zoning	I
19JK41	19JK41 - 6	1.9489	0.0418	0.1850	0.0020	169.8	277.2	0.61	2670	23	2697	9	2694	8	1.0	Core/rim overlap	
19JK41	19JK41 - 7	1.9264	0.0408	0.1853	0.0021	100.5	199.5	0.50	2695	23	2700	9	2699	9	0.2	Oscillatory zoning	I
19JK41	19JK41 - 8	2.0024	0.0441	0.1853	0.0019	267	461.3	0.58	2611	24	2700	8	2690	8	3.3	Oscillatory zoning	I
19JK41	19JK41 - 9	2.1101	0.0490	0.1883	0.0020	197.9	383	0.52	2501	24	2727	9	2703	8	8.3	>5% discordant	D
19JK41	19JK41 - 10	1.9964	0.0478	0.1849	0.0019	337	435	0.77	2618	26	2697	8	2689	8	2.9	Oscillatory zoning	I
19JK41	19JK41 - 11	1.9693	0.0427	0.1846	0.0022	164	218	0.75	2647	24	2694	10	2687	9	1.7	Oscillatory zoning	I
19JK41	19JK41 - 12	1.8965	0.0432	0.1845	0.0019	175.2	379.7	0.46	2730	25	2693	9	2697	8	-1.4	Oscillatory zoning	I
19JK41	19JK41 - 13	1.7634	0.0466	0.1845	0.0019	142.5	287.7	0.50	2896	31	2693	9	2709	9	-7.5	>5% discordant	D
19JK41	19JK41 - 14	1.9376	0.0413	0.1852	0.0019	125.1	299.6	0.42	2683	23	2699	8	2697	8	0.6	Oscillatory zoning	I
19JK41	19JK41 - 15	1.9246	0.0444	0.1844	0.0022	51.9	158.5	0.33	2697	25	2692	10	2693	9	-0.2	Oscillatory zoning	I
19JK41	19JK41 - 16	1.9157	0.0404	0.1862	0.0019	120.7	275.9	0.44	2708	23	2708	8	2708	8	0.0	Core/rim overlap	
19JK41	19JK41 - 17	1.9406	0.0452	0.1831	0.0018	143.2	436	0.33	2679	26	2680	8	2680	8	0.0	Oscillatory zoning	I
19JK41	19JK41 - 18	1.8060	0.0391	0.2137	0.0050	106.9	187.5	0.57	2841	25	2933	19	2899	15	3.2	Same $^{176}Hf/^{177}Hf$	H
19JK41	19JK41 - 19	1.9320	0.0448	0.1860	0.0019	106.8	374	0.29	2689	26	2706	8	2705	8	0.6	Oscillatory zoning	I
19JK41	19JK41 - 20	1.9908	0.0436	0.1844	0.0018	199.3	365.8	0.54	2624	24	2692	8	2685	8	2.5	Core/rim overlap	
19JK41	19JK41 - 21	2.1482	0.0554	0.1803	0.0019	180.7	373.3	0.48	2464	26	2655	9	2638	8	7.2	>5% discordant	D
19JK41	19JK41 - 22	1.9639	0.0424	0.1843	0.0019	72.72	291.1	0.25	2653	24	2691	9	2687	8	1.4	Oscillatory zoning	I
19JK41	19JK41 - 23	1.8706	0.0420	0.1859	0.0021	97.3	248.1	0.39	2761	25	2705	9	2712	9	-2.0	Oscillatory zoning	I
19JK41	19JK41 - 24	1.9666	0.0425	0.1837	0.0020	55.3	141.5	0.39	2650	24	2686	9	2681	8	1.3	Oscillatory zoning	I
19JK41	19JK41 - 25	1.9440	0.0416	0.1875	0.0020	79.3	183.4	0.43	2675	23	2720	9	2714	8	1.6	Xenocrystic	X

Table S3.2 (continued)

sample	spot id	$^{238}U/^{206}Pb$	2SE	$^{207}Pb/^{206}Pb$	2 SE	Th	U	Th/U	$^{238}U/^{206}Pb$	2SE	$^{207}Pb/^{206}Pb$	2 SE	Concordia	2 SE	Disc	Comment	Class
19JK43	19JK43 - 1	1.9223	0.0406	0.1849	0.0020	83.1	195	0.43	2700	23	2697	9	2697	8	-0.1	Oscillatory zoning	I
19JK43	19JK43 - 2	1.7379	0.0393	0.1896	0.0019	97.1	236.6	0.41	2930	27	2738	8	2756	8	-7.0	>5% discordant	D
19JK43	19JK43 - 3	2.1061	0.0488	0.1818	0.0017	164.1	787	0.21	2505	24	2669	8	2654	7	6.1	>5% discordant	D
19JK43	19JK43 - 4	1.6119	0.0390	0.1863	0.0018	145.6	434	0.34	3112	30	2709	8	2741	8	-14.9	>5% discordant	D
19JK43	19JK43 - 5	2.0580	0.0466	0.1865	0.0018	244.2	365	0.67	2553	24	2711	8	2696	7	5.8	>5% discordant	D
19JK43	19JK43 - 6	1.9417	0.0415	0.1840	0.0024	60	96.7	0.62	2678	23	2689	11	2687	10	0.4	Oscillatory zoning	I
19JK43	19JK43 - 7	2.0833	0.0477	0.1851	0.0018	111.3	423.2	0.26	2527	24	2698	8	2682	7	6.3	>5% discordant	D
19JK43	19JK43 - 8	1.7373	0.0392	0.1849	0.0020	51.5	132	0.39	2931	27	2697	9	2722	9	-8.7	>5% discordant	D
19JK43	19JK43 - 9	1.9044	0.0435	0.1855	0.0019	112.3	320	0.35	2721	25	2702	8	2704	8	-0.7	Oscillatory zoning	I
19JK43	19JK43 - 10	2.9976	0.0692	0.1812	0.0017	314	1566	0.20	1856	19	2663	8	2585	6	30.3	>5% discordant	D
19JK43	19JK43 - 11	1.9216	0.0443	0.1866	0.0018	218	457	0.48	2701	25	2712	8	2711	8	0.4	Metamict	
19JK43	19JK43 - 12	2.0610	0.0510	0.1841	0.0018	204	513	0.40	2550	26	2689	8	2678	7	5.2	>5% discordant	D
19JK43	19JK43 - 13	1.9387	0.0413	0.1848	0.0019	79.9	253.9	0.31	2681	23	2696	8	2694	8	0.5	Oscillatory zoning	I
19JK43	19JK43 - 14	1.9339	0.0411	0.1852	0.0021	101.1	162.3	0.62	2687	23	2699	9	2698	9	0.5	Oscillatory zoning	I
19JK43	19JK43 - 15	1.9798	0.0470	0.1849	0.0019	64.4	298	0.22	2636	26	2697	8	2691	8	2.3	Oscillatory zoning	I
19JK43	19JK43 - 16	1.8929	0.0430	0.1843	0.0019	101.6	310	0.33	2734	25	2691	9	2696	8	-1.6	Oscillatory zoning	I
19JK43	19JK43 - 17	2.1839	0.0525	0.1852	0.0018	129.3	520	0.25	2430	24	2699	8	2676	7	10.0	>5% discordant	D
19JK43	19JK43 - 18	1.6474	0.0489	0.2359	0.0071	43.8	187.5	0.23	3058	36	3092	24	3082	20	1.1	Same $^{176}Hf/^{177}Hf$	H
19JK43	19JK43 - 19	1.9183	0.0405	0.1849	0.0019	148.5	255.5	0.58	2705	23	2697	8	2698	8	-0.3	Oscillatory zoning	I
19JK43	19JK43 - 20	1.8155	0.0429	0.1844	0.0019	84.1	227.7	0.37	2829	27	2692	9	2705	8	-5.1	>5% discordant	D
19JK43	19JK43 - 21	1.8570	0.0414	0.1899	0.0021	110.9	245	0.45	2777	25	2741	9	2745	9	-1.3	Xenocrystic	X

Table S3.2 (continued)

sample	spot id	$^{238}U/^{206}Pb$	2SE	$^{207}Pb/^{206}Pb$	2 SE	Th	U	Th/U	$^{238}U/^{206}Pb$	2SE	$^{207}Pb/^{206}Pb$	2 SE	Concordia	2 SE	Disc	Comment	Class
19JK45B	19JK45B - 1	1.6949	0.0373	0.2078	0.0020	242.9	416	0.58	2989	26	2888	8	2896	8	-3.5	Oscillatory zoning	I
19JK45B	19JK45B - 2	1.8939	0.0574	0.2019	0.0028	467	632	0.74	2733	34	2841	11	2831	11	3.8	Possible Pb loss	
19JK45B	19JK45B - 3	1.7902	0.0385	0.2094	0.0020	238.5	433.3	0.55	2861	25	2900	8	2897	7	1.4	Oscillatory zoning	I
19JK45B	19JK45B - 4	1.7547	0.0369	0.2070	0.0020	146.6	308	0.48	2907	25	2881	8	2884	8	-0.9	Oscillatory zoning	I
19JK45B	19JK45B - 5	1.7838	0.0382	0.2076	0.0020	205	338.2	0.61	2869	25	2886	8	2885	7	0.6	Oscillatory zoning	I
19JK45B	19JK45B - 6	1.7794	0.0380	0.2070	0.0020	236.7	501.9	0.47	2875	25	2881	8	2881	7	0.2	Oscillatory zoning	I
19JK45B	19JK45B - 7	1.7835	0.0414	0.2078	0.0019	336	620	0.54	2870	27	2888	7	2886	7	0.6	Oscillatory zoning	I
19JK45B	19JK45B - 8	1.8678	0.0419	0.2078	0.0019	654	856	0.76	2764	25	2888	7	2878	7	4.3	Oscillatory zoning	I
19JK45B	19JK45B - 9	1.7334	0.0391	0.2067	0.0020	199.9	411	0.49	2936	27	2879	8	2884	8	-2.0	Oscillatory zoning	I
19JK45B	19JK45B - 10	1.7325	0.0390	0.2073	0.0020	185.1	349.8	0.53	2937	27	2884	8	2888	8	-1.9	Oscillatory zoning	I
19JK45B	19JK45B - 11	1.8312	0.0402	0.2076	0.0020	184	397	0.46	2809	25	2886	8	2880	7	2.7	Oscillatory zoning	I
19JK45B	19JK45B - 12	1.8519	0.0446	0.2036	0.0020	678	1163	0.58	2783	27	2855	8	2849	8	2.5	>1000 µg/g U	
19JK45B	19JK45B - 13	1.9569	0.0421	0.2072	0.0019	736	713	1.03	2661	24	2883	7	2865	7	7.7	>5% discordant	D
19JK45B	19JK45B - 14	1.7590	0.0371	0.2070	0.0021	130.9	252.5	0.52	2902	25	2881	8	2884	8	-0.7	Oscillatory zoning	I
19JK45B	19JK45B - 15	1.8064	0.0424	0.2070	0.0020	350.7	506	0.69	2840	27	2881	8	2878	7	1.4	Oscillatory zoning	I
19JK45B	19JK45B - 16	1.8560	0.0413	0.2068	0.0020	163.4	337.6	0.48	2778	25	2880	8	2871	7	3.5	Oscillatory zoning	I
19JK45B	19JK45B - 17	1.8765	0.0423	0.2077	0.0019	733	844	0.87	2754	25	2887	7	2877	7	4.6	Oscillatory zoning	I
19JK45B	19JK45B - 18	1.7227	0.0386	0.2076	0.0020	268.3	440	0.61	2951	27	2886	8	2891	8	-2.2	Oscillatory zoning	I
19JK45B	19JK45B - 19	1.8629	0.0416	0.2071	0.0019	296.8	549.7	0.54	2770	25	2882	7	2874	7	3.9	Oscillatory zoning	I
19JK45B	19JK45B - 20	1.7114	0.0381	0.2076	0.0020	256	425	0.60	2966	27	2886	8	2893	8	-2.8	Oscillatory zoning	I
19JK45B	19JK45B - 21	1.9290	0.0447	0.2013	0.0020	1591	1439	1.11	2692	26	2836	8	2824	7	5.1	>5% discordant	D
19JK45B	19JK45B - 22	1.7775	0.0411	0.2078	0.0019	341	614	0.56	2877	27	2888	7	2887	7	0.4	Oscillatory zoning	I
19JK45B	19JK45B - 23	1.7382	0.0393	0.2064	0.0020	191.9	381	0.50	2930	27	2877	8	2881	8	-1.8	Oscillatory zoning	I
19JK45B	19JK45B - 24	1.7188	0.0384	0.2077	0.0020	160.3	345.9	0.46	2956	27	2887	8	2893	8	-2.4	Oscillatory zoning	I
19JK45B	19JK45B - 25	1.7844	0.0382	0.2075	0.0020	287.8	504	0.57	2868	25	2885	8	2884	7	0.6	Oscillatory zoning	I
19JK45B	19JK45B - 26	1.7349	0.0421	0.2074	0.0020	258	579	0.45	2934	29	2885	8	2888	8	-1.7	Oscillatory zoning	I
19JK45B	19JK45B - 27	1.8474	0.0444	0.2070	0.0019	500.1	869	0.58	2789	27	2881	7	2875	7	3.2	Oscillatory zoning	I

Table S3.2 (continued)

sample	spot id	$^{238}U/^{206}Pb$	2SE	$^{207}Pb/^{206}Pb$	2 SE	Th	U	Th/U	$^{238}U/^{206}Pb$	2SE	$^{207}Pb/^{206}Pb$	2 SE	Concordia	2 SE	Disc	Comment	Class
18JK19	18JK19 - 1	1.9260	0.0408	0.1900	0.0019	105.3	216.5	0.49	2696	23	2741	8	2736	8	1.7	Oscillatory zoning	I
18JK19	18JK19 - 2	2.0530	0.0464	0.2021	0.0028	71.9	115	0.63	2558	24	2843	11	2794	10	10.0	>5% discordant	D
18JK19	18JK19 - 3	1.8646	0.0417	0.1880	0.0019	94.9	204.2	0.46	2768	25	2724	8	2728	8	-1.6	Oscillatory zoning	I
18JK19	18JK19 - 4	1.8907	0.0429	0.1872	0.0023	34.3	92.2	0.37	2737	25	2717	10	2720	9	-0.7	Oscillatory zoning	I
18JK19	18JK19 - 5	1.9073	0.0437	0.1882	0.0020	53.8	144.6	0.37	2717	25	2726	9	2725	8	0.3	Oscillatory zoning	I
18JK19	18JK19 - 6	1.9798	0.0431	0.1939	0.0021	52.46	136.2	0.39	2636	24	2775	9	2758	8	5.0	>5% discordant	D
18JK19	18JK19 - 7	1.8871	0.0427	0.1904	0.0020	77.5	153	0.51	2741	25	2745	9	2744	8	0.1	Oscillatory zoning	I
18JK19	18JK19 - 8	1.8727	0.0421	0.1879	0.0022	35.25	84.6	0.42	2758	25	2723	10	2728	9	-1.3	Oscillatory zoning	I
18JK19	18JK19 - 9	1.8893	0.0428	0.1906	0.0022	48.1	100.3	0.48	2739	25	2747	9	2746	9	0.3	Oscillatory zoning	I
18JK19	18JK19 - 10	1.8893	0.0428	0.1899	0.0025	34.1	71.3	0.48	2739	25	2741	11	2740	10	0.1	Oscillatory zoning	I
18JK19	18JK19 - 11	1.8786	0.0424	0.2053	0.0028	74.1	135.6	0.55	2751	25	2868	11	2850	10	4.1	Xenocrystic	X
18JK19	18JK19 - 12	1.8083	0.0425	0.1910	0.0021	56.9	106.5	0.53	2838	27	2750	9	2759	9	-3.2	Oscillatory zoning	I
18JK19	18JK19 - 13	1.9190	0.0405	0.1894	0.0020	78.4	201.4	0.39	2704	23	2736	9	2732	8	1.2	Oscillatory zoning	I
18JK19	18JK19 - 14	1.9091	0.0437	0.1938	0.0028	66.51	112.1	0.59	2715	25	2774	12	2764	11	2.1	Xenocrystic	X
18JK19	18JK19 - 15	1.9231	0.0407	0.1870	0.0020	63.13	176.1	0.36	2699	23	2715	9	2713	8	0.6	Oscillatory zoning	I
18JK19	18JK19 - 16	1.8864	0.0427	0.1884	0.0022	49.19	120.1	0.41	2742	25	2728	10	2729	9	-0.5	Oscillatory zoning	I
18JK19	18JK19 - 17	1.9272	0.0409	0.1872	0.0023	32.95	67.1	0.49	2695	23	2717	10	2713	9	0.8	Oscillatory zoning	I
18JK19	18JK19 - 18	2.0886	0.0480	0.1902	0.0019	166	308	0.54	2522	24	2743	8	2722	7	8.1	>5% discordant	D
18JK19	18JK19 - 19	1.9743	0.0429	0.1889	0.0020	127.2	249.8	0.51	2642	24	2732	9	2721	8	3.3	Oscillatory zoning	I
18JK19	18JK19 - 20	1.8574	0.0414	0.1941	0.0022	53.01	102.3	0.52	2777	25	2776	9	2777	9	0.0	Xenocrystic	X
18JK19	18JK19 - 21	1.8979	0.0432	0.1882	0.0023	40.8	92.5	0.44	2728	25	2726	10	2726	9	-0.1	Oscillatory zoning	I
18JK19	18JK19 - 22	1.9478	0.0417	0.1896	0.0021	46.56	120.9	0.39	2671	23	2738	9	2729	8	2.4	Oscillatory zoning	I
18JK19	18JK19 - 23	1.8723	0.0421	0.1892	0.0023	49	98.9	0.50	2759	25	2735	10	2738	9	-0.9	Oscillatory zoning	I
18JK19	18JK19 - 24	1.9956	0.0478	0.1952	0.0020	166	236.8	0.70	2619	26	2786	8	2771	8	6.0	>5% discordant	D
18JK19	18JK19 - 25	1.9361	0.0412	0.1892	0.0020	97.1	190.2	0.51	2684	23	2734	9	2728	8	1.8	Oscillatory zoning	I
18JK19	18JK19 - 26	1.9497	0.0418	0.1888	0.0022	62.3	110.1	0.57	2669	23	2731	10	2722	9	2.3	Oscillatory zoning	I
18JK19	18JK19 - 27	1.9113	0.0438	0.1883	0.0021	50.9	99.7	0.51	2713	25	2727	9	2725	9	0.5	Oscillatory zoning	I
18JK19	18JK19 - 28	1.9354	0.0412	0.1884	0.0020	77.6	128.5	0.60	2685	23	2728	9	2722	8	1.6	Oscillatory zoning	I
18JK19	18JK19 - 29	1.9433	0.0415	0.1878	0.0021	66.9	147.1	0.45	2676	23	2722	9	2716	9	1.7	Oscillatory zoning	I
18JK19	18JK19 - 30	1.8737	0.0421	0.1882	0.0023	34.9	73.1	0.48	2757	25	2726	10	2730	9	-1.1	Oscillatory zoning	I

Table S3.2 (continued)

sample	spot id	$^{238}U/^{206}Pb$	2SE	$^{207}Pb/^{206}Pb$	2 SE	Th	U	Th/U	$^{238}U/^{206}Pb$	2SE	$^{207}Pb/^{206}Pb$	2 SE	Concordia	2 SE	Disc	Comment	Class
17JK11	17JK11 - 1	1.9264	0.0408	0.2007	0.0018	740	825	0.90	2695	23	2831	7	2820	7	4.8	Oscillatory zoning	I
17JK11	17JK11 - 2	1.8146	0.0395	0.2009	0.0020	122.5	237.6	0.52	2830	25	2833	8	2832	8	0.1	Core/rim overlap	
17JK11	17JK11 - 3	1.8242	0.0399	0.2006	0.0019	271.1	375.1	0.72	2818	25	2830	8	2829	7	0.5	Oscillatory zoning	I
17JK11	17JK11 - 4	1.7775	0.0379	0.2018	0.0019	217.1	354	0.61	2877	25	2840	8	2843	7	-1.3	Oscillatory zoning	I
17JK11	17JK11 - 5	1.7743	0.0378	0.2038	0.0019	210	383.1	0.55	2882	25	2856	8	2858	7	-0.9	Oscillaotry zoning	I
17JK11	17JK11 - 6	1.7883	0.0384	0.2022	0.0019	248.5	433.7	0.57	2863	25	2843	8	2845	7	-0.7	Core/rim overlap	
17JK11	17JK11 - 7	1.7705	0.0376	0.2009	0.0019	179.4	323.8	0.55	2887	25	2833	8	2838	7	-1.9	Oscillatory zoning	I
17JK11	17JK11 - 8	1.8392	0.0406	0.1942	0.0021	287	327	0.88	2799	25	2777	9	2780	8	-0.8	Metamict	
17JK11	17JK11 - 9	1.8584	0.0414	0.1959	0.0019	197.8	378.6	0.52	2776	25	2792	8	2790	8	0.6	Core/rim overlap	
17JK11	17JK11 - 10	1.7832	0.0382	0.1998	0.0019	247	335	0.74	2870	25	2824	8	2828	7	-1.6	Core/rim overlap	
17JK11	17JK11 - 11	1.7976	0.0388	0.2005	0.0020	174.2	276.7	0.63	2851	25	2830	8	2832	8	-0.8	Oscillatory zoning	I
17JK11	17JK11 - 12	1.8295	0.0402	0.1995	0.0019	236.2	349.3	0.68	2811	25	2821	8	2820	7	0.4	Core/rim overlap	
17JK11	17JK11 - 13	1.8172	0.0396	0.2006	0.0019	323	502	0.64	2826	25	2830	8	2830	7	0.1	Oscillatory zoning	I
17JK11	17JK11 - 14	1.8073	0.0392	0.2001	0.0019	246	370.3	0.66	2839	25	2826	8	2827	7	-0.4	Core/rim overlap	
17JK11	17JK11 - 15	1.7819	0.0381	0.2001	0.0020	184.5	309	0.60	2872	25	2826	8	2831	8	-1.6	Oscillatory zoning	I
17JK11	17JK11 - 16	1.8335	0.0403	0.2011	0.0019	201.5	351	0.57	2806	25	2834	8	2832	7	1.0	Oscillatory zoning	I
17JK11	17JK11 - 17	1.7627	0.0373	0.2019	0.0019	236.2	384.7	0.61	2897	25	2841	8	2846	7	-2.0	Oscillatory zoning	I
17JK11	17JK11 - 18	1.8457	0.0409	0.2011	0.0019	529.9	666	0.80	2791	25	2834	8	2831	7	1.5	Oscillatory zoning	I
17JK11	17JK11 - 19	1.8495	0.0410	0.1956	0.0019	137.6	295.6	0.47	2786	25	2789	8	2789	8	0.1	Metamorphic	M
17JK11	17JK11 - 20	1.7665	0.0374	0.2015	0.0019	267.6	437	0.61	2892	25	2838	8	2843	7	-1.9	Oscillatory zoning	I
17JK11	17JK11 - 21	1.7867	0.0383	0.2075	0.0020	201.3	379	0.53	2865	25	2885	8	2884	7	0.7	Xenocrystic	X
17JK11	17JK11 - 22	1.5420	0.0380	0.2053	0.0020	328	441	0.74	3222	31	2868	8	2893	8	-12.4	>5% discordant	D

Table S3.2 (continued)

sample	spot id	$^{238}U/^{206}Pb$	2SE	$^{207}Pb/^{206}Pb$	2 SE	Th	U	Th/U	$^{238}U/^{206}Pb$	2SE	$^{207}Pb/^{206}Pb$	2 SE	Concordia	2 SE	Disc	Comment	Class
17JK26	17JK26 - 1	1.7835	0.0382	0.1984	0.0019	199	255.6	0.78	2870	25	2812	8	2818	8	-2.0	Oscillatory zoning	I
17JK26	17JK26 - 2	1.7844	0.0382	0.1986	0.0019	238.4	464.5	0.51	2868	25	2814	8	2819	8	-1.9	Oscillatory zoning	I
17JK26	17JK26 - 3	1.7851	0.0382	0.2003	0.0019	118.44	264.9	0.45	2867	25	2828	8	2831	7	-1.4	Oscillatory zoning	I
17JK26	17JK26 - 4	2.0137	0.0446	0.1966	0.0018	350.7	687	0.51	2599	24	2797	7	2781	7	7.1	>5% discordant	D
17JK26	17JK26 - 5	1.8265	0.0400	0.1994	0.0019	122.8	316	0.39	2815	25	2821	8	2820	7	0.2	Oscillatory zoning	I
17JK26	17JK26 - 6	1.8546	0.0413	0.1971	0.0020	146	189.6	0.77	2780	25	2802	8	2800	8	0.8	Core/rim overlap	
17JK26	17JK26 - 7	1.8911	0.0429	0.2004	0.0019	284.2	584	0.49	2736	25	2829	8	2821	7	3.3	Oscillatory zoning	I
17JK26	17JK26 - 8	1.7615	0.0403	0.2003	0.0019	147.6	312.7	0.47	2898	27	2828	8	2834	8	-2.5	Oscillatory zoning	I
17JK26	17JK26 - 9	1.8498	0.0411	0.1977	0.0020	178.4	191	0.93	2786	25	2807	8	2805	8	0.7	No oscillatory zoning	I
17JK26	17JK26 - 10	1.8786	0.0424	0.2000	0.0019	177.6	315.1	0.56	2751	25	2825	8	2819	7	2.6	Oscillatory zoning	I
17JK26	17JK26 - 11	1.8285	0.0401	0.1982	0.0020	130.3	285.5	0.46	2812	25	2811	8	2811	8	-0.1	Oscillatory zoning	I
17JK26	17JK26 - 12	1.8450	0.0408	0.1997	0.0019	247.9	484	0.51	2792	25	2823	8	2820	7	1.1	Oscillatory zoning	I
17JK26	17JK26 - 13	1.9055	0.0436	0.1990	0.0018	324	881.6	0.37	2720	25	2817	7	2810	7	3.5	Oscillatory zoning	I
17JK26	17JK26 - 14	1.7352	0.0391	0.2012	0.0021	74.6	199.8	0.37	2934	27	2835	9	2845	8	-3.5	Oscillatory zoning	I
17JK26	17JK26 - 15	1.8925	0.0430	0.1976	0.0019	307.7	564	0.55	2735	25	2806	8	2800	7	2.5	Oscillatory zoning	I
17JK26	17JK26 - 16	1.9873	0.0434	0.1792	0.0019	41.3	192.3	0.21	2628	24	2645	9	2643	8	0.7	Metamorphic	M
17JK26	17JK26 - 17	1.7538	0.0400	0.1988	0.0020	97.29	249	0.39	2909	27	2816	8	2824	8	-3.3	Oscillatory zoning	I
17JK26	17JK26 - 18	1.8136	0.0395	0.1942	0.0021	132.6	203.4	0.65	2831	25	2777	9	2783	8	-1.9	Core/rim overlap	

Table S3.2 (continued)

Secondary reference materials

sample	spot id	$^{238}U/^{206}Pb$	2SE	$^{207}Pb/^{206}Pb$	2 SE	Th	U	Th/U	$^{238}U/^{206}Pb$	2SE	$^{207}Pb/^{206}Pb$	2 SE	Concordia	2 SE	Disc
91500	91500 - 1	5.6786	0.1322	0.0742	0.0022	N/A	N/A	N/A	1046	11	1046	30	1046	11	0.0
91500	91500 - 2	5.7372	0.1317	0.0751	0.0022	N/A	N/A	N/A	1036	11	1070	29	1040	10	3.2
91500	91500 - 3	5.6593	0.1281	0.0755	0.0018	N/A	N/A	N/A	1049	11	1081	24	1054	10	3.0
91500	91500 - 4	5.6561	0.1280	0.0755	0.0017	N/A	N/A	N/A	1050	11	1081	23	1055	10	2.9
91500	91500 - 5	5.6306	0.1300	0.0745	0.0023	N/A	N/A	N/A	1054	11	1054	31	1054	11	0.0
91500	91500 - 6	5.6657	0.1316	0.0762	0.0022	N/A	N/A	N/A	1048	11	1099	29	1054	11	4.7
91500	91500 - 7	5.6433	0.1306	0.0741	0.0018	N/A	N/A	N/A	1052	11	1043	25	1050	10	-0.8
91500	91500 - 8	5.6370	0.1303	0.0746	0.0018	N/A	N/A	N/A	1053	11	1057	24	1054	10	0.4
91500	91500 - 9	5.7045	0.1302	0.0744	0.0018	N/A	N/A	N/A	1041	11	1051	24	1043	10	1.0
91500	91500 - 10	5.6915	0.1296	0.0789	0.0021	N/A	N/A	N/A	1043	11	1169	26	1059	11	10.7
91500	91500 - 11	5.6786	0.1290	0.074	0.0017	N/A	N/A	N/A	1046	11	1041	23	1045	10	-0.5
91500	91500 - 12	5.6818	0.1291	0.0754	0.0018	N/A	N/A	N/A	1045	11	1078	24	1051	10	3.1
91500	91500 - 13	5.6657	0.1284	0.075	0.0017	N/A	N/A	N/A	1048	11	1068	23	1051	10	1.9
91500	91500 - 14	5.6657	0.1284	0.0748	0.0019	N/A	N/A	N/A	1048	11	1062	26	1050	10	1.4
91500	91500 - 15	5.6338	0.1270	0.0763	0.0019	N/A	N/A	N/A	1053	11	1102	25	1061	10	4.4
91500	91500 - 16	5.6402	0.1272	0.0757	0.0017	N/A	N/A	N/A	1052	11	1086	23	1058	10	3.1
91500	91500 - 17	5.7803	0.1336	0.0735	0.002	N/A	N/A	N/A	1029	11	1027	28	1028	10	-0.2
91500	91500 - 18	5.7870	0.1340	0.0731	0.002	N/A	N/A	N/A	1028	11	1016	28	1026	10	-1.2
FC1	FC1 - 1	5.3758	0.1185	0.0760	0.0011	302.1	391	0.77	1100	11	1094	15	1098	9	-0.5
FC1	FC1 - 2	5.3622	0.1179	0.0764	0.0010	331.3	440	0.75	1102	11	1105	13	1103	8	0.2
FC1	FC1 - 3	5.3735	0.1184	0.0768	0.0010	412.3	559	0.74	1100	11	1115	13	1107	9	1.3
FC1	FC1 - 4	5.4558	0.1191	0.0762	0.0009	405.2	667	0.61	1085	11	1099	12	1092	8	1.3
FC1	FC1 - 6	5.3299	0.1165	0.0765	0.0010	332.3	485.1	0.69	1109	11	1107	13	1108	8	-0.1
FC1	FC1 - 7	5.3914	0.1192	0.0756	0.0009	295.6	461.1	0.64	1097	11	1084	12	1091	8	-1.2
FC1	FC1 - 8	5.3917	0.1192	0.0762	0.0011	137.2	283.4	0.48	1097	11	1099	14	1098	9	0.2
FC1	FC1 - 9	5.4206	0.1175	0.0763	0.0010	322.6	480	0.67	1091	11	1102	13	1096	8	1.0
FC1	FC1 - 10	5.4042	0.1168	0.0760	0.0010	438.6	641	0.68	1095	11	1094	13	1094	8	0.0

Table S3.2 (continued)

sample	spot id	$^{238}U/^{206}Pb$	2SE	$^{207}Pb/^{206}Pb$	2 SE	Th	U	Th/U	$^{238}U/^{206}Pb$	2SE	$^{207}Pb/^{206}Pb$	2 SE	Concordia	2 SE	Disc
Maniitsoq	macq - 2	1.7200	0.0385	0.2228	0.0024	146.6	129	1.14	2954	27	3000	9	2996	8	1.5
Maniitsoq	macq - 3	1.7292	0.0389	0.2209	0.0024	183.6	155.9	1.18	2942	27	2987	9	2982	8	1.5
Maniitsoq	macq - 4	1.7001	0.0376	0.2238	0.0024	132.7	131.1	1.01	2982	26	3008	9	3005	8	0.8
Maniitsoq	macq - 5	1.7027	0.0377	0.2231	0.0024	222.9	177.7	1.25	2979	26	3002	9	3000	8	0.8
Maniitsoq	macq - 6	1.7200	0.0385	0.2212	0.0023	303.5	200.3	1.52	2954	27	2989	8	2986	8	1.1
Maniitsoq	macq - 8	1.7185	0.0384	0.2205	0.0022	217.2	160.5	1.35	2957	27	2984	8	2981	8	0.9
Maniitsoq	macq - 9	1.7215	0.0385	0.2225	0.0023	293	204.2	1.43	2952	27	2998	8	2994	8	1.5
Maniitsoq	macq - 10	1.7501	0.0398	0.2240	0.0024	172.8	150.5	1.15	2914	27	3009	9	3000	8	3.2
GJ1	gj1 - 1	10.2859	0.2222	0.0596	0.0010	20.71	664	0.03	598	6	588	18	597	6	-1.7
GJ1	gj1 - 2	10.3520	0.2250	0.0597	0.0010	20.2	655	0.03	594	6	592	18	594	6	-0.5
GJ1	gj1 - 3	10.3552	0.2252	0.0601	0.0010	10.93	419.8	0.03	594	6	606	18	596	6	2.0
GJ1	gj1 - 4	10.4471	0.2292	0.0603	0.0010	8.52	348.5	0.02	589	6	613	18	592	6	3.9
GJ1	gj1 - 5	10.3178	0.2236	0.0605	0.0010	20.25	648	0.03	596	6	621	18	599	6	3.9
GJ1	gj1 - 6	10.3875	0.2266	0.0600	0.0011	18.77	624	0.03	593	6	603	20	593	6	1.7
GJ1	gj1 - 7	10.3391	0.2245	0.0610	0.0011	10.44	424	0.02	595	6	638	19	599	6	6.8
GJ1	gj1 - 8	10.3842	0.2264	0.0608	0.0011	10.88	433	0.03	593	6	631	20	596	6	6.1
GJ1	gj1 - 9	10.4603	0.2298	0.0603	0.0010	10.55	426.6	0.02	589	6	613	18	591	6	4.0
GJ1	gj1 - 10	10.3907	0.2267	0.0599	0.0011	10.94	434.1	0.03	592	6	599	20	593	6	1.1
GJ1	gj1 - 11	10.3767	0.2261	0.0603	0.0011	9.13	376.6	0.02	593	6	613	20	595	6	3.3
GJ1	gj1 - 12	10.4210	0.2281	0.0598	0.0011	9.31	386	0.02	591	6	595	20	591	6	0.8
GJ1	gj1 - 13	10.3413	0.2246	0.0604	0.0011	9.35	386	0.02	595	6	617	20	597	6	3.6
GJ1	gj1 - 14	10.3831	0.2264	0.0594	0.0010	9.02	370.3	0.02	593	6	581	18	592	6	-2.1
GJ1	gj1 - 15	10.3961	0.2270	0.0602	0.0010	8.83	360.5	0.02	592	6	610	18	594	6	2.9
GJ1	gj1 - 16	10.3821	0.2264	0.0600	0.0011	15.86	545	0.03	593	6	603	20	594	6	1.6
GJ1	gj1 - 17	10.4112	0.2276	0.0598	0.0010	18.32	620	0.03	591	6	595	18	592	6	0.7
GJ1	gj1 - 18	10.4384	0.2288	0.0602	0.0010	15.12	534	0.03	590	6	610	18	592	6	3.3

Table S3.3

LA-ICP-MS Hf isotopic data from zircon, including samples and standards. Meas = measured, DM = depleted mantle, calculated using a $^{176}Lu/^{177}Hf$ ratio of 0.023.

Sample results:

sample	spot id	$^{176}Hf/^{177}Hf$ meas	2SE	$^{178}Hf/^{177}Hf$	2SE	$^{180}Hf/^{177}Hf$	2SE	$^{176}Yb/^{177}Hf$	2SE	$^{176}Lu/^{177}Hf$	2SE	Age (Ma)	$^{176}Hf/^{177}Hf$ initial	εHf(t)	2SE	TDM
18JK08	18JK08 - 1	0.281205	0.000024	1.46691	0.00021	1.88673	0.00010	0.02113	0.00055	0.0005	1.10E-05	N/A				
18JK08	18JK08 - 2	0.281193	0.000021	1.46719	0.00013	1.8866	0.00007	0.01436	0.0004	0.0004	1.00E-05	N/A				
18JK08	18JK08 - 3	0.281181	0.000025	1.46709	0.00011	1.8867	0.00007	0.01458	0.00011	0.0004	1.90E-06	N/A				
18JK08	18JK08 - 4	0.281206	0.000023	1.46711	0.00013	1.88671	0.00009	0.01782	0.00067	0.0005	1.50E-05	2782	0.281181	6.28	1.37	2660
18JK08	18JK08 - 5	0.281199	0.000022	1.467	0.00012	1.88666	0.00009	0.0221	0.0014	0.0006	3.80E-05	N/A				
18JK08	18JK08 - 6	0.281181	0.000023	1.4672	0.00014	1.88665	0.0001	0.01868	0.00044	0.0005	1.20E-05	2727	0.281154	4.07	1.37	2861
18JK08	18JK08 - 7	0.281175	0.000024	1.46699	0.00013	1.88686	0.00009	0.02353	0.00036	0.0006	6.50E-06	N/A				
18JK08	18JK08 - 8	0.281153	0.000024	1.46707	0.00013	1.8868	0.00009	0.00958	0.00039	0.0003	1.30E-05	2685	0.281139	2.54	1.39	3011
18JK08	18JK08 - 9	0.28115	0.00002	1.46716	0.00014	1.88678	0.00008	0.01922	0.00043	0.0005	1.20E-05	N/A				
18JK08	18JK08 - 10	0.281193	0.00002	1.46714	0.0001	1.88669	0.00008	0.01376	0.00025	0.0004	6.00E-06	N/A				
18JK08	18JK08 - 11	0.281163	0.000022	1.46714	0.00013	1.88677	0.00009	0.01971	0.00021	0.0005	4.30E-06	2685	0.281136	2.44	1.35	3010
18JK08	18JK08 - 12	0.281196	0.000028	1.46717	0.00013	1.88675	0.0001	0.02537	0.00053	0.0007	1.10E-05	2664	0.281159	2.79	1.48	2923
18JK08	18JK08 - 13	0.281171	0.000024	1.46702	0.00012	1.88676	0.00008	0.0246	0.0019	0.0006	3.90E-05	N/A				
18JK08	18JK08 - 14	0.281185	0.000025	1.46706	0.00013	1.88669	0.0001	0.01868	0.00068	0.0005	1.40E-05	N/A				
18JK08	18JK08 - 15	0.281171	0.000023	1.46722	0.00012	1.88687	0.00011	0.0151	0.00016	0.0004	5.00E-06	2685	0.281149	2.91	1.37	2979
18JK08	18JK08 - 16	0.281152	0.000024	1.46729	0.00011	1.88673	0.00009	0.01659	0.00007	0.0005	3.00E-06	2685	0.281129	2.18	1.39	3052
18JK08	18JK08 - 17	0.281164	0.000022	1.46714	0.00012	1.88676	0.00011	0.01891	0.00026	0.0005	7.00E-06	N/A				
18JK08	18JK08 - 18	0.281155	0.000022	1.46723	0.00014	1.88685	0.00009	0.01945	0.00077	0.0005	1.80E-05	2685	0.281128	2.17	1.35	3041
18JK08	18JK08 - 19	0.281188	0.000022	1.46723	0.000099	1.8867	0.00008	0.01701	0.00074	0.0005	1.30E-05	N/A				
18JK08	18JK08 - 20	0.281152	0.000022	1.4671	0.00011	1.88666	0.00009	0.01190	0.00001	0.0003	2.60E-06	2685	0.281135	2.40	1.35	3052
18JK08	18JK08 - 21	0.281178	0.000028	1.46715	0.00012	1.88664	0.0001	0.01579	0.00024	0.0004	4.10E-06	N/A				

Table S3.3 (continued)

sample	spot id	$^{176}Hf/^{177}Hf$ meas	2SE	$^{178}Hf/^{177}Hf$	2SE	$^{180}Hf/^{177}Hf$	2SE	$^{176}Yb/^{177}Hf$	2SE	$^{176}Lu/^{177}Hf$	2SE	Age (Ma)	$^{176}Hf/^{177}Hf$ initial	εHf(t)	2SE	TDM
18JK53	18JK53 - 1	0.281176	0.000025	1.46714	0.00011	1.8867	0.00009	0.02642	0.00096	0.0008	2.90E-05	2696	0.281135	2.67	1.41	2939
18JK53	18JK53 - 2	0.281158	0.000021	1.4672	0.00014	1.88676	0.00007	0.00716	0.00011	0.0002	3.00E-06	2696	0.281147	3.08	1.33	3008
18JK53	18JK53 - 3	0.281178	0.000028	1.4671	0.00017	1.88656	0.00013	0.01688	0.00024	0.0005	7.10E-06	2745	0.281151	4.38	1.48	2838
18JK53	18JK53 - 4	0.281176	0.000025	1.46727	0.00012	1.88665	0.00009	0.01634	0.00032	0.0005	7.30E-06	N/A				
18JK53	18JK53 - 5	0.281155	0.000027	1.46724	0.00012	1.88672	0.00011	0.0177	0.00053	0.0005	1.70E-05	2696	0.281127	2.37	1.46	3020
18JK53	18JK53 - 6	0.281175	0.000023	1.46724	0.00014	1.88666	0.0001	0.02249	0.00064	0.0007	1.90E-05	2696	0.281141	2.86	1.37	2943
18JK53	18JK53 - 7	0.281186	0.000022	1.46722	0.000099	1.88677	0.00010	0.0299	0.0013	0.0009	3.30E-05	2696	0.281141	2.88	1.35	2901
18JK53	18JK53 - 8	0.281154	0.000026	1.4672	0.00011	1.8867	0.00010	0.01312	0.0001	0.0004	1.50E-06	2696	0.281133	2.59	1.43	3024
18JK53	18JK53 - 9	0.281167	0.000025	1.46715	0.00013	1.88659	0.00012	0.01545	0.00035	0.0005	6.90E-06	2696	0.281143	2.93	1.41	2974
18JK53	18JK53 - 10	0.281167	0.000025	1.4672	0.0001	1.88676	0.00010	0.02091	0.00025	0.0006	8.10E-06	2696	0.281135	2.65	1.41	2974
18JK53	18JK53 - 11	0.281178	0.000024	1.4671	0.00012	1.88657	0.00011	0.0206	0.00012	0.0006	3.10E-06	2696	0.281147	3.09	1.39	2932
18JK53	18JK53 - 12	0.281151	0.000023	1.46706	0.00013	1.88663	0.00013	0.01667	0.0004	0.0005	1.80E-05	2696	0.281124	2.26	1.37	3035
18JK53	18JK53 - 13	0.281175	0.000029	1.46718	0.00011	1.88663	0.00010	0.01982	0.00021	0.0006	4.60E-06	2696	0.281144	3.00	1.50	2943
18JK53	18JK53 - 14	0.281185	0.000026	1.46729	0.00013	1.8867	0.00010	0.02244	0.00018	0.0007	6.00E-06	2710	0.281150	3.54	1.43	2878
18JK53	18JK53 - 15	0.281154	0.000021	1.46717	0.00012	1.88674	0.00009	0.00645	0.00008	0.0002	2.20E-06	N/A				
18JK53	18JK53 - 16	0.281185	0.000028	1.46726	0.00013	1.88659	0.00011	0.02182	0.00077	0.0006	2.10E-05	2696	0.281152	3.26	1.48	2905
18JK53	18JK53 - 17	0.281136	0.000021	1.46719	0.0001	1.88678	0.00011	0.00652	0.00011	0.0002	3.90E-06	2696	0.281126	2.33	1.33	3093
18JK53	18JK53 - 18	0.281154	0.000028	1.46719	0.00012	1.88665	0.0001	0.00751	0.00025	0.0002	6.60E-06	2696	0.281142	2.91	1.48	3024
18JK53	18JK53 - 19	0.281145	0.000025	1.46704	0.00013	1.8867	0.0001	0.02398	0.00047	0.0007	1.30E-05	2696	0.281110	1.77	1.41	3058
18JK53	18JK53 - 20	0.281152	0.000023	1.46724	0.00011	1.88665	0.00009	0.01187	0.00056	0.0004	1.60E-05	N/A				
18JK53	18JK53 - 21	0.281143	0.000025	1.46729	0.00013	1.88673	0.00011	0.0223	0.0011	0.0007	3.20E-05	2696	0.281109	1.73	1.41	3066
18JK53	18JK53 - 22	0.281193	0.000027	1.46714	0.00011	1.8867	0.00012	0.03686	0.00074	0.0010	2.00E-05	2696	0.281139	2.82	1.46	2874
18JK53	18JK53 - 23	0.281199	0.000027	1.4671	0.00012	1.88657	0.0001	0.02914	0.0004	0.0008	1.40E-05	2696	0.281156	3.41	1.46	2851

Table S3.3 (continued)

sample	spot id	$^{176}Hf/^{177}Hf$ meas	2SE	$^{178}Hf/^{177}Hf$	2SE	$^{180}Hf/^{177}Hf$	2SE	$^{176}Yb/^{177}Hf$	2SE	$^{176}Lu/^{177}Hf$	2SE	Age (Ma)	$^{176}Hf/^{177}Hf$ initial	εHf(t)	2SE	TDM
19JK40	19JK40 - 1	0.281177	0.000022	1.46705	0.00011	1.88665	0.00008	0.01422	0.0003	0.0004	1.00E-05	2693	0.281157	3.39	1.35	2941
19JK40	19JK40 - 2	0.281171	0.00002	1.46727	0.00012	1.8867	0.00008	0.02049	0.00093	0.0005	2.00E-05	N/A				
19JK40	19JK40 - 3	0.281197	0.000028	1.46701	0.00015	1.88677	0.00012	0.02808	0.00075	0.0007	2.00E-05	N/A				
19JK40	19JK40 - 4	0.281151	0.000028	1.46728	0.00013	1.88663	0.00009	0.01902	0.00026	0.0005	7.50E-06	N/A				
19JK40	19JK40 - 5	0.281169	0.000026	1.46702	0.00019	1.88664	0.00009	0.02852	0.00048	0.0009	1.60E-05	N/A				
19JK40	19JK40 - 6	0.281161	0.00003	1.46706	0.00011	1.88671	0.00009	0.02304	0.00034	0.0006	9.50E-06	N/A				
19JK40	19JK40 - 7	0.281194	0.000022	1.46707	0.00011	1.88672	0.00009	0.05659	0.00096	0.0014	2.80E-05	N/A				
19JK40	19JK40 - 8	0.281149	0.000024	1.46717	0.00014	1.88672	0.0001	0.02068	0.00018	0.0006	4.20E-06	2693	0.281121	2.08	1.39	3048
19JK40	19JK40 - 9	0.281187	0.000027	1.46719	0.00014	1.88653	0.00012	0.01883	0.00017	0.0005	5.00E-06	N/A				
19JK40	19JK40 - 10	0.281157	0.000017	1.46709	0.00013	1.88676	0.00008	0.00928	0.00032	0.0003	7.90E-06	N/A				
19JK40	19JK40 - 11	0.281192	0.000022	1.46682	0.00015	1.88672	0.00007	0.01575	0.00034	0.0004	8.30E-06	N/A				
19JK40	19JK40 - 12	0.281143	0.000024	1.46716	0.00013	1.88684	0.00011	0.01157	0.00018	0.0003	5.20E-06	2716	0.281126	2.80	1.39	3027
19JK40	19JK40 - 13	0.281215	0.000029	1.46693	0.00016	1.88663	0.00009	0.0376	0.0019	0.0010	4.20E-05	N/A				
19JK40	19JK40 - 14	0.281179	0.000024	1.46704	0.00014	1.88671	0.00010	0.0622	0.0018	0.0016	3.50E-05	N/A				
19JK40	19JK40 - 15	0.281144	0.000028	1.46719	0.00012	1.88664	0.00009	0.01248	0.00019	0.0004	3.30E-06	N/A				
19JK40	19JK40 - 16	0.281152	0.000023	1.46711	0.00013	1.88665	0.00011	0.01487	0.00008	0.0004	2.40E-06	N/A				
19JK40	19JK40 - 17	0.281163	0.000027	1.46715	0.00012	1.88671	0.0001	0.02395	0.00078	0.0006	1.90E-05	N/A				
19JK40	19JK40 - 18	0.281157	0.000027	1.46709	0.00013	1.8866	0.0001	0.02199	0.00028	0.0006	8.80E-06	N/A				
19JK40	19JK40 - 19	0.281192	0.000025	1.46704	0.00016	1.88657	0.00011	0.01412	0.00075	0.0004	1.70E-05	N/A				
19JK40	19JK40 - 20	0.281171	0.000026	1.46709	0.00014	1.8866	0.00009	0.01934	0.00018	0.0005	5.90E-06	2702	0.281145	3.15	1.43	2947
19JK40	19JK40 - 21	0.281184	0.000025	1.46702	0.00011	1.88675	0.00010	0.02107	0.00038	0.0005	1.10E-05	N/A				
19JK40	19JK40 - 22	0.281207	0.000025	1.46723	0.00011	1.8867	0.00010	0.02641	0.00058	0.0007	1.90E-05	N/A				
19JK40	19JK40 - 23	0.281137	0.000029	1.46702	0.00017	1.8869	0.00010	0.01838	0.00019	0.0005	2.90E-06	2679	0.281112	1.44	1.50	3121
19JK40	19JK40 - 24	0.281164	0.000021	1.46715	0.00011	1.88673	0.00010	0.01947	0.00019	0.0005	4.50E-06	2706	0.281138	3.00	1.33	2965
19JK40	19JK40 - 25	0.281176	0.000026	1.46711	0.00011	1.88655	0.00009	0.02096	0.00053	0.0006	1.30E-05	2706	0.281145	3.27	1.43	2919
19JK40	19JK40 - 26	0.281172	0.000026	1.46717	0.00013	1.8866	0.00011	0.02018	0.00033	0.0005	7.80E-06	N/A				
19JK40	19JK40 - 27	0.281135	0.000032	1.46721	0.00016	1.8866	0.00009	0.01184	0.00012	0.0003	2.40E-06	2698	0.281117	2.09	1.58	3092
19JK40	19JK40 - 28	0.281181	0.000029	1.46708	0.00015	1.88657	0.00009	0.02906	0.00031	0.0008	7.50E-06	N/A				
19JK40	19JK40 - 29	0.281173	0.000019	1.4671	0.00011	1.88651	0.00011	0.01369	0.00072	0.0004	1.80E-05	N/A				

Table S3.3 (continued)

sample	spot id	$^{176}Hf/^{177}Hf$ meas	2SE	$^{178}Hf/^{177}Hf$	2SE	$^{180}Hf/^{177}Hf$	2SE	$^{176}Yb/^{177}Hf$	2SE	$^{176}Lu/^{177}Hf$	2SE	Age (Ma)	$^{176}Hf/^{177}Hf$ initial	εHf(t)	2SE	TDM
19JK41	19JK41 - 1	0.281193	0.000027	1.46712	0.00015	1.8868	0.00009	0.02797	0.00046	0.0008	1.20E-05	N/A				
19JK41	19JK41 - 2	0.281197	0.000028	1.46708	0.00012	1.88661	0.00010	0.0388	0.0011	0.0011	2.90E-05	2695	0.281141	2.85	1.48	2860
19JK41	19JK41 - 3	0.281197	0.000027	1.46721	0.00011	1.88665	0.00011	0.03518	0.00057	0.0010	2.10E-05	2697	0.281145	3.03	1.46	2857
19JK41	19JK41 - 4	0.281181	0.000026	1.46722	0.00012	1.88672	0.00011	0.0307	0.00033	0.0008	9.90E-06	2680	0.281137	2.39	1.43	2949
19JK41	19JK41 - 5	0.28119	0.000025	1.46726	0.00011	1.88668	0.00011	0.02081	0.00045	0.0006	1.30E-05	2691	0.281159	3.40	1.41	2894
19JK41	19JK41 - 6	0.281161	0.000019	1.46723	0.00012	1.8868	0.00011	0.02524	0.00021	0.0007	5.20E-06	N/A				
19JK41	19JK41 - 7	0.281194	0.000022	1.46715	0.00011	1.88674	0.00010	0.02573	0.00009	0.0008	5.00E-06	2700	0.281154	3.44	1.35	2862
19JK41	19JK41 - 8	0.281182	0.000022	1.46708	0.00011	1.88674	0.00008	0.02188	0.00054	0.0006	1.30E-05	2700	0.281150	3.30	1.35	2908
19JK41	19JK41 - 9	0.281186	0.000025	1.467	0.00012	1.88667	0.00010	0.02161	0.0008	0.0006	2.60E-05	N/A				
19JK41	19JK41 - 10	0.281183	0.000024	1.4672	0.00012	1.88662	0.00010	0.02878	0.00097	0.0008	2.40E-05	2697	0.281142	2.95	1.39	2911
19JK41	19JK41 - 11	0.281175	0.000029	1.46721	0.00013	1.88659	0.00011	0.0233	0.0019	0.0007	4.90E-05	2694	0.281141	2.82	1.51	2947
19JK41	19JK41 - 12	0.281119	0.000025	1.46721	0.00014	1.8867	0.00010	0.01439	0.00014	0.0004	3.20E-06	2693	0.281098	1.27	1.41	3163
19JK41	19JK41 - 13	0.281177	0.000025	1.46725	0.00013	1.8866	0.00009	0.01881	0.00045	0.0005	1.10E-05	N/A				
19JK41	19JK41 - 14	0.2812	0.000023	1.46721	0.00011	1.88659	0.00011	0.01597	0.00018	0.0005	5.20E-06	2699	0.281176	4.21	1.37	2840
19JK41	19JK41 - 15	0.2812	0.000026	1.46718	0.00013	1.88664	0.00012	0.03022	0.00041	0.0009	8.30E-06	2692	0.281154	3.27	1.43	2854
19JK41	19JK41 - 16	0.281169	0.000025	1.46718	0.00013	1.88659	0.00010	0.02066	0.00047	0.0006	1.20E-05	N/A				
19JK41	19JK41 - 17	0.281176	0.000023	1.46723	0.00011	1.88677	0.00009	0.01343	0.00031	0.0004	7.00E-06	2680	0.281156	3.06	1.37	2968
19JK41	19JK41 - 18	0.281201	0.000021	1.46702	0.0001	1.8866	0.00011	0.024	0.001	0.0007	2.60E-05	N/A				
19JK41	19JK41 - 19	0.28119	0.000023	1.46709	0.00014	1.88679	0.00010	0.01893	0.00048	0.0006	1.00E-05	2706	0.281161	3.85	1.37	2865
19JK41	19JK41 - 20	0.281173	0.00003	1.46724	0.0002	1.88659	0.00011	0.02794	0.00024	0.0008	1.00E-05	N/A				
19JK41	19JK41 - 21	0.281172	0.000026	1.46728	0.00012	1.8866	0.00009	0.02209	0.00021	0.0006	3.20E-06	N/A				
19JK41	19JK41 - 22	0.281147	0.000024	1.46727	0.00014	1.88666	0.00008	0.01084	0.00009	0.0003	3.40E-06	2691	0.281130	2.39	1.39	3059
19JK41	19JK41 - 23	0.281204	0.000032	1.46712	0.00015	1.88664	0.00012	0.01811	0.00046	0.0005	1.10E-05	2705	0.281177	4.38	1.58	2813
19JK41	19JK41 - 24	0.281219	0.000026	1.4672	0.00011	1.88654	0.00010	0.03496	0.00088	0.0010	1.80E-05	2686	0.281168	3.61	1.43	2793
19JK41	19JK41 - 25	0.281192	0.000022	1.46712	0.00013	1.88663	0.00009	0.01808	0.00069	0.0005	1.90E-05	2720	0.281166	4.31	1.35	2832

Table S3.3 (continued)

sample	spot id	$^{176}Hf/^{177}Hf$ meas	2SE	$^{178}Hf/^{177}Hf$	2SE	$^{180}Hf/^{177}Hf$	2SE	$^{176}Yb/^{177}Hf$	2SE	$^{176}Lu/^{177}Hf$	2SE	Age (Ma)	$^{176}Hf/^{177}Hf$ initial	εHf(t)	2SE	TDM
19JK43	19JK43 - 1	0.281206	0.000022	1.46717	0.00012	1.88662	0.00010	0.02771	0.00062	0.0008	1.60E-05	2696	0.281166	3.78	1.35	2823
19JK43	19JK43 - 2	0.281224	0.000026	1.4671	0.00013	1.88681	0.00011	0.03711	0.00043	0.0011	1.20E-05	N/A				
19JK43	19JK43 - 3	0.281187	0.000026	1.46728	0.00013	1.8867	0.00009	0.01833	0.00033	0.0005	1.00E-05	N/A				
19JK43	19JK43 - 4	0.281213	0.000026	1.46715	0.00011	1.88671	0.00010	0.03776	0.00084	0.0010	2.40E-05	N/A				
19JK43	19JK43 - 5	0.281212	0.000024	1.46719	0.00014	1.88667	0.00011	0.03105	0.00069	0.0009	1.60E-05	N/A				
19JK43	19JK43 - 6	0.281181	0.000027	1.46723	0.00013	1.88671	0.00011	0.03155	0.00048	0.0009	1.10E-05	2696	0.281134	2.65	1.46	2919
19JK43	19JK43 - 7	0.281199	0.000024	1.46723	0.00012	1.88668	0.00009	0.02517	0.00071	0.0007	1.70E-05	N/A				
19JK43	19JK43 - 8	0.281197	0.000032	1.46706	0.00013	1.88668	0.00012	0.02185	0.00052	0.0006	1.00E-05	N/A				
19JK43	19JK43 - 9	0.281236	0.000022	1.4671	0.00012	1.88664	0.00010	0.02237	0.00076	0.0006	1.00E-05	2696	0.281203	5.09	1.35	2708
19JK43	19JK43 - 10	0.28123	0.000025	1.46684	0.00013	1.88674	0.00010	0.02527	0.0003	0.0007	1.50E-05	N/A				
19JK43	19JK43 - 11	0.281193	0.000021	1.4671	0.00011	1.8868	0.00013	0.03215	0.00048	0.0008	1.20E-05	N/A				
19JK43	19JK43 - 12	0.281194	0.000027	1.46714	0.00013	1.88661	0.00009	0.0283	0.0021	0.0008	5.40E-05	N/A				
19JK43	19JK43 - 13	0.281173	0.000029	1.4672	0.00012	1.8867	0.00010	0.01709	0.00009	0.0005	3.90E-06	2696	0.281147	3.09	1.50	2950
19JK43	19JK43 - 14	0.28118	0.000024	1.46725	0.00014	1.88678	0.00011	0.03004	0.00042	0.0008	1.40E-05	2696	0.281137	2.75	1.39	2923
19JK43	19JK43 - 15	0.28122	0.000027	1.46684	0.00013	1.88672	0.00009	0.01867	0.00049	0.0006	1.50E-05	2696	0.281190	4.63	1.46	2769
19JK43	19JK43 - 16	0.281209	0.000021	1.46712	0.00013	1.88671	0.00010	0.02873	0.00091	0.0008	2.20E-05	2696	0.281167	3.81	1.33	2812
19JK43	19JK43 - 17	0.281197	0.000026	1.46718	0.00016	1.88654	0.00010	0.037	0.0025	0.0010	6.20E-05	N/A				
19JK43	19JK43 - 18	0.281192	0.000025	1.46737	0.00012	1.88665	0.00010	0.01362	0.00068	0.0004	1.70E-05	N/A				
19JK43	19JK43 - 19	0.281203	0.000028	1.46711	0.00014	1.88652	0.00011	0.03358	0.00077	0.0010	1.90E-05	2696	0.281153	3.33	1.48	2835
19JK43	19JK43 - 20	0.281155	0.000024	1.46722	0.00015	1.8865	0.00009	0.01613	0.00008	0.0005	2.00E-06	N/A				
19JK43	19JK43 - 21	0.281181	0.000029	1.46722	0.00012	1.88664	0.00011	0.0314	0.0012	0.0009	2.90E-05	2741	0.281136	3.72	1.51	2835

Table S3.3 (continued)

sample	spot id	$^{176}Hf/^{177}Hf$ meas	2SE	$^{178}Hf/^{177}Hf$	2SE	$^{180}Hf/^{177}Hf$	2SE	$^{176}Yb/^{177}Hf$	2SE	$^{176}Lu/^{177}Hf$	2SE	Age (Ma)	$^{176}Hf/^{177}Hf$ initial	εHf(t)	2SE	TDM
19JK45B	19JK45B - 1	0.281026	0.000029	1.46723	0.0001	1.88684	0.00010	0.0474	0.001	0.0013	3.20E-05	2885	0.280952	0.53	1.51	3155
19JK45B	19JK45B - 2	0.281057	0.000027	1.46711	0.00012	1.88666	0.00010	0.0659	0.0019	0.0018	5.30E-05	N/A				
19JK45B	19JK45B - 3	0.281011	0.000028	1.46714	0.0001	1.88665	0.00009	0.03345	0.00012	0.0009	2.40E-06	2885	0.280959	0.79	1.49	3213
19JK45B	19JK45B - 4	0.281027	0.000023	1.4672	0.00011	1.8867	0.00011	0.03909	0.00039	0.0011	8.80E-06	2885	0.280965	1.01	1.38	3151
19JK45B	19JK45B - 5	0.28102	0.000035	1.46702	0.00012	1.88642	0.00010	0.04541	0.00053	0.0013	1.60E-05	2885	0.280950	0.45	1.67	3178
19JK45B	19JK45B - 6	0.28103	0.000029	1.46711	0.00011	1.88667	0.00011	0.0474	0.0012	0.0013	3.20E-05	2885	0.280956	0.67	1.51	3140
19JK45B	19JK45B - 7	0.281005	0.000024	1.46719	0.00012	1.88671	0.00012	0.0496	0.0015	0.0014	3.40E-05	2885	0.280928	-0.32	1.40	3236
19JK45B	19JK45B - 8	0.281025	0.000027	1.46713	0.00009	1.88663	0.00007	0.06211	0.00089	0.0017	2.90E-05	2885	0.280930	-0.25	1.47	3159
19JK45B	19JK45B - 9	0.28102	0.000024	1.46716	0.00013	1.88667	0.00011	0.04094	0.00037	0.0012	1.00E-05	2885	0.280955	0.66	1.40	3178
19JK45B	19JK45B - 10	0.281003	0.000026	1.46718	0.00012	1.88672	0.00013	0.03714	0.00057	0.0011	2.00E-05	2885	0.280944	0.27	1.44	3243
19JK45B	19JK45B - 11	0.281017	0.000028	1.46712	0.00012	1.88688	0.00009	0.053	0.0015	0.0015	2.90E-05	2885	0.280936	-0.03	1.49	3190
19JK45B	19JK45B - 12	0.281042	0.000025	1.46719	0.00012	1.88677	0.00010	0.0604	0.0018	0.0017	4.10E-05	N/A				
19JK45B	19JK45B - 13	0.281111	0.000027	1.46712	0.00013	1.8868	0.00012	0.1025	0.0048	0.0028	1.10E-04	N/A				
19JK45B	19JK45B - 14	0.281029	0.000027	1.46718	0.0001	1.88668	0.00011	0.03032	0.00062	0.0009	1.30E-05	2885	0.280981	1.56	1.46	3144
19JK45B	19JK45B - 15	0.281082	0.000028	1.46713	0.00011	1.88674	0.00011	0.07454	0.00046	0.0020	1.20E-05	2885	0.280969	1.16	1.49	2940
19JK45B	19JK45B - 16	0.281019	0.000026	1.46713	0.0001	1.88658	0.00013	0.03244	0.00043	0.0009	1.50E-05	2885	0.280969	1.15	1.44	3182
19JK45B	19JK45B - 17	0.281063	0.000026	1.46709	0.00014	1.88657	0.00012	0.0917	0.0056	0.0025	1.30E-04	2885	0.280925	-0.41	1.46	3013
19JK45B	19JK45B - 18	0.280984	0.000026	1.46706	0.00012	1.88675	0.00011	0.04321	0.0003	0.0012	2.80E-06	2885	0.280916	-0.73	1.44	3316
19JK45B	19JK45B - 19	0.281002	0.000023	1.46719	0.00013	1.88665	0.00010	0.03609	0.00013	0.0010	5.80E-06	2885	0.280947	0.36	1.38	3247
19JK45B	19JK45B - 20	0.281037	0.000028	1.46726	0.00012	1.88669	0.00010	0.0512	0.0017	0.0014	3.90E-05	2885	0.280958	0.73	1.49	3113
19JK45B	19JK45B - 21	0.281204	0.000029	1.46713	0.00012	1.88674	0.00011	0.1858	0.0054	0.0050	1.40E-04	N/A				
19JK45B	19JK45B - 22	0.281004	0.000025	1.46714	0.00011	1.88672	0.00012	0.03746	0.00038	0.0011	5.70E-06	2885	0.280946	0.32	1.42	3239
19JK45B	19JK45B - 23	0.281004	0.000024	1.46716	0.00012	1.88665	0.00011	0.03068	0.0005	0.0009	8.70E-06	2885	0.280954	0.61	1.40	3239
19JK45B	19JK45B - 24	0.281004	0.000025	1.46722	0.00012	1.88686	0.00010	0.04254	0.00065	0.0012	2.10E-05	2885	0.280936	-0.03	1.42	3239
19JK45B	19JK45B - 25	0.281021	0.000023	1.46722	0.00014	1.8866	0.00011	0.03673	0.00073	0.0010	1.80E-05	2885	0.280964	0.95	1.38	3174
19JK45B	19JK45B - 26	0.281014	0.000025	1.4671	0.00010	1.8868	0.00012	0.04025	0.00046	0.0012	7.90E-06	2885	0.280950	0.46	1.42	3201
19JK45B	19JK45B - 27	0.281042	0.000028	1.46722	0.00011	1.88658	0.00010	0.04354	0.00018	0.0013	6.60E-06	2885	0.280973	1.28	1.49	3094

Table S3.3 (continued)

sample	spot id	$^{176}Hf/^{177}Hf$ meas	2SE	$^{178}Hf/^{177}Hf$	2SE	$^{180}Hf/^{177}Hf$	2SE	$^{176}Yb/^{177}Hf$	2SE	$^{176}Lu/^{177}Hf$	2SE	Age (Ma)	$^{176}Hf/^{177}Hf$ initial	εHf(t)	2SE	TDM
18JK19	18JK19 - 1	0.281192	0.000028	1.46713	0.00013	1.88658	0.00010	0.0352	0.00059	0.0010	1.60E-05	2741	0.281137	3.80	1.48	2791
18JK19	18JK19 - 2	0.281189	0.000024	1.46704	0.00012	1.8866	0.00010	0.01939	0.00026	0.0006	6.20E-06	N/A				
18JK19	18JK19 - 3	0.281195	0.000026	1.46713	0.00009	1.88668	0.00011	0.04128	0.0005	0.0012	1.40E-05	2724	0.281130	3.15	1.43	2812
18JK19	18JK19 - 4	0.281168	0.000028	1.4672	0.00011	1.88675	0.00009	0.01821	0.00019	0.0006	3.30E-06	2717	0.281139	3.29	1.48	2930
18JK19	18JK19 - 5	0.281186	0.000026	1.46715	0.00013	1.88666	0.00010	0.0276	0.0017	0.0008	5.20E-05	2726	0.281142	3.62	1.44	2844
18JK19	18JK19 - 6	0.281207	0.000026	1.4672	0.00013	1.88676	0.00012	0.02899	0.0008	0.0009	2.70E-05	N/A				
18JK19	18JK19 - 7	0.281189	0.00003	1.46716	0.00012	1.8866	0.00011	0.02249	0.00033	0.0007	6.70E-06	2745	0.281153	4.45	1.53	2796
18JK19	18JK19 - 8	0.281184	0.000025	1.46721	0.00011	1.88677	0.00010	0.02358	0.00097	0.0007	3.00E-05	2723	0.281147	3.71	1.41	2856
18JK19	18JK19 - 9	0.281188	0.000023	1.46727	0.00012	1.88675	0.00011	0.02644	0.00071	0.0008	1.80E-05	2747	0.281145	4.21	1.37	2796
18JK19	18JK19 - 10	0.281182	0.000022	1.46714	0.00014	1.88671	0.00010	0.01848	0.00048	0.0005	1.10E-05	2741	0.281153	4.36	1.35	2831
18JK19	18JK19 - 11	0.281174	0.000025	1.46726	0.00013	1.88686	0.00011	0.0339	0.0012	0.0010	3.10E-05	2868	0.281120	6.11	1.42	2616
18JK19	18JK19 - 12	0.281156	0.000024	1.46717	0.00014	1.88667	0.00010	0.02184	0.00099	0.0007	2.60E-05	2750	0.281122	3.45	1.39	2913
18JK19	18JK19 - 13	0.281188	0.000022	1.46723	0.00011	1.88654	0.00009	0.02187	0.00077	0.0007	2.00E-05	2736	0.281153	4.23	1.35	2816
18JK19	18JK19 - 14	0.281158	0.000029	1.46719	0.00012	1.88665	0.00010	0.02163	0.00047	0.0006	1.70E-05	2774	0.281124	4.10	1.51	2860
18JK19	18JK19 - 15	0.281187	0.000026	1.46719	0.00015	1.88662	0.00010	0.02727	0.00059	0.0008	2.00E-05	2715	0.281144	3.45	1.43	2860
18JK19	18JK19 - 16	0.281157	0.000023	1.46711	0.00014	1.8866	0.00010	0.01671	0.00042	0.0005	1.50E-05	2728	0.281130	3.23	1.37	2952
18JK19	18JK19 - 17	0.281168	0.000029	1.46725	0.00012	1.88675	0.00011	0.02309	0.00072	0.0007	2.10E-05	2717	0.281132	3.06	1.51	2930
18JK19	18JK19 - 18	0.281186	0.000027	1.46725	0.00013	1.88668	0.00008	0.0393	0.0034	0.0011	9.60E-05	N/A				
18JK19	18JK19 - 19	0.281168	0.000024	1.46724	0.00010	1.88676	0.00010	0.02635	0.00043	0.0008	1.60E-05	2732	0.281127	3.22	1.39	2901
18JK19	18JK19 - 20	0.281192	0.000029	1.46724	0.00013	1.88668	0.00011	0.03068	0.00049	0.0009	1.60E-05	2776	0.281143	4.82	1.51	2723
18JK19	18JK19 - 21	0.281184	0.000026	1.46713	0.00012	1.8866	0.00013	0.02246	0.0004	0.0007	1.10E-05	2726	0.281149	3.86	1.43	2851
18JK19	18JK19 - 22	0.281165	0.000028	1.46729	0.00014	1.88653	0.00009	0.02663	0.00032	0.0008	7.70E-06	2738	0.281122	3.19	1.48	2901
18JK19	18JK19 - 23	0.281188	0.000026	1.46726	0.00014	1.88674	0.00011	0.0244	0.00052	0.0007	1.60E-05	2735	0.281150	4.10	1.44	2819
18JK19	18JK19 - 24	0.281179	0.000028	1.46716	0.00013	1.88679	0.00012	0.03271	0.00054	0.0009	1.60E-05	N/A				
18JK19	18JK19 - 25	0.281169	0.000022	1.46719	0.00013	1.88665	0.00011	0.02732	0.00039	0.0008	1.00E-05	2734	0.281125	3.21	1.35	2892
18JK19	18JK19 - 26	0.281176	0.000031	1.46733	0.00012	1.88669	0.00011	0.0207	0.0018	0.0006	4.60E-05	2731	0.281144	3.81	1.56	2872
18JK19	18JK19 - 27	0.281152	0.000023	1.46722	0.00011	1.88668	0.00011	0.02281	0.00045	0.0007	1.10E-05	2727	0.281117	2.74	1.37	2973
18JK19	18JK19 - 28	0.281169	0.000025	1.46717	0.00014	1.88676	0.00010	0.03	0.0011	0.0009	3.10E-05	2728	0.281122	2.95	1.41	2906
18JK19	18JK19 - 29	0.281185	0.000028	1.4671	0.00012	1.88671	0.00010	0.03782	0.00007	0.0012	2.50E-06	2722	0.281125	2.90	1.48	2854
18JK19	18JK19 - 30	0.28117	0.000022	1.46729	0.00011	1.88678	0.00011	0.02511	0.00072	0.0008	2.30E-05	2726	0.281130	3.19	1.35	2905

Table S3.3 (continued)

sample	spot id	$^{176}Hf/^{177}Hf$ meas	2SE	$^{178}Hf/^{177}Hf$	2SE	$^{180}Hf/^{177}Hf$	2SE	$^{176}Yb/^{177}Hf$	2SE	$^{176}Lu/^{177}Hf$	2SE	Age (Ma)	$^{176}Hf/^{177}Hf$ initial	εHf(t)	2SE	TDM
17JK11	17JK11 - 1	0.281021	0.000029	1.46713	0.00014	1.88647	0.00011	0.0671	0.0043	0.0019	1.20E-04	2834	0.280917	-1.91	1.53	3669
17JK11	17JK11 - 2	0.280927	0.000028	1.46721	0.00015	1.88646	0.00009	0.01409	0.00024	0.0004	8.10E-06	N/A				
17JK11	17JK11 - 3	0.280933	0.000026	1.46712	0.00010	1.88659	0.00011	0.0379	0.0011	0.0011	2.80E-05	2834	0.280874	-3.44	1.44	3833
17JK11	17JK11 - 4	0.280926	0.000032	1.46715	0.00011	1.8865	0.0001	0.01678	0.00013	0.0005	3.20E-06	2834	0.280898	-2.56	1.58	3739
17JK11	17JK11 - 5	0.280928	0.000025	1.46725	0.00011	1.88669	0.00011	0.02046	0.00052	0.0007	1.60E-05	2856	0.280892	-2.25	1.42	3720
17JK11	17JK11 - 6	0.280943	0.00003	1.46722	0.00015	1.88671	0.00011	0.0293	0.0003	0.0009	8.50E-06	N/A				
17JK11	17JK11 - 7	0.280922	0.000023	1.46712	0.00012	1.88674	0.0001	0.01411	0.00018	0.0004	5.90E-06	2834	0.280898	-2.57	1.37	3740
17JK11	17JK11 - 8	0.281003	0.000028	1.46732	0.00011	1.88669	0.00010	0.075	0.011	0.0020	2.70E-04	N/A				
17JK11	17JK11 - 9	0.280918	0.000026	1.46723	0.00011	1.88653	0.00007	0.02583	0.00085	0.0007	2.70E-05	N/A				
17JK11	17JK11 - 10	0.280939	0.000024	1.46716	0.00010	1.88672	0.00009	0.0257	0.001	0.0008	2.90E-05	N/A				
17JK11	17JK11 - 11	0.280922	0.000029	1.46713	0.00011	1.88669	0.00011	0.02224	0.00036	0.0007	1.10E-05	2834	0.280885	-3.05	1.51	3791
17JK11	17JK11 - 12	0.280933	0.000025	1.46709	0.00014	1.88662	0.00011	0.02606	0.00069	0.0008	2.20E-05	N/A				
17JK11	17JK11 - 13	0.280948	0.000029	1.46706	0.00013	1.88655	0.00008	0.02025	0.00047	0.0006	1.20E-05	2834	0.280914	-2.01	1.51	3680
17JK11	17JK11 - 14	0.280923	0.000028	1.46714	0.00013	1.88657	0.00011	0.0248	0.0015	0.0008	4.70E-05	N/A				
17JK11	17JK11 - 15	0.280914	0.000023	1.46718	0.00013	1.88675	0.00011	0.01875	0.00042	0.0006	1.50E-05	2834	0.280882	-3.13	1.37	3800
17JK11	17JK11 - 16	0.280946	0.000022	1.4672	0.00015	1.88677	0.00009	0.02591	0.00071	0.0008	2.30E-05	2834	0.280903	-2.40	1.35	3721
17JK11	17JK11 - 17	0.280932	0.000021	1.46718	0.00012	1.88666	0.00010	0.02639	0.00042	0.0008	1.20E-05	2834	0.280888	-2.94	1.33	3779
17JK11	17JK11 - 18	0.28096	0.000028	1.46706	0.00013	1.88664	0.00012	0.02616	0.00032	0.0008	1.00E-05	2834	0.280917	-1.89	1.49	3667
17JK11	17JK11 - 19	0.280952	0.000027	1.46719	0.00013	1.88668	0.00009	0.015133	0.00007	0.0004	1.40E-06	2789	0.280928	-2.52	1.46	3708
17JK11	17JK11 - 20	0.280902	0.000026	1.46724	0.0001	1.88691	0.00011	0.02283	0.00029	0.0007	6.30E-06	2834	0.280864	-3.79	1.44	3869
17JK11	17JK11 - 21	0.280918	0.000022	1.46719	0.00011	1.8867	0.00010	0.01848	0.00014	0.0005	3.30E-06	2885	0.280888	-1.74	1.35	3682
17JK11	17JK11 - 22	0.280934	0.000026	1.46715	0.00014	1.88665	0.00010	0.03559	0.0009	0.0010	2.50E-05	N/A				

Table S3.3 (continued)

sample	spot id	$^{176}Hf/^{177}Hf$ meas	2SE	$^{178}Hf/^{177}Hf$	2SE	$^{180}Hf/^{177}Hf$	2SE	$^{176}Yb/^{177}Hf$	2SE	$^{176}Lu/^{177}Hf$	2SE	Age (Ma)	$^{176}Hf/^{177}Hf$ initial	εHf(t)	2SE	TDM
17JK26	17JK26 - 1	0.280943	0.000026	1.46712	0.00013	1.8866	0.00011	0.01126	0.00004	0.0003	2.80E-07	2812	0.280925	-2.09	1.44	3676
17JK26	17JK26 - 2	0.280938	0.000032	1.46718	0.00012	1.88678	0.00011	0.0483	0.0029	0.0013	8.10E-05	2814	0.280865	-4.19	1.59	3900
17JK26	17JK26 - 3	0.280922	0.000026	1.46723	0.00011	1.88667	0.0001	0.02502	0.00013	0.0007	5.80E-06	2828	0.280884	-3.22	1.44	3805
17JK26	17JK26 - 4	0.280941	0.000027	1.46702	0.00015	1.88675	0.00009	0.04026	0.00088	0.0011	1.70E-05	N/A				
17JK26	17JK26 - 5	0.280918	0.000024	1.46721	0.00018	1.88672	0.00011	0.0246	0.0017	0.0007	4.20E-05	2821	0.280879	-3.55	1.40	3836
17JK26	17JK26 - 6	0.280893	0.000026	1.46724	0.00014	1.88674	0.00009	0.01082	0.00006	0.0003	9.70E-07	N/A				
17JK26	17JK26 - 7	0.28096	0.000026	1.46716	0.00012	1.88667	0.00009	0.03734	0.00010	0.0010	1.60E-06	2829	0.280904	-2.48	1.44	3727
17JK26	17JK26 - 8	0.280918	0.000026	1.46723	0.00012	1.88658	0.00013	0.0321	0.0012	0.0009	2.80E-05	2828	0.280869	-3.72	1.44	3859
17JK26	17JK26 - 9	0.280901	0.000024	1.46721	0.00013	1.88663	0.0001	0.01126	0.00009	0.0003	1.20E-06	2807	0.280884	-3.71	1.39	3845
17JK26	17JK26 - 10	0.28093	0.000029	1.46725	0.00013	1.8867	0.0001	0.03143	0.00051	0.0009	1.60E-05	2825	0.280884	-3.27	1.51	3809
17JK26	17JK26 - 11	0.280951	0.000026	1.46719	0.00013	1.88656	0.00010	0.0311	0.0008	0.0009	1.90E-05	2811	0.280905	-2.85	1.44	3756
17JK26	17JK26 - 12	0.280959	0.000028	1.46711	0.00012	1.88671	0.00011	0.04348	0.00053	0.0012	1.90E-05	2823	0.280894	-2.95	1.49	3774
17JK26	17JK26 - 13	0.280912	0.000032	1.46726	0.00017	1.88679	0.00011	0.03393	0.00021	0.0010	8.10E-06	2817	0.280860	-4.29	1.58	3913
17JK26	17JK26 - 14	0.280888	0.000028	1.46736	0.00015	1.88676	0.00013	0.01839	0.00059	0.0005	1.30E-05	2835	0.280860	-3.90	1.49	3882
17JK26	17JK26 - 15	0.280951	0.000027	1.46714	0.00014	1.88676	0.00012	0.04015	0.00066	0.0012	1.10E-05	2806	0.280889	-3.55	1.46	3827
17JK26	17JK26 - 16	0.280948	0.000024	1.4673	0.00014	1.88672	0.00009	0.00071	0.00002	1.38E-05	5.20E-07	2645	0.280947	-5.20	1.39	3905
17JK26	17JK26 - 17	0.280932	0.000023	1.4671	0.00011	1.88654	0.0001	0.01406	0.00034	0.0004	1.00E-05	2816	0.280910	-2.56	1.37	3728
17JK26	17JK26 - 18	0.280918	0.000026	1.46724	0.00014	1.88661	0.00011	0.0107	0.00013	0.0003	5.80E-06	N/A				

Table S3.3 (continued)

Secondary standard results:

sample	spot id	$^{176}Hf/^{177}Hf$ meas	2SE	$^{178}Hf/^{177}Hf$	2SE	$^{180}Hf/^{177}Hf$	2SE	$^{176}Yb/^{177}Hf$	2SE	$^{176}Lu/^{177}Hf$	2SE
Mun0	mun0 - 1	0.282115	0.00003	1.46719	0.00011	1.8867	0.0001	0.00004	0.00001	1.98E-06	2.40E-07
Mun0	mun0 - 2	0.282106	0.000026	1.46717	0.00012	1.88656	0.0001	0.00004	0.00001	2.42E-06	2.90E-07
Mun0	mun0 - 3	0.282123	0.000021	1.46722	0.00011	1.88666	0.0001	0.00004	0.00001	2.12E-06	2.50E-07
Mun3	mun3 - 1	0.282144	0.000022	1.46724	0.00012	1.88666	0.0001	0.06167	0.00053	0.0017	5.30E-06
Mun3	mun3 - 2	0.282102	0.000032	1.46721	0.00013	1.88665	0.0001	0.07300	0.01100	0.0017	2.00E-04
Mun3	mun3 - 3	0.282171	0.000024	1.46727	0.00012	1.88663	0.0001	0.13449	0.00068	0.0035	3.10E-06
Mun1	mun1 - 1	0.282113	0.00003	1.46718	0.0001	1.88665	0.0001	0.03189	0.00006	0.0009	3.30E-06
Mun1	mun1 - 2	0.282122	0.00003	1.46721	0.00012	1.88669	0.0001	0.03169	0.00006	0.0009	3.40E-06
Mun1	mun1 - 3	0.282138	0.000026	1.46722	0.00013	1.88666	0.0001	0.03194	0.00007	0.0009	2.80E-06
FC1	FC1 - 1	0.28216	0.000023	1.46716	0.00012	1.88675	0.0001	0.04268	0.00064	0.0011	9.50E-06
FC1	FC1 - 2	0.282152	0.000027	1.46715	0.00013	1.88656	0.0001	0.05360	0.00021	0.0013	8.20E-07
FC1	FC1 - 3	0.282154	0.000027	1.46728	0.00012	1.88665	0.0001	0.05262	0.00019	0.0013	5.10E-07
FC1	FC1 - 4	0.282172	0.000036	1.46725	0.00014	1.88668	0.0001	0.05499	0.00014	0.0014	2.10E-06
FC1	FC1 - 5	0.282205	0.000027	1.46727	0.00012	1.8867	0.0001	0.05733	0.00018	0.0015	9.80E-07
FC1	FC1 - 6	0.282142	0.00002	1.46726	0.0001	1.88669	0.0001	0.04275	0.00031	0.0011	3.50E-06
FC1	FC1 - 7	0.282159	0.000025	1.46725	0.00013	1.88655	0.0001	0.04402	0.00052	0.0011	9.60E-06
FC1	FC1 - 8	0.282147	0.000028	1.46729	0.00013	1.88664	0.0001	0.02854	0.00020	0.0008	3.20E-06
FC1	FC1 - 9	0.282178	0.000027	1.46727	0.00011	1.88672	0.0001	0.03668	0.00047	0.0010	1.30E-05
FC1	FC1 - 10	0.282192	0.000027	1.46719	0.00015	1.88668	0.0001	0.06059	0.00015	0.0016	1.90E-06

Table S3.3 (continued)

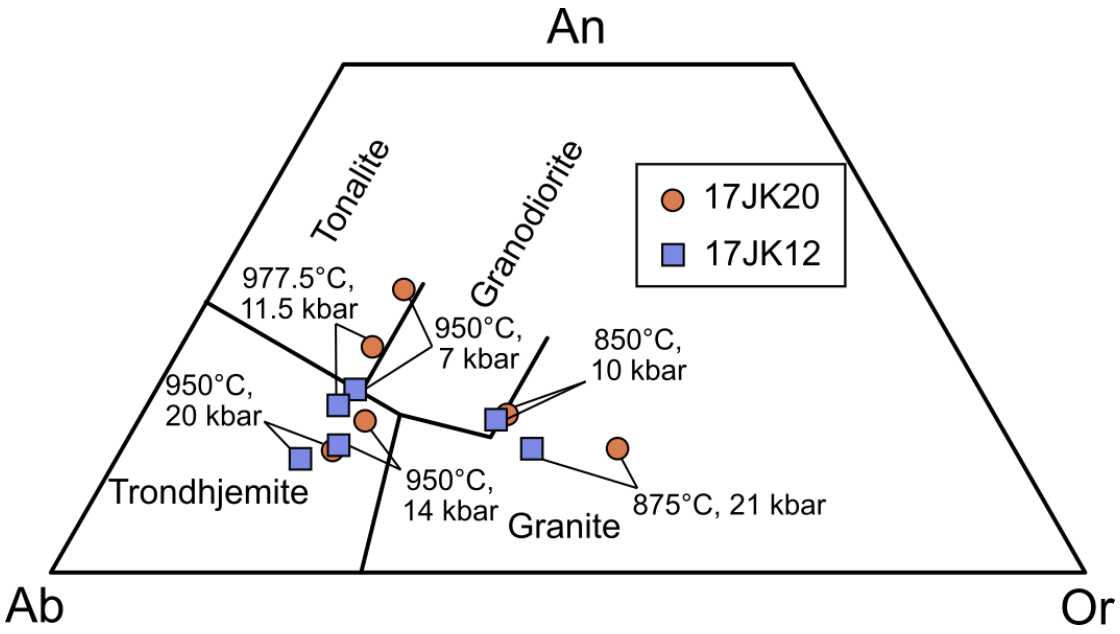
sample	spot id	$^{176}Hf/^{177}Hf$ meas	2SE	$^{178}Hf/^{177}Hf$	2SE	$^{180}Hf/^{177}Hf$	2SE	$^{176}Yb/^{177}Hf$	2SE	$^{176}Lu/^{177}Hf$	2SE
Maniitsoq	macq - 1	0.280836	0.000021	1.46716	0.00014	1.88679	0.0001	0.02100	0.00015	0.0006	2.00E-06
Maniitsoq	macq - 2	0.280829	0.000028	1.4672	0.00011	1.88677	0.0001	0.01626	0.00089	0.0004	2.10E-05
Maniitsoq	macq - 3	0.28083	0.000023	1.46715	0.00011	1.88673	0.0001	0.01661	0.00048	0.0005	1.10E-05
Maniitsoq	macq - 5	0.280874	0.000027	1.46709	0.00011	1.88662	0.0001	0.02557	0.00035	0.0007	1.00E-05
Maniitsoq	macq - 6	0.280837	0.000025	1.46724	0.0001	1.88654	0.0001	0.02959	0.00032	0.0008	3.70E-06
Maniitsoq	macq - 7	0.280845	0.000028	1.46724	0.00011	1.88667	0.0001	0.02991	0.00011	0.0008	1.20E-06
Maniitsoq	macq - 8	0.280851	0.000028	1.46709	0.00016	1.88663	0.0001	0.02633	0.00031	0.0007	8.90E-06
Maniitsoq	macq - 9	0.280828	0.000026	1.46732	0.00011	1.88669	0.0001	0.01919	0.00038	0.0005	8.30E-06
Maniitsoq	macq - 10	0.280876	0.000029	1.4672	0.00015	1.88662	0.0001	0.01645	0.00047	0.0005	1.20E-05
Plesovice	ples - 1	0.282459	0.000021	1.46721	0.00013	1.88668	0.0001	0.00908	0.00002	0.0002	4.50E-07
Plesovice	ples - 2	0.282459	0.000029	1.46722	0.00013	1.88671	0.0001	0.01006	0.00002	0.0002	1.10E-06
Plesovice	ples - 3	0.282455	0.000025	1.46724	0.00011	1.88672	0.0001	0.01101	0.00007	0.0002	2.50E-06
Plesovice	ples - 4	0.282454	0.000021	1.46731	0.0001	1.88674	0.0001	0.00832	0.00003	0.0002	4.10E-07
Plesovice	ples - 5	0.282476	0.000025	1.46722	0.00013	1.88673	0.0001	0.01245	0.00003	0.0002	7.30E-07
Plesovice	ples - 6	0.282431	0.000022	1.46718	0.00012	1.88658	0.0001	0.00924	0.00004	0.0002	2.80E-07
Plesovice	ples - 7	0.282446	0.000025	1.46721	0.00013	1.88673	0.0001	0.00794	0.00003	0.0001	2.50E-07
Plesovice	ples - 8	0.282423	0.000025	1.46721	0.00012	1.88669	0.0001	0.00712	0.00004	0.0001	2.50E-07
Plesovice	ples - 9	0.282446	0.000025	1.46721	0.00010	1.88679	0.0001	0.00659	0.00005	0.0001	3.90E-07
Plesovice	ples - 10	0.282475	0.000029	1.46726	0.00014	1.88666	0.0001	0.00645	0.00003	0.0001	2.40E-07

Table S3.3 (continued)

sample	spot id	$^{176}Hf/^{177}Hf$ meas	2SE	$^{178}Hf/^{177}Hf$	2SE	$^{180}Hf/^{177}Hf$	2SE	$^{176}Yb/^{177}Hf$	2SE	$^{176}Lu/^{177}Hf$	2SE
91500	91500 - 1	0.282259	0.000037	1.46727	0.00013	1.88655	0.0001	0.00580	0.00003	0.0002	3.90E-07
91500	91500 - 2	0.2823	0.000038	1.46733	0.00014	1.88669	0.0002	0.00601	0.00002	0.0002	4.90E-07
91500	91500 - 3	0.282279	0.000037	1.46716	0.00012	1.88655	0.0001	0.00985	0.00002	0.0003	1.40E-06
91500	91500 - 4	0.282256	0.000028	1.46728	0.00012	1.88672	0.0001	0.01262	0.00005	0.0004	5.50E-07
91500	91500 - 5	0.282283	0.000033	1.46724	0.00013	1.88676	0.0001	0.00624	0.00003	0.0002	4.30E-07
91500	91500 - 6	0.282311	0.000033	1.46724	0.00012	1.88668	0.0001	0.00600	0.00003	0.0002	4.20E-07
91500	91500 - 7	0.282292	0.000033	1.46725	0.00013	1.88673	0.0001	0.01012	0.00004	0.0003	1.90E-06
91500	91500 - 8	0.28228	0.000034	1.46727	0.00012	1.8867	0.0002	0.00993	0.00009	0.0003	9.90E-07
91500	91500 - 9	0.282291	0.000032	1.46725	0.00012	1.8868	0.0002	0.01032	0.00003	0.0003	9.90E-07
91500	91500 - 10	0.282285	0.000033	1.46733	0.00012	1.88658	0.0001	0.00938	0.00007	0.0003	8.20E-07
91500	91500 - 11	0.28232	0.000033	1.4673	0.00012	1.88679	0.0002	0.01160	0.00005	0.0003	4.70E-07
91500	91500 - 12	0.282291	0.000035	1.46722	0.0001	1.88662	0.0002	0.01144	0.00005	0.0003	4.90E-07
91500	91500 - 13	0.282289	0.000036	1.46723	0.00016	1.88656	0.0001	0.01170	0.00004	0.0003	6.30E-07
91500	91500 - 14	0.282268	0.000029	1.46723	0.00012	1.88677	0.0001	0.01171	0.00005	0.0003	5.20E-07
91500	91500 - 15	0.282292	0.000046	1.46728	0.00012	1.88659	0.0002	0.01174	0.00005	0.0003	3.70E-07
91500	91500 - 16	0.282292	0.000032	1.46719	0.00014	1.88662	0.0001	0.00795	0.00004	0.0002	3.70E-07
91500	91500 - 17	0.282249	0.000035	1.4672	0.00013	1.88665	0.0002	0.00734	0.00003	0.0002	5.00E-07
91500	91500 - 18	0.282264	0.000028	1.46719	0.00011	1.88676	0.0001	0.00879	0.00003	0.0003	5.00E-07
GJ1	gj1 - 1	0.281982	0.000031	1.46722	0.00013	1.88658	0.0001	0.01001	0.00003	0.0003	4.80E-07
GJ1	gj1 - 2	0.281992	0.000034	1.46714	0.00012	1.88655	0.0001	0.01002	0.00004	0.0003	3.20E-07
GJ1	gj1 - 3	0.281982	0.000029	1.46721	0.00011	1.88679	0.0001	0.01006	0.00004	0.0003	3.40E-07
GJ1	gj1 - 4	0.281988	0.000032	1.4672	0.00013	1.88661	0.0001	0.00997	0.00004	0.0003	4.10E-07
GJ1	gj1 - 5	0.281984	0.000025	1.4672	0.00011	1.88668	0.0001	0.00992	0.00004	0.0003	3.60E-07
GJ1	gj1 - 7	0.281997	0.000034	1.46737	0.00013	1.88664	0.0001	0.01000	0.00005	0.0003	4.20E-07
GJ1	gj1 - 8	0.282003	0.000035	1.4672	0.00012	1.88672	0.0001	0.01001	0.00003	0.0003	3.50E-07
GJ1	gj1 - 10	0.281991	0.000032	1.46723	0.00013	1.88663	0.0001	0.00998	0.00004	0.0003	3.90E-07
GJ1	gj1 - 11	0.282024	0.000036	1.46727	0.00012	1.88671	0.0001	0.01007	0.00004	0.0003	3.90E-07
GJ1	gj1 - 12	0.282001	0.000034	1.46722	0.00013	1.88668	0.0001	0.01007	0.00004	0.0003	3.30E-07
GJ1	gj1 - 13	0.282004	0.00003	1.46716	0.00013	1.88662	0.0001	0.01001	0.00004	0.0003	4.30E-07
GJ1	gj1 - 14	0.281979	0.00003	1.46727	0.00011	1.88669	0.0001	0.01005	0.00004	0.0003	3.10E-07
GJ1	gj1 - 15	0.282007	0.00003	1.46718	0.00011	1.88674	0.0001	0.01001	0.00004	0.0003	3.10E-07
GJ1	gj1 - 16	0.281995	0.000031	1.46731	0.00014	1.88666	0.0001	0.00993	0.00004	0.0003	3.30E-07
GJ1	gj1 - 17	0.282023	0.00003	1.46724	0.00012	1.88671	0.0001	0.01003	0.00004	0.0003	4.10E-07

Appendix S4

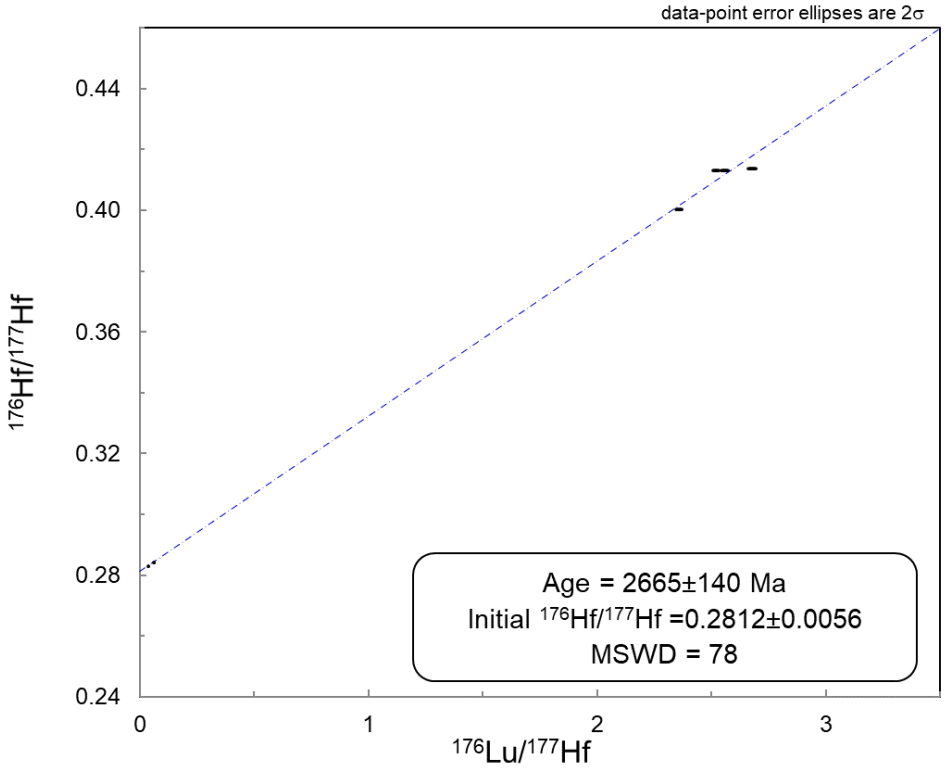
Figure S4.1



Modelled melt compositions plotted based on normative feldspar (An = anorthite, Ab = albite, Or = orthoclase) composition calculated using GCDkit, with granitoid classifications from Barker (1979).

Barker, F., 1979. Trondhjemite: definition, environment and hypotheses of origin. In: Barker, F. (Ed.), Trondhjemites, dacites, and related rocks. Amsterdam, Elsevier. Developments in Petrology 6, 1–12.

Figure S4.2



Errorchron for metabasite sample 17JK03 (data available in Table S4.4).

Table S4.1

Whole-rock major (wt.%) and trace element data (µg/g) for metabasite and leucosome samples investigated in this study.

Sample	Longitude	Latitude	Al_2O_3	BaO	CaO	Cr_2O_3	Fe_2O_3	K_2O	MgO	MnO	Na_2O	N	P_2O_5	SiO_2	TiO_2	Total	LOI
17JK08	48.014072	-82.811545	15.06	0.045	6.439	0.015	8.58	1.51	4.69	0.119	3.03	0.13	0.261	59.59	0.95	100.95	0.66
17JK09	48.013960	-82.812949	14.68	0.007	13.198	0.014	15.85	0.12	4.1	0.295	2.31	0.08	0.127	47.72	1.49	99.76	-0.13
17JK12	48.058977	-82.713142	15.69	0.013	10.057	0.032	14.07	0.74	6.35	0.207	2.94	0.12	0.083	48.26	1.16	100.93	1.33
17JK20	48.013574	-82.774865	14.6	0.009	9.306	0.01	17.55	0.54	4.84	0.28	1.97	0.09	0.199	48.44	1.69	99.44	-0.01
19JK13	48.095940	-82.667540	16.21	0.028	4.757	0.005	1.96	0.58	0.68	0.044	4.42	0.08	0.065	71.19	0.13	100.67	0.6
19JK16	48.013314	-82.776532	13.31	0.019	4.361	0.006	1.08	0.43	0.4	0.026	3.37	0.09	0.009	76.08	0.1	100.02	0.83

Sample	Crystalline Moisture	Free Moisture	FeO	La	Ce	Pr	Nd	Sm	Eu	Gd	Tb	Dy	Ho	Er	Yb	Lu	Hf
17JK08	1.03	0.58	6.42	22.5	51.16	6.528	26.3	5.353	1.3671	4.8	0.711	4.299	0.8571	2.46	2.22	0.331	4.43
17JK09	0.76	0.57	11.3	4.3	12.01	2.01	10.48	3.488	1.1868	4.53	0.7754	5.255	1.0995	3.177	3.108	0.452	1.56
17JK12	1.41	0.56	10.34	4.5	11.29	1.68	8.38	2.605	0.9556	3.317	0.5771	3.863	0.8385	2.414	2.365	0.354	1.49
17JK20	0.86	0.57	12.7	8.9	24.25	3.643	17.62	5.108	1.5271	6.031	1.0101	6.761	1.4371	4.216	4.055	0.614	1.97
19JK13	0.82	0.58	1.47	4.5	7.95	0.938	3.82	0.883	0.5933	0.947	0.1513	0.928	0.2112	0.602	212.9	0.556	0.09
19JK16	0.75	0.57	0.84	3.7	5.01	0.493	1.77	0.336	0.3275	0.347	0.0497	0.357	0.0746	0.219	157.2	0.192	0.03

Sample	Nb	Rb	Sr	Ta	Th	U	Y	Zr	Ba	Ti
17JK08	8.378	43.64	265.5	0.47	3.006	0.498	23.62	183	392.9	5414
17JK09	3.67	1.13	141.1	0.236	0.704	0.215	29.32	45	43.6	8652
17JK12	3.352	11.75	121	0.204	0.813	0.276	21.83	48	101.9	6516
17JK20	4.522	3.82	166.1	0.247	0.176	0.059	38.09	64	82.4	9600
19JK13	0.59	0.781	6.36	376.4	0.025	0.173	0.071	6.43	27	850
19JK16	1.76	0.452	4.92	215.2	0.031	0.402	0.164	2.16	84	661

Table S4.1.1

QA/QC for whole-rock major (wt.%) and trace element data (µg/g).

QA/QC type	Sample	Al_2O_3	BaO	CaO	Cr_2O_3	Fe_2O_3	K_2O	MgO	MnO	Na_2O	N	P_2O_5	SiO_2	TiO_2	Total	LOI
Detection limit		0.02	0.004	0.006	0.002	0.01	0.01	0.01	0.002	0.02		0.002	0.04	0.01		
Duplicate	17JK13	15.94	0.09	5.643	0.037	9.97	2.08	4.61	0.148	3.21	0.1	0.209	55.2	1.14	98.99	0.7
Duplicate	17JK13	16.13	0.092	5.686	0.038	10.06	2.11	4.68	0.149	3.22	0.12	0.21	55.69	1.16	99.92	0.69
Duplicate	17JK26	15.1	0.115	4.347	0.006	5.02	1.37	1.37	0.061	3.68	0.13	0.16	66.99	0.66	99.33	0.44
Duplicate	17JK26	15.22	0.112	4.359	0.006	5.04	1.36	1.38	0.061	3.57	0.12	0.16	67.45	0.67	99.82	0.44
Secondary reference	LK-NIP-1	15.15	0.018	10.131	0.021	13.48	0.47	7.25	0.189	2.4	0.11	0.111	48.75	1.15	99.21	0.09
Secondary reference	NPD-1	13.62	0.03	7.981	0.017	12.63	1.35	4.76	0.187	2.72	0.07	0.126	53.46	1.15	99.31	1.26
Secondary reference	GSP-2	14.84	0.149	2.077	0.004	4.88	5.35	0.97	0.042	2.85	0.06	0.302	66.4	0.67	99.23	0.7
Secondary reference	STSD-1	8.7	0.067	3.633	0.008	6.38	1.25	2.2	0.492	1.83	4.08	0.38	42.68	0.66	98.62	30.36
Duplicate	19JK10A	15.33	0.058	3.889	0.003	5.63	1.55	1.38	0.074	4.26	0.11	0.172	66.69	0.69	100.08	0.37
Duplicate	19JK10A	15.31	0.057	3.891	0.004	5.61	1.56	1.38	0.074	4.24	0.09	0.172	66.57	0.69	99.92	0.35
Duplicate	19JK19	30.24	0.004	16.061	0.019	2.71	0.17	2.02	0.035	1.82	0.06	0.014	46.49	0.2	100.46	0.68
Duplicate	19JK19	30.19	0.006	16.053	0.019	2.72	0.17	2	0.036	1.83	0.06	0.013	46.44	0.19	100.34	0.67
Duplicate	19JK23A	16.31	0.078	3.467	0.017	4.48	2.08	2.37	0.046	4.26	0.1	0.124	65.31	0.55	99.86	0.77
Duplicate	19JK23A	16.19	0.068	3.427	0.019	4.65	2.04	2.45	0.044	4.18	0.09	0.126	65.07	0.59	99.76	0.91
Duplicate	19JK29A	14.31	0.023	13.564	0.018	7.8	0.53	5.56	0.193	3.94	0.16	0.188	51.55	0.63	100.59	2.28
Duplicate	19JK29A	14.22	0.019	13.527	0.017	7.78	0.54	5.53	0.193	3.89	0.18	0.185	51.35	0.63	100.15	2.28
Duplicate	19JK32B	13.3	0.023	9.339	0.012	17.28	0.61	4.88	0.239	2.47	0.12	0.273	50.06	1.95	100.41	-0.02
Duplicate	19JK32B	13.2	0.023	9.364	0.012	17.33	0.6	4.94	0.239	2.45	0.15	0.266	50.03	1.95	100.41	0.01
Duplicate	19JK36B	15.87	0.052	3.124	0.005	2.46	1.34	0.76	0.029	5.14	0.1	0.076	70.39	0.31	100.18	0.61
Duplicate	19JK36B	16	0.053	3.145	0.007	2.49	1.37	0.77	0.03	5.18	0.11	0.077	70.69	0.31	100.74	0.63
Duplicate	19JK48A	14.05	0.194	1.39	0.003	1.85	5.37	0.35	0.018	3.24	0.05	0.06	73.14	0.13	100.17	0.39
Duplicate	19JK48A	14.27	0.198	1.454	0.004	1.86	5.29	0.33	0.017	3.36	0.06	0.062	73.3	0.12	100.61	0.34
Duplicate	19JK48B	16.49	0.013	3.17	0.003	0.39	0.76	0.16	0.007	5.9	0.07	0.012	73.28	0.05	100.55	0.32
Duplicate	19JK48B	16.19	0.011	3.14	0.004	0.43	0.78	0.18	0.007	5.78	0.06	0.016	73.43	0.06	100.3	0.28
Split	19JK07B	15.51	0.043	4.262	0.004	3.3	0.96	1.2	0.043	4.88	0.07	0.105	68.78	0.46	100.13	0.59
Split	19JK07B	15.54	0.043	4.183	0.004	3.12	0.95	1.12	0.041	4.92	0.07	0.098	69.59	0.43	100.63	0.6

Table S4.1.1 (continued)

QA/QC type	Sample	Crystalline Moisture	Free Moisture	FeO
Detection limit		0.03	0.01	0.06
Duplicate	17JK13	0.85	0.55	7.89
Duplicate	17JK13	1.06	0.58	7.86
Duplicate	17JK26	0.91	0.59	3.66
Duplicate	17JK26	0.78	0.58	3.7
Blank		0.17	0.16	
Blank		0.16	0.16	
Blank		0.15	0.16	
Secondary reference	MRB-12	4.72	0.64	
Secondary reference	MRB-12	5.17	0.61	
Secondary reference	MRB-12	5.22	0.64	
Secondary reference	JB-1b	1.96	1.12	
Secondary reference	JB-1b	1.95	1.21	
Secondary reference	LK-NIP-1			9.99
Secondary reference	LK-NIP-1			10.02
Secondary reference	PM-S			7.8
Secondary reference	FER-2			15.28
Secondary reference	FER-2			15.28
Secondary reference	BIR-1			8.43
Duplicate	19JK10A	0.83	0.58	3.11
Duplicate	19JK10A	0.83	0.56	3.13
Duplicate	19JK19	0.9	0.58	1.79
Duplicate	19JK19	0.76	0.54	1.78
Duplicate	19JK23A	1.2	0.62	3.44
Duplicate	19JK23A	1.28	0.61	3.52
Duplicate	19JK29A	1.49	0.67	5.61
Duplicate	19JK29A	1.38	0.64	5.5
Duplicate	19JK32B	1.14	0.59	12.51
Duplicate	19JK32B	1.17	0.6	12.63
Duplicate	19JK36B	0.84	0.57	1.59
Duplicate	19JK36B	0.77	0.56	1.5
Duplicate	19JK48A	0.71	0.55	0.73
Duplicate	19JK48A	0.68	0.54	0.9
Duplicate	19JK48B	0.66	0.54	0.17
Duplicate	19JK48B	0.61	0.53	0.9
Split	19JK07B	0.71	0.55	1.95
Split	19JK07B	0.8	0.56	1.75
Duplicate	19JK11			6.45
Duplicate	19JK11			6.43

Table S4.1.1 (continued)

QA/QC type	Sample	La	Ce	Pr	Nd	Sm	Eu	Gd	Tb	Dy	Ho	Er	Yb
Detection limit		0.1	0.12	0.014	0.06	0.026	0.0031	0.009	0.0023	0.009	0.0025	0.007	0.009
Duplicate	19JK01	51.5	84.65	7.787	22.2	1.986	0.6252	0.822	0.0705	0.346	0.053	0.148	0.165
Duplicate	19JK01	51.8	83.58	7.702	22.55	2.07	0.6304	0.815	0.0672	0.341	0.0576	0.15	0.165
Split	19JK07B	9	19.95	2.759	11.95	2.567	1.0071	2.095	0.2856	1.595	0.3006	0.826	0.743
Split	19JK07B SP	9.1	19.93	2.677	11.7	2.554	0.955	2.021	0.2669	1.477	0.2704	0.769	0.702
Duplicate	19JK11	15.2	26.11	2.632	9.2	1.807	0.7394	2.661	0.5221	3.703	0.8235	2.551	2.528
Duplicate	19JK11	15.2	25.88	2.61	9.2	1.884	0.7374	2.701	0.5157	3.672	0.7937	2.512	2.436
Duplicate	19JK20	42.2	78.5	8.593	30.81	5.398	1.2481	4.611	0.6877	4.284	0.8815	2.729	2.703
Duplicate	19JK20	40.5	75.33	8.238	28.91	5.092	1.2057	4.598	0.6669	4.198	0.8589	2.573	2.615
Duplicate	19JK23A	34.3	61.41	6.472	22.2	2.971	1.2185	1.923	0.2036	0.913	0.142	0.34	0.312
Duplicate	19JK23A	32.4	57.76	6.06	20.43	2.737	1.0672	1.685	0.1688	0.757	0.1197	0.295	0.269
Duplicate	19JK30	3	7.8	1.35	7.24	2.455	0.9271	3.394	0.6068	4.014	0.8907	2.638	2.59
Duplicate	19JK30	3.1	8.1	1.344	7.27	2.517	0.9475	3.5	0.6155	4.238	0.913	2.754	2.744
Duplicate	19JK32B	15.8	35.36	4.841	21.79	5.841	1.7856	6.796	1.1551	7.425	1.6032	4.816	4.598
Duplicate	19JK32B	15.5	34.92	4.744	21.33	5.652	1.8111	6.766	1.1574	7.458	1.6202	4.757	4.651
Duplicate	19JK36C	13.6	33.1	4.31	18.27	4.887	1.2946	6.12	1.0753	7.106	1.5088	4.587	4.375
Duplicate	19JK36C	13.2	32.56	4.304	18.12	4.951	1.306	6.218	1.0789	7.052	1.5238	4.537	4.394
Split	19JK36C SP	13	32.55	4.257	18.2	4.888	1.2772	6.016	1.0486	6.798	1.4761	4.341	4.203
Split	19JK36C SP	13	32.4	4.239	18.18	4.677	1.2753	6.079	1.0359	6.75	1.4467	4.417	4.168
Duplicate	19JK48A	72.3	130.25	12.805	38.43	4.435	0.6281	2.101	0.1924	0.771	0.1263	0.338	0.391
Duplicate	19JK48A	77.8	140.48	13.66	41.7	4.635	0.6743	2.289	0.1957	0.842	0.1403	0.337	0.361
Duplicate	19JK48B	2.3	3.79	0.367	1.32	0.16	0.4131	0.119	0.0131	0.08	0.0132	0.043	0.051
Duplicate	19JK48B	2.3	3.81	0.372	1.2	0.198	0.4204	0.129	0.0154	0.083	0.0151	0.035	0.057
Secondary reference	MRB-29	21.3	47.58	6.398	27.21	5.8	1.8765	6.007	0.8785	5.227	1.0313	2.832	2.426
Secondary reference	MRB-29	20.7	46.9	6.078	26.19	5.667	1.7788	5.662	0.8315	4.958	0.9428	2.645	2.23
Secondary reference	MRB-29	21.2	47.89	6.348	27.14	6.04	1.8557	5.842	0.8171	4.997	0.9614	2.673	2.355
Secondary reference	MRB-29	21	47.32	6.298	26.84	6.053	1.8514	5.828	0.8751	5.133	1.0021	2.83	2.339
Secondary reference	BHVO-2	14.9	35.85	5.151	24.19	6.002	2.038	6.046	0.8805	5.228	0.939	2.459	1.883
Secondary reference	AGV-2	36.6	66.91	8.046	29.51	5.473	1.5239	4.552	0.61	3.511	0.6588	1.837	1.62
Secondary reference	GSP-2	179	436.78	54.177	199.5	25.536	2.2131	11.94	1.2168	5.639	0.9253	2.301	1.604
Secondary reference	GSP-2	188	449.96	56.222	207.9	26.247	2.2581	12.04	1.2166	5.655	0.9374	2.33	1.659

Table S4.1.1 (continued)

QA/QC type	Sample	Lu	Hf	Nb	Rb	Sr	Ta	Th	U	Y	Zr	Ba	Ti
Duplicate	19JK01	0.025	3.84	2.399	49.53	553.3	0.129	9.049	0.225	1.56	175	507.8	2466
Duplicate	19JK01	0.028	3.49	2.416	49.5	555	0.139	8.912	0.202	1.54	157	516.9	2397
Split	19JK07B	0.11	2.85	4.233	19.23	752.3	0.226	1.33	0.188	8.21	127	379.3	2679
Split	19JK07B SP	0.097	2.73	3.939	17.27	748.2	0.201	1.285	0.18	7.67	126	360.5	2517
Duplicate	19JK11	0.379	3.84	6.714	74.66	250.6	0.283	3.245	0.328	23.51	160	890.2	4606
Duplicate	19JK11	0.369	3.82	6.854	76.06	254.4	0.292	3.36	0.328	23.57	159	883.4	4688
Duplicate	19JK20	0.42	7.32	6.989	34.97	345.9	0.353	11.338	0.611	24.03	336	631.3	4982
Duplicate	19JK20	0.41	7.8	7.018	35.19	346.5	0.345	11.582	0.634	24.26	370	611.1	4991
Duplicate	19JK23A	0.045	6.44	5.915	71.19	452	0.353	9.594	0.712	3.93	276	688.4	3256
Duplicate	19JK23A	0.037	5.57	5.667	69.19	446.2	0.317	8.268	0.617	3.34	241	589.2	3481
Duplicate	19JK30	0.393	1.48	2.229	1.77	95.9	0.125	0.184	0.055	25.05	52	43.4	6932
Duplicate	19JK30	0.396	1.52	2.211	1.6	93.6	0.126	0.169	0.053	24.54	51	45.4	6766
Duplicate	19JK32B	0.701	4.41	8.252	17.41	138.5	0.536	2.304	0.578	42.66	172	197	12390
Duplicate	19JK32B	0.709	4.37	8.185	16.63	133.5	0.531	2.334	0.573	42.25	167	196.4	11760
Duplicate	19JK36C	0.66	3.51	8.333	96.21	108.2	0.648	0.731	0.472	40.78	118	433.3	10941
Duplicate	19JK36C	0.653	3.48	8.228	95.74	109.3	0.639	0.684	0.477	40.68	120	429.4	10568
Split	19JK36C SP	0.634	3.33	8.326	98.57	103.9	0.627	0.614	0.442	39.43	116	444.7	10616
Split	19JK36C SP	0.632	3.39	8.287	103.73	107.4	0.613	0.618	0.46	40.39	123	450.2	10763
Duplicate	19JK48A	0.069	6.1	1.63	124.01	309.2	0.158	25.098	0.778	3.6	230	1669.4	841
Duplicate	19JK48A	0.062	6.41	1.015	111.54	313.3	0.066	27.819	0.909	3.57	234	>1740	794
Duplicate	19JK48B	0.009	0.9	0.546	14.5	404.2	0.041	0.484	0.144	0.46	32	84	266
Duplicate	19JK48B	0.012	0.83	0.551	13.81	409	0.025	0.379	0.117	0.44	32	89.6	310
Secondary reference	MRB-29	0.356	4.45	12.501	13.41	299.9	0.766	2.491	0.621	26.29	176	275.4	11148
Secondary reference	MRB-29	0.328	4.28	12.942	14.02	313.7	0.757	2.399	0.589	26.82	183	277.1	12118
Secondary reference	MRB-29	0.339	4.34	12.684	13.52	313.6	0.759	2.413	0.594	26.77	178	280.9	12254
Secondary reference	MRB-29	0.347	4.44	12.589	14.2	311.8	0.776	2.479	0.636	26.96	180	281.4	11879
Secondary reference	BHVO-2	0.254	4.43	17.437	8.57	388.8	1.083	1.152	0.407	25.45	175	125.6	16127
Secondary reference	AGV-2	0.236	5.22	13.297	66.36	658.7	0.795	5.803	1.829	18.82	243	1102.6	6256
Secondary reference	GSP-2	0.221	13.04	25.3	232.35	229.8	0.799	104.482	2.346	25.51	534	1302	3953
Secondary reference	GSP-2	0.225	14.04	25.061	229.4	227.5	0.806	108.667	2.44	26.19	560	1274.3	3923

Table S4.2

Mineral composition data for garnet, plagioclase, clinopyroxene, amphibole, and biotite obtained by electron probe microanalysis (EPMA).

Garnet data:

Comment	SiO_2 wt%	TiO_2 wt%	Al_2O_3 wt%	Cr_2O_3 wt%	MgO wt%	CaO wt%	MnO wt%	FeOt wt%	Na_2O wt%	K_2O wt%	Total
17JK08_grt1_1	38.24	0.05	21.47	N/A	5.24	7.75	1.62	26.19	N/A	N/A	100.55
17JK08_grt1_2	38.35	L.O.D.	21.48	N/A	5.73	6.34	1.75	27.10	N/A	N/A	100.74
17JK08_grt1_3	38.32	0.05	21.45	N/A	5.21	7.17	1.73	26.63	N/A	N/A	100.57
17JK08_grt1_4	38.25	0.08	21.41	N/A	5.24	6.70	1.76	27.12	N/A	N/A	100.55
17JK08_grt1_5	37.97	0.04	21.48	N/A	5.05	5.96	2.05	28.05	N/A	N/A	100.59
17JK08_grt1_6	38.27	0.04	21.59	N/A	5.24	5.98	1.92	27.82	N/A	N/A	100.86
17JK08_grt2_1	38.10	0.07	21.55	N/A	5.53	7.31	1.54	26.19	N/A	N/A	100.30
17JK08_grt2_2	38.08	L.O.D.	21.45	N/A	5.82	6.35	1.59	27.06	N/A	N/A	100.38
17JK08_grt2_3	38.39	0.06	21.59	N/A	5.65	6.86	1.57	26.64	N/A	N/A	100.76
17JK08_grt2_4	38.31	L.O.D.	21.64	N/A	5.72	6.32	1.61	27.03	N/A	N/A	100.66
17JK08_grt2_5	38.03	0.04	21.47	N/A	4.73	5.94	2.07	28.38	N/A	N/A	100.65
17JK08_grt2_6	38.11	0.03	21.56	N/A	5.36	7.42	1.55	26.12	N/A	N/A	100.15
17JK20_grt1_1	37.87	0.07	21.27	N/A	3.82	9.67	1.11	26.39	N/A	N/A	100.21
17JK20_grt1_2	37.96	0.06	21.30	N/A	3.82	9.40	1.17	26.64	N/A	N/A	100.35
17JK20_grt1_3	38.09	0.10	21.32	N/A	3.81	9.38	1.13	26.79	N/A	N/A	100.61
17JK20_grt1_4	37.79	0.04	21.19	N/A	4.02	8.34	1.20	27.69	N/A	N/A	100.28
17JK20_grt1_5	38.04	0.06	21.39	N/A	4.00	8.26	1.21	27.55	N/A	N/A	100.50
17JK20_grt1_6	37.76	0.05	21.50	N/A	3.79	8.00	1.28	27.94	N/A	N/A	100.33
17JK20_grt2_1	37.92	0.07	21.20	N/A	3.90	9.08	1.11	27.24	N/A	N/A	100.53
17JK20_grt2_2	38.14	0.06	21.72	N/A	3.96	8.81	1.15	27.17	N/A	N/A	101.01
17JK20_grt2_3	37.89	0.06	21.26	N/A	3.98	8.51	1.13	27.86	N/A	N/A	100.69
17JK20_grt2_4	38.14	L.O.D.	21.68	N/A	4.16	8.21	1.10	27.70	N/A	N/A	101.01
17JK20_grt2_5	38.07	0.06	21.67	N/A	4.08	8.14	1.17	27.49	N/A	N/A	100.68
17JK20_grt2_6	37.98	0.04	21.54	N/A	3.84	8.06	1.21	28.02	N/A	N/A	100.69
17JK12_grt1_line (Line) Pt 1	37.65	0.04	21.13	L.O.D.	4.28	7.10	1.77	27.53	L.O.D.	L.O.D.	99.51
17JK12_grt1_line (Line) Pt 2	37.73	0.04	21.08	0.05	4.12	7.41	1.72	28.00	L.O.D.	L.O.D.	100.13
17JK12_grt1_line (Line) Pt 3	37.64	L.O.D.	20.70	0.07	3.78	7.31	1.74	28.63	0.03	L.O.D.	99.92

Table S4.2 (garnet continued)

Comment	SiO_2 wt%	TiO_2 wt%	Al_2O_3 wt%	Cr_2O_3 wt%	MgO wt%	CaO wt%	MnO wt%	FeOt wt%	Na_2O wt%	K_2O wt%	Total
17JK12_grt1_line (Line) Pt 4	37.39	0.04	20.97	0.07	4.58	7.28	1.67	26.99	L.O.D.	L.O.D.	99.01
17JK12_grt1_line (Line) Pt 5	37.94	L.O.D.	21.32	0.03	4.65	7.35	1.91	26.87	L.O.D.	L.O.D.	100.10
17JK12_grt1_line (Line) Pt 6	37.59	L.O.D.	21.15	0.03	4.49	7.64	1.81	26.89	L.O.D.	L.O.D.	99.62
17JK12_grt1_line (Line) Pt 7	37.72	L.O.D.	21.29	0.03	4.44	7.60	1.87	27.10	L.O.D.	L.O.D.	100.10
17JK12_grt1_line (Line) Pt 8	37.61	L.O.D.	21.09	L.O.D.	4.52	7.67	1.90	26.67	L.O.D.	L.O.D.	99.49
17JK12_grt1_line (Line) Pt 9	37.58	L.O.D.	21.24	0.05	4.41	7.66	1.99	26.87	L.O.D.	L.O.D.	99.83
17JK12_grt1_line (Line) Pt 11	37.73	0.06	21.26	L.O.D.	4.56	7.55	1.84	26.72	L.O.D.	L.O.D.	99.73
17JK12_grt1_line (Line) Pt 12	37.61	0.05	21.14	0.04	4.71	7.43	1.70	26.69	L.O.D.	L.O.D.	99.37
17JK12_grt1_line (Line) Pt 13	37.70	0.06	21.05	0.04	4.75	7.40	1.80	27.28	L.O.D.	L.O.D.	100.09
17JK12_grt1_line (Line) Pt 14	37.82	0.05	21.18	0.03	4.71	7.23	1.76	27.31	L.O.D.	L.O.D.	100.09
17JK12_grt1_line (Line) Pt 15	37.35	L.O.D.	20.83	0.07	3.91	7.43	1.84	28.26	L.O.D.	L.O.D.	99.70
17JK12area2_grt (Line) Pt 1	37.17	0.06	20.96	0.05	3.77	7.11	1.79	28.55	L.O.D.	L.O.D.	99.45
17JK12area2_grt (Line) Pt 2	37.46	L.O.D.	20.95	0.10	4.41	7.48	1.65	27.49	L.O.D.	L.O.D.	99.55
17JK12area2_grt (Line) Pt 3	37.66	L.O.D.	21.04	0.11	4.45	7.45	1.66	27.50	L.O.D.	L.O.D.	99.91
17JK12area2_grt (Line) Pt 4	37.45	0.04	21.10	0.06	4.50	7.48	1.60	27.35	L.O.D.	L.O.D.	99.56
17JK12area2_grt (Line) Pt 5	37.56	L.O.D.	21.29	0.10	4.54	7.38	1.70	27.57	L.O.D.	L.O.D.	100.17
17JK12area2_grt (Line) Pt 6	37.80	L.O.D.	21.24	0.08	4.38	7.43	1.66	27.47	0.03	L.O.D.	100.12
17JK12area2_grt (Line) Pt 7	37.91	L.O.D.	20.73	0.08	4.23	7.41	1.63	27.71	L.O.D.	L.O.D.	99.73
17JK12area2_grt (Line) Pt 8	37.97	L.O.D.	21.25	0.07	3.66	7.25	1.81	28.46	L.O.D.	L.O.D.	100.52
17JK12area2_grt2_c	37.50	L.O.D.	21.03	L.O.D.	4.37	7.38	1.78	27.54	L.O.D.	L.O.D.	99.65
17JK12area2_grt2_r	36.83	0.08	20.76	0.06	3.45	7.31	1.86	29.14	L.O.D.	L.O.D.	99.48
17JK12area5_grt_c1	37.59	L.O.D.	21.25	0.05	4.71	7.59	1.66	27.04	L.O.D.	L.O.D.	99.93
17JK12area5_grt_c2	37.64	L.O.D.	21.27	0.04	4.51	7.11	1.68	27.98	L.O.D.	L.O.D.	100.25
17JK12area5_grt_c3	37.04	L.O.D.	21.02	0.04	4.68	7.44	1.64	27.45	L.O.D.	L.O.D.	99.32
17JK09_grt1 (Line) Pt 1	37.97	0.07	20.87	0.03	2.59	9.94	1.01	28.28	0.02	L.O.D.	100.79
17JK09_grt1 (Line) Pt 2	37.62	0.04	20.89	L.O.D.	2.87	9.89	1.05	27.68	L.O.D.	L.O.D.	100.07
17JK09_grt1 (Line) Pt 3	37.49	0.05	20.84	L.O.D.	2.90	9.97	1.07	27.80	L.O.D.	L.O.D.	100.14
17JK09_grt1 (Line) Pt 4	37.41	0.05	20.58	0.03	2.78	9.99	0.93	27.98	L.O.D.	L.O.D.	99.76
17JK09_grt1 (Line) Pt 5	37.56	0.10	20.93	L.O.D.	2.85	9.80	0.99	27.66	L.O.D.	L.O.D.	99.87
17JK09_grt1 (Line) Pt 6	37.25	L.O.D.	20.63	L.O.D.	2.84	10.04	0.99	27.81	L.O.D.	L.O.D.	99.58

Table S4.2 (garnet continued)

Comment	SiO_2 wt%	TiO_2 wt%	Al_2O_3 wt%	Cr_2O_3 wt%	MgO wt%	CaO wt%	MnO wt%	FeOt wt%	Na_2O wt%	K_2O wt%	Total
17JK09_grt1 (Line) Pt 7	37.36	L.O.D.	20.50	L.O.D.	2.78	9.85	0.95	27.73	L.O.D.	L.O.D.	99.19
17JK09_grt1 (Line) Pt 8	37.41	L.O.D.	20.81	L.O.D.	2.83	9.80	1.06	27.48	L.O.D.	L.O.D.	99.39
17JK09_grt1 (Line) Pt 9	38.09	L.O.D.	21.03	L.O.D.	2.85	9.86	1.05	27.75	L.O.D.	L.O.D.	100.64
17JK09_grt1 (Line) Pt 10	37.55	0.05	20.62	L.O.D.	2.74	9.73	1.06	27.72	L.O.D.	L.O.D.	99.49
17JK09_grt1 (Line) Pt 11	37.62	0.08	20.67	L.O.D.	2.78	9.92	0.99	27.89	L.O.D.	L.O.D.	99.95
17JK09_grt1 (Line) Pt 12	37.63	0.04	20.95	L.O.D.	2.90	9.81	0.93	27.49	L.O.D.	L.O.D.	99.75
17JK09_grt1 (Line) Pt 13	37.70	0.05	20.83	0.03	2.82	9.81	0.97	27.93	L.O.D.	L.O.D.	100.14
17JK09_grt1 (Line) Pt 14	37.76	L.O.D.	20.51	L.O.D.	2.69	10.16	0.92	28.03	L.O.D.	L.O.D.	100.12
17JK09_grt1 (Line) Pt 15	37.02	0.07	20.63	0.05	2.45	10.22	0.97	27.91	L.O.D.	L.O.D.	99.32
17JK09_area2_grt_c	37.04	0.09	20.65	0.03	2.59	10.30	0.89	27.74	L.O.D.	L.O.D.	99.34
17JK09_area2_grt_r	37.35	0.09	20.73	L.O.D.	2.41	10.50	0.90	27.94	L.O.D.	L.O.D.	99.93
17JK09_grt2 (Line) Pt 1	37.34	0.08	20.66	L.O.D.	2.25	10.39	0.94	27.98	L.O.D.	L.O.D.	99.67
17JK09_grt2 (Line) Pt 2	37.09	0.05	20.58	L.O.D.	2.29	10.64	0.95	27.78	L.O.D.	L.O.D.	99.39
17JK09_grt2 (Line) Pt 3	37.28	0.11	20.63	0.05	2.45	10.33	0.89	27.97	L.O.D.	0.02	99.74
17JK09_grt2 (Line) Pt 4	37.67	0.09	20.84	L.O.D.	2.55	10.18	0.91	27.60	L.O.D.	L.O.D.	99.85
17JK09_grt2 (Line) Pt 5	37.53	0.04	21.08	L.O.D.	2.59	10.08	0.98	27.70	L.O.D.	L.O.D.	100.02
17JK09_grt2 (Line) Pt 6	37.65	0.04	20.88	L.O.D.	2.59	10.06	0.97	27.97	L.O.D.	L.O.D.	100.17
17JK09_grt2 (Line) Pt 7	37.49	0.05	20.70	0.04	2.58	10.36	0.96	27.50	L.O.D.	L.O.D.	99.69
17JK09_grt2 (Line) Pt 8	37.57	0.07	20.75	L.O.D.	2.60	10.20	0.97	27.60	L.O.D.	L.O.D.	99.78
17JK09_grt2 (Line) Pt 9	37.59	0.06	20.55	L.O.D.	2.58	10.22	0.92	27.82	L.O.D.	L.O.D.	99.77
17JK09_grt2 (Line) Pt 10	37.67	0.06	20.72	0.03	2.63	10.26	1.00	27.97	L.O.D.	L.O.D.	100.35
17JK09_grt2 (Line) Pt 11	37.49	L.O.D.	20.85	L.O.D.	2.62	10.13	1.01	27.71	L.O.D.	L.O.D.	99.87
17JK09_grt2 (Line) Pt 12	37.40	0.09	20.49	0.03	2.54	10.46	0.95	27.97	L.O.D.	L.O.D.	99.93
17JK09_grt2 (Line) Pt 13	37.60	0.08	20.50	0.03	2.51	10.39	1.01	28.06	L.O.D.	L.O.D.	100.18
17JK09_grt2 (Line) Pt 14	37.22	0.04	20.54	L.O.D.	2.39	10.59	0.94	27.90	L.O.D.	L.O.D.	99.64
17JK09_grt2 (Line) Pt 15	37.31	0.08	20.38	0.05	2.34	10.52	0.90	28.46	L.O.D.	L.O.D.	100.06

Table S4.2 (continued)

Plagioclase data:

Comment	SiO_2 wt%	TiO_2 wt%	Al_2O_3 wt%	Cr_2O_3 wt%	MgO wt%	CaO wt%	MnO wt%	FeOt wt%	SrO wt%	BaO wt%	Na_2O wt%	K_2O wt%	Total
17JK08_area1_pl1	60.32	N/A	26.94	N/A	N/A	7.34	N/A	0.04	N/A	N/A	7.06	0.14	101.84
17JK08_area1_pl2	60.23	N/A	26.88	N/A	N/A	7.36	N/A	0.05	N/A	N/A	7.17	0.10	101.80
17JK08_area1_pl3	60.40	N/A	26.80	N/A	N/A	7.34	N/A	0.02	N/A	N/A	7.16	0.14	101.86
17JK08_area2_pl1	60.10	N/A	26.85	N/A	N/A	7.35	N/A	0.03	N/A	N/A	7.12	0.16	101.61
17JK08_area2_pl2	59.99	N/A	26.85	N/A	N/A	7.26	N/A	L.O.D.	N/A	N/A	7.27	0.15	101.52
17JK08_area2_pl3	60.12	N/A	27.02	N/A	N/A	7.36	N/A	0.02	N/A	N/A	7.16	0.12	101.81
17JK08_area2_pl4	59.97	N/A	26.96	N/A	N/A	7.26	N/A	L.O.D.	N/A	N/A	7.21	0.14	101.54
17JK08_area3_pl1	60.04	N/A	26.85	N/A	N/A	7.28	N/A	0.03	N/A	N/A	7.17	0.20	101.56
17JK08_area3_pl2	60.12	N/A	26.93	N/A	N/A	7.38	N/A	0.03	N/A	N/A	7.27	0.16	101.89
17JK08_area3_pl3	60.13	N/A	26.81	N/A	N/A	7.41	N/A	0.02	N/A	N/A	7.26	0.15	101.79
17JK08_area3_pl4	60.09	N/A	26.73	N/A	N/A	7.33	N/A	0.10	N/A	N/A	7.11	0.15	101.52
17JK08_area3_pl5	59.83	N/A	26.90	N/A	N/A	7.40	N/A	0.04	N/A	N/A	7.23	0.17	101.57
17JK08_area2_pl5	60.19	N/A	26.91	N/A	N/A	7.34	N/A	0.03	N/A	N/A	7.36	0.15	101.99
17JK20_area1_pl1	59.85	N/A	27.30	N/A	N/A	7.77	N/A	0.05	N/A	N/A	6.80	0.19	101.95
17JK20_area1_pl2	59.15	N/A	27.05	N/A	N/A	7.80	N/A	0.05	N/A	N/A	6.55	0.18	100.80
17JK20_area1_pl3	59.84	N/A	27.00	N/A	N/A	7.62	N/A	0.05	N/A	N/A	6.94	0.18	101.63
17JK20_area1_pl4	59.46	N/A	27.40	N/A	N/A	7.83	N/A	0.11	N/A	N/A	6.92	0.18	101.91
17JK20_area2_pl1	59.54	N/A	27.14	N/A	N/A	7.66	N/A	0.02	N/A	N/A	6.98	0.18	101.53
17JK20_area2_pl2	59.64	N/A	27.33	N/A	N/A	7.88	N/A	0.05	N/A	N/A	6.83	0.13	101.85
17JK20_area2_pl3	59.84	N/A	26.99	N/A	N/A	7.61	N/A	0.08	N/A	N/A	6.78	0.19	101.48
17JK20_area2_pl4	59.44	N/A	27.35	N/A	N/A	7.77	N/A	0.03	N/A	N/A	6.69	0.22	101.50
17JK20_area2_pl5	59.65	N/A	27.29	N/A	N/A	7.64	N/A	0.06	N/A	N/A	7.07	0.16	101.88
17JK20_area3_pl1	59.61	N/A	27.26	N/A	N/A	7.70	N/A	0.07	N/A	N/A	6.99	0.16	101.79
17JK20_area3_pl2	59.48	N/A	27.16	N/A	N/A	7.72	N/A	0.03	N/A	N/A	6.73	0.19	101.30
17JK20_area3_pl3	59.71	N/A	27.19	N/A	N/A	7.72	N/A	0.09	N/A	N/A	6.88	0.16	101.75
17JK12area1_pl1_c	58.05	L.O.D.	26.14	L.O.D.	L.O.D.	8.05	L.O.D.	L.O.D.	L.O.D.	0.07	7.30	0.04	99.72
17JK12area1_pl1_r	58.16	L.O.D.	26.12	L.O.D.	L.O.D.	8.18	L.O.D.	0.07	L.O.D.	L.O.D.	7.20	L.O.D.	99.85

Table S4.2 (plagioclase continued)

Comment	SiO_2 wt%	TiO_2 wt%	Al_2O_3 wt%	Cr_2O_3 wt%	MgO wt%	CaO wt%	MnO wt%	FeOt wt%	SrO wt%	BaO wt%	Na_2O wt%	K_2O wt%	Total
17JK12area1_pl2	57.28	L.O.D.	25.79	L.O.D.	L.O.D.	8.71	L.O.D.	0.04	L.O.D.	L.O.D.	7.19	0.07	99.13
17JK12area3_pl1_c	58.82	L.O.D.	25.92	L.O.D.	L.O.D.	7.89	L.O.D.	L.O.D.	L.O.D.	L.O.D.	7.30	0.13	100.17
17JK12area3_pl1_r	58.65	L.O.D.	25.83	L.O.D.	L.O.D.	7.71	L.O.D.	0.08	L.O.D.	L.O.D.	7.41	0.12	99.85
17JK12area3_pl2	58.25	L.O.D.	26.09	L.O.D.	L.O.D.	8.06	L.O.D.	0.06	L.O.D.	L.O.D.	7.15	0.08	99.71
17JK12area3_pl3_c1	58.59	L.O.D.	25.96	L.O.D.	L.O.D.	7.99	L.O.D.	L.O.D.	L.O.D.	L.O.D.	7.22	0.10	99.94
17JK12area3_pl3_c2	58.61	L.O.D.	26.17	L.O.D.	L.O.D.	7.99	L.O.D.	L.O.D.	L.O.D.	L.O.D.	7.27	0.10	100.23
17JK12area3_pl3_c3	58.46	L.O.D.	25.81	L.O.D.	L.O.D.	7.82	L.O.D.	L.O.D.	0.13	L.O.D.	7.26	0.09	99.58
17JK12area3_pl3_r1	59.54	L.O.D.	25.59	L.O.D.	L.O.D.	7.31	L.O.D.	0.12	L.O.D.	L.O.D.	7.66	0.06	100.39
17JK12area3_pl3_r2	58.76	L.O.D.	25.80	L.O.D.	L.O.D.	7.75	L.O.D.	0.10	L.O.D.	L.O.D.	7.40	0.06	99.94
17JK12area3_pl4_c	58.76	L.O.D.	25.76	0.03	L.O.D.	7.61	L.O.D.	L.O.D.	L.O.D.	L.O.D.	7.41	0.10	99.76
17JK12area3_pl4_r	59.43	0.03	25.70	L.O.D.	L.O.D.	7.46	L.O.D.	0.09	0.14	L.O.D.	7.54	0.09	100.54
17JK09_area1_pl1_c	57.91	L.O.D.	26.51	L.O.D.	L.O.D.	8.56	L.O.D.	0.04	L.O.D.	L.O.D.	6.85	0.20	100.10
17JK09_area1_pl1_r	58.41	L.O.D.	26.56	L.O.D.	L.O.D.	8.36	L.O.D.	0.06	L.O.D.	L.O.D.	7.06	0.18	100.70
17JK09_area1_pl2_c	57.79	L.O.D.	26.42	L.O.D.	L.O.D.	8.59	L.O.D.	0.05	0.10	L.O.D.	6.76	0.23	100.01
17JK09_area1_pl2_r	58.32	L.O.D.	26.12	L.O.D.	L.O.D.	8.01	L.O.D.	0.09	0.12	L.O.D.	7.15	0.17	99.99
17JK09_area1_pl3_c	57.99	L.O.D.	26.42	L.O.D.	L.O.D.	8.49	L.O.D.	0.05	L.O.D.	L.O.D.	6.90	0.20	100.12
17JK09_area1_pl3_r	57.82	L.O.D.	26.36	L.O.D.	L.O.D.	8.36	L.O.D.	0.07	L.O.D.	L.O.D.	6.94	0.16	99.81
17JK09_area1_pl4_inc	59.53	L.O.D.	25.61	L.O.D.	L.O.D.	7.37	L.O.D.	0.07	L.O.D.	L.O.D.	7.84	0.04	100.50
17JK09_area1_pl5_inc	58.42	L.O.D.	26.28	L.O.D.	L.O.D.	8.24	L.O.D.	0.20	L.O.D.	L.O.D.	7.13	0.03	100.34
17JK09_area2_pl1_c	58.01	L.O.D.	26.67	L.O.D.	L.O.D.	8.73	L.O.D.	0.09	L.O.D.	L.O.D.	6.77	0.19	100.53
17JK09_area2_pl1_r	57.92	L.O.D.	26.43	L.O.D.	L.O.D.	8.71	L.O.D.	0.10	0.13	L.O.D.	6.88	0.18	100.36
17JK09_area2_pl2_c	58.11	L.O.D.	26.61	0.03	L.O.D.	8.80	L.O.D.	0.03	L.O.D.	L.O.D.	6.66	0.18	100.49
17JK09_area2_pl2_r	58.26	L.O.D.	26.47	L.O.D.	L.O.D.	8.60	L.O.D.	0.03	0.13	L.O.D.	6.76	0.20	100.54
17JK09_area3_pl1_c	57.67	L.O.D.	26.60	L.O.D.	L.O.D.	8.63	L.O.D.	L.O.D.	L.O.D.	L.O.D.	6.70	0.28	99.94
17JK09_area3_pl1_r	57.86	L.O.D.	26.54	L.O.D.	L.O.D.	8.65	L.O.D.	0.11	L.O.D.	L.O.D.	6.86	0.13	100.19
17JK09_area3_pl2	62.77	L.O.D.	23.45	L.O.D.	L.O.D.	4.93	L.O.D.	0.09	L.O.D.	L.O.D.	9.13	0.07	100.45

Table S4.2 (continued)

Clinopyroxene data:

Comment	SiO_2 wt%	TiO_2 wt%	Al_2O_3 wt%	V_2O_3 wt%	Cr_2O_3 wt%	MgO wt%	CaO wt%	MnO wt%	FeOt wt%	NiO wt%	Na_2O wt%	K_2O wt%	Total
17JK20_area1_cpx1	51.08	0.26	2.47	N/A	L.O.D.	11.28	21.85	0.18	12.13	N/A	0.54	N/A	99.79
17JK20_area1_cpx2	51.43	0.21	2.46	N/A	L.O.D.	11.26	21.77	0.17	12.37	N/A	0.60	N/A	100.28
17JK20_area2_cpx1	51.44	0.23	2.27	N/A	L.O.D.	11.65	21.96	0.13	11.67	N/A	0.56	N/A	99.89
17JK20_area2_cpx2	51.51	0.25	2.34	N/A	L.O.D.	11.75	21.93	0.14	11.66	N/A	0.56	N/A	100.14
17JK20_area2_cpx3	51.97	0.13	1.85	N/A	L.O.D.	11.93	22.17	0.11	11.08	N/A	0.54	N/A	99.79
17JK20_area2_cpx4	51.38	0.21	2.26	N/A	L.O.D.	11.75	21.89	0.12	11.85	N/A	0.55	N/A	100.01
17JK20_area2_cpx5	51.57	0.21	2.22	N/A	L.O.D.	11.77	21.90	0.14	11.45	N/A	0.57	N/A	99.82
17JK20_area2_cpx6	51.79	0.16	2.00	N/A	L.O.D.	11.83	22.23	0.13	10.96	N/A	0.56	N/A	99.65
17JK20_grt2_cpx1	51.46	0.25	2.41	N/A	L.O.D.	11.60	21.87	0.15	12.17	N/A	0.59	N/A	100.51
17JK20_grt2_cpx2	51.44	0.23	2.28	N/A	0.03	11.38	21.94	0.14	12.07	N/A	0.53	N/A	100.03
17JK20_grt2_cpx3	51.25	0.24	2.36	N/A	L.O.D.	11.33	21.76	0.16	12.10	N/A	0.57	N/A	99.77
17JK09_area1_px1_c	50.25	0.22	2.58	0.11	L.O.D.	9.67	21.99	0.10	13.88	L.O.D.	0.64	L.O.D.	99.43
17JK09_area1_px1_r	50.42	0.19	2.08	0.07	L.O.D.	9.97	22.10	0.15	13.76	L.O.D.	0.57	L.O.D.	99.31
17JK09_area1_px2_c	49.18	0.35	2.85	0.12	0.05	9.20	21.74	0.13	14.40	L.O.D.	0.67	L.O.D.	98.69
17JK09_area1_px2_r	50.38	0.24	2.20	0.13	0.06	9.65	21.98	0.15	13.64	L.O.D.	0.60	L.O.D.	99.02
17JK09_area1_px3_c	50.45	0.34	2.88	0.11	0.03	9.56	21.89	0.12	14.01	L.O.D.	0.68	L.O.D.	100.08
17JK09_area1_px3_r	50.76	0.18	2.35	0.08	L.O.D.	9.71	21.95	0.11	13.85	0.03	0.59	L.O.D.	99.62
17JK09_area2_px1_c	50.29	0.29	2.80	L.O.D.	L.O.D.	9.26	21.89	0.11	14.43	L.O.D.	0.66	L.O.D.	99.72
17JK09_area2_px1_r	50.45	0.28	2.52	0.08	0.03	9.49	22.07	0.11	14.15	L.O.D.	0.62	L.O.D.	99.81
17JK09_area2_px2_c	49.76	0.34	2.89	0.11	L.O.D.	8.94	21.64	0.17	14.77	L.O.D.	0.62	L.O.D.	99.24
17JK09_area2_px2_r	50.20	0.25	2.42	0.10	L.O.D.	9.48	22.09	0.13	14.08	L.O.D.	0.60	L.O.D.	99.36
17JK09_area3_px1_c	49.86	0.29	2.75	0.14	L.O.D.	9.23	22.04	0.13	14.62	L.O.D.	0.64	L.O.D.	99.72
17JK09_area3_px1_r	50.23	0.17	2.09	0.14	L.O.D.	9.64	22.29	0.12	13.85	L.O.D.	0.54	L.O.D.	99.06
17JK09_area3_px2	50.69	0.12	1.81	0.07	L.O.D.	9.92	22.39	0.06	13.42	L.O.D.	0.55	L.O.D.	99.02
17JK09_area3_px3	50.61	0.28	2.40	0.07	L.O.D.	9.41	22.04	0.13	14.42	L.O.D.	0.60	L.O.D.	99.94
17JK09_area1_px2_c repeat	49.86	0.34	2.90	0.11	0.04	9.22	21.68	0.14	14.41	L.O.D.	0.65	L.O.D.	99.34

Table S4.2 (continued)

Amphibole data:

Comment	SiO_2 wt%	TiO_2 wt%	Al_2O_3 wt%	V_2O_3 wt%	Cr_2O_3 wt%	MgO wt%	CaO wt%	MnO wt%	FeOt wt%	Na_2O wt%	K_2O wt%	F wt%	Cl wt%	Total
17JK08_area1_hbl1	42.90	1.78	12.08	N/A	N/A	10.35	11.08	N/A	16.07	1.59	1.11	N/A	N/A	96.97
17JK08_area1_hbl2	42.96	1.59	12.24	N/A	N/A	10.52	11.25	N/A	15.67	1.41	1.05	N/A	N/A	96.70
17JK08_area3_hbl1	43.22	1.82	11.84	N/A	N/A	10.71	11.15	N/A	15.88	1.55	1.06	N/A	N/A	97.24
17JK08_area3_hbl2	42.94	1.95	12.41	N/A	N/A	10.11	11.40	N/A	15.55	1.34	1.07	N/A	N/A	96.76
17JK08_area3_hbl3	42.93	1.81	12.00	N/A	N/A	10.49	11.32	N/A	15.89	1.53	1.06	N/A	N/A	97.03
17JK08_area3_hbl4	43.08	1.73	12.26	N/A	N/A	10.49	11.27	N/A	15.77	1.53	1.06	N/A	N/A	97.19
17JK08_area3_hbl5	43.53	1.63	12.64	N/A	N/A	10.45	11.54	N/A	15.05	1.38	1.10	N/A	N/A	97.32
17JK08_area3_hbl6	43.21	1.74	12.22	N/A	N/A	10.63	11.34	N/A	15.77	1.45	1.07	N/A	N/A	97.42
17JK08_grt2_hbl_inclusion	43.96	1.60	12.24	N/A	N/A	12.44	11.10	N/A	13.35	1.68	0.75	N/A	N/A	97.12
17JK20_area1_hbl1	41.77	1.92	12.24	N/A	N/A	8.94	11.43	N/A	17.66	1.52	1.32	N/A	N/A	96.80
17JK20_area1_hbl2	41.94	1.53	13.21	N/A	N/A	8.92	11.52	N/A	17.18	1.25	1.42	N/A	N/A	96.98
17JK20_area1_hbl3	41.68	1.97	12.23	N/A	N/A	9.13	11.31	N/A	17.77	1.51	1.32	N/A	N/A	96.90
17JK20_area1_hbl4	41.56	2.12	12.73	N/A	N/A	9.11	11.36	N/A	16.92	1.43	1.43	N/A	N/A	96.65
17JK20_area1_hbl5	41.72	2.18	12.17	N/A	N/A	9.24	11.32	N/A	17.52	1.55	1.37	N/A	N/A	97.06
17JK20_area3_hbl1	41.23	2.03	12.11	N/A	N/A	8.94	11.26	N/A	17.84	1.52	1.33	N/A	N/A	96.24
17JK20_area3_hbl2	41.61	1.82	12.30	N/A	N/A	9.03	11.30	N/A	17.66	1.50	1.35	N/A	N/A	96.57
17JK20_area3_hbl3	41.38	2.16	12.37	N/A	N/A	8.87	11.24	N/A	18.25	1.53	1.37	N/A	N/A	97.17
17JK20_area3_hbl4	41.76	2.14	12.46	N/A	N/A	9.07	11.28	N/A	17.58	1.54	1.36	N/A	N/A	97.20
17JK20_area3_hbl5	41.37	2.12	12.30	N/A	N/A	8.82	11.29	N/A	17.76	1.55	1.33	N/A	N/A	96.54
17JK12area2_hbl1_c	42.47	1.93	11.80	L.O.D.	0.05	9.76	11.09	0.12	17.31	1.62	1.11	L.O.D.	0.02	97.27
17JK12area2_hbl1_r1	42.68	1.91	12.46	L.O.D.	0.08	9.77	11.10	0.13	16.49	1.66	0.99	L.O.D.	0.02	97.29
17JK12area2_hbl1_r2	42.71	2.17	12.02	0.09	0.08	9.69	11.36	0.12	16.74	1.61	1.07	L.O.D.	L.O.D.	97.66
17JK12area2_hbl2_c	42.41	1.95	12.33	0.07	0.07	9.66	11.17	0.12	16.83	1.69	1.18	L.O.D.	L.O.D.	97.48
17JK12area2_hbl2_r	42.86	2.04	12.32	L.O.D.	0.08	10.06	11.24	0.12	16.07	1.64	1.12	L.O.D.	L.O.D.	97.54
17JK12area2_hbl3	42.58	2.02	12.33	0.09	0.07	10.35	11.19	0.06	15.79	1.68	1.09	L.O.D.	0.02	97.28
17JK12area2_hbl4_inc	43.12	2.01	12.03	L.O.D.	0.07	10.22	11.29	0.12	16.31	1.56	1.23	L.O.D.	0.02	97.99
17JK12area2_hbl5_c	42.81	2.04	12.23	0.06	0.07	9.43	11.10	0.08	17.27	1.70	1.12	L.O.D.	0.02	97.93

Table S4.2 (amphibole continued)

Comment	SiO_2 wt%	TiO_2 wt%	Al_2O_3 wt%	V_2O_3 wt%	Cr_2O_3 wt%	MgO wt%	CaO wt%	MnO wt%	FeOt wt%	Na_2O wt%	K_2O wt%	F wt%	Cl wt%	Total
17JK12area2_hbl5_r	42.78	1.91	11.87	0.07	0.08	9.61	11.07	0.13	17.30	1.60	1.13	L.O.D.	0.02	97.55
17JK12area2_hbl6	43.84	0.89	12.01	L.O.D.	0.05	10.23	10.88	0.13	16.95	1.61	0.58	L.O.D.	0.02	97.18
17JK12area3_hbl1_c	42.71	2.10	11.97	0.07	0.08	9.53	11.16	0.16	17.35	1.64	1.16	L.O.D.	L.O.D.	97.93
17JK12area3_hbl1_r	43.11	1.60	12.64	0.10	0.07	9.91	11.29	0.13	16.61	1.46	0.89	0.08	0.02	97.90
17JK12area3_hbl2_c	42.99	2.07	11.98	0.10	0.06	9.61	11.18	0.17	17.15	1.72	1.16	L.O.D.	0.02	98.21
17JK12area3_hbl2_r	42.64	1.62	12.82	0.11	0.08	8.89	11.22	0.09	17.88	1.49	1.07	0.10	0.03	98.04
17JK09_area3_hbl1_inc	40.98	1.14	13.09	0.22	0.05	7.18	11.29	0.04	20.23	1.60	1.13	L.O.D.	L.O.D.	96.94
17JK09_area3_hbl1_inc repeat	41.14	1.15	13.04	0.21	L.O.D.	7.29	11.23	0.06	20.48	1.60	1.05	L.O.D.	L.O.D.	97.24
17JK09_area2_hbl2	41.20	1.79	12.51	0.20	L.O.D.	7.23	11.49	0.06	20.31	1.37	1.43	L.O.D.	L.O.D.	97.60
17JK09_area3_hbl3	41.04	1.54	12.39	0.11	L.O.D.	7.07	11.70	0.06	20.63	1.41	1.35	L.O.D.	L.O.D.	97.28
17JK09_area3_hbl4	41.71	1.64	11.84	0.21	0.04	7.25	11.64	0.06	20.45	1.23	1.46	L.O.D.	L.O.D.	97.51
17JK09_area4_hbl1	41.21	1.91	12.44	0.09	L.O.D.	7.62	11.34	L.O.D.	19.85	1.52	1.31	L.O.D.	L.O.D.	97.27
17JK09_area4_hbl2	41.05	2.55	12.11	0.15	0.03	7.79	11.48	0.05	19.59	1.85	1.21	0.08	L.O.D.	97.94
17JK09_area4_hbl3	43.50	1.16	10.56	0.09	L.O.D.	8.54	11.39	0.08	19.69	1.53	0.52	L.O.D.	L.O.D.	97.05
17JK09_area4_hbl3 repeat	44.05	1.15	10.41	L.O.D.	L.O.D.	8.68	11.44	0.07	19.28	1.44	0.51	L.O.D.	L.O.D.	97.02
17JK09_area4_hbl4	43.18	1.12	10.82	0.20	0.03	8.40	11.41	0.08	19.43	1.29	0.77	L.O.D.	L.O.D.	96.73
17JK09_area4_hbl4 repeat	43.59	1.18	10.85	0.17	L.O.D.	8.39	11.47	0.13	19.66	1.35	0.74	0.09	L.O.D.	97.59
17JK09_area4_hbl5	45.37	0.89	9.49	0.14	0.03	9.11	11.39	0.08	19.48	1.21	0.35	L.O.D.	0.01	97.54

Table S4.2 (continued)

Biotie data:

Comment	SiO_2 wt%	TiO_2 wt%	Al_2O_3 wt%	V_2O_3 wt%	Cr_2O_3 wt%	MgO wt%	CaO wt%	MnO wt%	FeOt wt%	Na_2O wt%	K_2O wt%	F wt%	Cl wt%	Total
17JK08_area1_bt1	36.20	4.22	16.17	N/A	N/A	11.56	N/A	N/A	17.15	N/A	9.79	L.O.D.	L.O.D.	95.04
17JK08_area1_bt2	36.43	4.22	16.37	N/A	N/A	11.98	N/A	N/A	16.67	N/A	9.73	L.O.D.	L.O.D.	95.33
17JK08_area1_bt3	36.59	4.02	16.59	N/A	N/A	12.06	N/A	N/A	16.93	N/A	9.70	L.O.D.	L.O.D.	95.83
17JK08_area2_bt1	36.40	4.40	16.47	N/A	N/A	11.29	N/A	N/A	17.47	N/A	9.77	L.O.D.	L.O.D.	95.67
17JK08_area2_bt2	36.08	4.54	16.48	N/A	N/A	11.13	N/A	N/A	17.32	N/A	9.95	L.O.D.	L.O.D.	95.41
17JK08_area3_bt1	36.13	4.35	16.05	N/A	N/A	11.61	N/A	N/A	17.36	N/A	9.72	L.O.D.	L.O.D.	95.16
17JK08_area3_bt2	36.04	4.46	16.06	N/A	N/A	11.56	N/A	N/A	17.47	N/A	9.81	L.O.D.	L.O.D.	95.33
17JK08_area3_bt3	36.21	4.35	16.20	N/A	N/A	11.66	N/A	N/A	17.39	N/A	9.69	L.O.D.	L.O.D.	95.42
17JK08_area3_bt4	36.23	4.23	16.11	N/A	N/A	11.56	N/A	N/A	17.55	N/A	9.71	L.O.D.	L.O.D.	95.33
17JK08_area3_bt5	36.14	4.50	15.93	N/A	N/A	11.37	N/A	N/A	17.61	N/A	9.77	L.O.D.	L.O.D.	95.21
17JK08_grt2_bt_inclusion	36.92	3.15	16.71	N/A	N/A	14.26	N/A	N/A	14.33	N/A	9.29	L.O.D.	L.O.D.	94.66
17JK20_area4_bt1	36.14	3.83	16.68	N/A	N/A	11.10	N/A	N/A	18.56	N/A	9.17	L.O.D.	L.O.D.	95.38
17JK12area3_bt	36.18	3.26	15.53	L.O.D.	0.05	11.77	L.O.D.	L.O.D.	17.50	0.10	9.44	0.15	0.02	93.99
17JK12area3_bt repeat	36.00	3.45	15.58	0.08	0.07	11.83	L.O.D.	0.05	17.43	0.12	9.33	0.13	0.02	94.09
17JK09_area5_bt1	36.08	2.70	15.73	0.11	L.O.D.	10.53	0.07	L.O.D.	20.57	0.05	9.63	L.O.D.	L.O.D.	95.45
17JK09_area5_bt2	35.53	3.73	15.26	0.05	0.02	9.22	0.12	L.O.D.	21.04	0.07	9.46	L.O.D.	L.O.D.	94.51
17JK09_area5_bt2 repeat	35.51	3.59	14.90	0.09	0.03	9.36	0.12	L.O.D.	21.46	0.05	9.53	0.06	L.O.D.	94.70

Table S4.3

Data from secondary reference materials (concentration in µg/g) and mass spectrometer dwell times for elements analyzed during laser ablation inductively coupled plasma mass spectrometry (LA-ICP-MS) of garnet.

Secondary reference: BHVO-2G

Date	Sample analyzed	Li	Be	Na	Mg	Al	P	Ca	Sc	Ti	V	Cr	Mn
7/17/2019	17JK20	4.01	0.77	1.56E+04	4.36E+04	7.91E+04	1357	7.86E+04	30.2	1.79E+04	318	280	1297
7/17/2019	17JK20	3.94	0.43	1.50E+04	3.41E+04	7.96E+04	891	7.91E+04	32.4	1.66E+04	315	275	1226
7/17/2019	17JK20	3.98	0.51	1.58E+04	3.73E+04	8.09E+04	1095	8.38E+04	33.4	1.67E+04	325	268	1369
7/17/2019	17JK20	4.01	1.15	1.53E+04	3.10E+04	8.46E+04	787	8.24E+04	33.8	1.80E+04	334	275	1320
7/17/2019	17JK20	4.23	1.67	1.63E+04	3.29E+04	8.74E+04	940	8.56E+04	35.1	1.89E+04	338	292	1346
7/17/2019	17JK20	4.33	1.47	1.50E+04	5.14E+04	8.29E+04	1120	8.77E+04	32.7	1.86E+04	336	286	1390
7/17/2019	17JK20	3.75	0.94	1.48E+04	4.18E+04	8.35E+04	1056	8.27E+04	34.1	1.84E+04	326	279	1390
7/17/2019	17JK20	4.09	0.96	1.54E+04	4.39E+04	8.27E+04	1126	8.70E+04	33.4	1.86E+04	336	284	1294
7/17/2019	17JK20	3.74	0.31	1.62E+04	4.64E+04	8.76E+04	1249	9.00E+04	35.1	1.96E+04	339	295	1376
7/17/2019	17JK20	4.28	0.14	1.55E+04	4.40E+04	8.42E+04	1244	8.48E+04	33.6	1.93E+04	341	283	1376
7/17/2019	17JK20	4.34	0.91	1.56E+04	4.89E+04	8.39E+04	1263	8.78E+04	33.7	1.99E+04	335	292	1321
7/17/2019	17JK20	4.09	1.05	1.61E+04	4.55E+04	8.64E+04	1091	8.44E+04	33.9	1.84E+04	341	276	1291
7/17/2019	17JK20	4.19	1.14	1.55E+04	4.47E+04	8.09E+04	1239	8.06E+04	32.1	1.71E+04	317	269	1229
7/17/2019	17JK20	4.22	0.78	1.60E+04	4.54E+04	8.04E+04	1199	8.27E+04	32.1	1.76E+04	320	266	1316
7/17/2019	17JK20	4.69	0.79	1.68E+04	4.88E+04	8.88E+04	1476	9.03E+04	35.5	2.02E+04	349	298	1377
7/17/2019	17JK20	4.41	0.69	1.47E+04	4.41E+04	8.20E+04	1568	8.60E+04	32.8	1.85E+04	327	271	1349
7/17/2019	17JK20	4.17	0.85	1.50E+04	4.75E+04	8.05E+04	1062	8.66E+04	33.0	1.90E+04	316	270	1328
7/30/2020	17JK08	3.43	0.77	1.48E+04	3.28E+04	7.14E+04	970	7.79E+04	27.1	1.57E+04	276	251	1174
7/30/2020	17JK08	3.71	1.33	1.47E+04	3.61E+04	7.88E+04	1031	8.25E+04	29.2	1.75E+04	297	275	1232
7/30/2020	17JK08	3.29	0.97	1.51E+04	3.64E+04	7.84E+04	1115	7.58E+04	28.3	1.76E+04	304	264	1235
7/30/2020	17JK08	3.97	1.72	1.56E+04	4.06E+04	8.41E+04	1221	8.90E+04	31.2	1.85E+04	322	270	1330
7/30/2020	17JK08	3.58	1.19	1.48E+04	3.74E+04	7.85E+04	1066	7.82E+04	26.8	1.73E+04	306	282	1219

Table S4.3 (continued)

Secondary reference: BHVO-2G

Date	Sample analyzed	Li	Be	Na	Mg	Al	P	Ca	Sc	Ti	V	Cr	Mn
7/30/2020	17JK08	3.76	1.07	1.49E+04	3.65E+04	7.78E+04	1103	8.44E+04	29.1	1.67E+04	293	250	1203
7/30/2020	17JK08	3.82	1.26	1.55E+04	3.75E+04	7.86E+04	1057	8.12E+04	29.2	1.83E+04	294	267	1349
7/30/2020	17JK08	4.17	1.33	1.60E+04	3.91E+04	7.61E+04	1138	8.24E+04	30.4	1.75E+04	289	266	1308
7/30/2020	17JK08	3.91	0.59	1.39E+04	3.52E+04	7.54E+04	962	7.84E+04	28.8	1.59E+04	292	241	1234
7/30/2020	17JK08	3.82	0.94	1.65E+04	3.75E+04	8.07E+04	999	8.47E+04	28.7	1.71E+04	303	260	1282
7/30/2020	17JK08	4.22	0.63	1.59E+04	3.82E+04	7.74E+04	1041	8.07E+04	29.7	1.74E+04	298	268	1258
7/30/2020	17JK08	4.71	1.54	1.77E+04	3.98E+04	8.09E+04	1057	8.25E+04	30.6	1.80E+04	314	257	1312
7/30/2020	17JK08	4.03	0.71	1.67E+04	3.80E+04	7.85E+04	1008	8.29E+04	28.0	1.72E+04	294	244	1284
7/30/2020	17JK08	3.78	1.29	1.49E+04	3.60E+04	7.36E+04	983	7.45E+04	27.1	1.58E+04	293	235	1159
7/30/2020	17JK08	4.52	1.04	1.77E+04	3.99E+04	8.57E+04	1137	9.09E+04	29.4	1.82E+04	328	267	1334
7/30/2020	17JK08	3.71	0.73	1.55E+04	3.79E+04	7.74E+04	1038	8.19E+04	28.7	1.65E+04	300	262	1249
7/30/2020	17JK08	3.95	1.36	1.50E+04	3.73E+04	7.83E+04	1088	8.17E+04	30.9	1.71E+04	299	258	1235
7/30/2020	17JK08	3.98	1.01	1.53E+04	3.69E+04	8.15E+04	1119	8.05E+04	30.0	1.73E+04	309	241	1243
7/30/2020	17JK08	3.97	1.39	1.56E+04	3.79E+04	8.32E+04	1120	8.76E+04	29.8	1.76E+04	307	262	1344
7/30/2020	17JK08	4.05	0.66	1.55E+04	3.65E+04	7.99E+04	1096	8.20E+04	27.9	1.68E+04	305	236	1254
7/30/2020	17JK08	4.25	0.83	1.58E+04	3.85E+04	8.09E+04	1071	8.77E+04	31.4	1.80E+04	299	252	1301
7/30/2020	17JK08	3.96	0.78	1.49E+04	3.86E+04	7.91E+04	984	8.37E+04	30.7	1.73E+04	297	249	1262
7/30/2020	17JK08	3.99	1.01	1.57E+04	3.83E+04	7.64E+04	1030	7.95E+04	26.7	1.66E+04	321	259	1255
7/30/2020	17JK08	3.90	1.07	1.65E+04	3.80E+04	7.88E+04	1047	8.30E+04	28.6	1.69E+04	324	259	1291
7/30/2020	17JK08	3.69	0.59	1.56E+04	3.84E+04	7.99E+04	1021	8.37E+04	28.6	1.69E+04	311	253	1293
7/30/2020	17JK08	3.98	1.35	1.66E+04	3.60E+04	7.60E+04	1031	7.69E+04	26.8	1.60E+04	317	255	1277
7/30/2020	17JK08	4.44	0.90	1.64E+04	3.79E+04	7.65E+04	1124	8.10E+04	27.5	1.69E+04	319	247	1256
7/30/2020	17JK08	4.15	0.58	1.61E+04	3.57E+04	7.14E+04	1060	7.26E+04	25.8	1.51E+04	306	243	1199
7/30/2020	17JK08	4.27	1.05	1.73E+04	3.86E+04	7.30E+04	1094	7.71E+04	25.7	1.61E+04	311	259	1226
7/30/2020	17JK08	4.32	0.87	1.75E+04	3.76E+04	7.50E+04	1142	7.82E+04	25.8	1.66E+04	338	255	1253
7/30/2020	17JK08	4.32	1.02	1.69E+04	3.80E+04	6.98E+04	1087	6.97E+04	25.2	1.52E+04	323	257	1238
7/30/2020	17JK08	4.41	0.68	1.69E+04	3.66E+04	6.89E+04	1174	6.96E+04	24.2	1.58E+04	321	259	1171
7/30/2020	17JK08	4.22	0.83	1.70E+04	3.64E+04	6.84E+04	1137	7.17E+04	24.4	1.62E+04	324	252	1220

Table S4.3 (continued)

Secondary reference: BHVO-2G

Date	Sample analyzed	Li	Be	Na	Mg	Al	P	Ca	Sc	Ti	V	Cr	Mn
7/30/2020	17JK08	4.18	0.79	1.60E+04	3.47E+04	6.93E+04	1057	7.28E+04	25.1	1.58E+04	310	255	1151
7/30/2020	17JK08	3.99	0.93	1.57E+04	3.73E+04	7.26E+04	1050	7.66E+04	25.1	1.58E+04	310	253	1165
7/30/2020	17JK08	3.73	0.63	1.58E+04	3.62E+04	7.01E+04	1063	7.30E+04	26.2	1.55E+04	278	244	1164
7/30/2020	17JK08	4.14	0.98	1.64E+04	3.84E+04	7.04E+04	1121	7.55E+04	25.3	1.57E+04	286	257	1179
7/30/2020	17JK08	4.25	0.84	1.59E+04	3.56E+04	6.90E+04	1047	7.40E+04	24.8	1.59E+04	331	256	1213
7/30/2020	17JK08	4.14	1.26	1.60E+04	3.65E+04	7.11E+04	1054	7.34E+04	26.4	1.60E+04	313	267	1205
7/30/2020	17JK08	4.30	0.96	1.54E+04	3.71E+04	7.08E+04	1057	7.17E+04	25.6	1.59E+04	307	262	1229
7/30/2020	17JK08	4.18	0.69	1.53E+04	3.65E+04	7.27E+04	986	7.19E+04	26.1	1.60E+04	309	252	1186
7/30/2020	17JK08	4.01	1.11	1.61E+04	3.90E+04	7.40E+04	1098	7.42E+04	26.0	1.62E+04	325	276	1195
7/30/2020	17JK08	3.95	0.89	1.76E+04	3.76E+04	7.43E+04	1088	7.60E+04	27.5	1.63E+04	310	269	1242
7/30/2020	17JK08	4.29	0.77	1.70E+04	3.95E+04	7.19E+04	1067	7.62E+04	27.8	1.57E+04	317	276	1251
7/30/2020	17JK08	4.16	1.14	1.68E+04	3.72E+04	6.75E+04	1075	7.24E+04	26.0	1.58E+04	317	264	1225
7/30/2020	17JK08	4.03	0.80	1.51E+04	3.66E+04	6.58E+04	929	6.86E+04	23.9	1.52E+04	291	256	1155
7/30/2020	17JK08	4.27	0.86	1.71E+04	3.61E+04	7.35E+04	971	7.75E+04	26.2	1.62E+04	311	278	1183
7/30/2020	17JK08	4.17	0.92	1.57E+04	3.63E+04	6.88E+04	974	7.11E+04	24.1	1.55E+04	313	261	1150
7/30/2020	17JK08	4.11	0.85	1.64E+04	3.93E+04	7.64E+04	1069	8.12E+04	28.2	1.68E+04	310	270	1268
7/30/2020	17JK08	4.18	1.18	1.68E+04	3.87E+04	7.37E+04	1063	7.37E+04	27.4	1.63E+04	322	271	1263
7/30/2020	17JK08	4.47	0.87	1.55E+04	3.90E+04	7.65E+04	1112	7.98E+04	28.3	1.68E+04	311	275	1324
7/30/2020	17JK08	4.50	1.17	1.65E+04	3.64E+04	7.21E+04	1129	7.72E+04	25.3	1.60E+04	310	274	1241
7/30/2020	17JK08	3.89	0.97	1.67E+04	3.68E+04	6.87E+04	1089	7.60E+04	26.3	1.54E+04	317	276	1196
7/30/2020	17JK08	4.02	0.71	1.66E+04	3.62E+04	6.97E+04	1035	7.46E+04	26.4	1.56E+04	319	266	1153
7/30/2020	17JK08	4.14	1.09	1.71E+04	3.66E+04	7.59E+04	1088	8.08E+04	28.2	1.65E+04	330	276	1266
7/30/2020	17JK08	3.86	0.97	1.61E+04	3.62E+04	7.19E+04	1059	7.60E+04	26.0	1.62E+04	315	279	1218
7/30/2020	17JK08	4.39	1.01	1.54E+04	3.54E+04	7.21E+04	1064	7.38E+04	25.2	1.62E+04	309	274	1164
7/30/2020	17JK08	4.05	1.45	1.64E+04	3.70E+04	7.53E+04	1027	7.97E+04	26.6	1.68E+04	323	279	1198
7/30/2020	17JK08	3.95	0.69	1.47E+04	3.27E+04	7.46E+04	957	7.01E+04	24.9	1.56E+04	297	277	1136
7/30/2020	17JK08	3.98	0.92	1.57E+04	3.37E+04	7.68E+04	961	7.61E+04	27.2	1.66E+04	298	293	1146
8/7/2020	17JK12	4.10	0.41	1.69E+04	3.07E+04	7.34E+04	1028	7.83E+04	27.4	1.60E+04	318	288	1319

Table S4.3 (continued)

Secondary reference: BHVO-2G

Date	Sample analyzed	Li	Be	Na	Mg	Al	P	Ca	Sc	Ti	V	Cr	Mn
8/7/2020	17JK12	4.26	0.78	1.69E+04	2.65E+04	6.91E+04	1037	7.48E+04	27.0	1.60E+04	322	294	1206
8/7/2020	17JK12	3.69	0.52	1.61E+04	2.56E+04	6.71E+04	1012	6.92E+04	24.9	1.55E+04	314	263	1209
8/7/2020	17JK12	4.10	0.81	1.72E+04	2.79E+04	6.99E+04	1046	7.55E+04	26.5	1.61E+04	317	273	1305
8/7/2020	17JK12	3.53	0.63	1.59E+04	2.81E+04	6.86E+04	979	7.21E+04	25.3	1.52E+04	273	287	1123
8/7/2020	17JK12	4.38	0.24	1.70E+04	2.77E+04	7.18E+04	973	7.49E+04	26.8	1.64E+04	315	275	1230
8/7/2020	17JK12	3.71	1.01	1.69E+04	2.56E+04	6.63E+04	936	6.87E+04	26.1	1.47E+04	309	254	1167
8/7/2020	17JK12	4.12	0.92	1.56E+04	2.74E+04	6.83E+04	968	7.23E+04	24.8	1.53E+04	323	264	1190
8/7/2020	17JK12	3.67	1.10	1.83E+04	2.74E+04	6.79E+04	1029	7.19E+04	25.3	1.51E+04	319	265	1186
8/7/2020	17JK12	3.95	0.63	1.71E+04	2.82E+04	7.20E+04	995	7.55E+04	26.8	1.60E+04	306	281	1238
8/7/2020	17JK12	4.07	0.94	1.71E+04	2.73E+04	7.19E+04	1046	7.41E+04	25.0	1.60E+04	309	266	1199
8/7/2020	17JK12	4.05	0.69	1.71E+04	2.66E+04	6.93E+04	1000	7.48E+04	25.8	1.62E+04	321	272	1311
8/7/2020	17JK12	4.42	0.86	1.59E+04	3.17E+04	7.35E+04	1057	7.51E+04	26.9	1.63E+04	319	264	1218
8/7/2020	17JK12	4.18	<LOD	1.76E+04	2.78E+04	7.04E+04	1043	7.39E+04	24.4	1.58E+04	309	282	1188
8/7/2020	17JK12	3.90	0.67	1.59E+04	2.60E+04	7.13E+04	984	7.85E+04	27.0	1.69E+04	313	259	1156
8/7/2020	17JK12	4.45	0.69	1.68E+04	2.79E+04	7.26E+04	1022	7.65E+04	25.5	1.64E+04	315	293	1247
8/7/2020	17JK12	4.07	0.67	1.65E+04	2.83E+04	6.86E+04	1074	7.27E+04	24.8	1.53E+04	308	279	1231
8/7/2020	17JK12	3.90	0.80	1.75E+04	2.68E+04	6.92E+04	983	7.38E+04	23.3	1.59E+04	328	280	1220
8/7/2020	17JK12	3.89	1.15	1.73E+04	2.49E+04	6.52E+04	947	6.90E+04	23.6	1.55E+04	300	263	1190
8/7/2020	17JK12	3.69	0.94	1.76E+04	2.70E+04	7.01E+04	1077	7.44E+04	26.9	1.58E+04	295	286	1153
8/7/2020	17JK12	4.34	1.29	1.68E+04	2.62E+04	7.02E+04	838	7.63E+04	25.5	1.58E+04	295	273	1180
8/7/2020	17JK12	4.42	0.45	1.54E+04	2.72E+04	6.66E+04	942	7.48E+04	25.7	1.57E+04	342	278	1189
8/7/2020	17JK12	4.31	0.65	1.79E+04	2.67E+04	6.98E+04	947	7.72E+04	26.2	1.63E+04	327	289	1234
8/7/2020	17JK12	3.68	0.97	1.66E+04	2.59E+04	6.83E+04	947	7.40E+04	25.2	1.54E+04	331	270	1208
8/7/2020	17JK12	3.82	0.54	1.76E+04	2.64E+04	6.82E+04	884	7.58E+04	25.5	1.59E+04	315	269	1247
8/7/2020	17JK12	4.29	0.89	1.84E+04	2.90E+04	7.23E+04	1049	7.63E+04	28.0	1.61E+04	321	282	1282
8/7/2020	17JK12	4.13	1.03	1.87E+04	2.72E+04	6.53E+04	850	6.77E+04	23.2	1.48E+04	314	265	1085
8/7/2020	17JK12	4.19	0.91	1.79E+04	2.70E+04	6.67E+04	917	7.50E+04	24.6	1.57E+04	329	269	1213
8/7/2020	17JK12	4.43	0.92	1.74E+04	2.72E+04	6.82E+04	1000	7.61E+04	25.3	1.61E+04	338	296	1231

Table S4.3 (continued)

Secondary reference: BHVO-2G

Date	Sample analyzed	Li	Be	Na	Mg	Al	P	Ca	Sc	Ti	V	Cr	Mn
8/7/2020	17JK12	4.14	1.18	1.77E+04	2.76E+04	7.13E+04	995	7.56E+04	27.0	1.60E+04	333	280	1194
8/7/2020	17JK12	4.34	0.52	1.71E+04	2.79E+04	7.27E+04	971	7.39E+04	27.4	1.60E+04	338	262	1216
8/18/2020	17JK12, 17JK20	3.66	0.91	1.35E+04	2.91E+04	6.08E+04	820	6.11E+04	24.0	1.42E+04	270	237	1064
8/18/2020	17JK12, 17JK20	3.05	0.59	1.33E+04	2.78E+04	5.96E+04	914	6.52E+04	22.5	1.31E+04	271	226	1035
8/18/2020	17JK12, 17JK20	4.11	1.24	1.50E+04	2.97E+04	6.35E+04	902	6.84E+04	25.3	1.48E+04	282	237	1113
8/18/2020	17JK12, 17JK20	3.67	0.37	1.43E+04	3.02E+04	6.62E+04	1119	7.19E+04	25.4	1.60E+04	289	241	1113
8/18/2020	17JK12, 17JK20	3.42	<LOD	1.41E+04	2.98E+04	6.71E+04	1122	6.98E+04	27.4	1.63E+04	272	229	1052
8/18/2020	17JK12, 17JK20	4.01	<LOD	1.47E+04	2.96E+04	7.42E+04	1023	7.63E+04	29.5	1.64E+04	273	234	1096
8/18/2020	17JK12, 17JK20	3.07	<LOD	1.50E+04	3.05E+04	7.21E+04	855	7.52E+04	30.4	1.58E+04	267	241	1077
8/18/2020	17JK12, 17JK20	3.78	0.83	1.66E+04	2.74E+04	6.67E+04	810	7.16E+04	25.7	1.52E+04	303	251	1135
8/18/2020	17JK12, 17JK20	3.89	<LOD	1.45E+04	2.31E+04	6.57E+04	818	6.91E+04	25.2	1.48E+04	309	244	1095
8/18/2020	17JK12, 17JK20	3.93	0.74	1.60E+04	2.52E+04	6.64E+04	852	7.12E+04	26.8	1.56E+04	303	237	1123
8/18/2020	17JK12, 17JK20	3.81	1.00	1.55E+04	2.48E+04	6.97E+04	951	7.44E+04	26.7	1.58E+04	297	247	1148
8/18/2020	17JK12, 17JK20	3.87	1.03	1.61E+04	2.48E+04	6.84E+04	811	7.30E+04	27.4	1.56E+04	293	250	1085
8/18/2020	17JK12, 17JK20	3.99	<LOD	1.50E+04	2.56E+04	6.96E+04	864	7.01E+04	26.7	1.57E+04	290	256	1057
8/18/2020	17JK12, 17JK20	4.12	0.80	1.65E+04	2.65E+04	7.22E+04	930	7.57E+04	28.2	1.63E+04	310	251	1104
8/18/2020	17JK12, 17JK20	3.50	0.81	1.52E+04	2.35E+04	6.55E+04	809	6.90E+04	24.8	1.46E+04	277	225	1036
8/18/2020	17JK12, 17JK20	3.82	0.24	1.63E+04	2.78E+04	6.91E+04	898	7.47E+04	26.9	1.57E+04	292	243	1053
8/18/2020	17JK12, 17JK20	4.18	0.97	1.57E+04	2.42E+04	6.70E+04	940	7.37E+04	25.7	1.51E+04	283	237	1053
8/18/2020	17JK12, 17JK20	3.44	0.45	1.64E+04	2.52E+04	7.24E+04	794	7.94E+04	28.3	1.60E+04	314	261	1068
9/17/2020	17JK09	4.56	0.85	1.56E+04	3.80E+04	7.28E+04	1040	7.80E+04	29.1	1.72E+04	336	283	1257
9/17/2020	17JK09	4.24	0.95	1.65E+04	4.00E+04	7.32E+04	943	8.10E+04	27.9	1.75E+04	353	285	1261
9/17/2020	17JK09	4.31	0.62	1.55E+04	3.80E+04	6.95E+04	798	7.56E+04	25.9	1.63E+04	333	272	1234
9/17/2020	17JK09	4.35	1.28	1.74E+04	3.86E+04	7.62E+04	934	8.00E+04	28.4	1.80E+04	372	292	1369
9/17/2020	17JK09	4.33	0.94	1.58E+04	3.76E+04	7.26E+04	905	7.57E+04	29.2	1.71E+04	362	296	1282
9/17/2020	17JK09	4.03	0.69	1.59E+04	3.75E+04	7.15E+04	935	7.36E+04	27.7	1.63E+04	324	284	1272
9/17/2020	17JK09	4.49	1.32	1.58E+04	4.06E+04	7.09E+04	1040	7.52E+04	28.9	1.73E+04	350	300	1337
9/17/2020	17JK09	4.03	0.57	1.64E+04	3.87E+04	7.09E+04	1045	7.32E+04	27.4	1.65E+04	332	277	1282

Table S4.3 (continued)

Secondary reference: BHVO-2G

Date	Sample analyzed	Li	Be	Na	Mg	Al	P	Ca	Sc	Ti	V	Cr	Mn
9/17/2020	17JK09	4.48	0.46	1.66E+04	3.91E+04	7.17E+04	1042	7.56E+04	27.1	1.68E+04	340	297	1283
9/17/2020	17JK09	4.51	0.39	1.71E+04	3.91E+04	7.24E+04	1085	7.68E+04	28.0	1.68E+04	353	308	1329
9/17/2020	17JK09	3.81	1.13	1.63E+04	3.65E+04	7.14E+04	934	7.45E+04	26.4	1.60E+04	333	273	1245
9/17/2020	17JK09	4.37	<LOD	1.57E+04	3.55E+04	6.79E+04	897	7.63E+04	26.9	1.63E+04	364	294	1255
9/17/2020	17JK09	4.31	<LOD	1.68E+04	3.87E+04	6.82E+04	887	7.37E+04	26.0	1.65E+04	360	302	1275
9/17/2020	17JK09	4.46	0.35	1.60E+04	3.73E+04	6.88E+04	813	7.36E+04	25.6	1.63E+04	330	283	1238
9/17/2020	17JK09	4.36	1.05	1.68E+04	3.87E+04	7.30E+04	859	7.46E+04	27.2	1.70E+04	336	306	1273
9/17/2020	17JK09	4.00	0.41	1.59E+04	3.79E+04	6.98E+04	947	7.50E+04	27.5	1.65E+04	348	287	1271
9/17/2020	17JK09	4.58	0.62	1.71E+04	3.83E+04	7.27E+04	1036	7.64E+04	27.0	1.61E+04	342	293	1309
9/17/2020	17JK09	4.39	<LOD	1.61E+04	4.06E+04	7.11E+04	994	7.48E+04	28.1	1.62E+04	334	289	1267
9/17/2020	17JK09	4.26	0.42	1.63E+04	4.38E+04	7.52E+04	1097	8.23E+04	30.6	1.74E+04	356	297	1324
9/17/2020	17JK09	3.70	0.66	1.69E+04	4.05E+04	7.33E+04	1181	7.68E+04	27.7	1.71E+04	331	285	1307
9/17/2020	17JK09	3.74	0.36	1.57E+04	4.01E+04	6.95E+04	1260	7.15E+04	27.3	1.59E+04	329	277	1239
9/17/2020	17JK09	4.33	0.38	1.67E+04	4.12E+04	7.28E+04	1308	7.64E+04	28.4	1.70E+04	337	291	1281
9/17/2020	17JK09	4.06	0.65	1.54E+04	3.99E+04	6.86E+04	1338	7.17E+04	26.8	1.61E+04	320	290	1216
9/17/2020	17JK09	3.79	0.87	1.58E+04	3.97E+04	6.98E+04	1422	7.18E+04	27.4	1.57E+04	329	283	1203
9/17/2020	17JK09	4.78	0.60	1.64E+04	4.20E+04	7.16E+04	1481	7.80E+04	28.7	1.66E+04	341	304	1287
9/17/2020	17JK09	4.06	0.76	1.64E+04	3.98E+04	7.49E+04	1360	7.79E+04	29.1	1.69E+04	338	298	1299
9/17/2020	17JK09	4.23	0.78	1.79E+04	4.16E+04	7.63E+04	1458	7.80E+04	29.2	1.73E+04	343	302	1349
9/17/2020	17JK09	4.26	0.69	1.69E+04	4.27E+04	7.51E+04	1518	7.81E+04	28.3	1.71E+04	332	311	1279
9/17/2020	17JK09	4.54	0.33	1.67E+04	4.19E+04	7.48E+04	1453	7.72E+04	28.7	1.69E+04	347	306	1343
9/17/2020	17JK09	4.26	0.42	1.60E+04	4.09E+04	6.91E+04	1463	7.56E+04	28.1	1.59E+04	319	286	1229
9/17/2020	17JK09	3.94	0.29	1.63E+04	3.88E+04	7.12E+04	1495	7.79E+04	28.5	1.66E+04	341	308	1284

Table S4.3 (continued)

Secondary reference: BHVO-2G

Date	Sample analyzed	Fe	Co	Ni	Cu	Zn	Ga	Sr	Y	Zr	Nb	La	Ce	Pr	Nd
7/17/2019	17JK20	7.34E+04	44.4	108	106	93.6	19.3	374	21.2	150	N/A	13.6	35.4	5.07	24.0
7/17/2019	17JK20	5.62E+04	44.3	104	86	59.0	18.6	388	23.1	146	N/A	14.5	35.5	4.87	23.7
7/17/2019	17JK20	6.55E+04	43.9	107	88	79.2	19.6	377	23.1	146	N/A	14.3	36.4	4.88	22.9
7/17/2019	17JK20	4.89E+04	46.9	100	74	53.6	19.2	403	24.4	154	N/A	15.4	36.3	5.10	24.5
7/17/2019	17JK20	6.68E+04	46.5	108	89	61.3	20.1	418	25.1	164	N/A	15.8	37.7	5.34	25.3
7/17/2019	17JK20	9.62E+04	44.9	118	116	106.0	19.2	389	24.1	158	N/A	15.1	36.5	4.97	23.0
7/17/2019	17JK20	7.47E+04	45.1	112	98	76.5	19.7	399	24.0	160	N/A	15.5	36.7	5.25	24.0
7/17/2019	17JK20	8.18E+04	45.1	102	101	88.6	19.8	409	24.2	160	N/A	15.2	37.0	5.25	24.0
7/17/2019	17JK20	8.33E+04	44.9	110	103	87.5	20.1	420	24.3	168	N/A	16.5	36.9	5.28	24.3
7/17/2019	17JK20	8.29E+04	46.6	108	103	85.7	21.1	409	25.2	172	N/A	15.9	37.6	5.20	23.4
7/17/2019	17JK20	8.87E+04	46.6	119	116	103.5	21.0	419	25.1	170	N/A	16.0	37.3	5.41	24.8
7/17/2019	17JK20	8.70E+04	46.1	127	109	90.9	19.4	409	23.9	163	N/A	15.4	38.8	5.30	24.0
7/17/2019	17JK20	8.05E+04	43.2	116	113	93.9	18.7	389	23.6	154	N/A	14.6	35.3	4.96	23.3
7/17/2019	17JK20	8.28E+04	43.5	117	114	99.1	19.7	394	22.9	156	N/A	14.4	34.8	4.87	23.9
7/17/2019	17JK20	9.78E+04	46.6	120	121	98.9	21.4	427	25.7	173	N/A	16.0	38.3	5.31	25.3
7/17/2019	17JK20	8.98E+04	44.6	116	113	90.1	18.8	401	23.7	165	N/A	14.7	36.2	4.81	24.2
7/17/2019	17JK20	9.05E+04	41.7	114	120	87.1	19.4	409	24.1	161	N/A	15.5	34.7	4.86	22.9
7/30/2020	17JK08	6.25E+04	38.8	94	81	81.8	18.7	382	19.2	128	N/A	13.0	33.6	4.62	22.2
7/30/2020	17JK08	7.03E+04	41.2	104	84	70.7	18.7	385	19.2	134	N/A	13.7	35.2	4.77	22.1
7/30/2020	17JK08	8.11E+04	43.7	116	89	75.2	18.0	385	19.2	137	N/A	13.7	33.5	4.74	21.5
7/30/2020	17JK08	8.41E+04	49.1	108	90	72.2	19.9	423	21.1	140	N/A	14.2	37.9	5.28	22.0
7/30/2020	17JK08	7.87E+04	41.0	98	91	68.8	18.7	390	20.4	130	N/A	13.8	36.3	5.12	21.9
7/30/2020	17JK08	6.75E+04	42.7	107	92	64.8	18.6	391	18.2	135	N/A	13.9	36.2	4.53	22.5
7/30/2020	17JK08	8.28E+04	44.9	122	91	70.9	18.2	407	21.4	141	N/A	14.1	36.6	4.73	23.6
7/30/2020	17JK08	7.55E+04	44.2	105	92	71.5	19.0	358	19.9	136	N/A	14.5	35.2	5.08	21.5
7/30/2020	17JK08	7.22E+04	40.0	96	83	62.1	18.0	384	19.9	131	N/A	13.4	33.9	4.78	21.5
7/30/2020	17JK08	7.84E+04	42.4	108	86	69.2	20.2	373	20.0	138	N/A	13.9	34.8	5.01	21.6
7/30/2020	17JK08	6.54E+04	43.0	103	91	63.9	18.2	377	19.8	136	N/A	13.5	35.8	4.54	21.5

Table S4.3 (continued)

Secondary reference: BHVO-2G

Date	Sample analyzed	Fe	Co	Ni	Cu	Zn	Ga	Sr	Y	Zr	Nb	La	Ce	Pr	Nd
7/30/2020	17JK08	7.14E+04	46.1	107	102	77.9	20.4	421	20.8	137	N/A	15.2	37.3	5.08	22.8
7/30/2020	17JK08	6.30E+04	41.5	105	92	63.1	19.5	393	19.5	136	N/A	15.5	35.1	4.81	23.2
7/30/2020	17JK08	6.19E+04	40.3	100	84	61.7	18.6	368	17.6	125	N/A	13.6	34.0	4.67	20.8
7/30/2020	17JK08	7.88E+04	44.8	109	91	75.8	19.1	422	20.7	139	N/A	14.8	37.4	5.11	23.5
7/30/2020	17JK08	6.50E+04	41.6	107	86	68.7	18.7	389	19.9	132	N/A	14.0	36.3	4.93	23.4
7/30/2020	17JK08	7.18E+04	44.4	105	90	66.7	18.2	407	19.8	139	N/A	13.4	34.5	4.76	21.0
7/30/2020	17JK08	7.19E+04	43.6	98	92	75.1	19.2	391	21.4	144	N/A	14.1	35.4	4.95	23.1
7/30/2020	17JK08	7.00E+04	44.0	110	89	69.9	19.4	411	20.3	138	N/A	14.8	36.6	5.06	23.1
7/30/2020	17JK08	6.27E+04	43.0	100	91	66.8	18.6	388	20.5	135	N/A	14.2	36.7	5.17	20.9
7/30/2020	17JK08	8.08E+04	42.0	107	93	70.9	18.8	403	19.8	142	N/A	14.7	36.9	5.16	23.2
7/30/2020	17JK08	7.04E+04	42.2	98	84	65.9	19.0	387	18.8	136	N/A	14.5	35.7	5.07	21.6
7/30/2020	17JK08	6.91E+04	43.9	101	89	70.0	18.9	380	19.5	128	N/A	12.8	34.6	4.58	21.5
7/30/2020	17JK08	6.68E+04	44.6	109	90	67.3	19.7	370	19.4	132	N/A	13.5	35.7	5.07	22.4
7/30/2020	17JK08	6.80E+04	41.7	105	85	68.1	18.9	377	19.4	133	N/A	13.4	36.2	4.74	22.1
7/30/2020	17JK08	6.95E+04	43.9	104	93	78.9	19.6	346	17.9	123	N/A	12.8	34.1	4.55	20.9
7/30/2020	17JK08	6.80E+04	45.3	107	96	79.9	19.1	352	19.1	126	N/A	12.8	34.0	4.67	20.3
7/30/2020	17JK08	6.06E+04	41.7	102	92	76.6	18.8	329	17.8	117	N/A	11.8	32.0	4.26	19.5
7/30/2020	17JK08	5.50E+04	43.7	112	101	72.6	20.4	347	16.6	115	N/A	12.3	32.7	4.21	19.4
7/30/2020	17JK08	6.75E+04	45.9	118	101	79.6	21.3	349	17.7	118	N/A	12.3	33.9	4.45	20.0
7/30/2020	17JK08	6.73E+04	43.9	113	91	78.9	20.2	331	17.6	110	N/A	11.7	33.1	4.21	18.3
7/30/2020	17JK08	6.79E+04	43.3	109	92	79.1	20.1	334	16.6	108	N/A	11.9	33.1	4.41	19.4
7/30/2020	17JK08	7.38E+04	42.3	108	89	76.7	19.2	350	15.3	111	N/A	11.7	32.8	4.48	19.0
7/30/2020	17JK08	6.28E+04	43.7	106	90	76.2	19.4	336	16.8	116	N/A	11.9	32.6	4.40	19.1
7/30/2020	17JK08	6.74E+04	41.8	106	89	79.8	18.9	343	16.9	117	N/A	12.2	32.7	4.53	18.7
7/30/2020	17JK08	6.17E+04	39.7	97	86	78.5	18.7	344	16.5	115	N/A	11.8	31.9	4.31	19.0
7/30/2020	17JK08	6.09E+04	42.3	103	88	76.9	19.8	347	17.3	112	N/A	12.6	34.0	4.09	19.5
7/30/2020	17JK08	6.07E+04	43.6	111	87	79.5	19.0	349	17.1	114	N/A	12.4	34.3	4.50	19.5

Table S4.3 (continued)

Secondary reference: BHVO-2G

Date	Sample analyzed	Fe	Co	Ni	Cu	Zn	Ga	Sr	Y	Zr	Nb	La	Ce	Pr	Nd
7/30/2020	17JK08	6.73E+04	43.3	109	88	78.8	20.3	348	16.7	110	N/A	11.9	32.2	4.31	19.1
7/30/2020	17JK08	5.89E+04	42.5	105	86	80.5	20.0	344	16.7	114	N/A	11.9	32.3	4.16	18.6
7/30/2020	17JK08	5.54E+04	43.6	101	87	81.7	19.9	356	17.3	121	N/A	12.5	32.7	4.43	19.3
7/30/2020	17JK08	6.29E+04	44.8	105	87	81.5	20.2	353	16.9	123	N/A	12.7	33.6	4.29	20.7
7/30/2020	17JK08	5.95E+04	44.0	108	84	79.2	20.6	354	16.9	117	N/A	12.4	34.0	4.45	19.5
7/30/2020	17JK08	6.20E+04	42.4	104	88	85.6	21.8	346	16.9	117	N/A	12.0	34.1	4.36	18.6
7/30/2020	17JK08	5.89E+04	43.3	100	83	75.8	20.3	343	17.7	116	N/A	12.0	33.0	4.37	19.4
7/30/2020	17JK08	5.20E+04	40.6	93	79	71.9	18.4	329	15.7	111	N/A	11.1	31.8	4.22	18.7
7/30/2020	17JK08	6.21E+04	42.9	102	80	77.8	19.9	359	17.9	121	N/A	12.7	33.5	4.58	20.4
7/30/2020	17JK08	5.64E+04	40.8	94	75	78.9	20.4	331	16.7	115	N/A	12.0	32.6	4.13	19.3
7/30/2020	17JK08	6.47E+04	44.3	108	82	84.2	20.6	377	18.8	131	N/A	13.1	36.3	4.47	21.6
7/30/2020	17JK08	6.38E+04	44.7	106	82	84.4	20.8	342	17.9	121	N/A	12.6	33.2	4.40	19.8
7/30/2020	17JK08	6.67E+04	44.0	108	82	84.8	19.0	370	19.7	132	N/A	13.3	33.2	4.74	22.4
7/30/2020	17JK08	5.51E+04	44.5	102	84	83.9	20.2	339	17.8	118	N/A	13.1	34.1	4.15	20.4
7/30/2020	17JK08	5.96E+04	44.1	104	78	86.0	19.7	348	17.8	120	N/A	12.5	32.3	4.35	19.4
7/30/2020	17JK08	5.77E+04	42.0	101	83	85.6	20.2	338	16.9	118	N/A	12.2	32.0	4.24	18.6
7/30/2020	17JK08	6.15E+04	45.0	109	88	88.5	22.1	352	18.2	124	N/A	12.8	34.7	4.44	20.4
7/30/2020	17JK08	5.71E+04	43.4	101	84	84.8	19.4	345	16.8	122	N/A	12.9	34.7	4.52	19.7
7/30/2020	17JK08	5.74E+04	43.7	101	84	84.6	18.9	363	18.1	122	N/A	12.6	33.6	4.15	20.1
7/30/2020	17JK08	4.40E+04	43.0	102	89	71.8	19.3	356	17.8	122	N/A	12.5	34.2	4.70	20.0
7/30/2020	17JK08	3.73E+04	39.3	99	84	64.5	18.5	329	16.8	109	N/A	12.3	32.5	4.27	19.4
7/30/2020	17JK08	3.96E+04	42.1	100	83	69.7	19.7	371	17.1	115	N/A	12.9	35.0	4.55	19.8
8/7/2020	17JK12	4.26E+04	48.5	115	73	94.7	20.8	376	18.3	133	17.1	13.5	34.5	4.26	20.3
8/7/2020	17JK12	4.41E+04	44.0	121	72	97.8	20.2	365	18.9	130	16.2	12.4	34.6	4.61	21.1
8/7/2020	17JK12	4.00E+04	43.0	108	67	104.7	21.5	341	16.0	119	15.5	11.7	33.3	4.11	18.5
8/7/2020	17JK12	4.18E+04	45.2	114	67	106.8	21.9	348	17.7	128	15.8	12.5	33.7	4.30	19.6
8/7/2020	17JK12	4.29E+04	42.2	104	63	106.4	19.5	331	18.0	130	15.7	11.8	32.5	4.47	19.6

Table S4.3 (continued)

Secondary reference: BHVO-2G

Date	Sample analyzed	Fe	Co	Ni	Cu	Zn	Ga	Sr	Y	Zr	Nb	La	Ce	Pr	Nd
8/7/2020	17JK12	4.40E+04	44.5	109	71	107.9	20.1	354	18.1	125	16.2	12.8	34.8	4.38	21.2
8/7/2020	17JK12	3.97E+04	40.7	106	65	98.2	19.2	308	16.6	117	15.7	11.4	31.9	4.20	18.8
8/7/2020	17JK12	4.45E+04	42.1	109	68	107.6	20.5	321	16.8	117	15.4	11.8	32.4	4.41	18.5
8/7/2020	17JK12	4.01E+04	43.0	104	64	104.2	20.1	332	17.0	124	15.7	12.2	33.1	4.12	19.1
8/7/2020	17JK12	4.33E+04	42.4	110	62	103.4	20.8	353	17.8	126	15.8	12.5	33.6	4.50	18.9
8/7/2020	17JK12	5.06E+04	43.7	107	66	106.3	21.1	338	17.2	123	16.3	11.9	32.9	4.21	19.4
8/7/2020	17JK12	4.10E+04	44.2	107	65	108.7	20.5	340	17.2	124	16.4	12.2	33.1	4.28	19.2
8/7/2020	17JK12	4.35E+04	43.5	115	69	111.5	21.5	359	17.9	130	16.4	12.5	33.6	4.28	19.9
8/7/2020	17JK12	4.81E+04	44.3	105	63	114.8	21.7	338	17.1	121	15.8	12.2	32.9	4.22	19.4
8/7/2020	17JK12	4.40E+04	45.9	113	67	115.5	20.9	355	19.1	130	17.0	12.6	33.1	4.38	19.3
8/7/2020	17JK12	4.80E+04	43.6	113	74	111.3	21.5	351	18.3	120	16.1	12.3	34.0	4.31	19.5
8/7/2020	17JK12	4.41E+04	46.9	103	66	106.5	20.8	331	17.1	122	15.3	12.2	32.5	4.11	18.3
8/7/2020	17JK12	4.49E+04	42.9	115	72	110.0	21.7	342	16.4	119	16.2	12.0	32.6	4.21	18.7
8/7/2020	17JK12	4.35E+04	42.5	102	67	105.2	20.1	332	15.9	113	15.6	11.5	31.2	3.98	18.0
8/7/2020	17JK12	4.58E+04	43.5	116	68	113.6	19.6	344	17.8	130	16.7	12.3	34.7	4.66	20.2
8/7/2020	17JK12	4.24E+04	40.4	104	64	105.2	20.1	338	17.8	130	15.3	12.7	33.0	4.37	20.8
8/7/2020	17JK12	5.11E+04	43.2	111	72	108.0	20.8	349	19.1	128	16.2	12.0	34.0	4.47	20.4
8/7/2020	17JK12	4.99E+04	43.8	106	66	108.9	20.7	330	17.4	122	16.4	12.0	33.1	4.37	18.5
8/7/2020	17JK12	4.55E+04	42.4	111	70	104.4	20.7	326	16.8	114	15.9	11.5	32.4	4.16	19.3
8/7/2020	17JK12	4.58E+04	44.6	105	62	108.5	19.7	343	17.9	127	16.3	12.8	33.5	4.33	20.1
8/7/2020	17JK12	5.33E+04	44.2	117	63	104.1	22.3	360	18.8	126	17.2	12.3	33.3	4.76	20.7
8/7/2020	17JK12	4.36E+04	40.8	110	63	103.5	19.7	324	16.4	115	15.5	11.5	31.5	4.10	18.9
8/7/2020	17JK12	5.19E+04	42.8	113	70	100.7	20.9	341	15.7	114	15.8	11.6	33.6	4.40	19.6
8/7/2020	17JK12	5.19E+04	45.0	118	72	106.9	21.2	348	17.7	120	16.2	12.0	34.8	4.31	20.5
8/7/2020	17JK12	5.27E+04	43.6	111	73	104.4	20.6	341	17.5	123	16.6	12.4	34.0	4.43	20.1
8/7/2020	17JK12	5.99E+04	43.0	106	69	105.3	21.1	331	18.5	126	16.2	12.7	33.9	4.39	21.3
8/18/2020	17JK12, 17JK20	5.10E+04	38.3	92	66	93.0	16.9	300	15.7	111	14.9	10.9	29.7	4.05	17.4

Table S4.3 (continued)

Secondary reference: BHVO-2G

Date	Sample analyzed	Fe	Co	Ni	Cu	Zn	Ga	Sr	Y	Zr	Nb	La	Ce	Pr	Nd
8/18/2020	17JK12, 17JK20	4.82E+04	36.6	96	65	88.4	18.6	293	14.6	104	14.0	10.2	30.0	3.84	16.0
8/18/2020	17JK12, 17JK20	5.23E+04	39.7	93	67	96.0	18.7	325	16.7	123	15.2	12.2	31.5	4.16	19.1
8/18/2020	17JK12, 17JK20	5.31E+04	38.5	99	66	94.1	19.0	326	17.9	127	15.1	12.2	32.5	4.26	19.0
8/18/2020	17JK12, 17JK20	5.21E+04	37.1	95	65	104.4	15.7	332	19.5	133	15.2	13.6	29.7	4.33	19.2
8/18/2020	17JK12, 17JK20	5.28E+04	38.5	94	61	97.0	17.7	348	20.5	143	16.8	13.1	31.3	4.52	21.1
8/18/2020	17JK12, 17JK20	5.20E+04	38.1	93	64	99.5	19.1	357	21.0	149	17.0	13.1	32.9	4.31	20.7
8/18/2020	17JK12, 17JK20	5.14E+04	38.6	102	64	92.0	18.3	338	17.8	127	16.0	12.1	32.7	4.14	20.3
8/18/2020	17JK12, 17JK20	5.09E+04	38.1	98	62	87.6	18.6	316	17.6	116	14.8	11.6	31.2	4.14	18.6
8/18/2020	17JK12, 17JK20	5.20E+04	38.1	97	60	88.3	18.5	334	18.2	123	15.5	11.7	31.5	4.17	19.5
8/18/2020	17JK12, 17JK20	5.27E+04	39.5	94	63	90.6	18.5	333	18.3	129	15.7	12.2	31.2	4.30	20.5
8/18/2020	17JK12, 17JK20	5.36E+04	39.2	98	57	86.2	17.8	335	18.8	128	15.8	12.4	31.4	4.32	20.0
8/18/2020	17JK12, 17JK20	4.99E+04	38.1	92	59	79.4	19.1	340	17.9	127	15.0	12.0	30.7	4.21	19.3
8/18/2020	17JK12, 17JK20	5.55E+04	39.9	100	60	90.9	19.2	369	18.9	131	16.8	12.8	33.9	4.70	21.0
8/18/2020	17JK12, 17JK20	5.00E+04	35.1	92	62	82.2	18.4	327	17.0	117	15.0	11.8	29.6	3.96	18.3
8/18/2020	17JK12, 17JK20	5.10E+04	38.2	97	66	85.9	19.1	340	18.0	124	15.7	12.1	30.5	4.36	19.2
8/18/2020	17JK12, 17JK20	5.33E+04	35.2	91	55	81.1	18.3	347	18.0	122	15.8	12.1	31.9	4.25	18.7
8/18/2020	17JK12, 17JK20	5.22E+04	39.0	97	62	84.4	18.6	369	18.8	130	16.3	13.0	32.8	4.38	20.0
9/17/2020	17JK09	5.75E+04	45.0	111	99	95.8	20.0	358	20.7	137	16.8	13.3	35.8	4.69	22.2
9/17/2020	17JK09	5.37E+04	47.0	111	104	93.8	21.1	368	20.3	135	16.4	13.5	35.6	4.70	22.0
9/17/2020	17JK09	5.29E+04	43.0	108	91	93.6	20.4	344	18.2	120	15.8	12.6	33.8	4.35	19.6
9/17/2020	17JK09	5.50E+04	49.1	120	100	99.7	21.7	371	19.6	128	17.0	12.8	38.3	4.68	22.0
9/17/2020	17JK09	6.68E+04	45.9	122	101	97.9	18.6	351	20.0	129	16.1	13.0	36.7	4.60	20.4
9/17/2020	17JK09	6.05E+04	46.5	117	96	96.1	19.6	349	18.7	127	16.0	12.6	35.0	4.53	20.1
9/17/2020	17JK09	7.85E+04	46.5	123	106	96.4	21.7	371	18.9	135	16.7	13.1	36.0	4.54	21.1
9/17/2020	17JK09	6.60E+04	46.8	113	93	93.5	20.7	350	19.5	130	16.2	12.5	34.5	4.54	20.2
9/17/2020	17JK09	7.05E+04	46.5	120	100	97.1	19.8	352	19.4	131	16.4	12.9	35.3	4.42	20.9
9/17/2020	17JK09	6.24E+04	47.9	121	99	100.6	21.1	356	19.5	133	16.6	13.4	37.0	4.64	20.0

Table S4.3 (continued)

Secondary reference: BHVO-2G

Date	Sample analyzed	Fe	Co	Ni	Cu	Zn	Ga	Sr	Y	Zr	Nb	La	Ce	Pr	Nd
9/17/2020	17JK09	6.51E+04	46.9	116	99	88.1	20.0	341	18.5	125	15.7	12.7	34.2	4.36	18.5
9/17/2020	17JK09	5.67E+04	46.3	115	95	90.1	20.8	352	19.3	129	16.3	12.8	35.8	4.55	20.5
9/17/2020	17JK09	6.72E+04	47.7	123	100	100.0	22.9	334	18.8	126	16.2	12.9	36.7	4.48	20.6
9/17/2020	17JK09	6.64E+04	45.0	107	95	89.8	19.9	350	18.0	122	16.0	12.8	35.1	4.66	19.5
9/17/2020	17JK09	5.75E+04	47.9	120	100	97.8	20.6	365	19.6	129	16.6	12.9	36.6	4.49	19.8
9/17/2020	17JK09	6.20E+04	46.2	118	102	90.9	20.1	351	19.3	126	16.7	12.6	35.0	4.20	20.0
9/17/2020	17JK09	4.52E+04	47.2	118	107	93.7	20.9	352	18.7	125	16.7	12.9	34.7	4.56	20.0
9/17/2020	17JK09	8.45E+04	47.2	117	99	86.3	20.8	360	20.3	131	17.4	13.2	35.9	4.71	20.2
9/17/2020	17JK09	7.51E+04	49.1	121	110	93.6	20.5	382	21.3	139	18.4	13.9	36.4	4.67	22.1
9/17/2020	17JK09	7.12E+04	47.3	114	98	84.9	21.7	371	19.6	136	15.9	13.7	36.3	4.40	21.5
9/17/2020	17JK09	7.15E+04	43.4	110	103	83.4	21.7	352	18.3	126	16.5	12.6	35.7	4.33	20.3
9/17/2020	17JK09	7.58E+04	46.6	113	106	79.7	22.1	372	19.5	132	16.8	12.9	36.4	4.76	20.9
9/17/2020	17JK09	7.04E+04	45.1	106	96	82.4	20.3	348	18.4	124	16.5	12.2	34.3	4.48	19.4
9/17/2020	17JK09	7.09E+04	44.8	111	100	84.4	20.8	357	19.2	127	15.9	12.1	35.7	4.47	20.4
9/17/2020	17JK09	6.78E+04	46.8	117	106	83.4	21.0	379	19.8	135	17.0	13.2	36.4	4.53	21.2
9/17/2020	17JK09	6.80E+04	45.4	115	103	83.9	21.1	375	19.6	132	16.8	13.2	37.0	4.72	20.1
9/17/2020	17JK09	7.90E+04	49.0	125	111	87.5	20.6	391	20.2	138	17.7	13.1	37.0	4.64	22.1
9/17/2020	17JK09	6.27E+04	47.7	124	112	85.7	20.0	380	19.6	133	16.9	13.5	36.3	4.33	22.3
9/17/2020	17JK09	6.72E+04	49.0	122	105	80.4	19.7	384	21.2	138	17.5	12.9	36.7	4.86	20.8
9/17/2020	17JK09	7.13E+04	45.2	118	102	81.2	19.6	354	19.7	130	16.2	13.2	34.8	4.55	20.6
9/17/2020	17JK09	6.68E+04	47.0	118	105	86.7	22.0	380	19.7	134	16.7	13.8	35.1	4.98	21.5

Table S4.3 (continued)

Secondary reference: BHVO-2G

Date	Sample analyzed	Sm	Eu	Gd	Tb	Dy	Ho	Er	Tm	Yb	Lu	Hf	Pb	Th	U
7/17/2019	17JK20	5.86	2.09	5.52	0.82	5.05	0.89	2.47	0.34	1.78	0.22	4.21	1.57	1.14	0.47
7/17/2019	17JK20	6.06	2.01	5.47	0.79	4.76	0.95	2.51	0.29	2.15	0.25	4.31	1.67	1.14	0.39
7/17/2019	17JK20	6.28	2.14	5.71	0.85	4.95	0.96	2.35	0.30	1.91	0.25	4.10	1.79	1.16	0.46
7/17/2019	17JK20	6.08	2.25	6.34	0.91	5.32	0.96	2.55	0.32	2.11	0.29	4.17	1.76	1.16	0.44
7/17/2019	17JK20	6.55	2.03	6.81	0.77	5.89	0.96	2.46	0.32	2.06	0.34	4.66	1.83	1.33	0.40
7/17/2019	17JK20	5.69	2.02	5.66	0.86	4.72	0.97	2.14	0.34	1.69	0.22	4.17	1.63	1.14	0.46
7/17/2019	17JK20	6.20	1.81	5.10	0.97	5.08	0.86	2.63	0.34	1.88	0.25	4.56	1.85	1.15	0.41
7/17/2019	17JK20	6.47	1.87	5.32	0.86	5.90	0.85	2.43	0.31	1.74	0.26	4.38	1.54	1.30	0.35
7/17/2019	17JK20	6.32	2.22	6.12	1.02	6.29	0.88	2.45	0.31	2.39	0.29	4.64	1.43	1.17	0.47
7/17/2019	17JK20	6.55	2.10	5.89	0.78	5.29	1.02	2.69	0.29	2.17	0.26	4.56	1.59	1.31	0.43
7/17/2019	17JK20	6.16	1.97	7.10	0.98	4.73	1.02	2.13	0.31	2.19	0.26	4.74	1.94	1.17	0.36
7/17/2019	17JK20	6.43	2.21	7.14	1.02	5.49	0.94	2.62	0.25	2.01	0.28	4.56	1.62	1.31	0.43
7/17/2019	17JK20	6.01	2.08	5.98	0.92	4.98	0.97	2.37	0.26	1.70	0.22	4.04	1.98	1.37	0.40
7/17/2019	17JK20	5.41	2.09	5.86	0.87	5.09	0.95	2.69	0.32	2.13	0.24	4.23	1.69	1.15	0.43
7/17/2019	17JK20	6.51	2.24	5.52	1.05	5.12	0.92	2.98	0.39	2.33	0.30	4.39	1.79	1.33	0.48
7/17/2019	17JK20	6.16	2.03	6.18	0.90	5.43	1.02	2.23	0.35	1.97	0.24	4.54	1.82	1.34	0.37
7/17/2019	17JK20	6.25	2.33	6.11	0.94	5.08	0.97	2.31	0.26	1.54	0.22	4.42	1.88	1.28	0.44
7/30/2020	17JK08	5.82	2.04	5.88	0.56	3.67	0.80	2.28	0.21	1.24	0.22	3.99	1.39	1.00	0.40
7/30/2020	17JK08	5.84	2.16	5.52	0.60	4.50	0.71	2.33	0.26	1.54	0.25	3.33	1.60	1.11	0.38
7/30/2020	17JK08	5.58	1.90	4.67	0.80	4.97	0.81	2.15	0.15	1.27	0.17	3.10	1.40	0.94	0.48
7/30/2020	17JK08	5.80	1.95	7.04	0.91	4.14	0.81	2.44	0.20	1.89	0.23	4.16	1.69	1.06	0.42
7/30/2020	17JK08	5.10	2.14	5.75	0.69	3.87	1.02	1.95	0.18	1.90	0.19	3.83	1.40	1.14	0.34
7/30/2020	17JK08	5.37	2.07	6.16	0.66	4.60	0.85	1.93	0.25	1.54	0.18	3.48	1.57	1.06	0.50
7/30/2020	17JK08	5.13	2.29	5.38	0.73	4.69	0.86	2.18	0.41	1.68	0.27	3.77	1.90	1.11	0.40
7/30/2020	17JK08	5.63	1.96	4.90	0.82	4.55	0.70	1.78	0.25	2.01	0.27	3.43	1.61	1.14	0.36
7/30/2020	17JK08	5.06	1.63	4.15	0.86	4.10	0.75	1.99	0.21	1.38	0.17	3.50	1.89	1.04	0.42
7/30/2020	17JK08	5.46	2.01	5.49	0.78	3.80	0.85	1.82	0.25	2.20	0.24	3.74	1.73	0.92	0.47
7/30/2020	17JK08	6.64	1.94	5.31	0.91	4.27	0.74	2.17	0.27	1.10	0.27	3.55	1.91	1.26	0.44

Table S4.3 (continued)

Secondary reference: BHVO-2G

Date	Sample analyzed	Sm	Eu	Gd	Tb	Dy	Ho	Er	Tm	Yb	Lu	Hf	Pb	Th	U
7/30/2020	17JK08	6.02	1.79	4.91	0.83	4.21	0.75	2.39	0.27	1.69	0.25	3.60	2.16	1.14	0.50
7/30/2020	17JK08	5.44	2.18	5.18	0.71	4.33	0.77	2.04	0.32	2.09	0.29	3.63	1.67	1.07	0.46
7/30/2020	17JK08	5.68	1.75	4.92	0.75	3.59	0.72	1.90	0.25	1.68	0.22	3.64	1.76	1.19	0.30
7/30/2020	17JK08	6.41	2.07	5.41	0.84	4.43	0.87	1.97	0.29	2.02	0.24	3.81	1.80	1.17	0.38
7/30/2020	17JK08	5.90	1.94	5.34	0.82	4.55	0.91	2.45	0.18	1.95	0.22	3.98	1.60	0.98	0.39
7/30/2020	17JK08	5.75	2.16	5.09	0.73	3.89	0.80	2.18	0.24	2.18	0.21	3.21	1.80	1.13	0.43
7/30/2020	17JK08	5.76	1.80	3.87	0.87	4.89	1.10	2.14	0.30	2.08	0.19	3.87	1.55	1.02	0.47
7/30/2020	17JK08	6.21	1.98	6.11	0.73	4.96	0.77	2.06	0.33	1.72	0.24	3.51	1.86	1.11	0.42
7/30/2020	17JK08	5.60	1.98	5.44	0.70	3.84	0.88	1.68	0.28	1.56	0.21	3.26	1.75	0.96	0.43
7/30/2020	17JK08	5.47	1.90	5.27	0.67	5.04	0.74	2.47	0.31	1.52	0.21	3.80	1.96	1.08	0.46
7/30/2020	17JK08	5.40	2.01	4.41	0.79	4.35	0.71	1.92	0.21	1.31	0.25	3.90	2.03	1.16	0.45
7/30/2020	17JK08	5.11	2.01	4.71	0.79	4.65	0.74	2.06	0.20	1.78	0.21	3.29	1.44	0.92	0.46
7/30/2020	17JK08	4.77	1.86	5.32	0.74	4.30	0.64	2.32	0.26	1.42	0.22	3.33	1.64	1.02	0.43
7/30/2020	17JK08	5.50	1.98	5.59	0.76	3.94	0.82	2.04	0.24	1.83	0.21	3.47	1.60	1.16	0.39
7/30/2020	17JK08	4.65	1.88	4.42	0.67	4.34	0.69	2.08	0.21	1.48	0.18	3.28	1.86	1.02	0.44
7/30/2020	17JK08	5.01	1.78	4.46	0.73	3.79	0.64	1.96	0.25	1.89	0.22	3.24	1.86	1.02	0.46
7/30/2020	17JK08	4.60	1.67	4.38	0.62	3.51	0.60	1.74	0.21	1.66	0.19	3.03	1.74	0.97	0.38
7/30/2020	17JK08	4.97	1.77	4.06	0.63	3.71	0.66	1.83	0.22	1.39	0.20	2.86	1.87	0.92	0.43
7/30/2020	17JK08	4.89	1.74	4.44	0.63	3.69	0.74	1.89	0.25	1.59	0.19	2.90	1.82	0.82	0.46
7/30/2020	17JK08	4.57	1.61	4.21	0.62	3.53	0.67	1.43	0.19	1.57	0.17	2.85	1.74	0.96	0.40
7/30/2020	17JK08	4.76	1.82	4.01	0.57	3.98	0.67	1.77	0.20	1.19	0.21	2.99	1.92	0.86	0.44
7/30/2020	17JK08	4.61	1.67	4.39	0.63	3.15	0.65	1.42	0.20	1.43	0.19	3.03	1.73	0.81	0.40
7/30/2020	17JK08	4.92	1.59	4.64	0.60	3.26	0.68	1.80	0.18	1.51	0.19	3.13	1.53	0.89	0.41
7/30/2020	17JK08	4.68	1.80	4.42	0.68	3.67	0.66	1.66	0.23	1.25	0.16	3.03	1.61	0.83	0.33
7/30/2020	17JK08	4.69	1.65	4.54	0.64	3.93	0.67	1.59	0.22	1.57	0.20	3.12	1.66	0.90	0.40
7/30/2020	17JK08	4.80	1.86	4.34	0.62	3.87	0.73	1.77	0.24	1.32	0.19	3.36	1.57	1.02	0.34
7/30/2020	17JK08	5.23	1.78	4.84	0.61	3.71	0.72	1.69	0.23	1.63	0.20	3.25	1.70	0.89	0.40
7/30/2020	17JK08	4.41	1.67	3.98	0.69	3.85	0.70	1.84	0.26	1.54	0.21	3.10	1.58	0.94	0.43

Table S4.3 (continued)

Secondary reference: BHVO-2G

Date	Sample analyzed	Sm	Eu	Gd	Tb	Dy	Ho	Er	Tm	Yb	Lu	Hf	Pb	Th	U
7/30/2020	17JK08	4.65	1.62	4.12	0.67	3.95	0.65	1.84	0.24	1.41	0.15	2.99	1.65	0.95	0.42
7/30/2020	17JK08	4.93	1.64	4.03	0.72	3.32	0.64	1.76	0.21	1.41	0.21	3.25	1.80	0.99	0.36
7/30/2020	17JK08	4.85	1.74	4.70	0.71	4.25	0.65	1.61	0.22	1.27	0.20	3.25	1.56	0.99	0.42
7/30/2020	17JK08	4.61	1.85	4.39	0.64	3.68	0.77	1.62	0.20	1.54	0.17	3.26	1.89	0.87	0.40
7/30/2020	17JK08	4.53	1.81	4.56	0.65	3.69	0.70	1.63	0.20	1.46	0.19	3.22	1.67	0.88	0.38
7/30/2020	17JK08	4.37	1.78	4.47	0.57	3.66	0.66	1.70	0.19	1.47	0.19	3.16	1.68	0.86	0.40
7/30/2020	17JK08	4.49	1.57	4.41	0.64	3.30	0.58	1.61	0.23	1.32	0.19	3.00	1.50	0.94	0.39
7/30/2020	17JK08	4.72	1.81	4.84	0.76	3.86	0.71	1.79	0.23	1.54	0.15	3.12	1.68	0.92	0.38
7/30/2020	17JK08	4.99	1.64	3.77	0.56	3.83	0.68	1.58	0.21	1.40	0.20	3.16	1.65	1.04	0.39
7/30/2020	17JK08	5.01	1.87	4.90	0.68	3.92	0.76	1.96	0.23	1.85	0.20	3.24	1.84	0.97	0.44
7/30/2020	17JK08	4.66	1.72	4.38	0.62	3.95	0.69	1.85	0.25	1.40	0.22	3.31	1.94	0.99	0.46
7/30/2020	17JK08	5.66	1.72	5.29	0.78	4.37	0.74	2.01	0.24	1.74	0.22	3.69	1.72	0.93	0.41
7/30/2020	17JK08	4.77	1.74	4.56	0.71	3.65	0.75	1.79	0.23	1.34	0.19	3.28	1.65	0.90	0.44
7/30/2020	17JK08	4.40	1.69	5.02	0.65	3.79	0.72	1.64	0.23	1.29	0.17	3.10	1.46	0.97	0.40
7/30/2020	17JK08	4.63	1.76	4.57	0.72	3.73	0.71	1.88	0.20	1.26	0.20	3.04	1.63	0.88	0.44
7/30/2020	17JK08	5.27	1.84	4.74	0.68	3.48	0.69	1.82	0.24	1.47	0.16	3.33	1.78	1.07	0.39
7/30/2020	17JK08	5.21	1.66	4.65	0.70	3.75	0.71	1.79	0.21	1.55	0.18	3.04	1.71	0.84	0.39
7/30/2020	17JK08	4.94	1.74	4.35	0.67	3.65	0.60	1.63	0.23	1.50	0.18	3.07	1.63	0.86	0.47
7/30/2020	17JK08	5.05	1.85	4.99	0.65	4.21	0.64	1.79	0.28	1.38	0.20	3.16	1.68	1.02	0.40
7/30/2020	17JK08	4.78	1.78	5.16	0.63	3.47	0.63	1.79	0.20	1.34	0.18	3.01	1.42	0.96	0.42
7/30/2020	17JK08	5.24	1.74	4.50	0.68	3.23	0.76	1.69	0.27	1.30	0.20	3.41	1.52	0.89	0.38
8/7/2020	17JK12	5.12	1.77	5.41	0.73	3.94	0.62	1.89	0.22	1.38	0.22	3.06	1.84	0.95	0.37
8/7/2020	17JK12	5.29	1.83	4.89	0.72	3.91	0.63	2.12	0.22	1.61	0.20	3.46	1.98	0.98	0.47
8/7/2020	17JK12	4.60	1.71	4.57	0.57	3.67	0.69	1.76	0.20	1.47	0.22	3.07	1.95	0.89	0.41
8/7/2020	17JK12	4.82	1.48	4.59	0.75	4.32	0.55	1.70	0.20	1.52	0.18	3.01	1.56	0.99	0.42
8/7/2020	17JK12	5.33	1.74	4.43	0.69	3.90	0.65	1.62	0.24	1.55	0.22	3.50	1.80	0.86	0.43
8/7/2020	17JK12	5.22	1.53	4.75	0.57	3.54	0.73	1.78	0.23	1.55	0.18	3.36	1.61	0.90	0.41
8/7/2020	17JK12	4.56	1.56	4.05	0.58	3.75	0.74	1.83	0.20	1.41	0.21	3.22	1.46	0.85	0.38

Table S4.3 (continued)

Secondary reference: BHVO-2G

Date	Sample analyzed	Sm	Eu	Gd	Tb	Dy	Ho	Er	Tm	Yb	Lu	Hf	Pb	Th	U
8/7/2020	17JK12	4.75	1.64	4.39	0.57	3.84	0.59	1.67	0.19	1.50	0.18	3.00	1.74	0.88	0.39
8/7/2020	17JK12	4.82	1.73	4.72	0.59	3.68	0.76	2.04	0.23	1.59	0.19	3.00	1.61	0.92	0.34
8/7/2020	17JK12	4.71	1.86	4.24	0.79	3.69	0.65	1.73	0.20	1.76	0.19	3.13	1.92	0.92	0.41
8/7/2020	17JK12	4.78	1.76	4.71	0.73	4.06	0.72	1.64	0.20	1.57	0.19	3.21	1.77	0.95	0.39
8/7/2020	17JK12	5.06	1.61	4.95	0.68	3.98	0.61	1.88	0.26	1.45	0.21	3.00	1.73	0.82	0.37
8/7/2020	17JK12	4.80	1.67	4.71	0.63	4.09	0.75	1.79	0.19	1.46	0.20	3.14	1.99	0.98	0.38
8/7/2020	17JK12	4.48	1.63	4.74	0.61	3.75	0.74	1.74	0.24	1.81	0.19	3.09	2.03	1.01	0.39
8/7/2020	17JK12	5.20	1.77	4.44	0.74	4.05	0.67	2.05	0.22	1.57	0.18	3.47	1.79	0.93	0.40
8/7/2020	17JK12	4.79	1.74	4.41	0.67	3.61	0.69	1.70	0.17	1.41	0.17	3.09	1.66	0.92	0.46
8/7/2020	17JK12	4.63	1.68	4.96	0.64	3.53	0.73	1.64	0.26	1.33	0.18	3.00	1.80	1.00	0.40
8/7/2020	17JK12	4.21	1.59	4.25	0.70	3.22	0.65	1.56	0.24	1.19	0.21	2.85	1.81	0.86	0.38
8/7/2020	17JK12	4.25	1.51	4.44	0.56	3.66	0.61	1.49	0.22	1.56	0.21	3.20	1.79	0.81	0.37
8/7/2020	17JK12	5.04	1.73	4.51	0.76	4.35	0.75	1.86	0.18	1.43	0.22	3.14	1.69	0.99	0.43
8/7/2020	17JK12	4.73	1.77	4.34	0.64	3.61	0.78	1.63	0.26	1.33	0.22	3.30	1.85	1.03	0.47
8/7/2020	17JK12	4.75	1.55	4.13	0.71	3.61	0.71	1.74	0.18	1.69	0.19	2.98	1.72	0.95	0.39
8/7/2020	17JK12	5.02	1.81	4.31	0.57	4.04	0.61	1.96	0.20	1.74	0.21	3.13	2.00	0.96	0.40
8/7/2020	17JK12	4.58	1.60	4.10	0.66	3.34	0.72	1.43	0.22	1.29	0.14	3.02	1.67	0.79	0.36
8/7/2020	17JK12	5.03	1.66	4.54	0.65	3.38	0.65	1.73	0.23	1.35	0.19	3.53	1.76	0.98	0.40
8/7/2020	17JK12	5.16	1.66	5.81	0.77	4.48	0.70	1.80	0.25	1.53	0.18	3.66	1.96	0.94	0.41
8/7/2020	17JK12	4.59	1.71	4.20	0.59	3.55	0.66	1.55	0.22	1.25	0.21	2.94	1.78	0.93	0.39
8/7/2020	17JK12	4.53	1.60	4.83	0.60	3.78	0.62	1.55	0.21	1.58	0.20	3.09	1.66	0.81	0.45
8/7/2020	17JK12	4.66	1.77	4.31	0.62	3.48	0.78	1.59	0.22	1.52	0.19	2.97	1.78	0.94	0.43
8/7/2020	17JK12	5.14	1.88	4.27	0.64	4.09	0.68	1.72	0.24	1.86	0.22	3.19	1.76	0.85	0.37
8/7/2020	17JK12	4.75	1.93	4.56	0.72	4.45	0.72	1.82	0.24	1.51	0.24	2.91	1.74	0.96	0.44
8/18/2020	17JK12, 17JK20	4.38	1.54	4.61	0.65	3.84	0.63	1.50	0.21	1.31	0.17	3.00	1.46	0.83	0.35
8/18/2020	17JK12, 17JK20	3.97	1.40	3.85	0.55	3.38	0.58	1.59	0.18	1.20	0.18	2.83	1.52	0.73	0.32
8/18/2020	17JK12, 17JK20	5.26	1.88	4.22	0.63	3.26	0.71	1.89	0.26	1.80	0.25	3.03	1.65	0.97	0.39
8/18/2020	17JK12, 17JK20	4.60	1.62	4.63	0.61	3.93	0.69	2.04	0.27	1.12	0.23	3.50	1.68	1.00	0.41

Table S4.3 (continued)

Secondary reference: BHVO-2G

Date	Sample analyzed	Sm	Eu	Gd	Tb	Dy	Ho	Er	Tm	Yb	Lu	Hf	Pb	Th	U
8/18/2020	17JK12, 17JK20	4.86	1.59	4.88	0.56	4.96	0.94	1.83	0.25	1.57	0.25	3.58	1.50	0.91	0.27
8/18/2020	17JK12, 17JK20	4.99	1.54	5.58	0.72	5.00	0.90	2.09	0.30	2.11	0.19	3.68	1.49	1.09	0.33
8/18/2020	17JK12, 17JK20	4.80	1.99	5.56	0.77	4.17	0.90	2.04	0.31	1.56	0.19	4.13	1.52	1.07	0.32
8/18/2020	17JK12, 17JK20	4.81	1.71	4.71	0.61	3.99	0.75	1.80	0.28	1.68	0.19	3.48	1.57	0.87	0.38
8/18/2020	17JK12, 17JK20	4.98	1.67	4.57	0.68	3.92	0.66	1.74	0.20	1.25	0.19	3.34	1.66	0.88	0.32
8/18/2020	17JK12, 17JK20	4.78	1.64	4.28	0.70	3.50	0.67	1.75	0.24	1.47	0.19	2.91	1.88	0.83	0.37
8/18/2020	17JK12, 17JK20	4.54	1.71	4.64	0.71	4.12	0.75	1.84	0.27	1.71	0.21	3.53	1.85	0.93	0.38
8/18/2020	17JK12, 17JK20	5.18	1.72	4.54	0.73	4.01	0.63	2.00	0.20	1.49	0.20	3.32	1.62	0.89	0.33
8/18/2020	17JK12, 17JK20	4.78	1.38	4.95	0.75	3.50	0.74	2.14	0.27	1.32	0.21	3.45	1.76	1.04	0.35
8/18/2020	17JK12, 17JK20	5.06	1.94	5.40	0.72	4.27	0.77	1.99	0.25	1.92	0.20	3.49	2.08	0.97	0.36
8/18/2020	17JK12, 17JK20	4.45	1.64	3.84	0.65	4.03	0.72	1.54	0.22	1.32	0.19	3.06	1.86	0.88	0.34
8/18/2020	17JK12, 17JK20	5.01	1.61	4.34	0.63	3.90	0.73	1.86	0.24	1.60	0.20	3.54	1.84	1.01	0.44
8/18/2020	17JK12, 17JK20	4.77	1.59	4.78	0.66	3.73	0.70	1.80	0.19	1.27	0.18	3.28	1.80	0.87	0.37
8/18/2020	17JK12, 17JK20	4.99	1.76	4.13	0.72	3.78	0.68	2.00	0.27	1.59	0.20	3.61	1.80	1.00	0.37
9/17/2020	17JK09	5.32	1.85	4.37	0.83	4.46	0.76	2.03	0.31	1.74	0.22	3.80	1.70	1.19	0.42
9/17/2020	17JK09	5.27	1.99	5.69	0.74	4.22	0.95	2.15	0.26	2.08	0.27	3.64	1.85	1.02	0.48
9/17/2020	17JK09	5.05	1.63	4.97	0.70	3.91	0.69	1.88	0.25	1.37	0.21	3.45	1.91	0.86	0.37
9/17/2020	17JK09	5.58	1.74	4.22	0.81	4.31	0.82	2.24	0.30	1.69	0.24	3.34	2.12	1.07	0.52
9/17/2020	17JK09	4.76	1.97	5.00	0.73	4.26	0.78	2.18	0.24	1.58	0.21	3.74	1.80	1.14	0.46
9/17/2020	17JK09	5.26	1.86	5.35	0.79	3.99	0.73	1.88	0.22	1.75	0.25	3.49	1.89	0.94	0.41
9/17/2020	17JK09	4.97	1.82	4.45	0.75	3.88	0.79	2.05	0.27	1.69	0.23	3.77	1.96	1.00	0.48
9/17/2020	17JK09	5.25	1.63	4.99	0.73	4.49	0.83	2.07	0.22	1.74	0.24	3.56	1.94	0.93	0.41
9/17/2020	17JK09	5.52	1.82	5.41	0.78	4.48	0.83	1.98	0.27	1.42	0.24	3.81	1.54	1.00	0.47
9/17/2020	17JK09	4.83	1.70	5.62	0.73	4.12	0.77	2.03	0.30	1.79	0.24	3.53	2.18	0.97	0.47
9/17/2020	17JK09	4.58	1.63	4.82	0.66	3.76	0.73	1.93	0.21	1.70	0.21	3.68	2.09	1.04	0.39
9/17/2020	17JK09	4.98	1.86	5.09	0.85	3.91	0.88	2.08	0.20	1.55	0.21	3.75	1.71	1.02	0.37
9/17/2020	17JK09	5.10	1.89	4.89	0.76	4.01	0.72	1.89	0.28	1.39	0.23	3.20	2.16	0.90	0.40
9/17/2020	17JK09	5.15	1.64	3.91	0.73	3.60	0.63	2.12	0.16	1.40	0.20	3.24	1.69	1.05	0.43

Table S4.3 (continued)

Secondary reference: BHVO-2G

Date	Sample analyzed	Sm	Eu	Gd	Tb	Dy	Ho	Er	Tm	Yb	Lu	Hf	Pb	Th	U
9/17/2020	17JK09	5.27	1.78	4.14	0.82	4.38	0.74	1.93	0.28	1.54	0.20	3.32	1.91	1.04	0.46
9/17/2020	17JK09	4.92	1.86	4.73	0.73	4.00	0.75	1.95	0.28	1.85	0.25	3.28	1.89	0.83	0.40
9/17/2020	17JK09	5.20	1.86	5.10	0.75	4.17	0.77	1.80	0.25	1.37	0.23	3.22	2.35	0.97	0.46
9/17/2020	17JK09	5.00	1.79	4.35	0.70	3.91	0.83	1.95	0.29	1.62	0.21	3.26	1.68	1.00	0.45
9/17/2020	17JK09	5.51	1.99	5.14	0.77	4.13	0.89	2.31	0.29	1.57	0.24	3.54	1.68	1.09	0.36
9/17/2020	17JK09	5.16	1.72	5.35	0.90	4.74	0.78	1.96	0.30	1.87	0.24	3.65	1.79	1.13	0.58
9/17/2020	17JK09	5.11	1.84	5.32	0.73	4.14	0.78	1.87	0.20	1.54	0.20	3.57	1.90	0.97	0.37
9/17/2020	17JK09	5.15	1.96	4.41	0.77	4.13	0.80	2.47	0.24	1.84	0.25	3.51	1.87	0.99	0.34
9/17/2020	17JK09	4.71	1.81	5.52	0.64	3.50	0.85	2.03	0.23	1.36	0.20	3.17	1.60	0.95	0.36
9/17/2020	17JK09	5.43	1.84	5.11	0.69	4.84	0.77	1.87	0.19	1.56	0.20	3.42	1.89	0.85	0.40
9/17/2020	17JK09	5.65	1.90	4.71	0.73	4.09	0.77	1.80	0.22	1.90	0.23	3.94	1.56	1.14	0.39
9/17/2020	17JK09	5.08	1.65	4.33	0.68	4.39	0.80	2.00	0.23	1.46	0.21	3.60	1.76	1.04	0.41
9/17/2020	17JK09	5.51	2.13	5.35	0.79	3.96	0.79	2.08	0.27	2.04	0.24	3.55	1.99	1.10	0.40
9/17/2020	17JK09	5.02	1.82	5.57	0.63	4.25	0.84	1.84	0.24	1.43	0.26	3.49	1.94	1.04	0.44
9/17/2020	17JK09	5.18	1.76	4.55	0.73	4.20	0.76	1.98	0.31	1.62	0.23	3.65	1.93	1.02	0.45
9/17/2020	17JK09	5.11	1.80	4.95	0.64	4.09	0.75	1.99	0.19	1.61	0.19	3.65	1.55	1.02	0.47
9/17/2020	17JK09	4.78	1.68	5.33	0.71	3.83	0.68	2.17	0.20	1.64	0.21	3.36	1.81	1.07	0.52

Table S4.3 (continued)

Secondary reference: NIST610

Date	Sample analyzed	Li	Be	Na	Mg	Al	P	Ca	Sc	Ti	V	Cr	Mn
7/17/2019	17JK20	460	463	1.02E+05	495	1.12E+04	532	8.53E+04	486	515	447	399	449
7/17/2019	17JK20	451	484	1.00E+05	418	1.12E+04	359	8.73E+04	487	468	453	406	425
7/17/2019	17JK20	435	463	9.94E+04	461	1.13E+04	455	8.66E+04	481	461	438	395	444
7/17/2019	17JK20	450	463	9.83E+04	375	1.15E+04	298	8.93E+04	498	489	440	405	427
7/17/2019	17JK20	449	448	1.00E+05	365	1.15E+04	348	8.71E+04	494	506	425	399	446
7/17/2019	17JK20	455	461	1.02E+05	597	1.15E+04	451	8.79E+04	499	519	449	412	461

Table S4.3 (continued)

Secondary reference: NIST610

Date	Sample analyzed	Li	Be	Na	Mg	Al	P	Ca	Sc	Ti	V	Cr	Mn
7/17/2019	17JK20	446	457	9.99E+04	500	1.15E+04	431	8.53E+04	486	513	441	393	453
7/17/2019	17JK20	446	463	9.96E+04	480	1.10E+04	434	8.70E+04	496	497	448	409	441
7/17/2019	17JK20	451	452	9.88E+04	529	1.14E+04	463	8.52E+04	479	517	437	402	439
7/17/2019	17JK20	465	455	9.91E+04	471	1.11E+04	496	8.55E+04	486	519	444	397	447
7/17/2019	17JK20	465	462	1.00E+05	518	1.10E+04	470	8.70E+04	485	513	454	419	459
7/17/2019	17JK20	457	449	1.02E+05	522	1.12E+04	444	8.58E+04	489	499	448	404	438
7/17/2019	17JK20	450	450	1.02E+05	513	1.09E+04	462	8.44E+04	486	489	446	402	420
7/17/2019	17JK20	452	452	1.02E+05	510	1.12E+04	450	8.51E+04	490	504	447	405	447
7/17/2019	17JK20	463	473	1.00E+05	505	1.12E+04	517	8.59E+04	493	515	452	390	451
7/17/2019	17JK20	464	475	1.02E+05	502	1.12E+04	581	8.46E+04	485	503	458	408	456
7/17/2019	17JK20	468	479	1.02E+05	530	1.15E+04	429	8.94E+04	501	516	455	404	454
8/7/2020	17JK12	471	377	1.10E+05	348	9.01E+03	387	7.46E+04	367	439	473	434	435
8/7/2020	17JK12	483	389	1.18E+05	316	9.61E+03	414	7.86E+04	411	485	490	452	443
8/7/2020	17JK12	456	393	1.13E+05	309	9.43E+03	398	7.54E+04	399	451	459	414	419
8/7/2020	17JK12	447	370	1.07E+05	334	9.16E+03	409	7.21E+04	389	444	450	397	412
8/7/2020	17JK12	428	366	1.06E+05	332	8.88E+03	405	7.28E+04	376	416	439	388	407
8/7/2020	17JK12	428	380	1.08E+05	319	8.97E+03	393	7.40E+04	387	427	435	407	403
8/7/2020	17JK12	469	399	1.13E+05	351	9.97E+03	426	7.71E+04	416	478	466	423	430
8/7/2020	17JK12	452	391	1.13E+05	319	9.57E+03	420	7.43E+04	394	456	457	410	414
8/7/2020	17JK12	427	400	1.08E+05	313	9.46E+03	422	7.54E+04	388	454	451	395	413
8/7/2020	17JK12	437	391	1.09E+05	349	9.74E+03	424	7.89E+04	412	463	468	425	409
8/7/2020	17JK12	449	409	1.13E+05	327	9.80E+03	420	7.65E+04	410	475	477	418	415
8/7/2020	17JK12	448	386	1.06E+05	318	9.53E+03	412	7.65E+04	408	437	447	401	418
8/7/2020	17JK12	470	414	1.15E+05	361	9.86E+03	421	8.01E+04	433	477	467	423	435
8/7/2020	17JK12	455	405	1.10E+05	336	9.47E+03	402	7.52E+04	408	459	461	408	417
8/7/2020	17JK12	451	401	1.07E+05	316	9.34E+03	416	7.66E+04	400	457	464	411	415
8/7/2020	17JK12	459	406	1.09E+05	318	9.49E+03	424	7.45E+04	387	450	447	422	415
8/7/2020	17JK12	471	404	1.12E+05	328	9.65E+03	404	7.63E+04	399	441	447	427	407

Table S4.3 (continued)

Secondary reference: NIST610

Date	Sample analyzed	Li	Be	Na	Mg	Al	P	Ca	Sc	Ti	V	Cr	Mn
8/7/2020	17JK12	448	397	1.11E+05	316	9.43E+03	404	7.50E+04	398	458	467	437	419
8/7/2020	17JK12	448	401	1.11E+05	318	9.63E+03	410	7.34E+04	394	455	456	426	419
8/7/2020	17JK12	451	389	1.13E+05	311	9.48E+03	403	7.66E+04	393	454	448	432	402
8/7/2020	17JK12	462	391	1.12E+05	327	9.60E+03	408	7.63E+04	406	451	466	421	409
8/7/2020	17JK12	462	396	1.14E+05	323	9.35E+03	398	7.62E+04	406	446	454	415	422
8/7/2020	17JK12	452	381	1.10E+05	302	9.00E+03	384	7.41E+04	393	443	455	419	410
8/7/2020	17JK12	467	373	1.16E+05	301	9.14E+03	384	7.58E+04	396	442	448	421	424
8/7/2020	17JK12	462	405	1.15E+05	329	9.46E+03	389	8.17E+04	428	471	479	446	436
8/7/2020	17JK12	459	386	1.11E+05	317	9.50E+03	397	7.76E+04	404	463	480	440	412
8/7/2020	17JK12	464	389	1.12E+05	309	9.44E+03	368	7.57E+04	403	455	466	425	416
8/7/2020	17JK12	444	382	1.13E+05	309	8.76E+03	386	7.40E+04	399	449	460	414	413
8/7/2020	17JK12	463	392	1.13E+05	321	9.04E+03	397	7.60E+04	408	449	473	435	408
8/7/2020	17JK12	456	418	1.13E+05	329	9.71E+03	394	7.76E+04	420	460	478	424	421
8/7/2020	17JK12	461	408	1.11E+05	339	9.99E+03	417	7.74E+04	431	450	465	407	418
8/18/2020	17JK12, 17JK20	460	472	1.01E+05	445	1.12E+04	370	7.99E+04	482	500	423	398	422
8/18/2020	17JK12, 17JK20	448	440	1.05E+05	424	1.06E+04	411	7.82E+04	456	471	445	405	425
8/18/2020	17JK12, 17JK20	448	435	1.04E+05	425	1.07E+04	456	8.08E+04	458	466	445	412	435
8/18/2020	17JK12, 17JK20	431	427	1.03E+05	389	1.03E+04	420	7.62E+04	442	453	433	388	416
8/18/2020	17JK12, 17JK20	429	445	1.01E+05	415	1.05E+04	402	7.83E+04	451	466	428	418	430
8/18/2020	17JK12, 17JK20	439	446	1.08E+05	387	1.09E+04	434	8.28E+04	469	492	459	419	443
8/18/2020	17JK12, 17JK20	429	446	1.05E+05	437	1.08E+04	506	8.32E+04	450	506	438	407	425
8/18/2020	17JK12, 17JK20	452	449	1.06E+05	417	1.18E+04	559	8.60E+04	472	509	461	413	427
8/18/2020	17JK12, 17JK20	421	461	1.01E+05	426	1.22E+04	535	8.00E+04	450	492	421	391	435
8/18/2020	17JK12, 17JK20	420	429	1.01E+05	414	1.16E+04	550	7.76E+04	444	522	433	401	435
8/18/2020	17JK12, 17JK20	405	422	9.61E+04	374	1.15E+04	486	7.92E+04	436	484	431	387	406
8/18/2020	17JK12, 17JK20	452	453	1.05E+05	421	1.19E+04	444	8.84E+04	468	516	453	409	435
8/18/2020	17JK12, 17JK20	430	443	9.88E+04	423	1.14E+04	394	8.04E+04	454	467	445	397	426
8/18/2020	17JK12, 17JK20	416	447	1.01E+05	400	1.14E+04	361	8.35E+04	467	470	439	397	433

Table S4.3 (continued)

Secondary reference: NIST610

Date	Sample analyzed	Li	Be	Na	Mg	Al	P	Ca	Sc	Ti	V	Cr	Mn
8/18/2020	17JK12, 17JK20	407	451	9.98E+04	381	1.14E+04	372	7.88E+04	451	466	432	395	420
8/18/2020	17JK12, 17JK20	416	447	9.99E+04	375	1.08E+04	362	8.47E+04	472	506	433	391	430
8/18/2020	17JK12, 17JK20	411	446	9.86E+04	358	1.08E+04	364	8.37E+04	479	489	427	377	411
8/18/2020	17JK12, 17JK20	412	455	1.00E+05	350	1.07E+04	365	8.41E+04	482	499	415	386	411
8/18/2020	17JK12, 17JK20	442	480	1.03E+05	376	1.12E+04	368	8.41E+04	503	502	437	403	441
8/18/2020	17JK12, 17JK20	420	443	1.01E+05	344	1.07E+04	376	8.23E+04	480	489	433	386	409
8/18/2020	17JK12, 17JK20	434	463	1.04E+05	355	1.13E+04	422	8.52E+04	500	479	437	398	420
8/18/2020	17JK12, 17JK20	423	462	1.03E+05	361	1.07E+04	433	8.40E+04	486	495	432	396	423
8/18/2020	17JK12, 17JK20	428	474	1.05E+05	349	1.12E+04	412	8.58E+04	497	518	440	401	433
8/18/2020	17JK12, 17JK20	425	487	1.01E+05	343	1.11E+04	401	8.73E+04	501	506	440	407	428
8/18/2020	17JK12, 17JK20	433	468	1.03E+05	364	1.15E+04	390	8.78E+04	497	514	435	400	428
8/18/2020	17JK12, 17JK20	413	468	1.01E+05	378	1.18E+04	432	8.60E+04	502	522	438	398	421
8/18/2020	17JK12, 17JK20	415	471	9.95E+04	368	1.19E+04	430	8.57E+04	492	500	432	393	415
8/18/2020	17JK12, 17JK20	407	476	1.00E+05	344	1.18E+04	416	8.47E+04	492	496	420	392	418
8/18/2020	17JK12, 17JK20	401	460	1.00E+05	363	1.20E+04	415	8.66E+04	488	480	419	382	419
8/18/2020	17JK12, 17JK20	418	475	1.02E+05	379	1.14E+04	389	8.88E+04	508	495	428	399	433
8/18/2020	17JK12, 17JK20	409	477	9.93E+04	394	1.13E+04	391	8.84E+04	499	503	429	395	430
8/18/2020	17JK12, 17JK20	421	465	1.04E+05	416	1.16E+04	410	8.97E+04	505	491	433	400	426
8/18/2020	17JK12, 17JK20	422	478	9.99E+04	386	1.14E+04	418	8.34E+04	497	503	428	390	429
8/18/2020	17JK12, 17JK20	414	479	1.02E+05	384	1.15E+04	396	8.65E+04	503	514	443	405	425
8/18/2020	17JK12, 17JK20	413	469	1.02E+05	366	1.14E+04	400	8.87E+04	504	498	430	400	423
8/18/2020	17JK12, 17JK20	401	468	1.02E+05	360	1.12E+04	356	9.07E+04	494	468	426	391	414
8/18/2020	17JK12, 17JK20	420	488	1.06E+05	386	1.19E+04	356	9.23E+04	523	474	441	411	448
9/17/2020	17JK09	455	398	1.01E+05	463	9.68E+03	399	7.81E+04	403	460	444	410	427
9/17/2020	17JK09	459	402	1.03E+05	456	9.71E+03	352	7.73E+04	401	454	452	390	423
9/17/2020	17JK09	440	388	9.59E+04	431	9.46E+03	314	7.52E+04	389	454	441	384	406
9/17/2020	17JK09	459	400	1.01E+05	450	9.60E+03	342	7.70E+04	404	503	459	406	431
9/17/2020	17JK09	451	388	9.71E+04	442	9.33E+03	336	7.39E+04	390	463	442	396	415

Table S4.3 (continued)

Secondary reference: NIST610

Date	Sample analyzed	Li	Be	Na	Mg	Al	P	Ca	Sc	Ti	V	Cr	Mn
9/17/2020	17JK09	447	388	1.02E+05	435	9.77E+03	359	7.48E+04	404	457	450	409	421
9/17/2020	17JK09	446	389	9.89E+04	457	9.98E+03	380	7.50E+04	404	449	459	405	432
9/17/2020	17JK09	451	395	9.77E+04	460	9.76E+03	405	7.50E+04	405	452	459	403	428
9/17/2020	17JK09	449	391	9.99E+04	453	1.04E+04	412	7.39E+04	398	451	445	399	422
9/17/2020	17JK09	450	402	1.02E+05	448	9.68E+03	405	7.49E+04	403	448	451	404	425
9/17/2020	17JK09	450	387	9.88E+04	443	9.40E+03	371	7.46E+04	396	421	438	396	412
9/17/2020	17JK09	439	371	9.53E+04	419	8.89E+03	332	7.34E+04	386	440	439	392	403
9/17/2020	17JK09	448	397	9.99E+04	439	9.24E+03	323	7.57E+04	398	451	470	414	435
9/17/2020	17JK09	446	382	9.74E+04	443	9.60E+03	338	7.20E+04	392	453	446	396	423
9/17/2020	17JK09	445	373	9.79E+04	425	9.39E+03	336	7.14E+04	388	444	450	397	422
9/17/2020	17JK09	440	378	9.81E+04	434	9.23E+03	347	7.13E+04	388	426	431	383	414
9/17/2020	17JK09	449	373	9.96E+04	442	9.35E+03	376	7.15E+04	391	430	438	392	414
9/17/2020	17JK09	466	386	1.02E+05	429	9.05E+03	395	7.37E+04	399	439	453	407	440
9/17/2020	17JK09	466	399	1.05E+05	465	9.74E+03	424	7.72E+04	417	448	454	421	447
9/17/2020	17JK09	456	397	1.02E+05	469	9.26E+03	430	7.37E+04	408	460	451	416	438
9/17/2020	17JK09	466	401	1.01E+05	464	9.66E+03	522	7.43E+04	395	459	455	419	444
9/17/2020	17JK09	444	392	9.90E+04	459	9.04E+03	534	7.05E+04	377	421	429	399	415
9/17/2020	17JK09	475	422	1.03E+05	495	9.48E+03	861	7.50E+04	406	447	464	422	454
9/17/2020	17JK09	457	398	1.02E+05	482	9.61E+03	526	7.33E+04	399	452	451	428	427
9/17/2020	17JK09	450	392	9.78E+04	464	9.26E+03	721	7.16E+04	387	429	455	425	416
9/17/2020	17JK09	464	402	1.01E+05	497	9.49E+03	675	7.30E+04	392	439	446	423	433
9/17/2020	17JK09	468	407	1.06E+05	461	9.73E+03	525	7.91E+04	415	460	475	444	454
9/17/2020	17JK09	464	390	1.04E+05	470	9.64E+03	627	7.36E+04	407	437	450	418	430
9/17/2020	17JK09	459	399	9.96E+04	458	9.26E+03	558	7.48E+04	406	454	449	421	430
9/17/2020	17JK09	456	416	9.88E+04	475	9.69E+03	777	7.86E+04	418	437	461	441	447
9/17/2020	17JK09	458	404	1.00E+05	497	9.66E+03	956	7.50E+04	426	458	471	434	435

Table S4.3 (continued)

Secondary reference: NIST610

Date	Sample analyzed	Fe	Co	Ni	Cu	Zn	Ga	Sr	Y	Zr	Nb	La	Ce	Pr	Nd
7/17/2019	17JK20	406	406	440	412	412	427	533	476	460	N/A	447	451	454	446
7/17/2019	17JK20	324	412	407	320	267	441	525	483	432	N/A	454	460	455	443
7/17/2019	17JK20	382	404	420	365	351	433	528	488	430	N/A	446	453	449	436
7/17/2019	17JK20	274	413	399	287	242	443	529	500	451	N/A	460	463	466	448
7/17/2019	17JK20	352	399	414	314	249	436	528	491	461	N/A	463	451	464	443
7/17/2019	17JK20	561	415	459	454	455	440	534	496	464	N/A	464	468	471	444
7/17/2019	17JK20	449	405	422	385	343	426	540	479	457	N/A	452	459	463	436
7/17/2019	17JK20	455	407	426	389	375	431	528	477	450	N/A	455	463	464	443
7/17/2019	17JK20	462	402	418	389	372	434	527	482	456	N/A	457	450	446	438
7/17/2019	17JK20	469	411	436	389	354	427	533	488	482	N/A	467	461	456	441
7/17/2019	17JK20	461	416	451	429	442	442	535	485	471	N/A	460	466	456	446
7/17/2019	17JK20	482	409	478	417	398	432	542	487	464	N/A	461	462	465	448
7/17/2019	17JK20	433	416	449	410	407	433	551	469	440	N/A	453	465	459	444
7/17/2019	17JK20	460	401	470	418	434	434	548	477	458	N/A	453	457	461	449
7/17/2019	17JK20	474	407	444	425	407	419	544	483	463	N/A	451	463	455	450
7/17/2019	17JK20	486	411	445	415	397	427	546	482	453	N/A	448	461	459	442
7/17/2019	17JK20	475	407	458	439	400	430	550	509	477	N/A	473	464	471	452
8/7/2020	17JK12	285	419	463	309	465	480	467	391	391	418	374	415	394	366
8/7/2020	17JK12	271	434	462	300	498	499	480	422	411	439	403	453	417	391
8/7/2020	17JK12	257	415	423	286	483	477	489	409	397	432	396	431	404	385
8/7/2020	17JK12	238	395	419	262	494	448	436	398	388	418	382	417	388	371
8/7/2020	17JK12	259	386	404	262	466	444	451	393	383	404	377	400	388	367
8/7/2020	17JK12	274	391	424	267	480	447	444	406	390	408	381	415	395	379
8/7/2020	17JK12	272	416	422	278	514	472	474	423	405	435	404	431	411	397
8/7/2020	17JK12	282	407	429	270	500	464	460	409	398	439	391	427	396	381
8/7/2020	17JK12	245	411	410	269	486	465	442	402	395	428	386	413	393	376
8/7/2020	17JK12	268	414	443	274	513	472	467	415	412	440	402	425	415	398
8/7/2020	17JK12	287	420	431	268	519	465	468	417	414	428	399	429	408	391

Table S4.3 (continued)

Secondary reference: NIST610

Date	Sample analyzed	Fe	Co	Ni	Cu	Zn	Ga	Sr	Y	Zr	Nb	La	Ce	Pr	Nd
8/7/2020	17JK12	247	403	418	265	489	458	450	405	402	418	391	407	391	380
8/7/2020	17JK12	277	413	451	280	528	468	480	439	428	442	417	442	411	394
8/7/2020	17JK12	282	411	436	270	504	472	460	414	408	429	395	431	400	385
8/7/2020	17JK12	281	414	433	262	502	465	451	404	392	426	386	419	394	379
8/7/2020	17JK12	277	411	427	265	505	470	453	396	386	420	380	420	396	374
8/7/2020	17JK12	276	404	436	273	506	462	467	403	397	434	394	424	396	379
8/7/2020	17JK12	287	416	439	275	504	479	471	399	400	423	391	424	410	386
8/7/2020	17JK12	285	424	442	273	511	464	456	394	389	416	378	418	390	380
8/7/2020	17JK12	282	403	427	269	498	460	466	399	393	418	387	418	398	385
8/7/2020	17JK12	276	407	430	271	492	466	469	410	402	419	383	427	398	383
8/7/2020	17JK12	294	421	452	276	494	473	476	414	400	425	392	434	402	390
8/7/2020	17JK12	295	406	422	268	484	454	452	401	385	401	382	415	389	374
8/7/2020	17JK12	292	419	441	278	512	463	469	398	377	414	383	423	393	373
8/7/2020	17JK12	286	432	456	289	501	486	488	419	413	443	396	430	408	397
8/7/2020	17JK12	306	423	442	286	508	470	473	402	392	419	389	421	393	378
8/7/2020	17JK12	290	414	442	275	494	473	466	398	386	417	383	415	394	369
8/7/2020	17JK12	309	412	432	276	492	470	454	391	375	415	379	408	388	371
8/7/2020	17JK12	313	416	454	286	486	488	481	415	395	427	393	436	405	386
8/7/2020	17JK12	320	423	459	283	499	465	467	415	393	426	391	429	415	390
8/7/2020	17JK12	384	415	442	288	507	473	449	443	407	423	401	428	409	401
8/18/2020	17JK12, 17JK20	367	411	421	293	500	436	527	463	455	483	444	445	449	429
8/18/2020	17JK12, 17JK20	366	407	418	280	510	446	508	436	433	457	425	443	415	410
8/18/2020	17JK12, 17JK20	367	409	423	293	518	444	505	443	434	455	426	441	438	413
8/18/2020	17JK12, 17JK20	364	407	411	276	483	432	491	431	426	446	417	437	423	399
8/18/2020	17JK12, 17JK20	404	401	427	287	487	435	515	445	430	456	420	445	434	410
8/18/2020	17JK12, 17JK20	383	414	442	259	505	445	515	454	445	462	436	458	440	423
8/18/2020	17JK12, 17JK20	384	409	411	282	485	445	504	443	433	448	426	439	432	412
8/18/2020	17JK12, 17JK20	408	421	419	285	514	449	529	454	454	463	438	461	449	428

Table S4.3 (continued)

Secondary reference: NIST610

Date	Sample analyzed	Fe	Co	Ni	Cu	Zn	Ga	Sr	Y	Zr	Nb	La	Ce	Pr	Nd
8/18/2020	17JK12, 17JK20	364	394	418	282	479	436	492	428	428	441	418	431	424	408
8/18/2020	17JK12, 17JK20	427	394	420	300	474	445	497	437	427	439	430	442	423	413
8/18/2020	17JK12, 17JK20	363	389	414	266	461	428	480	430	419	428	406	421	422	403
8/18/2020	17JK12, 17JK20	407	422	445	267	494	456	524	457	451	475	448	456	446	434
8/18/2020	17JK12, 17JK20	360	386	416	265	476	446	492	438	429	436	431	451	431	415
8/18/2020	17JK12, 17JK20	375	399	424	263	483	429	499	448	441	459	426	444	433	423
8/18/2020	17JK12, 17JK20	366	390	405	263	465	436	477	435	422	439	411	417	420	404
8/18/2020	17JK12, 17JK20	405	402	418	264	475	439	512	448	442	464	434	448	449	430
8/18/2020	17JK12, 17JK20	384	386	410	257	461	430	503	451	442	463	432	444	436	421
8/18/2020	17JK12, 17JK20	380	386	408	257	469	428	510	443	434	461	428	432	436	420
8/18/2020	17JK12, 17JK20	403	400	423	260	488	451	534	471	461	480	448	458	457	444
8/18/2020	17JK12, 17JK20	378	383	412	245	459	435	515	451	434	458	435	440	436	426
8/18/2020	17JK12, 17JK20	389	388	424	256	465	444	531	466	449	474	441	453	446	439
8/18/2020	17JK12, 17JK20	390	379	409	263	454	439	534	461	448	465	441	453	447	433
8/18/2020	17JK12, 17JK20	399	393	422	251	468	454	554	475	459	479	457	456	459	447
8/18/2020	17JK12, 17JK20	393	396	425	245	457	457	536	476	462	483	460	454	460	448
8/18/2020	17JK12, 17JK20	388	390	423	253	451	443	540	476	469	482	458	450	456	451
8/18/2020	17JK12, 17JK20	397	394	428	257	470	453	550	481	467	485	462	466	468	447
8/18/2020	17JK12, 17JK20	371	381	409	243	444	441	538	474	456	478	452	455	455	446
8/18/2020	17JK12, 17JK20	374	373	404	237	443	434	544	467	453	476	446	439	456	444
8/18/2020	17JK12, 17JK20	385	374	405	244	431	432	525	467	457	479	452	435	448	438
8/18/2020	17JK12, 17JK20	388	395	423	261	444	451	566	488	470	495	465	462	467	462
8/18/2020	17JK12, 17JK20	396	393	426	269	449	446	558	482	468	488	456	446	468	454
8/18/2020	17JK12, 17JK20	410	391	423	279	455	449	561	489	466	486	465	458	472	452
8/18/2020	17JK12, 17JK20	381	384	417	252	449	437	553	475	460	487	458	451	463	447
8/18/2020	17JK12, 17JK20	387	385	420	246	444	443	565	488	473	499	470	457	462	455
8/18/2020	17JK12, 17JK20	389	387	422	246	454	449	550	487	470	481	465	456	463	449
8/18/2020	17JK12, 17JK20	376	373	402	248	435	445	559	482	467	475	458	450	469	441

Table S4.3 (continued)

Secondary reference: NIST610

Date	Sample analyzed	Fe	Co	Ni	Cu	Zn	Ga	Sr	Y	Zr	Nb	La	Ce	Pr	Nd
8/18/2020	17JK12, 17JK20	411	404	424	266	467	459	594	512	496	514	510	486	497	477
9/17/2020	17JK09	339	409	416	377	419	454	466	400	377	428	387	432	414	390
9/17/2020	17JK09	289	413	416	374	416	442	460	386	362	418	378	430	403	377
9/17/2020	17JK09	312	397	410	338	397	425	451	380	348	403	371	426	393	369
9/17/2020	17JK09	308	415	449	356	420	447	474	393	364	428	386	445	409	387
9/17/2020	17JK09	391	399	441	345	406	426	458	371	343	407	368	426	389	367
9/17/2020	17JK09	371	409	457	363	424	445	457	375	357	415	376	429	397	372
9/17/2020	17JK09	433	409	446	363	432	456	467	381	365	409	384	432	401	372
9/17/2020	17JK09	389	397	440	339	418	453	455	383	358	417	382	431	400	377
9/17/2020	17JK09	401	401	438	362	416	442	443	378	362	407	374	428	391	368
9/17/2020	17JK09	345	415	434	357	421	451	450	383	361	427	381	433	402	372
9/17/2020	17JK09	371	406	428	354	403	443	457	371	351	411	375	429	392	364
9/17/2020	17JK09	310	406	410	340	415	424	454	363	347	404	366	416	384	358
9/17/2020	17JK09	405	424	433	336	416	454	474	379	362	425	387	442	400	375
9/17/2020	17JK09	386	411	418	353	413	435	453	374	352	411	369	427	390	367
9/17/2020	17JK09	317	413	435	341	400	443	459	374	349	404	366	421	385	363
9/17/2020	17JK09	321	404	416	346	396	436	445	369	343	408	368	409	385	359
9/17/2020	17JK09	224	402	434	366	387	446	435	370	344	406	373	417	381	365
9/17/2020	17JK09	596	410	434	379	392	458	463	380	354	423	377	424	396	366
9/17/2020	17JK09	409	435	438	411	408	466	490	410	382	444	402	449	418	394
9/17/2020	17JK09	389	413	431	391	379	446	459	385	368	426	390	434	404	380
9/17/2020	17JK09	413	429	444	390	393	449	484	393	368	423	388	442	418	389
9/17/2020	17JK09	399	404	429	386	366	426	456	366	346	404	370	431	392	366
9/17/2020	17JK09	420	426	440	404	383	451	487	388	366	429	383	463	416	395
9/17/2020	17JK09	393	412	421	375	391	471	465	382	363	430	379	437	405	380
9/17/2020	17JK09	353	415	447	371	369	441	445	380	355	413	371	434	393	377
9/17/2020	17JK09	379	407	445	395	379	444	477	386	356	422	372	434	407	378
9/17/2020	17JK09	440	424	480	394	392	461	481	404	383	438	397	448	415	389

Table S4.3 (continued)

Secondary reference: NIST610

Date	Sample analyzed	Fe	Co	Ni	Cu	Zn	Ga	Sr	Y	Zr	Nb	La	Ce	Pr	Nd
9/17/2020	17JK09	354	414	458	394	361	444	463	390	370	426	386	439	407	383
9/17/2020	17JK09	369	419	446	390	387	443	464	391	363	432	388	429	407	378
9/17/2020	17JK09	399	431	465	388	377	459	468	402	376	439	396	446	424	388
9/17/2020	17JK09	382	420	466	392	397	458	491	401	377	434	394	453	419	390

Table S4.3 (continued)

Secondary reference: NIST610

Date	Sample analyzed	Sm	Eu	Gd	Tb	Dy	Ho	Er	Tm	Yb	Lu	Hf	Pb	Th	U
7/17/2019	17JK20	463	456	476	464	457	474	480	451	486	464	448	413	463	443
7/17/2019	17JK20	464	458	464	455	451	477	472	455	490	460	446	410	467	456
7/17/2019	17JK20	464	449	454	456	444	478	470	452	481	463	451	406	473	444
7/17/2019	17JK20	483	465	470	468	459	486	481	474	502	476	462	413	477	455
7/17/2019	17JK20	474	468	466	464	455	481	475	466	491	468	456	408	476	451
7/17/2019	17JK20	477	467	476	472	461	484	478	464	489	462	456	409	468	449
7/17/2019	17JK20	466	463	460	458	447	473	472	457	489	457	445	415	464	440
7/17/2019	17JK20	462	460	464	464	455	467	475	460	488	457	447	424	466	450
7/17/2019	17JK20	462	463	454	457	453	473	479	449	476	457	442	408	464	444
7/17/2019	17JK20	466	463	459	462	451	476	476	456	482	463	447	411	475	443
7/17/2019	17JK20	463	462	454	452	450	467	468	448	479	460	447	424	473	462
7/17/2019	17JK20	472	458	464	467	460	481	482	453	493	468	458	414	480	454
7/17/2019	17JK20	459	460	466	463	450	475	476	447	483	451	440	413	458	448
7/17/2019	17JK20	468	463	466	463	452	473	477	453	487	462	444	418	468	458
7/17/2019	17JK20	469	469	470	467	461	481	473	462	494	466	452	403	472	455
7/17/2019	17JK20	468	462	460	456	457	464	468	451	485	455	439	408	458	458
7/17/2019	17JK20	491	488	474	480	475	495	497	478	502	482	473	430	499	457
8/7/2020	17JK12	379	382	380	369	366	376	376	362	391	370	362	449	395	480
8/7/2020	17JK12	417	408	414	405	385	414	408	390	430	398	394	468	418	499

Table S4.3 (continued)

Secondary reference: NIST610

Date	Sample analyzed	Sm	Eu	Gd	Tb	Dy	Ho	Er	Tm	Yb	Lu	Hf	Pb	Th	U
8/7/2020	17JK12	407	393	397	405	385	408	393	381	420	399	385	468	414	485
8/7/2020	17JK12	392	371	388	395	372	384	380	365	399	377	375	431	389	446
8/7/2020	17JK12	391	381	374	383	362	384	383	366	406	382	370	435	393	435
8/7/2020	17JK12	395	379	385	386	382	391	389	379	413	389	377	422	393	452
8/7/2020	17JK12	411	406	398	411	395	414	409	396	434	406	394	466	418	465
8/7/2020	17JK12	405	394	401	402	389	402	405	387	419	395	385	445	408	471
8/7/2020	17JK12	394	385	399	391	384	396	391	384	405	392	380	446	402	462
8/7/2020	17JK12	419	409	418	413	404	413	411	392	426	405	384	452	417	474
8/7/2020	17JK12	415	406	415	414	405	414	419	400	424	407	397	455	421	468
8/7/2020	17JK12	397	387	400	397	389	401	413	387	412	397	385	437	408	447
8/7/2020	17JK12	416	406	419	413	407	420	417	408	428	413	402	461	430	475
8/7/2020	17JK12	399	394	409	396	390	408	409	394	418	396	385	445	413	460
8/7/2020	17JK12	395	392	406	393	381	400	407	393	414	395	377	442	411	473
8/7/2020	17JK12	388	388	396	393	379	396	390	382	401	384	372	442	406	471
8/7/2020	17JK12	395	390	401	397	376	400	400	389	413	390	373	447	397	468
8/7/2020	17JK12	402	389	386	397	383	401	398	393	416	396	380	458	397	476
8/7/2020	17JK12	401	389	378	394	386	394	389	381	407	384	376	436	399	467
8/7/2020	17JK12	392	390	385	391	384	400	396	381	407	392	380	450	404	482
8/7/2020	17JK12	394	392	386	398	384	403	405	389	425	392	389	457	407	468
8/7/2020	17JK12	401	392	392	406	391	411	409	390	419	400	387	451	415	476
8/7/2020	17JK12	388	383	379	396	375	401	393	374	407	390	377	438	403	465
8/7/2020	17JK12	396	382	384	390	380	399	392	370	405	383	366	459	394	469
8/7/2020	17JK12	415	404	403	416	401	420	412	395	421	406	399	462	420	476
8/7/2020	17JK12	391	386	393	389	377	403	395	378	406	390	378	447	402	470
8/7/2020	17JK12	388	389	385	387	372	390	385	377	407	385	377	455	395	468
8/7/2020	17JK12	389	380	393	386	379	390	386	378	406	384	373	458	391	459
8/7/2020	17JK12	404	401	407	404	393	404	403	396	415	399	388	465	408	465
8/7/2020	17JK12	407	398	407	415	407	412	409	398	421	405	391	471	415	482

Table S4.3 (continued)

Secondary reference: NIST610

Date	Sample analyzed	Sm	Eu	Gd	Tb	Dy	Ho	Er	Tm	Yb	Lu	Hf	Pb	Th	U
8/7/2020	17JK12	416	411	412	419	423	432	427	412	432	427	406	473	430	468
8/18/2020	17JK12, 17JK20	464	440	443	457	458	464	456	452	481	461	443	424	483	460
8/18/2020	17JK12, 17JK20	438	419	431	425	418	435	425	413	456	423	404	415	443	442
8/18/2020	17JK12, 17JK20	440	434	435	431	431	447	440	421	472	436	417	431	450	455
8/18/2020	17JK12, 17JK20	426	408	414	414	407	430	425	409	443	412	398	405	431	436
8/18/2020	17JK12, 17JK20	439	428	426	428	418	437	435	421	445	428	414	415	440	444
8/18/2020	17JK12, 17JK20	446	424	444	434	432	438	445	427	448	437	420	423	457	444
8/18/2020	17JK12, 17JK20	438	426	435	427	413	433	440	423	445	430	416	410	444	444
8/18/2020	17JK12, 17JK20	451	442	452	446	429	452	451	433	459	448	429	416	457	466
8/18/2020	17JK12, 17JK20	429	415	427	421	417	434	428	417	448	426	418	411	438	437
8/18/2020	17JK12, 17JK20	431	429	420	421	414	434	431	410	451	425	410	418	443	451
8/18/2020	17JK12, 17JK20	419	418	417	410	399	417	425	407	443	412	401	401	430	436
8/18/2020	17JK12, 17JK20	461	449	447	450	433	455	464	441	469	450	440	447	462	458
8/18/2020	17JK12, 17JK20	436	432	431	427	412	424	435	416	437	435	420	411	442	432
8/18/2020	17JK12, 17JK20	445	428	434	434	421	441	446	431	443	440	426	423	450	431
8/18/2020	17JK12, 17JK20	422	414	420	419	405	426	423	415	430	427	418	390	440	421
8/18/2020	17JK12, 17JK20	446	443	438	441	430	439	444	428	454	437	427	406	452	437
8/18/2020	17JK12, 17JK20	444	438	439	440	424	445	448	423	467	436	433	414	455	431
8/18/2020	17JK12, 17JK20	439	428	431	429	431	441	439	422	463	437	428	414	454	421
8/18/2020	17JK12, 17JK20	465	452	452	458	456	474	464	445	496	459	448	427	473	436
8/18/2020	17JK12, 17JK20	448	438	436	439	437	457	440	428	473	440	431	406	456	418
8/18/2020	17JK12, 17JK20	458	448	455	450	442	462	461	446	493	457	447	433	471	445
8/18/2020	17JK12, 17JK20	457	454	456	453	439	465	460	444	483	451	446	420	468	434
8/18/2020	17JK12, 17JK20	470	462	454	460	439	467	469	454	485	465	458	434	475	433
8/18/2020	17JK12, 17JK20	471	465	461	468	455	470	474	455	485	468	458	445	477	433
8/18/2020	17JK12, 17JK20	476	464	459	464	447	471	473	462	491	471	458	426	480	448
8/18/2020	17JK12, 17JK20	477	459	457	470	452	469	469	453	493	461	453	438	474	433
8/18/2020	17JK12, 17JK20	470	460	453	461	455	471	465	454	486	462	455	425	482	426

Table S4.3 (continued)

Secondary reference: NIST610

Date	Sample analyzed	Sm	Eu	Gd	Tb	Dy	Ho	Er	Tm	Yb	Lu	Hf	Pb	Th	U
8/18/2020	17JK12, 17JK20	460	459	446	454	453	461	465	457	473	456	451	407	474	419
8/18/2020	17JK12, 17JK20	463	455	454	450	448	467	462	452	472	456	445	418	471	424
8/18/2020	17JK12, 17JK20	479	471	474	480	473	483	476	472	484	471	465	420	484	436
8/18/2020	17JK12, 17JK20	475	473	464	469	455	479	472	467	498	470	460	419	481	436
8/18/2020	17JK12, 17JK20	473	471	475	472	461	485	476	468	503	469	463	422	488	443
8/18/2020	17JK12, 17JK20	466	468	458	456	446	470	466	457	492	461	451	412	478	436
8/18/2020	17JK12, 17JK20	473	471	473	477	465	473	475	468	495	479	467	426	484	440
8/18/2020	17JK12, 17JK20	471	470	465	467	462	476	473	460	500	473	459	414	483	439
8/18/2020	17JK12, 17JK20	471	469	465	463	460	476	469	456	492	471	458	408	470	428
8/18/2020	17JK12, 17JK20	501	509	502	492	477	507	501	484	521	500	487	424	506	450
9/17/2020	17JK09	401	402	381	379	376	382	387	362	395	371	359	425	389	460
9/17/2020	17JK09	391	390	374	373	366	375	374	364	391	366	351	426	385	464
9/17/2020	17JK09	381	381	365	363	365	371	369	351	385	362	350	414	375	443
9/17/2020	17JK09	395	407	380	383	373	384	382	374	398	375	360	429	388	462
9/17/2020	17JK09	376	386	365	366	354	371	372	356	388	361	349	412	379	439
9/17/2020	17JK09	387	388	363	372	360	380	379	356	382	365	354	421	387	451
9/17/2020	17JK09	390	394	373	376	362	381	377	364	388	374	364	425	390	454
9/17/2020	17JK09	387	393	375	377	359	383	377	363	395	377	360	419	387	450
9/17/2020	17JK09	378	381	366	372	364	376	373	359	392	365	361	426	384	450
9/17/2020	17JK09	387	389	376	378	371	379	379	365	395	375	361	427	387	460
9/17/2020	17JK09	380	384	373	370	365	374	370	357	382	363	354	418	382	456
9/17/2020	17JK09	376	371	356	364	353	364	352	345	374	354	343	399	367	439
9/17/2020	17JK09	392	398	374	376	366	376	372	360	395	369	361	429	387	462
9/17/2020	17JK09	384	382	362	369	355	363	360	355	380	359	350	419	379	444
9/17/2020	17JK09	377	379	355	361	358	359	357	351	379	358	348	414	381	444
9/17/2020	17JK09	369	372	348	354	350	357	360	345	374	354	341	417	377	449
9/17/2020	17JK09	371	377	360	364	354	363	366	351	375	358	348	421	379	448
9/17/2020	17JK09	379	388	370	373	356	371	377	354	380	368	354	419	382	455

Table S4.3 (continued)

Secondary reference: NIST610

Date	Sample analyzed	Sm	Eu	Gd	Tb	Dy	Ho	Er	Tm	Yb	Lu	Hf	Pb	Th	U
9/17/2020	17JK09	415	414	401	394	390	398	401	384	410	394	379	429	409	478
9/17/2020	17JK09	403	397	376	378	372	383	379	373	390	369	363	426	384	466
9/17/2020	17JK09	408	409	386	392	372	399	391	379	408	385	377	437	406	487
9/17/2020	17JK09	382	373	361	369	351	363	358	353	369	358	342	415	374	435
9/17/2020	17JK09	403	401	385	385	377	392	387	379	398	386	373	440	397	467
9/17/2020	17JK09	399	393	375	383	369	389	370	367	391	372	362	439	401	463
9/17/2020	17JK09	387	385	369	371	362	374	363	362	376	365	352	435	382	458
9/17/2020	17JK09	393	395	365	372	359	384	371	365	391	369	356	426	386	455
9/17/2020	17JK09	404	411	392	388	375	401	390	382	413	388	378	444	404	468
9/17/2020	17JK09	389	403	374	376	367	389	375	368	393	372	362	426	391	465
9/17/2020	17JK09	391	398	372	377	368	385	373	369	397	371	365	427	388	446
9/17/2020	17JK09	402	409	389	391	379	403	385	379	409	388	374	436	409	471
9/17/2020	17JK09	398	403	385	377	368	387	375	362	401	386	368	430	395	470

Table S4.3.1

Mass spectrometer dwell times for each element

Element	Dwell time (ms)
^{7}Li	10
^{9}Be	10
^{23}Na	5
^{24}Mg	5
^{27}Al	5
^{29}Si	5
^{31}P	10
^{43}Ca	5
^{45}Sc	10
^{47}Ti	10
^{51}V	10
^{52}Cr	10
^{55}Mn	5
^{56}Fe	5
^{59}Co	10
^{60}Ni	10
^{63}Cu	10
^{66}Zn	10
^{71}Ga	10
^{86}Sr	10
^{89}Y	10
^{90}Zr	10
^{93}Nb	10
^{139}La	10
^{140}Ce	10
^{141}Pr	10
^{146}Nd	20
^{147}Sm	20
^{153}Eu	10
^{157}Gd	10
^{159}Tb	10

Table S4.3.1 (continued)

Element	Dwell time (ms)
^{163}Dy	10
^{165}Ho	10
^{166}Er	10
^{169}Tm	10
^{172}Yb	10
^{175}Lu	20
^{178}Hf	20
^{208}Pb	10
^{232}Th	10
^{238}U	10

Table S4.4

Lu and Hf data obtained by isotope dilution from garnet and whole rock fractions of metabasite and metatonalite. Results are shown for an additional metabasite sample that was analyzed (17JK03) but yielded an errorchron (Figure S4.2).

Sample	Lu (µg/g)	Hf (µg/g)	^{175}Lu (V)	^{176}Hf (V)	^{176}Lu/^{175}Lu	^{175}Lu/^{177}Hf	^{173}Yb/^{177}Hf	^{176}Lu/^{177}Hf	^{176}Hf/^{177}Hf	err
17JK20WRS	0.660	1.138	8.957	0.487	0.203292	0.000021	0.000012	0.0823	0.285316	0.000005
17JK20WRB	0.723	2.710	7.798	0.477	0.159140	0.000005	0.000002	0.0379	0.283107	0.000005
17JK20G1	2.229	0.254	7.979	0.484	0.205794	0.000028	0.000015	1.2603	0.345330	0.000005
17JK20G2	2.131	0.221	7.801	0.718	0.141476	0.000251	0.000187	1.3882	0.352558	0.000005
17JK20G3	2.223	0.238	7.886	0.499	0.179470	0.000015	0.000005	1.3410	0.349090	0.000006
17JK20G4	2.150	0.260	7.842	0.584	0.200684	0.000087	0.000051	1.1874	0.342068	0.000018
17JK12WRS	0.538	2.171	8.90	0.46	0.166139	0.000000	0.000000	0.0351	0.282897	0.000005
17JK12WRB	0.561	2.506	4.87	0.38	0.196483	0.000009	0.000008	0.0318	0.282716	0.000007
17JK12G1	3.507	0.293	8.93	0.47	0.155032	0.000000	0.000002	1.7262	0.367133	0.000007
17JK12G2	3.439	0.332	8.08	0.59	0.134320	0.000035	0.000034	1.4909	0.355567	0.000006
17JK12G3	3.382	0.297	7.16	0.54	0.120713	0.000018	0.000025	1.6398	0.363321	0.000006
17JK12G4	3.480	0.318	7.70	0.54	0.123490	0.000103	0.000062	1.5750	0.359586	0.000014
17JK09 WRS	0.478	0.999	2.267	1.291	0.096817	0.000020	0.000033	0.0680	0.284621	0.000003
17JK09 WRB	0.502	2.651	2.770	1.919	0.187432	0.000009	0.000007	0.0268	0.282549	0.000003
17JK09G1	1.407	0.154	3.208	1.108	0.133208	0.000261	0.000175	1.3140	0.347842	0.000006
17JK09G2	1.406	0.164	3.801	0.703	0.134810	0.000027	0.000020	1.2274	0.343455	0.000005
17JK09G3	1.415	0.156	5.070	1.101	0.114705	0.000047	0.000070	1.2998	0.346397	0.000004
17JK09G4	1.398	0.161	2.018	1.089	0.120352	0.000035	0.000075	1.2466	0.344209	0.000004
17JK08WRS	0.408	4.291	7.703	0.484	0.421491	0.000017	0.000005	0.0135	0.281830	0.000004
17JK08WRB	0.430	4.283	7.842	0.500	0.459971	0.000015	0.000003	0.0142	0.281872	0.000004
17JK08G1	5.140	3.155	9.439	0.477	0.108480	0.000026	0.000031	0.2316	0.292993	0.000037
17JK08G2	5.109	3.286	8.838	0.486	0.097474	0.000000	0.000000	0.2210	0.292553	0.000005
17JK08G3	5.130	3.271	7.272	0.490	0.105843	0.000000	0.000000	0.2229	0.292565	0.000004
17JK08G4	5.072	3.138	8.558	0.500	0.106216	0.000001	0.000002	0.2298	0.292953	0.000004
17JK03WRS	0.271	0.655	5.22	0.44	0.352905	0.000021	0.000000	0.0587	0.284127	0.000004
17JK03WRB	0.282	1.058	6.84	0.43	0.158917	0.000001	0.000000	0.0378	0.283120	0.000005
17JK03G1	1.940	0.110	5.47	0.30	0.104503	0.000001	0.000000	2.5574	0.413302	0.000007
17JK03G2	2.120	0.130	5.14	0.29	0.090697	0.000012	0.000013	2.3586	0.400562	0.000009
17JK03G3	1.952	0.113	5.37	0.37	0.117865	0.000018	0.000012	2.5187	0.413289	0.000010
17JK03G4	2.180	0.118	5.36	0.39	0.097687	0.000030	0.000079	2.6770	0.413853	0.000007

Table S4.4 (continued)

Sample	$^{176}Lu/^{177}Hf$	2s (abs)	$^{176}Hf/^{177}Hf$	2s (abs)
17JK20WRS	0.0823	0.0004	0.285316	0.000015
17JK20WRB	0.0379	0.0002	0.283107	0.000015
17JK20G1	1.2603	0.0063	0.345330	0.000018
17JK20G2	1.3882	0.0069	0.352558	0.000018
17JK20G3	1.3410	0.0067	0.349090	0.000018
17JK20G4	1.1874	0.0059	0.342068	0.000025
17JK12WRS	0.0351	0.0002	0.282897	0.000015
17JK12WRB	0.0318	0.0002	0.282716	0.000016
17JK12G1	1.7262	0.0086	0.367133	0.000020
17JK12G2	1.4909	0.0075	0.355567	0.000019
17JK12G3	1.6398	0.0082	0.363321	0.000019
17JK12G4	1.5750	0.0079	0.359586	0.000023
17JK09 WRS	0.0680	0.0003	0.284621	0.000015
17JK09 WRB	0.0268	0.0001	0.282549	0.000014
17JK09G1	1.3140	0.0066	0.347842	0.000018
17JK09G2	1.2274	0.0061	0.343455	0.000018
17JK09G3	1.2998	0.0065	0.346397	0.000018
17JK09G4	1.2466	0.0062	0.344209	0.000018
17JK08WRS	0.0135	0.0001	0.281830	0.000015
17JK08WRB	0.0142	0.0001	0.281872	0.000015
17JK08G1	0.2316	0.0012	0.292993	0.000040
17JK08G2	0.2210	0.0011	0.292553	0.000015
17JK08G3	0.2229	0.0011	0.292565	0.000015
17JK08G4	0.2298	0.0011	0.292953	0.000015
17JK03WRS	0.0587	0.0003	0.284127	0.000015
17JK03WRB	0.0378	0.0002	0.283120	0.000015
17JK03G1	2.5574	0.0128	0.413302	0.000022
17JK03G2	2.3586	0.0118	0.400562	0.000022
17JK03G3	2.5187	0.0126	0.413289	0.000023
17JK03G4	2.6770	0.0134	0.413853	0.000022

Table S4.5

U, Pb, Lu, and Hf data obtained by laser ablation split stream ICP-MS of zircon in leucosome samples. Concentrations of Th and U in µg/g. Results from secondary reference materials are also included. Calculated dates ($^{238}U/^{206}Pb$ – column 10, $^{207}Pb/^{206}Pb$ – column 12, concordia age – column 14) are in Ma. Disc = discordance

Data from samples:

Sample	spot id	$^{238}U/^{206}Pb$	2SE	$^{207}Pb/^{206}Pb$	2 SE	Th	U	Th/U	$^{238}U/^{206}Pb$	2SE	$^{207}Pb/^{206}Pb$	2 SE	Concordia	2SE	Disc
19JK15	19JK15 - 1	1.9908	0.0436	0.1806	0.0026	38.9	44.3	0.88	2624	24	2658	12	2651	11	1.3
19JK15	19JK15 - 2	1.9920	0.0437	0.1791	0.0020	46.35	176.7	0.26	2622	24	2644	9	2641	9	0.8
19JK15	19JK15 - 3	1.9976	0.0439	0.1754	0.0021	48.13	110.8	0.43	2616	24	2609	10	2610	9	-0.3
19JK15	19JK15 - 4	1.9944	0.0438	0.1809	0.0025	29.47	72.67	0.41	2620	24	2660	12	2653	10	1.5
19JK15	19JK15 - 5	1.9547	0.0420	0.1876	0.0021	44.07	117	0.38	2663	23	2720	9	2713	9	2.1
19JK15	19JK15 - 6	2.1820	0.0524	0.1539	0.0024	42.64	97.9	0.44	2432	24	2389	13	2399	12	-1.8
19JK15	19JK15 - 7	1.9889	0.0435	0.1811	0.0022	50	99.9	0.50	2626	24	2662	10	2657	9	1.4
19JK15	19JK15 - 8	1.9697	0.0427	0.1804	0.0022	27.52	121	0.23	2647	24	2656	10	2654	9	0.3
19JK15	19JK15 - 9	2.0101	0.0444	0.1816	0.0024	51.83	72.44	0.72	2603	24	2667	11	2656	10	2.4
19JK15	19JK15 - 10	1.6469	0.0380	0.1793	0.0021	30	110.9	0.27	3059	28	2646	10	2696	10	-15.6
19JK15	19JK15 - 11	1.8202	0.0431	0.1816	0.0027	21.7	59.4	0.37	2823	27	2667	12	2695	11	-5.8
19JK15	19JK15 - 12	1.9861	0.0434	0.1806	0.0018	96.88	263.7	0.37	2629	24	2658	8	2655	8	1.1
19JK15	19JK15 - 13	2.0101	0.0444	0.1812	0.0021	71.6	134.7	0.53	2603	24	2663	10	2655	9	2.3
19JK15	19JK15 - 14	2.0052	0.0442	0.1803	0.0024	68.85	72.49	0.95	2608	24	2655	11	2647	10	1.8
19JK15	19JK15 - 15	1.9689	0.0426	0.1822	0.0026	35.98	70.4	0.51	2648	24	2672	12	2667	11	0.9
19JK15	19JK15 - 16	2.0218	0.0450	0.1776	0.0036	12.36	29.35	0.42	2591	24	2630	17	2617	14	1.5
19JK15	19JK15 - 17	2.0346	0.0455	0.1779	0.0029	15.75	58.51	0.27	2577	24	2633	14	2619	12	2.1
19JK15	19JK15 - 18	1.9920	0.0437	0.1794	0.0023	30.54	121.7	0.25	2622	24	2647	11	2643	10	0.9
19JK15	19JK15 - 19	1.9673	0.0426	0.1834	0.0028	17.64	52.4	0.34	2649	24	2683	13	2676	11	1.3
19JK15	19JK15 - 20	2.0820	0.0477	0.1730	0.0022	70.9	144.2	0.49	2529	24	2586	11	2577	10	2.2

Table S4.5 (continued)

Sample	spot id	$^{238}U/^{206}Pb$	2SE	$^{207}Pb/^{206}Pb$	2 SE	Th	U	Th/U	$^{238}U/^{206}Pb$	2SE	$^{207}Pb/^{206}Pb$	2 SE	Concordia	2SE	Disc
19JK16	19JK16 - 1	1.9662	0.0425	0.1792	0.0017	243	776	0.31	2651	24	2645	8	2645	7	-0.2
19JK16	19JK16 - 2	1.9736	0.0428	0.1789	0.0017	343.3	995	0.35	2643	24	2642	8	2642	7	0.0
19JK16	19JK16 - 3	1.9893	0.0435	0.1799	0.0017	398.9	1191	0.33	2625	24	2651	8	2649	7	1.0
19JK16	19JK16 - 4	1.9670	0.0426	0.1786	0.0017	260.1	786	0.33	2650	24	2639	8	2640	8	-0.4
19JK16	19JK16 - 5	1.9782	0.0430	0.1784	0.0017	246	812	0.30	2637	24	2637	8	2637	8	0.0
19JK16	19JK16 - 6	2.0178	0.0448	0.1793	0.0020	72.5	250	0.29	2595	24	2646	9	2639	9	1.9
19JK16	19JK16 - 7	2.0064	0.0443	0.1800	0.0019	142.5	289.9	0.49	2607	24	2652	9	2647	8	1.7
19JK16	19JK16 - 8	2.0153	0.0447	0.1802	0.0019	77.7	278.7	0.28	2598	24	2654	9	2647	8	2.1
19JK16	19JK16 - 9	1.9554	0.0459	0.1862	0.0018	190.5	594	0.32	2663	26	2708	8	2704	8	1.7
19JK16	19JK16 - 10	1.9482	0.0417	0.1795	0.0017	216.1	733.1	0.29	2671	23	2648	8	2650	7	-0.9
19JK16	19JK16 - 11	2.1272	0.0453	0.1801	0.0017	768.1	2260	0.34	2484	22	2653	8	2635	7	6.4
19JK16	19JK16 - 12	2.0218	0.0450	0.1757	0.0017	158	503.4	0.31	2591	24	2612	8	2610	8	0.8
19JK16	19JK16 - 13	1.9440	0.0416	0.1804	0.0022	43.1	162	0.27	2675	23	2656	10	2659	9	-0.7
19JK16	19JK16 - 14	2.0429	0.0459	0.1797	0.0020	69.1	228.5	0.30	2569	24	2649	9	2639	9	3.1
19JK16	19JK16 - 15	1.8932	0.0430	0.1784	0.0018	219.5	525	0.42	2734	25	2637	8	2647	8	-3.7
19JK16	19JK16 - 16	1.9301	0.0410	0.1801	0.0018	112.4	300.1	0.37	2691	23	2653	8	2657	8	-1.4
19JK16	19JK16 - 17	1.8667	0.0453	0.1951	0.0021	127.6	369	0.35	2765	27	2785	9	2783	8	0.7
19JK16	19JK16 - 18	1.9608	0.0423	0.1764	0.0024	29.55	97.9	0.30	2657	24	2619	11	2626	10	-1.5
19JK16	19JK16 - 19	2.0305	0.0454	0.1743	0.0019	68.9	251.6	0.27	2581	24	2599	9	2596	8	0.7
19JK16	19JK16 - 20	1.9639	0.0424	0.1797	0.0018	115.1	424	0.27	2653	24	2649	8	2650	8	-0.1
19JK16	19JK16 - 21	1.9264	0.0445	0.1793	0.0019	102.4	331.8	0.31	2695	25	2646	9	2651	8	-1.9

Table S4.5 (continued)

Sample	spot id	$^{176}Hf/^{177}Hf$ measured	2SE	$^{178}Hf/^{177}Hf$	2SE	$^{180}Hf/^{177}Hf$	2SE	$^{176}Yb/^{177}Hf$	2SE	$^{176}Lu/^{177}Hf$	2SE	Comment
19JK15	19JK15 - 1	0.281158	0.000024	1.46726	0.00013	1.88668	0.00009	0.00115	0.00009	3.45E-05	3.90E-06	Leucosome population
19JK15	19JK15 - 2	0.281178	0.000026	1.46724	0.00011	1.88659	0.00010	0.00091	0.00001	1.96E-05	2.80E-07	Leucosome population
19JK15	19JK15 - 3	0.281174	0.00003	1.46728	0.00013	1.88652	0.00009	0.00050	0.00001	9.93E-06	2.40E-07	Leucosome population
19JK15	19JK15 - 4	0.281179	0.000022	1.46728	0.00012	1.8867	0.00008	0.00077	0.00001	1.73E-05	2.90E-07	Leucosome population
19JK15	19JK15 - 5	0.281171	0.000028	1.46724	0.00016	1.8867	0.00012	0.00389	0.00010	1.02E-04	2.60E-06	Inherited
19JK15	19JK15 - 6	0.281188	0.000025	1.46729	0.00012	1.88669	0.00008	0.00041	0.00001	9.02E-06	2.50E-07	Crack - not included
19JK15	19JK15 - 7	0.281161	0.000025	1.46721	0.00011	1.88684	0.00010	0.00056	0.00004	1.18E-05	8.40E-07	Leucosome population
19JK15	19JK15 - 8	0.281169	0.000029	1.46737	0.00014	1.88678	0.00010	0.00384	0.00002	1.01E-04	4.60E-07	Leucosome population
19JK15	19JK15 - 9	0.28117	0.000019	1.46726	0.00013	1.88669	0.00009	0.00051	0.00001	1.07E-05	2.40E-07	Leucosome population
19JK15	19JK15 - 10	0.281153	0.000023	1.46731	0.00012	1.88676	0.00010	0.00036	0.00001	6.37E-06	2.70E-07	>5% discordant
19JK15	19JK15 - 11	0.281177	0.000025	1.46726	0.00014	1.88671	0.00010	0.00069	0.00003	1.61E-05	9.60E-07	>5% discordant
19JK15	19JK15 - 12	0.281182	0.000027	1.46727	0.00012	1.88666	0.00010	0.00066	0.00001	1.47E-05	2.20E-07	Leucosome population
19JK15	19JK15 - 13	0.281173	0.000026	1.46727	0.00013	1.88664	0.00010	0.00212	0.00006	6.08E-05	2.30E-06	Leucosome population
19JK15	19JK15 - 14	0.281158	0.000022	1.46725	0.00011	1.88667	0.00008	0.00087	0.00003	2.03E-05	7.40E-07	Leucosome population
19JK15	19JK15 - 15	0.281177	0.00002	1.46725	0.00013	1.88651	0.00010	0.00131	0.00001	3.01E-05	3.30E-07	Leucosome population
19JK15	19JK15 - 16	0.281163	0.000021	1.46728	0.00012	1.88675	0.00010	0.00045	0.00001	9.60E-06	2.20E-07	Leucosome population
19JK15	19JK15 - 17	0.281172	0.000023	1.46737	0.00011	1.88664	0.00009	0.00051	0.00002	1.03E-05	5.30E-07	Leucosome population
19JK15	19JK15 - 18	0.281185	0.000023	1.4673	0.00013	1.88682	0.00008	0.00047	0.00001	8.60E-06	2.10E-07	Leucosome population
19JK15	19JK15 - 19	0.281173	0.000029	1.46718	0.00014	1.88655	0.00009	0.00034	0.00001	6.83E-06	2.80E-07	Leucosome population
19JK15	19JK15 - 20	0.281199	0.000027	1.46721	0.00012	1.88674	0.00010	0.00028	0.00001	6.64E-06	2.00E-07	Late metamorphic

Table S4.5 (continued)

Sample	spot id	$^{176}Hf/^{177}Hf$ measured	2SE	$^{178}Hf/^{177}Hf$	2SE	$^{180}Hf/^{177}Hf$	2SE	$^{176}Yb/^{177}Hf$	2SE	$^{176}Lu/^{177}Hf$	2SE	Comment
19JK16	19JK16 - 1	0.281139	0.000026	1.46725	0.00013	1.88664	0.00010	0.00295	0.00002	7.62E-05	7.60E-07	Leucosome population
19JK16	19JK16 - 2	0.281179	0.000025	1.46715	0.00013	1.88677	0.00010	0.00368	0.00005	9.13E-05	1.20E-06	Leucosome population
19JK16	19JK16 - 3	0.281162	0.000027	1.46719	0.00014	1.88671	0.00011	0.00188	0.00009	4.16E-05	2.10E-06	Leucosome population
19JK16	19JK16 - 4	0.281184	0.000029	1.46721	0.00012	1.88671	0.00011	0.00238	0.00003	6.01E-05	7.50E-07	Leucosome population
19JK16	19JK16 - 5	0.281174	0.000026	1.46725	0.00013	1.88663	0.00009	0.00308	0.00004	7.87E-05	5.20E-07	Leucosome population
19JK16	19JK16 - 6	0.281208	0.000021	1.46719	0.00012	1.88637	0.00010	0.00126	0.00005	3.23E-05	1.20E-06	Leucosome population
19JK16	19JK16 - 7	0.2812	0.000027	1.46722	0.00011	1.88663	0.00009	0.00288	0.00008	7.28E-05	1.80E-06	Leucosome population
19JK16	19JK16 - 8	0.281183	0.000024	1.46723	0.00012	1.88663	0.00013	0.00112	0.00004	2.84E-05	8.50E-07	Leucosome population
19JK16	19JK16 - 9	0.281169	0.000029	1.46718	0.00014	1.88665	0.00012	0.00310	0.00016	7.66E-05	3.30E-06	Inherited
19JK16	19JK16 - 10	0.281164	0.000028	1.46722	0.00013	1.88667	0.00012	0.00184	0.00004	4.58E-05	8.00E-07	Leucosome population
19JK16	19JK16 - 11	0.281147	0.000026	1.4672	0.00013	1.88668	0.00008	0.00339	0.00024	7.90E-05	5.50E-06	>5% discordant
19JK16	19JK16 - 12	0.281169	0.000028	1.46719	0.00014	1.88671	0.00010	0.00157	0.00002	4.22E-05	7.40E-07	Leucosome population
19JK16	19JK16 - 13	0.281215	0.000032	1.46724	0.00014	1.8866	0.00013	0.00216	0.00019	5.87E-05	5.30E-06	Leucosome population
19JK16	19JK16 - 14	0.281158	0.000026	1.46723	0.00012	1.88668	0.00010	0.00187	0.00004	5.18E-05	7.70E-07	Leucosome population
19JK16	19JK16 - 15	0.281168	0.000026	1.46718	0.00012	1.88661	0.00011	0.00170	0.00004	3.97E-05	7.80E-07	Leucosome population
19JK16	19JK16 - 16	0.281174	0.000023	1.46724	0.00014	1.88667	0.00012	0.00584	0.00005	1.79E-04	1.80E-06	Leucosome population
19JK16	19JK16 - 17	0.281174	0.000025	1.46718	0.00013	1.88672	0.00011	0.00199	0.00006	4.76E-05	1.90E-06	Inherited
19JK16	19JK16 - 18	0.281174	0.000029	1.46718	0.00014	1.88661	0.00012	0.00033	0.00001	7.84E-06	2.40E-07	Leucosome population
19JK16	19JK16 - 19	0.281195	0.000028	1.46728	0.00013	1.88665	0.00011	0.00127	0.00002	3.42E-05	5.90E-07	Leucosome population
19JK16	19JK16 - 20	0.281159	0.000024	1.46721	0.00014	1.88682	0.00011	0.00356	0.00008	1.03E-04	2.10E-06	Leucosome population
19JK16	19JK16 - 21	0.281177	0.000024	1.46717	0.00012	1.8867	0.00011	0.00198	0.00002	5.15E-05	9.40E-07	Leucosome population

Table S4.5 (continued)

Data from secondary reference materials (U–Pb).

sample	spot id	$^{238}U/^{206}Pb$	2SE	$^{207}Pb/^{206}Pb$	2 SE	Th	U	Th/U	$^{238}U/^{206}Pb$	2SE	$^{207}Pb/^{206}Pb$	2 SE	Concordia	2 SE	Disc
91500	91500 - 1	5.6786	0.1322	0.0742	0.0022	N/A	N/A	0.38	1046	11	1046	30	1046	11	0.0
91500	91500 - 2	5.7372	0.1317	0.0751	0.0022	N/A	N/A	0.38	1036	11	1070	29	1040	10	3.2
91500	91500 - 3	5.6593	0.1281	0.0755	0.0018	N/A	N/A	0.38	1049	11	1081	24	1054	10	3.0
91500	91500 - 4	5.6561	0.1280	0.0755	0.0017	N/A	N/A	0.37	1050	11	1081	23	1055	10	2.9
91500	91500 - 5	5.6306	0.1300	0.0745	0.0023	N/A	N/A	0.38	1054	11	1054	31	1054	11	0.0
91500	91500 - 6	5.6657	0.1316	0.0762	0.0022	N/A	N/A	0.37	1048	11	1099	29	1054	11	4.7
91500	91500 - 7	5.6433	0.1306	0.0741	0.0018	N/A	N/A	0.37	1052	11	1043	25	1050	10	-0.8
91500	91500 - 8	5.6370	0.1303	0.0746	0.0018	N/A	N/A	0.38	1053	11	1057	24	1054	10	0.4
91500	91500 - 9	5.7045	0.1302	0.0744	0.0018	N/A	N/A	0.38	1041	11	1051	24	1043	10	1.0
91500	91500 - 10	5.6915	0.1296	0.0789	0.0021	N/A	N/A	0.37	1043	11	1169	26	1059	11	10.7
91500	91500 - 11	5.6786	0.1290	0.0740	0.0017	N/A	N/A	0.38	1046	11	1041	23	1045	10	-0.5
91500	91500 - 12	5.6818	0.1291	0.0754	0.0018	N/A	N/A	0.38	1045	11	1078	24	1051	10	3.1
91500	91500 - 13	5.6657	0.1284	0.0750	0.0017	N/A	N/A	0.38	1048	11	1068	23	1051	10	1.9
91500	91500 - 14	5.6657	0.1284	0.0748	0.0019	N/A	N/A	0.37	1048	11	1062	26	1050	10	1.4
91500	91500 - 15	5.6338	0.1270	0.0763	0.0019	N/A	N/A	0.37	1053	11	1102	25	1061	10	4.4
91500	91500 - 16	5.6402	0.1272	0.0757	0.0017	N/A	N/A	0.38	1052	11	1086	23	1058	10	3.1
91500	91500 - 17	5.7803	0.1336	0.0735	0.0020	N/A	N/A	0.38	1029	11	1027	28	1028	10	-0.2
91500	91500 - 18	5.7870	0.1340	0.0731	0.0020	N/A	N/A	0.38	1028	11	1016	28	1026	10	-1.2
FC1	FC1 - 1	5.3758	0.1185	0.0760	0.0011	302.1	391	0.77	1100	11	1094	15	1098	9	-0.5
FC1	FC1 - 2	5.3622	0.1179	0.0764	0.0010	331.3	440	0.75	1102	11	1105	13	1103	8	0.2
FC1	FC1 - 3	5.3735	0.1184	0.0768	0.0010	412.3	559	0.74	1100	11	1115	13	1107	9	1.3
FC1	FC1 - 4	5.4558	0.1191	0.0762	0.0009	405.2	667	0.61	1085	11	1099	12	1092	8	1.3
FC1	FC1 - 6	5.3299	0.1165	0.0765	0.0010	332.3	485.1	0.69	1109	11	1107	13	1108	8	-0.1
FC1	FC1 - 7	5.3914	0.1192	0.0756	0.0009	295.6	461.1	0.64	1097	11	1084	12	1091	8	-1.2
FC1	FC1 - 8	5.3917	0.1192	0.0762	0.0011	137.2	283.4	0.48	1097	11	1099	14	1098	9	0.2
FC1	FC1 - 9	5.4206	0.1175	0.0763	0.0010	322.6	480	0.67	1091	11	1102	13	1096	8	1.0
FC1	FC1 - 10	5.4042	0.1168	0.0760	0.0010	438.6	641	0.68	1095	11	1094	13	1094	8	0.0

Table S4.5 (continued)

sample	spot id	$^{238}U/^{206}Pb$	2SE	$^{207}Pb/^{206}Pb$	2 SE	Th	U	Th/U	$^{238}U/^{206}Pb$	2SE	$^{207}Pb/^{206}Pb$	2 SE	Concordia	2 SE	Disc
Maniitsoq	macq - 2	1.7200	0.0385	0.2228	0.0024	146.6	129	1.14	2954	27	3000	9	2996	8	1.5
Maniitsoq	macq - 3	1.7292	0.0389	0.2209	0.0024	183.6	155.9	1.18	2942	27	2987	9	2982	8	1.5
Maniitsoq	macq - 4	1.7001	0.0376	0.2238	0.0024	132.7	131.1	1.01	2982	26	3008	9	3005	8	0.8
Maniitsoq	macq - 5	1.7027	0.0377	0.2231	0.0024	222.9	177.7	1.25	2979	26	3002	9	3000	8	0.8
Maniitsoq	macq - 6	1.7200	0.0385	0.2212	0.0023	303.5	200.3	1.52	2954	27	2989	8	2986	8	1.1
Maniitsoq	macq - 8	1.7185	0.0384	0.2205	0.0022	217.2	160.5	1.35	2957	27	2984	8	2981	8	0.9
Maniitsoq	macq - 9	1.7215	0.0385	0.2225	0.0023	293	204.2	1.43	2952	27	2998	8	2994	8	1.5
Maniitsoq	macq - 10	1.7501	0.0398	0.2240	0.0024	172.8	150.5	1.15	2914	27	3009	9	3000	8	3.2
GJ1	gj1 - 1	10.2859	0.2222	0.0596	0.0010	20.71	664	0.03	598	6	588	18	597	6	-1.7
GJ1	gj1 - 2	10.3520	0.2250	0.0597	0.0010	20.2	655	0.03	594	6	592	18	594	6	-0.5
GJ1	gj1 - 3	10.3552	0.2252	0.0601	0.0010	10.93	419.8	0.03	594	6	606	18	596	6	2.0
GJ1	gj1 - 4	10.4471	0.2292	0.0603	0.0010	8.52	348.5	0.02	589	6	613	18	592	6	3.9
GJ1	gj1 - 5	10.3178	0.2236	0.0605	0.0010	20.25	648	0.03	596	6	621	18	599	6	3.9
GJ1	gj1 - 6	10.3875	0.2266	0.0600	0.0011	18.77	624	0.03	593	6	603	20	593	6	1.7
GJ1	gj1 - 7	10.3391	0.2245	0.0610	0.0011	10.44	424	0.02	595	6	638	19	599	6	6.8
GJ1	gj1 - 8	10.3842	0.2264	0.0608	0.0011	10.88	433	0.03	593	6	631	20	596	6	6.1
GJ1	gj1 - 9	10.4603	0.2298	0.0603	0.0010	10.55	426.6	0.02	589	6	613	18	591	6	4.0
GJ1	gj1 - 10	10.3907	0.2267	0.0599	0.0011	10.94	434.1	0.03	592	6	599	20	593	6	1.1
GJ1	gj1 - 11	10.3767	0.2261	0.0603	0.0011	9.13	376.6	0.02	593	6	613	20	595	6	3.3
GJ1	gj1 - 12	10.4210	0.2281	0.0598	0.0011	9.31	386	0.02	591	6	595	20	591	6	0.8
GJ1	gj1 - 13	10.3413	0.2246	0.0604	0.0011	9.35	386	0.02	595	6	617	20	597	6	3.6
GJ1	gj1 - 14	10.3831	0.2264	0.0594	0.0010	9.02	370.3	0.02	593	6	581	18	592	6	-2.1
GJ1	gj1 - 15	10.3961	0.2270	0.0602	0.0010	8.83	360.5	0.02	592	6	610	18	594	6	2.9
GJ1	gj1 - 16	10.3821	0.2264	0.0600	0.0011	15.86	545	0.03	593	6	603	20	594	6	1.6
GJ1	gj1 - 17	10.4112	0.2276	0.0598	0.0010	18.32	620	0.03	591	6	595	18	592	6	0.7
GJ1	gj1 - 18	10.4384	0.2288	0.0602	0.0010	15.12	534	0.03	590	6	610	18	592	6	3.3

Table S4.5 (continued)

Data from secondary reference materials (Lu–Hf).

sample	spot id	$^{176}Hf/^{177}Hf$ measured	2SE	$^{178}Hf/^{177}Hf$	2SE	$^{180}Hf/^{177}Hf$	2SE	$^{176}Yb/^{177}Hf$	2SE	$^{176}Lu/^{177}Hf$	2SE
Mun0	mun0 - 1	0.282115	0.00003	1.46719	0.00011	1.8867	0.00011	0.00004	0.00001	1.98E-06	2.40E-07
Mun0	mun0 - 2	0.282106	0.000026	1.46717	0.00012	1.88656	0.00010	0.00004	0.00001	2.42E-06	2.90E-07
Mun0	mun0 - 3	0.282123	0.000021	1.46722	0.00011	1.88666	0.00012	0.00004	0.00001	2.12E-06	2.50E-07
Mun3	mun3 - 1	0.282144	0.000022	1.46724	0.00012	1.88666	0.00008	0.06167	0.00053	0.0017	5.30E-06
Mun3	mun3 - 2	0.282102	0.000032	1.46721	0.00013	1.88665	0.00011	0.07300	0.01100	0.0017	2.00E-04
Mun3	mun3 - 3	0.282171	0.000024	1.46727	0.00012	1.88663	0.00009	0.13449	0.00068	0.0035	3.10E-06
Mun1	mun1 - 1	0.282113	0.00003	1.46718	0.0001	1.88665	0.00012	0.03189	0.00006	0.0009	3.30E-06
Mun1	mun1 - 2	0.282122	0.00003	1.46721	0.00012	1.88669	0.00011	0.03169	0.00006	0.0009	3.40E-06
Mun1	mun1 - 3	0.282138	0.000026	1.46722	0.00013	1.88666	0.00012	0.03194	0.00007	0.0009	2.80E-06
FC1	FC1 - 1	0.28216	0.000023	1.46716	0.00012	1.88675	0.00010	0.04268	0.00064	0.0011	9.50E-06
FC1	FC1 - 2	0.282152	0.000027	1.46715	0.00013	1.88656	0.00010	0.05360	0.00021	0.0013	8.20E-07
FC1	FC1 - 3	0.282154	0.000027	1.46728	0.00012	1.88665	0.00011	0.05262	0.00019	0.0013	5.10E-07
FC1	FC1 - 4	0.282172	0.000036	1.46725	0.00014	1.88668	0.00009	0.05499	0.00014	0.0014	2.10E-06
FC1	FC1 - 5	0.282205	0.000027	1.46727	0.00012	1.8867	0.00010	0.05733	0.00018	0.0015	9.80E-07
FC1	FC1 - 6	0.282142	0.00002	1.46726	0.0001	1.88669	0.00010	0.04275	0.00031	0.0011	3.50E-06
FC1	FC1 - 7	0.282159	0.000025	1.46725	0.00013	1.88655	0.00010	0.04402	0.00052	0.0011	9.60E-06
FC1	FC1 - 8	0.282147	0.000028	1.46729	0.00013	1.88664	0.00012	0.02854	0.00020	0.0008	3.20E-06
FC1	FC1 - 9	0.282178	0.000027	1.46727	0.00011	1.88672	0.00012	0.03668	0.00047	0.0010	1.30E-05
FC1	FC1 - 10	0.282192	0.000027	1.46719	0.00015	1.88668	0.00010	0.06059	0.00015	0.0016	1.90E-06
Maniitsoq	macq - 1	0.280836	0.000021	1.46716	0.00014	1.88679	0.00009	0.02100	0.00015	0.0006	2.00E-06
Maniitsoq	macq - 2	0.280829	0.000028	1.4672	0.00011	1.88677	0.00010	0.01626	0.00089	0.0004	2.10E-05
Maniitsoq	macq - 3	0.28083	0.000023	1.46715	0.00011	1.88673	0.00010	0.01661	0.00048	0.0005	1.10E-05
Maniitsoq	macq - 5	0.280874	0.000027	1.46709	0.00011	1.88662	0.00010	0.02557	0.00035	0.0007	1.00E-05
Maniitsoq	macq - 6	0.280837	0.000025	1.46724	0.0001	1.88654	0.00010	0.02959	0.00032	0.0008	3.70E-06
Maniitsoq	macq - 7	0.280845	0.000028	1.46724	0.00011	1.88667	0.00010	0.02991	0.00011	0.0008	1.20E-06
Maniitsoq	macq - 8	0.280851	0.000028	1.46709	0.00016	1.88663	0.00009	0.02633	0.00031	0.0007	8.90E-06
Maniitsoq	macq - 9	0.280828	0.000026	1.46732	0.00011	1.88669	0.00010	0.01919	0.00038	0.0005	8.30E-06
Maniitsoq	macq - 10	0.280876	0.000029	1.4672	0.00015	1.88662	0.00011	0.01645	0.00047	0.0005	1.20E-05
Plesovice	ples - 1	0.282459	0.000021	1.46721	0.00013	1.88668	0.00010	0.00908	0.00002	0.0002	4.50E-07
Plesovice	ples - 2	0.282459	0.000029	1.46722	0.00013	1.88671	0.00010	0.01006	0.00002	0.0002	1.10E-06
Plesovice	ples - 3	0.282455	0.000025	1.46724	0.00011	1.88672	0.00010	0.01101	0.00007	0.0002	2.50E-06

Table S4.5 (continued)

sample	spot id	$^{176}Hf/^{177}Hf$ measured	2SE	$^{178}Hf/^{177}Hf$	2SE	$^{180}Hf/^{177}Hf$	2SE	$^{176}Yb/^{177}Hf$	2SE	$^{176}Lu/^{177}Hf$	2SE
Plesovice	ples - 4	0.282454	0.000021	1.46731	0.0001	1.88674	0.00010	0.00832	0.00003	0.0002	4.10E-07
Plesovice	ples - 5	0.282476	0.000025	1.46722	0.00013	1.88673	0.00007	0.01245	0.00003	0.0002	7.30E-07
Plesovice	ples - 6	0.282431	0.000022	1.46718	0.00012	1.88658	0.00011	0.00924	0.00004	0.0002	2.80E-07
Plesovice	ples - 7	0.282446	0.000025	1.46721	0.00013	1.88673	0.00010	0.00794	0.00003	0.0001	2.50E-07
Plesovice	ples - 8	0.282423	0.000025	1.46721	0.00012	1.88669	0.00009	0.00712	0.00004	0.0001	2.50E-07
Plesovice	ples - 9	0.282446	0.000025	1.46721	0.00010	1.88679	0.00010	0.00659	0.00005	0.0001	3.90E-07
Plesovice	ples - 10	0.282475	0.000029	1.46726	0.00014	1.88666	0.00010	0.00645	0.00003	0.0001	2.40E-07
91500	91500 - 1	0.282259	0.000037	1.46727	0.00013	1.88655	0.00014	0.00580	0.00003	0.0002	3.90E-07
91500	91500 - 2	0.2823	0.000038	1.46733	0.00014	1.88669	0.00016	0.00601	0.00002	0.0002	4.90E-07
91500	91500 - 3	0.282279	0.000037	1.46716	0.00012	1.88655	0.00014	0.00985	0.00002	0.0003	1.40E-06
91500	91500 - 4	0.282256	0.000028	1.46728	0.00012	1.88672	0.00014	0.01262	0.00005	0.0004	5.50E-07
91500	91500 - 5	0.282283	0.000033	1.46724	0.00013	1.88676	0.00013	0.00624	0.00003	0.0002	4.30E-07
91500	91500 - 6	0.282311	0.000033	1.46724	0.00012	1.88668	0.00011	0.00600	0.00003	0.0002	4.20E-07
91500	91500 - 7	0.282292	0.000033	1.46725	0.00013	1.88673	0.00013	0.01012	0.00004	0.0003	1.90E-06
91500	91500 - 8	0.28228	0.000034	1.46727	0.00012	1.8867	0.00015	0.00993	0.00009	0.0003	9.90E-07
91500	91500 - 9	0.282291	0.000032	1.46725	0.00012	1.8868	0.00017	0.01032	0.00003	0.0003	9.90E-07
91500	91500 - 10	0.282285	0.000033	1.46733	0.00012	1.88658	0.00014	0.00938	0.00007	0.0003	8.20E-07
91500	91500 - 11	0.28232	0.000033	1.4673	0.00012	1.88679	0.00016	0.01160	0.00005	0.0003	4.70E-07
91500	91500 - 12	0.282291	0.000035	1.46722	0.0001	1.88662	0.00016	0.01144	0.00005	0.0003	4.90E-07
91500	91500 - 13	0.282289	0.000036	1.46723	0.00016	1.88656	0.00014	0.01170	0.00004	0.0003	6.30E-07
91500	91500 - 14	0.282268	0.000029	1.46723	0.00012	1.88677	0.00013	0.01171	0.00005	0.0003	5.20E-07
91500	91500 - 15	0.282292	0.000046	1.46728	0.00012	1.88659	0.00015	0.01174	0.00005	0.0003	3.70E-07
91500	91500 - 16	0.282292	0.000032	1.46719	0.00014	1.88662	0.00014	0.00795	0.00004	0.0002	3.70E-07
91500	91500 - 17	0.282249	0.000035	1.4672	0.00013	1.88665	0.00016	0.00734	0.00003	0.0002	5.00E-07
91500	91500 - 18	0.282264	0.000028	1.46719	0.00011	1.88676	0.00014	0.00879	0.00003	0.0003	5.00E-07
GJ1	gj1 - 1	0.281982	0.000031	1.46722	0.00013	1.88658	0.00011	0.01001	0.00003	0.0003	4.80E-07
GJ1	gj1 - 2	0.281992	0.000034	1.46714	0.00012	1.88655	0.00014	0.01002	0.00004	0.0003	3.20E-07
GJ1	gj1 - 3	0.281982	0.000029	1.46721	0.00011	1.88679	0.00014	0.01006	0.00004	0.0003	3.40E-07
GJ1	gj1 - 4	0.281988	0.000032	1.4672	0.00013	1.88661	0.00011	0.00997	0.00004	0.0003	4.10E-07
GJ1	gj1 - 5	0.281984	0.000025	1.4672	0.00011	1.88668	0.00013	0.00992	0.00004	0.0003	3.60E-07
GJ1	gj1 - 7	0.281997	0.000034	1.46737	0.00013	1.88664	0.00012	0.01000	0.00005	0.0003	4.20E-07
GJ1	gj1 - 8	0.282003	0.000035	1.4672	0.00012	1.88672	0.00013	0.01001	0.00003	0.0003	3.50E-07
GJ1	gj1 - 10	0.281991	0.000032	1.46723	0.00013	1.88663	0.00011	0.00998	0.00004	0.0003	3.90E-07
GJ1	gj1 - 11	0.282024	0.000036	1.46727	0.00012	1.88671	0.00012	0.01007	0.00004	0.0003	3.90E-07
GJ1	gj1 - 12	0.282001	0.000034	1.46722	0.00013	1.88668	0.00012	0.01007	0.00004	0.0003	3.30E-07
GJ1	gj1 - 13	0.282004	0.00003	1.46716	0.00013	1.88662	0.00014	0.01001	0.00004	0.0003	4.30E-07
GJ1	gj1 - 14	0.281979	0.00003	1.46727	0.00011	1.88669	0.00013	0.01005	0.00004	0.0003	3.10E-07
GJ1	gj1 - 15	0.282007	0.00003	1.46718	0.00011	1.88674	0.00012	0.01001	0.00004	0.0003	3.10E-07
GJ1	gj1 - 16	0.281995	0.000031	1.46731	0.00014	1.88666	0.00011	0.00993	0.00004	0.0003	3.30E-07
GJ1	gj1 - 17	0.282023	0.00003	1.46724	0.00012	1.88671	0.00013	0.01003	0.00004	0.0003	4.10E-07

Table S4.6

Calculated major (wt.%) and trace (µg/g) element compositions of model melt. P = pressure, T = temperature

Sample	P (kbar)	T (°C)	H_2O	SiO_2	Al_2O_3	CaO	MgO	FeO	K_2O	Na_2O
17JK12	7	950	3.21	56.48	14.53	2.97	3.20	12.98	2.08	4.56
17JK12	14	950	5.62	61.39	17.03	2.58	0.91	3.66	2.76	6.05
17JK12	11.5	977.5	4.08	58.94	16.21	3.10	2.01	8.02	2.26	5.37
17JK12	20	950	7.18	63.21	17.43	2.06	0.22	0.85	2.43	6.63
17JK12	10	850	5.92	66.49	14.67	2.39	0.44	2.36	3.90	3.82
17JK12	21	875	9.28	63.20	16.38	2.02	0.05	0.21	4.87	4.00
17JK20	7	950	2.99	59.23	13.89	3.78	2.19	12.81	1.76	3.34
17JK20	14	950	4.78	65.74	15.37	2.70	0.60	3.20	2.59	5.03
17JK20	11.5	977.5	3.40	64.37	14.81	3.52	1.24	6.49	1.98	4.19
17JK20	20	950	6.62	65.32	16.34	2.07	0.18	0.94	2.63	5.91
17JK20	10	850	5.93	66.81	14.71	2.46	0.38	2.03	3.99	3.71
17JK20	21	875	9.32	63.29	15.99	1.99	0.05	0.28	5.82	3.25

Sample	Rb	Ba	Th	U	Nb	Ta	La	Ce	Sr	Nd
17JK12	14.66	75.67	74.87	104.2	29.67	31.21	39.51	34.07	8.72	25.31
17JK12	20.23	117.4	101.2	139.0	20.01	15.87	57.78	48.82	15.73	35.49
17JK12	15.88	91.87	80.93	111.7	32.85	34.34	45.84	39.65	12.28	29.95
17JK12	22.84	168.2	110.4	153.1	18.07	13.61	75.85	65.11	38.03	50.30
17JK12	29.15	108.8	142.2	201.1	43.41	42.11	55.69	42.57	9.24	25.64
17JK12	29.64	247.4	135.1	193.2	19.48	14.24	99.19	81.20	88.48	58.31
17JK20	15.13	65.64	74.08	104.2	28.06	33.51	44.41	43.14	9.25	43.54
17JK20	7.92	110.9	26.13	34.64	18.43	12.25	146.6	139.1	25.08	107.8
17JK20	5.72	78.96	19.25	25.91	44.34	44.89	108.4	107.8	17.65	92.30
17JK20	11.02	195.6	34.80	46.42	19.75	12.68	212.3	187.4	67.69	128.6
17JK20	12.43	110.3	39.15	53.39	65.09	62.09	157.4	135.6	15.99	85.87
17JK20	15.56	323.5	45.37	62.15	20.80	13.05	297.5	243.1	187.0	150.4

Sample	Zr	Sm	Eu	Gd	Dy	Er	Yb	Y	Lu
17JK12	25.93	18.98	12.91	15.80	14.55	15.00	16.38	13.17	17.06
17JK12	23.65	16.94	13.26	7.31	3.42	2.14	1.73	2.56	1.64
17JK12	23.74	18.03	13.54	9.79	5.30	3.53	2.92	4.07	2.79
17JK12	22.57	17.82	15.16	6.21	2.64	1.58	1.26	1.94	1.19
17JK12	31.02	15.45	11.31	9.75	6.25	4.64	4.07	5.02	3.95
17JK12	24.35	18.40	16.39	6.20	2.61	1.56	1.24	1.92	1.17
17JK20	28.30	40.83	14.45	37.24	33.80	31.85	30.95	51.62	30.34
17JK20	29.99	35.33	21.80	11.24	4.55	2.72	2.12	3.30	2.02
17JK20	29.51	40.60	22.69	14.83	6.31	3.84	3.01	4.61	2.87
17JK20	31.07	34.14	23.87	10.19	4.05	2.41	1.87	2.93	1.79
17JK20	38.36	35.81	20.40	14.12	6.37	3.97	3.15	4.70	3.03
17JK20	33.21	35.04	25.49	10.15	4.01	2.38	1.85	2.89	1.76

Table S4.7

Compiled geochronological data previously collected from granitoids in the Michipicoten Greenstone Belt (MGB) and the Wawa Gneiss Domain (WGD). Data references are available within the table, see references for details of age and error calculation.

Geochronological data compilation.

Reference	Sample Number	Sample description	Rock classification
Moser et al. 1996	A1	Lineated, biotite/amphibole-bearing tonalite orthogneiss	Tonalite
Turek et al 1984	670	Sample of massive biotite granite.	Granite
Kendrick et al [Chapter 4]	19JK45B	TTG	Tonalite-trondhjemite
Turek et al 1982	646	Black and white, medium-grained equigranular trondhjemite	Trondhjemite
Sullivan et al 1985	GoO240	Small, foliated, granodiorite and diorite synvolcanic pluton	Diorite, quartz diorite, granodiorite, tonalite
Turek et al 1996	69	Sample of foliated biotite tonalite.	Tonalite
Turek et al 1982	664	Coarse grained massive granodiorite	Granodiorite
Ciufo et al 2020	SH-3	tonalite-trondhjemite	Tonalite-trondhjemite
Turek et al 1996	101	Foliated biotite tonalite.	Tonalite
Turek et al 1984	672	Quartz diorite from a quartz diorite to trondhjemite body	Quartz diorite
Kamo, 2015	14LR-183	tonalite	Tonalite
Petrus, 2015	13LR-066A	tonalite	Tonalite
Kamo, 2014	13RL-207	weakly foliated biotite tonalte	Tonalite
Percival & Krogh, 1983	5 gneissic tonalite	Thinly layered hornblende-biotite tonalite orthogneiss	Tonalite
Kamo, 2016a	15LR-163A	tonalite	Tonalite
Turek et al 1984	674	Foliated trondhjemite from the southwestern granitic terrane.	Trondhjemite
Corfu & Sage, 1992	DSc	Clasts in Dore conglomerate	Tonalite-trondhjemite
Kendrick et al [Chapter 4]	19JK43	TTG	Tonalite-trondhjemite
Kendrick et al [Chapter 4]	18JK53	TTG	Tonalite-trondhjemite
Turek et al 1996	102	Sample of foliated biotite tonalite.	Tonalite
Kamo, 2015	14LR-111	granodiorite	Granodiorite
Turek et al 1992	755	Massive, equigranular granodiorite	Granodiorite

Table 4.7 (continued)

Reference	Sample Number	Sample description	Rock classification
Kendrick et al [Chapter 4]	18JK08	TTG	Tonalite-trondhjemite
Farey & Krogh, 1986	FE-9-76	Massive to weakly foliated, coarse grained quartz monzonite.	Quartz monzonite
Turek et al 1996	78	Sample of foliated biotite tonalite.	Tonalite
Davis, 2016	15BT-038A	granite	Granite
Percival & Krogh, 1983	6 granodiorite	gneissic foliated granodiorite	Granodiorite
Turek et al 1992	326/GoO231	Sample is granite, a minor phase of the syenite pluton.	Granite
Sutcliffe & Davis, 2019	18JW-534	granite	Granite
Moser et al. 1996	C6	Tonalite gneiss from a horizontal shear zone	Tonalite
Corfu & Sage, 1992	RPS-2-92	Sample is of a medium-grained biotite granodiorite.	Granodiorite
Corfu & Sage, 1992	C-91-1	Sample is of a medium- to coarse-grained biotite granodiorite.	Granodiorite
Smith et al 1987	#26	rapikivi granite	Granite
Turek et al 1996	1114	Sample of non-foliated, leucrocratic granodiorite.	Granodiorite
Turek et al 1996	113	granodiorite	Granodiorite
Kamo, 2014	13LR-224	granite, late stock, #2 P3787	Granite
Turek et al 1992	758	Massive, equigranular granodiorite	Granodiorite
Turek et al 1984	673	Sample of non-foliated quartz monzonite.	Quartz monzonite
Moser et al. 1996	C5	Biotite tonalite pegmatite, 5 cm wide steeply dipping leucosome	Tonalite
Turek et al 1996	123	Sample of porphyritic quartz monzonite.	Quartz monzonite
Moser et al. 1996	B3	One 2 m-thick sill of lineated tonalite gneiss	Tonalite
Moser et al. 1996	A2	Massive, coarse-grained biotite-tonalite veins and veinlets.	Tonalite

Table 4.7 (continued)

Reference	Domain	Age (Ma)	Plus	Minus	Age notes	Latitude	Longitude
Moser et al. 1996	WGD	2925	35	35	Upper intercept	47.8601	-83.9099
Turek et al 1984	MGB/WGD	2889	2	2	Upper intercept	48.0767	-84.5835
Kendrick et al [Chapter 4]	MGB/WGD	2884.8	2	2	207/206 weighted mean age		
Turek et al 1982	MGB/WGD	2747	6	6	Upper intercept	48.0717	-84.5485
Sullivan et al 1985	MGB	2745	3	3	Upper intercept	47.9222	-84.7249
Turek et al 1996	MGB/WGD	2741	21	21	upper intercept	48.3750	-83.8546
Turek et al 1982	MGB	2737	6	6	Upper intercept	47.9222	-84.7249
Ciufo et al 2020	MGB	2724.1	4.3	4.3	207/206 weighted mean age		
Turek et al 1996	MGB/WGD	2723	13	13	Upper intercept	48.1623	-84.0666
Turek et al 1984	MGB	2722	11	8	Upper intercept	48.2206	-84.6213
Kamo, 2015	MGB/WGD	2720.8	1.4	1.4	mean 207Pb/206Pb	48.3760	-83.8670
Petrus, 2015	MGB/WGD	2716	2	2	concordia age	48.1972	-83.9599
Kamo, 2014	MGB/WGD	2713.6	1.1	1.1	mean 207Pb/206Pb	48.2457	-83.7720
Percival & Krogh, 1983	WGD	2707	1	1	Upper intercept	47.8254	-83.3489
Kamo, 2016a	MGB/WGD	2699.7	1.4	1.4	mean 207Pb/206Pb	48.4452	-83.9769
Turek et al 1984	MGB/WGD	2699	1	1	Upper intercept	48.0762	-84.9308
Corfu & Sage, 1992	MGB	2698	2	2	Upper intercept		
Kendrick et al [Chapter 4]	WGD	2696.1	3.1	3.1	207/206 weighted mean age		
Kendrick et al [Chapter 4]	WGD	2695.7	2.8	2.8	207/206 weighted mean age		
Turek et al 1996	MGB/WGD	2688	14	14	Upper intercept	48.4278	-83.9257
Kamo, 2015	MGB/WGD	2688	2	2	Youngest concordant zircon	48.3619	-83.7975
Turek et al 1992	MGB/WGD	2686	9	9	Upper intercept	48.3620	-84.5202
Kendrick et al [Chapter 4]	WGD	2684.8	3.3	3.3	207/206 weighted mean age		
Farey & Krogh, 1986	MGB	2684.5	2.7	2.6	None	48.2834	-84.2832
Turek et al 1996	MGB	2678.5	4.6	4.6	Upper intercept	48.3161	-84.0599
Davis, 2016	MGB	2678	4	4	mean 207Pb/206Pb	48.3734	-83.9797
Percival & Krogh, 1983	WGD	2677	4.5	2.8	Upper intercept	47.8056	-83.3499
Turek et al 1992	MGB	2677	9	9	Upper intercept	48.2450	-84.9119
Sutcliffe & Davis, 2019	MGB	2676	1	1	Estimate of emplacement	48.3642	-84.0714
Moser et al. 1996	WGD	2674	1	1	207Pb/206Pb age	47.7501	-83.3199
Corfu & Sage, 1992	MGB	2671	2	2	Upper intercept	48.3197	-84.4107
Corfu & Sage, 1992	MGB	2671	2	2	Upper intercept	48.2832	-84.5521

Table 4.7 (continued)

Reference	Domain	Age (Ma)	Plus	Minus	Age notes	Latitude	Longitude
Smith et al 1987	MGB	2670	10	10	Upper intercept?		
Turek et al 1996	MGB	2669.8	7.7	7.7	Upper intercept	48.3495	-84.2243
Turek et al 1996	MGB	2668	1	1		48.3803	-83.9561
Kamo, 2014	MGB/WGD	2666	2	2	Youngest concordant grain	48.2099	-83.8224
Turek et al 1992	MGB	2662.4	6.1	6.1	Upper intercept	48.2525	-84.7735
Turek et al 1984	MGB	2662	1	1	Upper intercept	48.2914	-84.5505
Moser et al. 1996	WGD	2661	1	1	Upper intercept	47.7501	-83.3199
Turek et al 1996	MGB	2661	11	11	Upper intercept	48.3070	-83.8977
Moser et al. 1996	WGD	2660	2	2	Upper intercept	47.7801	-83.5499
Moser et al. 1996	WGD	2645	2	2	Upper intercept	47.8601	-83.9099

Table S4.7.1

References

Ciufo, T. J., Jellicoe, K., Yakymchuk, C., Lin, S., Mercier-Langevin, P., Wodicka, N. 2020. Geology, structural evolution, and hydrothermal alteration of the Island gold deposit, Michipicoten greenstone belt, Ontario. In: Mercier-Langevin, P., Lawley, C. J. M. & Castonguay, S. (eds) Targeted Geoscience Initiative 5: Contributions to the Understanding of Canadian Gold Systems. Geological Survey of Canada, Open File 8712, 143–156.

Corfu, F., Sage, R.P., 1992. U–Pb age constraints for deposition of clastic metasedimentary rocks and late-tectonic plutonism, Michipicoten Belt, Superior Province. Can. J. Earth Sci. 29, 1640–1651.

Davis, D.W., 2016. Geochronology of rocks from northwest Ontario 2015–2016. Part 2: LA-ICP-MS geochronology. Internal report, Jack Satterly Geochronology Laboratory and Ontario Geological Survey (unpublished).

Frarey, M.J., Krogh, T.E., 1986. U–Pb zircon ages of late internal plutons of the Abitibi and eastern Wawa subprovinces, Ontario and Quebec, in: Current Research, Part A. Geological Survey of Canada, Paper 86-1A, pp. 43–48.

Kamo, S.L., 2014. Report on U-Pb CA-ID-TIMS geochronology on volcanic and plutonic rocks, Superior and Grenville provinces, Ontario. Internal report, Jack Satterly Geochronology Laboratory and Ontario Geological Survey (unpublished).

Kamo, S.L., 2015. Report on the U-Pb ID-TIMS geochronology on volcanic and plutonic rocks, Superior and Grenville Provinces, Ontario. Internal report, Jack Satterly Geochronology Laboratory and Ontario Geological Survey (unpublished).

Kamo, S.L., 2016. Report on U-Pb ID-TIMS geochronology for the Ontario Geological Survey: Bedrock mapping projects, Ontario. Internal report, Jack Satterly Geochronology Laboratory and Ontario Geological Survey (unpublished).

Kendrick, J., Duguet, M., Kirkland, C.L., Liebmann, J., Lin, S., Moser, D.E., Yakymchuk, C., (submitted). Anatomy of a craton: isotopic heterogeneity across an Archean crustal cross-section.

Moser, D.E., Heaman, L.M., Krogh, T.E., Hanes, J.A., 1996. Intracrustal extension of an Archean orogen revealed using single-grain U-Pb zircon geochronology. Tectonics 15, 1093–1109. https://doi.org/10.1029/96TC00130

Percival, J.A., Krogh, T.E., 1983. U–Pb zircon geochronology of the Kapuskasing structural zone and vicinity in the Chapleau–Foleyet area, Ontario. Can. J. Earth Sci. 20, 830–843. https://doi.org/10.1139/e83-073

Petrus, J. 2015. Report on U-Pb geochronology. Internal report for Precambrian Geoscience Section, Ontario Geological Survey, by the Mineral Exploration Research Centre, Department of Earth Sciences, Laurentian University (unpublished).

Table S4.7.1 (continued)

Smith, P.E., Tatsumoto, M., Farquhar, R.M., 1987. Zircon Lu-Hf systematics and the evolution of the Archean crust in the southern Superior Province, Canada. Contrib. to Mineral. Petrol. 97, 93–104. https://doi.org/10.1007/BF00375217

Sullivan, R.W., Sage, R.P., Card, K.D., 1985. U-Pb zircon age of the Jubilee Stock in the Michipicoten Greenstone Belt near Wawa, Ontario, in: Current Research, Part B. Geological Survey of Canada, Paper 85-1B, pp. 361–365.

Sutcliffe, C.N., Davis, D.W., 2019. U-Pb geochronology by LA-ICP-MS in samples from northern Ontario. Internal report, Jack Satterly Geochronology Laboratory and Ontario Geological Survey (unpublished).

Turek, A., Smith, P.E., Van Schmus, W.R., 1982. Rb–Sr and U–Pb ages of volcanism and granite emplacement in the Michipicoten belt—Wawa, Ontario. Can. J. Earth Sci. 19, 1608–1626.

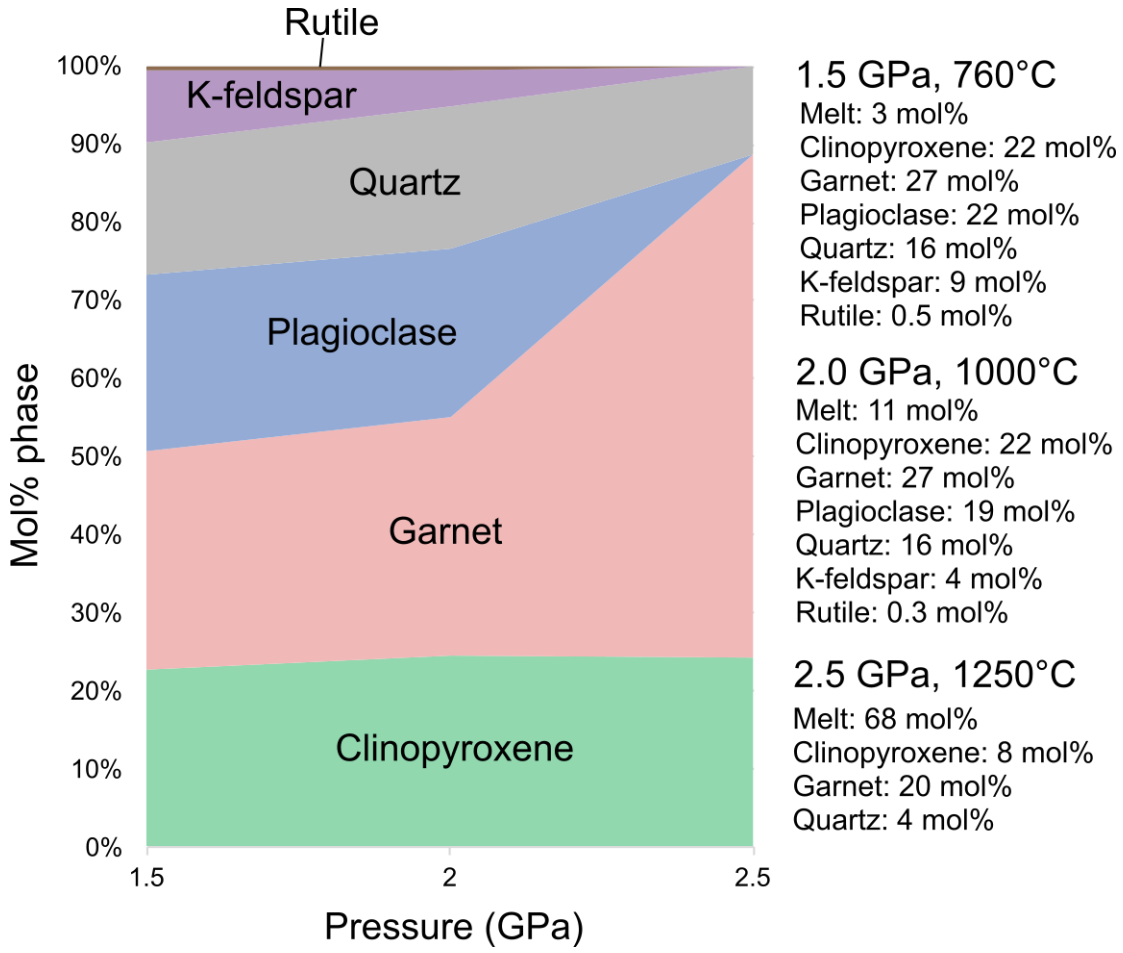
Turek, A., Smith, P.E., Van Schmus, W.R., 1984. U-Pb zircon ages and the evolution of the Michipicoten plutonic-volcanic terrane of the Superior Province, Ontario. Can. J. Earth Sci. 21, 457–464.

Turek, A., Sage, R.P., Van Schmus, W.R., 1992. Advances in the U-Pb zircon geochronology of the Michipicoten greenstone belt, Superior Province, Ontario. Can. J. Earth Sci. 29, 1154–1165. https://doi.org/10.1139/e92-093

Turek, A., Heather, K.B., Sage, R.P., Van Schmus, W.R., 1996. U-Pb zircon ages for the Missanabie-Renabie area and their relation to the rest of the Michipicoten greenstone belt, Superior Province, Ontario, Canada. Precambrian Res. 76, 191–211. https://doi.org/10.1016/0301-9268(95)00063-1

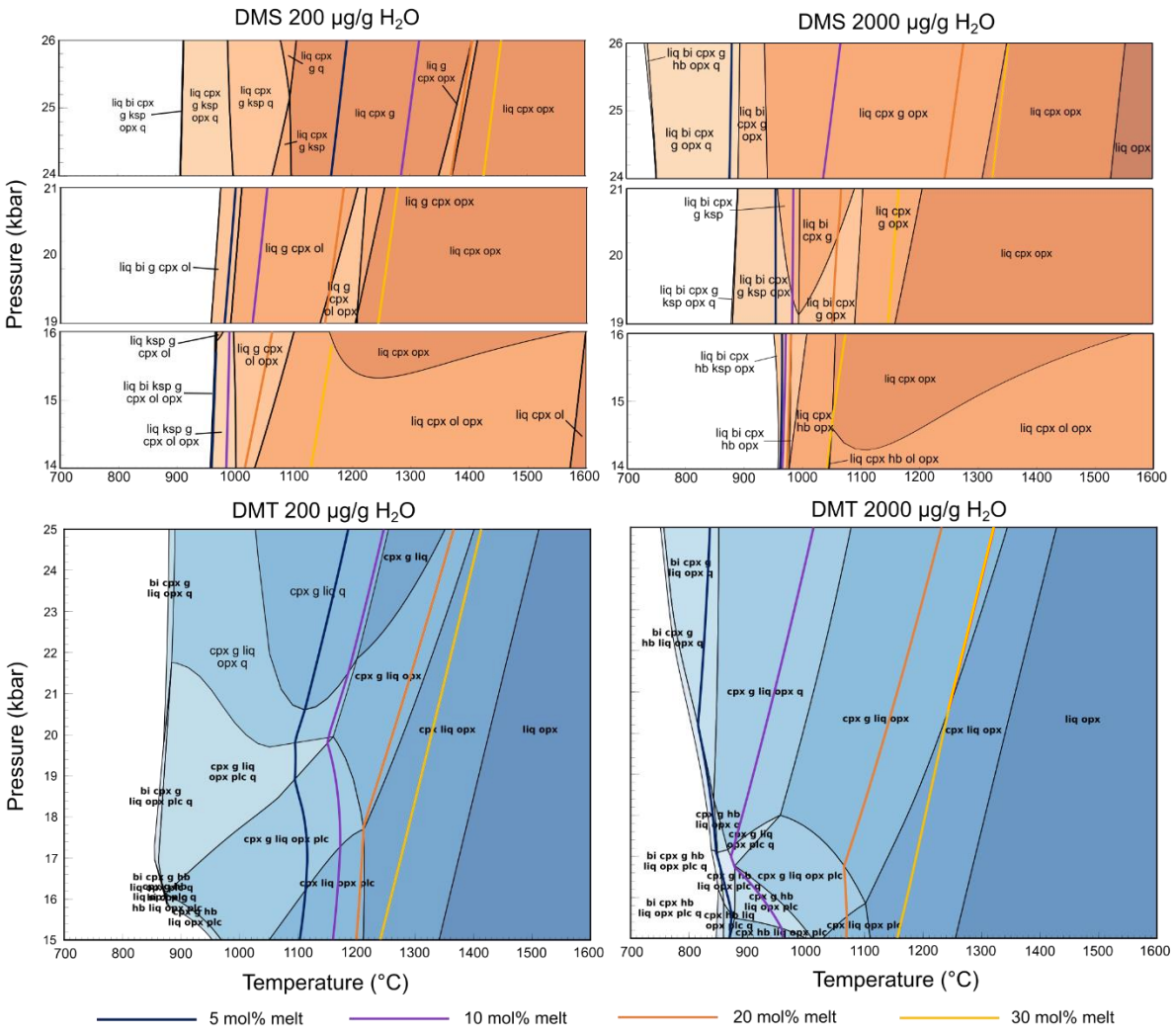
Appendix S5

Figure S5.1



Results of phase equilibrium modelling of Archean upper crust composition (AUC1.5, AUC2.0, AUC2.5, see Table 6.1)

Figure S5.2



Phase diagrams for DMT (TTG-metasomatized depleted mantle) and DMS (metasediment-melt-metasomatized depleted mantle) calculated using 200 µg/g H_2O and 2000 µg/g H_2O.

Table S5.1

Compilation of major (wt.%) and trace (µg/g) element data of sanukitoid samples from literature sources.

Reference	sample no.	craton	SiO_2	Al_2O_3	FeOt	MgO	CaO	Na_2O	K_2O	TiO_2
De Oliveira et al 2010	MD-02B	Amazonia	56.86	13.42	8.25	6.78	6.40	2.66	5.08	0.56
De Oliveira et al 2010	MD-02A	Amazonia	55.03	12.69	9.48	7.67	7.66	2.39	4.37	0.71
De Oliveira et al 2010	Cr-71	Amazonia	53.01	13.31	10.78	9.24	8.62	2.38	1.96	0.71
De Oliveira et al 2010	MFR-07B	Amazonia	52.96	12.60	10.09	10.34	8.54	2.59	2.12	0.76
De Oliveira et al 2010	299	Amazonia	54.05	13.82	9.62	8.55	7.94	2.93	2.36	0.73
De Oliveira et al 2010	ADR-2	Amazonia	56.81	14.82	7.62	6.01	6.95	3.99	3.17	0.63
De Oliveira et al 2010	MFR-12A	Amazonia	55.47	15.33	8.82	6.21	8.18	3.11	2.08	0.81
De Oliveira et al 2010	MFR-07D	Amazonia	52.15	13.60	10.76	8.82	9.16	2.70	1.79	1.01
De Oliveira et al 2010	ADR-1	Amazonia	57.31	13.81	6.87	7.82	8.64	3.03	1.85	0.67
De Oliveira et al 2010	ADR-4A	Amazonia	60.41	14.49	6.36	6.00	6.08	3.90	2.28	0.49
De Oliveira et al 2010	MFR-27C	Amazonia	52.48	16.82	9.37	5.87	7.91	4.22	2.42	0.91
De Oliveira et al 2010	MD-02C	Amazonia	52.91	14.18	10.33	7.60	8.61	3.63	2.00	0.74
De Oliveira et al 2010	MFR-12B	Amazonia	54.86	11.38	9.29	10.96	9.70	2.15	1.07	0.58
De Oliveira et al 2010	MD-03B	Amazonia	58.01	13.60	8.34	6.77	6.68	3.92	1.80	0.87
De Oliveira et al 2010	MD-03A	Amazonia	54.20	16.02	8.83	6.44	7.85	4.84	1.13	0.71
Egorova, 2014	351/1	Baltic shield	51.18	11.71	10.07	16.14	7.21	0.63	2.49	0.57
Egorova, 2014	212	Baltic shield	53.00	6.23	8.34	12.25	16.47	0.86	2.03	0.83
Egorova, 2014	K-17-2	Baltic shield	54.27	15.92	9.39	6.41	5.86	2.79	4.40	0.97
Egorova, 2014	118	Baltic shield	55.43	15.70	6.55	7.32	5.80	3.50	4.83	0.87
Egorova, 2014	53	Baltic shield	53.45	15.16	9.51	8.10	5.79	3.16	3.87	0.96
Egorova, 2014	124	Baltic shield	55.87	13.48	7.60	9.09	6.85	3.15	3.16	0.80
Egorova, 2014	36/3	Baltic shield	60.64	16.29	6.51	3.99	5.55	3.74	2.76	0.52
Egorova, 2014	K-10-2	Baltic shield	51.81	17.49	10.22	5.50	6.36	4.32	2.99	1.32
Egorova, 2014	36/2	Baltic shield	57.29	17.01	7.37	4.18	5.65	4.88	2.89	0.73
Egorova, 2014	37	Baltic shield	60.42	16.47	6.70	3.53	5.23	4.50	2.53	0.62
Egorova, 2014	351	Baltic shield	59.74	14.80	5.47	5.10	7.28	4.71	2.24	0.65
Lobach-Zhuchenko et al., 2005	124	Baltic shield	55.87	13.48	7.60	9.09	6.85	3.15	3.16	0.80
Lobach-Zhuchenko et al., 2005	134a	Baltic shield	56.82	7.45	11.53	8.37	11.11	1.98	1.60	1.14
Lobach-Zhuchenko et al., 2005	1113	Baltic shield	61.21	17.28	5.93	3.21	4.75	4.29	2.78	0.54

Table S5.1 (continued)

Reference	sample no.	craton	SiO_2	Al_2O_3	FeOt	MgO	CaO	Na_2O	K_2O	TiO_2
Lobach-Zhuchenko et al., 2005	100-12	Baltic shield	61.05	15.29	5.92	2.45	4.17	6.62	3.50	0.99
Lobach-Zhuchenko et al., 2005	a29	Baltic shield	55.85	17.09	8.69	6.29	5.67	4.23	1.48	0.71
Lobach-Zhuchenko et al., 2008	238/11-03	Baltic shield	54.78	15.32	7.71	6.25	6.59	4.24	4.27	0.83
Lobach-Zhuchenko et al., 2008	561	Baltic shield	53.80	16.35	9.94	5.33	5.98	3.86	3.83	0.90
Lobach-Zhuchenko et al., 2008	204-04	Baltic shield	55.40	16.66	6.95	5.10	5.91	4.74	4.53	0.72
Lobach-Zhuchenko et al., 2008	201a	Baltic shield	53.35	13.08	10.82	6.66	8.21	3.43	3.23	1.22
Lobach-Zhuchenko et al., 2008	236/3	Baltic shield	58.48	16.84	5.85	4.11	4.73	5.12	4.23	0.63
Lobach-Zhuchenko et al., 2008	42948	Baltic shield	57.52	16.71	6.35	4.47	5.54	4.81	3.92	0.68
Lobach-Zhuchenko et al., 2008	551	Baltic shield	58.99	16.38	5.81	4.60	4.79	5.22	3.64	0.57
Lobach-Zhuchenko et al., 2008	42894	Baltic shield	50.31	13.58	11.61	8.12	8.62	3.85	2.68	1.23
Lobach-Zhuchenko et al., 2008	42769	Baltic shield	54.82	16.42	8.59	5.07	6.55	5.61	2.24	0.70
Heilimo et al 2010	223-AML-87	Karelian Province	56.41	17.10	6.24	5.41	7.27	5.10	1.77	0.70
Heilimo et al 2010	225-TMB-87	Karelian Province	58.21	16.59	6.66	4.65	7.40	4.49	1.36	0.64
Heilimo et al 2010	26-AML-87	Karelian Province	61.47	16.03	5.42	4.19	5.60	4.80	1.91	0.59
Heilimo et al 2010	299-TMB-87	Karelian Province	60.86	16.03	5.25	4.68	5.49	4.51	2.59	0.60
Heilimo et al 2010	397-ATK-83	Karelian Province	54.69	18.43	6.91	5.28	7.22	5.02	1.77	0.68
Heilimo et al 2010	61-1-ATK-86	Karelian Province	56.02	16.45	6.83	6.29	6.80	4.69	2.12	0.79
Heilimo et al 2010	72-AML-87	Karelian Province	59.08	16.68	5.25	4.35	6.08	4.93	3.02	0.60
Heilimo et al 2010	AAK-02-177B	Karelian Province	58.39	14.68	8.61	5.82	4.72	3.39	3.76	0.64
Heilimo et al 2010	AAK-02-57B	Karelian Province	61.31	14.24	7.21	5.55	3.78	2.71	4.67	0.53
Heilimo et al 2010	EPHE-2004-320.1	Karelian Province	60.44	16.76	5.98	4.04	5.41	4.76	1.82	0.78
Heilimo et al 2010	EPHE-2004-334.1	Karelian Province	59.63	13.48	7.52	7.40	5.78	2.70	2.70	0.79
Heilimo et al 2010	EPHE-2004-336.2	Karelian Province	61.14	15.82	5.85	4.20	6.02	4.54	1.70	0.73
Heilimo et al 2010	EPHE-2004-336.3	Karelian Province	57.72	11.77	7.96	9.29	7.83	2.64	1.91	0.86
Heilimo et al 2010	EPHE-2004-345.1	Karelian Province	60.90	15.71	5.77	4.80	5.95	4.22	1.96	0.70
Heilimo et al 2010	EPHE-2004-346.1	Karelian Province	61.51	15.61	5.63	4.87	5.66	4.63	1.41	0.69
Heilimo et al 2010	EPHE-2004-347.1	Karelian Province	60.63	16.63	5.36	4.51	5.77	4.18	2.17	0.74
Heilimo et al 2010	EPHE-2004-347.2	Karelian Province	58.19	12.23	8.52	8.50	7.38	2.78	1.79	0.61
Heilimo et al 2010	EPHE-2004-353.2	Karelian Province	57.14	14.39	7.49	7.54	8.27	3.63	0.78	0.75
Heilimo et al 2010	EPHE-2005-13.2	Karelian Province	60.22	14.24	6.94	5.34	6.68	3.88	2.12	0.57
Heilimo et al 2010	HJO-87-138	Karelian Province	60.98	19.21	5.02	2.75	2.01	5.80	3.64	0.58
Heilimo et al 2010	TTU$-2004-143	Karelian Province	58.43	18.60	6.35	3.37	6.10	4.77	1.66	0.71
Heilimo et al 2010	TTU$-2004-148	Karelian Province	61.34	18.98	4.60	3.23	3.74	4.60	3.04	0.47

Table S5.1 (continued)

Reference	sample no.	craton	SiO_2	Al_2O_3	FeOt	MgO	CaO	Na_2O	K_2O	TiO_2
Heilimo et al 2010	TTU$-2004-162	Karelian Province	57.99	18.79	6.14	3.20	6.15	5.17	1.80	0.76
Heilimo et al 2010	TTU$-2004-193	Karelian Province	60.40	17.86	5.37	2.96	5.32	5.39	2.01	0.69
Heilimo et al 2010	TTU$-2004-202	Karelian Province	61.81	17.18	5.41	2.35	4.95	4.71	2.82	0.77
Heilimo et al 2010	TTU$-2004-263	Karelian Province	57.54	17.92	6.59	3.85	6.58	5.35	1.30	0.87
Laurent et al 2014	BUL-01A	Kaapvaal	48.21	16.98	12.89	3.92	8.47	3.68	2.82	3.02
Laurent et al 2014	BUL-02	Kaapvaal	50.18	18.03	10.68	3.73	8.33	4.03	2.58	2.43
Laurent et al 2014	BUL-11	Kaapvaal	54.50	19.11	7.22	2.66	6.10	3.73	4.80	1.88
Laurent et al 2014	BUL-14	Kaapvaal	60.13	17.24	6.21	2.00	4.53	3.41	5.02	1.46
Laurent et al 2014	BUL-34	Kaapvaal	55.63	17.34	7.71	4.05	7.66	3.60	2.23	1.79
Laurent et al 2014	BUL-35	Kaapvaal	57.06	17.37	7.16	3.56	6.91	3.63	2.57	1.73
Laurent et al 2014	BUL-36	Kaapvaal	54.84	17.60	7.93	4.16	8.01	3.45	2.12	1.91
Laurent et al 2014	BUL-48	Kaapvaal	52.27	18.68	8.72	4.09	7.23	3.89	2.92	2.20
Laurent et al 2014	BUL-49	Kaapvaal	56.68	17.74	6.71	3.49	6.80	3.88	3.12	1.59
Jiang et al 2016	JN1313	North China	61.24	16.17	5.10	3.88	5.74	4.06	3.17	0.65
Jiang et al 2016	JN1312	North China	59.81	16.38	5.59	4.57	5.92	4.38	2.65	0.69
Jiang et al 2016	JN1317	North China	53.57	16.83	7.55	6.71	8.49	4.42	1.56	0.87
Wang et al 2009	05SD-87	North China	59.96	13.86	7.38	5.57	6.92	3.50	2.17	0.64
Wang et al 2009	05SD-88	North China	59.82	13.78	7.43	5.66	7.01	3.54	2.14	0.62
Wang et al 2009	05SD-89	North China	60.12	13.79	7.35	5.55	6.90	3.45	2.21	0.63
Wang et al 2009	05SD-90	North China	60.32	13.64	7.35	5.55	6.94	3.43	2.13	0.63
Wang et al 2009	05SD-91	North China	60.05	13.87	7.40	5.58	6.81	3.49	2.17	0.63
Wang et al 2009	05SD-92	North China	59.70	13.75	7.58	5.70	6.97	3.51	2.16	0.64
Wang et al 2009	05SD-93	North China	59.71	13.69	7.52	5.79	7.04	3.50	2.13	0.62
Wang et al 2009	05SD-94	North China	59.74	13.85	7.54	5.68	6.98	3.45	2.13	0.63
Wang et al 2009	05SD-97	North China	58.61	14.08	7.55	6.51	6.94	3.72	2.01	0.57
Wang et al 2009	06TK-1	North China	56.65	14.40	7.90	7.71	7.32	3.63	1.84	0.55
Wang et al 2009	06TK-2	North China	56.12	14.58	8.20	7.97	7.66	3.39	1.62	0.46
Wang et al 2009	06TK-3	North China	56.60	14.60	8.00	7.73	7.30	3.73	1.51	0.53
Wang et al 2009	06TK-4	North China	57.06	14.36	7.71	7.61	6.93	3.46	2.35	0.52
Wang et al 2009	06TK-5	North China	56.95	14.57	7.78	7.57	7.17	3.57	1.89	0.50
Wang et al 2009	06TK-6	North China	56.87	14.21	7.86	7.78	7.22	3.38	2.18	0.51

Table S5.1 (continued)

Reference	sample no.	craton	SiO_2	Al_2O_3	FeOt	MgO	CaO	Na_2O	K_2O	TiO_2
Wang et al 2009	06TK-7	North China	57.83	14.33	7.70	6.88	7.00	3.85	1.84	0.56
Stern and Hanson, 1991	06	Superior Province	59.51	16.60	5.00	3.68	5.31	4.94	4.32	0.63
Stern and Hanson, 1991	13	Superior Province	61.59	15.90	4.09	3.33	5.31	4.91	4.28	0.60
Stern and Hanson, 1991	114	Superior Province	60.90	16.89	4.15	3.17	5.05	5.57	3.61	0.66
Stern and Hanson, 1991	58	Superior Province	58.89	16.92	4.81	3.95	6.38	5.26	3.31	0.48
Stern and Hanson, 1991	92a	Superior Province	58.10	16.88	5.24	4.26	6.30	5.25	3.27	0.69
Stern and Hanson, 1991	12	Superior Province	60.96	16.35	4.60	3.40	5.37	5.49	3.22	0.62
Stern and Hanson, 1991	07	Superior Province	59.54	16.35	4.82	4.35	6.39	5.29	2.77	0.49
Stern and Hanson, 1991	115	Superior Province	58.95	16.82	5.10	3.92	6.77	5.35	2.38	0.70
Stern and Hanson, 1991	57	Superior Province	57.89	16.58	5.22	4.84	7.68	5.72	1.67	0.39
Stevenson et al, 1999	WS-1A	Superior Province	52.16	14.95	11.12	6.83	7.27	3.27	3.06	1.34
Stevenson et al, 1999	NwL226	Superior Province	55.70	16.54	7.35	5.43	6.77	4.22	3.15	0.85
Stevenson et al, 1999	NwL229	Superior Province	58.08	16.28	5.65	3.02	7.90	4.90	3.24	0.92
Stevenson et al, 1999	NwL227	Superior Province	53.20	18.53	8.52	4.15	7.71	4.23	2.76	0.89
Stevenson et al, 1999	WS-1C	Superior Province	53.05	16.69	9.88	5.56	7.39	4.03	2.30	1.10

Reference	sample no.	Sr	Ba	Cr	Zr	La	Ce	Nd	Sm	Eu	Gd	Dy	Er	Yb	Lu
De Oliveira et al 2010	MD-02B	338	1382	465	103	18.4	50.2	32.8	6.62	1.27	5.4	3.83	1.88	1.69	0.26
De Oliveira et al 2010	MD-02A	357.7	1088	506	118	22.4	64.8	43	8.61	1.75	6.92	4.66	2.33	2.3	0.34
De Oliveira et al 2010	Cr-71	422	n.d.	n.d.	116	n.d.	n.d.	n.d.	n.d.	n.d.	n.d.	n.d.	n.d.	n.d.	n.d.
De Oliveira et al 2010	MFR-07B	477	511	253	97	33	62.8	25.1	4.8	1.29	4.04	2.82	1.51	1.55	0.22
De Oliveira et al 2010	299	445	1145	n.d.	129	n.d.	n.d.	n.d.	n.d.	n.d.	n.d.	n.d.	n.d.	n.d.	n.d.
De Oliveira et al 2010	ADR-2	463	876	281	105	29	72.1	40.4	7.5	1.52	5.8	4	2.04	1.73	0.29
De Oliveira et al 2010	MFR-12A	604	711	171	99	27.6	53.9	27.1	5.3	1.59	4.74	3.37	1.82	1.48	0.25
De Oliveira et al 2010	MFR-07D	494	608	212	87	31.8	67.2	28.9	6.1	1.69	5.06	3.9	2.14	1.8	0.3
De Oliveira et al 2010	ADR-1	507	527	239	92	25.4	55.2	24.5	4.5	1.33	3.64	2.89	1.68	1.41	0.23
De Oliveira et al 2010	ADR-4A	745	812	308	94	23.7	51.1	21.4	3.6	1.02	2.78	2.25	1.03	0.93	0.15
De Oliveira et al 2010	MFR-27C	800	344	103	165	28.5	77.1	44	8.6	1.73	5.71	4.35	2.05	1.7	0.25
De Oliveira et al 2010	MD-02C	508	468	397	140	25	67.2	41.6	8.4	1.58	6.65	4.94	2.41	2.24	0.32
De Oliveira et al 2010	MFR-12B	335	442	417	81	24.3	43.7	20.9	4.1	1.14	3.59	2.79	1.52	1.36	0.2
De Oliveira et al 2010	MD-03B	436	417	335	153	30.8	71	41.8	7.91	1.59	6.7	4.5	2.16	1.88	0.28
De Oliveira et al 2010	MD-03A	544.8	199	226	151	25.4	60.4	43.5	8.35	1.62	6.64	4.36	2.14	1.85	0.28

Table S5.1 (continued)

Reference	sample no.	Sr	Ba	Cr	Zr	La	Ce	Nd	Sm	Eu	Gd	Dy	Er	Yb	Lu
Egorova, 2014	351/1														
Egorova, 2014	212		1120	338		259	596	294	45.3	7.83	38.8	11.5	3.67	2.95	0.38
Egorova, 2014	K-17-2	929	1113	120	249	76	172.3	78.93	13.48	3.13	8.84	5.32	2.56	2.28	0.33
Egorova, 2014	118	711	1676	164	162										
Egorova, 2014	53	1060	824	147	213	89.4	174	99	15.2	3.62				2.34	0.32
Egorova, 2014	124	1089	2542	202	99	50.3	107.4	61.2	10.9	3.2	9	4.9	2.2	1.8	0.2
Egorova, 2014	36/3	659	1202	74	120	36.3	73.7	35.64	6.03	1.49	4.08	2.3	1.13	0.99	0.14
Egorova, 2014	K-10-2	912	995	21	184	58	139.5	69.83	12.61	2.97	8.26	4.95	2.1	1.64	0.23
Egorova, 2014	36/2	744	1149	45	113	36.2	72.1	40	6.53	1.28	3.6	1.99	1.15	0.92	0.13
Egorova, 2014	37	649	961	39	138										
Egorova, 2014	351														
Lobach-Zhuchenko et al., 2005	124	1089	2542	202	99	50.3	107.4	61.2	10.9	3.2	5.3	2.7	1	1.77	0.1
Lobach-Zhuchenko et al., 2005	134a	1279	734	36	47	49.9	251		17.4	3.8				2.3	
Lobach-Zhuchenko et al., 2005	1113	852	1307	140	33	19	43	21	4.6	1.4	20.3	8.9	3.1	0.8	0.1
Lobach-Zhuchenko et al., 2005	100-12	2383	2807	261	60	124.2	377.5		26.1	6.4				1.9	0.2
Lobach-Zhuchenko et al., 2005	a29	618	774	50	84	149.9	20	40.2	1.4	0.5				0.7	0.4
Lobach-Zhuchenko et al., 2008	238/11-03	1432	1740	275	233	83.6	180	87	15.7	3.91	11	6.09	2.27	2.07	0.32
Lobach-Zhuchenko et al., 2008	561	1334	1090	110	146	48	106	nd	8.7	2.65	nd	nd	nd	1.9	nd
Lobach-Zhuchenko et al., 2008	204-04	1554	1880	188	216	86.6	180	78.8	13.3	3.51	9.99	5.34	2.07	1.7	0.25
Lobach-Zhuchenko et al., 2008	201a	1371	2090	144	195	87.4	190	93.3	17.1	4.48	11.9	6.53	2.48	2.27	0.32
Lobach-Zhuchenko et al., 2008	236/3	1603	2080	138	207	64	118	53.5	8.97	2.51	5.88	3.4	1.4	1.18	0.12
Lobach-Zhuchenko et al., 2008	42948	2090	2820	168	238	63.8	123	55.5	9.4	2.64	6.1	3.55	1.58	1.2	0.3
Lobach-Zhuchenko et al., 2008	551	1885	1668	141	215	56.7	126	58	9.29	2.42	nd	nd	nd	1.42	0.18
Lobach-Zhuchenko et al., 2008	42894	1880	910	153	154	49.7	115.3	60.6	11.1	3.2	8.4	5.4	2.4	1.8	0.2
Lobach-Zhuchenko et al., 2008	42769	2321	1361	157	125	33.1	69.1	40.7	6.4	2.8	4.7	2.6	0.9	0.8	0.1
Heilimo et al 2010	223-AML-87	1160	960	200	230	n.a.	n.a.	n.a.	n.a.	n.a.	n.a.	n.a.	n.a.	n.a.	n.a.
Heilimo et al 2010	225-TMB-87	840	490	180	210	n.a.	n.a.	n.a.	n.a.	n.a.	n.a.	n.a.	n.a.	n.a.	n.a.
Heilimo et al 2010	26-AML-87	790	690	160	170	n.a.	n.a.	n.a.	n.a.	n.a.	n.a.	n.a.	n.a.	n.a.	n.a.
Heilimo et al 2010	299-TMB-87	760	1240	180	200	n.a.	n.a.	n.a.	n.a.	n.a.	n.a.	n.a.	n.a.	n.a.	n.a.
Heilimo et al 2010	397-ATK-83	730	570	150	180	n.a.	n.a.	n.a.	n.a.	n.a.	n.a.	n.a.	n.a.	n.a.	n.a.
Heilimo et al 2010	61-1-ATK-86	989	999	208	147	58.3	134	73.3	12.1	3.05	9.67	4.34	1.88	1.56	0.22
Heilimo et al 2010	72-AML-87	1040	1770	150	200	65.2	140	72.7	11.6	2.9	8.49	3.66	1.42	1.35	0.17
Heilimo et al 2010	AAK-02-177B	679	855	183	179	53.3	99.7	42.6	6.55	1.55	5.34	2.31	0.91	0.86	0.14

Table S5.1 (continued)

Reference	sample no.	Sr	Ba	Cr	Zr	La	Ce	Nd	Sm	Eu	Gd	Dy	Er	Yb	Lu
Heilimo et al 2010	AAK-02-57B	634	750	338	110	36.8	58.8	23.7	3.7	0.78	2.87	1.62	0.68	0.67	<0.1
Heilimo et al 2010	EPHE-2004-320.1	633	875	81	125	25.7	53.4	26.4	4.83	1.2	4.1	2.48	1.16	0.9	0.14
Heilimo et al 2010	EPHE-2004-334.1	369	851	298	77.9	10.7	31.9	24.1	5.15	1.02	4.03	3.04	1.43	1.38	0.17
Heilimo et al 2010	EPHE-2004-336.2	491	352	129	149	30	70.2	40.7	7.1	1.2	6.45	4.11	2.04	1.71	0.28
Heilimo et al 2010	EPHE-2004-336.3	354	417	626	66.7	32.5	67.2	30.4	5.36	1.18	4.82	2.82	1.47	1.31	0.21
Heilimo et al 2010	EPHE-2004-345.1	549	788	167	56.4	27.1	58.1	25.5	4.48	0.9	3.2	2.56	1.21	1.35	0.18
Heilimo et al 2010	EPHE-2004-346.1	553	565	197	123	30.7	58.3	26.7	4.68	1.05	3.68	2.44	1.13	1.25	0.15
Heilimo et al 2010	EPHE-2004-347.1	643	778	169	78.4	25.4	46.1	19.2	3.2	0.79	2.35	1.41	0.68	0.68	0.1
Heilimo et al 2010	EPHE-2004-347.2	376	597	514	111	24.6	51.4	24.5	4.7	0.92	4.74	2.89	1.66	1.37	0.2
Heilimo et al 2010	EPHE-2004-353.2	500	407	407	37.3	22.2	54.2	29.4	5.33	1.24	4.67	3.18	2.01	1.42	0.2
Heilimo et al 2010	EPHE-2005-13.2	442	1403	275	83.8	22.6	56.3	31.7	5.92	1.23	5.57	3.5	1.96	1.63	0.24
Heilimo et al 2010	HJO-87-138	304	1200	122	126	b.d.l.	b.d.l.	b.d.l.	b.d.l.	b.d.l.	b.d.l.	b.d.l.	b.d.l.	b.d.l.	b.d.l.
Heilimo et al 2010	TTU$-2004-143	1266	769	<30	199	24.1	59.9	34.1	6.06	1.57	5.37	2.92	1.42	1.49	0.21
Heilimo et al 2010	TTU$-2004-148	883	1742	<30	73.2	21.7	45	23.2	3.67	0.88	2.87	1.53	0.76	0.74	<0.1
Heilimo et al 2010	TTU$-2004-162	1175	799	<30	69.2	24.1	56.2	34.1	5.95	1.3	4.97	2.73	1.35	1.3	0.17
Heilimo et al 2010	TTU$-2004-193	934	675	51	159	56	115	53.1	9.41	1.65	8.13	3.8	1.58	1.27	0.2
Heilimo et al 2010	TTU$-2004-202	1092	1311	<30	214	52.3	107	47.2	8.53	2.17	7.09	3.47	1.37	1.34	0.17
Heilimo et al 2010	TTU$-2004-263	1257	544	72	155	69.4	138	60.6	10.1	1.97	8.46	4.3	1.57	1.56	0.21
Laurent et al 2014	BUL-01A	691	1337	61.58	697.1	197	448.3	245.1	40.63	5.51	30.73	17.89	7.54	5.86	0.72
Laurent et al 2014	BUL-02	794.1	1340	41.06	939.1	202.7	435.8	216.2	35.75	5.43	25.88	15.08	6.26	4.77	0.63
Laurent et al 2014	BUL-11	1405	4407	20.53	660.5	171.2	286	150.7	23.16	5.42	16.09	8.14	3.12	2.71	0.35
Laurent et al 2014	BUL-14	987.3	2322	27.37	505.1	125.9	269.2	130.1	21.94	4.54	15.52	8.74	3.4	2.92	0.41
Laurent et al 2014	BUL-34	637.2	1304	102.6	554.2	127.4	280.3	140	23.49	4.05	17.36	11.15	4.38	3.24	0.43
Laurent et al 2014	BUL-35	597.1	1515	88.95	768.5	141.8	305	142.1	22.93	3.96	16.63	10.21	4.09	3.08	0.43
Laurent et al 2014	BUL-36	662.4	1209	109.5	608.4	127.5	278.1	128.5	20.01	3.74	14.62	8.63	3.43	2.78	0.38
Laurent et al 2014	BUL-48	510.1	949	109.5	767	152.3	329.3	147	22.79	3.43	15.8	9.69	3.72	2.74	0.4
Laurent et al 2014	BUL-49	536.7	1063	54.74	513.9	109.4	246.6	121.7	19.55	3.78	13.46	8.08	3.16	2.51	0.34
Jiang et al 2016	JN1313	1239	1325	136	177	70.46	154.96	69.79	11.19	2.88	6.85	3.31	1.14	1.02	0.14
Jiang et al 2016	JN1312	1381	1281	139	215	77.63	167.33	77.68	13.42	3.21	7.74	3.62	1.28	0.94	0.15
Jiang et al 2016	JN1317	1090	541	178	206	60.17	140.68	85.21	17.18	4.12	10.92	5.31	1.96	1.43	0.21
Wang et al 2009	05SD-87	609	633	223	113	27.55	62.89	34.62	6	1.56	4.81	2.64	1.24	1.13	0.18

Table S5.1 (continued)

Reference	sample no.	Sr	Ba	Cr	Zr	La	Ce	Nd	Sm	Eu	Gd	Dy	Er	Yb	Lu
Wang et al 2009	05SD-88	623	633	241	108	27.97	63.92	34.8	5.92	1.62	4.71	2.62	1.25	1.1	0.17
Wang et al 2009	05SD-89	609	635	228	110	27.62	63.36	34.04	5.94	1.52	4.58	2.62	1.18	1.09	0.17
Wang et al 2009	05SD-90	608	613	236	113	27.61	60.34	31.88	5.81	1.54	4.62	2.63	1.18	1.08	0.17
Wang et al 2009	05SD-91	609	623	230	110	27.79	63.2	33.71	5.77	1.55	4.6	2.49	1.21	1.08	0.17
Wang et al 2009	05SD-92	624	600	232	108	27.44	58.72	32.51	5.65	1.52	4.43	2.55	1.18	1.06	0.17
Wang et al 2009	05SD-93	615	618	244	105	27.07	61.99	33.83	6.01	1.53	4.73	2.71	1.24	1.08	0.16
Wang et al 2009	05SD-94	617	613	245	108	28.47	62.61	34.78	5.95	1.63	4.81	2.73	1.24	1.13	0.19
Wang et al 2009	05SD-97	689	618	299	104	32.75	73.55	39.34	6.84	1.83	5.05	2.74	1.21	1.06	0.17
Wang et al 2009	06TK-1	791	624	375	97	38.76	88.93	45.75	8.09	2.12	5.38	2.75	1.17	0.96	0.14
Wang et al 2009	06TK-2	966	576	385	71	38.4	90.23	47.55	8.22	2.13	5.54	2.88	1.16	0.97	0.14
Wang et al 2009	06TK-3														
Wang et al 2009	06TK-4	860	747	394	110	42.42	96.42	49.42	8.6	2.2	5.72	2.99	1.22	1.05	0.15
Wang et al 2009	06TK-5	822	724	387	96	37.66	84.71	45.08	8.07	2.34	5.56	2.74	1.15	0.96	0.14
Wang et al 2009	06TK-6	835	651	402	115	40.48	94.26	49.45	8.53	2.2	5.84	2.9	1.16	1.01	0.15
Wang et al 2009	06TK-7	763	696	334	108	36.3	82.69	43.2	7.56	1.93	5.32	2.88	1.22	1.06	0.16
Stern and Hanson, 1991	06	1472	2698	85	147		139.2	63.47	10.7	2.466	6.824	3.27	1.226	0.933	
Stern and Hanson, 1991	13	1407	1982	86	123		141.1	67.2	11.7	2.577	7.485	3.52	1.307	0.953	
Stern and Hanson, 1991	114	1782	2174	87	257										
Stern and Hanson, 1991	58	1879	2132	115	50		99.77	51.41	9.198	2.695	6.038	2.79	1.023	0.75	
Stern and Hanson, 1991	92a	1867	2575	137	209	62.01	135.9	67.41	11.5	2.988	7.325	3.42	1.265	0.934	
Stern and Hanson, 1991	12	1435	1669	100	172		131	56.32	9.14	2.217	5.67	2.65	0.999	0.756	
Stern and Hanson, 1991	07	1890	2153	143	79	57.9	122.2	57.81	9.7	2.709	6.106	2.79	1.027	0.751	
Stern and Hanson, 1991	115	1913	1302	107	248										
Stern and Hanson, 1991	57	2230	1146	150	66		101.0	52.08	9.109	2.603	5.928	2.78	1.026	0.753	
Stevenson et al, 1999	WS-1A	1096	3254		112	59.8	144	75.8	15.7	3.74	12.7	6.48	3.32	2.22	
Stevenson et al, 1999	NwL226	1070	1181		124	64.4	142.2	65.6	10.96	2.56	6.89	2.7	1.18	0.75	
Stevenson et al, 1999	NwL229	2466	1711		84	94.5	207	93.4	15.31	3.63	9.49	3.12	1.19	0.64	
Stevenson et al, 1999	NwL227	2239	1675		54	51.3	118.8	60.3	10.79	3.13	7.34	2.4	1.01	0.51	
Stevenson et al, 1999	WS-1C	1226	973		166	56.32	136	71.1	14.4	3.35	10.8	6.22	3.13	2.47	

Appendix S6

Table S6.1

Results of Re–Os geochronology of molybdenite collected in the Kapuskasing Uplift, conducted at University of Alberta. λ = ^{187}Re–^{187}Os decay constant.

Sample	Re (µg/g)	± 2σ	^{187}Re (µg/g)	± 2σ	^{187}Os (µg/g)	± 2σ	Model Age (Ma)	± 2σ (Ma)	± 2σ (Ma) with λ
19JK08	33.58	0.1	21.11	0.1	933	0.7	2596.5	8	11.5
19JK49	97.53	0.29	61.3	0.2	2737	5	2621.8	9.2	12.4

Table S6.2

Results of Sm–Nd analysis of metabasite sample 17JK09 from the Kapuskasing Structural Zone. Analysis of garnet separates and whole-rock fractions was done at Radiogenic Isotope and Geochronology Laboratory (RIGL) at Washington State University.

Sample	Sm (µg/g)	Nd (µg/g)	$^{147}Sm/^{144}Nd$	2s (abs)	$^{143}Nd/^{144}Nd$	2s (abs)
Garnet-1	4.217	5.584	0.45718	0.00229	0.517071	0.000026
Garnet-2	4.305	5.618	0.46388	0.00232	0.517184	0.000027
Garnet-3	4.328	5.716	0.45845	0.00229	0.517084	0.000026
Garnet-4	4.339	5.830	0.45065	0.00225	0.516958	0.000027
Whole rock - Bomb	3.541	10.665	0.20084	0.00100	0.512824	0.000026
Whole rock - Savillex	3.484	10.668	0.19753	0.00099	0.512789	0.000026